

**Article 1:**

*A derivative based method for cost optimal area allocation in heat exchanger networks*

**Walmsley, T.G.**, Walmsley, M.R.W., Morrison, A.S., Atkins, M.J., Neale, J.R., 2014.

Applied Thermal Engineering 70, 1084–1096.

DOI: 10.1016/j.applthermaleng.2014.03.044

Citations: 22

Elsevier



# A derivative based method for cost optimal area allocation in heat exchanger networks



Timothy G. Walmsley\*, Michael R.W. Walmsley, Andrew S. Morrison, Martin J. Atkins, James R. Neale

Energy Research Centre, School of Engineering, University of Waikato, Hamilton, New Zealand

## HIGHLIGHTS

- A novel cost derivative approach to allocating area in a HEN is developed.
- The new CDM method is applied to a distillation process and milk powder plant.
- Total cost savings of 5–7% are obtain compared to PDM solutions.

## ARTICLE INFO

### Article history:

Received 4 January 2014

Received in revised form

16 March 2014

Accepted 19 March 2014

Available online 5 April 2014

### Keywords:

Process integration

Heat recovery

Heat exchanger network

## ABSTRACT

This paper presents a novel Cost Derivative Method (CDM) for finding the optimal area allocation for a defined Heat Exchanger Network (HEN) structure and stream data to achieve minimum total cost. Using the Pinch Design Method (PDM) to determine the HEN structure, the approach attempts to add, remove and shift area to exchangers where economic benefits are returned. From the derivation of the method, it is found that the slope of the  $\epsilon$ -NTU relationship for the specific heat exchanger type, in combination with the difference in exchanger inlet temperatures and the overall heat transfer coefficient, are critical to calculating the extra overall duty each incremental area element returns. The approach is able to account for differences in film coefficients, heat exchanger types, flow arrangements, exchanger cost functions, and utility pricing. Incorporated into the method is the newly defined “heat duty flow-on” factor,  $\theta$ , which evaluates downstream effects on utility use and cost that are caused by changing the area of one exchanger. To illustrate the method, the CDM is illustrated by application to a simple distillation process and a milk powder plant case study. After applying the new CDM, the total annual cost was reduced by 7.1% for the distillation problem and 5.8% for the milk powder plant. For the distillation process, the CDM solution was found to give a comparable minimum total area and cost to four recently published programming HEN synthesis solutions for the same problem without requiring the increased network complexity through multiple stream splits. The CDM has significant potential and is expected to improve with further development.

© 2014 Elsevier Ltd. All rights reserved.

## 1. Introduction

Heat Exchanger Network (HEN) synthesis has been the focus of numerous studies [4]. The most significant contribution in this field over the past four decades has been the development of Pinch Analysis and the Pinch Design Method (PDM) [8]. Pinch is a holistic approach to network synthesis that now has a proven track record for achieving energy savings in a range of industries. Extensions to

the original method, such as targeting total area, Heat Exchanger (HE) shells [1] and pressure drop [10], have been developed to improve its industrial relevance and profitability. Much less, however, has been published on improving the area allocation within HEN structures as an approach to reducing total cost.

Pinch Analysis applies fundamental thermodynamic principles to identify temperatures that constrain process heat recovery assuming a minimum approach temperature,  $\Delta T_{\min}$ . But the  $\Delta T_{\min}$  constraint for most problems results in non-cost optimal HEN area allocation mostly due to differences in utility costs, stream heat transfer film coefficients, HE types and flow arrangements, HE capital costs, and approach temperatures. To an extent the  $\Delta T$

\* Corresponding author.

E-mail address: [tgw7@waikato.ac.nz](mailto:tgw7@waikato.ac.nz) (T.G. Walmsley).

**Nomenclature***Roman*

<i>A</i>	area (m <sup>2</sup> )
<i>b</i>	capital cost coefficient (\$/m <sup>2</sup> )
<i>C</i>	heat capacity flow rate (kW/°C)
<i>C*</i>	ratio of minimum to maximum heat capacity flow rates for $\epsilon$ -NTU method
<i>CC</i>	annualised capital cost (\$/y)
<i>FC</i>	annualised fixed cost (\$/y)
<i>G</i>	a product of variables
<i>I</i>	cost index
<i>NTU</i>	number of (heat) transfer units
<i>n</i>	capital cost exponent
<i>P</i>	temperature effectiveness
<i>p</i>	utility price (\$/kWh)
$\hat{p}$	annual utility price (\$/kW/y)
<i>Q</i>	heat duty (kW)
<i>R</i>	ratio of minimum to maximum heat capacity flow rates for P-NTU method
<i>S</i>	annual savings (\$/y)
<i>T</i>	temperature (°C)
<i>TC</i>	total annual cost (\$/y)
<i>U</i>	overall heat transfer coefficient (kW/°C/m <sup>2</sup> )
<i>UC</i>	utility cost (\$/y)

*Greek*

$\beta$	stream split fraction
$\Delta$	positive difference between two states
$\epsilon$	heat exchanger effectiveness
$\theta$	heat duty flow-on factor

*Subscripts/superscripts*

add	additional
cap	capital
in	inlet
max	maximum
min	minimum
out	outlet
p	process
ut	utility

*Abbreviations*

CDM	Cost Derivative Method
CIP	clean-in-place
COW	water removed from milk
HE	heat exchanger
HEN	heat exchanger network
MER	maximum energy recovery network
PDM	pinch design method
RE	heat recovery exchanger
TE	terminal heat recovery exchanger
UE	utility exchanger

contribution concept for individual streams, in place of a global  $\Delta T_{\min}$ , was developed to account for large differences in film coefficients, although optimal area allocation is not ensured by this method. Simple methods for  $\Delta T_{\min}$  relaxation through dual minimum approach temperatures, where one  $\Delta T_{\min}$  is selected for heat recovery targeting and the other  $\Delta T_{\min}$  is applied to individual exchangers, have also been proposed [11].

Ait-Ali and Wade [2] derived conditions to determine the optimal heat recovery area allocation in multi stage heat exchanger systems with any number of exchangers in series. The derivation was based on the Log-Mean Temperature Difference heat exchanger design method. Limitations of the method are that it only applies to multi-stage heat exchanger systems – not HEN's in general – and assumes counter flow heat transfer. Focus is directed towards achieving maximum heat recovery for a given total area, which does not necessarily equate to minimum total cost. The method of Ait-Ali and Wade [2] is one of the few published methods on optimising area allocation in literature other than pure computer programming based approaches.

Computer programming has been applied to develop cost effective heat exchanger networks with optimal area allocation. Gorji-Bandpy et al. [5] applied a two stage optimisation approach using the Genetic Algorithm for HEN synthesis and Sequential Quadratic Programming for heat duty and area distribution. Nemet et al. [9] applied deterministic and stochastic multi-period Mixed-Integer Nonlinear Programming models for HEN synthesis. Their investigation incorporated projections for future utility prices to ensure the cost-benefit of the HEN was maximised across the lifetime of the project. Escobar and Trierweiler [3] summarised the various approaches to HEN synthesis using linear programming, non-linear programming, mixed integer linear programming, and mixed integer non-linear programming, together with the major solution algorithms relating to these classes.

In this paper, a novel Cost Derivative Method (CDM) is developed and applied to obtain minimum total annual cost through (near) optimal area allocation within a HEN structure using the first derivative of the total cost function of a heat exchanger in a HEN. The intention is for this method to be applied after HEN structures are developed by the PDM or some other synthesis approach. The derivative approach attempts to add/shift area to the recovery exchangers (RE) where the greatest incremental cost benefit is returned. Effectiveness–Number of Transfer Units ( $\epsilon$ -NTU) relationships for sizing heat exchangers [7] form an essential part of the method. The CDM is able to account for differences in film coefficients, HE flow arrangements, HE cost functions, and utility costs. The method is applied to the simple distillation example of [6] and the milk powder plant case study of [12] to illustrate the potential cost savings, although results are case specific. Both Walmsley et al. [12] and Gundersen [6] applied the PDM to develop their respective HEN's and as a result this work presents the CDM as using the PDM solutions as a key input to the method. An earlier version of this method has been published in Chemical Engineering Transactions by the authors [13].

## 2. Derivation of the Cost Derivative Method for cost optimal area allocation

This section presents the derivation of fundamental equations that may be applied to a HEN to optimally allocate HE area (and duty) so that the total annual cost of the system is minimised. The scope of the derivation includes both utility and capital cost but ignores pumping and piping costs. The intention is for this method to be applied to a HEN during the design stage. Significant structural change to the heat recovery side of the HEN is not considered.

Necessary conditions for optimal area allocation are derived by focusing on how incrementally adding area to a single heat

exchanger affects Total annual Cost (TC). The overall goal is to identify which heat exchangers can economically afford more area, whereas other heat exchangers may need to reduce in area because the heat recovery cost savings are insufficient to justify the capital expenditure. A challenge in this approach is to accurately account for the several flow-on effects that occur from changing the area of one HE in a network.

2.1. Derivative of a heat exchanger's total cost function

Consider the design of a large HEN containing several Recovery Exchangers (RE) and Utility Exchangers (UE) where RE<sub>1</sub> is the match between hot stream “x” and cold stream “y”.

The total annual cost, TC, of the HEN, ignoring piping and pumping costs, is

$$TC = CC_{RE} + CC_{ut} + UC \tag{1}$$

Where CC is the annualised capital cost, and subscript ut refers to utility. Each cost component is comprised of fixed and variable costs. If the area, A, of RE<sub>1</sub> is increased by ΔA, then the resulting change in total annual cost, i.e. ΔTC, is

$$\Delta TC = \Delta CC_1 + \sum \Delta CC_{ut} - \sum \Delta S_{ut} \tag{2}$$

Where S is the annual utility savings due to heat recovery and subscript 1 refers to the stream match between streams x and y.

Fig. 1 illustrates the effects of increasing the area of RE<sub>1</sub> by a very small amount, i.e. dA, on the exit temperatures from RE<sub>1</sub>, which propagates to downstream RE's. As the change in stream temperatures, dT<sub>y2</sub> and dT<sub>x2</sub>, flows on to the next network RE, it affects the RE's duty and outlet temperatures. Eventually the change temperature propagates to a UE affecting is required utility load and design area.

After dividing by dA<sub>1</sub> and converting to derivative form, Eq. (2) is rewritten

$$\frac{dTC}{dA_1} = \frac{dCC_1}{dA_1} + \sum \frac{dCC_{ut(i)}}{dA_1} - \sum \frac{dS_{ut(i)}}{dA_1} \tag{3}$$

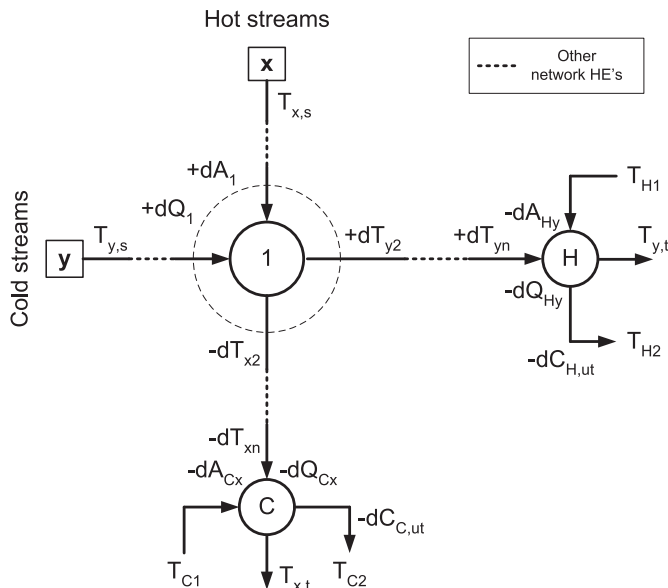


Fig. 1. Impact of increasing the area of recovery exchanger 1 by dA.

By setting dTC/dA<sub>1</sub> to zero the cost “optimum” area for RE<sub>1</sub> may be solved. To find the solution to Eq. (3) each differential element is now analysed.

The incremental annualised heat recovery savings in Eq. (3) is the product of the annual utility price, p, (\$/kW<sub>y</sub>) and the change in utility consumption, dQ<sub>ut(i)</sub>,

$$\sum \frac{dS_{ut(i)}}{dA_1} = \sum \left( -p_{ut(i)} \frac{dQ_{ut(i)}}{dA_1} \right), \quad \text{where } p_{ut} = \hat{p}_{ut} t \tag{4}$$

In Eq. (4),  $\hat{p}$  is the specific utility price (\$/kWh) and t is the plant production hours per year (h/y). After applying the chain rule to dQ<sub>ut(i)</sub>/dA<sub>1</sub> and recognising that the new term dQ<sub>1</sub>/dA<sub>1</sub> is the constant for all UE's, Eq. (4) becomes

$$\sum \frac{dS_{ut(i)}}{dA_1} = \frac{dQ_1}{dA_1} \sum \left( -p_{ut(i)} \frac{dQ_{ut(i)}}{dQ_1} \right) \tag{5}$$

We may choose to (newly) define the heat duty flow-on factor, θ, as the ratio of the reduction in duty of UE<sub>i</sub> to the increase in duty of RE<sub>1</sub>,

$$\theta_1^{ut(i)} \equiv \frac{-dQ_{ut(i)}}{dQ_1} \tag{6}$$

The negative sign in Eq. (6) is included so that positive values for θ represent an increase in heat recovery and a reduction in utility use. Substituting Eq. (6) into Eq. (5) gives

$$\sum \frac{dS_{ut}}{dA_1} = \frac{dQ_1}{dA_1} \sum \left( p_{ut(i)} \theta_1^{ut(i)} \right) \tag{7}$$

The other derivative terms in Eq. (3) are related to capital cost. The general annualised heat exchanger capital cost formula is

$$CC = FC + bA^n \tag{8}$$

Where FC is a fixed cost, b is a positive constant and n is a positive constant less than unity. In the context of this study coefficients FC and b are annualised to take into account the time value of money. Taking the derivative of Eq. (8) with respect to area gives

$$\frac{dCC}{dA} = bnA^{n-1} \tag{9}$$

Eq. (9) may be applied directly to the RE capital cost component in Eq. (3). However, to apply Eq. (9) to the UE capital cost component requires application of the chain rule, as presented in Eq. (10), since dA<sub>1</sub> ≠ dA<sub>ut(i)</sub>.

$$\sum \frac{dCC_{ut(i)}}{dA_1} = \sum \left( \frac{dCC_{ut(i)}}{dA_{ut(i)}} \cdot \frac{dA_{ut(i)}}{dQ_{ut(i)}} \cdot \frac{dQ_{ut(i)}}{dQ_1} \cdot \frac{dQ_1}{dA_1} \right) \tag{10}$$

Eq. (11) is obtained by substituting Eqs. (6) and (9) into Eq. (10) and once again recognising that dQ<sub>1</sub>/dA<sub>1</sub> is the same for all UE's.

$$\sum \frac{dCC_{ut(i)}}{dA_1} = \frac{dQ_1}{dA_1} \sum \left( \frac{(bnA^{n-1})_{ut(i)} \theta_1^{ut(i)}}{dQ_{ut(i)}/dA_{ut(i)}} \right) \tag{11}$$

Each component of Eq. (3) has now been analysed. Substituting Eqs. (7), (9) and (11) into Eq. (3) and simplifying gives

$$\frac{dT_C}{dA_1} = (bnA^{n-1})_1 - \frac{dQ_1}{dA_1} \sum \left( \theta_1^{ut(i)} \left( p_{ut(i)} + \frac{(bnA^{n-1})_{ut(i)}}{dQ_{ut(i)}/dA_{ut(i)}} \right) \right) \quad (12)$$

By setting  $dT_C/dA$  to zero and rearranging, Eq. (12) becomes

$$(bnA^{n-1})_1 = \frac{dQ_1}{dA_1} \sum \left( \theta_1^{ut(i)} \left( p_{ut(i)} + \frac{(bnA^{n-1})_{ut(i)}}{dQ_{ut(i)}/dA_{ut(i)}} \right) \right) \quad (13)$$

Eq. (13) represents the cost to savings trade-off. On the left hand side of Eq. (13) is the incremental RE capital cost, whereas on the right hand side is the incremental heat recovery and UE capital savings. Three elements in Eq. (13) that need further analysis to be able to solve for area are: (1)  $dQ_1/dA_1$ , (2)  $dQ_{ut(i)}/dA_{ut(i)}$  and (3)  $\theta$ .

## 2.2. Analysis of $dQ/dA$ for heat exchangers

### 2.2.1. Case 1: heat recovery exchangers

When area is added to a heat recovery exchanger, the duty increases and the outlet temperatures change, whereas the stream flow rates are constant. The expression for  $dQ/dA$  is obtained by substituting the definitions for  $Q$  and  $A$  from the  $\varepsilon$ -NTU heat exchanger design method [7] while assuming the overall heat transfer coefficient ( $U$ ), the difference in inlet temperature of the streams ( $\Delta T_{max}$ ) and the flow rates of the streams, are unaffected by the additional area. As a result Eq. (14) is obtained.

$$\frac{dQ}{dA} = U\Delta T_{max} \frac{d\varepsilon}{dNTU} \quad (14)$$

The term  $d\varepsilon/dNTU$  is specific to a heat exchanger flow arrangement. The derivative of the counterflow  $\varepsilon$ -NTU relationship is

$$\frac{d\varepsilon}{dNTU} = (1 - \varepsilon)(1 - \varepsilon C^*), \quad [0 \leq C^* \leq 1] \quad (15)$$

### 2.2.2. Case 2: utility heat exchangers

The second case of  $dQ/dA$  is for UE's where a change in inlet temperature of a process stream affects the required utility duty, utility flow rate and exchanger area. For a UE, the outlet temperature of the process stream is a fixed (target) temperature and the inlet and outlet temperatures of the utility are also fixed. It's important to note that the derivation (not presented in this paper) uses temperature effectiveness,  $P$ , in place of effectiveness,  $\varepsilon$ , because the stream with  $C_{min}$  is not always obvious. P-NTU relationships are the same as  $\varepsilon$ -NTU relationships. The  $dQ/dA$  expression for utility exchangers is

$$\frac{dQ}{dA} = \frac{U\Delta T_{max}}{1 - P_p} \frac{dP_p}{dNTU_p}, \quad \text{where } P_p = \frac{\Delta T_p}{\Delta T_{max}}, \quad R_p = \frac{C_p}{C_{ut}} \quad (16)$$

The counterflow solution for  $dP_p/dNTU_p$  is

$$\frac{dP_p}{dNTU_p} = \frac{P_p(1 - P_p)(1 - R_p)}{\frac{P_p}{1 - P_p R_p} - \frac{R_p}{1 - R_p} \ln \left| \frac{1 - P_p R_p}{1 - P_p} \right|}, \quad [0 \leq R_p \neq 1] \quad (17a)$$

$$\frac{dP_p}{dNTU_p} = (1 - P_p)^2, \quad [R_p = 1] \quad (17b)$$

## 2.3. Heat duty flow-on factor

### 2.3.1. Origin, propagation and termination of the heat duty flow-on effect

The heat duty flow-on factor,  $\theta$ , as defined in Eq. (6) needs to be determined to find the minimum total annual cost solution of a network. In this section, a derivation based on the  $\varepsilon$ -NTU (and P-NTU) method is presented to demonstrate how network specific equations for  $\theta$  may be quickly formulated.

**2.3.1.1. Origin of heat duty flow-on "effect".** When  $dA$  is added to  $RE_1$ , the change in outlet temperature of hot stream  $x$  (Eq. (18a)) and cold stream  $y$  (Eq. (18b)) are

$$dT_{1,x}^{out} = -\frac{dQ_1}{C_x}, \quad x \in \text{hot streams} \quad (18a)$$

$$dT_{1,y}^{out} = \frac{dQ_1}{C_y}, \quad y \in \text{cold streams} \quad (18b)$$

The change in outlet temperature of streams  $x$  and  $y$  from  $RE_1$  propagates through the network affecting the inlet temperatures to and duties of downstream recovery exchangers.

**2.3.1.2. Heat duty flow-on through downstream heat recovery exchangers.** Now consider recovery exchanger  $n$ ,  $RE_n$ , that is positioned at the intersection of two other streams,  $v$  and  $w$ , which is downstream of  $RE_1$  and illustrated in Fig. 2. It is important to note that the change in inlet temperature for stream  $v$  is  $dT_{n,v}$ , whereas for stream  $w$  the change in inlet temperature,  $dT_{n,w}$  is zero.

The total duty of  $RE_n$  is

$$Q_n = (\varepsilon C_{min} \Delta T_{max})_n \quad (19)$$

The derivative of Eq. (19) with respect to temperature, recognizing  $\varepsilon$  and  $C_{min}$  are constants, is

$$dQ_n = (\varepsilon C_{min})_n dT_{n,v}^{in}, \quad \text{where } dT_{n,v}^{in} = d(\Delta T_{max}) \quad (20)$$

The change inlet and outlet temperatures of stream  $v$  to/from  $RE_n$  are related by energy balance

$$dT_{n,v}^{out} = dT_{n,v}^{in} - \frac{dQ_n}{C_v} \quad (21)$$

Substituting Eq. (20) into Eq. (21) and simplifying gives

$$dT_{n,v}^{out} = dT_{n,v}^{in}(1 - P_{n,v}), \quad \text{where } P_{n,v} = \frac{(\varepsilon C_{min})_n}{C_v} \quad (22)$$

Using temperature effectiveness,  $P$ , in the above equation enables useful simplification. Eq. (22) may be modified to account for stream splits. Consider if stream  $v$  is split into  $i$  number of streams and each branch passes through  $RE_{n1}, \dots, RE_{ni}$ , then the change in temperature before and after the stream split is

$$dT_{n,v}^{out} = dT_{n,v}^{in} - \frac{1}{C_v} \sum_{i_0=1}^i dQ_{n(i)} \quad (23)$$

By substituting Eq. (20) into Eq. (23) and simplifying gives

$$dT_{n,v}^{out} = dT_{n,v}^{in} \left( 1 - \sum_{i_0=1}^i \beta_{v(i)} P_{n,v(i)} \right), \quad \text{where} \quad (24)$$

$$P_{n,v(i)} = \frac{(\varepsilon C_{min})_{n(i)}}{C_{v(i)}}, \quad \beta_{v(i)} \equiv \frac{C_{v(i)}}{C_v}$$

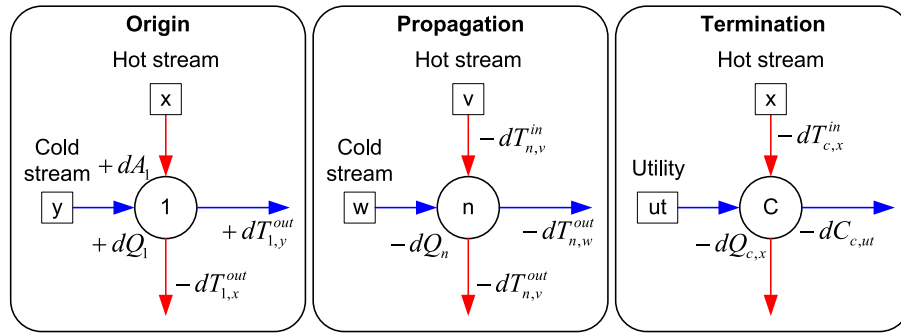


Fig. 2. Analysis of heat duty flow-on through heat exchanger networks.

In Eq. (24),  $\beta$  is the split fraction. Eq. (24) is correct for splits on either hot or cold streams.

The next part of the analysis focuses on how the outlet temperature of stream  $w$  is affected (Fig. 2). The energy balance for stream  $w$  is

$$dT_{n,w}^{\text{out}} = dT_{n,w}^{\text{in}} + \frac{dQ_n}{C_w} \quad (25)$$

Since  $dT_{n,w}^{\text{in}}$  is nil, then substituting Eq. (20) into Eq. (25) simplifies to

$$dT_{n,w}^{\text{out}} = dT_{n,v}^{\text{in}} P_{n,w}, \quad \text{where } P_{n,w} = \frac{(\varepsilon C_{\min})_n}{C_w} \quad (26)$$

It is important to note that the values of  $P_{n,v}$  and  $P_{n,w}$  always fall between zero and one, which implies that the heat duty and temperature flow-on effects from RE<sub>1</sub> are dampened as the change in temperature propagates through the HEN.

**2.3.1.3. Termination of heat duty flow-on effect.** Eventually the change in exchanger duties and temperatures propagates to a UE, where utility stream flow rates are adjusted to ensure the process stream's target temperature is achieved (Fig. 2). Changes in heat duty from RE<sub>1</sub> may propagate along multiple different downstream paths to the same UE. Each flow-on path may be treated independently and summed to find the combined effect on utility use. We now consider how the change in inlet temperatures to the UE's on streams  $x$  and  $y$  affect its duty, assuming these  $dT$ 's are caused by  $j$  number of flow-on paths. The change in utility duty for the heater and cooler may be expressed as

$$dQ_{c,x} = C_x \sum_{j_0=1}^j dT_{c,x(j)}^{\text{in}}, \quad x \in \text{hot streams} \quad (27a)$$

$$dQ_{h,y} = -C_y \sum_{j_0=1}^j dT_{h,y(j)}^{\text{in}}, \quad y \in \text{cold streams} \quad (27b)$$

**2.3.1.4. Steps for deriving complete heat duty flow-on factor equations.** Eqs. (18), (24), (26) and (27) provide a framework to construct formulas for individual heat duty flow-on factors for an RE/UE match. The steps for constructing equations for  $\theta$  are:

1. Identify flow-on pathways between selected RE <sub>$n$</sub>  (origin) and UE<sub>ut</sub> (termination)
2. For one pathway, write the energy balance for UE<sub>ut</sub> using Eq. (27)
3. Move toward the RE using flow-on pathway by substituting in Eq. (24) or 26 for  $dT$

4. Once the RE is reached, apply Eq. (18) for RE <sub>$n$</sub> .
5. Rearrange to form an equation for  $\theta$  as defined in Eq. (6) for the flow-on path.
6. If applicable, repeat steps 2–5 for other flow-on pathways
7. Sum equations for the different pathways to find  $\theta$ .

### 2.3.2. General principles for finding the heat duty flow-on factor

The general formulas presented in previous section are the foundation for finding heat duty flow-on factors. In addition to these equations, there are a few general principles that are useful for forming equations for the heat duty flow-on factor and implementing the factor as part of a computer program.

The generalised formula for a heat duty flow-on factor is

$$\theta_n^{\text{ut}} = \frac{-dQ_{\text{ut}}}{dQ_n} = \pm \sum \left( \frac{C_{\text{ut},p(i)}}{C_{n,s(i)}} G_i \right) \quad (28)$$

Where subscript  $ut,p$  refers to the process stream being cooled/heated by utility,  $n,s$  refers initial stream that the heat duty flow-on effect is propagated along, and  $i$  refers to the selected heat duty flow-on pathway. Function  $G$  is used to describe the heat duty flow-on effect along a pathway with an unspecified number and arrangement of RE's such that

$$dT_{G_i}^{\text{out}} = G_i dT_{G_i}^{\text{in}}, \quad \text{where } G_i = \Pi(P_j, 1 - P_j) \quad (29)$$

For the general case, the inlet temperature to  $G$  is from RE <sub>$n$</sub> , i.e. the RE where  $dA$  is added, and the outlet temperature from  $G$  is the inlet temperature of the process stream to UE<sub>ut</sub>.

Heat duty flow-on factors for a single pathway may be positive or negative. This sign may be determined using the rules in Table 1. For example, if the heat duty flow-on effect is propagated from the origin RE along a hot stream to a hot utility, then the sign of heat duty flow-on factor is negative, i.e. utility increases.

The heat duty flow-on factor of RE<sub>1</sub> often has common flow-on pathways with other RE's to some downstream UE<sub>ut</sub> as illustrated in Fig. 3.

In general, the heat duty flow-on factor for RE<sub>1</sub> to UE<sub>ut</sub> is

$$\theta_1^{\text{ut}} = \theta_{1(x)}^{\text{ut}} + \theta_{1(y)}^{\text{ut}} \quad (30)$$

Table 1

Sign of heat duty flow-on factor. Positive is increased heat recovery, negative is increased utility use.

	Hot stream (origin RE)	Cold stream (origin RE)
Hot utility	–	+
Cold utility	+	–

which is the sum of the heat duty flow-on effects along streams  $x$  and  $y$ . The heat duty flow-on factor for pathways along streams  $x$  and  $y$  may be related to the heat duty flow-on factors for downstream RE's 2 and 3.

$$\theta_{1(x)}^{ut} = \left( 1 - \sum_{i_0=1}^i \beta_{x(i)} P_{3,x(i)} \right) \theta_{3(x)}^{ut} - P_{3,y1} \theta_{3(y1)}^{ut}, \quad \text{where}$$

$$\theta_3^{ut} = \theta_{3(x)}^{ut} + \theta_{3(y1)}^{ut} \tag{31a}$$

$$\theta_{1(y)}^{ut} = \left( 1 - \sum_{i_0=1}^i \beta_{y(i)} P_{2,y(i)} \right) \theta_{2(y)}^{ut} - P_{2,x1} \theta_{2(x1)}^{ut}, \quad \text{where}$$

$$\theta_2^{ut} = \theta_{2(y)}^{ut} + \theta_{2(x1)}^{ut} \tag{31b}$$

Relating the heat duty flow-on factor of RE<sub>1</sub> to the heat duty flow-on factor of downstream RE's 2 and 3 (Fig. 3) is very useful from a practical computer programming implementation point of view. By effective use of these equations, one may eliminate the need to derive complete heat duty flow-on factor equations from every RE to every UE in a network.

2.3.3. Heat duty flow-on for closed loops – a special case

The idea of heat loops in a HEN is a well-known Pinch Analysis concept. In many cases it is advantageous to break a heat loop to reduce the number of heat exchanger units often as a trade-off for reduced heat recovery. Fig. 4 is a schematic of two simple HEN's that contain: (a) a non-self-interacting loop (i.e. open loop) and (b) a self-interacting loop (i.e. closed loop). Arrows are included to highlight the important heat duty flow-on pathways.

Fig. 4 illustrates the differences between an open loop and closed loop in the context of a HEN. In Fig. 4(a), the heat duty flow-on effects do not interact with itself whereas in Fig. 4(b) the heat loop interacts with itself. In a so-called closed heat loop, adding  $dA$  to one of the RE's affects at least one of the inlet temperatures to the same RE. Self-interacting closed heat loops presents an interesting challenge for determining an exact equation for the heat duty flow-on factor. In addition, interacting loops also presents a significant process control issue due to the closed loop feedback that occurs for disturbances in temperature or flow rate in any RE forming the loop.

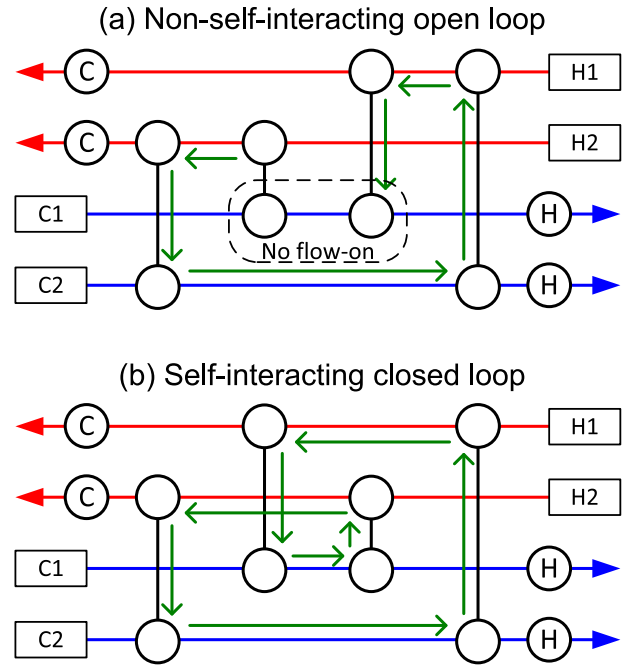


Fig. 4. Non-self-interacting (a) and self-interacting (b) heat loops.

For the closed loop situation, it is necessary to clarify the definition of the heat duty flow-on factor, i.e. the ratio of  $dQ_{ut}$  to  $dQ_1$ . Normally when  $dQ_1$  is calculated the  $dQ$  solely occurs due the increase in area and heat exchanger effectiveness. However, when there is a closed heat loop, the heat duty change flows around the loop affecting the inlet temperature to RE<sub>1</sub>, which implies

$$dQ_1 = dQ_{1(eff)} + \varepsilon_1 C_{min,1} d(\Delta T_{max,1}), \quad \text{where}$$

$$dQ_{1(eff)} = C_{min,1} \Delta T_{max,1} d\varepsilon_1 \tag{32}$$

One portion of  $dQ_1$  is directly attributed to the change in effectiveness of the heat exchanger, whereas the second portion of  $dQ_1$  is due to the change in an inlet temperature to RE<sub>1</sub>. To be consistent with the previous cost derivatives, the heat duty flow one factor for closed loops is based on  $dQ_{1(eff)}$ , i.e.  $-dQ_{ut}/dQ_{1(eff)}$ , rather than the actual  $dQ$  for RE<sub>1</sub>.

Fig. 5 presents four generalised HEN cases where the heat duty flow-on factor is affected by a closed heat loop. For each case in Fig. 5,  $dA$  is added to RE<sub>1</sub>, which is the match between streams  $s$  and  $t$ . Streams  $s$  and  $t$  are labelled so that the heat duty flow-on effect primarily flows along stream  $s$  to UE<sub>ut</sub>. Circles in Fig. 5 represent individual heat exchangers whereas rectangular boxes represent a function  $G$  that describes the heat duty flow-on effect through an unspecified number and arrangement of RE's (Eq. (29)). Table 2 presents the generalised heat duty flow-on factors relating to the four situations outlined in Fig. 5.

It is interesting to note that Eq. (35) bears some resemblance to the general formula for closed loop transfers functions in process control. The ratio of heat capacities at the front of the equation is analogous to a proportionality constant. In process control the numerator is the closed loop function and the denominator is one plus the open loop function.

The term  $1 - G_L$  appears on the denominator of all three generalised equations in Table 2. Since  $G_L$  must be a positive value less than unity, it is deduced that the presence of the closed heat loop tends to amplify the heat duty flow-on factor. It maybe, therefore, possible to find a situation where an individual heat duty

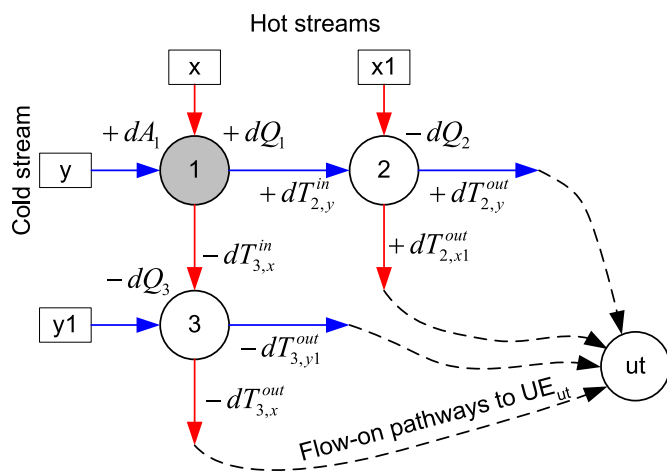


Fig. 3. Heat duty flow-on pathways.

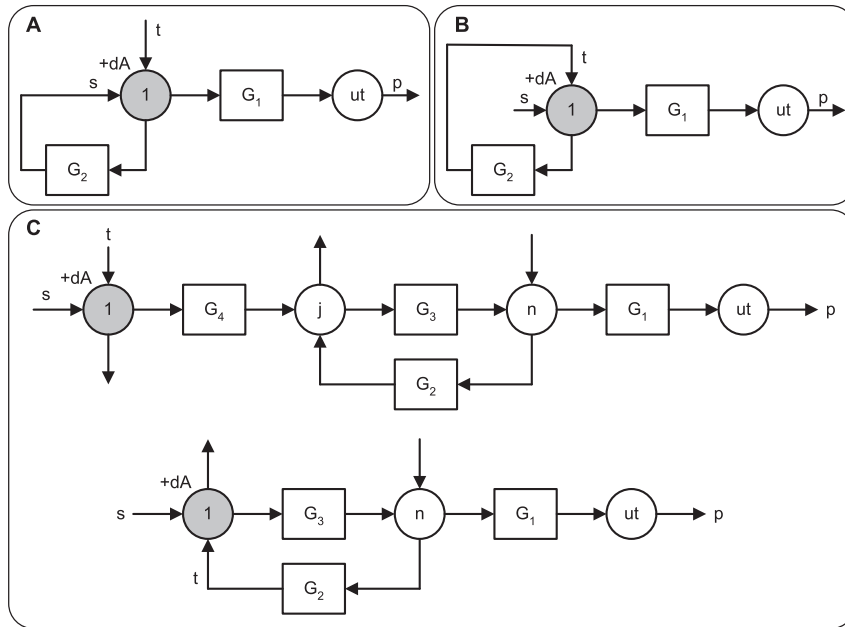


Fig. 5. Heat duty flow-on in self-interacting closed heat loops.

flow-on factor is greater than one, although the sum of individual heat duty flow-on factors to all heaters or coolers must collectively be less than one.

2.3.4. Overall heat duty flow-on factor

It is useful to define the overall heat duty flow-on factor,  $\theta$ ,

$$\theta_1 \equiv \sum \theta_1^{h(i)} = \sum \theta_1^{c(i)} \tag{36}$$

Where subscript 1 refers to the RE and superscripts  $h$  and  $c$  refer to the heaters and coolers. Using Fig. 3, the overall heat duty flow-on factor may be also described in terms of downstream flow-on factors,

$$\theta_1 = 1 - \sum_{i_0=1}^i (\beta_{y(i)} P_{2,y(i)} \theta_{2(i)}) - \sum_{j_0=1}^j (\beta_{x(j)} P_{3,x(j)} \theta_{3(j)}) \tag{37}$$

The derivation of Eq. (37) is not presented in this paper. Two important properties of the heat duty flow-on factor are:

- (1) The heat duty flow-on factor is nearly always independent of the area of the RE where heat duty flow-on effect originates, i.e.  $RE_n$ .
- (2) The overall heat duty flow-on factor has the limits of  $-1$  and  $1$  where negative overall heat duty flow-on factors indicate that a stream match is actually detrimental to network heat recovery.

Since  $\theta$  for  $RE_n$  is nearly always independent the area of  $RE_n$ , it follows that the heat recovery,  $Q_{add}$ , unique to  $RE_n$  is

$$Q_{add} = \theta_{RE} Q_{RE}, \quad \text{where } Q_{RE} = Q_{net} + Q_{add} \tag{38}$$

Where  $Q_{add}$  is the portion of  $RE_n$ 's duty that goes to increasing the total network heat recovery and  $Q_{net}$  is the portion of  $RE_n$ 's duty that is substituting heat recovery from other RE's in the network. Such a breakdown of an RE's duty assumes the area and effectiveness of all other RE's in the network is constant. When the heat duty flow-on factor is negative, it follows that  $Q_{add}$  is also negative even though  $Q_{net}$  and  $Q_{RE}$  may both be positive. Eq. (38) does not

hold true in the case of an RE in a closed heat loop where the HE area for  $RE_n$  does affect the heat duty flow-on factor.

2.4. Modifications for minimum HEN total annual cost

Calculating a solution based on the cost optimum areas for each individual RE (i.e. the solution to Eq. (13) as presently interpreted) in the network does not ensure the overall minimum total cost for the entire HEN. Two common HEN situations where such is the case are:

1. The size of RE's are constrained by a stream's target temperature
2. A small duty UE may be eliminated by shifting the utility load to RE's or other UE's, thus saving a significant fixed installation fixed cost

To illustrate the first situation, consider the simple HEN in Fig. 6. The cost optimum areas of the two RE's are calculated and applied. However the target temperature of stream Y is exceeded and as a result the area of  $RE_2$  is scaled back such that  $dTC/dA$  is less than zero.

The second situation is encountered when the final temperature of a process stream (after heat recovery) does not quite reach its target temperature and requires the installation of a small UE, which incurs a significant fixed capital cost. In this situation it is sometimes possible to obtain a lower total cost solution by increasing the area of RE's in the network and eliminating the need of the UE. However there is a tension between eliminating UE's to reduce capital cost and the controllability of a network [15].

2.4.1. Recovery exchangers as terminal recovery exchangers

When a stream is able to thermodynamically and economically reach its target temperature with heat recovery, the final RE on the stream may be viewed as a pseudo UE. In Fig. 6,  $RE_2$  is unable to achieve its optimum area because of the target temperature constraint on stream y. As a result  $RE_2$  may be treated as a UE such that its area is sized to obtain the remaining required duty. The final RE on a stream not needing utility, e.g.  $RE_2$  on stream y, is referred to as a Terminal Exchanger (TE) to distinguish these exchangers from regular RE's and UE's.

**Table 2**

General formulas for heat duty flow-on factors in interacting closed heat loops where  $G_L$  is the function describing the closed loop and  $G_{OL}$  is the function describing the open loop.

Position of RE <sub>1</sub>	General formula
(A) "Corner" of a closed loop	$\theta_1^{ut} = \pm \frac{C_{ut,p}}{C_{1,s}} G_1 \left( \frac{P_{1,s} - G_L}{P_{1,s}(1 - G_L)} \right) \quad (33)$
(B) "Edge" of a closed loop	$\theta_1^{ut} = \pm \frac{C_{ut,p}}{C_{1,s}} G_1 \left( \frac{(1 - P_{1,t}) - G_L}{(1 - P_{1,t})(1 - G_L)} \right) \quad (34)$
(C) Upstream or in other positions of a closed loop	$\theta_1^{ut} = \pm \frac{C_{ut,p}}{C_{1,s}} \frac{G_{OL}}{1 - G_L} \quad (35)$

Fig. 7 presents two general cases of how a change in area on two upstream RE's (1 and 3) affect the duty and outlet temperatures from a TE (2). In case A,  $dA$  is added to RE<sub>1</sub>, which lessens the required duty on TE<sub>2</sub>. In turn, the area of TE<sub>2</sub> is reduced saving some capital cost, but no additional utility savings on stream y are gained. In case B,  $dA$  is added to RE<sub>3</sub>, which affects the inlet temperature to TE<sub>2</sub>. The change in  $\Delta T_{max}$  for TE<sub>2</sub> affects the required area and capital cost of TE<sub>2</sub> although the duty of TE<sub>2</sub> remains constant. These two cases have been analysed in detail and expressions for the capital cost savings, i.e.  $dCC/dA$ , and the heat duty flow-on factor for TE's have been obtained, which may be used to reinterpret Eq. (7) for utility cost savings and Eq. (11) for capital cost savings resulting from adding  $dA$  to an RE. The summary of the detailed analysis is presented in Table 3.

**2.5. Solutions accounting for future utility and capital price ratio changes**

For purposes of capital cost estimation, utility prices ( $p$ ) and capital cost coefficients ( $k$ ) are normally indexed to a particular base year. Indices,  $I$ , are a non-dimensional way of presenting trends in price for various commodities. Eq. (13) may be modified to include utility price ( $I_{ut}$ ) and capital cost ( $I_{cap}$ ) indices using the same base year and index,  $I_0$ ,

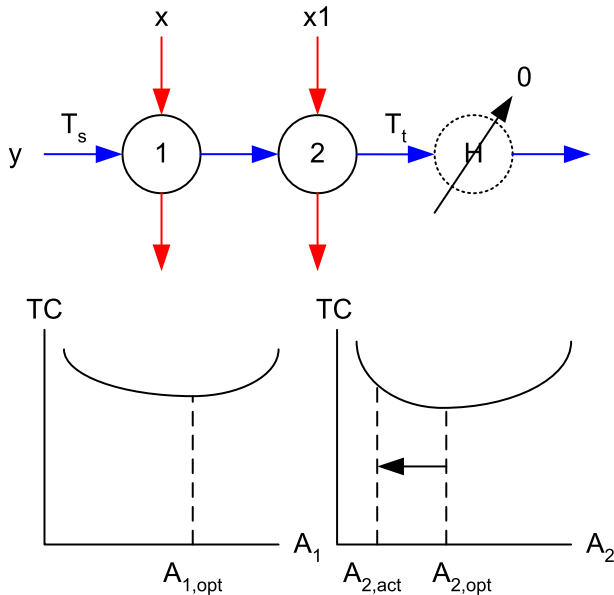


**Fig. 6.** The impact of target temperature constraints on heat exchanger sizing.

$$\left( \frac{I_{cap}}{I_0} bnA^{n-1} \right)_1 = \frac{dQ_1}{dA_1} \sum \left( \theta_1^{ut(i)} \left( \frac{I_{ut}}{I_0} p_{ut(i)} + \frac{I_{cap}}{I_0} \frac{(bnA^{n-1})_{ut(i)}}{dQ_{ut(i)}/dA_{ut(i)}} \right) \right) \quad (39)$$

which is multiplied by  $I_0/I_{cap}$  to obtain

$$(bnA^{n-1})_1 = \frac{dQ_1}{dA_1} \sum \left( \theta_1^{ut(i)} \left( \frac{I_{ut}}{I_{cap}} p_{ut(i)} + \frac{(bnA^{n-1})_{ut(i)}}{dQ_{ut(i)}/dA_{ut(i)}} \right) \right) \quad (40)$$

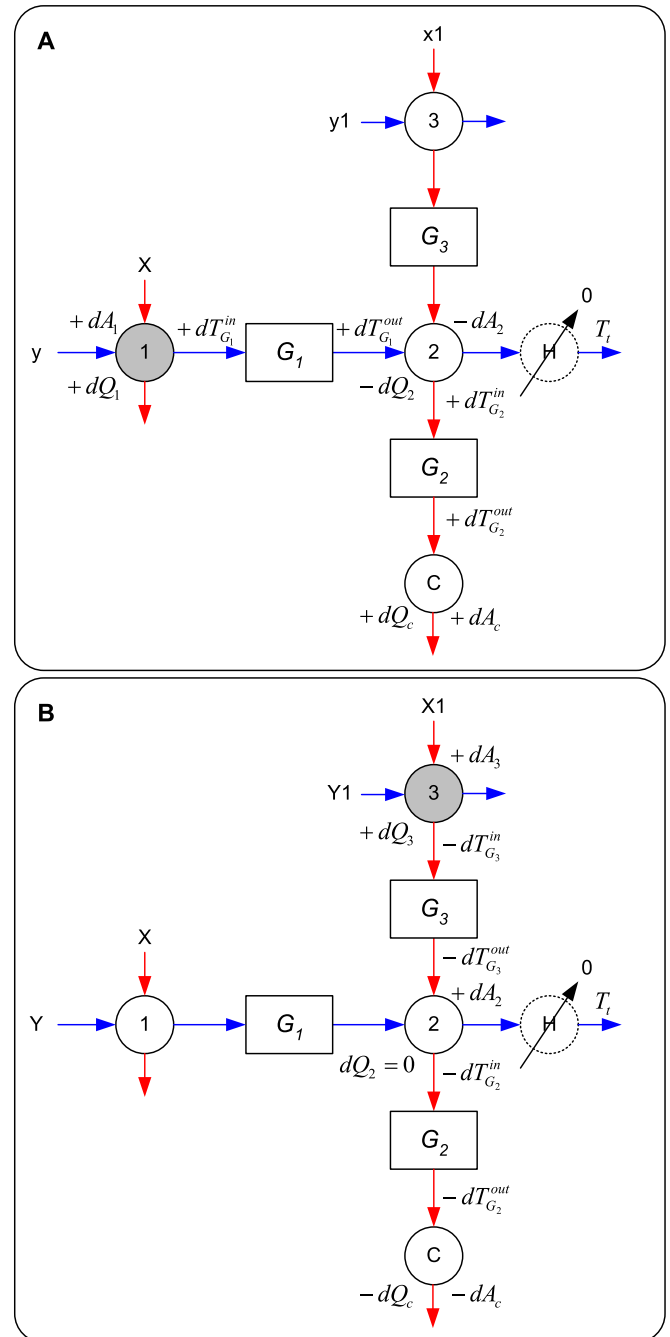


**Fig. 7.** Impact of increasing area of RE 1 and 3 on the duty of RE<sub>2</sub> that is constrained by a target temperature.

**Table 3**  
Expression for terminal exchangers for two cases presented in Fig. 7.

Objective	Case A	Case B
$\frac{dCC_{TE}}{dA_{RE}}$	$\frac{dCC_2}{dA_1} = -\frac{dQ_1}{dA_1} \frac{(bnA^{n-1})_2 \theta_1^2}{(dQ_2/dA_2)_{TE}}$	$\frac{dCC_2}{dA_3} = -\frac{dQ_3}{dA_3} \frac{(bnA^{n-1})_2 \theta_2^2}{(dQ_{2,x1}/dA_2)_{TE}}$
$\left(\frac{dQ}{dA}\right)_{TE}$	$\frac{dQ_2}{dA_2} = \frac{U\Delta T_{max}}{1-P_{2,y}} \frac{dP_y}{dNTU_y}$	$\frac{dQ_{2,x1}^{in}}{dA_2} = \frac{U\Delta T_{max}}{P_{x1}} \frac{dP_{x1}}{dNTU_{x1}}$ where $dQ_{2,x1}^{in} = C_{x1} dT_{2,x1}^{in}$
$\left(\frac{dP}{dNTU}\right)_{TE}$	$\frac{dP_y}{dNTU_y} = (1 - P_y)(1 - P_y R_y)$	$\frac{dP_{x1}}{dNTU_{x1}} = (1 - P_{x1})(1 - P_{x1} R_{x1})$
$dT_{TE}^{out} = f(dT_{TE}^{in})$	$dT_{2,x1}^{out} = \frac{C_y}{C_{x1}} dT_{2,y}^{in}$	$dT_{2,x1}^{out} = dT_{2,x1}^{in}$
$\theta_{RE}^{TE}$	$\theta_1^2 = G_1$	$\theta_3^2 = G_3$
$\theta_{RE}^{UE}$	$\theta_1^{c,x1} = -G_1 G_2$	$\theta_1^{c,x1} = G_3 G_2$

Eq. (40) demonstrates the importance of the ratio of utility to capital cost. If the initial value  $I_{ut}/I_{cap}$  is unity, then inputting values greater than one represents the fact that utility prices tend to rise over time whereas capital is paid for immediately. Higher utility to capital cost ratios result in HEN solutions with increased heat recovery due to increased justifiable capital cost.

**3. Application of the Cost Derivative Method**

The conditions arising from the previous derivations may be applied to find a cost optimal solution for area allocation for a given HEN structure. The method is referred to as the Cost Derivative Method (CDM).

In this study, the CDM has been applied in an Excel™ Spreadsheet. A flow diagram of the method is provided in Fig. 8. For the case studies analysed, the initial HEN structures were generated using the Pinch Design Method (PDM) and supplied as the main input, together with stream and cost data, into the CDM. Previously applied  $\Delta T_{min}$  constraints from the PDM are removed, although heat exchanger duties and areas may be used as initial values prior to optimisation. In the model, zero duty UE's are added to streams not requiring utility to ensure target temperatures are met while the model iterates through to find an overall solution.

The spreadsheet iteratively solves for the cost optimal area allocation in a HEN. In the spreadsheet, the value of  $dQ/dA$  from Eq. (8) for each heat exchanger is determined based on some initial sizing values (obtained in this case from the PDM solution). Using Eqs. (14) and (15) together with  $dQ/dA$ , the required effectiveness of the recovery exchanger is calculated, from which the NTU and heat exchanger area is determined. The new heat exchanger areas and duties are now used to recalculate  $dQ/dA$  forming an iterative loop. After a few iterations, the changes to the calculated areas are negligible and a solution is found. If the solution contains a limiting target temperature and/or a small duty UE that can be thermodynamically removed, the total cost of the solution may be potentially reduced by identifying some RE's as TE's. TE's are not sized according to Eq. (13) but according to the remaining duty required for a stream to achieve its target temperature. It is important to note that Eq. (15) may be substituted with the first derivative of the  $\epsilon$ -NTU relationship applicable to the specific heat exchanger type.

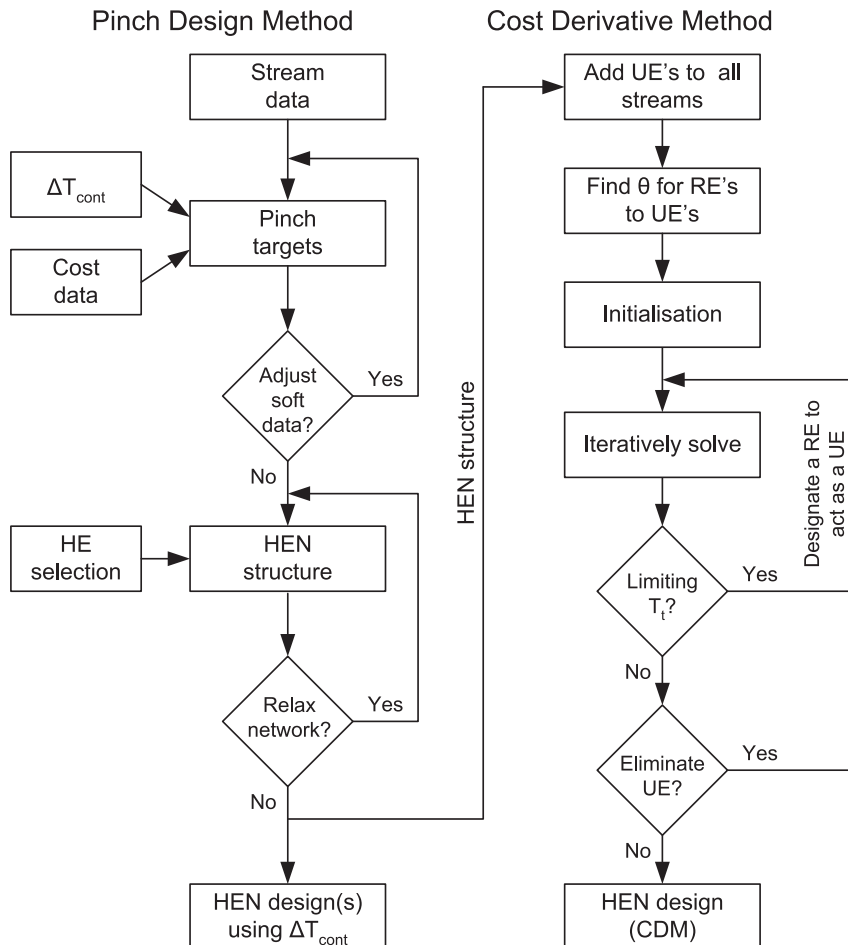


**Fig. 8.** Flow sheet of Pinch Design Method and Cost Derivative Method.

Solutions to the CDM were obtained in less than a few seconds. In practice, the CDM may be repeated for different RE network structures and the minimum cost solutions compared to decide on the final network design.

#### 4. Milk powder plant case study

The milk powder plant case study is taken from Ref. [12]. Focus in this case study is directed towards the integration of waste heat leaving the milk evaporator train in the powder plant. CDM solutions for two Maximum Energy Recovery networks (MER A and B) are compared to the Pinch Design Method (PDM) solutions. Refer to [12] for stream data and cost data.

##### 4.1. Comparison of the CDM and PDM solutions

A feature of MER A is the split of the milk stream to match with COW and the condenser vapour (Fig. 9). The stream split fraction is a degree of freedom that may be utilised to minimise total annual cost, TC, of HEN of the evaporator and CIP zones. Fig. 10 presents TC of the PDM and CDM solutions for milk split fractions between 0.0 and 0.2, where the fraction is for the milk/condenser match. For the PDM, a slight improvement (1.5%) is gained over the original solution. The CDM applies a significant lower milk split fraction while attempting to optimally allocate HEN area and the CDM solution (\$5.56/t<sub>p</sub>) gives a 5.8% total cost reduction compared to the original solution (\$5.91/t<sub>p</sub>).

Fig. 9 compares the heat exchanger area solutions for the PDM and CDM of MER A. The lower milk split fraction in the CDM is reflected in the allocation of area and duty in the HEN. The duty of the RE<sub>1</sub> is increased by 229 kW whereas RE<sub>2</sub> is decreased by 298 kW in the CDM compared to the PDM (Table 4). The economic balance in the CDM favoured increasing the duty of RE<sub>3</sub> by 299 kW

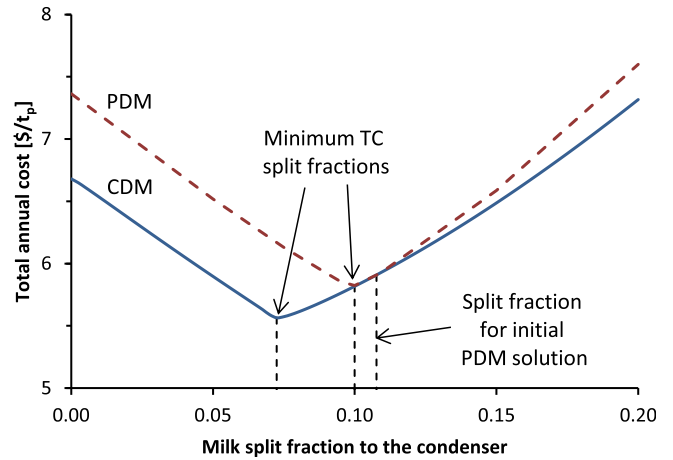


Fig. 10. Optimising the milk split fraction to milk/condenser vapour match.

in compensation for the reduction in duty on the RE<sub>2</sub> so that no utility cooling of the condenser load is required. As a result, the CDM solution viewed the CIP/condenser match as a terminal exchanger. In general the selection of  $\Delta T_{cont}$  in the PDM appears to have been conservative as indicated by the lower  $\Delta T_{LM}$ 's in the CDM and the negative dTC/dA values. For this particular HEN, the heat duty flow-on factors for all the heat recovery exchangers were all unity due to the split and the temperature effectiveness (*P*) of the condensing fluid being close to zero, i.e. no temperature change.

The CDM solution for MER B reduced total cost by 5.4% from \$5.45/t<sub>p</sub> for the PDM to \$5.16/t<sub>p</sub>. These two solutions are compared in Fig. 11. In the CDM, there is a significant shift of 279 kW from RE<sub>B</sub> to RE<sub>D</sub> compared to the PDM. This allows a rebalance and increase in total duty for the cyclic matches between milk/COW streams. As a result the duty of RE<sub>C</sub> increases by 1003 kW, although at the expense of a 549 kW reduction on RE<sub>A</sub>.

A detailed comparison including duty, area, log-mean temperature difference, heat duty flow-on factor and dTC/dA for individual heat exchangers is presented in Table 5. Although the duty of RE<sub>B</sub> is less in the CDM, its area is increased by 34% to compensate for a lower  $\Delta T_{LM}$ . The  $\Delta T_{LM}$  of RE<sub>A</sub> and RE<sub>C</sub> are also lower requiring significantly more area on RE<sub>C</sub> to deliver an increase in duty. The heat duty flow-on factors for the PDM and CDM are similar. RE<sub>D</sub> is identified as a terminal exchanger and the cyclic match on the milk stream forms an interacting closed heat loop. Like the PDM for MER A, the selection of  $\Delta T_{cont}$  generally appears to have been too conservative as indicated by the negative dTC/dA values whereas the dTC/dA values for the CDM are zero.

##### 4.2. Solutions based on different utility-capital cost ratios

The relationship between utility and capital costs is dynamic. Utility prices are normally expected to rise although new

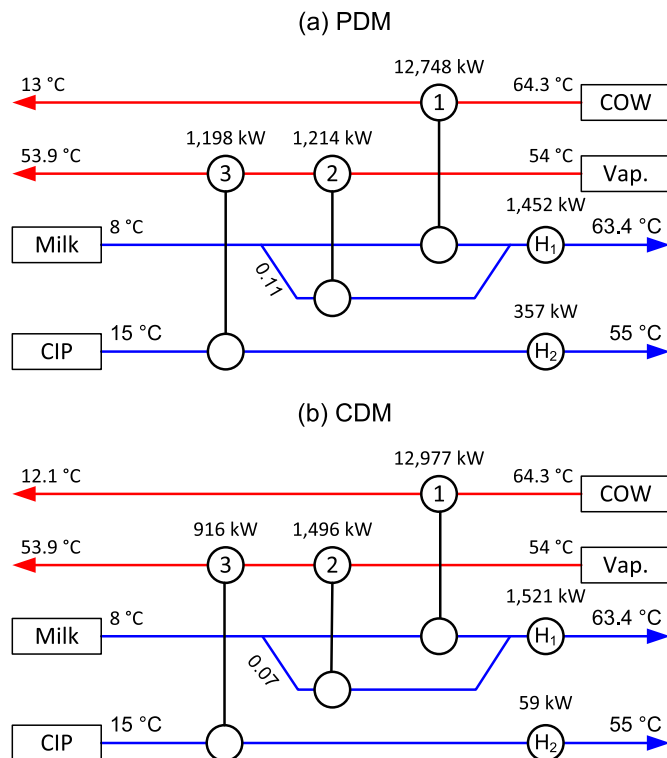


Fig. 9. Heat exchanger network design solutions of the PDM and CDM for MER A. Duties based on a milk powder plant producing 23 t<sub>p</sub>/h.

Table 4  
A detailed comparison of PDM and CDM solutions for MER A.

HE	Duty [kW]		Area [m <sup>2</sup> ]		$\Delta T_{LM}$ [°C]		$\Sigma\theta$		dT/dA [\$/kW/y]	
	PDM	CDM	PDM	CDM	PDM	CDM	PDM	CDM	PDM	CDM
1	12,748	12,977	1275	1297	5.0	5.0	1.00	1.00	-21	0
2	1214	916	42	58	19.1	10.6	1.00	1.00	-219	0
3	1198	1496	41	114	19.7	8.8	1.00	1.00	-225	0
H <sub>1</sub>	1452	1521	25	26	29.2	29.3				
H <sub>2</sub>	357	59	19	7	9.6	4.5				

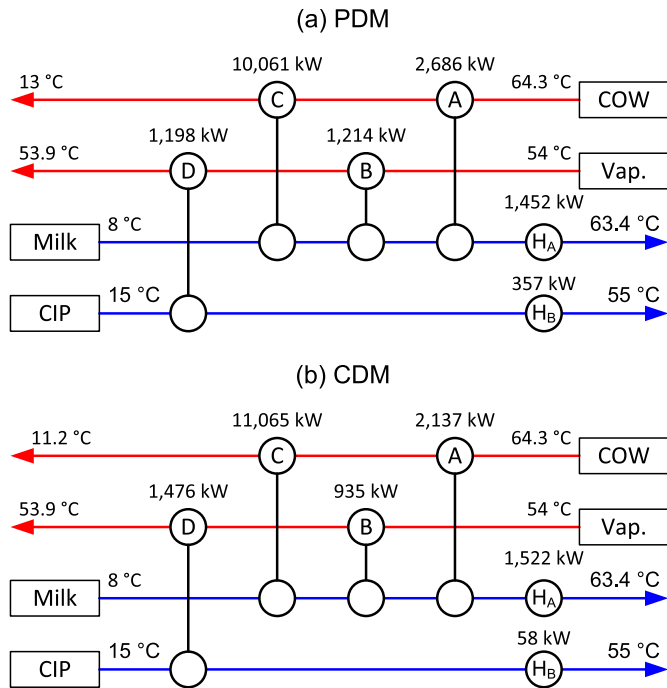


Fig. 11. Heat exchanger network design solutions of the PDM and CDM for MER B. Duties based on a milk powder plant producing 23  $t_p/h$ .

discoveries of resources can lead to dramatic reductions in price due to increased confidence in long term energy supply. A prime example of this has been the rapid growth of shale oil and gas recovery in the United States and Canada. On the other hand, cost estimation invariably involves significant errors even with the best available data. It is important, therefore, to test a wide range of utility-capital ratios ( $I_{ut}/I_{cap}$ ) to understand the impact on the final solution. Fig. 12 presents the results for total area and heat recovery efficiency for utility-capital ratios between 0.05 and 1.95. A utility-capital ratio of unity is the solution for the current costs. The heat recovery efficiency is based on a maximum heat recovery of 16,401 kW, which was obtained using Pinch targeting with  $\Delta T_{min} \rightarrow 0$  °C. For the entire range of utility-capital ratios, Fig. 12 shows the MER B solutions, which uses a cyclic match to preheat the milk instead of a split, result in slightly more heat recovery than MER A, but at the expense of slightly increased total area.

## 5. Simple distillation case study

Process and utility stream data for the simple distillation process from Ref. [6] are given in Table 6. Heat exchangers are assumed to be counterflow and exchanger capital costs are estimated using

$$CC = 4000 + 500A^{0.83} \quad (41)$$

Table 5

A detailed comparison of PDM and CDM solutions for MER B.

HE	Duty [kW]		Area [m <sup>2</sup> ]		$\Delta T_{LM}$ [°C]		$\Sigma\theta$		dTC/dA [\$/kW/y]	
	PDM	CDM	PDM	CDM	PDM	CDM	PDM	CDM	PDM	CDM
A	2686	2137	241	211	5.6	5.1	0.72	0.76	-600	0
B	1214	935	108	145	7.5	4.3	0.56	0.56	-1232	0
C	10,061	11,065	723	1063	7.0	5.2	0.31	0.26	118	0
D	1198	1476	41	94	19.7	10.4	1.00	1.00	-3594	0
H <sub>A</sub>	1452	1277	25	22	29.2	28.8				
H <sub>B</sub>	357	79	19	8	9.6	5.0				

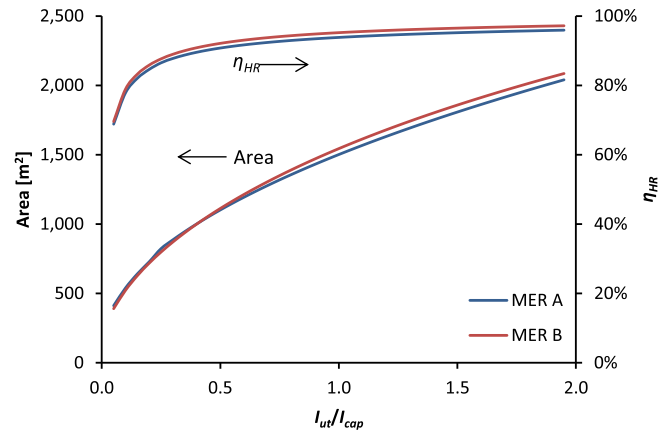


Fig. 12. The impact of the utility-capital ratio on the total area and heat recovery of the CDM solution for MER A and B.

To select an initial (pre-design) value of  $\Delta T_{min}$ , Gundersen applied a super targeting approach to calculate  $\Delta T_{min} = 10$  °C. As a result the HEN structure in Fig. 13 is based on  $\Delta T_{min} = 10$  °C. This work also calculates a post-synthesis optimisation of  $\Delta T_{min}$  (12.5 °C) to further minimise total cost. The CDM is applied to the HEN structure in Fig. 13 to solve for near cost optimal area allocation.

The CDM solution achieves a similar level of heat recovery to the PDM solutions although the CDM solution has one less cooler and one extra heater than the PDM. Table 7 compares the duty, area, log-mean temperature difference ( $\Delta T_{LM}$ ), overall heat duty flow-on factor ( $\Sigma\theta$ ) and dTC/dA, for each heat exchanger in the two solutions. In both solutions RE<sub>D</sub> has the highest duty with the PDM assigning a duty of 2200 kW and the CDM allocating 1933 kW. As suggested by the positive value for dTC/dA of \$111/kW/y for RE<sub>D</sub> in the PDM solution, the additional heat exchanger duty and area allocated to RE<sub>D</sub> in the PDM solution compared to the CDM solution comes at the expense of increased total cost.

Interestingly the duty of RE<sub>A</sub> in the PDM is only 65% of the duty of RE<sub>A</sub> in the CDM solution; yet the value of dTC/dA is positive for the PDM and zero for the CDM, which may appear counterintuitive. However one should note the significant difference in the overall heat duty flow-on factor,  $\Sigma\theta$ , which may be applied to calculate  $Q_{add}$  (Eq. (38)). Only 115 kW for RE<sub>A</sub> in the PDM is additional heat recovery ( $Q_{add}$ ) compared to 266 kW for the CDM solution. In calculating the CDM solution, RE<sub>B</sub> is a terminal exchanger due to utility C<sub>1</sub> being nil. Using the concept of the final RE on some streams as a TE, it was possible to achieve dTC/dA of zero for all RE's in the CDM solution and obtained the lowest total cost.

The PDM and CDM solutions are compared to four solutions for the same problem generated by Non-Linear Programming, Superstructure, Hyperstructure and Synheat computer programming

**Table 6**  
Process and utility stream data for a simple distillation process from Ref. [6].

Stream	Code	$T_s$ [°C]	$T_t$ [°C]	$C$ [kW/°C]	$Q$ [kW]	$h$ [kW/ m <sup>2</sup> °C]	$p$ [\$/y/ kW]
Reactor outlet	H1	270	160	18	1980	0.5	
Product	H2	220	60	22	3520	0.5	
Feed	C1	50	210	20	3200	0.5	
Recycle	C2	160	210	50	2500	0.5	
Steam	HU	250	249			2.5	200
Cooling water	CU	15	20			1.0	20

HEN synthesis methods (Table 8) given in Ref. [3]. The CDM solution requires 11% less HEN area, recovers a similar quantity of heat, and saves 7.6% of the total cost when compared to the PDM with  $\Delta T_{min} = 12.5$  °C. The programming synthesis methods developed new HEN structures that reduced total cost. Even so, for this case study the CDM obtained the lowest total cost using the same structure as the PDM. The programming methods also increased network complexity as indicated by the increased number of stream splits and exchanger units, whereas the CDM focuses solely on cost optimal area allocation within a HEN. However the programming methods were constrained to obtain the same heat recovery target as the PDM with  $\Delta T_{min} = 10$  °C and, as a result, the total costs achieved by the programming methods do not necessarily represent the best solution the method could find without such a constraint.

**6. Method limitations and future developments**

The CDM has a number of limitations, which will likely be areas of future work:

- Optimisation methods rely on obtaining accurate stream data, utility prices, and capital cost functions. Gaining an additional 5% cost savings through optimisation can only be translated to actual industrial savings by supplementing the optimisation with quality information.
- The method does not deal with synthesis of the HEN. Future work will look at how the CDM can be useful in HEN synthesis.
- Solutions to the CDM are calculated iteratively. Like most programming synthesis methods, there is substantial incentive to automate procedures and algorithms to find the best solution for a given method. The CDM may be implemented in software such as Excel™ or Matlab™ to automatically iterate and solve the necessary equations.
- The method looks at only the variable cost components of the total cost function. To an extent, the method overcomes this problem by viewing some RE's as a terminal recovery exchanger that is required to recover sufficient heat for the stream to reach its target temperature.

**Table 7**  
A detailed comparison of PDM ( $\Delta T_{min} = 12.5$  °C) and CDM solutions for the distillation process.

HE	$Q$ [kW]		$A$ [m <sup>2</sup> ]		$\Delta T_{LM}$ [°C]		$\Sigma\theta$		$dTC/dA$ [\$/kW/y]	
	PDM	CDM	PDM	CDM	PDM	CDM	PDM	CDM	PDM	CDM
A	754	1166	51	119	60	39	0.15	0.23	21	0
B	1000	814	264	210	15	16	1.00	1.00	4	0
C	1044	1159	179	254	23	18	0.77	0.71	-126	0
D	2200	1933	516	312	17	25	0.24	0.31	111	0
H <sub>1</sub>	0	453	0	22	-	50				
H <sub>2</sub>	702	175	36	10	46	41				
C <sub>1</sub>	226	0	5	0	149	-				
C <sub>2</sub>	276	428	17	25	49	52				

- Stream split fractions are optimised individually, which increases the degrees of freedom.
- Heat transfer film coefficients and heat exchanger pressure drop are assumed independent of heat exchanger area. These assumptions are made because the trade-off between heat transfer and pressure drop is strongly dependent on the physical heat exchanger dimensions, which in most cases is undetermined at the time of designing the network. If the information is available, correlations between overall/individual stream film coefficients and area may be included by making the necessary adjustments to the derivation of  $dQ/dA$ . A correlation between pumping costs, i.e. pressure drop, and area may also be added to the overall cost derivative. This is an area of future development of the method.
- The controllability of a network is not considered in the present method. The CDM attempts to optimally allocate area based on a number of simplified constraints and often eliminates the need of some utility exchangers. However by doing so, the network solution may encounter control difficulties. For example if the solution increases the number of paths or decreases the number of heat loops, there is an increase in the degrees of freedom resulting in improved control. Future work may look at how the controllability of a HEN and the cost of process control can be included in the overall optimisation. One possible method is to incorporate a controllability index [14] to identify solutions with serious control issues so that these issues may be resolved.

**7. Conclusion**

The novel Cost Derivative Method (CDM) derived in this paper has significant potential for improving the area allocation in Heat Exchanger Networks (HEN) to reduce total cost without increasing network complexity. Unlike the Pinch approach, the CDM (near) optimally accounts for differences in film coefficients, heat exchanger types and arrangements, exchanger cost functions, and

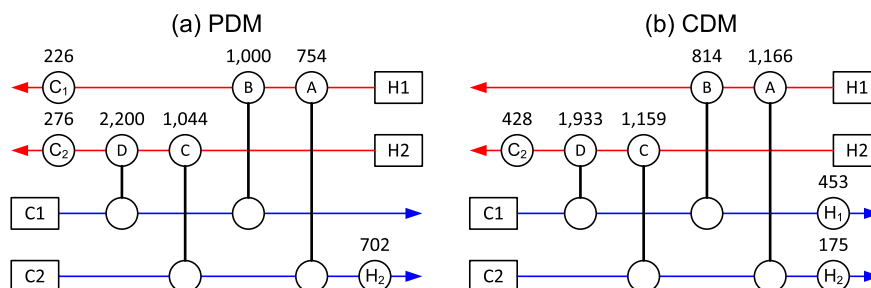


**Fig. 13.** Heat exchanger network for a distillation process using the PDM with  $\Delta T_{min} = 12.5$  °C and the CDM. Duties are in kW.

**Table 8**  
Comparison of heat integration solutions for the distillation process. Non-Linear Programming (NLP), Superstructure, Hyperstructure and Synheat solutions are taken from Ref. [3].

	CDM	PDM ( $\Delta T_{\min}$ opt.)	PDM	NLP	Super-structure	Hyper-structure	Synheat model
$\Delta T_{\min}$ ( $^{\circ}\text{C}$ )	7.3	12.5	10.0	10.0	10.0	6.9	9.9
RE	4	4	4	4	4	4	5
UE	3	3	3	3	2	2	2
Splits	0	0	0	2	2	4	3
$\Sigma A$ ( $\text{m}^2$ )	952	1067	1244	1170	1148	1105	1065
$Q_r$ (MW)	5072	4998	5100	5100	5100	5100	5100
CC (\$/y)	222,037	235,242	261,486	251,120	247,842	232,927	239,047
UC (\$/y)	134,139	150,396	128,000	128,000	128,000	128,000	128,000
TC (\$/y)	356,176	385,638	389,486	379,120	375,842	360,927	367,047

utility pricing. The new CDM is applied to a simple distillation process and a milk powder plant to illustrate its effectiveness in reducing total cost. For the distillation case study, total cost was reduced by 7.1% compared to the best Pinch Design Method (PDM) solution and, for the milk powder plant case study, the total cost was decreased by 5.8% compared to the PDM solution. Cost reductions between 5 and 6% may appear trivial; however, the CDM has much wider appeal since the CDM is generally applicable. In industries such as oil refining where energy represents a larger portion of the total production cost and the scale is a couple of magnitudes larger, a 5–6% savings can be in the order of tens of millions rather than tens of thousands.

## References

- [1] S. Ahmad, R. Smith, Targets and design for minimum number of shells in heat exchanger networks, *ChERD* 67 (1989) 481–494.
- [2] M.A. Ait-Ali, D.J. Wilde, Optimal area allocation in multistage heat exchanger systems, *J. Heat. Transf.* 102 (1980) 199–201.
- [3] M. Escobar, J.O. Trierweiler, Optimal heat exchanger network synthesis: a case study comparison, *Appl. Therm. Eng.* 51 (2013) 801–826.
- [4] K.C. Furman, N.V. Sahinidis, A critical review and annotated bibliography for heat exchanger network synthesis in the 20th century, *Ind. Eng. Chem. Res.* 41 (2002) 2335–2370.
- [5] M. Gorji-Bandpy, H. Yahyazadeh-Jelodar, M. Khalili, Optimization of heat exchanger network, *Appl. Therm. Eng.* 31 (2011) 779–784.
- [6] T. Gundersen, A Process Integration PRIMER, SINTEF Energy Research, Trondheim, Norway, 2000.
- [7] W.M. Kays, A.L. London, Compact Heat Exchangers, third ed., Krieger Pub. Co., Malabar, USA, 1998.
- [8] B. Linnhoff, E. Hindmarsh, The pinch design method for heat exchanger networks, *Chem. Eng. Sci.* 38 (1983) 745–763.
- [9] A. Nemet, J.J. Klemeš, Z. Kravanja, Minimisation of a heat exchanger networks' cost over its lifetime, *Energy* 45 (2012) 264–276.
- [10] G.T. Polley, M.H. Panjeh Shahi, F.O. Jegede, Pressure drop considerations in the retrofit of heat exchanger networks, *ChERD* 68 (1990) 211–220.
- [11] U.V. Shenoy, Heat Exchanger Network Synthesis: Process Optimization by Energy and Resource Analysis, Gulf Professional Publishing, Houston, USA, 1995.
- [12] T.G. Walmsley, M.R.W. Walmsley, M.J. Atkins, J.R. Neale, Improving energy recovery in milk powder production through soft data optimisation, *Appl. Therm. Eng.* 61 (2013a) 80–87.
- [13] T.G. Walmsley, M.R.W. Walmsley, A.S. Morrison, M.J. Atkins, J.R. Neale, A derivative method to minimising total cost in heat exchanger networks through optimal area allocation, *Chem. Eng. Trans.* 35 (2013b) 1171–1176.
- [14] D.L. Westphalen, B.R. Young, W.Y. Svrcek, A controllability index for heat exchanger networks, *Ind. Eng. Chem. Res.* 42 (2003) 4659–4667.
- [15] B.R. Young, R. Tellez, W.Y. Svrcek, Towards integrated process and control system synthesis for heat-integrated plants, *Can. J. Chem. Eng.* 84 (2006) 219–229.

**Article 2:**

*A Novel Heat Exchanger Network Bridge Retrofit Method using  
the Modified Energy Transfer Diagram*

Lal, N., **Walmsley, T.G.**, Walmsley, M.R.W., Atkins, M.J., Neale, J.R.,  
2018.

Energy 155, 190–204.

DOI: 10.1016/j.energy.2018.05.019

Elsevier



# A novel Heat Exchanger Network Bridge Retrofit method using the Modified Energy Transfer Diagram

Nathan S. Lal<sup>a</sup>, Timothy G. Walmsley<sup>b,\*</sup>, Michael R.W. Walmsley<sup>a</sup>, Martin J. Atkins<sup>a</sup>, James R. Neale<sup>a</sup>

<sup>a</sup> Energy Research Centre, School of Engineering, University of Waikato, Private Bag 3105, Hamilton, New Zealand

<sup>b</sup> Sustainable Process Integration Laboratory – SPIL, NETME Centre, Faculty of Mechanical Engineering, Brno University of Technology - VUT Brno, Technická 2896/2, 616 69, Brno, Czech Republic

## ARTICLE INFO

### Article history:

Received 15 February 2018

Received in revised form

28 April 2018

Accepted 3 May 2018

Available online 4 May 2018

### Keywords:

Process retrofit

Pinch analysis

Heat exchanger network

Energy transfer diagram

Heat recovery

## ABSTRACT

The aim of this paper is to develop a novel method for the retrofit of Heat Exchanger Networks based on Bridge Retrofit analysis. The method identifies Retrofit Bridges that correspond to energy saving modifications using two new proposed tools: The Heat Surplus–Deficit Table and the Modified Energy Transfer Diagram. These tools both allow the identification and quantification of Retrofit Bridges. These tools have been developed following conventional Pinch Analysis tools such as the Composite Curve and Grand Composite Curve. The connection between the conventional Heat Exchanger Network synthesis tools and the proposed retrofit tools is established to improve understanding of the method and relate it to what is currently used in both literature and industry. The method is demonstrated with a simple illustrative example and a more detail paper mill case study. The paper mill incorporates a paper machine and paper recycling plant and is co-located with a Kraft pulp mill in New Zealand. Results from the retrofit method suggest a retrofit design that will achieve an annualised profit of NZD 570,000/y (USD 414,000/y) with a payback of 2.4 y.

© 2018 Elsevier Ltd. All rights reserved.

## 1. Introduction

Increasing global focus on energy generation and consumption as well as its cost, sustainability, and environmental impacts, have provided the industrial sector with a strong incentive to look for opportunities for process improvement [1] and process sustainability through renewable energy [2]. Process improvement can be achieved through Process Integration to reduce energy consumption and environmental impacts for the same production and/or through debottlenecking to increase production using the same equipment and lower specific energy consumption [3]. A key pathway to improve Process Integration is through the retrofit of the Heat Exchanger Network (HEN) [4]. The subject of this paper focuses on HEN retrofit.

There are three general approaches to deciding how to retrofit a HEN [5]: (1) Pinch Analysis (PA)-based graphical procedures, (2) Mathematical Programming (MP) through the formulation of a retrofit superstructure and its optimisation, and (3) a combination

of both graphical and Mathematical Programming techniques. PA techniques rely on thermodynamics to express the potential retrofit heat savings for a HEN using graphs. Inherent with these procedures is a high degree of input from the engineer, which helps lead to practical solutions that meet all the requirements of the considered process and site. Graphical approaches often double as effective communication tools to walk industrial engineers through the process from which a solution is derived. The disadvantage of PA techniques is the “optimal” solution will rarely be obtained. MP, on the other hand, seeks to find the global optimal solution given a set of variables, superstructure relationships, and constraints. Besides the model formulation, there is minimal opportunity for input by the engineer. Most Mathematical Programming models for both inputs and outputs are often displayed from a command line, creating a key barrier to the communication of the ideas with industry. This work continues a recent resurgence in the development of graphical PA techniques for HEN retrofit.

PA encompasses well-known tools such as Composite Curves (CC) and Grand Composite Curves (GCC) [6] that also lead to Total Site Heat Integration tools such as Total Site Profiles and Site Utility Grand Composite Curves [7]. These sets of tools have been effectively applied to address the problem of individual process and

\* Corresponding author.

E-mail address: [walmsley@fme.vutbr.cz](mailto:walmsley@fme.vutbr.cz) (T.G. Walmsley).

Nomenclature		Subscripts	
<i>Roman</i>		cont	contribution
A	Area (m <sup>2</sup> )	c	cold
ACC	Annualised Capital Cost (NZD/y)	h	hot
b	Capital cost proportional constant (NZD/m <sup>2</sup> )	min	minimum
CI	Capital Investment (NZD)	<i>Abbreviations</i>	
CP	Specific Heat Capacity Flow Rate (kW/°C)	C#	Cooler
f	Fixed investment cost (NZD)	CC	Composite Curves
H	Enthalpy (kW)	E#	Exchanger
H*	Superimposed Enthalpy Cascade (kW)	E-PTA	Exchanger Problem Table Algorithm
LF	Lang Factor	EGCC	Exchanger Grand Composite Curve
n	Capital cost exponent	ETD	Energy Transfer Diagram
PB	Simple Payback Period (y)	GCC	Grand Composite Curve
Q	Exchanger Duty (kW)	H#	Heater
S	Utility Savings (NZD/y)	HEN	Heat Exchanger Network
T	Temperature (°C)	HSDT	Heat Surplus-Deficit Table
T*	Shifted Temperature (°C)	HTE	Heat Transfer Enhancement
TRP	Total Retrofit Profit (NZD/y)	MER	Maximum Energy Recovery
UC	Utility Cost (NZD/y)	METD	Modified Energy Transfer Diagram
<i>Greek</i>		N#	New Exchanger
Δ	difference between two states	PA	Pinch Analysis
		SCC	Shifted Composite Curve

Total Site integration and provide an avenue to convince the industrial end-user to adopt the solution. As a result, PA and Total Site Heat Integration have successfully been applied to define how new chemical and processing plants and sites can increase overall energy efficiency and environmental performance. However, the insights from PA and Total Site Heat Integration are often aggregated across an entire process or site such that the fidelity of a retrofit problem, including the design of the current HEN, is lost.

Many recent studies have sought to develop HEN retrofit methods that maximise energy savings through improved design. Smith et al. [8] reviewed and extended the Network Pinch retrofit method to provide a coherent step-wise design strategy to move from an existing level of integration towards maximum energy recovery in a sequence of steps. Ochoa-Estopier et al. [9] undertook a comprehensive three-part industrial case study that combined both process models of a Crude-oil Distillation system [9] and HEN retrofit method and model [10] into a single optimisation framework [11] to generate a highly integrated, low energy solution. Realizing that adding new exchangers or repiping existing ones are often costly, Jiang et al. [12] focused on increasing energy savings for a fixed network structure developing sensitivity curves to predict how increases in heat exchanger area may provide utility reduction. This was followed by Akpomimie and Smith [13] who undertook greater depth of heat exchanger modelling in conjunction with the installation of Heat Transfer Enhancement (HTE) to identify the increase in the duty of critical heat exchangers. Next, Pan et al. [14] added pressure drop constraints and fouling mitigation potential into the retrofit analysis of using HTE in a fixed HEN structure. Akpomimie and Smith [15] combined their team's recent efforts on both structural and enhancement type retrofit methods to comprise an overall cost-effective strategy to increase energy efficiency. Ayotte-Sauvé et al. [16] applied a Mixed Integer Nonlinear Programming technique to solve a retrofit superstructure using a step-wise approach with the possibility of user intervention after each step.

The challenge of developing new PA-based tools that use thermodynamics to express the current HEN and potential retrofit

modifications has been recognised in several recent papers. Recent examples include the development of Advanced Composite Curves [17], the extension of the Stream Temperature versus Enthalpy Plot to HEN retrofit [18], new Temperature Driving Force Curves [19], an extended Network Pinch method [20], a Shifted Retrofit Thermodynamic Grid Diagram [21], and Bridge Analysis based on the new Energy Transfer Diagram [22]. Each of these approaches deserves further consideration and development with the selected focus of this paper being to extend the Energy Transfer Diagram. Bonhivers et al. [22] recognised the need to develop a new retrofit tool that synthesised the HEN with the background process. The new tool was the Energy Transfer Diagram (ETD). In addition, Bonhivers et al. [23] explained a set of concepts related to the ETD with emphasis on the advantage of a Retrofit Bridge over a Path Retrofit. The ETD provides a visual and numerical expression of each individual component of a HEN and its potential to be reintegrated more efficiently. The heat exchanger pockets that comprise the ETD show where heat is transferred across the Pinch, which heat exchangers have excessive temperature driving forces that can be better exploited, and target the potential for retrofit. Combined with these efforts, a new retrofit method based on the ETD was developed called Bridge Analysis. Similar to the conventional Pinch-based Loops and Paths retrofit method [24], Bridge Analysis aims to find energy savings pathways between cold and hot utility use. However, these pathways are not constrained to the present structure of the HEN, which provides a key advantage in that all combinations of bridges including those attained by structural HEN modification can be found [22]. Later, Bonhivers et al. [25] took the concept a step further to develop a heat exchanger load diagram followed by a hybrid CC and ETD plot [26].

In the four years since publication, Bridge Analysis and the ETD has not received much attention beyond Bonhivers and co. At present, there are three published case studies using the technique: (1) Bonhivers et al. [25] for a Kraft pulp mill, (2) Jahromi and Beheshti [27] for a methanol-to-propylene plant, and (3) Chen et al. [28] with the optimisation of a single-effect ammonia-water absorption system. Despite its usefulness and validity, its

communication and connection with well-known Pinch tools needed greater consideration to be understood by many in the Process Integration research community and improve its uptake. As examples, the original works plotted enthalpy on the y-axis and temperature on the x-axis, which runs counter to the convention of nearly all published research in the PA space [3]. The ETD diagram was plotted in an uncoordinated random colour scheme that provided little to the HEN characterisation and offered no assistance to the bridge identification procedure [25]. The link between the ETD and PA tools – CC and GCC – was initially overlooked [22] while later attempts focused on comparing end products rather than building and linking the ETD method with standard PA techniques and terms [29]. The procedure was chiefly explained in graphical terms without reference to the supporting tables and algorithms. These deficiencies from the previous studies represent gaps in the literature, many of which are the target of the current study.

The aim of this paper is to develop an improved HEN Bridge Retrofit method through the development of novel graphical and tabular tools that more effectively support the identification of step-wise retrofit changes for an existing HEN that results in energy savings and total cost reduction. The new graphical and tabular tools are the Modified Energy Transfer Diagram (METD) and the Heat Surplus-Deficit Table (HSDT). The METD appropriately represents the cascade and distribution of heat from the hot utilities to the cold utilities. The METD shows the heat surpluses and deficits within the HEN to improve bridge analysis and the identification of new heat exchanger matches. The HSDT allows for the numerical evaluation of these new exchanger matches. The method will be demonstrated with a simple illustrative example and a paper mill case study, which is co-located with a Kraft Mill in New Zealand.

The novel contributions of this research to literature are:

- The development of the Modified Energy Transfer Diagram as a graphical tool for HEN retrofit analysis, which uses colour to provide more insights into the retrofit problem.
- The development of the new Heat Surplus-Deficit Table as a numerical tool for HEN retrofit analysis, which has the greater potential for future automation and scalability.
- The application of the novel retrofit design method to an illustrative example and a Paper Plant.

## 2. Theory

### 2.1. Pinch Analysis

In conventional PA, there are two CCs, a cold CC and a hot CC, representing all cold streams and all hot streams as shown in

Fig. 1a. After performing appropriate temperature shifts for a minimum temperature driving force,  $\Delta T_{\min}$ , the shifted cold CC is moved to the left and pinched against the shifted hot CC, as shown for the Shifted Composite Curves (SCC) in Fig. 1b. The horizontal enthalpy difference between the hot and cold CCs is the basis for generating the Grand Composite Curve (GCC) in Fig. 1c. In short, the GCC defines which temperature intervals have heat surpluses and which have heat deficits.

The GCC is one of the most powerful tools in Pinch Analysis but is not as practical for retrofit analysis. The use of the GCC in retrofit analysis is limited because it does not provide any information about the individual streams nor is it able to represent an existing network. The GCC does, however, allow the Pinch Temperature and minimum energy targets to be determined, i.e. the minimum utility targets. These targets set the limits for what is thermodynamically achievable for a given minimum approach temperature and provide the goals for the HEN design. The GCC also provides information about the near Pinch point(s), the presence of heat recovery 'pockets', and multiple utility placement options.

### 2.2. Exchanger Grand Composite Curve and Energy Transfer Diagram

Many researchers have made attempts to adapt the GCC to retrofit analysis, and the Energy Transfer Diagram (ETD) is the result of one recent attempt. The ETD is constructed by combining multiple Energy Transfer Curves [22], which are more appropriately termed Exchanger GCCs (EGCC) to align with standard PA definitions. EGCCs are calculated for each individual heat recovery exchanger and utility exchanger in the HEN. While the GCC is constructed from the entire set of stream data, an EGCC is based on a particular stream match with their inlet (supply) and outlet (target) temperatures as shown in Fig. 2. The shape of the EGCC provides a lot of information as well. Large areas under the curve ( $T^* \cdot \Delta H$ ) enclosed with the y-axis indicate a large thermodynamic driving force across a significant duty. If near or crossing the Pinch region, this indicates that stream segments matched in an existing exchanger may be reintegrated to successfully transfer heat from a heat surplus being cooled, across the Pinch, to a heat deficit being heated, therefore reducing utility consumption. Small areas under the curve indicate that a match is already highly efficient with approach temperatures similar to the minimum. As a result, there is little opportunity to reintegrate the heat from the EGCC in a more effective way.

The ETD is constructed by stacking the EGCC of each individual exchanger in the HEN. The EGCC is plotted with temperature on the y-axis. The construction of the ETD is demonstrated in Fig. 3. To follow the original ETD style, the temperature and enthalpy axes are switched and the original formatting approach applied.

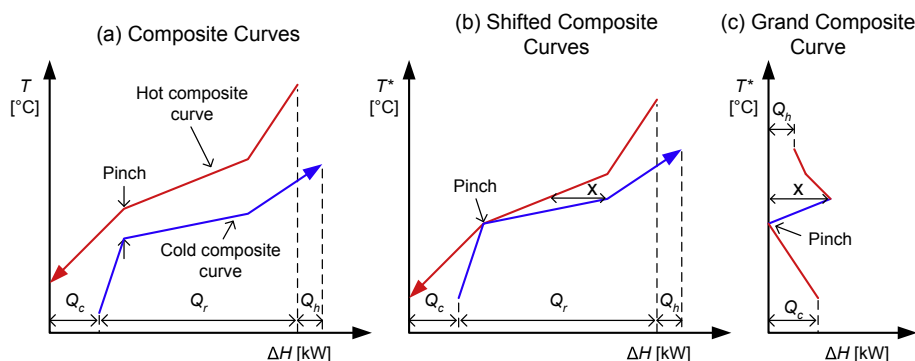


Fig. 1. Relationship between the (a) Composite Curves, (b) Shifted Composite Curves, and (c) Grand Composite Curve. Adapted from Klemeš et al. [3].

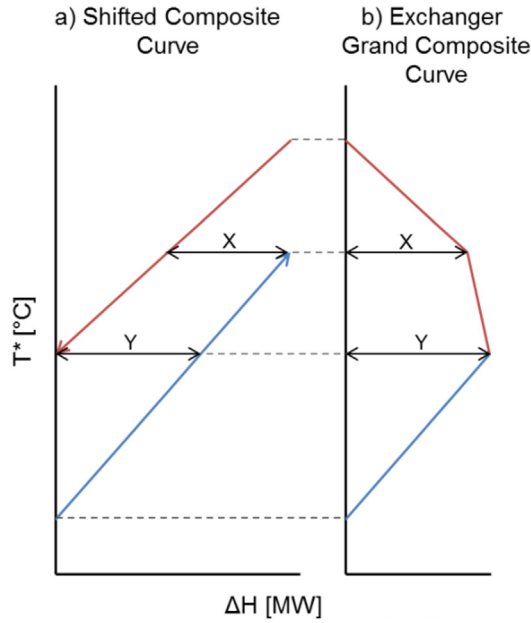


Fig. 2. Development of the EGCC for an individual exchanger.

An example of the ETD from Bonhivers et al. [30] is presented in Fig. 4. The ETD shows the current hot and cold utilities and the maximum energy savings. The maximum energy savings is determined by the lowest point in the outermost curve, which is the overall Heat Exchanger Network cascade profile. The maximum energy savings is effectively the minimum energy target from the conventional GCC. The lowest point is also the Pinch point for the

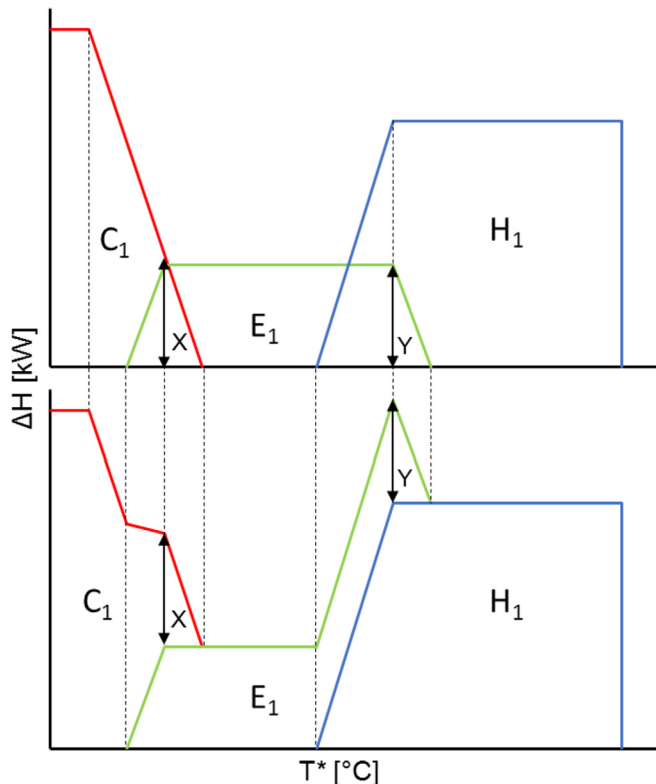


Fig. 3. Construction of the Energy Transfer Diagram using the EGCCs (top) and stacking them (bottom). Adapted from Bonhivers et al. [22].

system and can be used to identify any cross-Pinch heat transfer.

Conceptually, the ETD represents the cascade of process heat from the hot utilities to the cold utilities. The general aim of a retrofit is to improve the heat recovery performance of the HEN by minimising the degradation of cascaded process heat through the system leading to reduced hot and cold utility consumption. Effective HEN modifications can be identified using Bridge Analysis, which uses the ETD to identify pathways, or bridges, that indicate how the existing HEN can be modified to save energy. A Retrofit Bridge creates a path between a cooler and heater such that heat can be shifted away from cold utility exchangers to recovery exchangers and then to replace hot utility. Fig. 4 presents an example of a Retrofit Bridge using Bonhivers et al.'s original ETD method and notation. In this instance, the Retrofit Bridge identifies a pathway from cooler C1 to heat recovery exchanger E3 and then to heater H1.

A significant weakness of the original method of Bonhivers et al. [30] was the connection between the ETD and the idea of exchanger GCC level heat surplus/deficit. Each EGCC shows the heat surplus/deficit for individual temperature intervals but this was not translated over to the ETD. As a result, the identification of Retrofit Bridges on the original ETD is difficult due to the lack of clarity as to which segments are heat surpluses and which segments are heat deficits. In this paper, the ETD is modified, i.e. the Modified Energy Transfer Diagram – METD, to provide greater insight into a retrofit problem while also expressing the METD and its explanation using standard Pinch terms.

### 3. Method

The proposed method builds upon the original Bridge Analysis developed by Bonhivers et al. [30] and uses Process Integration and Pinch Analysis techniques. The proposed method introduces the METD and the HSDDT to improve the identification and qualification of bridges for the retrofit design with the goal of reducing the utility load of the HEN. Fig. 5 presents an overview of the proposed method.

#### Step 1 Extract Retrofit Steam Data

The HEN to be retrofitted will consist of any number of hot utilities (heaters), cold utilities (coolers), process-to-process exchangers (heat exchangers), and process streams. All streams in the HEN should already be matched and balanced such that stream target temperatures are achieving in the existing design. Like conventional PA, the following retrofit stream data is required: specific heat capacity flow rate, supply (inlet) and target (outlet)

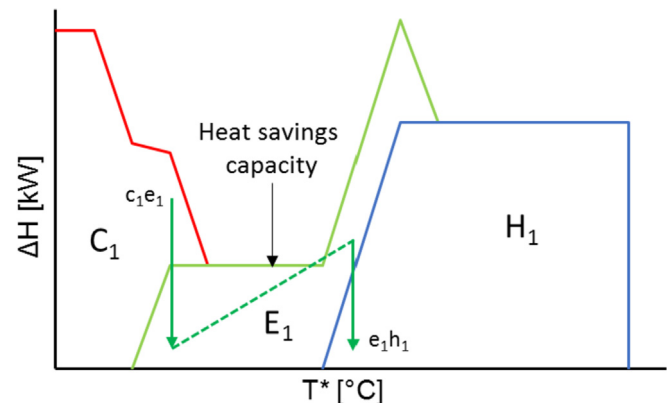


Fig. 4. Energy Transfer Diagram using original representation style. Adapted from Bonhivers et al. [22].

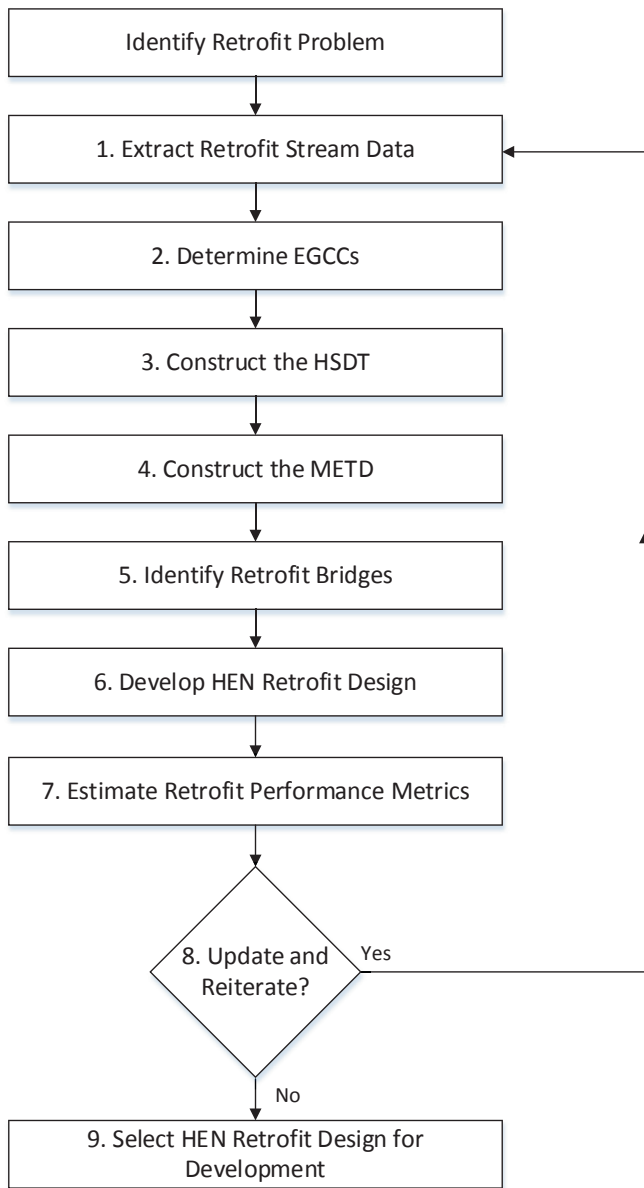


Fig. 5. Improved Bridge Retrofit Analysis method using the HSST and METD.

temperatures for each stream segment in each heat exchanger, existing exchanger duties, and the HEN structure. Either a global minimum approach temperature,  $\Delta T_{min}$ , or stream-specific minimum approach temperatures,  $\Delta T_{cont}$ , are set to determine the retrofit targets.

Step 2 Determine Exchanger Grand Composite Curves (EGCC)

In this step, the EGCCs for each individual exchanger are calculated using the Exchanger Problem Table Algorithm (E-PTA) (Table 1). Unlike conventional PA, where the Problem Table Algorithm [6] is used for the full set of stream data (without a defined HEN), the E-PTA considers each exchanger as a separate problem. The E-PTA is a simplified case of the standard Problem Table Algorithm where there is most often only one hot stream ( $CP_h$ ) and one cold stream ( $CP_c$ ) accounted for in each temperature interval and where, for a balanced heat exchanger, the first and last enthalpy values,  $H$ , must be zero. The  $\Delta H$  is the net heat surplus or deficit within each temperature interval. The heat surplus/deficit

Table 1  
Exchanger problem table algorithm – E-PTA.

$T^*$ (°C)	$\Delta T^*$ (°C)	$CP_{net}$ (kW/°C)	$\Delta H$ (kW)	$H$ (kW)
$T_1$	$T_1 - T_2$	$(CP_h - CP_c)_{1-2}$	$(\Delta T \cdot CP_{net})_{1-2}$	$H_1 = \Delta H_{HU,E}$
$T_2$	$T_2 - T_3$	$(CP_h - CP_c)_{2-3}$	$(\Delta T \cdot CP_{net})_{2-3}$	$H_1 + \Delta H_{1-2}$
$\vdots$	$\vdots$	$\vdots$	$\vdots$	$\vdots$
$T_n$	$T_{n-1} - T_n$	$(CP_h - CP_c)_{[n-1]-n}$	$(\Delta T \cdot CP_{net})_{[n-1]-n}$	$H_{n-1} + \Delta H_{[n-1]-n}$

values provide valuable information about opportunities for heat in existing heat exchanger matches may be re-integrated through retrofits to achieve external heat savings. The final column in Table 1 is the overall heat cascade,  $H$ . The initial value at the beginning of the cascade is the total hot utility demand by the heat exchanger,  $\Delta H_{HU,E}$ . For recovery exchangers and cold utility matches,  $H_1$  is zero while for hot utility exchangers  $H_1$  is the hot utility duty for the exchanger.

The E-PTA is repeated multiple times considering each individual heat exchanger as separate cases. The EGCC plots the shifted temperatures,  $T^*$ , on the y-axis with the heat cascade,  $H$ , on the x-axis. When formulating the  $T^*$  intervals, it is strongly recommended to include the shifted temperatures for all heat exchangers in every E-PTA. By doing so, the temperature intervals for each EGCC will match, simplifying the calculation of the METD. The EGCCs provide valuable information that can be used in the following steps.

Step 3 Construct the HSST

The Heat Surplus-Deficit Table – HSST, Table 2, is the collection of  $\Delta H$  columns (Table 1) from each EGCC. It is the first tool that can be applied to identify and quantify Retrofit Bridges. The recommended order of  $\Delta H$  columns is to write all coolers, followed by recovery exchangers and, lastly, heaters. The HSST enables tabular visualisation and identification of Retrofit Bridge options with the HEN that lead to energy savings. In the HSST, positive  $\Delta H$  values refer to heat surpluses while negative  $\Delta H$  values refer to heat deficits.

Step 4 Construct the METD

The METD is constructed by stacking each EGCC (determined in Step 2) by superimposing each profile on top of one another. The tabular data for the METD is calculated as:

$$H_{j(i)}^* = H_{j(i)} + H_{j(i-1)} \tag{1}$$

Where  $H$  is the cascade from the final column of Table 1,  $H^*$  is the cascade of superimposed  $H$  values, subscript  $j$  refers to each temperature interval, and subscript  $i$  refers to each EGCC.

Using the  $H^*$  data set, the outlines of each EGCC can be plotted to

Table 2  
Heat surplus-deficit table – HSST.

$T^*$ (°C)	$\Delta H_{(C)}$ (kW)	$\dots$	$\Delta H_{(R)}$ (kW)	$\dots$	$\Delta H_{(H)}$ (kW)
$T_1$	$\Delta H_{1-2(C)}$	$\dots$	$\Delta H_{1-2(R)}$	$\dots$	$\Delta H_{1-2(H)}$
$T_2$	$\Delta H_{2-3(C)}$	$\dots$	$\Delta H_{2-3(R)}$	$\dots$	$\Delta H_{2-3(H)}$
$\vdots$	$\vdots$	$\dots$	$\vdots$	$\dots$	$\vdots$
$T_n$	$\Delta H_{[n-1]-n(C)}$	$\dots$	$\Delta H_{[n-1]-n(R)}$	$\dots$	$\Delta H_{[n-1]-n(H)}$

form the METD with temperature on the y-axis and enthalpy on the x-axis. The line colour convention for the METD applies red to represent segments with heat surplus, blue for heat deficit segments, and black for zero heat surplus/deficit. The HSDT provides the required information to know which segments are heat surplus, deficit, or neutral.

The METD, as an improved version of the ETD, aims to increase the visual comprehension of the retrofit problem and strengthen its relationship with conventional PA tools, especially the GCC. The key differences between the ETD and the METD are:

- The temperature and enthalpy axes are switched such that the METD follow PA convention becoming more easily understood by the Process Integration community.
- The use of colour is different where the METD shows which segments represent heat surpluses and deficits and the original ETD coloured EGCC to distinguish between exchangers. As a result, the METD accurately identifies and quantifies the maximum heat savings of a Retrofit Bridge whereas the ETD lacks the required information precisely identify a Retrofit Bridge on its own.
- The METD, in some cases, contains stream labels for the heat surplus/deficit segments to improve connection back to the required modifications to achieve the full energy savings of a Retrofit Bridge.

#### Step 5 Identify Retrofit Bridges

Retrofit bridges are identified using both the METD and the HSDT by finding sets of matches that link a cooler to a heater. Each match within the bridge matches a heat surplus with a heat deficit. Surpluses are represented in the METD as red curves and as positive numbers in the HSDT. Deficits are represented in the METD as blue curves and as negative numbers in the HSDT. The following rules can be applied when identifying the retrofit bridges:

- A bridge only links a single cooler to a single heater.
- A bridge is a set of matches between surpluses and deficits.
- Each surplus or deficit refers to a hot or cold stream, respectively.
- A surplus can only be matched with a deficit within the same temperature interval or a lower temperature interval. This complies with the Second Law of Thermodynamics.
- With respect to the METD, the bridge moves up the cascade following the temperature axis.

After identifying the retrofit bridges, the bridges can be quantified based on the resulting energy savings, or utility reductions. Each match allows a certain amount of heat transfer based on the available enthalpies of the surplus and deficit within the given temperature interval. The allowable heat transfer of a match is limited by the lesser of the surplus or deficit enthalpies, like a bottleneck. The lowest allowable heat transfer out of all the matches is then taken as the overall energy savings of the entire bridge. The quantification can be done using the x-axis on the METD but is much easier when using the HSDT as the HSDT is the numerical representation of the METD.

#### Step 6 Develop HEN retrofit design

The retrofit bridges identified in the previous step indicate where matches could be made to increase heat recovery and reduce utility load. The set of matches includes existing matches and non-existing matches. To complete the retrofit, new exchangers are added to match the streams that weren't already matched, as indicated by the selected bridge.

The hot and cold utility are each then reduced according to the savings indicated by the bridge and the HEN is rebalanced. Rebalancing will often require adding additional heat transfer area to the starting exchangers to compensate for changes in temperatures and duties. The addition of new exchangers and new heat transfer area are the only retrofit modifications to be considered in this paper. The result is a retrofitted HEN.

#### Step 7 Estimate retrofit performance metrics

Currently, the METD offers little insight into the cost of a retrofit and further steps are required to compare the designs on an economic basis. For each design option, the utility savings (S), annualised capital cost (ACC), total retrofit profit (TRP), and simple payback (PB) were determined.

The utility savings (S) is the difference between the initial and final utility cost (UC) as defined as follows:

$$\Delta S = UC_i - UC_f = \sum_{i=1}^n (p_{h,i} \Delta Q_{hu,i}) + \sum_{j=1}^m (p_{c,j} \Delta Q_{cu,j}) \quad (2)$$

Where  $p_{h,i}$  is the price of hot utility  $i$ ,  $p_{c,j}$  is the price of cold utility  $j$ ,  $\Delta Q_{hu,i}$  is the reduction in duty of hot utility  $i$ , and  $\Delta Q_{cu,j}$  is the reduction in duty of cold utility  $j$ .

The capital investment (CI) for a retrofit is estimated using a capital cost estimation correlation for the specified type of heat exchanger multiplied by a Lang Factor (LF), as shown as follows:

$$CI = (f + bA^n)LF \quad (3)$$

Where  $f$  is the fixed investment cost and  $b$  and  $n$  are capital cost function constants.

The ACC is calculated as the product of the estimated CI of the retrofit project and the annualization factor, which depends on the specified discount rate and project life.

TRP is the amount of annual profit gained from implementing a retrofit and is calculated as follows:

$$TRP = \Delta S - ACC \quad (4)$$

Additional piping and pumping costs are not explicitly stated in Eq. (4) and will be the subject of future work.

The PB was calculated as follows:

$$PB = \frac{CI}{\Delta S} \quad (5)$$

#### Step 8 Update HEN design and reiterate

The proposed method can be reiterated to provide step-wise retrofit designs. After application of a Retrofit Bridge, the new HEN becomes the input to another iteration of retrofit identification and quantification. Once a Maximum Energy Recovery network (MER) is obtained, resetting the HEN provides the opportunity to explore a different sequence of Retrofit Bridges.

#### Step 9 Select HEN retrofit design for detailed business case development

After all potential bridges have been identified and the corresponding HEN retrofit designs have been costed, a HEN retrofit design can be selected for further business case development. TRP and PB guide the decision-making process to select retrofit options that are attractive to present to the end-user.

### 4. Illustrative example

#### 4.1. Retrofit problem and stream data extraction

To demonstrate the method, a four-stream illustrative example is used. The four-stream problem with HEN has been adapted from Klemeš et al. [31] to demonstrate HEN retrofit with the goal of reaching a MER. The adapted HEN is presented in Fig. 6. Currently, there are two heat exchangers (E1 and E2), two cold utilities/coolers (C1 and C2), and one hot utility/heater (H1) that transfer heat between the four streams (F1 to F4). The heater duty is 2,700 kW and the combined cooler duty is 2,950 kW. The example applies a global  $\Delta T_{cont}$  of 5 °C and the Pinch temperature is 145 °C (150 °C hot and 140 °C cold).

The retrofit stream data, Table 3, are the specific heat capacity flowrates and supply and target temperature limits for each stream, the duties and temperature limits of each exchanger and utility, and the existing matches. The grid diagram in Fig. 6 contains all necessary information to formulate Table 3, which forms the input for an Excel spreadsheet calculation tool to construct the HSDT and METD.

#### 4.2. Retrofit analysis using the Heat Surplus-Deficit Table

Retrofit analysis can be conducted using both the HSDT and the METD. In this section, the use of the HSDT will be demonstrated. The HSDT is constructed using the E-PTA of each of the five heat exchangers (including utility exchangers) that comprise the original network. Considering the HSDT in Fig. 7, many different Retrofit Bridges can be identified. In this section, only one will be demonstrated. This example identifies Retrofit Bridge Option 1 that will be discussed in more detail in later sections as well. Following the arrows, one finds a surplus of 2,350 kW in C1 can match with a deficit of -1,480 kW in E1. The match is allowed as the temperature of the deficit is always equal to or lower than the temperature of the surplus. Following from the deficit in E1 to the potential surplus due to re-integration, the METD shows a surplus of 1,250 kW in E1 can match with a deficit of -1,500 kW in H1. E1 has another 230 kW of surplus that cannot further fulfil the deficit in H1 because but its temperature is lower. Including the additional 230 kW in the match violates the basic thermodynamic law of heat must transfer from heat to cold. For a shifted temperature plot, this law extends to horizontal heat transfer, which represents heat transfer at the minimum approach temperature. The heat surplus in E1 limits the maximum overall savings of Retrofit Bridge Option 1 to 1,250 kW, acting as a bottleneck and Pinch point to retrofit energy savings.

The bridge information from the HSDT is then translated into an implementable retrofit design. The allowable modifications include new exchanger units, additional heat transfer area, re-piping of a heat exchanger, stream splits, or a combination of modifications.

**Table 3**  
Stream data for the four-stream retrofit problem from Klemeš et al. [31].

Unit	Stream	$T_s$ (°C)	$T_t$ (°C)	$\Delta H$ (kW)
H1	F3	140.0	230.0	2,700
E1	F4	200.0	104.0	2,400
E1	F1	20.0	140.0	2,400
E2	F2	250.0	196.7	800
E2	F1	140.0	180.0	800
C2	F2	196.7	40.0	2,350
C1	F4	104.0	80.0	600

$T^*$ °C	C2 $\Delta H_{net}$ kW	C1 $\Delta H_{net}$ kW	E1 $\Delta H_{net}$ kW	E2 $\Delta H_{net}$ kW	H1 $\Delta H_{net}$ kW
245	-	-	-	150	-
235	-	-	-	600	-1,200
195	-	-	83	50	-100
191.7	-	100	167		-200
185	-	600	1,000	-800	-1,200
145	-	690	230	-	-
99	600	360	-480	-	-
75	-	600	-800	-	-
35	-	-	-200	-	-
25	-	-	-	-	-
$\Sigma \Delta H_{Surplus}$		2,350	1,250		
$\Sigma \Delta H_{Deficit}$			-1,480		-1,500

Fig. 7. Heat Surplus-Deficit Table for the illustrative four-stream problem.

#### 4.3. Retrofit analysis using the Modified Energy Transfer Diagram

Analysing the retrofit stream data, application of the E-PTA determines the data set for the five EGCCs that superimpose to construct the METD in Fig. 8 and applied to find Retrofit Bridges.

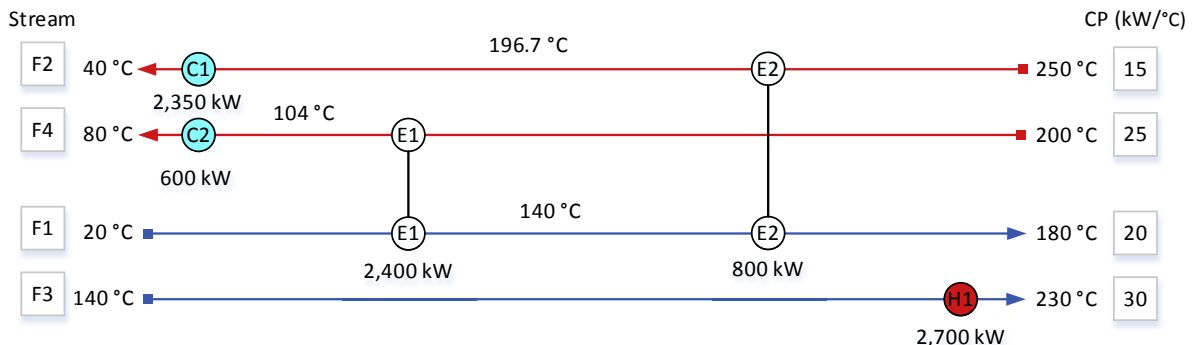


Fig. 6. Existing Heat Exchanger Network for a four-stream problem from Klemeš et al. [31].

The bridges found with the METD will be the same as those found using the HSDT, as the HSDT is a numerical version of the METD. Either method can be followed with success.

The METD contains exchanger labels, stream segment labels, as well as colours that indicate segments with heat surplus and deficit to assist with the retrofit analysis. The right-hand profile of the METD – the network curve has identical shape to the GCC shifted to the right by the amount of cross-Pinch heat transfer. The point of lowest enthalpy in the network curve is 1,950 kW, which is the maximum energy savings for the given  $\Delta T_{cont}$ . If the maximum energy savings are achieved, then the METD will show that the cold and hot utilities are 1,000 kW and 750 kW which will match the minimum utility targets obtained with the GCC.

Examining the METD, it is evident that there is significant cross-Pinch heat transfer in exchanger E1 and cooler C1. Using the METD, Retrofit Bridges are located by linking a cooler with a heater with a series of matches between heat surpluses and heat deficits. There are often many different Retrofit Bridge options and, in this instance, there are six possibilities. Three different bridges (using the initial METD) are presented in Fig. 9 to demonstrate the ways in which bridges may be recognised. Stream information has been left off but remains the same as in Fig. 8. The amount of heat transfer that each match and bridge allows is shown as well as the path of the bridge.

As an example, Retrofit Bridge Option 1 in Fig. 9a is discussed in detail to explain how the bridge is identified, its matches and magnitude. The bridge links the cooler C1 with the heater H1 with two matches. On the METD, the bridge is represented by the green line going from the C1 curve along E1 to the H1 curve. The Retrofit Bridge begins with the heat surplus stream F2 in cooler C1 matching with the heat deficit stream F1 in exchanger E1, reducing

the utility load on C1. The match is denoted as C1-E1. By planning heat transfer between F2 to F1, the duty of E1 reduces by the same amount, freeing up higher temperature surplus heat above the Pinch in stream F4. As a result, a dotted line is drawn along E1 indicating that surplus heat in E1 is now available for re-integration. To complete the bridge between cooler and heater, a second match connects the surplus stream F4 to the deficit stream F3 in heater H1. The match is denoted as E1-H1. The magnitude of each involved heat surplus and deficit, as shown on Fig. 9a, is used to quantify the maximum retrofit energy savings that the bridge can achieve. For C1-E1, there is a surplus of 2,350 kW and a deficit of 1,480 kW. For E1-H1, there is a surplus of 1,250 kW and a deficit of 1,500 kW. The bottleneck of the Retrofit Bridge is, therefore, the heat surplus in E1 of 1250 kW, which defines the required duty of the two new matches. This is the same result as observed with the HSDT in the previous section.

4.4. Retrofit Bridge Option 1

Retrofit Bridge Option 1 has been thoroughly explained using both the HSDT and the METD. To continue the example, the corresponding HEN retrofit design for Retrofit Bridge Option 1 is presented in Fig. 10. In this case, there are two new exchangers, N1 and N2, with duties of 1,250 kW. The utilities C1 and H1 have been reduced by 1,250 kW, and exchanger E2 has been left intact while the duty of E1 has reduced by 1,250 kW. Checks are made to ensure exchanger has sufficient area to achieve the new inlet/outlet temperature of each exchanger. Where the existing area is insufficient, additional area through an extra exchanger is added during the economic analysis phase.

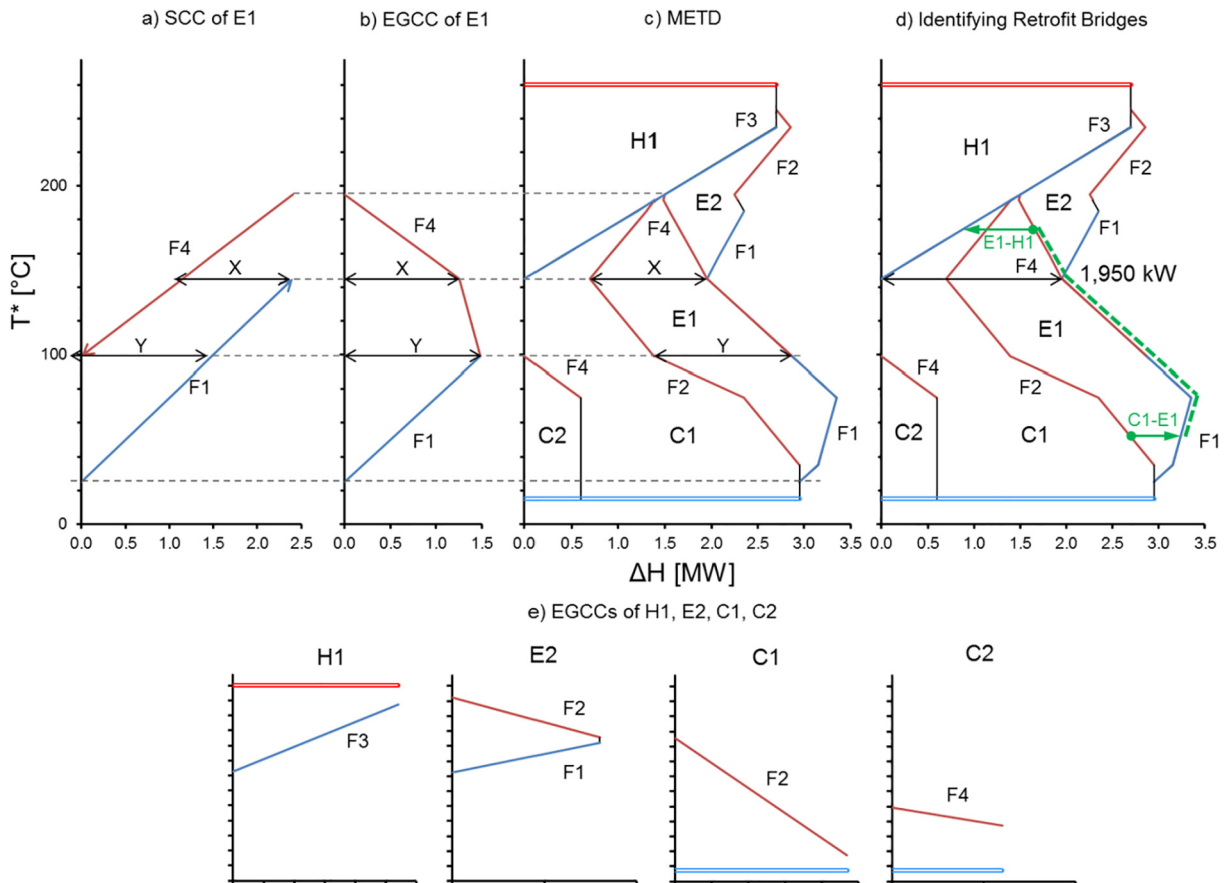


Fig. 8. Development of the METD with the identification of one Retrofit Bridge option for the illustrative four-stream problem.

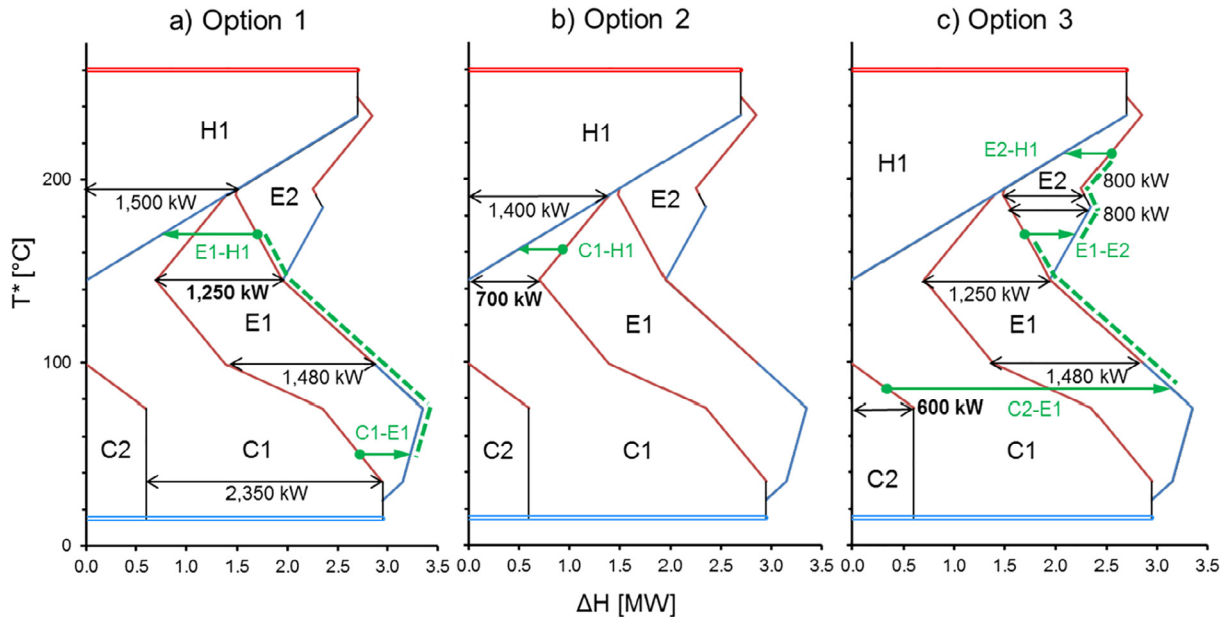


Fig. 9. Three different bridges identified using the Modified Energy Transfer Diagram.

Retrofit Bridge Option 1 is one of several possible Retrofit Bridge options, which are explored in the next section to identify option that is best to implement.

4.5. Retrofit economic performance for design selection

Following the method with several iterations, it is possible to generate several of Retrofit Bridge options. Many of these options are the result of updating the HEN to find new bridges, i.e., the next step in the retrofit design. The results for each retrofit design are presented in Fig. 11. Here, the hot utility is shown to demonstrate how the load has been reduced by the retrofit. The retrofit area (new exchangers and additional area) has been compared with the hot utility to show how much area is required to achieve the savings. Retrofit Bridge options have also been distinguished based on how many new exchangers (HX) are needed. The retrofit target of 750 kW is achieved in four different retrofit designs and either requires three or five new exchangers. As expected, increasing the number of exchangers results in an increase in retrofit area and a decrease in hot utility.

For each design option, the TRP was determined, as outlined in the method. The assumed steam price is NZD 35/MWh while the cost of cold utility is not considered. The annualised ACC for each design has been calculated using the following:

$$ACC_{new} = 4,000 + 500 A^{0.83} \tag{6}$$

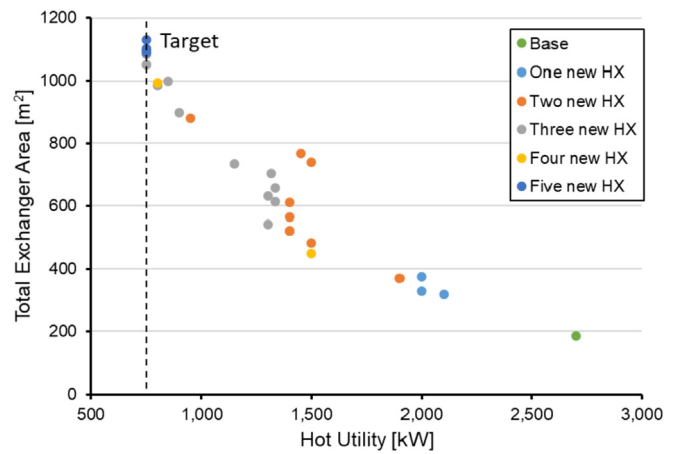


Fig. 11. Relationship between hot utility and the total exchanger area for each retrofit design option.

$$ACC_{existing} = 2,000 + 500A^{0.83} \tag{7}$$

Where A is the new heat transfer area required.

Fig. 12 compares each of the Retrofit Bridge options based on their TRP and current hot utility. Fig. 12 shows that it is possible to achieve the target of 750 kW but it requires five new heat exchangers and is significantly unprofitable. It is apparent that ACC

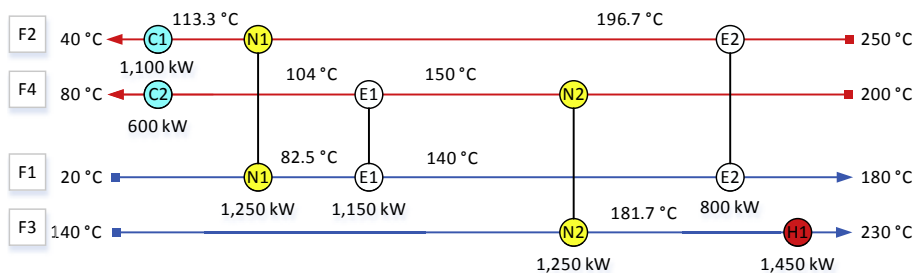


Fig. 10. HEN retrofit design after applying Retrofit Bridge Option 1.

has a significant effect on the retrofit profit as the most profitable designs tend to only have one or two new heat exchangers. The two most profitable retrofit designs have been indicated in Fig. 12. The most profitable design has a hot utility of 1,500 kW and a TRP of NZD 105,426/y, followed by a design with a hot utility of 1,950 kW and a TRP of NZD 96,610/y. Considering profitability as the only economic performance metric, these two designs can be selected for further development.

The first design was reached in two modification steps. In the first step, the cooling load of C2 is compensated for by E1 and a third exchanger is added to the HEN. A fourth new exchanger is then added in a second retrofit step. The resulting HEN is shown in Fig. 13a. The two exchangers are labelled N1 and N2. N1 has a duty of 600 kW and has a heat exchanger area of 134 m<sup>2</sup>, while E4 has a duty of 2,400 kW and has a heat exchanger area of 95 m<sup>2</sup>. Of the original exchangers, only E1 required an increase in area with 70 m<sup>2</sup>

needed through the addition of a heat exchanger. The duties of the original exchangers have been left the same. The retrofit has reduced the hot utility load to 1,500 kW, a decrease of 44%.

The second design was achieved in one modification step. A new exchanger (N1) has been added matching stream F2 with stream F4. N1 has a duty of 700 kW and a heat exchanger area of 145 m<sup>2</sup>. This reduces the hot utility from 2,700 kW to 2,000 kW, or a 25.9% reduction. The resulting HEN is shown in Fig. 13b.

### 5. Case study: paper plant

#### 5.1. Background

The considered case study in this paper is based on a Paper Plant located next to a Kraft Pulp Mill in New Zealand. The Kraft Mill cluster is an important part of New Zealand's forestry sector and is one of the largest chemical processing plants in the country. The Paper Plant consists of a paper machine and an adjacent recycle paper plant and derives benefits from co-location through vertical integration of products and a common centralised utility system. The paper machine can process a pulp suspension into several different grades of Kraft liner board paper. The recycling plant recycles and reuses white water (water drained from the paper during the process). The current HEN consumes a total hot utility of 9,143 kW and has a total cold utility of 20,067 kW. The process heat is distributed throughout the HEN with two coolers, five heaters, and five heat recovery exchangers. Three hot streams are currently discharged from the plant as warm air and water with some heat recovery potential. To account for this, three additional pseudo-coolers have been added to the HEN to represent the heat recovery opportunity of these hot streams. The stream data, including existing matches, is presented in Table 4.

Conventional Pinch Analysis of the Paper Plant determined a minimum hot utility load of 4,317 kW and minimum cold utility load of 15,241 kW. These targets were based on a  $\Delta T_{cont}$  for gaseous flows of 10 °C and a  $\Delta T_{cont}$  for liquid flows of 5 °C. The maximum retrofit

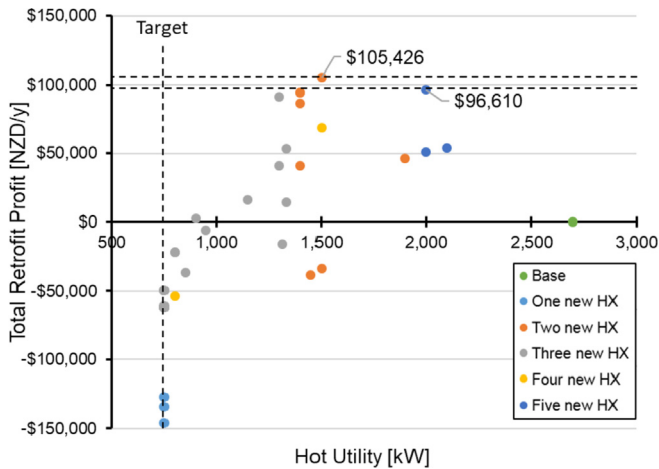


Fig. 12. Relationship between the total profit of the retrofit and the hot utility required.

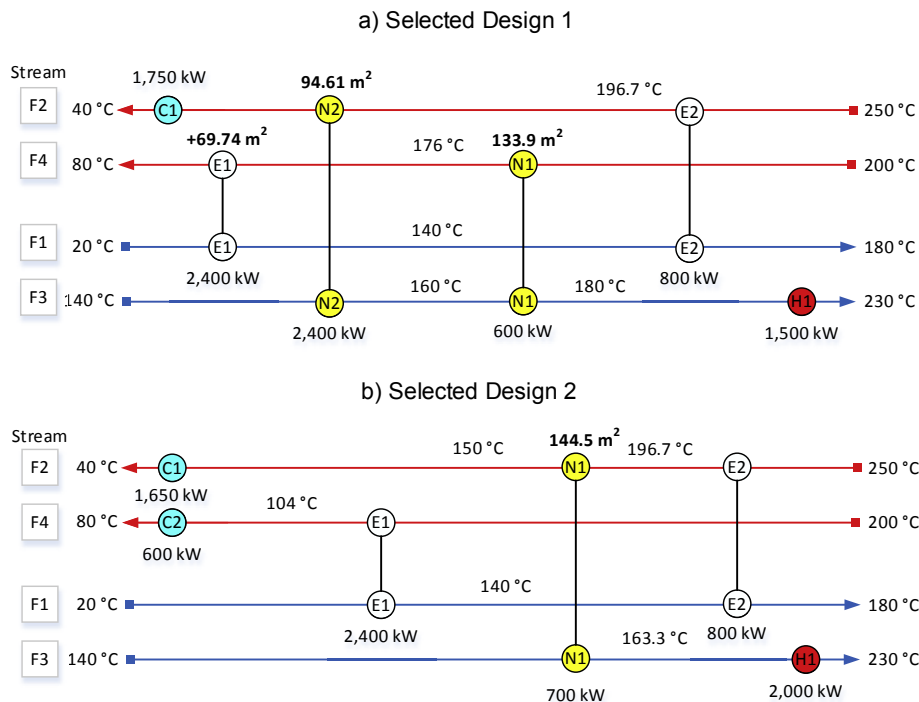


Fig. 13. Selected HEN retrofit designs with the highest total retrofit profits.

**Table 4**  
Retrofit stream data for the Paper Plant.

Unit	Stream	T <sub>s</sub> °C	T <sub>T</sub> °C	ΔH kW	ΔT <sub>cont</sub> °C
C1	WW Overflow (WW)	34	30 <sup>a</sup>	1,283	5
C2	RC Waste Water (RC)	50	30 <sup>a</sup>	1,527	5
C3	Exhaust Air 1 (EX 1)	73	40 <sup>b</sup>	8,332	10
C4	Exhaust Air 2 (EX 2)	70	40 <sup>b</sup>	7,708	10
C5	Press Seal Tank Overflow (PS)	28	20 <sup>b</sup>	1,217	5
E1	Exhaust Air 1	80	73	1,884	10
E1	PV Air (PV)	20	60	1,884	10
E2	Blow Box Air (BB)	20	60	2,508	10
E2	Exhaust Air 2	80	70	2,508	10
E3	Bore Water (BW)	11	48	7,951	5
E3	WW Overflow	58	34	7,951	5
E4	Press Seal Tank Overflow	70	28	6,306	5
E4	Repulper (RP)	11	60	6,306	5
E5	Other Inputs (OI)	30	50	727	5
E5	RC Waste Water	60	50	727	5
H1	Bore Water	48	61	2,794	5
H2	Hot Water (HW)	50	61	2,032	5
H3	Blow Box Air	60	80	1,255	10
H4	PV Air	60	125	3,062	10

<sup>a</sup> Soft target temperature constrained by consented maximum discharge temperature limits.

<sup>b</sup> Soft target temperatures for streams that can be directly discharged without utility cooling but contain heat recovery potential.

energy recovery target, 4,826 kW, is the difference between current use and the utility targets. Based on the current HEN and the retrofit stream data table, the HSDT and METD (Fig. 15) can be constructed and used to conduct a Retrofit Analysis of the Paper Plant. The network grid diagram for the current HEN is presented in Fig. 14.

5.2. Heat Exchanger Network Bridge Retrofit analysis

Following the method, the HSDT and METD for the retrofit problem have been constructed. For the HSDT, please refer to

Table A in the Appendix. The METD for the Paper Plant is presented in Fig. 16 and will be referred to in detail. The maximum energy savings that can be achieved by a retrofit is 4,826 kW, as seen by the outermost curve's point of least enthalpy (the Pinch point). There is a large amount of cold utility being utilised by the HEN but it is only the hot utility that crosses the Pinch of 70 °C, specifically heaters H1 and H2. As the combined hot utility of H1 and H2 is 4,826 kW, the removal of these two heaters will achieve the maximum energy

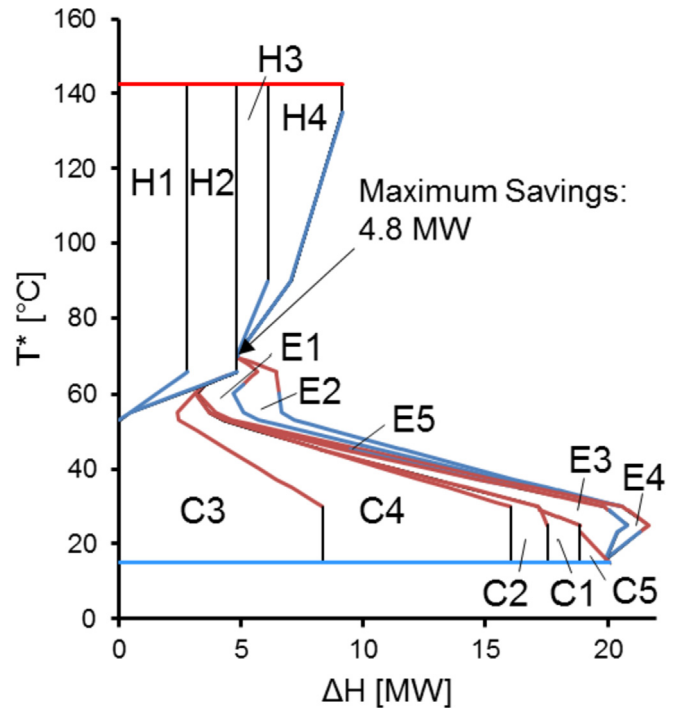


Fig. 15. METD for the paper plant.

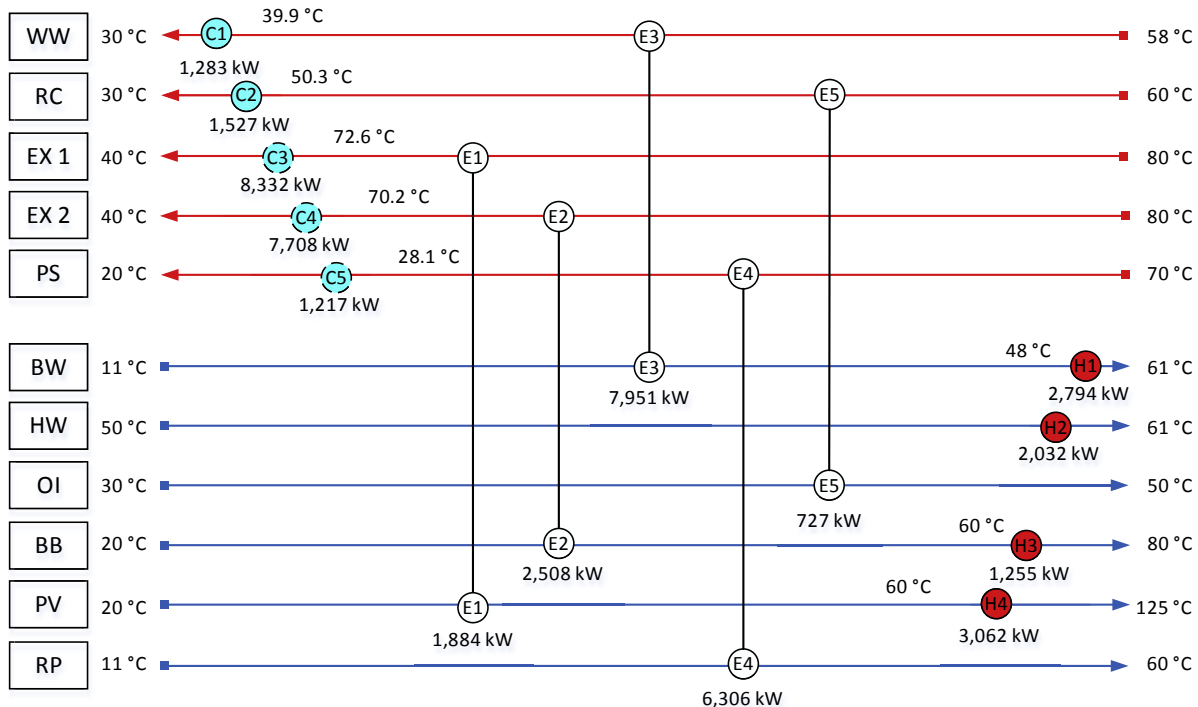


Fig. 14. Heat exchanger network of the paper plant.

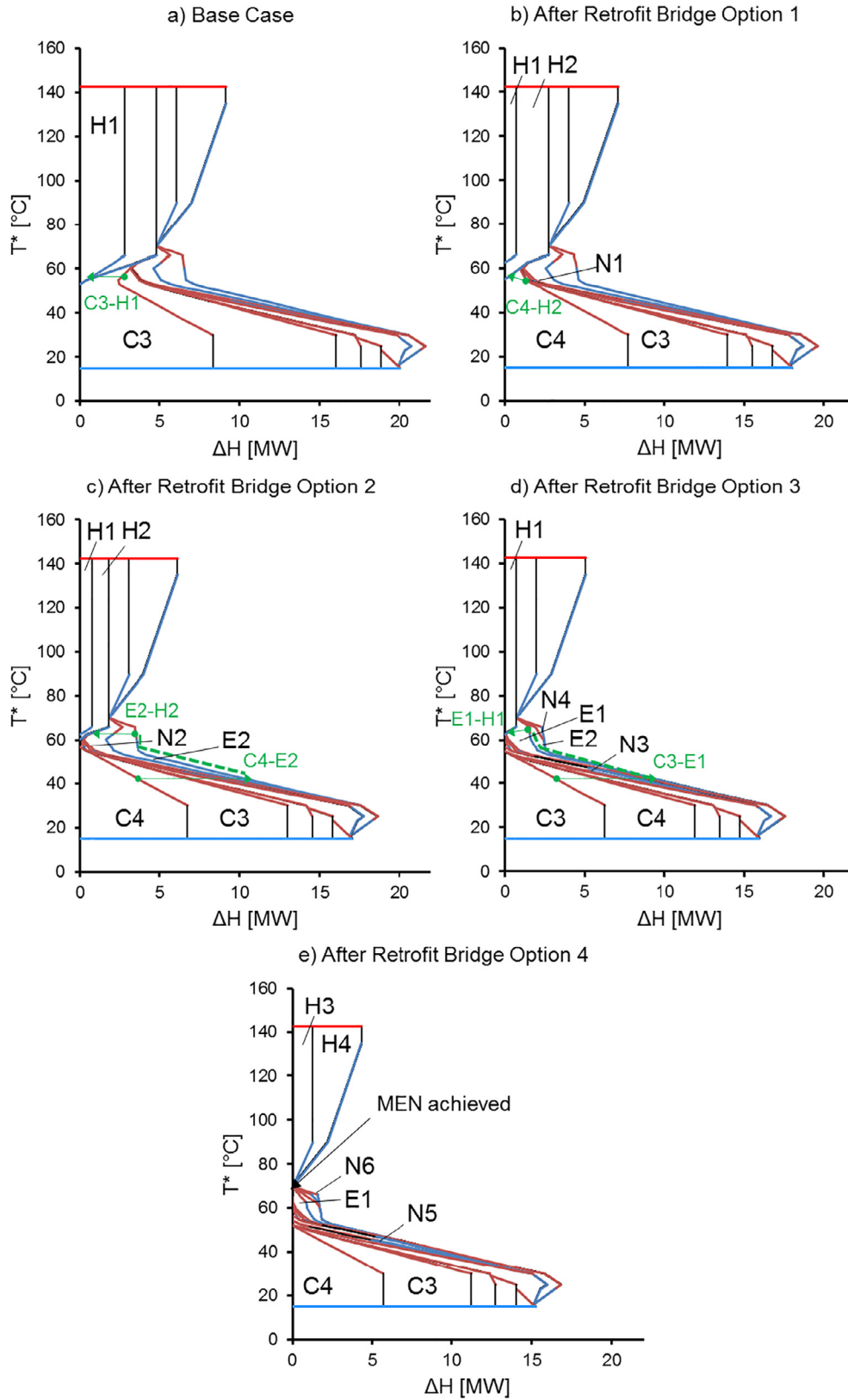


Fig. 16. Four different Retrofit Bridge options showing the evolution of the METD as the MER is achieved.

savings and will result in a MER network. These heaters are linked to Bore Water and Hot Water, respectively.

Using the tools introduced by the method, several Retrofit Bridge options can be identified and quantified. These Retrofit

Bridge options seek to reach the MER and each option builds upon the previous, continuing to reduce the utility in H1 and H2. Four Retrofit Bridge options are presented in Fig. 16 using five different METDs. Only relevant exchangers have been labelled, including

**Table 5**  
Design and economic performance metrics for Retrofit Bridge options of the Paper Plant including capital cost sensitivity.

Option	Retrofit Bridges	$\Delta Q_r$ (kW)	Mod.#	Add. Area (m <sup>2</sup> )	$\Delta S$ (NZD/y)	ACC (NZD/y)	TRP (NZD/y)	PB (y)
Original capital cost estimate								
1	C3-H1	2,067	1	1,874	633,804	232,465	401,338	2.25
2	Opt. 1 +C4-H2	3,024	2	2,745	927,189	356,867	570,322	2.36
3	Opt. 2 +C4-E2-H2	4,099	4	4,520	1,256,815	609,703	647,112	2.98
4	Opt. 3 +C3-E1-H1	4,826	6	5,727	1,479,652	794,252	685,400	3.30
Capital cost +30%								
1	C3-H1	2,067	1	1,874	633,804	302,205	331,598	2.93
2	Opt. 1 +C4-H2	3,024	2	2,745	927,189	463,927	463,262	3.07
3	Opt. 2 +C4-E2-H2	4,099	4	4,520	1,256,815	792,614	464,201	3.88
4	Opt. 3 +C3-E1-H1	4,826	6	5,727	1,479,652	1,032,527	447,124	4.29

new exchangers (in their first appearance on the METD).

The five different METDs each represent different stages of the retrofit. In the first METD (Fig. 16a), the first Retrofit Bridge between C3 and H1 is introduced. The second METD (Fig. 16b) then shows the resulting METD after updating the HEN and reiterating the method. The second METD also shows the next Retrofit Bridge. The same has been applied in Fig. 16c and d with Fig. 16e showing the final METD once the MER has been achieved. In order to apply Retrofit Bridge options 3 and 4, stream splitting has been used on either Exhaust Air 2 or Exhaust Air 1, respectively.

Interestingly, each Retrofit Bridge only requires new exchangers and not additional heat transfer area to the existing exchangers. These new exchangers can be located on the METDs but the size of the exchangers on the METD (i.e., the size of their EGCCs) are very small relative to other exchangers. Evidently, the heat flow of the corresponding heat surpluses and deficits are significantly low and are unlikely to be involved in further retrofitting.

### 5.3. Economic performance and sensitivity of retrofit design options

To select a design for further development, the economic performance metrics of each retrofit design are considered. UC was calculated based on a hot utility cost of NZD 35/MWh and negligible cold utility costs. ACC has been annualised based on a discount rate of 10% and a lifespan of 10 years. An LF of 3.5 has also been applied in determining the constants for the costing equations. ACC was calculated with the following:

$$ACC = 1800 + 200A \quad (8)$$

$$ACC = 500A^{0.815} \quad (9)$$

Where A is the required heat transfer area. Eq. (8) is used for exchanger matches between two liquids while Eq. (9) is used for exchanger matches between a gas and either a gas or a liquid.

With the design and economic performance metrics presented in Table 5, a decision can be reached and justified. Retrofit Bridge Option 4 is the most profitable of the options, owing to the substantial energy savings, but also has the greatest PB. On the other hand, Option 1 has the lowest profitability with the shortest PB. After considering the capital cost sensitivity analysis (+30%), Option 2 has been selected for further development. Option 2 has a reasonable PB and significant retrofit profit in both analyses. Option 2 also has the added benefit of only requiring two modifications. Options 3 and 4 suffer from a high number of modifications, long PB, and increased sensitivity to capital cost. Considering the trade-

off between utility costs and capital costs, Option 2 is the better option.

Applying Retrofit Bridge Option 2 results in a 3,024 kW reduction in hot utility and NZD 570,000/y in total retrofit profit. The changes made to the HEN, including the two new exchangers, can be seen in Fig. 17. Two new exchangers have been added, N1 and N2, with 1,874 m<sup>2</sup> and 870 m<sup>2</sup> of heat transfer required, respectively. Fortunately, no additional heat transfer area was required or stream splitting. The resulting changes affect streams Hot Water, Bore Water, Exhaust Air 1, and Exhaust Air 2 only, and make significant reductions in cross-Pinch heat transfer.

### 5.4. Advantages and limitations

The key advantage of the METD over other graphical retrofit methods is the existing familiarity. The METD relates directly to the GCC, a very common and well-understood graphical tool used in PA for HEN synthesis, and therefore, the concepts involved in the METD will already be familiar to most PA practitioners. This familiarity is advantage for the METD as it means that the METD should be easy to understand and follow. Other graphical methods can involve many new curves and concepts that can create a barrier to entry. The METD requires no other graphical tools alongside it, and is able to represent the existing HEN's exchanger topology. Other graphical tools do not always achieve this. The METD is also simple to use and the potential energy savings can be easily identified, for most retrofit problems.

The METD is limited by what can be ascertained visually. In

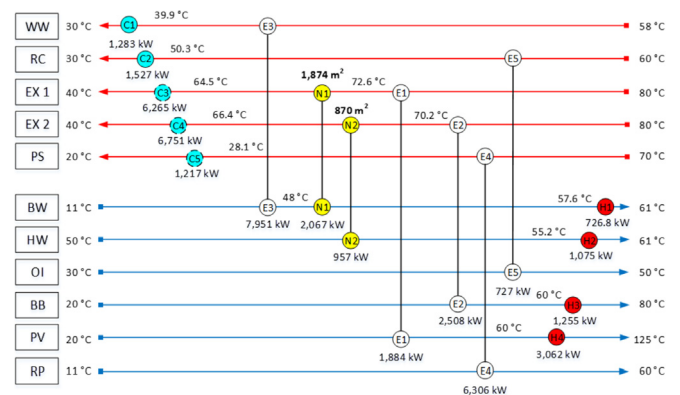


Fig. 17. Proposed heat exchanger network for retrofit bridge option 2.



## References

- [1] Zore Ž, Čuček L, Kravanja Z. Syntheses of sustainable supply networks with a new composite criterion – sustainability profit. *Comput Chem Eng* 2017;102:139–55. <https://doi.org/10.1016/j.compchemeng.2016.12.003>.
- [2] Liew PY, Theo WL, Wan Alwi SR, Lim JS, Abdul Manan Z, Klemeš JJ, et al. Total Site Heat Integration planning and design for industrial, urban and renewable systems. *Renew Sustain Energy Rev* 2017;68:964–85. <https://doi.org/10.1016/j.rser.2016.05.086>.
- [3] *Handbook of process integration (PI): minimisation of energy and water use*. In: Klemeš JJ, editor. Waste and emissions. Cambridge, UK: Woodhead Publishing; 2013.
- [4] Sreepathi BK, Rangaiah GP. Review of heat exchanger network retrofitting methodologies and their applications. *Ind Eng Chem Res* 2014;53:11205–20. <https://doi.org/10.1021/ie403075c>.
- [5] Klemeš JJ, Kravanja Z. Forty years of heat integration: pinch analysis (PA) and mathematical programming (MP). *Curr Opin Chem Eng* 2013;2:461–74. <https://doi.org/10.1016/j.coche.2013.10.003>.
- [6] Linnhoff B, editor. *User guide on process integration for the efficient use of energy*. Oxford, UK: Pergamon Press; 1982.
- [7] Klemeš JJ, Dhole VR, Raissi K, Perry SJ, Puigjaner L. Targeting and design methodology for reduction of fuel, power and CO<sub>2</sub> on Total Sites. *Appl Therm Eng* 1997;17:993–1003. [https://doi.org/10.1016/S1359-4311\(96\)00087-7](https://doi.org/10.1016/S1359-4311(96)00087-7).
- [8] Smith R, Jobson M, Chen L. Recent development in the retrofit of heat exchanger networks. *Appl Therm Eng* 2010;30:2281–9. <https://doi.org/10.1016/j.applthermaleng.2010.06.006>.
- [9] Ochoa-Estropier LM, Jobson M. Optimization of heat-integrated Crude oil distillation systems. Part I: the distillation model. *Ind Eng Chem Res* 2015;54:4988–5000. <https://doi.org/10.1021/ie503802j>.
- [10] Ochoa-Estropier LM, Jobson M, Chen L, Rodriguez-Forero CA, Smith R. Optimization of heat-integrated Crude oil distillation systems. Part II: heat exchanger network retrofit model. *Ind Eng Chem Res* 2015;54:5001–17. <https://doi.org/10.1021/ie503804u>.
- [11] Ochoa-Estropier LM, Jobson M. Optimization of heat-integrated Crude oil distillation systems. Part III: optimization framework. *Ind Eng Chem Res* 2015;54:5018–36. <https://doi.org/10.1021/ie503805s>.
- [12] Jiang N, Shelley JD, Doyle S, Smith R. Heat exchanger network retrofit with a fixed network structure. *Appl Energy* 2014;127:25–33. <https://doi.org/10.1016/j.apenergy.2014.04.028>.
- [13] Akpomimie MO, Smith R. Retrofit of heat exchanger networks with heat transfer enhancement based on an area ratio approach. *Appl Energy* 2016;165:22–35. <https://doi.org/10.1016/j.apenergy.2015.11.056>.
- [14] Pan M, Bulatov I, Smith R. Improving heat recovery in retrofitting heat exchanger networks with heat transfer intensification, pressure drop constraint and fouling mitigation. *Appl Energy* 2016;161:611–26. <https://doi.org/10.1016/j.apenergy.2015.09.073>.
- [15] Akpomimie MO, Smith R. Cost-effective strategy for heat exchanger network retrofit. *Energy* 2017. <https://doi.org/10.1016/j.energy.2017.09.005>.
- [16] Ayotte-Sauvé E, Ashrafi O, Bédard S, Rohani N. Optimal retrofit of heat exchanger networks: a stepwise approach. *Comput Chem Eng* 2017;106:243–68. <https://doi.org/10.1016/j.compchemeng.2017.06.008>.
- [17] Nordman R, Berntsson T. Use of advanced composite curves for assessing cost-effective HEN retrofit I: theory and concepts. *Appl Therm Eng* 2009;29:275–81. <https://doi.org/10.1016/j.applthermaleng.2008.02.021>.
- [18] Lai YQ, Manan ZA, Wan Alwi SR. Heat exchanger network retrofit using individual stream temperature vs enthalpy plot. *Chem Eng Trans* 2017;61:1651–6. <https://doi.org/10.3303/CET1761273>.
- [19] Kamel DA, Gadalla MA, Abdelaziz OY, Labib MA, Ashour FH. Temperature driving force (TDF) curves for heat exchanger network retrofit – a case study and implications. *Energy* 2017;123:283–95. <https://doi.org/10.1016/j.energy.2017.02.013>.
- [20] Gadalla MA. A new graphical method for Pinch Analysis applications: heat exchanger network retrofit and energy integration. *Energy* 2015;81:159–74. <https://doi.org/10.1016/j.energy.2014.12.011>.
- [21] Yong JY, Varbanov PS, Klemeš JJ. Heat exchanger network retrofit supported by extended Grid Diagram and heat path development. *Appl Therm Eng* 2015;89:1033–45. <https://doi.org/10.1016/j.applthermaleng.2015.04.025>.
- [22] Bonhivers J-C, Korbel M, Sorin M, Savulescu L, Stuart PR. Energy transfer diagram for improving integration of industrial systems. *Appl Therm Eng* 2014;63:468–79. <https://doi.org/10.1016/j.applthermaleng.2013.10.046>.
- [23] Bonhivers J-C, Srinivasan B, Stuart PR. New analysis method to reduce the industrial energy requirements by heat-exchanger network retrofit: Part 1 – Concepts. *Appl Therm Eng* 2017;119:659–69. <https://doi.org/10.1016/j.applthermaleng.2014.04.078>.
- [24] Varbanov PS, Klemeš JJ. Rules for paths construction for HENs debottlenecking. *Appl Therm Eng* 2000;20:1409–20. [https://doi.org/10.1016/S1359-4311\(00\)00015-6](https://doi.org/10.1016/S1359-4311(00)00015-6).
- [25] Bonhivers J-C, Svensson E, Sorin MV, Berntsson TS, Stuart PR. Energy transfer diagram for site-wide analysis and application to a kraft pulp mill. *Appl Therm Eng* 2015;75:547–60. <https://doi.org/10.1016/j.applthermaleng.2014.09.045>.
- [26] Bonhivers J-C, Moussavi A, Alva-Argaez A, Stuart PR. Linking pinch analysis and bridge analysis to save energy by heat-exchanger network retrofit. *Appl Therm Eng* 2016;106:443–72. <https://doi.org/10.1016/j.applthermaleng.2016.05.174>.
- [27] Jahromi FS, Beheshti M. An extended energy saving method for modification of MTP process heat exchanger network. *Energy* 2017;140:1059–73. <https://doi.org/10.1016/j.energy.2017.09.032>.
- [28] Chen X, Wang RZ, Du S. Heat integration of ammonia-water absorption refrigeration system through heat-exchanger network analysis. *Energy* 2017;141:1585–99. <https://doi.org/10.1016/j.energy.2017.11.100>.
- [29] Bonhivers JC, Svensson E, Berntsson T, Stuart PR. Comparison between pinch analysis and bridge analysis to retrofit the heat exchanger network of a kraft pulp mill. *Appl Therm Eng* 2014;70:369–79. <https://doi.org/10.1016/j.applthermaleng.2014.04.052>.
- [30] Bonhivers J-C, Alva-Argaez A, Srinivasan B, Stuart PR. New analysis method to reduce the industrial energy requirements by heat-exchanger network retrofit: Part 2 – stepwise and graphical approach. *Appl Therm Eng* 2017;119:670–86. <https://doi.org/10.1016/j.applthermaleng.2015.05.085>.
- [31] Klemeš JJ, Varbanov PS, Wan ASRW, Manan ZA. *Process integration and intensification, saving energy, water and resources*. Berlin, Boston: De Gruyter; 2014.

**Article 3:**

*Combined numerical pinch and exergy analysis for low temperature heat exchanger network*

Hamsani, M.N., **Walmsley, T.G.**, Liew, P.Y., Wan Alwi, S.R., 2018.

Energy 153, 100-112.

DOI: [10.1016/j.energy.2018.04.023](https://doi.org/10.1016/j.energy.2018.04.023)

Elsevier



# Combined Pinch and exergy numerical analysis for low temperature heat exchanger network

Muhammad Nurheilmi Hamsani<sup>a</sup>, Timothy Gordon Walmsley<sup>b</sup>, Peng Yen Liew<sup>a, c, \*</sup>, Sharifah Rafidah Wan Alwi<sup>b, d</sup>

<sup>a</sup> Malaysia – Japan International Institute of Technology (MJIT), Universiti Teknologi Malaysia, Jalan Sultan Yahya Petra, 54100 Kuala Lumpur, Malaysia

<sup>b</sup> Sustainable Process Integration Laboratory (SPIL), NETME Centre, Faculty of Mechanical Engineering, Brno University of Technology, Technická 2896/2, 616 00 Brno, Czech Republic

<sup>c</sup> Process Systems Engineering Centre (PROSPECT), Research Institute of Sustainability Environment (RISE), Universiti Teknologi Malaysia, 81310 UTM Johor Bahru, Malaysia

<sup>d</sup> Faculty of Chemical and Energy Engineering, Universiti Teknologi Malaysia, 81310 UTM Johor Bahru, Malaysia

## ARTICLE INFO

### Article history:

Received 27 January 2018

Received in revised form

21 March 2018

Accepted 5 April 2018

Available online 6 April 2018

### Keywords:

Process integration

Pinch analysis

Exergy analysis

Low temperature

Heat exchanger network

## ABSTRACT

To reduce the dependence on fossil fuel, Process Integration and energy efficiency are crucial in chemical process industry to minimise the consumption of fossil fuels and electricity demand through Heat Exchanger Network (HEN). Pinch Analysis is well established to optimal HEN design to maximize the energy recovery in a process. The stream matches for energy recovery in HEN is important to ensure the temperature potential is not wasted, which the temperature potential could be converted into mechanical work. Therefore, Exergy Analysis has been introduced to work with Pinch Analysis, which ensure the heat recovery stream matches with appropriate temperature differences to minimise the work potential (exergy) loss. This paper demonstrates how Pinch Analysis and Exergy Analysis is simultaneously applied to determine exergy targets (rejection, requirement and avoidable losses) in low temperature HEN. A novel numerical tool known as Exergy Problem Table Algorithm (Ex-PTA), is proposed in this paper as a numerical method to the conventional graphical representation in Extended Pinch Analysis and Design (ExPAnD) method. The proposed tool produces more realistic and achievable results. The net shaft work requirement of the refrigeration system is also determined together with the system COP. This paper explored the effect of setting heat exchangers' minimum approach temperature ( $\Delta T_{\min}$ ) on the exergy targets for low temperature HEN design. The external utility requirement and unavoidable exergy losses increased with  $\Delta T_{\min}$ , while avoidable exergy losses and energy recovery reduced with respect to  $\Delta T_{\min}$ . The net power requirement of the system increased with the  $\Delta T_{\min}$  increment, however, the system COP reduced due to higher increment rate of compression compared to expansion work generation. The optimal  $\Delta T_{\min}$  was determined at 2 °C for heat recovery system in the case study based on super-targeting approach, which considers the total annualized cost, operating cost and capital cost.

© 2018 Elsevier Ltd. All rights reserved.

## 1. Introduction

Energy is one of the important resources in the world. Due to high production demand in the chemical industries, energy demand is also increasing exponentially every year over the last few

decades. The dependence of fossil fuels in the industries gives harmful effects to the environment as a significant amount of greenhouse gases emitted to the atmosphere which causes global warming. Several agreements, such as Kyoto Protocol and Paris Agreement, have been introduced at inter-governmental levels in effort to curb global warming internationally. The actions taken aim to minimise the greenhouse gasses emissions, which has been mainly generated from fossil fuel. It is crucial to reduce industrial energy consumption as large quantities of carbon dioxide will be emitted throughout the energy production process. One of the

\* Corresponding author. Malaysia – Japan International Institute of Technology (MJIT), Universiti Teknologi Malaysia, Jalan Sultan Yahya Petra, 54100 Kuala Lumpur, Malaysia.

E-mail address: [pyliew@utm.my](mailto:pyliew@utm.my) (P.Y. Liew).

Nomenclature			
CC	Composite Curve	$\Delta X$	Exergy difference for a temperature range
ECC	Exergy Composite Curve	$\Delta T_{\min}$	Minimum approach temperature
EGCC	Exergy Grand Composite Curve	$\eta_{\text{ex}}$	Exergetic efficiency
Ex-PTA	Exergy Problem Table Algorithm	<i>Subscript</i>	
ExPAnD	Extended Pinch Analysis and Design	comp	compressor
GCC	Grand Composite Curve	def	deficit
HEN	Heat Exchanger Network	ext	external heat requirement profile
PTA	Problem Table Algorithm	f	final
TSHI	Total Site Heat Integration	i	initial
WHEN	Work and Heat Exchanger Network	loss(above pinch)	Exergy loss above exergetic Pinch (below heat Pinch)
<i>Symbol</i>		loss(below pinch)	loss below exergetic Pinch (above heat Pinch)
Cp	Heat capacity	net	net
CP	Heat capacity flowrate	o	reference
$Q_{H\min}$	Minimum heating utility requirement	p	heat recovery pocket profile
$Q_{C\min}$	Minimum cooling utility requirement	req	requirement
$T^E$	Exergetic temperature	rej	rejection
$T^*$	Shifted temperature	s	supply
W	Compressor shaft work	sur	surplus
X	Exergy/Exergy Cascade	t	target
$\Delta H$	Enthalpy difference for a temperature range	turb	turbine

corrective actions to reduce energy consumption is through Process Integration and energy efficiency. The advantages of energy efficiency towards the industry including reduce energy bills, increase productivity, maximize profits and reduce greenhouse gases emissions.

Pinch Analysis is a widely used approach for Process Integration to target and optimise the energy utilisation in a process plant. It was first developed by Linnhoff and Flower [1] at the University of Leeds in the late 1970s. The method has been further developed to improve the industrial energy efficiency and increase the profit margin of a company. Previous studies have shown that through Pinch Analysis, energy savings of 20% up to 40% can be achieved [2]. Instead of focusing on Heat Integration for a single process, Pinch Analysis has been extended to multiple sites heat integration known as Total Site Heat Integration (TSHI) [3]. The TSHI concept integrates heating and cooling supply and demands of co-located processes via the centralised site utility system [4]. Heating or cooling deficit of a process may be indirectly satisfied by excess heating or cooling capacity of a different process through the generation and consumption of a common utility level. An improved TSHI method has been developed by Klemeš, Dhole [5] to enhance the energy efficiency of large industrial scale. More recently, Tarighaleslami, Walmsley [6] further developed the graphical TSHI method for improved application to low temperature processes that require non-isothermal utility (e.g. hot water) and use these utility systems to indirectly recover heat. Total Site utility temperature selection can also be optimized to realise even greater benefits [7]. One of the advantages of these graphical representations is that it provides good and clear visualisation advantage, however, it may encounter some difficulties and inaccuracies for large and complicated problems. Therefore, further development of TSHI has been introduced by Liew, Alwi [8] to come out with a novel numerical algorithm for a better outcome in terms of accuracy and efficiency. Later, an improved method has been developed to account for stream variations [9].

Over the last few decades, Pinch Analysis provides physical insights to synthesise Heat Exchanger Network (HEN) in various production processes. Gundersen and Naess [10] have published a

review paper related to synthesis of cost-optimal heat exchanger networks. Heuristic-based HEN design method [11] has been used widely for achieving the targeted minimum utility. More recently, a novel tool [12] has been introduced for simultaneous targeting and designing HEN. HEN synthesis has been further extended by Aghahosseini and Dincer [13] to include exergy loss cost for industrial applications. The exergy loss cost is used as a trade-off between the capital cost of heat exchangers to determine the optimum minimum approach temperature ( $\Delta T_{\min}$ ) in HEN design.

Exergy Analysis is defined as a systematic tool to determine exergy content in the processes so that compressor shaft work can be analysed. Umeda, Harada [14] first introduced a novel diagram known as energy availability diagram where the axes of the diagram are Carnot factor and enthalpy. Later, Linnhoff and Dhole [15] renamed the diagram as Exergy Composite Curves (ECCs) and Exergy Grand Composite Curves (EGCCs). The work has extended a combined Pinch and Exergy Analysis method from a conventional Pinch Analysis for sub-ambient, low temperature process design. The proposed combined method also considers both temperature and pressure as design variables, whereas temperature is the only design variable in Pinch Analysis. Dhole and Linnhoff [16] further developed a method for overall low temperature process design and analysis. Application of the method has been done by Fritsson and Berntsson [17] to measure energy efficiency in a slaughter and meat processing plant. Marechal and Favrat [18] used the combined Pinch and Exergy Analysis approach to investigate the optimal energy conversion technologies integration opportunities. Hirata [19] described on how Pinch Analysis can be performed to integrate the heat in low temperature processes. Hirata and Kakiuchi [20] further investigated the heat integration opportunities of adsorption heat pumps to satisfy cooling demand in the refrigeration system in an ethylene manufacturing process. Ataei [21] applied the combined Pinch and Exergy Analysis method to minimise the power consumption of an olefin plant. Ghorbani, Salehi [22] later applied the same method for designing the refrigeration cycle in liquefied natural gas industry. Aspelund, Berstad [23] extended Pinch and Exergy Analysis concepts to design sub-ambient processes, known as the Extended Pinch Analysis and Design (ExPAnD)

procedure. The main purpose of the method is to utilise heating and cooling capacity by manipulating the pressure of streams to reduce net shaft work. Later, expanders [24] and compressors [25] are integrated into HENs in sub-ambient processes using ExPAnD graphical representation, known as Work and Heat Exchanger Networks (WHEN) design [26], which contribute to sub-ambient process design method. Marmolejo-Correa and Gundersen [27] then described several challenges that encountered when using exergy efficiency as a performance indicator in sub-ambient process design. Later, Marmolejo-Correa and Gundersen [28] introduced a new parameter called as exergetic temperature ( $T^E$ ) to enable a linear graphical representation of improved exergetic Composite Curves.

Several studies have developed and utilised a combined Pinch and Exergy Analysis. ExPAnD method has improved the visual impact of exergy analysis tools for practising engineers. To enhance the visibility of the research, Exergy Analysis research needs to bridge with HEN design using simple graphical and numerical tools for highlighting the importance of exergy. In addition,  $\Delta T_{\min}$  is essential for heat exchanger design, which affects the size and cost of the equipment. Typically, lower  $\Delta T_{\min}$  contributes to larger heat transfer area and thus higher investment cost. Super-targeting has been developed with Pinch Analysis for the economic trade-off between energy and capital cost of a HEN design. The graphical method proposed by Marmolejo-Correa and Gundersen [28] considered a  $\Delta T_{\min}$  of 0 °C, which the effect of  $\Delta T_{\min}$  in exergy analysis has not been explored for HEN design. The effect could be insignificant for WHEN design for sub-ambient processes, however,  $\Delta T_{\min}$  is still important for HEN design for low temperature processes.

In this study, a numerical exergy targeting approach – the Exergy Problem Table Algorithm (Ex-PTA), which is aided by the conventional Problem Table Algorithm – is proposed to determine the avoidable exergy losses and exergy targets (requirement, rejection, deficit and surplus) of a system. A systematic numerical tool is required to provide achievable results. The method considers a unified  $\Delta T_{\min}$  for HEN to enhance the validity of the assumptions of the method. This paper also includes the investigation of the driving force effects by  $\Delta T_{\min}$  to exergy targets and losses in a HEN design. This method focuses on the analysis of avoidable exergy losses for low temperature HEN, however, the pressure change requirements for process streams have not been considered.

## 2. Theory

ExPAnD method [29] estimated exergy recovery and decomposition by assuming vertical heat transfer for process-to-process heat recovery in the system. In the same enthalpy interval, hot streams are assumed to exchange with the cold streams at the temperature below it. This type of heat exchange involves more heat exchanger area and stream split, thus requires higher investment cost. Fig. 1(a) illustrates vertical heat exchange on Composite Curve (CC) and Grand Composite Curve (GCC). The heat recovery focuses at temperature interval nearer to Pinch temperature.

Horizontal heat exchange is illustrated in Fig. 1(b), which the heat recovery is distributed at each temperature interval. The excess enthalpy in an interval is then recovered for cold streams at lower temperature in lower temperature interval, which is illustrated as a heat recovery pocket in the GCC in Fig. 1(b). This type of heat exchange is incorporated into the proposed method in this paper.

## 3. Method

The proposed numerical exergy losses and targets

determination for low temperature HEN design is presented in this section. The method is then demonstrated in detail using a case study in next section. The method is summarised as shown in Fig. 2.

### 3.1. Step 1: data extraction

The hot and cold stream data for the refrigeration system are extracted from the process design flowsheet. The process stream data required in Pinch Analysis study includes heat capacity flow-rate (CP) data, supply temperature ( $T_s$ ) and target temperature ( $T_t$ ) in Celsius. If minimum approach temperature ( $\Delta T_{\min}$ ) is required in the case, the shifted temperatures ( $T^*$ ) must be determined. Note that, the shifted temperatures are determined by subtracting half of the minimum approach temperature,  $\Delta T_{\min}/2$  from all hot stream supply and target temperatures, while half of the minimum approach temperature,  $\Delta T_{\min}/2$  is added to all cold stream supply and target temperatures. The exergetic temperature ( $T^E$ ) is then calculated using Eq. (1). The reference temperature in the system ( $T_o$ ) is also required to determine the exergetic temperature. If  $\Delta T_{\min}$  is zero,  $T^*$  is the same as the actual process temperatures,  $T$ .

$$T^{*E} = \left[ T_o \left( \frac{T^*}{T_o} - \ln \frac{T^*}{T_o} - 1 \right) \right] \quad (1)$$

### 3.2. Step 2: conventional Problem Table Algorithm

The process Pinch temperature and energy targets (minimum heating and cooling requirement) are determined using a numerical tool – Problem Table Algorithm (PTA) – or graphical representation – Composite Curve (CC) and Grand Composite Curve (GCC). The analysis determines the requirements for heating and cooling in the process, including both temperature and duty. Table 1 presents the standard method for calculating the PTA [1].

### 3.3. Step 3: decomposition of enthalpy cascade

The Final Enthalpy Cascade (Table 1) is decomposed in this step into the two parts: (1) External Heat Requirement Profile, i.e. stream segments needing external heating and cooling, and (2) Heat Recovery Pockets Profile, i.e. segments in surplus/deficit that may be internally heat integrated. The general tabular approach is presented in Table 2. The difference between the External Heat Requirement Profile and Heat Recovery Pockets Profile is most easily understood using the graphical representation of the data set – the Grand Composite Curve (GCC).

Fig. 3 presents an example showing the decomposition of the Final Enthalpy Cascade into the Net External Heat Requirement and Heat Recovery Pockets Profiles. The step is to ensure sufficient temperature intervals are contained within the PTA. To identify necessary additional temperature intervals, the minimum and maximum temperatures of each pocket are determined from the GCC (or PTA), as shown in Fig. 3(a), and added as temperature intervals in the PTA using linear interpolation of existing temperature intervals. For example, Points 1 and 2 are the maximum and minimum temperatures of the heat recovery pocket above the Pinch in the example GCC. For this case, Point 1 will be an existing temperature interval (as indicated by the change in CP above/below this point), while Point 2 is likely required to be determined via linear interpolation. It is known that Point 1 and 2 shares the same relative enthalpy. Using the aid of the GCC, the intervals that contribute to the External Net Surplus/Deficit, i.e. the segments that require utility according to the GCC, can be identified. The  $\Delta H$  profile can then be cascaded to find the Initial External Heat

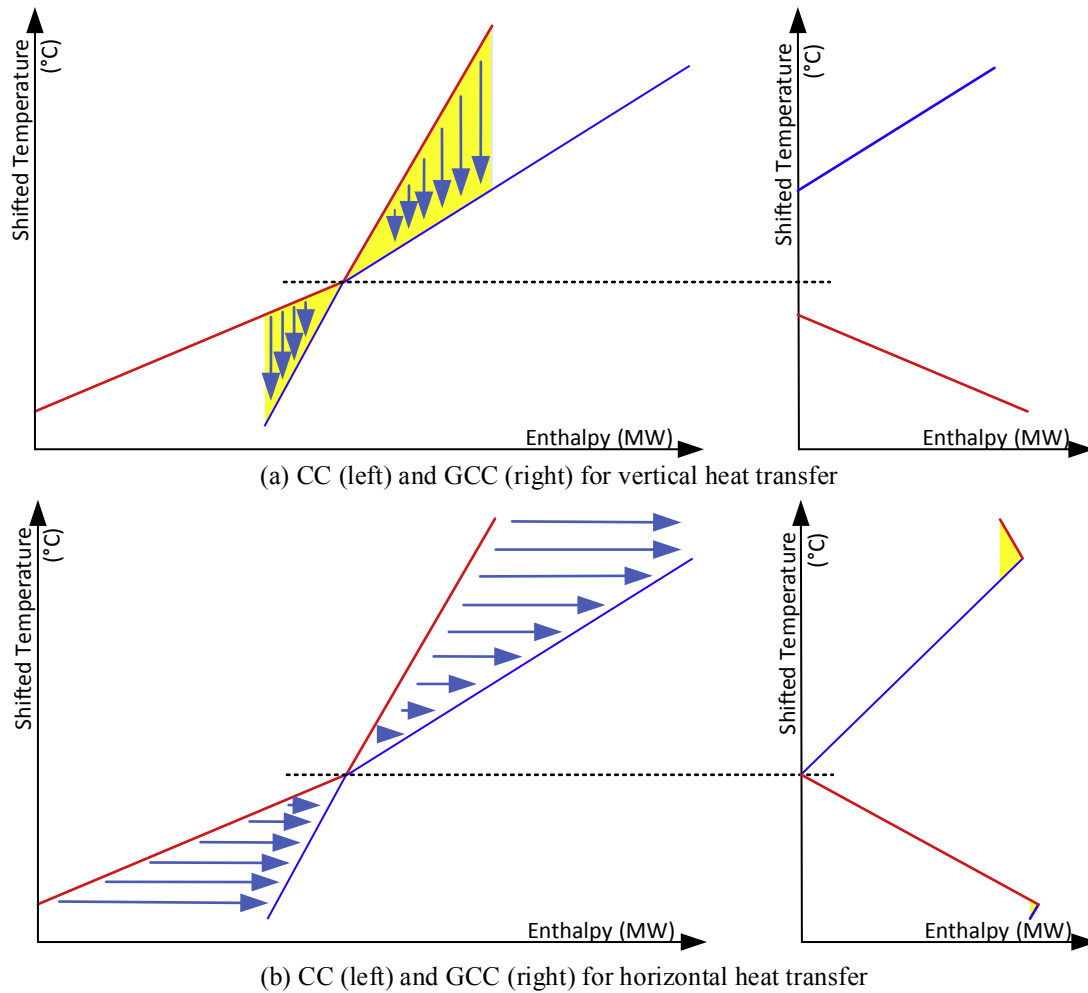


Fig. 1. Illustration of vertical and horizontal heat transfer.

Requirement Cascade and the External Heat Requirement Profile. To complete the decomposition, the Heat Recovery Pockets Profile is found as the difference between the Final Enthalpy Cascade and the External Heat Requirement Profile.

#### 3.4. Step 4: exergy Problem Table Algorithm

In this step, the Exergy PTA (Ex-PTA), presented in Table 3, is applied separately to the External Heat Requirement and Heat Recovery Pockets Profiles (Table 2), as well as the Final Heat Cascade (Table 1). The Ex-PTA method follows a similar pattern to the conventional PTA. A key difference is the input enthalpy cascade,  $H_{input}$ . The first column is the shifted temperature intervals followed  $H_{input}$  which is defined in separate tables for External Heat Requirement Profile, Heat Recovery Pockets Profile, and the Final Heat Cascade. Column 3 is the shifted exergetic temperatures ( $T^{*E}$ ) followed by columns that mirror the conventional enthalpy PTA. Another difference is the  $CP_{net}$  values are determined using the  $H_{input}$  cascade. The surplus/deficit exergy values ( $\Delta X$ ) which calculated by Eq. (2) as well as the initial and final exergy cascades ( $X_i$  and  $X_f$ ) follow the same procedure as the standard PTA. The initial exergy cascade is performed from the first temperature row with an enthalpy value of 0 MW, while the final exergy cascade is cascaded from top to bottom with the modulus of the negative value present at the Pinch (as defined by the enthalpy PTA) in the initial exergy cascade. Since exergy does not follow the law of

conservation, it is normal for negative exergy values to be present in the final cascade,  $X_f$ .

$$\Delta X = \dot{m} \cdot C_p \cdot \Delta T^{*E} = CP \cdot \Delta T^{*E} \quad (2)$$

#### 3.5. Step 5: exergy requirement, rejection and losses targeting

The two Ex-PTA from Step 4 are used for determining the exergy requirement ( $X_{req}$ ), exergy rejection ( $X_{rej}$ ) and avoidable exergy losses. The Ex-PTA of the External Heat Requirement Profile is constructed to target the  $X_{req}$  and  $X_{rej}$  in the process, while the second Ex-PTA of the Heat Recovery Pockets Profile is constructed to determine avoidable exergy losses within the process, i.e. exergy losses that occur with temperature driving force above the predefined minimum,  $\Delta T_{min}$ . From the Ex-PTA for External Heat Requirement Profile, exergy requirement and exergy rejection are directly determined in the final exergy cascade column,  $X_f$ . The top value of the cascade is the target for maximum exergy rejection if below ambient temperature (or minimum exergy requirement if above ambient). The bottom value of the cascade is the minimum exergy requirement if below ambient temperature (or maximum exergy rejection if above ambient). For processes that cross ambient temperature, it is possible to have two minimum exergy requirement targets. The final exergy cascade of the Ex-PTA for the Heat

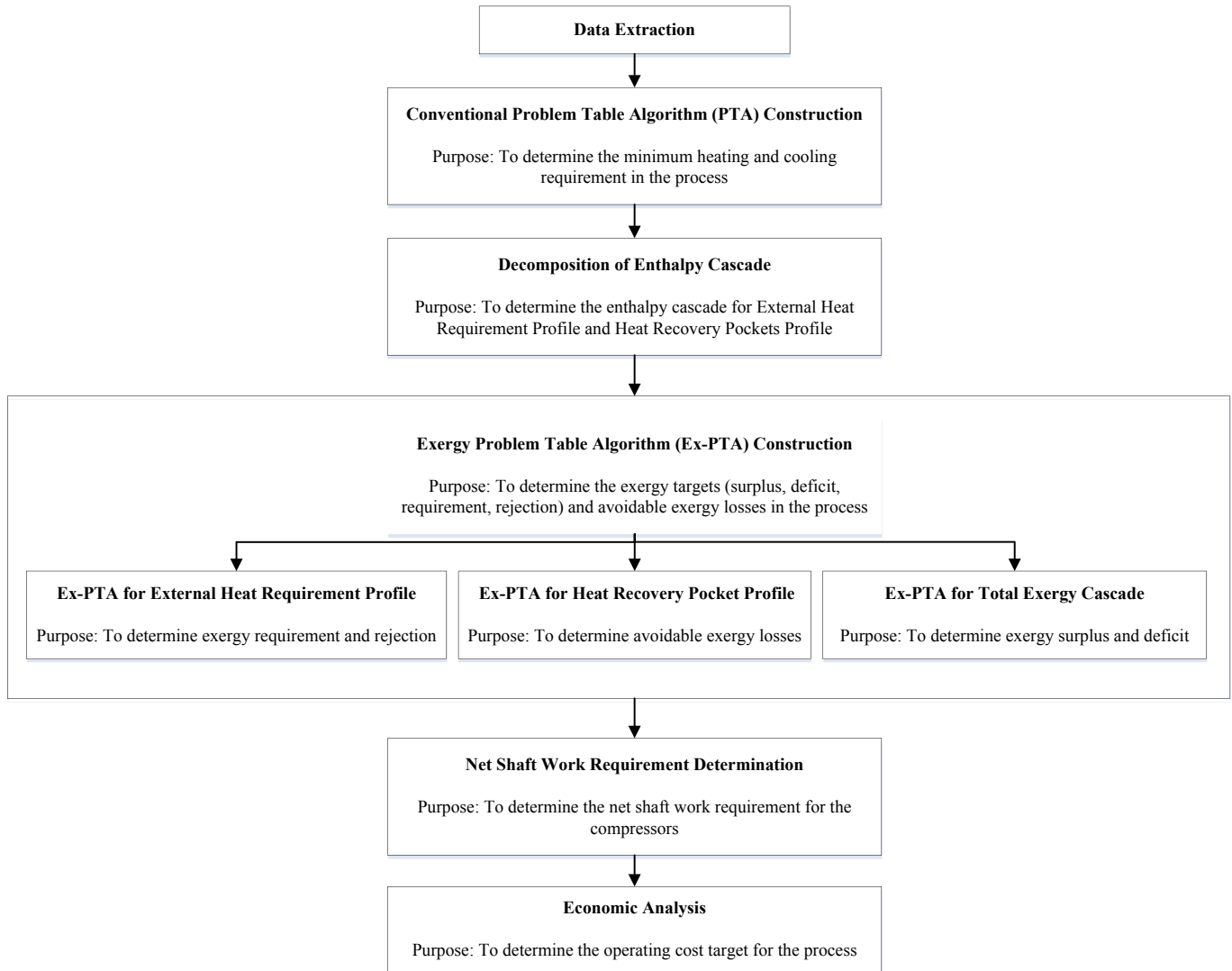


Fig. 2. Summary of the proposed method.

**Table 1**  
Conventional problem table algorithm – PTA.

$T^*$ (°C)	$\Delta T^*$ (K)	$CP_{net}$ (MW/K)	Net Surplus/Deficit $\Delta H$ (MW)	Initial (i) Enthalpy Cascade (MW)	Final (f) Enthalpy Cascade (MW)
$T_1$				$H_{1(i)} = 0$	$H_{1(f)} = \min H_i $
$T_2$	$T_1 - T_2$	$(\sum CP_h - \sum CP_c)_{1-2}$	$(\Delta T \cdot CP_{net})_{1-2}$	$H_{1(i)} + \Delta H_{1-2}$	$H_{1(f)} + \Delta H_{1-2}$
$T_3$	$T_2 - T_3$	$(\sum CP_h - \sum CP_c)_{2-3}$	$(\Delta T \cdot CP_{net})_{2-3}$	$H_{2(i)} + \Delta H_{2-3}$	$H_{2(f)} + \Delta H_{2-3}$
$T_4$	$T_3 - T_4$	$(\sum CP_h - \sum CP_c)_{3-4}$	$(\Delta T \cdot CP_{net})_{3-4}$	...	...
...	...	...	...	...	...
$T_n$	$T_{n-1} - T_n$	$(\sum CP_h - \sum CP_c)_{[n-1]-n}$	$(\Delta T \cdot CP_{net})_{[n-1]-n}$	$H_{n-1(i)} + \Delta H_{[n-1]-n}$	$H_{n-1(f)} + \Delta H_{[n-1]-n}$

Recovery Pockets Profile determines the total avoidable exergy losses above and below the Pinch.

### 3.6. Step 6: net shaft work requirement and economic analysis

This step quantifies the net shaft work consumption, i.e. compression work minus expansion work. The net shaft work requirement is determined from process exergy requirements and

rejection. To determine compressor and turbine shaft works, the exergetic efficiency ( $\eta_{ex}$ ) needs to be defined and the net shaft work estimated using Eq. (3). The estimated operating cost is calculated from the net shaft work consumption target multiplied by the electricity price.

$$W_{net} = W_{comp} - W_{turb} \approx X_{req}/\eta_{ex} - \eta_{ex}X_{rej} \quad (3)$$

**Table 2**  
Decomposed enthalpy cascades.

$T^*$ (°C)	$H_f$ (MW)	External Net Surplus/Deficit ( $^*$ ) (MW)	Initial External Heat Requirement (r,i) Cascade (MW)	External Heat Requirement (r) Profile (MW)	Heat Recovery Pockets (p) Profile (MW)
$T_1$	$H_{1(f)}$	$\Delta H_{1-2}^*$	$H_{1(r,i)} = 0$	$H_{1(r)} = \min H_i $	$H_{1(p)} = H_{1(f)} - H_{1(r)}$
$T_2$	$H_{2(f)}$	$\Delta H_{2-3}^*$	$H_{1(r,i)} + \Delta H_{1-2}^*$	$H_{1(r)} + \Delta H_{1-2}^*$	$H_{2(p)} = H_{2(f)} - H_{2(r)}$
$T_3$	$H_{3(f)}$	$\Delta H_{3-4}^*$	$H_{2(r,i)} + \Delta H_{2-3}^*$	$H_{2(r)} + \Delta H_{2-3}^*$	$H_{3(p)} = H_{3(f)} - H_{3(r)}$
...	...	...	...	...	...
$T_n$	$H_{n(f)}$	$\Delta H_{[n-1]-n}^*$	$H_{n-1(r,i)} + \Delta H_{[n-1]-n}^*$	$H_{n-1(r)} + \Delta H_{[n-1]-n}^*$	$H_{n(p)} = H_{n(f)} - H_{n(r)}$

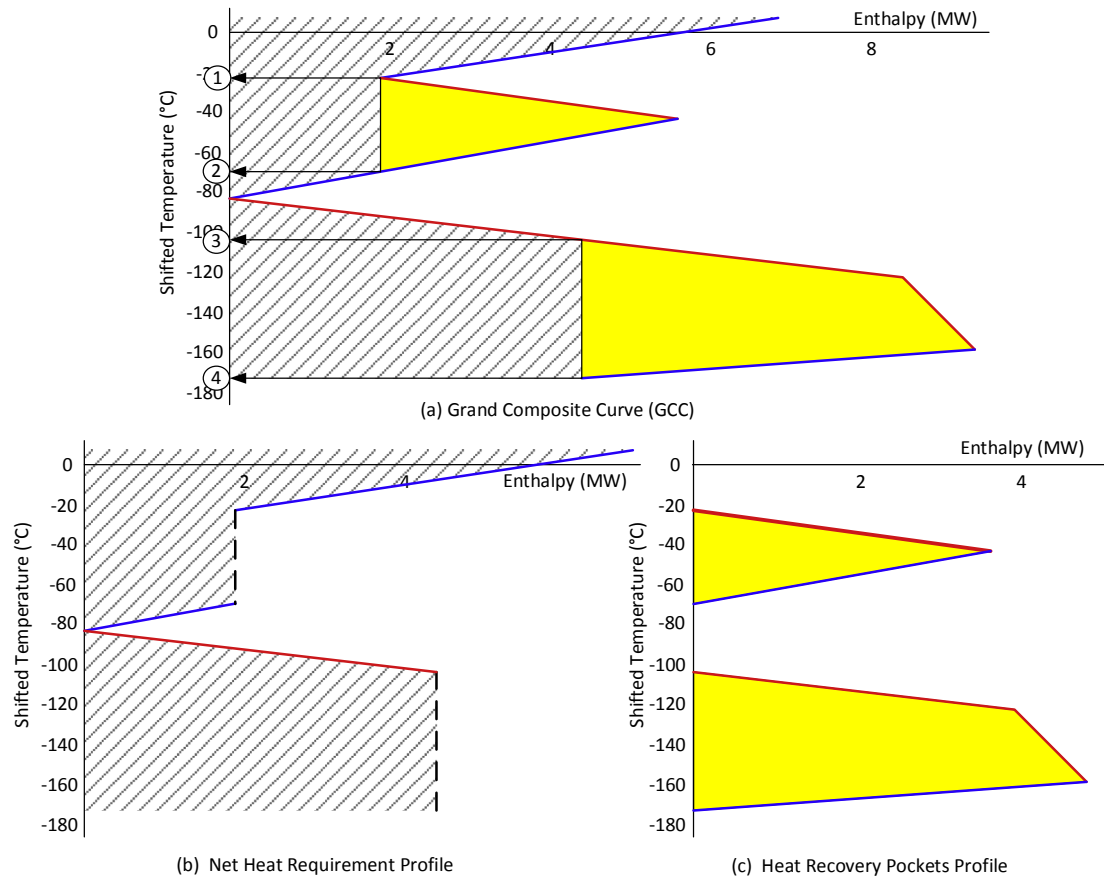


**Fig. 3.** (a) Grand composite curve (GCC), (b) External heat requirement profile, and (c) Heat recovery pockets profile.

**Table 3**  
Exergy problem table algorithm – Ex-PTA.

$T^*$ (°C)	$H_{input}$ (MW)	$T^{E*}$ (K)	$\Delta T^{E*}$ (K)	$CP_{net}$ (MW/K)	$\Delta X$ (MW)	$X_i$ (MW)	$X_f$ (MW)
$T_1$	$H_1$	$T_1^E$	$T_1^E - T_2^E$	$(-\Delta H/\Delta T)_{1-2}$	$(\Delta T^{E*} \cdot CP_{net})_{1-2}$	$X_{1(i)} = 0$	$X_{1(f)} = (-X_i)_{pinch}$
$T_2$	$H_2$	$T_2^E$	$T_2^E - T_3^E$	$(-\Delta H/\Delta T)_{2-3}$	$(\Delta T^{E*} \cdot CP_{net})_{2-3}$	$X_{1(i)} + \Delta X_{1-2}$	$X_{1(f)} + \Delta X_{1-2}$
$T_3$	$H_3$	$T_3^E$	$T_3^E - T_4^E$	$(-\Delta H/\Delta T)_{3-4}$	$(\Delta T^{E*} \cdot CP_{net})_{3-4}$	$X_{2(i)} + \Delta X_{2-3}$	$X_{2(f)} + \Delta X_{2-3}$
...	...	...	...	...	...	...	...
$T_n$	$H_n$	$T_n^E$	$T_{n-1}^E - T_n^E$	$(-\Delta H/\Delta T)_{[n-1]-n}$	$(\Delta T^{E*} \cdot CP_{net})_{[n-1]-n}$	$X_{n-1(i)} + \Delta X_{[n-1]-n}$	$X_{n-1(f)} + \Delta X_{[n-1]-n}$

The Coefficient of Performance for the entire refrigeration system can also be determined according to Eq. (4).

$$\text{COP}_R = Q_C/W_{\text{net}} \quad (4)$$

The estimated operating cost of the compressor is then used in super-targeting analysis [30] in addition to capital cost of heat exchanger to determine optimal  $\Delta T_{\text{min}}$  for HEN design. The net shaft work consumption target can be minimised through process modification and optimisation. For example, if the exergy losses are minimised in heat recovery pockets through pressure manipulation for the same  $\Delta T_{\text{min}}$ , the exergy requirement/rejection targets will improve and the net shaft work consumption target decrease. This extension will be the subject of future work.

#### 4. Case study

The procedure is illustrated using a case study adopted from Marmolejo-Correa [29]. Several situations are considered to demonstrate the method. In the first case study which is the base case, no minimum approach temperature ( $\Delta T_{\text{min}}$ ) is used in order to compare the outcomes with the method of Marmolejo-Correa [29]. To illustrate the  $\Delta T_{\text{min}}$  consideration, the case study is repeated with 10 °C global  $\Delta T_{\text{min}}$ . This case study is demonstrated step-by-step for better understanding of the proposed method, as following:

##### 4.1. Step 1: data extraction

Table 4 shows the process stream data of a sub-ambient process. The reference temperature in the system are 15 °C ( $T_0$ ). A theoretical  $\Delta T_{\text{min}}$  of 0K is assumed for the process. H1 and H2 are categorised as hot streams while C1 and C2 are cold streams. Both initial and target temperatures are converted to exergetic temperature ( $T^E$ ) using Eq (1) [28]. Note that the highest  $T^E$  has the highest amount of exergy and vice versa. Unlike above-ambient processes, hot streams are classified as the exergy sinks and cold streams are the exergy sources in the sub-ambient processes. In this case study, the streams do not require any change in pressure as the main aim is to determine the avoidable exergy losses in low temperature HEN.

##### 4.2. Step 2: conventional Problem Table Algorithm

The Problem Table Algorithm (PTA) in Pinch Analysis is constructed to determine the minimum energy requirement and energy transfer beyond temperature intervals through energy cascades. Supporting the graphical representation of the GCC, this numerical method provides the calculation of the net heat cascade from which energy requirements targets may be set for a process. In each temperature interval, the heat capacities of all the hot streams which exist in the interval are added together and subtracted with the heat capacities of all the cold streams, which results in a net heat capacity flow ( $CP_{\text{net}}$ ). Then, the  $CP_{\text{net}}$  for each temperature intervals are multiplied by temperature range in the intervals to

**Table 4**  
Process stream data of base case [29].

	$T_s$ (°C)	$T_t$ (°C)	CP (MW/K)	$T_s^{E^*}$ (K)	$T_t^{E^*}$ (K)
H1	6.85	−123.15	0.185	0.12	50.01
H2	−23.15	−158.15	0.35	2.77	91.62
C1	−173.15	−43.15	0.325	116.93	6.80
C2	−83.15	6.85	0.35	21.87	0.12

give the enthalpy in each temperature intervals. The initial enthalpy cascade is then performed with an initial zero input at the highest temperature, adding on the net enthalpy in each temperature intervals down the table. The modulus of the largest negative value in the initial enthalpy cascade is initiated at the highest temperature in the final enthalpy cascade. As a result, 6.85 MW of external hot utility ( $Q_{H\text{min}}$ ) and 4.40 MW of external cooling utility ( $Q_{C\text{min}}$ ) are required with a Pinch temperature of −83.15 °C, as shown in Table 5.

##### 4.3. Step 3: decomposition of enthalpy cascade

The Final Enthalpy Cascade is decomposed into Net External Heat Requirement Profile and Heat Recovery Pockets Profile. Using the visual representation of the data, which was previously presented as Fig. 3, one can identify that two temperature intervals at −69.58 and −104.10 °C should be added. The additional temperatures could also be identified through linear interpolation. Also, with the aid of Fig. 3, the intervals relating to external heating requirement can be identified and cascaded to determine the External Heat Requirement Profile and then, by difference, the Heat Recovery Pockets Profile (see Table 6). An asterisk "\*" is used for indicating a temperature interval that involves in the heat pocket in the External Net Surplus/Deficit column.

##### 4.4. Step 4: exergy Problem Table Algorithm

Three Exergy Problem Tables Algorithm (Ex-PTA) are then constructed from the External Heat Requirement Profile (Table 7), Heat Recovery Pockets Profile (Table 8), and the Final Enthalpy Cascade (Table 9). Instead of using normal temperatures in the interval of a conventional PTA, the exergetic temperatures are used in Ex-PTA. Then, exergy in each temperature interval is determined before the exergy cascade is performed using a similar approach as a heat cascade in the conventional PTA from the top to the bottom of the table.

In addition to the two Ex-PTA required to set exergy targets, a third Ex-PTA is presented. Table 9 shows the exergy cascade based on the Final Enthalpy Cascade from Table 5, i.e. the GCC. The method for constructing this cascade is the same as the previous Ex-PTA. It is important to note that the Pinch is correlated back to the Heat Pinch on Table 5, it is not redefined for each Ex-PTA.

##### 4.5. Step 5: exergy requirement, rejection and losses targeting

Exergy rejection and requirement targets are determined from Table 7, while avoidable exergy losses are determined from Table 8. Exergy value at the lowest exergetic temperature, 1.33 MW, represents the target for maximum exergy rejection ( $X_{\text{rej}}$ ), whereas the exergy value at the highest exergetic temperature, 2.67 MW, is the target for the minimum exergy requirement ( $X_{\text{req}}$ ). These values differ with the result obtained from ExPanD method, which gives a maximum exergy rejection of 0.46 MW and minimum exergy requirement of 6.07 MW [29]. The ExPanD method assumes vertical process-process heat transfer as defined by the Composite Curve. The new method in this paper assumes horizontal process-process heat transfer viewed on the Composite Curve. As a result, the new method is expected to allow for greater rejection of exergy while also requiring less exergy. For the new method, if the exergy rejection of the process exceeds 1.33 MW, exergy transfer across the Pinch will occur and the exergy requirement will increase by (at least) the same amount of excess exergy rejection.

From Table 8, the avoidable exergy loss below the exergetic Pinch temperature (but above the heat Pinch) is 0.48 MW and the avoidable exergy loss above the exergetic Pinch temperature (but

**Table 5**  
PTA for heat cascade.

T (°C)	ΔT (°C)	CP				CP <sub>net</sub> (MW/°C)	ΔH (MW)	H <sub>i</sub> (MW)	H <sub>f</sub> (MW)
		H1 (MW/°C)	H2	C1	C2				
6.85	30	0.185			0.35	-0.17	-4.95	0	6.85
-23.15	20	0.185	0.35		0.35	0.19	3.70	-4.95	1.90
-43.15	40	0.185	0.35	0.325	0.35	-0.14	-5.60	-1.25	5.60
<b>-83.15</b>	40	0.185	0.35	0.325	0.35	0.21	8.40	<b>-6.85</b>	<b>0 (Pinch)</b>
-123.15	35		0.35	0.325		0.03	0.88	1.55	8.40
-158.15	15			0.325		-0.33	-4.88	2.43	9.28
-173.15								-2.45	4.40

**Table 6**  
Decomposed enthalpy cascades.

T <sup>a</sup> (°C)	H <sub>f</sub> (MW)	External Net Surplus/Deficit ( <sup>a</sup> ) (MW)	Initial External Heat Requirement (r,i) Cascade (MW)	External Heat Requirement (r) Profile, H <sub>ext</sub> (MW)	Heat Recovery Pockets (p) Profile, H <sub>p</sub> (MW)
6.85	6.85	-4.95	0	6.85	0.00
-23.15	1.90	<sup>a</sup>	-4.95	1.90	0.00
-43.15	5.60	<sup>a</sup>	-4.95	1.90	3.70
-69.58	1.90	-1.9	-4.95	1.90	0.00
<b>-83.15</b>	<b>0.00</b>	<b>4.4</b>	<b>-6.85</b>	<b>0.00</b>	<b>0.00</b>
-104.10	4.40	<sup>a</sup>	-2.45	4.40	0.00
-123.15	8.40	<sup>a</sup>	-2.45	4.40	4.00
-158.15	9.28	<sup>a</sup>	-2.45	4.40	4.88
-173.15	4.40		-2.45	4.40	0.00

<sup>a</sup> Heat surplus/deficit values relating to heat recovery pockets.

**Table 7**  
Ex-PTA for external heat requirement profile.

T (°C)	H <sub>ext</sub> (MW)	T <sup>E</sup> (K)	ΔT <sup>E</sup> (K)	CP <sub>net</sub> (MW/K)	ΔX <sub>ext</sub> (MW)	X <sub>ext,i</sub> (MW)	X <sub>ext,f</sub> (MW)
6.85	6.85	0.12	2.65	-0.17	-0.45	0.00	1.33
-23.15	1.90	2.77	4.03	0	0	-0.45	0.88
-43.15	1.90	6.80	8.74	0	0	-0.45	0.88
-69.58	1.90	15.54	6.31	-0.14	-0.88	-0.45	0.88
<b>-83.15</b>	<b>0 (Pinch)</b>	<b>21.87</b>	12.70	0.21	2.67	<b>-1.33</b>	<b>0</b>
-104.10	4.40	34.57	15.40	0	0	1.34	2.67
-123.15	4.40	49.97	41.65	0	0	1.34	2.67
-158.15	4.40	91.62	25.31	0	0	1.34	2.67
-173.15	4.40	116.93				1.34	2.67

**Table 8**  
Ex-PTA for heat recovery pocket profile.

T (°C)	H <sub>p</sub> (MW)	T <sup>E</sup> (K)	ΔT <sup>E</sup> (K)	CP <sub>net</sub> (MW/K)	ΔX <sub>p</sub> (MW)	X <sub>p,i</sub> (MW)	X <sub>p,f</sub> (MW)
6.85	0	0.12	2.65	0	0	0	0.48
-23.15	0	2.77	4.03	0.19	0.74	0	0.48
-43.15	3.70	6.80	8.74	-0.14	-1.22	0.74	1.22
-69.58	0	15.54	6.31	0	0	-0.48	0
<b>-83.15</b>	<b>0 (Pinch)</b>	<b>21.87</b>	12.70	0	0	<b>-0.48</b>	<b>0</b>
-104.10	0	34.57	15.40	0.21	3.23	-0.48	0
-123.15	4.00	49.97	41.65	0.02	1.04	2.75	3.23
-158.15	4.88	91.62	25.31	-0.33	-8.21	3.79	4.27
-173.15	0	116.93				-4.42	-3.94

below the heat Pinch) is 3.94 MW. The combined avoidable exergy loss is 4.42 MW, which is also the total exergy loss due to process-

process heat transfer. If the external exergy source (utility) supplies exergy greater than the exergy requirement (assuming no exergy

**Table 9**  
Ex-PTA for the total exergy cascade.

T (°C)	H <sub>f</sub> (MW)	T <sup>E</sup> (K)	ΔT <sup>E</sup> (K)	CP <sub>net</sub> (MW/K)	ΔX <sub>f</sub> (MW)	X <sub>fi</sub> (MW)	X <sub>ff</sub> (MW)
6.85	6.85	0.12				0.00	1.80
			2.65	-0.17	-0.44		
-23.15	1.90	2.77	4.03	0.19	0.75	-0.44	1.36
			15.07	-0.14	-2.11	0.31	2.11
<b>-83.15</b>	<b>0 (Pinch)</b>	<b>21.87</b>	28.14	0.21	5.91	<b>-1.80</b>	<b>0</b>
			41.61	0.03	1.04	4.11	5.91
-123.15	8.40	50.01	25.31	-0.33	-8.23	5.15	6.95
			116.93			-3.08	-1.28

transfer across the Pinch), exergy loss (due to process-utility heat transfer) occurs due to an increase in approach temperature for process-utility heat transfer above the exergetic Pinch. Cross-Pinch addition of exergy to below the exergetic Pinch or the rejection of exergy from above the exergetic Pinch causes the increment of exergy requirement for the process.

The problem can also be represented graphically to help with a more complete understanding of the three sets of exergy cascades. Fig. 4 shows the Exergy Grand Composite Curve (Ex-GCC) based on the Ex-PTA for net exergy cascade in Table 9. The upper and lower values of the net exergy cascade in Table 9 provide net surplus and deficit exergy targets. These targets are not the same as the minimum exergy requirement and maximum exergy rejection targets. This is due to the presence of heat recovery pockets, within which exergy loss occurs. The heat recovery pockets are shaded in yellow, showing that X<sub>source</sub> for the pocket is of great magnitude than the X<sub>sink</sub> with the difference being the exergy loss due to heat transfer within the pocket.

The relationships between exergy surplus/deficit (Table 9) to exergy rejection/requirement (Table 7) is defined by Eqs. (5) and (6).

$$X_{\text{req}} = X_{\text{def}} + X_{\text{loss(above pinch)}}, \text{ i.e. } X_{\text{req}} = -1.28 + 3.94 = 2.67 \text{ MW} \quad (5)$$

$$X_{\text{rej}} = X_{\text{sur}} - X_{\text{loss(below pinch)}}, \text{ i.e. } X_{\text{rej}} = 1.80 - 0.48 = 1.33 \text{ MW} \quad (6)$$

#### 4.6. Step 6: net shaft work requirement determination and economic analysis

After quantifying avoidable exergy loss in the system, the net shaft work requirement is calculated using Eq. (3). The use of exergetic efficiency is significant in this study to measure the performance of sub-ambient processes [27]. Linnhoff and Dhole [15] proposed a value of 0.59 for  $\eta_{\text{ex}}$  while Smith [31] used a value of 0.60. The previous work done by Linnhoff and Dhole [15] showed that there was only 1.9% difference between the proposed  $\eta_{\text{ex}}$  value and the simulation result. In this study, a value of 0.6 is used for  $\eta_{\text{ex}}$  to determine the net compressor shaft work requirement. In terms of exergy rejection ( $X_{\text{rej}}$ ), it can be calculated by multiplying by 0.6 to estimate the work of expansion through a turbine, 0.80 MW. For the required work of compression, the exergy requirement ( $X_{\text{req}}$ ) is divided by 0.6 to estimate 4.45 MW. The net shaft work requirement is determined as 3.65 MW (4.45 MW–0.80 MW). This means that 3.65 MW of power will need to be drawn from the grid to drive the required refrigeration compressors. The COP for the entire refrigeration system is 1.205. Assuming the running hours of the compressor on a yearly basis is 7920 h (330 d), the total power consumption is 28,900 MWh. The tariff for high voltage industrial sector is set at 110 USD/MWh for the case study. As a result, the operating cost target for the process is 3,180,000 USD/y.

#### 5. Reanalysis of the case study with $\Delta T_{\text{min}} = 10^\circ \text{C}$

In this section, the problem is reanalysed using various  $\Delta T_{\text{min}}$  values to demonstrate its effect on process exergy targets. This case analyses the same problem using a  $\Delta T_{\text{min}}$  of  $10^\circ \text{C}$ . The process stream data for the case study is the same as previous with the addition of stream temperature shifts by  $\Delta T_{\text{min}}/2$ . Shifted temperatures ( $T^*$ ) for all supply and target temperatures are added in the column of Table 10 due to introduction of  $\Delta T_{\text{min}}$ . In the next step, the PTA is applied to set process energy targets, as shown in Appendix 1. These targets are 12.2 MW of hot utility, 9.75 MW of cold utility and a Pinch of  $-78.15^\circ \text{C}$ . After that, exergy cascade is performed using Ex-PTA to determine exergy surplus and deficit in

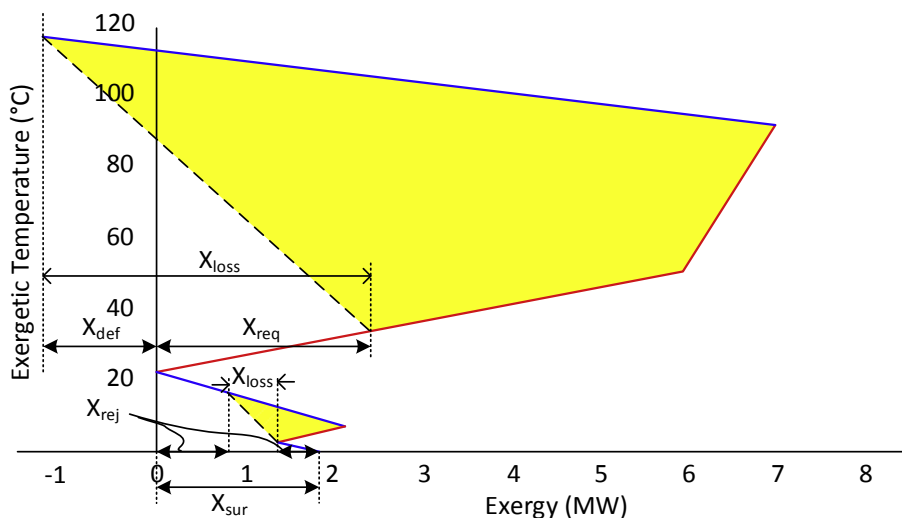


**Fig. 4.** Exergy targets and avoidable exergy losses on an Ex-GCC.

the process which are 2.20 MW and 5.82 MW.

The Grand Composite Curve (GCC) is illustrated in Appendix 2 and the heat recovery pocket region is eliminated to determine avoidable exergy losses. Additional temperature points which are Points 2 and 3 are then determined to remove the heat recovery pockets. By using linear interpolation, Point 2 is  $-51.36\text{ }^{\circ}\text{C}$  and Point 3 is  $-124.58\text{ }^{\circ}\text{C}$ .

The Ex-PTA for the External Heat Requirement Profile (Table 11) and Heat Recovery Pockets Profile (Table 12) are then constructed. From Ex-PTA for the External Heat Requirement Profile, exergy value at the lowest exergetic temperature (2.09 MW) represents the target for exergy rejection, whereas exergy value at the highest exergetic temperature (6.71 MW) is the target for exergy requirement. In Ex-PTA for Heat Recovery Pockets Profile, 0.11 MW is determined as the avoidable exergy loss at below exergetic Pinch temperature and 0.90 MW at above the exergetic Pinch, which contributes to total exergy losses of 1.01 MW. Fig. 5 shows exergy targets illustration in the process. The inclined dashed lines represent exergy loss due to heat transfer in the process. In general term, to determine exergy requirement above exergetic Pinch, exergy deficit is added with exergy losses while exergy surplus is subtracted with exergy losses below exergetic Pinch to get exergy rejection as shown in Eqs. (5) and (6) (see Table 13).

The net compressor shaft work requirement is then analysed. Exergetic efficiency ( $\eta_{ex}$ ) is again assumed as 0.6. To determine the net shaft work requirement of compressor, Eq. (3) is applied, where work consumption ( $X_{req}/\eta_{ex}$ ) of compressor is subtracted with work production by turbine ( $\eta_{ex} X_{rej}$ ). As a result, the net shaft work requirement is 9.93 MW (11.18 MW – 1.25 MW). The running hours of the compressor and tariff for high voltage industrial sector are assumed to be 7920 h in a year and 110 USD/MWh, respectively. Therefore, the total power consumption is estimated around 78,650 MWh. The annual operating cost for refrigerant compression is USD 8,651,500.

**6. Discussion**

The case study results are tabulated in Table 14 for comparing the findings from the ExPAnD method of Marmolejo-Correa [29], the base case (Section 4.1) and additional cases with  $\Delta T_{min}$  of 1, 2, 5 and  $10\text{ }^{\circ}\text{C}$  (Section 4.2). The range of  $\Delta T_{min}$  values provides a better understanding of its impact on the exergy targets (rejection, requirement and avoidable loss). All the cases share the same system assumptions, where the  $\Delta T_{min}$  of the HEN is the only manipulating variable. Since total exergy losses is determined in the ExPAnD method, the total exergy loss is also calculated for each of these cases for comparing the ExPAnD method and the proposed method, as listed in Table 14.

As shown in Table 14, types of exergy losses are divided into three categories: (1) unavoidable exergy losses due to process-process heat transfer at  $\Delta T_{min}$ , (2) avoidable exergy losses due to process-process heat transfer at driving forces greater than  $\Delta T_{min}$ ,

**Table 10**  
Process stream data for the case study with  $\Delta T_{min} = 10\text{ }^{\circ}\text{C}$  [29].

	$T_s$	$T_t$	$T_s^*$	$T_t^*$	$T_t^{*E}$	$T_t^E$	CP
	( $^{\circ}\text{C}$ )	( $^{\circ}\text{C}$ )	( $^{\circ}\text{C}$ )	( $^{\circ}\text{C}$ )	(K)	(K)	(MW/K)
H1	6.85	-123.15	1.85	-128.15	0.31	54.78	0.185
H2	-23.15	-158.15	-28.15	-163.15	3.6	99.44	0.35
C1	-173.15	-43.15	-168.15	-38.15	107.85	5.61	0.325
C2	-83.15	6.85	-78.15	11.85	19.38	0.02	0.35

**Table 11**  
Ex-PTA for External Heat Requirement Profile of the case study with  $\Delta T_{min} = 10\text{ }^{\circ}\text{C}$ .

T	$H_{ext}$	$T^E$	$\Delta T^E$	$CP_{net}$	$\Delta X_{ext}$	$X_{ext,i}$	$X_{ext,f}$
( $^{\circ}\text{C}$ )	(MW)	(K)	(K)	(MW/K)	(MW)	(MW)	(MW)
11.85	12.20	0.02	0.29	-0.35	-0.10	0.00	2.09
1.85	8.70	0.31	3.29	-0.17	-0.54	-0.10	1.99
-28.15	3.75	3.59	2.01	0.00	0.00	-0.64	1.45
-38.15	3.75	5.60	3.46	0.00	0.00	-0.64	1.45
-51.36	3.75	9.06	10.30	-0.14	-1.44	-0.64	1.45
<b>-78.15</b>	<b>0.00</b>	<b>19.37</b>	31.93	0.21	6.71	<b>-2.09</b>	<b>0 (Pinch)</b>
-124.58	9.75	51.30	3.44	0.00	0.00	4.62	6.71
-128.15	9.75	54.74	44.60	0.00	0.00	4.62	6.71
-163.15	9.75	99.34	8.40	0.00	0.00	4.62	6.71
-168.15	9.75	107.74				4.62	6.71

**Table 12**  
Ex-PTA for Heat Recovery Pocket Profile of the case study with  $\Delta T_{min} = 10\text{ }^{\circ}\text{C}$ .

T	$H_p$	$T^E$	$\Delta T^E$	$CP_{net}$	$\Delta X_p$	$X_{p,i}$	$X_{p,f}$
( $^{\circ}\text{C}$ )	(MW)	(K)	(K)	(MW/K)	(MW)	(MW)	(MW)
11.85	0.00	0.02	0.29	0.00	0.00	0.00	0.11
1.85	0.00	0.31	3.29	0.00	0.00	0.00	0.11
-28.15	0.00	3.59	2.01	0.19	0.37	0.00	0.11
-38.15	1.85	5.60	3.46	-0.14	-0.48	0.37	0.48
-51.36	0.00	9.06	10.30	0.00	0.00	-0.11	0.00
<b>-78.15</b>	<b>0.00</b>	<b>19.37</b>	31.93	0.00	0.00	<b>-0.11</b>	<b>0 (Pinch)</b>
-124.58	0.00	51.30	3.44	0.21	0.72	-0.11	0.00
-128.15	0.75	54.74	44.60	0.02	1.12	0.61	0.72
-163.15	1.62	99.34	8.40	-0.32	-2.73	1.72	1.83
-168.15	0.00	107.74				-1.01	-0.90

**Table 13**  
Ex-PTA for total exergy cascade of the case study with  $\Delta T_{min} = 10\text{ }^{\circ}\text{C}$ .

$T^*$	$H_f$	$T^{*E}$	$\Delta T^{*E}$	$CP_{net}$	$\Delta X_f$	$X_{f,i}$	$X_{f,f}$
( $^{\circ}\text{C}$ )	(MW)	(K)	(K)	(MW/K)	(MW)	(MW)	(MW)
11.85	12.2	0.02	0.29	-0.35	-0.10	0	2.20
1.85	8.70	0.31	3.29	-0.17	-0.54	-0.10	2.10
-28.15	3.75	3.6	2.01	0.19	0.37	-0.64	1.56
-38.15	5.60	5.61	13.77	-0.14	-1.93	-0.27	1.93
<b>-78.15</b>	<b>0 (Pinch)</b>	<b>19.38</b>	35.4	0.21	7.43	<b>-2.20</b>	<b>0 (Pinch)</b>
-128.15	10.50	54.78	44.66	0.03	1.12	5.23	7.43
-163.15	11.38	99.44	8.41	-0.33	-2.73	6.35	8.55
-168.15	9.75	107.85				3.62	5.82

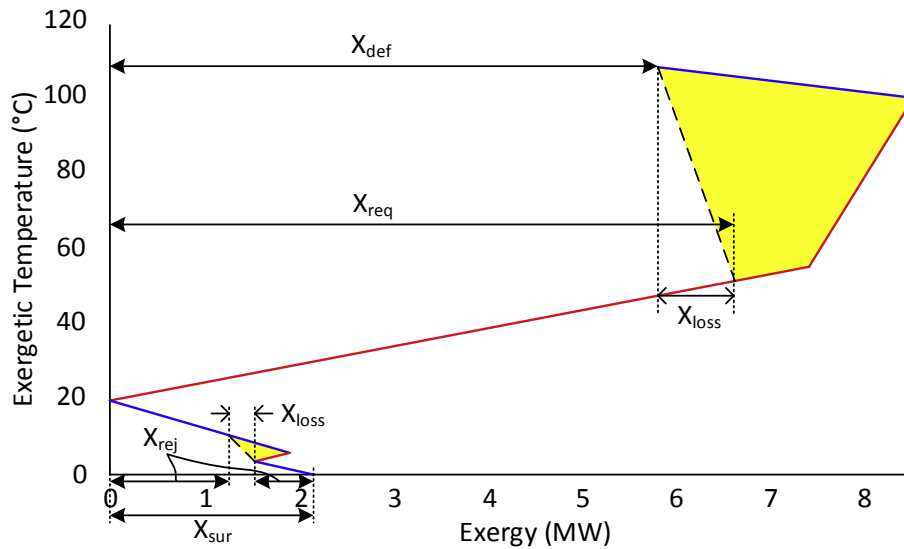


Fig. 5. Exergy Grand Composite Curve (Ex-GCC) of the case study with  $\Delta T_{\min} = 10^\circ\text{C}$ .

Table 14

Comparison of the ExPANd method to the new exergy targeting method for a range of  $\Delta T_{\min}$ .

	ExPANd [29]	Base Case	Case 1	Case 2	Case 3	Case 4
$\Delta T_{\min}$ ( $^\circ\text{C}$ )	0	0	1	2	5	10
Minimum Heating Requirement (MW)	6.85	6.85	7.39	7.92	9.53	12.20
Minimum Cooling Requirement (MW)	4.40	4.40	4.93	5.47	7.07	9.75
Maximum Heat Recovery (MW)	66.90	66.90	66.37	65.84	64.23	61.55
Exergy Surplus (MW)	1.80	1.80	1.84	1.88	2.00	2.20
Exergy Deficit (MW)	-1.27	-1.27	-0.57	0.14	2.27	5.82
Type of Exergy Losses	Total <sup>a</sup>	Total <sup>a</sup>	Avoidable	Avoidable	Avoidable	Avoidable
Exergy Losses –above exergetic Pinch (MW)	7.34	3.94	3.60	3.26	2.29	0.90
Exergy Losses –below exergetic Pinch (MW)	1.34	0.48	0.43	0.38	0.26	0.11
Maximum Exergy Rejection (MW)	0.46	1.33	1.41	1.50	1.74	2.09
Minimum Exergy Requirement (MW)	6.07	2.67	3.03	3.40	4.56	6.71
Expansion Shaft Work Target (MW)	0.28	0.80	0.85	0.90	1.04	1.25
Compression Shaft Work Target (MW)	10.12	4.45	5.05	5.67	7.60	11.18
Net Shaft Work Requirement (MW)	9.84	3.65	4.20	4.77	6.56	9.93
COP Target for Refrigeration	0.447	1.205	1.173	1.146	1.078	0.982
Annual Operating Cost (USD/y)	8,572,600	3,180,000	3,667,900	4,157,700	5,717,500	8,648,100

<sup>a</sup> With  $\Delta T_{\min} = 0^\circ\text{C}$ , all exergy losses due to process-to-process heat transfer are avoidable, i.e. heat transfer at driving forces greater than  $\Delta T_{\min}$ .

and (3) exergy losses due to process-utility heat transfer. Since the  $\Delta T_{\min}$  for base case study is  $0^\circ\text{C}$ , unavoidable process-process exergy loss is nil. Avoidable exergy loss, on the other hand, is proportional to size and location of the heat recovery pockets. The exergy rejection and requirement targets from ExPANd and the proposed (base case) method are different due to the targeting approaches. The ExPANd method aims to determine the exergy targets (rejection, requirement and total loss) considering vertical heat transfer according to Composite Curve. The proposed method determines the exergy targets (rejection, requirement and avoidable loss) based on the concept of horizontal heat transfer as defined during the formation of the Grand Composite Curve. The new method estimates the avoidable exergy losses based on heat recovery pockets and assumes that heat transfer at  $\Delta T_{\min}$  is unavoidable. This change is expected to produce more optimistic but still achievable results. As such, the exergy targets from the proposed method have higher exergy rejection and lower exergy requirement. During the rejection of exergy, there is an opportunity to design a system to recover work through turbine expansion. Whereas the exergy requirement is fulfilled for low temperature processes via the shaft work of compressors. As a result, the new method demonstrates the benefits of horizontal heat transfer, which tends to produce a HEN with more even driving forces

through-out the network.

Exploring the driving force effect from  $\Delta T_{\min}$  in Table 14 shows the exergy rejection and exergy requirement targets increased with the  $\Delta T_{\min}$  increment, while the exergy and energy recovery rate reduced. Fig. 6 shows the changes of estimated shaft work generation and consumption as well as the trend for COP with respect to the  $\Delta T_{\min}$ . For increasing  $\Delta T_{\min}$ , the increases in compression shaft work are at a greater rate than expansion work generation. As a result, the overall impact on COP is a negative trend with respect to  $\Delta T_{\min}$ .

Exergy losses due to heat transfer is inevitable for Process Integration and heat recovery. There should be an acceptable (minimal) exergy loss in any heat transfer system. The total exergy loss from ExPANd method is not comparable with the avoidable exergy losses targeted by the proposed method. Avoidable exergy losses exponentially decreased due to more exergy has been lost during heat exchange within  $\Delta T_{\min}$  interval.

To study the effect of  $\Delta T_{\min}$  on heat and exergy analysis, the operating (net compression) and capital cost for the heat recovery system is required to be estimated as in super-targeting technique. The capital cost estimation is simplified by assuming four heat exchanges are used in the system, which includes heater and cooler, as well as heat recovery heat exchanger at above and below Pinch

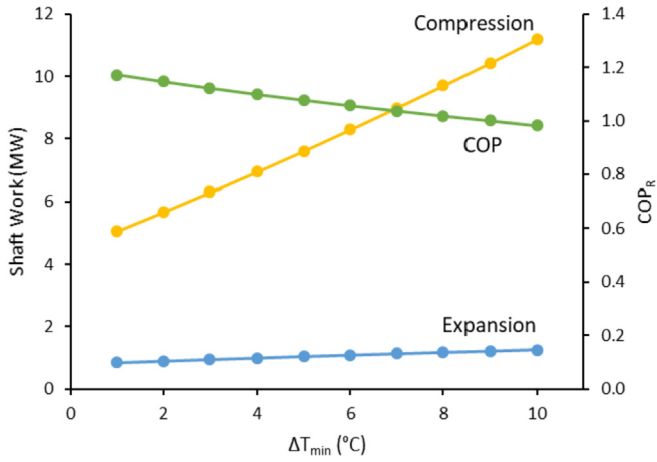


Fig. 6. Shaft work (compression requirement and expansion generation) and Coefficient of Performance (COP) for different  $\Delta T_{min}$ .

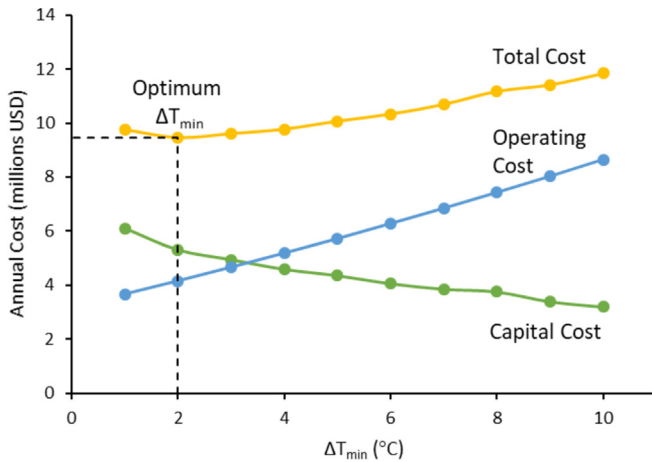


Fig. 7. Super-targeting for optimal  $\Delta T_{min}$ .

temperature. Super-targeting approach is then continued with optimal  $\Delta T_{min}$  determination based on total annualized cost for HEN design. The optimal  $\Delta T_{min}$  is chosen at a point where the lowest total annualized cost and high operating cost are present. As shown in Fig. 7, the optimal  $\Delta T_{min}$  is estimated to be approximately 2 °C, the point of lowest total annualized cost.

## 7. Conclusion

A combined Pinch and Exergy Analysis is performed to analyse energy saving opportunities with minimal exergy losses in low temperature Heat Exchanger Network (HEN). In this study, a novel numerical tool known as, Exergy Problem Table Algorithm (Ex-PTA), are introduced to determine the exergy targets (rejection, requirement and avoidable losses). This numerical tool results in more realistic and achievable findings as compared to the graphical method since this method applies horizontal process-process heat transfer instead of vertical heat transfer. Exergy analysis performed by Ex-PTA is aided by the traditional PTA as for heat cascade. The tool was then illustrated using illustrative case studies. In base case study without minimum approach temperature ( $\Delta T_{min}$ ) assumed, the result showed that exergy rejection and exergy requirement were identified as 1.33 MW and 2.67 MW. Avoidable exergy losses and net shaft work requirement of compressor were 4.42 MW and 3.65 MW. Based on the economic evaluation, 3,180,000 USD/y worth of potential compressor shaft work were lost throughout the process. The effect of  $\Delta T_{min}$  on the energy and exergy targets was then evaluated. The external utility requirement increased with  $\Delta T_{min}$ , while avoidable exergy losses and energy recovery reduced with respect to  $\Delta T_{min}$ . The compression shaft work increases at a higher rate than expansion work generation, along with  $\Delta T_{min}$  increment. The overall impact on COP for the overall refrigeration system decreases with respect to  $\Delta T_{min}$ . The optimal  $\Delta T_{min}$  for HEN design was determined as 2 °C via a super-targeting approach and selection of the point with lowest total annualized cost. The present work can be further developed with focus on pressure changes in low temperature HEN to analyse the effect of pressure manipulation towards Pinch and Exergy Analysis.

## Acknowledgments

This work was carried out under the financial support from Universiti Teknologi Malaysia through UTM Flagship Grant (Q.K130000.2443.03G84). Additional support has also been provided through the collaboration agreement between Universiti Teknologi Malaysia and Brno University of Technology, supported by the EU project “Sustainable Process Integration Laboratory – SPIL”, project No. CZ.02.1.01/0.0/0.0/15\_003/0000456 funded by EU “CZ Operational Programme Research and Development, Education”, Priority 1: Strengthening capacity for quality research.

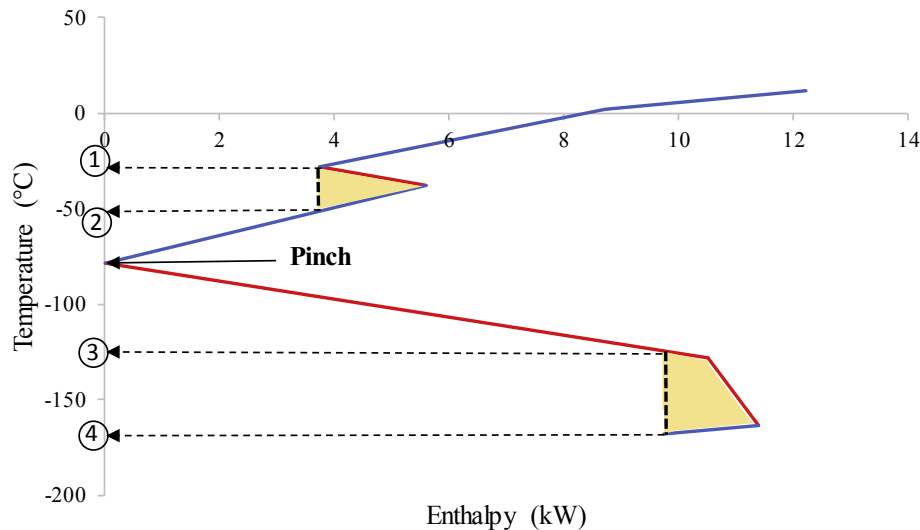
## Appendix 1

PTA for heat cascade of the case study with  $\Delta T_{min} = 10$  °C.

T* (°C)	CP (MW/°C)				$\Delta T$ (°C)	CP <sub>net</sub> (MW/°C)	$\Delta H$ (MW)	H <sub>i</sub> (MW)	H <sub>f</sub> (MW)
	H1	H2	C1	C2					
11.85								0	12.2
1.85				0.35	10	-0.35	-3.50	-3.50	8.70
-28.15	0.185			0.35	30	-0.17	-4.95	-8.45	3.75
-38.15	0.185	0.35		0.35	10	0.19	1.85	-6.60	5.60
-78.15	0.185	0.35	0.325	0.35	40	-0.14	-5.60	-12.20	0 (Pinch)
-128.15	0.185	0.35	0.325		50	0.21	10.50	-1.70	10.50
-163.15		0.35	0.325		35	0.03	0.87	-0.83	11.38
-168.15			0.325		5	-0.33	-1.63	-2.45	9.75

## Appendix 2

Grand Composite Curve (GCC) including pockets for modified case.



## References

- [1] Linnhoff B, Flower JR. Synthesis of heat exchanger networks: I. Systematic generation of energy optimal networks. *AIChE J* 1978;24(4):633–42.
- [2] Hackl R, Harvey S. Total site analysis (TSA) and exergy analysis for shaft work and associated steam and electricity savings in low temperature processes in industrial clusters. *Chem Eng Trans* 2012;29:1974–1979.
- [3] Liew PY, Theo WL, Wan Alwi SR, Lim JS, Abdul Manan Z, Klemeš JJ, et al. Total Site Heat Integration planning and design for industrial, urban and renewable systems. *Renew Sustain Energy Rev* 2017;68(Part 2):964–85.
- [4] Dhole VR, Linnhoff B. Total site targets for fuel, co-generation, emissions, and cooling. *Comput Chem Eng* 1993;17(Supplement 1):S101–9.
- [5] Klemeš J, Dhole VR, Raissi K, Perry SJ, Puigjaner L. Targeting and design methodology for reduction of fuel, power and CO2 on total sites. *Appl Therm Eng* 1997;17(8–10):993–1003.
- [6] Tarighaleslami AH, Walmsley TG, Atkins MJ, Walmsley MR, Liew PY, Neale JR. A Unified Total Site Heat Integration targeting method for isothermal and non-isothermal utilities. *Energy* 2017;119:10–25.
- [7] Tarighaleslami AH, Walmsley TG, Atkins MJ, Walmsley MR, Neale JR. Optimisation of non-isothermal utilities using the unified total site heat integration method. *Chem Eng Trans* 2016;52:457–62.
- [8] Liew PY, Alwi SRW, Varbanov PS, Manan ZA, Klemeš JJ. A numerical technique for total site sensitivity analysis. *Appl Therm Eng* 2012;40:397–408.
- [9] Liew PY, Wan Alwi SR, Klemeš JJ, Varbanov PS, Abdul Manan Z. Algorithmic targeting for Total Site Heat Integration with variable energy supply/demand. *Appl Therm Eng* 2014;70(2):1073–83.
- [10] Gundersen T, Naess L. The synthesis of cost optimal heat exchanger networks: an industrial review of the state of the art. *Comput Chem Eng* 1988;12:503–30.
- [11] Gundersen T. Heat integration: targets and heat exchanger network design. *Handbook of Process Integration (PI)*. London, U.K: Woodhead Publishing; 2013. p. 129–67.
- [12] Wan Alwi SR, Manan ZA. STEP—a new graphical tool for simultaneous targeting and design of a heat exchanger network. *Chem Eng J* 2010;162(1):106–21.
- [13] Aghahosseini S, Dincer I. Exergy-based design and analysis of heat exchanger networks. In: Dincer I, Colpan CO, Kizilkan O, Ezan MA, editors. *Progress in clean energy*, vol. 1. Analysis and Modeling. Cham: Springer International Publishing; 2015. p. 371–87.
- [14] Umeda T, Harada T, Shiroko K. A thermodynamic approach to the synthesis of heat integration systems in chemical processes. *Comput Chem Eng* 1979;3(1–4):273–82.
- [15] Linnhoff B, Dhole VR. Shaftwork targets for low-temperature process design. *Chem Eng Sci* 1992;47(8):2081–91.
- [16] Dhole VR, Linnhoff B. Overall design of low temperature processes. *Comput Chem Eng* 1994;18:S105–11.
- [17] Fritzson A, Berntsson T. Efficient energy use in a slaughter and meat processing plant—opportunities for process integration. *J Food Eng* 2006;76(4):594–604.
- [18] Marechal F, Favrat D. Combined exergy and pinch analysis for the optimal integration of energy conversion technologies. 18th International conference on efficiency, cost, optimization, simulation and environmental impact of energy systems. Trondheim, Norway 2005. p. 177–a.
- [19] Hirata K. Energy saving for ethylene process by advanced process integration. *Chem Eng Trans* 2011;25:81–6.
- [20] Hirata K, Kakiuchi H. Energy saving for ethylene process by adsorption heat pump. *Appl Therm Eng* 2011;31(13):2115–22.
- [21] Ataei A. Application of combined pinch and exergy analysis in retrofit of an olefin plant for energy conservation. *Sci Res Essays* 2011;6(12):2437–46.
- [22] Ghorbani B, Salehi G, Ghaemmaleki H, Amidpour M, Hamed M. Simulation and optimization of refrigeration cycle in NGL recovery plants with exergy-pinch analysis. *J Nat Gas Sci Eng* 2012;7:35–43.
- [23] Aspelund A, Berstad DO, Gundersen T. An Extended Pinch Analysis and Design procedure utilizing pressure based exergy for subambient cooling. *Appl Therm Eng* 2007;27(16):2633–49.
- [24] Fu C, Gundersen T. Sub-ambient heat exchanger network design including expanders. *Chem Eng Sci* 2015;138(Suppl. C):712–29.
- [25] Fu C, Gundersen T. Sub-ambient heat exchanger network design including compressors. *Chem Eng Sci* 2015;137(Suppl. C):631–45.
- [26] Huang K, Karimi IA. Work-heat exchanger network synthesis (WHENS). *Energy* 2016;113(Suppl. C):1006–17.
- [27] Marmolejo-Correa D, Gundersen T. Low temperature process design: challenges and approaches for using exergy efficiencies. *Comput Aided Chem Eng* 2011;29:1909–13.
- [28] Marmolejo-Correa D, Gundersen T. A new graphical representation of exergy applied to low temperature process design. *Comput Aided Chem Eng* 2012;31:1180–4.
- [29] Marmolejo-Correa D. Analysis and design of low temperature processes with focus on LNG. Trondheim, Norway: Norwegian University of Science and Technology; 2013.
- [30] Klemeš J, Friedler F, Bulatov I, Varbanov P. Sustainability in the process industry: integration and optimization: integration and optimization. McGraw-Hill Education; 2010.
- [31] Smith R. Chemical process: design and integration. London, UK: John Wiley & Sons; 2005.

**Article 4:**

*Appropriate placement of vapour recompression in ultra-low energy industrial milk evaporation systems using Pinch Analysis*

**Walmsley, T.G.**, Atkins, M.J., Walmsley, M.R.W., Neale, J.R., 2016.

Energy 116, Part 2, 1269–1281.

DOI: [10.1016/j.energy.2016.04.026](https://doi.org/10.1016/j.energy.2016.04.026)

Citations: 13

Elsevier



# Appropriate placement of vapour recompression in ultra-low energy industrial milk evaporation systems using Pinch Analysis



Timothy G. Walmsley<sup>\*</sup>, Martin J. Atkins, Michael R.W. Walmsley, James R. Neale

University of Waikato, Energy Research Centre, School of Engineering, Hamilton, New Zealand

## ARTICLE INFO

### Article history:

Received 31 December 2015

Received in revised form

6 March 2016

Accepted 6 April 2016

Available online 28 April 2016

### Keywords:

Pinch Analysis

Evaporation systems

Process Integration

Dairy processing

Vapour recompression

## ABSTRACT

This study focuses on applying Pinch Analysis to an industrial milk evaporator case study to quantify the potential energy savings. Modern milk evaporators are typically integrated using both mechanical and thermal vapour recompression technologies as the primary means for attaining a high level of energy efficiency. A significant step change in energy efficiency for milk evaporators is achieved in this study by appropriate placement of vapour recompression in a new improved two-effect milk evaporation system design. The Grand Composite Curve helps identify areas for process modifications and placements of vapour recompression that result in energy reduction. In particular, the innovative placement of Mechanical Vapour Recompression in the system unlocks significant energy, energy cost, and emissions savings. The new design requires 78% less steam (6397 kW) at the expense of 16% (364 kW<sub>elec</sub>) more electricity use. The estimated cost savings associated with the improved design is \$942,601/y and the emissions reduction is 3416 t CO<sub>2</sub>-e/y. Further energy efficiency improvements and cost savings of \$1,411,844/y are gained through improved Total Site Heat Integration through recovery of waste heat from the dryer exhaust air and boiler return condensate streams.

© 2016 Elsevier Ltd. All rights reserved.

## 1. Introduction

Increasing sustainability in food processing through increased processing energy efficiency is a topic of significant global interest [1]. Rising pressure to lower energy use and emissions in all sectors of society are driving the need for energy efficiency related research and implementation [2]. In New Zealand, the food processing sector is dominated by dairy processing with milk powders being the principal product for export. Conversion of liquid milk to powdered milk is an energy intensive two-stage process that uses between 5.2 and 11.1 GJ/t of product depending on the plant's vintage [3]. The first dewatering stage, which is the focal point of the present study, is a multi-effect evaporator train. The second dewatering stage is spray drying, which typically has minimal heat integration [4].

A series of recent studies into the reduction of energy use of milk powder production using Process Integration techniques have chiefly given attention to spray dryer exhaust heat recovery as the key to advancing to the next level of energy efficiency. Focuses of these studies have included optimisation of soft temperatures for

minimising energy use [5], development of HEN (Heat Exchanger Networks) [6], dryer heat recovery modelling [7], and development of a comprehensive economic optimisation of the dryer exhaust heat recovery system [8]. Although the evaporation system was included in some of these studies, the finer details and constraints surrounding the entire evaporation system, including the milk heat treatment section, were not fully appreciated. As a result, improvements in the thermal and electrical energy efficiency for the milk evaporator plant were limited.

Published studies on milk evaporation systems have chiefly focused on the stand-alone energy efficiency of the individual process; without considering a holistic Process Integration approach to designing an evaporation system that optimally integrates with the entire milk powder process [9]. For example, Hanneman and Robertson [10] compared a five-effect milk evaporator train integrated with TVR (thermal vapour recompression) to a single evaporator effect integrated with MVR (mechanical vapour recompression). Their analysis reported the MVR scheme required 55% less fuel use, however their analysis failed to account for any required vapour bleeds and condensers that may be integrated as a heat source in the surrounding process. Available industrial documentation from GEA Niro, a global industrial milk evaporator supplier, presents set-ups and operation techniques for

<sup>\*</sup> Corresponding author.

E-mail address: [timgw@waikato.ac.nz](mailto:timgw@waikato.ac.nz) (T.G. Walmsley).

## Nomenclature

### Roman

<i>COP</i>	coefficient of performance
<i>H</i>	heat flow (kW)
<i>HSR</i>	heat savings ratio (kW/kW)
<i>PR</i>	thermo-compressor performance ratio (kg/kg)
<i>PT</i>	Pinch Temperature (°C)
<i>Q</i>	duty (kW)
<i>T</i>	temperature (°C)
<i>T*</i>	shifted temperature (°C)
<i>TS</i>	supply temperature (°C)
<i>TT</i>	target temperature (°C)
<i>W</i>	work (kW)

### Greek

$\Delta$	difference between two states
----------	-------------------------------

### Subscripts

<i>bleed</i>	vapour bleed
<i>c</i>	cold
<i>cond</i>	condensation/condenser
<i>comp</i>	compression
<i>cont</i>	contribution
<i>ele</i>	electrical

<i>evap</i>	evaporation
<i>feed</i>	feed to evaporator effect
<i>flash</i>	flash vapour of the liquid feed
<i>h</i>	hot
<i>in</i>	inlet
<i>r</i>	recovery
<i>sens</i>	sensible heating of the liquid feed
<i>steam</i>	steam utility use

### Abbreviations

CC	Composite Curves
CIP	clean-in-place
DSI	direct steam injection
FB	fluidised bed
GCC	Grand Composite Curve
HEN	heat exchanger network
HPS	high pressure steam
HT	high temperature
HTHW	high temperature hot water
HVAC	heating, ventilation and cooling
LTHW	low temperature hot water
MPS	medium pressure steam
MVR	mechanical vapour recompression
TSHI	Total Site Heat Integration
TVR	thermal vapour recompression

milk evaporators, which achieve a high-energy economy [11], but these are often sub-optimal with respect to an entire site. It is anticipated that applications of Process Integration techniques to the milk evaporation system problem will yield substantial economic steam savings, as have been found for other industries [12].

Thermal and mechanical vapour recompression technologies find excellent application in a wide range of processing systems. TVR uses a thermocompressor with high pressure vapour (steam utility) to recompress low pressure vapour (often under vacuum) to a slightly higher pressure and temperature. MVR uses a mechanical fan, normally driven by electricity, to recompress low pressure vapour to a slightly higher pressure and temperature. In distillation systems, MRV can directly compress top distillate vapour for use in the reboiler or can indirectly recover heat from the distillate vapour using a separate working fluid such as n-pentane before upgrade and use in the reboiler. These processing structures led to a step-change in energy integration [13]. In desalination systems, multi-effect evaporation systems integrated with an absorption heat pump and vapour compression cycles can effectively synthesize to generate cooling and fresh clean water at 26% lower total cost compared to [14]. TVR has found application in carbon capture processes to upgrade and recovery of waste, resulting in energy savings between 10 and 14% [15]. In milk evaporation systems, vapour recompression units directly compress vapour flows drawn from the product on the tube-side (“evaporator”) to a higher pressure and temperature for use as the condensing vapour on the shell-side (“condenser”). As a result, this arrangement creates a so called open cycle heat pump. The analogy between vapour recompression and conventional heat pumps also extends to the idea of appropriate placement in Pinch Analysis, which states that a heat pump should upgrade heat from below the Pinch for use above the Pinch [16].

Purposeful design and integration of the evaporation system to complement the heat demands of neighbouring processes provides greater opportunities for energy and emissions savings. TSHI (Total

Site Heat Integration) provides a valuable framework for understanding and optimising the site-wide heat balance [17,18]. Application of TSHI has recently led to substantial utility savings in slaughter and meat processing [19], large industrial parks in Japan [20] and Thailand [21], chemical processing clusters [16,17], and Kraft pulp mills [23]. With respect to the milk evaporation system design problem, TSHI can help determine the value of heat exports from the evaporation system to neighbouring processes.

The aim of this study is to develop an ultra-low energy design for a milk evaporation system through the appropriate placement of vapour recompression, given the context of a stand-alone milk powder factory. To achieve this aim, a combination of Pinch Analysis, TSHI, and process modelling techniques are applied to the milk evaporation system problem to identify critical components of an ultra-low energy evaporation system design. A modern industrial two-effect evaporator case study provides a useful starting point, comparison, and scope for the new evaporation system design. To ensure a fair comparison, the new design is constrained to have the same number of effects as the industrial base case. Milk processing constraints related to product quality, thermal treatment, and thermophile growth, are important considerations in the solution development. In particular, the GCC (Grand Composite Curve) plays an important role in the analysis to help identify where process modifications and vapour recompression can be considered to provide a step change in energy efficiency. Targets for energy use, energy cost, and emissions are calculated to determine the benefits of shifting towards an ultra-low energy milk evaporation system. The presented analysis is an extension of the early work by the authors [9].

## 2. Historical developments in energy efficiency of industrial milk evaporation systems in New Zealand

Over the past four decades, there has been significant progress in the design and efficiency of milk evaporators in the New Zealand

dairy industry. The presented historical developments are based on generalised historical design trends for New Zealand milk powder factories, but there are individual exceptions.

Plants built in the 1980s tended to have installed either a conventional four or seven-effect milk evaporator system. Four-effect milk evaporators have a *COP* (Co-efficient of Performance), i.e. the ratio of evaporation in kJ to energy input in kJ, of about 4 and the systems reject 560 MJ/ $t_{\text{evap}}$  of low-grade heat through cooling towers and in discharged warm condensate streams due to low overall heat integration.

In the early 1990's, the new vintage of plants favoured four-effect evaporation systems with integrated TVR. These evaporation systems achieve a *COP* of about 7. Heat integration between the evaporators and the background processes was also improved compared to earlier designs and, consequently, about 300 MJ/ $t_{\text{evap}}$  of heat is rejected in cooling towers and discharged condensate flows.

Milk evaporator designs since mid-1990 have mostly used a combination of MVR and TVR technologies in either two or three effect arrangements. The overall *COP* of these evaporation systems are about 30 and may no longer need a cooling tower to reject low-grade heat. However, unrecovered low-grade heat of about 83 MJ/ $t_{\text{evap}}$  is contained in discharged condensate streams (25–35 °C) that are seemingly above the milk powder plant's hot Pinch Temperature (13 °C) [5].

Improvements in energy efficiency of milk evaporation systems in New Zealand, however, have been marginal since the shift to MVR/TVR combinations. Industry practice with respect to energy efficiency of the evaporation system has plateaued. The questions addressed by this work are: Does the current energy efficiency plateau represents a thermodynamic limit for these systems? Are further step-changes in energy efficiency possible? And, what are the key design elements that will enable such a step change in energy efficiency?

### 3. An elementary analysis of integrated evaporation systems

The design and set-up of an evaporation system plays a fundamental role in determining the thermodynamic energy efficiency potentials of a system. As a result, it is first important to understand the simple Pinch Analysis concept of an ideal integrated evaporation system [12], which can help maximise the degree of energy recovery for an entire system. Simple illustrations in Fig. 1 are used to describe this concept for multi-effect evaporation systems with and without vapour recompression. The effect of vapour recompression on the overall heat balance is also critical to the present work. As a result, heat balances of single effect evaporation systems with MVR and TVR and various liquid feed temperatures,  $T_{\text{feed}}$ , relative to the evaporation temperature, which affect the availability of heat for recovery from an evaporation system, are illustrated in Fig. 2. To help demonstrate various principles in this section, the heat load profiles of the evaporation system, i.e. the evaporation and condensation heat loads in each effect, are presented separate to the background process heat load.

The ideal integration of evaporation systems depends on the required evaporation load compared to the heating and cooling needs of the background processes, which can be represented as a GCC (Fig. 1). Multi-effect evaporation systems are preferably integrated so that the system fits either above the Pinch as a source (Fig. 1a), below the Pinch as a sink (Fig. 1b), or inside a heat recovery pocket of the background GCC (not shown), in such a way that no extra utility is needed beyond the demands of the background processes [24]. It is also possible to position evaporator effects either side of the Pinch Temperature without increasing overall utility consumption, but not across the Pinch Temperature.

If the hypothetical net heat load cascade of the background processes is reduced relative to the evaporation system load as illustrated in Fig. 1c and d, one may choose to increase the number of evaporator effects to offset the lower inter-system heat integration potential. However, there are many situations where increasing the number of effects is not technically feasible and/or economically viable. For such situations, integration of vapour recompression in evaporation systems provides an alternate method for reducing utility demand while potentially using less evaporator effects.

TVR appropriately integrates into evaporation systems that are above the Pinch Temperature of the background processes, as illustrated in Fig. 1c. TVR uses high-pressure steam utility to provide the work to recompress some of the low-pressure evaporated vapour using a thermocompressor (Fig. 2a, c, and e). The remaining low-pressure vapour exiting the tube-side condenses in a condenser. The condenser duty depends on the performance ratio of the thermocompressor, which is characteristic to a particular design [25], and the liquid feed temperature. Thermocompressor performance ratio, *PR*, is

$$PR \equiv \frac{\dot{m}_{\text{upg}}}{\dot{m}_{\text{ut,st}}} \quad (1)$$

Heat from the condenser and subsequent warm condensate streams ideally cascade as a heat sources for the background processes. If not, utility use will increase by  $\Delta Q_h$  and  $\Delta Q_c$ , as illustrated for the TVR system in Fig. 1c. As a result, if the condenser heat is composited into the background process GCC, the inclusion will change the Pinch Temperature to be driven by the evaporation system, such as the condenser pressure. For such situations, MVR may consider as an alternate vapour recompression method because that inputs less energy (electricity) and therefore outputs less waste heat, preventing the increase in steam consumption.

MVR also appropriately integrates into evaporation systems that are above the Pinch Temperature of the background process (Fig. 1d), although it may also be used below Pinch if multi-effect evaporation is not possible. It is important to note that if the evaporation and condensation loads of the evaporator were added to the background, the Pinch Temperature of the combined process would be driven by the evaporation system. Implementation of MVR therefore follows the appropriate placement principle for heat pumps, i.e. heat is upgraded from below the Pinch to above the Pinch.

MVR integrated effects commonly recompress all the low-pressure evaporated vapour on the tube-side to the shell-side pressure (Fig. 2 b, d, and f). A vapour bleed from the shell-side of the effect is normally requisite to balance the evaporation and condensation loads. The vapour bleed is an additional heat source for the background processes. If liquid feed is overly subcooled, i.e.  $T_{\text{feed}} < T_{\text{evap}}$ , steam utility (or recovered heat) may be consumed to pre-heat the liquid feed before entering the evaporator (or to inject it into the shell-side of the evaporator) in order to reach the desired evaporation load and therefore production rate (Fig. 2e). The required work of compression,  $W_{\text{comp}}$ , is primarily dependent on the initial vapour pressure and its required temperature lift. Unlike TVR systems, MVR integrated systems does not benefit from multi-effect arrangements. A limitation of MVR units is the maximum saturation temperature lift achieved by a single MVR unit is nominally 8 °C. When larger pressure and temperature lifts are needed, MVR fans can be placed in series. Combinations of MVR and TVR as part of an evaporation system above the Pinch may also be designed to match the GCC of the background processes, which minimises utility consumption and operating energy cost.

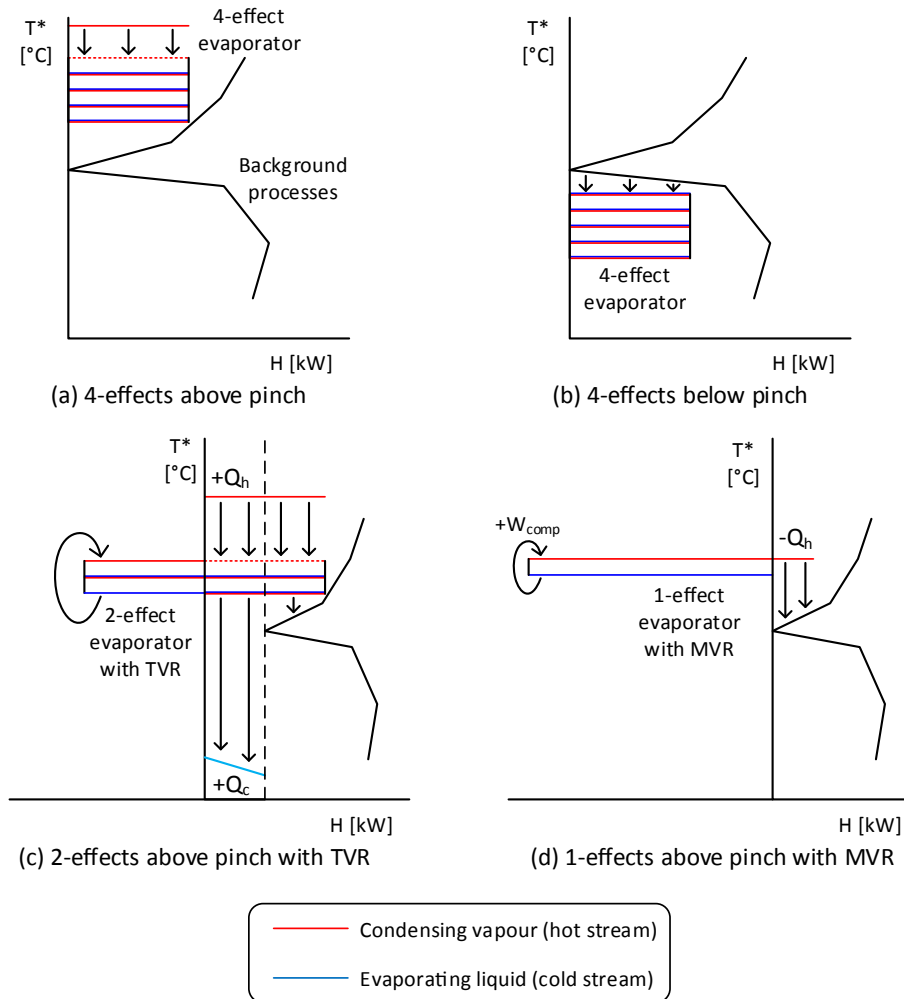


Fig. 1. Conceptual integration of evaporation systems including vapour recompression with background processes.

#### 4. Methodology

A sequential design and optimisation approach following the process design analogy of the Onion Diagram [26] has been taken in this investigation. At the core of the Onion Diagram is the reactor system, followed (in order) by layers for the separation system, the HEN, the utility system, and waste treatment. In the case of a milk evaporation system, there is no so called reactor; rather, the evaporator design, which includes the arrangement and number of effects, may be considered as the core of the system (i.e. the separation system), which is surrounded by a HEN. Starting with a modern evaporation system design as the base case, the study presents analysis of the following scenarios:

1. Improvements for the HEN given the base case evaporator design;
2. Process temperature modification for improved heat recovery given the base case evaporator design;
3. Appropriate selection and placement of vapour recompression for a new evaporator system design;
4. Design of the HEN; and,
5. Heat import and export targets for TSHI for the base case design and new designs.

To target these scenarios, a combination of process modelling, Pinch Analysis, and TSHI form the basis of the targeting, design, and optimisation analysis for milk evaporators. Process modelling helps determine the multiple downstream effects from making a process modification. Pinch Analysis is applied to calculate heat recovery and utility targets for a given set of stream data. The Pinch Design Method is applied to design the HEN. TSHI helps determine the value of heat exports from the evaporation system given a correctly integrated site.

##### 4.1. Process model description

A detailed heat and mass balance process model of a multi-effect falling film milk evaporator system, including both MVR and/or TVR, has been implemented in an Excel™ spreadsheet. The model has been validated for the current set-up using the industrial plant data. The model applies standard water/steam properties (IAPWS IF-97) and milk properties [27]. Based on industrial data, low pressure mechanical compressors (MVR) have a calculated isentropic efficiency of 80%. Thermocompressor performance is modelled using the model of Sargolzaei et al. [28], assuming choked flow through the thermocompressor. The model was applied to test various retrofit and new build concepts to determine the impact on overall energy efficiency. As the proposed concepts are applied, the

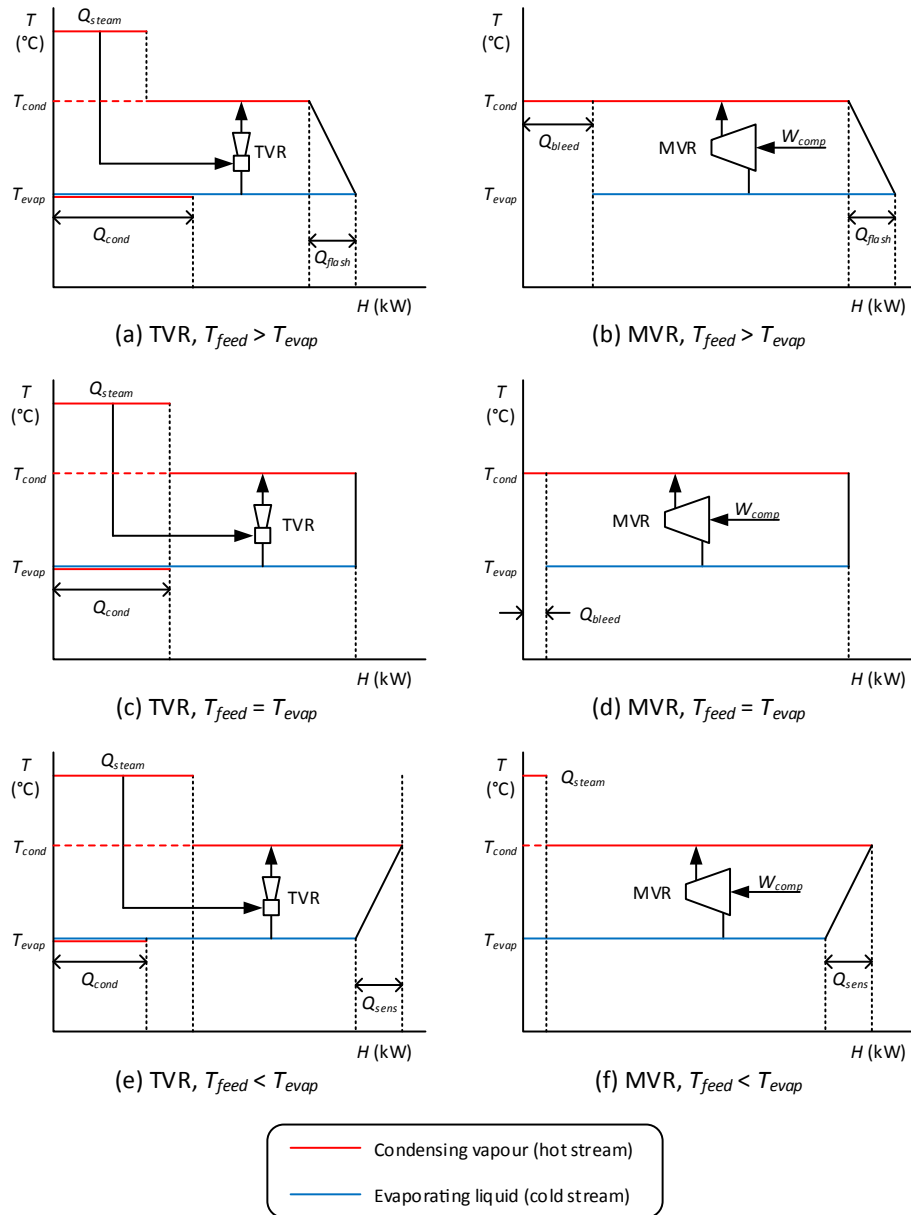


Fig. 2. Heat balances of single evaporator effects integrated with MVR and TVR with the same evaporation duty.

mass and energy balance model recalculates, which in turn affects the PA stream data and the calculated Pinch targets.

4.2. Process and Total Site Heat Integration targeting

Pinch Analysis techniques for evaporation systems [12] have been applied to calculate utility and heat recovery targets for the evaporation processing zone. The inclusion of vapour recompression into the evaporation system is based on the appropriate placement principle for heat pumps [16]. A Heat Savings Ratio is calculated to determine the effectiveness of integrating vapour recompression into the evaporation system. The HSR is defined as

$$HSR = \frac{Q_{h, reduction}}{Q_{in}}, \text{ where } Q_{in} = \begin{cases} W_{comp} \in \text{MVR} \\ Q_{steam} \in \text{TVR} \end{cases} \quad (2)$$

TSHI (Total Site Heat Integration) [18] has been applied to understand the integration potential between the evaporation system

and the remainder of the milk powder processes. Utility use has been targeted at the process level and later combined and matched for TSHI. Targeting utilities at the process level ensures targets for hot water systems are realistic.

5. Industrial milk evaporation system case study

5.1. Process description and processing constraints

Milk evaporators have several upstream and downstream processes that provide opportunities for heat integration. These milk processing steps also have a number of processing constraints that must be satisfied to obtain an industrially acceptable solution.

Important upstream processes of the evaporation system include a milk separation process, which includes cream pasteurisation, and a milk heat treatment process. At modern factories, the milk separation process separates raw milk from the farm into skim

milk and cream, while the fluids are cold ( $\sim 8$  °C). Older designs use a hot separation process ( $\sim 45$  °C) with greater energy demand. The new cold milk separation technology requires about 10 MJ/ $t_p$  of hot water utility and 10 MJ/ $t_p$  of chilled water utility, which is primarily associated with cream pasteurisation. The older hot separation technology demands about 170 MJ/ $t_p$  of hot water utility and 170 MJ/ $t_p$  of chilled water utility. The milk separation process usually services multiple dairy processing plants, e.g. milk powder plant, cream plant, and butter plant. As a result, the scheduling of the milk separation process tends to depend on the timing of the in-flow of milk from the farm, which may differ from the production schedule of the milk powder plant. Steam availability due to differences in production schedules should be considered when analysing heat integration opportunities. In the case study, direct integration between the evaporator system and milk separation process is disallowed, rather integration through the utility system, Total Site Heat Integration, is required.

The milk heat treatment process is a combination of holding temperature (80–120 °C) and time (1–60 s), which affect the degree of protein denaturation [29] and the flavour of the milk powder [30]. Milk enters the heat treatment process at about 8 °C, i.e. its storage temperature, and heats to the heat treatment temperature, which is 94.5 °C for the case study. Conventional heat recovery via heat exchangers normally heats milk to about 80 °C. During the preheat phase, it is important to recognise that rapid thermophile growth occurs in the temperature range of 45–60 °C [31]. If conventional heat exchangers are used to preheat milk through the thermophile temperature range, two parallel processing lines, which includes duplicate heat recovery exchangers, are needed to allow for mid-evaporator run cleaning (about every 4 h). If direct vapour (or steam) injection is used to heat the milk through the thermophile temperature range, the requirement of mid-run washing is avoidable, i.e. no need for parallel processing lines. Once milk exceeds 80 °C, it is important to limit contact between milk and processing equipment surfaces and to tightly control the residence time of the milk at a specific heat treatment temperature. To fulfil this constraint, DSI (direct steam injection) rapidly heats the milk to 94.5 °C, the heat treatment temperature. After being held for a short time, milk is flashed to between 80 and 85 °C for instantaneous cooling and generation of low-pressure vapour for heat recovery. In New Zealand factories, the milk heat treatment process operates on the same schedule as the evaporation system and it is directly integrated with the evaporation system.

The evaporation system follows the heat treatment process. The multi-train, multi-effect falling film evaporation system concentrates standardised milk from about 12% to 52% solids. Multiple effects improve the energy efficiency of the evaporator and the multiples train enable continuous operation. Each evaporator train is washed CIP (clean-in-place) about every 16 h to maintain food grade processing hygiene. The common temperature-operating window of industrial evaporator systems is 45–73 °C. The upper temperature limit relates to avoiding further denaturing of proteins, which adversely affects the flavour of the final milk powder product [31].

The final processing step is the spray dryer system. After exiting the final milk evaporator effect, milk is heated to about 75 °C and homogenised before being atomised and co-currently spray dried using hot air (210 °C) to form milk powder. Partially dry powder from the main spray dryer chambers exits through a series of fluidised beds that provides sufficient residence time to complete the drying process and cools the powder from around 80 °C in the main chamber to about 35 °C in the final fluidised bed. Spent dryer air passes through cyclones and/or baghouses to help capture any entrained particles before being exhausted to the atmosphere at

about 75 °C. The spray dryer and its auxiliary processing equipment is washed every 2–4 weeks.

## 5.2. Evaporation system process design and stream data

The base-case site has a 2-effect evaporator system with integrated vapour recompression (Fig. 3). The first effect is integrated with MVR and the second effect is integrated with TVR. The MVR effect currently operates at 68 °C (milk-side) with a duty of 115 MW and the TVR effect operates at 56 °C (milk-side) with a duty of 5 MW. Both effects have approach temperatures of 5 °C (condensation temperature to evaporation temperature). Some vapour from the TVR effect is upgraded in a secondary thermocompressor to indirectly pre-heat milk via the shell-side of the MVR effect. Table 1 presents the measured stream data for the base case design set-up for the evaporation system, including the heat treatment process, and the spray dryer process. For Pinch Analysis, the heat treatment process is counted as part of the evaporation system zone. The Exhaust Air stream from the dryer for the purpose of the Total Site Analysis forms its own zone because it is physical distant from the other streams in the Spray Dryer Zone.

Stream flow rates are a function of the scale of production, i.e. tonnes of powder produced per hour,  $t_p/h$ . Most stream temperatures, including the evaporator pressures/temperatures, are soft and independent of production scale. Hard temperatures include the incoming temperature of the standardised milk (8 °C), the milk heat treatment temperature (94.5 °C), the final temperature of the milk concentrate (70 °C), and the CIP water supply and target temperatures (15 °C and 85 °C). Utility prices for the site in New Zealand dollars are \$25.00/t for steam and hot water heating and \$100/MWh for electricity. Site utility stream data is given in Table 2. Heat integration targets are based on a  $\Delta T_{cont}$  of 2.5 °C for liquid and vapour streams and 12.5 °C for gas streams, which reflect the difference in typical heat transfer coefficients for the various fluids (2–8 kW/[m<sup>2</sup>°C] for liquid and vapour streams and 0.1 kW/[m<sup>2</sup>°C] for gas streams).

## 6. Results and discussion for milk evaporation system case study

### 6.1. Pinch Analysis targets for base case evaporation design

Initial applications of Pinch Analysis focus on improving the HEN of the evaporation system. CC (Composite Curves) and GCC are plotted in Fig. 4 based on the base case design. Heat transfer within the evaporator effects, which total 120,560 kW, have been excluded from the CCs and GCCs. Heat recovery for the base case design is 18,309 kW. The Pinch Analysis target suggests an additional heat recovery of 1322 kW is possible compared to the base design. The Pinch Temperature is 80.5 °C. The Pinch occurs between the HT Milk Flash stream and the composite of the Cold Milk and CIP Water streams. There is also a near Pinch at 70.5 °C driven by the operating pressure of the shell-side of Effect 1 from which vapour is bled, i.e. the Vapour Bleed stream. If the minimum approach temperature is hypothetically set near 0 °C, the maximum thermodynamic heat recovery is 21,037 kW, which is 2728 kW (or 15%) greater than the base case. In this extreme case, the Pinch Temperature remains driven by the soft temperature of the HT Milk Flash stream.

### 6.2. Process temperature modifications for base case evaporation design

Further energy savings can be obtained through minor process modifications. Process modifications have been implemented in the

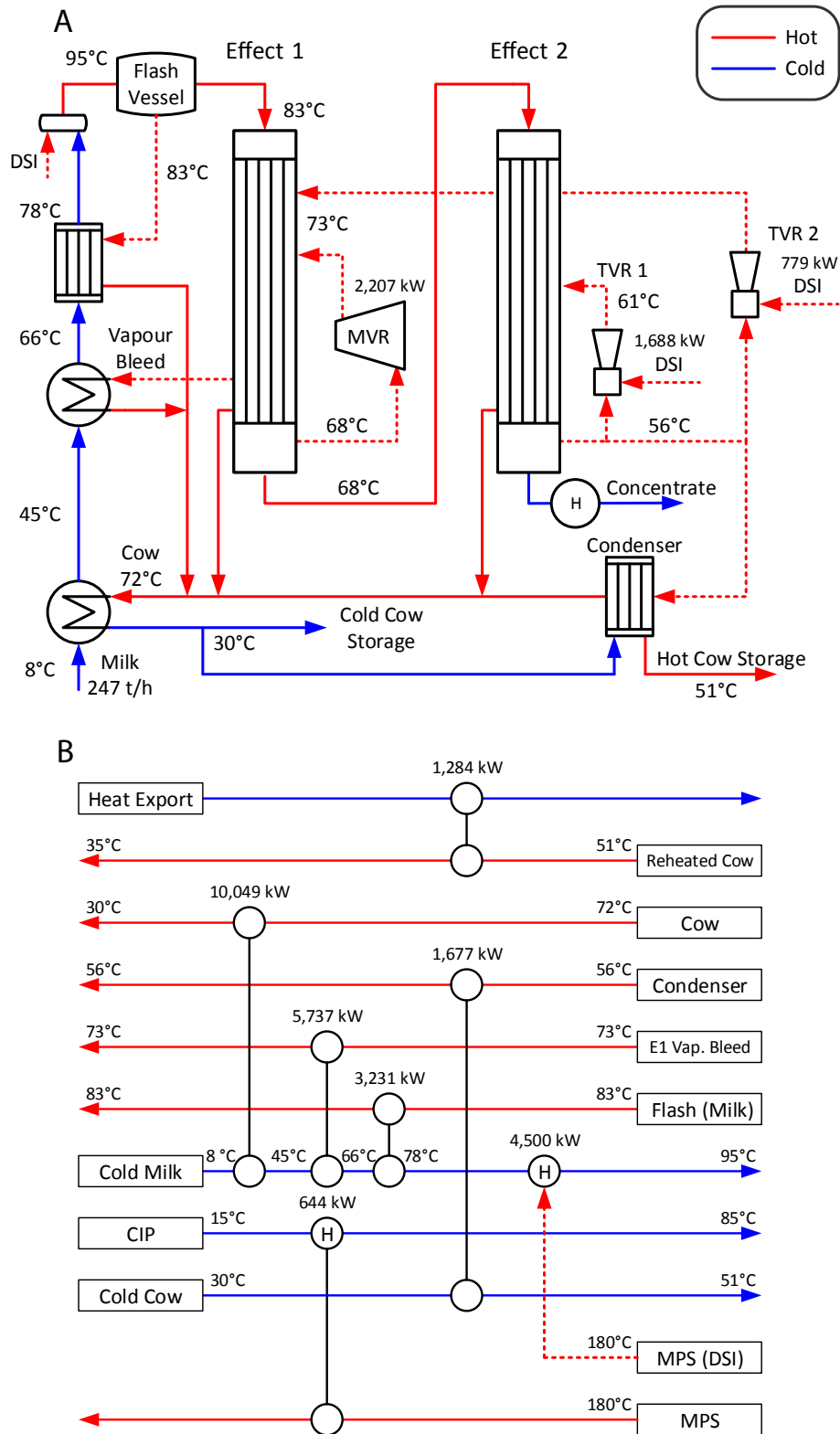


Fig. 3. Base-case industrial milk evaporator integration illustrated using a process flow diagram (A) and grid diagram (B).

detailed process model to ensure the numerous downstream impacts of changing a process variable, e.g. temperature, for the evaporation system are accounted for. New stream data may then be extracted from the model for reapplication of Pinch Analysis. When considering process modifications, the Plus/Minus Principle

recommends to keep hot streams hot and to keep cold streams cold [26]. This principle is most effective for increasing energy recovery when applied to the stream that drives the Pinch [6], which in this case is the HT Milk Flash stream. There are multiple downstream effects from changing the HT Milk Flash temperature. This flash

**Table 1**  
Base case site stream data.

Process stream	TS [°C]	TT [°C]	CP [kW/°C]	$\Delta H$ [kW]
<i>Heat treatment and evaporator zone</i>				
Cold milk	8	95	272	23,557
HT flash vapour	83	83		3231
E1 vapour bleed	73	73		5733
E2 Condenser	56	56		1677
COW	73	13	237	14,103
CIP Water	15	85	9	644
<i>Spray dryer zone</i>				
Concentrate	56	70	49	692
Dryer inlet air	15	210	132	25,757
FB inlet air	15	95	66	5301
HVAC	15	25	53	531
<i>Dryer roof zone</i>				
Exhaust air	75	55	279	5714
<i>Boiler</i>				
Condensate	85	40	50	2250

**Table 2**  
Base case site utility stream data.

Utility stream	Type	TS [°C]	TT [°C]
HPS	Hot	250	250
MPS	Hot	180	180
HTHW	Hot	80	65
LTHW	Hot	55	35
Cooling Water	Cold	25	30

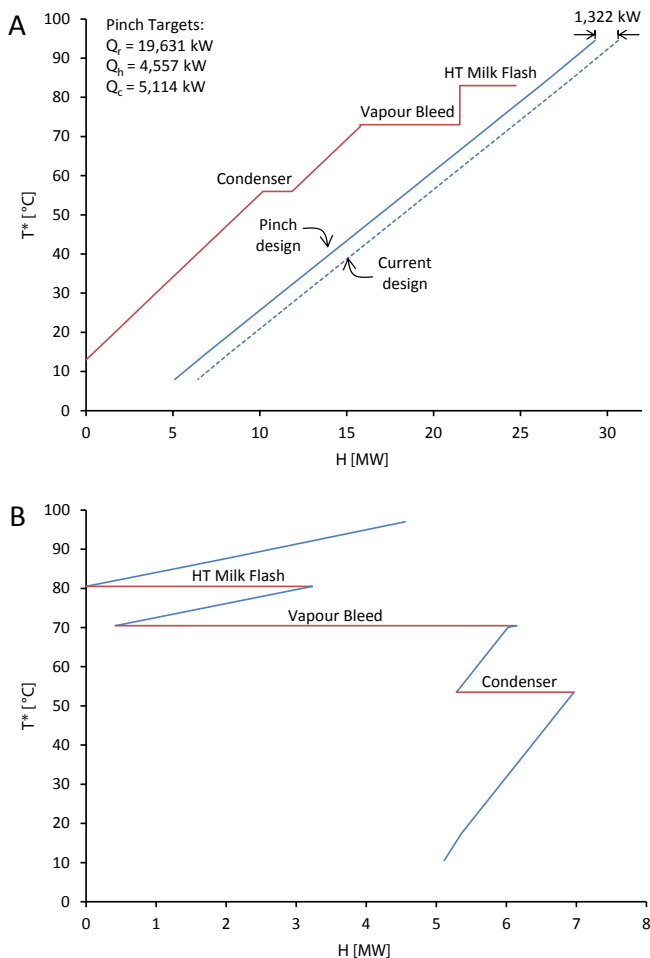


**Fig. 4.** CCs (A) and GCC (B) for the current evaporator design.

temperature primarily affects: (1) the amount of flashing that occurs as the liquid milk feed enters the first evaporator effect; (2) the amount of required heat transfer in the first effect; (3) the required duty of the vapour bleed from the first effect; and, (4) the condenser duty. The development of a comprehensive process model was therefore an essential part of the Pinch Analysis and heat recovery design optimisation investigation.

Following the Plus/Minus Principle, the HT Milk Flash temperature has been increased by 0.7 °C in the process model and new targets calculated (Fig. 5). The new HT Milk Flash temperature was chosen so that two Pinches would occur on the GCC, which is an indication of maximum heat recovery [6]. As a result the heat recovery target increases by 199 kW. Further increases in the HT Milk Flash temperature yield no additional benefit due to the second Pinch Temperature at 70.5 °C driven by the Vapour Bleed stream. The Vapour Bleed temperature, which is determined by the shell-side operating pressure of Effect 1, is constrained by the allowable operating temperature window for milk evaporators, which means it cannot be increased. As a result, the heat recovery target of 19,826 kW represents the best case design for the given evaporation system design.

### 6.3. Appropriate placement of vapour recompression in new evaporation system designs

A new evaporation system design can be developed by considering the appropriate use of vapour recompression. The integration of vapour recompression (either MVR or TVR) into an evaporation system should be ideally applied according to the appropriate placement principle for heat pumps. To develop the new design, the effects of the vapour recompression units in the current evaporation system on the stream data are removed and the evaporation/condensation occurring in the evaporator effects are added as stream data for the Pinch Analysis.

The GCC in Fig. 6A suggests Effect 1 should be integrated using MVR, as it is in the base case design. MVR is preferred since there is minimal opportunity to cascade heat through the evaporation system to heat other sinks [9]. The HSR (Heat Savings Ratio), which is defined in Eq. (2), for Effect 1 with MVR is 52. The GCC in Fig. 6B results from assuming Effect 1 is integrated with MVR and heat transfer within the MVR effect is removed from subsequent GCCs. The tube-side temperature of Effect 2 now drives the Pinch Temperature at 53.5 °C. There are three options to further improve energy efficiency: (1) integrate Effect 2 using TVR, (2) integrate

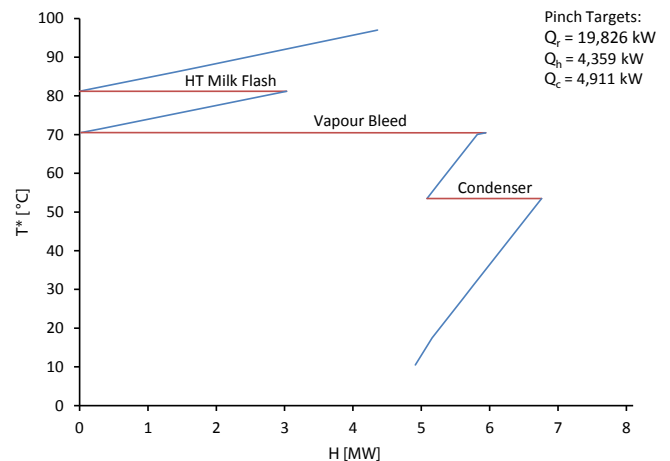


**Fig. 5.** GCC with new HT Milk Flash temperatures of 83.7 °C, given the current two-effect evaporator set-up integrated with one MVR and two TVR units.

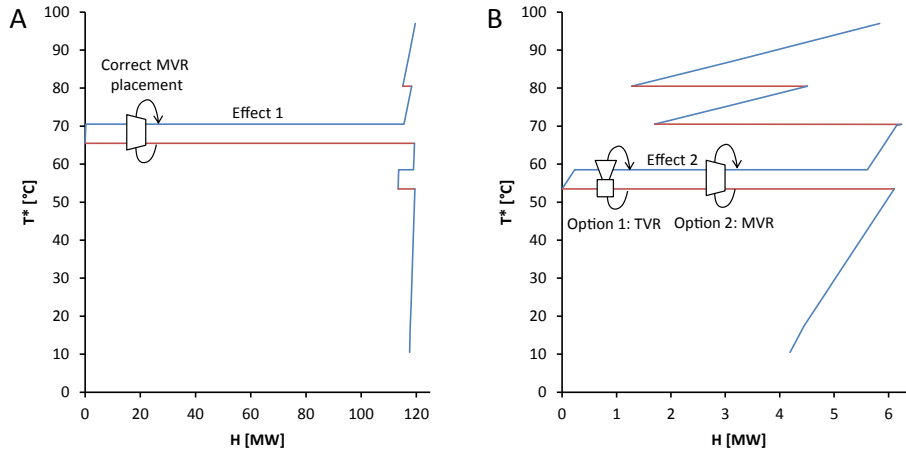


Fig. 6. GCC for evaporation system problem without vapour recompression (A) and with MVR for Effect 1 (B).

Effect 2 using MVR, and (3) add another effect that operates at 61 °C with heat cascading from Effect 2. This paper focuses on the first two options, while the third option, which requires an additional effect, is beyond the current scope. Using either MVR or TVR to integrate with Effect 2 also opens the possibility of additional vapour recompression for use in the milk heat treatment process. These options are explored using the GCC as an important tool for identifying the integration of vapour recompression in Figs. 7 and 8, with a summary of the corresponding energy targets in Table 3.

Fig. 7 presents the graphical development of a new MVR/TVR evaporation system design given Effect 1 uses MVR and Effect 2 uses TVR. The HSR for Effect 2 with TVR is  $-0.2$  (Fig. 7A), which means the total steam use increased after including TVR for Effect 2. However, the use of TVR for Effect 2 helps identify that MVR should upgrade 3770 kW of heat from the shell-side of Effect 1 to directly heat milk above the HT Milk Flash temperature. Implementation of the changes shown in Fig. 7A results in an overall reduction in steam utility of 3835 kW, which means the net HSR is 10.1 for the secondary MVR unit. The final GCC for the new MVR/TVR evaporation system is presented in Fig. 7B.

A second new evaporation system design may be developed given Effects 1 and 2 both use MVR (Fig. 8). The HSR for the MVR integrated with Effect 2 is 12.2, which is substantially better than using TVR for this effect. Fig. 8A identifies MVR may be used to

upgrade excess vapour from the shell-side of Effect 1 using 245 kW<sub>ele</sub> to supply 2638 kW of heat to the cold milk sink. After implementing this additional MVR as well as the process temperature modification in Fig. 8A, a GCC for the new MVR/MVR evaporation system design may be determined as shown in Fig. 8B. The Pinch Region spans from 10.5 °C to 81.2 °C with no potential for heat export (unlike the current design) to neighbouring zones.

The new MVR/MVR design, from an energy use point of view, has marginally lower electricity and thermal energy use compared to the new MVR/TVR design. More important is the relaxed constraint around the Condenser load in the GCC of Fig. 8B compared the GCC of Fig. 7B. Since the Condenser is a significantly lower at a slightly higher temperature, it opens up more possibilities around the preheating of the milk. One unique milk processing constraint is only one heat exchange match should be used to heat milk through the high thermophile growth temperature range of 45–60 °C, as to minimize the duplication of process lines. The new MVR/TVR design has a Pinch at 53.5 °C, which means this constraint cannot be met. As a consequence, only the new MVR/MVR design has been progressed to the HEN design stage.

#### 6.4. New ultra-low energy evaporation system design

A new HEN for an ultra-low energy system has been developed given the placement of three MVR units as shown in Fig. 9. The

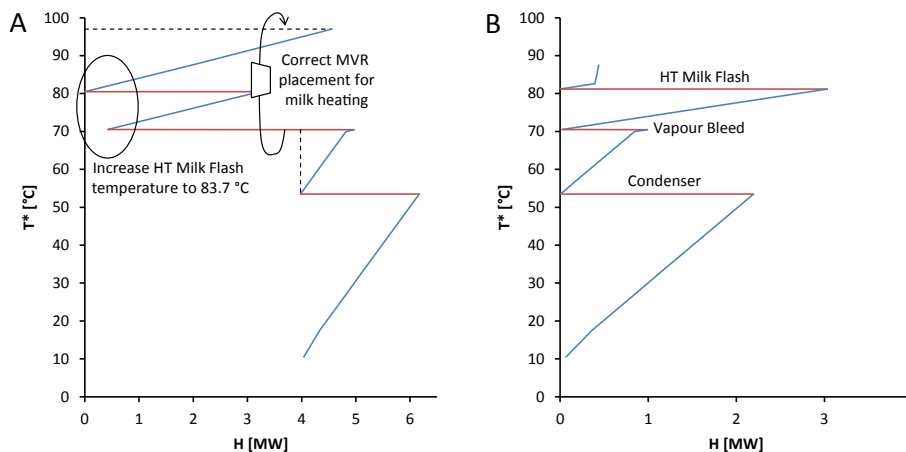
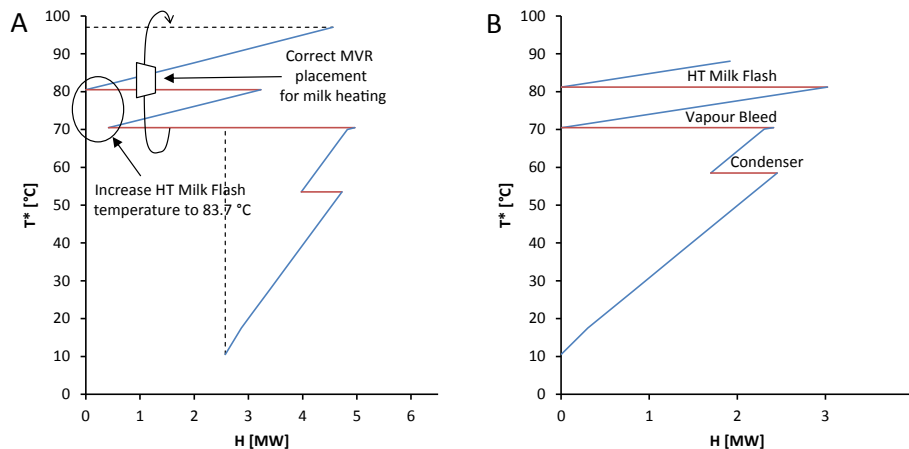


Fig. 7. Development of an evaporation system design using the GCC, given Effects 1 and 2 are integrated with MVR and TVR respectively. (A) Identification of potential energy savings. (B) Final GCC for new MVR/TVR evaporation system design.



**Fig. 8.** Development of an evaporation system design using the GCC, given Effects 1 and 2 are both integrated with MVR. (A) Identification of potential energy savings. (B) Final GCC for new MVR/MVR evaporation system design.

**Table 3**

Summary of evaporation system energy targets for Figs. 4–9.

Scheme (Figure)	PT [°C]	$Q_{ele,MVR}$ [kW]	$Q_{h,TVR}$ [kW]	$Q_{h,other}$ [kW]	$\Sigma Q_h$ [kW]	$\Sigma Q_c$ [kW]
Current (3)	–	2207	2373	5878	8251	6435
4	80.5	2207	2373	4558	6931	5114
5	70.5–81.2	2207	2373	4359	6732	4911
6A	65.5	–	–	19,621	19,621	117,546
6B	53.5	2207	–	5838	5838	4189
7A	80.5	2207	1624	4557	6181	4038
7B	53.5–81.2	2582	1624	438	2003	65
8A	80.5	2312	–	4557	4557	2566
8B	10.5–81.2	2557	–	1919	1919	–
New (9)	10.5	2571	–	1854	1854	–

estimated electrical and thermal energy uses for the completed new design are compared to the current design and various Pinch targets in Table 3. Compared to the current design, the new MVR/MVR evaporation system design reduces steam utility use by 78% (6397 kW) at the expense of 16% (364 kW<sub>ele</sub>) increase in electricity use.

The HEN in Fig. 9 has four notable differences compared to the base case design in Fig. 3. First, there is a higher milk outlet temperature from the Milk/Cow match. The new design mixes lower temperature heat from the Condenser with the other condensate streams while also reducing the approach temperature of the Milk/Cow match. This change results in an additional 4344 kW of heat transfer. The higher outlet temperature of 61 °C also means the milk pass through the high thermophile growth temperature range in this heat exchanger. As a result, duplicate heat exchangers are required to ensure continuous processing, which is an important processing constraint. Second, there is a multi-stage MVR unit that upgrades heat from the shell-side of the first effect to heat milk. This important change was identified using the GCC in Fig. 8. Third, there is no longer excess low-grade heat available from the Condenser for export to heat dryer air flows. Fourth, Effect 2 is integrated with MVR instead of TVR. Fifth, there is now heat recovery to CIP water, where previously there was none.

Capital cost is also an important factor in determining the most economic evaporation system design and the total cost of a project. This paper focused on exploring to what extent energy reductions are possible in the milk evaporation system given certain processing constraints, without too much concern for capital cost

implications. Rigorous capital costings of these designs compared to the current design will be the focus of future work.

#### 6.5. Total Site Heat Integration for the milk powder factory

The milk evaporation system is a critical component and energy user of the milk powder production process. Major changes to the energy use profile of the evaporation system affect the site-wide heat balance. A comparison of four TSHI targets for the current plant design, the pinched current plant design, TSHI with the pinched current plant, and TSHI with the new MVR/MVR evaporation system design are presented in Table 4. It is important to note that the electricity use column only includes MVR electricity from the evaporation system.

An important difference between the first two targets and the last two targets in Table 4 is the inclusion of the Exhaust Air and Condensate streams as heat sources. Recovering heat from these streams can be challenging [32], but it is likely to happen in the near future as pressure on energy use and emissions increases. In the current design, 1284 kW of low-grade heat exports, which is counted as generation of LTHW, from the evaporation system are used to heat air streams in the Spray Dryer Zone. However, if heat is recovered from the Exhaust Air and Condensate streams, the marginal value of the heat exports from the evaporation system becomes nil. It is important to note that in practice there would not be a surplus of LTHW needing cooling, as indicated in Table 4. Instead, the design will only recover the amount of heat that is needed from the Exhaust Air flow given the balance of LTHW sources and sinks on the Total Site.

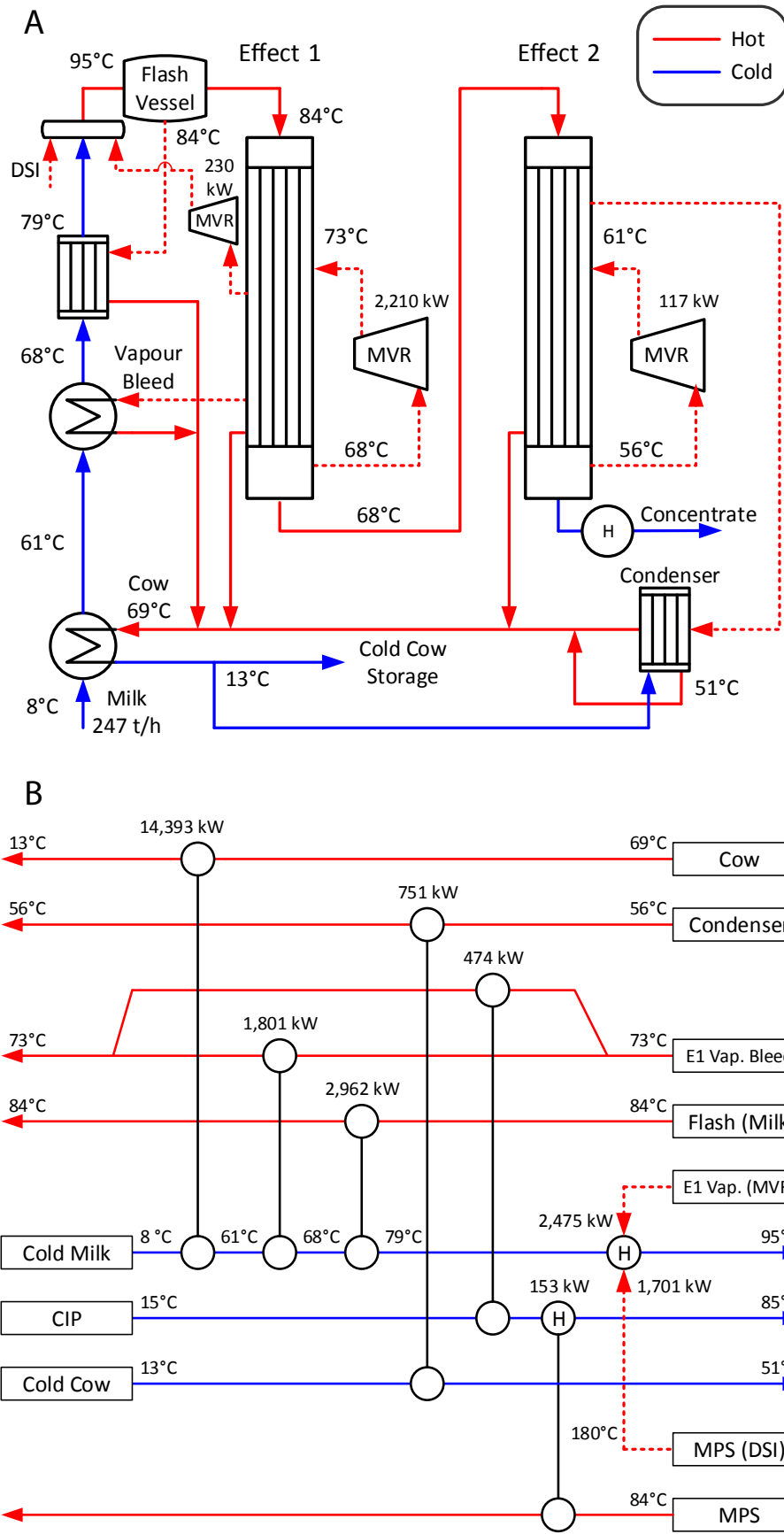


Fig. 9. New ultra-low energy milk evaporation system design illustrated using a process flow diagram (A) and grid diagram (B).

**Table 4**  
Summary of TSHI energy targets, energy cost savings, and emissions reduction.

Scheme		Electricity [kW]	HPS [kW]	MPS [kW]	HTHW [kW]	LTHW [kW]	Utility savings [\$y]	Emissions reduction [t CO <sub>2</sub> -e/y]
Current	Consumption	2207	5944	32,175	692	1815		
	Generation	–	–	–	–	1284		
	Net	2207	5944	32,175	692	531	–	–
Pinched current design	Consumption	2207	5944	22,220	5650	5490		
	Generation	–	–	–	–	2922		
	Net	2207	5944	22,220	5650	2568	\$ 665,667	2297
Pinched current design and TSHI <sup>a</sup>	Consumption	2207	5944	22,220	5650	5490		
	Generation	–	–	–	750 <sup>a</sup>	10,136 <sup>a</sup>		
	Net	2207	5944	22,220	4900	–4646	\$ 1,411,844	4872
New evap. design <sup>a</sup> and TSHI <sup>a</sup>	Consumption	2571	5944	17,057	5650	5490		
	Generation	–	–	–	750 <sup>a</sup>	7214 <sup>a</sup>		
	Net	2571	5944	17,057	4900	–1725	\$ 2,354,446	8288

<sup>a</sup> Additional HTHW and LTHW generation from Exhaust Air and Condensate streams in TSHI schemes.

The utility savings from improving the current evaporation system design is \$665,667/y. About 45% of the utility savings arises from improved intra-Process Integration within the evaporation system, while the remaining 55% of cost savings comes from increased LTHW generation. Heat recovery from Exhaust Air and Condensate has potential to contribute an additional \$746,177/y savings. Implementation of the new MVR/MVR evaporation system design delivers a further \$942,601/y. In total, the achievable energy cost reduction is 23.1%. For the final two targets, there is a lack of LTHW sinks within the milk powder process and so one option is to export heat to co-located plants (e.g. cheese, whey, casein, or butter plants) for large multi-plant sites using hot water loops [33].

The emissions reductions from implementing the various energy efficiency concepts have also been calculated. In New Zealand, the cost efficient replacement of thermal energy with electricity is a beneficial method for lowering emissions since the Emissions Factor from electricity (0.129 t CO<sub>2</sub>-e/MWh) is approximately half that of thermal energy from coal (0.270 t CO<sub>2</sub>-e/MWh) [34]. As presented in Table 4, the emissions reduction potential for a 30 t/h milk powder factory by implementing the new evaporation system design provides an additional 3416 t CO<sub>2</sub>-e/y beyond the 4872 t CO<sub>2</sub>-e/y obtained by TSHI with a Pinched version of the current design. Overall this represents a 24.3% decrease in emissions from the entire site.

## 7. Conclusions

A new ultra-low energy, two-effect milk evaporation system design has been successfully developed. The Grand Composite Curve played a critical role in identifying process modifications and the appropriate placements of vapour recompression so to minimise energy use. In particular, the additional application of Mechanical Vapour Recompression in the system unlocks significant energy, cost, and emissions savings. The new design requires 78% less steam (6397 kW) at the expense of 16% (364 kW<sub>ele</sub>) more electricity use. The estimated cost savings associated with the improved design is \$942,601/y and the emissions reduction is 3416 t CO<sub>2</sub>-e/y. Further energy efficiency improvements are gained through improved Total Site Heat Integration by recovering heat from the dryer exhaust air and boiler return condensate streams.

## References

- [1] Klemes JJ, Smith R, Kim JK. Handbook of water and energy management in food processing. Cambridge, UK: Woodhead Publishing; 2008.
- [2] Klemes JJ, editor. Handbook of process integration: minimisation of energy and water use, waste and emissions. Cambridge, UK: Woodhead Publishing; 2013.
- [3] Ramirez CA, Patel M, Blok K. From fluid milk to milk powder: energy use and energy efficiency in the European dairy industry. Energy 2006;31:1984–2004. <http://dx.doi.org/10.1016/j.energy.2005.10.014>.
- [4] Reay D. A selection of heat recovery applications illustrated by means of case studies. J Heat Recovery Syst 1982;2:401–18. [http://dx.doi.org/10.1016/0198-7593\(82\)90028-5](http://dx.doi.org/10.1016/0198-7593(82)90028-5).
- [5] Walmsley TG, Walmsley MRW, Atkins MJ, Fodor Z, Neale JR. Optimal stream discharge temperatures for a dryer operation using a thermo-economic assessment. Chem Eng Trans 2012;29:403–8. <http://dx.doi.org/10.3303/CET1229252>.
- [6] Walmsley TG, Walmsley MRW, Atkins MJ, Neale JR. Improving energy recovery in milk powder production through soft data optimisation. Appl Therm Eng 2013;61:80–7. <http://dx.doi.org/10.1016/j.applthermaleng.2013.01.051>.
- [7] Atkins MJ, Walmsley MRW, Neale JR. Integrating heat recovery from milk powder spray dryer exhausts in the dairy industry. Appl Therm Eng 2011;31:2101–6. <http://dx.doi.org/10.1016/j.applthermaleng.2011.03.006>.
- [8] Walmsley TG, Walmsley MRW, Atkins MJ, Neale JR, Tarighaleslami AH. Thermo-economic optimisation of industrial milk spray dryer exhaust to inlet air heat recovery. Energy 2015;90(Part 1):95–104. <http://dx.doi.org/10.1016/j.energy.2015.03.102>.
- [9] Walmsley TG, Walmsley MRW, Neale JR, Atkins MJ. Pinch analysis of an industrial milk evaporator with vapour recompression technologies. Chem Eng Trans 2015;45:7–12. <http://dx.doi.org/10.3303/CET1545002>.
- [10] Hanneman H, Robertson LJ. Heat recovery systems. In: Energy use dairy process. Brussels, Belgium: International Dairy Federation; 2005.
- [11] Westergaard V. Milk powder technology. 5th ed. Copenhagen, Denmark: GEA Niro; 2010.
- [12] Westphalen DL, Wolf Maciel MR. Pinch analysis of evaporation systems. Braz J Chem Eng 2000;17:525–38. <http://dx.doi.org/10.1590/S0104-6632200000400017>.
- [13] Modla G, Lang P. Heat pump systems with mechanical compression for batch distillation. Energy 2013;62:403–17. <http://dx.doi.org/10.1016/j.energy.2013.09.036>.
- [14] Janghorban Esfahani I, Kang YT, Yoo C. A high efficient combined multi-effect evaporation-absorption heat pump and vapor-compression refrigeration part 1: energy and economic modeling and analysis. Energy 2014;75:312–26. <http://dx.doi.org/10.1016/j.energy.2014.07.081>.
- [15] Reddick C, Sorin M, Sapoundjiev H, Aidoun Z. Carbon capture simulation using ejectors for waste heat upgrading. Energy 2016;100:251–61. <http://dx.doi.org/10.1016/j.energy.2016.01.099>.
- [16] Townsend DW, Linnhoff B. Heat and power networks in process design. Part I: criteria for placement of heat engines and heat pumps in process networks. AIChE J 1983;29:742–8. <http://dx.doi.org/10.1002/aic.690290508>.
- [17] Klemes JJ, Dhole VR, Raissi K, Perry SJ, Puigjaner L. Targeting and design methodology for reduction of fuel, power and CO<sub>2</sub> on total sites. Appl Therm Eng 1997;17:993–1003. [http://dx.doi.org/10.1016/S1359-4311\(96\)00087-7](http://dx.doi.org/10.1016/S1359-4311(96)00087-7).
- [18] Klemes JJ, Varbanov PS, Wan ASRW, Manan ZA. Process integration and intensification, saving energy, water and resources. Berlin, Boston: De Gruyter; 2014. <http://www.degruyter.com/view/product/204103> [accessed 04.03.16].
- [19] Fritzon A, Berntsson T. Energy efficiency in the slaughter and meat processing industry—opportunities for improvements in future energy markets. J Food Eng 2006;77:792–802. <http://dx.doi.org/10.1016/j.jfoodeng.2005.08.005>.
- [20] Matsuda K, Hirochi Y, Tatsumi H, Shire T. Applying heat integration total site based pinch technology to a large industrial area in Japan to further improve performance of highly efficient process plants. Energy 2009;34:1687–92. <http://dx.doi.org/10.1016/j.energy.2009.05.017>.
- [21] Matsuda K, Hirochi Y, Kurosaki D, Kado Y. Application of area-wide pinch technology to a large industrial area in Thailand. Chem Eng Trans 2014;39:1027–32. <http://dx.doi.org/10.3303/CET1439172>.
- [22] Bonhivers JC, Svensson E, Berntsson T, Stuart PR. Comparison between pinch analysis and bridge analysis to retrofit the heat exchanger network of a kraft

- pulp mill. *Appl Therm Eng* 2014;70:369–79. <http://dx.doi.org/10.1016/j.applthermaleng.2014.04.052>.
- [24] Feng X, Smith R. Case studies of heat integration of evaporation systems. *Chin J Chem Eng* 2001;9:224–7.
- [25] Al-Juwayhel F, El-Dessouky H, Ettouney H. Analysis of single-effect evaporator desalination systems combined with vapor compression heat pumps. *Desalination* 1997;114:253–75. [http://dx.doi.org/10.1016/S0011-9164\(98\)00017-4](http://dx.doi.org/10.1016/S0011-9164(98)00017-4).
- [26] Linnhoff B. *Introduction to pinch technology*. Northwich, UK: Linnhoff March; 1998.
- [27] MAF Quality Management. *Physical properties of dairy products*. 3rd ed. Hamilton, New Zealand: MAF Quality Management; 1996.
- [28] Sargolzaei J, Pirzadi Jahromi MR, Saljoughi E. Triple-choking model for ejector. *J Therm Sci Eng Appl* 2010;2. <http://dx.doi.org/10.1115/1.4002752>. 021009-021009-10.
- [29] Oldfield DJ, Taylor MW, Singh H. Effect of preheating and other process parameters on whey protein reactions during skim milk powder manufacture. *Int Dairy J* 2005;15:501–11. <http://dx.doi.org/10.1016/j.idairyj.2004.09.004>.
- [30] Baldwin AJ, Cooper HR, Palmer KC. Effect of preheat treatment and storage on the properties of whole milk powder. Changes in sensory properties. *Neth Milk Dairy J* 1991;45:97–116.
- [31] Hinton AR. Thermophiles and fouling deposits in milk powder plants [PhD thesis]. Massey University; 2003. <http://muir.massey.ac.nz/handle/10179/1861> [accessed 03.07.12].
- [32] Walmsley TG, Walmsley MRW, Atkins MJ, Neale JR. Fouling and pressure drop analysis of milk powder deposition on the front of parallel fins. *Adv Powder Technol* 2013;24:780–5. <http://dx.doi.org/10.1016/j.apt.2013.04.004>.
- [33] Walmsley TG, Walmsley MRW, Atkins MJ, Neale JR. Integration of industrial solar and gaseous waste heat into heat recovery loops using constant and variable temperature storage. *Energy* 2014;75:53–67. <http://dx.doi.org/10.1016/j.energy.2014.01.103>.
- [34] Walmsley MRW, Walmsley TG, Atkins MJ, Kamp PJJ, Neale JR. Minimising carbon emissions and energy expended for electricity generation in New Zealand through to 2050. *Appl Energy* 2014;135:656–65. <http://dx.doi.org/10.1016/j.apenergy.2014.04.048>.

**Article 5:**

*Thermo-economic optimisation of industrial milk spray dryer  
exhaust to inlet air heat recovery*

**Walmsley, T.G.**, Walmsley, M.R.W., Atkins, M.J., Neale, J.R.,  
Tarighaleslami, A.H., 2015.

Energy 90, Part 1, 95–104.

DOI: 10.1016/j.energy.2015.03.102

Citations: 9

Elsevier



# Thermo-economic optimisation of industrial milk spray dryer exhaust to inlet air heat recovery



Timothy G. Walmsley<sup>\*</sup>, Michael R.W. Walmsley, Martin J. Atkins, James R. Neale, Amir H. Tarighaleslami

University of Waikato, Energy Research Centre, School of Engineering, Hamilton, New Zealand

## ARTICLE INFO

### Article history:

Received 19 December 2014

Received in revised form

5 March 2015

Accepted 7 March 2015

Available online 30 April 2015

### Keywords:

Process integration

Heat transfer

Particulate fouling

Spray dryer

## ABSTRACT

This study reports a thermo-economic design optimisation of an industrial milk spray dryer liquid coupled loop exhaust heat recovery system. Incorporated into the analysis is the ability to predict the level of milk powder fouling over time and its impacts on heat transfer and pressure drop. Focus is given to a finned round tube, a bare round tube and a bare elliptical tube. Modelling results show that spray exhaust heat recovery is economically viable for the considered industrial case study. Based on the results, the best liquid coupled loop heat exchange system uses a finned tube heat exchanger to recover heat from the exhaust air with a face velocity of 4 m/s and 14 tube rows, which gives a net present value of NZ\$2.9 million and an internal rate of return of 71%. The developed thermo-economic assessment method has the ability to cater to site specific needs that affect the utility savings and the capital cost for implementing exhaust heat recovery.

© 2015 Elsevier Ltd. All rights reserved.

## 1. Introduction

Spray dryer exhaust heat recovery can typically increase dryer energy efficiency by 10–20% [1], but it is complicated by the low heat transfer coefficient of air and the presence of powder particulates that may foul the heat exchanger surfaces. Several case studies on spray dryer heat integration for a range of industries from the 1980's, which was subsidised by the UK's energy efficiency demonstration scheme, showed 2–4 years as a typical payback and a steam savings of 10% [1,2]. In general, dryer exhaust heat recovery is applicable to a wide range of other industries. For example, Laurijssen et al. [3] demonstrated that dryer exhaust heat recovery for a conventional multi-cylinder dryer used in the paper industry plays a critical role in lowering thermal energy use by 32%. Han et al. [4] modelled a lignite-fired power station under variable load and proposed to use the hot flue for drying the incoming fuel as a means for heat recovery and boiler efficiency increases in the order of 1–2%. Tippayawong et al. [5] analysed industrial longan drying practice to show that dryer heat recovery can increase thermal efficiency by 21%.

Increasing energy efficiency in milk spray drying is an important topic for New Zealand because the results of the New Zealand dairy industry heavily impacts the national economy. The installed capacity of milk spray drying in New Zealand reached an estimate of 300 t/h in 2013 with a consumption of around 29 PJ/y of thermal energy. Milk powders supply about 20% of New Zealand's exports. As a consequence, energy efficiency in milk powder production is therefore a prime concern for industry and the New Zealand government as a means of lifting national economic performance. Spray dryer exhaust heat recovery represents a great remaining opportunity for significantly increasing heat recovery in the milk powder production process. In the United States, many milk powder plants have installed exhaust heat recovery systems for pre-heating the inlet air. Besides heat recovery, another benefit for this practice is to minimise inlet dryer air humidity. For these plants, hot air for drying is generated using direct fired natural gas combustion, which combustion reaction increases the air's moisture content. Inlet air pre-heating reduces the fuel consumption, which reduces moisture in the air, which maximises the drying capacity of the air. New Zealand plants, however, favour indirect heating methods of the dryer air using steam or indirect gas fired air heaters. The additional benefit of lower inlet air humidity is not present in the New Zealand case.

The New Zealand dairy industry has been cautious to uptake spray dryer exhaust heat recovery. In the mid-1980's, the Plains Co-

<sup>\*</sup> Corresponding author.

E-mail address: [timgw@waikato.ac.nz](mailto:timgw@waikato.ac.nz) (T.G. Walmsley).

Nomenclature		Greek	
<i>Roman</i>		$\Delta$	positive difference between two states
$A$	area ( $\text{m}^2$ )	$\epsilon$	heat exchanger effectiveness
$C$	heat capacity flow rate ( $\text{kW}/^\circ\text{C}$ )	$\tau$	time constant (s)
$C^*$	ratio of minimum to maximum heat capacity flow rates for $\epsilon$ -NTU method	$\phi$	probability
$c_b$	particulate concentration in air flow ( $\text{kg}/\text{kg}$ )	<i>Subscripts/superscripts</i>	
$d_p$	particle diameter (m)	c	cold stream
$h$	heat transfer film coefficient ( $\text{kW}/^\circ\text{C} \cdot \text{m}^2$ )	f	fouling
$j$	Colburn $j$ factor	F	frontal
$NTU$	number of transfer units	h	hot stream
$Nu$	Nusselt number	HX	heat exchanger
$\Delta P$	pressure drop (Pa or %)	i	impact
$P$	temperature effectiveness	l	loop
$Q$	heat duty (kW)	min	minimum
$R$	heat transfer resistance ( $^\circ\text{C} \cdot \text{m}^2/\text{kW}$ )	o	overall
$r$	radius ( $\mu\text{m}$ )	p	pass
$t$	time (s)	r	recovery
$U$	overall heat transfer coefficient ( $\text{kW}/^\circ\text{C} \cdot \text{m}^2$ )	s	sticking
		tot	total
		tube	heat exchanger tube
		w	wall

Op Dairy Ltd factory installed a glass tube air-to-air exhaust heat recovery system. However, energy surveys of its performance showed that heat recovery levels decreased by as much 40% after 13 h of operation due to milk powder fouling. In 2008, a New Zealand South Island dairy factory built a new state-of-the-art dryer, which was also the world's largest milk dryer at the time, and had plans to install a liquid coupled loop exhaust heat recovery system. The exhaust heat exchanger was built but never installed due to concerns over milk powder fouling causing disruptions to plant production. Since that time an additional twelve milk powder spray dryers have been built in New Zealand all without exhaust heat recovery, which evidences that exhaust heat recovery is not standard industry practice in New Zealand.

Within the field of Process Integration, PA (Pinch Analysis) is an established methodology originally proposed by Linnhoff et al. [6] for targeting heat recovery and utility use for industrial processes using Problem Tables and Composite Curves, and developing cost-effective heat exchanger networks. Recent PA studies on milk powder production have shown that to significantly increase heat recovery, heat is required to be recovered from the exhaust air for either intra-plant [7] or inter-plant heat integration [8]. Selection of soft target temperatures in the milk powder plant such as the final temperature of the exhaust air critically affects the shape of the Grand Composite Curve and the location of the Pinch temperature [9]. The exhaust air temperature of milk spray dryers is typically 65–85 °C. Walmsley et al. [7] showed there is no additional steam savings value in recovering dryer exhaust heat below the temperature range of 50–55 °C based on a minimum approach temperature. Atkins et al. [10] modelled the benefit of spray dryer exhaust heat recovery using a liquid coupled loop heat exchanger system to the overall heat recovery in the milk powder process. However their study was confined to the heat transfer characteristics of the liquid coupled loop heat exchanger system. This study furthers the work of Atkins et al. [10] to look closely at the fouling and cost elements of installing exhaust heat recovery systems in industry.

This paper reports the application of a comprehensive thermo-economic assessment tool for modelling a dryer exhaust-to-inlet air indirect heat recovery system to maximise key economic indicators such as NPV (Net Present Value) and IRR (Internal Rate of Return). The model quantifies the trade-off between heat transfer,

pressure drop and fouling in terms of cost so that an optimisation can be performed. Literature correlations for the Colburn  $j$  factor and Fanning friction factor  $f$  of various heat transfer surfaces from Kays and London [11] form the basis for estimating the overall heat recovery of the system. An estimate of the fouling on the heat exchanger surface based on the milk powder deposition model presented by Walmsley et al. [12] is incorporated into the thermo-economic analysis. The comprehensive model is anticipated to demonstrate whether or not milk spray dryer exhaust heat recovery can be economic for a case study of a New Zealand dairy plant. In the general, the tool developed in this optimisation study has the potential to be applied to any dairy plant.

## 2. The milk spray dryer exhaust heat recovery system design problem

The design challenge and potential optimisation associated with spray dryer exhaust heat recovery can be expressed diagrammatically as presented in Fig. 1. The up-side down triangle represents the possible exhaust heat exchanger solutions. On the one hand, exhaust heat exchangers with a greater number of tube rows can

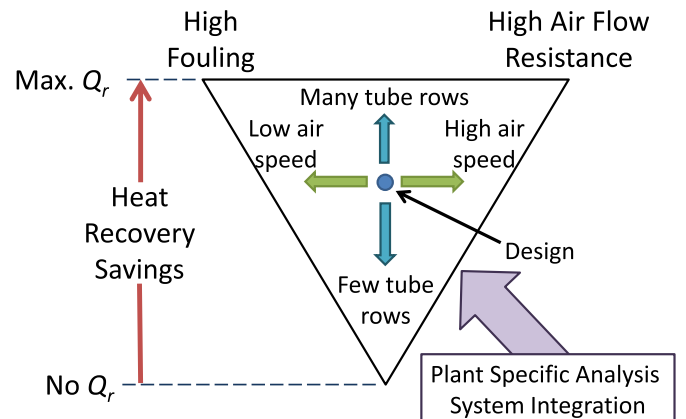


Fig. 1. The exhaust heat exchanger design challenge.

recover more heat ( $Q_r$ ) but this increases both pressure drop and fouling. Fewer tube rows recover less heat with lower fouling and pressure drop. The air face velocity on the heat exchanger is also important and may be manipulated by changing the duct dimensions. High air velocities reduce fouling and improve heat transfer but also increase pressure drop. Lower air velocities have the opposite effect. Finding the right balance between heat recovery, fouling, and pressure drop is chiefly governed by the number of tube rows of the heat exchanger, the face velocity and the geometry of the heat exchanger surface. These parameters are important degrees of freedom that may be manipulated to maximise the economic benefit of an exhaust heat recovery project.

### 3. Development of a comprehensive thermo-economic dryer exhaust heat recovery model

#### 3.1. Heat transfer and friction factor modelling for liquid coupled loop heat exchanger systems

##### 3.1.1. Heat exchanger system inputs

The exhaust-inlet liquid coupled loop heat recovery model is set-up to allow user-defined inputs for the design and modelling parameters of the heat recovery system. Fig. 2 is a screenshot from the spreadsheet of the key design parameter inputs. Dimensions of the heat exchangers are calculated based on air mass flow rate in conjunction with the heat exchanger face velocity for the height and width, and the number of tube rows for the depth. The model uses a height to width ratio of 1:1, i.e. square face, which is typically of spray dryer exhaust roof ducts. There is the option of inputting a specific loop flow rate or allowing the tool to calculate the optimum loop flow rate. In Fig. 2, the tube type number refers to a particular tube geometry and arrangement. Each tube geometry and arrangement has been assigned a number and a new tube type maybe selected via a drop down menu.

##### 3.1.2. Governing heat transfer equations based on effectiveness

The concept of a LCHE (liquid coupled loop heat exchanger) for indirect heat transfer is presented in Fig. 3. This indirect heat exchange system consists of two heat exchangers coupled using an intermediate loop fluid [13]. The loop fluid transports heat from the source stream to the sink stream. LCHE systems are most applicable to situations where source and sink streams are physically distant as is the case with spray dryer exhaust heat recovery for New Zealand dairy plants.

The model uses the effectiveness-NTU approach to solve the LCHE system from Kays and London [11]. The governing overall

effectiveness ( $\epsilon_0$ ) relationship for the performance of LCHE systems is

$$\frac{1}{\epsilon_0} = \frac{C_{\min,o}/C_{\min,c}}{\epsilon_c} + \frac{C_{\min,o}/C_{\min,h}}{\epsilon_h} + \frac{C_{\min,o}}{C_l} \quad (1)$$

Each heat exchanger has the option to contain multiple liquid fluid passes to produce a near counter flow heat exchanger arrangement for enhanced heat transfer but at the expense of pumping power. Kays and London provide the following relationship (Eq. (2)) for determining the effectiveness of a multi-pass heat exchanger unit based on  $n$  number of passes and an effectiveness of a pass,  $\epsilon_p$ , defined by the applicable  $\epsilon$ -NTU relationship, which is the unmixed–unmixed cross-flow relationship for this situation. The unmixed–unmixed cross-flow correlation is selected because there is minimal transverse mixing on both the air and water sides within a pass of a finned tube heat exchanger.

$$\epsilon = \frac{\left(\frac{1-\epsilon_p C^*}{1-\epsilon_p}\right)^n - 1}{\left(\frac{1-\epsilon_p C^*}{1-\epsilon_p}\right)^n - C^*} \quad (2)$$

The model contains an iterative calculation system so that once the heat exchanger outlet temperatures are known, the air and water properties update, which impacts the inputs to the model, and the system re-solves until the solution converges. Convergence in the solution was based on the changes in the temperatures being less than 0.1 °C. Air properties are called using Excel™ functions from the commercial add-in package @Air ([www.techwareeng.com](http://www.techwareeng.com)). Water properties are called from built-in spreadsheet functions powered by the open source XSteam tables ([www.x-eng.com](http://www.x-eng.com)), which are based on IAPWS IF97 steam and water properties.

Once the model finds a solution, the quality of the solution is checked. The model checks to ensure the temperatures in and out of the heat exchangers are thermodynamically feasible, i.e. no temperature cross, and the duties of the two heat exchangers are the same. The model ensures the number of passes is valid for the number of tube rows. To further clarify, the model assumes that there is an equal number of tube rows per pass. Warning messages appear in the spreadsheet results and are recorded when heat transfer and/or friction factor correlation limits are exceeded.

##### 3.1.3. Heat transfer and pressure drop heat exchanger surface characteristics

Heat transfer and friction factor correlations have been formulated using the tabulated data presented in Kays and London [11] for staggered finned tube banks, bare tube banks and plain plate surfaces, and the data in Walmsley et al. [14] for bare circular and elliptical tube geometries. A power law based equation provided sufficiently good correlation for the data of most tube types and arrangements from Kays and London [11]. Correlations for bare and finned tubes and plain plate air–water geometries are built into the spreadsheet. Table 1 provides the essential heat exchanger surface design variables such as tube diameter, tube/plate arrangements, etc.

In practice, the average heat transfer coefficient varies from row-to-row in a finned tube heat exchanger [11]. Literature correlations applied in the spreadsheet are corrected for the row effect such that the reported Nusselt number or  $j$  factor correlations are based on a heat exchanger with infinite rows. There are two methods to account for the row-effect on the heat transfer coefficient: (1) adjust the heat transfer coefficient and (2) use row specific  $\epsilon$ -NTU relationships. The approach taken in this work is that of

User Defined Design Parameters			
	Exh. HX	Inlet HX	
Air Mass Flow Rate	76	56	kg/s
Temperature In	75.0	15.0	°C
Abs Humidity	50.0	10.0	g/kg
Face Velocity	4.0	4.0	m/s
Tube Type	19	6	
Tube Rows	10	6	
Number of Passes	10	6	
Loop Flow Rate	Optimum		kg/s

Fig. 2. Screenshot from the spreadsheet model showing heat exchanger user defined parameters.

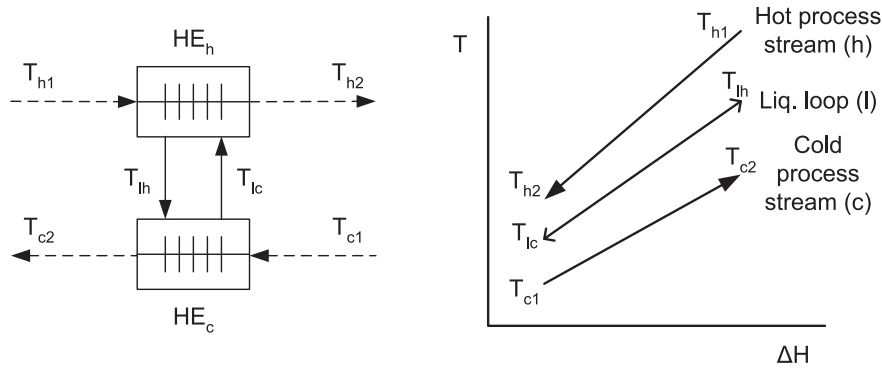


Fig. 3. Liquid couple loop heat exchanger system.

applying the row specific  $\epsilon$ -NTU relationships from ESDU (Engineering Science Data Unit) 86018 cited by Wang et al. [15]. This approach is taken because the row specific  $\epsilon$ -NTU relationships are less affected by the tube and fin geometry.

3.1.4. Liquid couple loop heat exchanger system optimisation

Holmberg [16] derived the optimum loop heat capacity flow rate assuming counter-flow heat exchanger arrangement,

$$C_l = \frac{(UA)_h + (UA)_c}{\frac{(UA)_h}{C_h} + \frac{(UA)_c}{C_c}} \quad (3)$$

where  $U$  is overall heat transfer coefficient and  $A$  is heat exchanger area,  $C$  is the heat capacity flow rate and subscripts  $h$  refers to the hot fluid,  $c$  refers to the cold fluid and  $l$  refers to the loop fluid.

When  $(UA)_h \gg (UA)_c$ , then  $C_l$  in Eq. (3) approaches  $C_h$ . The reverse is also true; when  $(UA)_c \gg (UA)_h$ , then  $C_l$  approaches  $C_c$ . Thus, the optimum  $C_l$  always falls somewhere between  $C_h$  and  $C_c$ . Using a simple spreadsheet, a preliminary investigation into the applicability of Eq. (3) to non-counter-flow heat exchanger arrangements, including the unmixed–unmixed cross-flow arrangement, has been undertaken. The investigation looked at cases where the LCHE system involved two heat exchangers with the same arrangement and varied the  $UA$  values for the heat exchangers across a wide range. Preliminary checks using Excel™ Solver showed that Eq. (3) is sufficiently accurate to predict the optimum loop flow rate to achieve a heat transfer within 0.1% of the maximum possible.

The approach applied in the spreadsheet tool to optimise a LCHE system is, first, to select areas for the exhaust and inlet air heat

Table 1 Heat exchanger geometry information. Key for heat exchanger surface codes: C – circular (round); E – elliptical; B – bare; F – finned; KL – Kays and London [11]; W – Walmsley et al. [14].

Source	Tube type (code)	$D_o$ mm	$D_i$ mm	$X$ tube/plate mm	$d_{h,air}$ mm	$\sigma_{air}$ m <sup>2</sup> /m <sup>2</sup>	$\alpha$ m <sup>2</sup> /m <sup>3</sup>	$S_T$ mm	$S_L$ mm	Fin pitch fins/m	$x_{fin}$ mm	$d_{fin}$ mm	$\Phi$ m <sup>2</sup> /m <sup>2</sup>
<i>Bare tube – staggered arrangement</i>													
KL	CB-1.5:1.25-3/8	9.5	6.2	1.7	7.6	0.333	175	14.3	11.9				
W	CB-1.5:1.25 (CFD)	20.0	16.7	1.7	15.9	0.333	84	30.0	25.0				
W	CB-2:1 (CFD)	20.0	16.7	1.7	25.5	0.500	79	40.0	20.0				
W	EB-1.5:1.25 (CFD)	30.8	27.5	1.7	15.9	0.333	84	30.0	38.5				
W	EB-2:1 (CFD)	25.9	22.6	1.7	25.5	0.500	79	40.0	30.8				
<i>Circular finned tube – staggered arrangement</i>													
KL	CF-7.34	9.7	7.2	1.2	4.8	0.538	459	24.8	20.3	289	0.460	23.4	0.892
KL	CF-8.72	9.7	7.2	1.2	3.9	0.524	535	24.8	20.3	343	0.460	23.4	0.910
KL	CF-8.72c	10.7	8.2	1.2	4.4	0.494	446	24.8	20.3	343	0.480	23.4	0.876
KL	CF-7.0-5/8J	16.4	13.1	1.7	6.7	0.449	269	31.3	34.3	276	0.250	28.5	0.830
KL	CF-8.7-5/8J (A)	16.4	13.1	1.7	5.5	0.443	324	31.3	34.3	343	0.250	28.5	0.862
KL	CF-8.7-5/8J (B)	16.4	13.1	1.7	11.7	0.628	216	46.9	34.3	343	0.250	28.5	0.862
KL	CF-9.05-3/4J (A)	19.7	16.4	1.7	5.1	0.455	354	39.5	44.5	356	0.305	37.2	0.917
KL	CF-9.05-3/4J (B)	19.7	16.4	1.7	8.2	0.572	279	50.3	44.5	356	0.305	37.2	0.917
KL	CF-9.05-3/4J (C)	19.7	16.4	1.7	13.6	0.688	203	69.2	44.5	356	0.305	37.2	0.917
KL	CF-9.05-3/4J (D)	19.7	16.4	1.7	4.8	0.537	443	69.2	20.3	356	0.305	37.2	0.917
KL	CF-9.05-3/4J (E)	19.7	16.4	1.7	6.4	0.572	354	50.3	34.9	356	0.305	37.2	0.917
KL	CF-8.8–1.0J (A)	26.0	22.7	1.7	5.9	0.439	299	49.8	52.4	346	0.305	44.1	0.825
KL	CF-8.8–1.0J (B)	26.0	22.7	1.7	13.2	0.642	191	78.2	52.4	346	0.305	44.1	0.825
<i>Plain plate</i>													
KL	2.0 T			0.3	14.5		250	19.1	304.8	79	0.813		0.606
KL	3.01 T			0.3	10.8		323	19.1	304.8	119	0.813		0.706
KL	3.97 T			0.3	8.6		392	19.1	304.8	156	0.813		0.766
KL	5.3 S			0.3	6.1		617	11.9	304.8	209	0.152		0.719
KL	6.2 B			0.3	5.5		669	10.3	304.8	244	0.254		0.728
KL	9.03 SB			0.3	4.6		801	6.4	304.8	356	0.203		0.888
KL	11.1 B			0.3	3.5		1024	12.2	304.8	437	0.203		0.854
KL	14.77 ST			0.3	2.6		1378	8.4	304.8	582	0.152		0.844
KL	15.08 SB			0.3	2.7		1358	6.4	304.8	594	0.152		0.870
KL	19.86 ST			0.3	1.9		1841	10.6	304.8	782	0.152		0.849

exchangers, and then, to determine the near optimum loop flow rate using Eq. (3). With a defined loop flow rate,  $C_l$ , and heat exchanger areas, the effectiveness of the exhaust and inlet exchangers may be calculated, from which the loop temperatures ( $T_{l,c}$  and  $T_{l,h}$ ) of the LCHE system may be calculated using

$$T_{l,c} = \frac{\epsilon_h C_{h,\min} \left(1 - \frac{\epsilon_c C_{c,\min}}{C_l}\right) T_{h1} + \epsilon_c C_{c,\min} T_{c1}}{\epsilon_h C_{h,\min} \left(1 - \frac{\epsilon_c C_{c,\min}}{C_l}\right) + \epsilon_c C_{c,\min}} \quad (4)$$

$$T_{l,h} = \frac{\epsilon_h C_{h,\min} T_{h1} + \epsilon_c C_{c,\min} \left(1 - \frac{\epsilon_h C_{h,\min}}{C_l}\right) T_{c1}}{\epsilon_h C_{h,\min} \left(1 - \frac{\epsilon_c C_{c,\min}}{C_l}\right) + \epsilon_c C_{c,\min}} \quad (5)$$

The above formulas have been derived based on energy continuity across the LCHE system and assume that heat loss is minimal. Once the intermediate hot and cold loop temperatures are found, the overall duty of the system may be calculated.

### 3.2. Modelling fouling and its effects on heat transfer and pressure drop

#### 3.2.1. Predicting fouling build-up on the exhaust heat exchanger

The inputs to the model that relate to the build-up of fouling are presented in Fig. 4. Elsewhere in the spreadsheet the user may also input a particle size distribution. Using these parameters the spreadsheet applies the deposition model from Walmsley et al. [12] to estimate the amount of powder that sticks for each time step. The model of Walmsley et al. [12] was originally based on a series of experiments of milk powder deposition on a flat plate in an impingement jet. This model has been recently successfully applied to predict the key deposition characteristics on round and elliptical tubes by Walmsley et al. [17].

The method for estimating the amount of deposition is explained in Fig. 5. After entering the required inputs, the spreadsheet calculates the overall heat recovery system duty and estimates the air temperature profile within the exhaust heat exchanger based on a constant average heat transfer coefficient for each tube row, which results in a constant  $NTU$  for all tube rows.

The temperature profile is used to calculate a critical impact angle using the deposition model on Walmsley et al. [12] for each combination of tube row and particle size. Once the critical impact is known, the position on the tube that is the boundary of particle's sticking and rebounding, and the frontal area of the sticking region ( $A_s$ ), can be determined. A probability of sticking ( $\phi_s$ ), which is defined the probability that a particle which impacts a tube will stick, can be estimated by dividing the frontal area of the sticking region by the total frontal area of a row of tubes, i.e.  $A_s/A_F$ . To

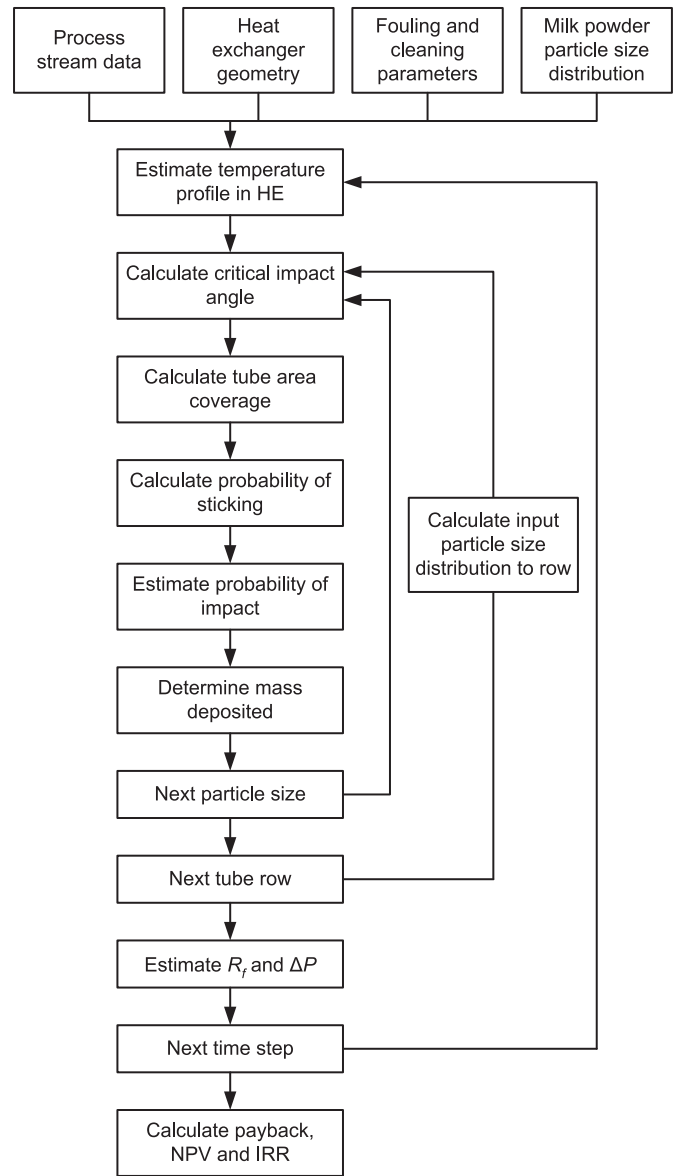


Fig. 5. Heat exchanger fouling model flow diagram.

determine the total increase in foulant mass, the probability of impact ( $\phi_i$ ), which is the probability that a particle will impact a tube, must also be considered. For this work, the probability of impact is assumed constant and estimated as fraction of frontal tube area to total cross-sectional area of the duct, i.e.  $A_F/A_{tot}$ . Particles are assumed to be evenly distributed throughout the air flow and duct and, with presuming only minor deviations in a particle's flow path, particles that are aligned with the frontal area of a tube are likely to impact a surface, whereas particles in a gap are unlikely to impact the row. Using these assumptions, the fraction of particles impacting a tube can be estimated as  $A_F/A_{tot}$ . There is opportunity in future work to input a probability of impact that is row and particle size specific. In reality, smaller particles are expected to have lower probabilities due to the smaller particle relaxation times. At present, this is a limitation of the model.

The product of the probabilities of impact and sticking, i.e.  $\phi_s \phi_i$ , give the percentage of particle mass entering a row that will deposit. This process of calculating the mass deposited is repeated for each combination of particle size fraction and tube row within a single time-step using Visual Basic based macros. The effect of the

Fouling and Cleaning Parameters		
Concentration	3.5	mg/m <sup>3</sup>
Run time	672	h
Time Step	5.0	h
Wash Length	1.0	h
Start Clean?	TRUE	
Optimum Clean?	FALSE	

Fig. 4. Screenshot from the spreadsheet model showing fouling and cleaning user defined parameters.

fouling build-up on  $R_f$  and  $f$  is discussed in detail in the next two sections. For each new time-step, the performance of the heat recovery system and the exhaust heat exchanger temperature profile is recalculated. Once the run-time is complete, the model uses the cumulative heat recovery savings and costs to estimate the payback, NPV and IRR for the system.

The Excel spreadsheet tool incorporating the fouling model required 2.5 h on average to complete the analysis for one heat exchanger design using a time step of 5 h for a total cycle of 672 h. The fouling model was computed on an Intel™ i7 3.4 GHz processor. Test cases were used to determine the appropriate time step as to minimise its impact on the final solution.

The fouling build-up model makes several simplifications and assumptions. Uniform distribution along the length of each tube is assumed, although in recent experiments conducted by the authors [17], the particle distribution, which is often related to the airflow distribution, may be maldistributed causing a non-uniform profile along the length of a tube. Deposition is also likely to be heavier near the heat exchanger outer walls as shown in the experimental work of Walmsley et al. [17]. The probability of impact is constant for all rows and particle sizes. The probability of sticking has no respect for the surface condition and assumes the probability of a particle sticking to the tube wall is similar to a particle sticking to a particle. This simplification is supported by the work of Nijdam and Langrish [18], who found pre-coating the inside of a dryer with powder had little effect on the rate of deposition build-up.

### 3.2.2. Particle size distribution

Fig. 6 shows the particle size distributions of SMP (Skim Milk Powder) product compared to the size distribution collected in the bag house, which is assumed to be similar to the size distribution emitted out the exhaust duct. The particle size distribution was measured in iso-propanol using a Malvern Mastersizer 2000 according to the method of Pisecky [19]. The average particle size for bag house powder is significantly lower than bulk product, but the distributions span similar size ranges. The baghouse powder particle size distribution is entered into the spreadsheet tool as an input to the fouling model.

The particle size distributions in Fig. 6 were experimentally obtained using a light ray diffraction method using such instruments as a Malvern Mastersizer. Commonly food powders are added to a solvent and analysed. The standard method for analysis of milk powders is to place a small sample in isopropanol and test every two minutes until readings are constant [18,19].

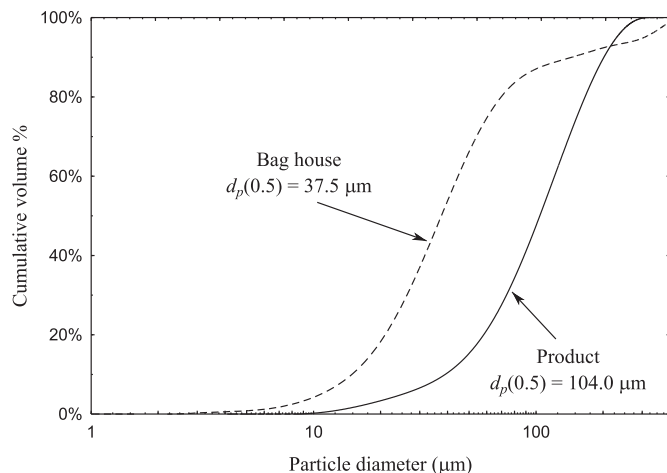


Fig. 6. Particle size distribution of baghouse and bulk product SMP.

### 3.2.3. The effect of fouling on heat transfer

Fouling affects heat transfer due to adding a layer of resistance. If the fouling was assumed to be perfectly uniform in thickness around a circular tube, the resistance due to fouling may be estimated using

$$R_{f,tube} = \frac{r_{tube}}{k_f} \ln\left(\frac{r_f}{r_{tube}}\right) \quad (6)$$

where  $R_{f,tube}$  is the fouling resistance using the air-side tube area as the basis,  $k_f$  is the thermal conductivity of the foulant layer,  $r_f$  is the radius of the fouling and  $r_{tube}$  is the outside radius of the tube. As a simplification, it is assumed that the fouling build-up on the front of the tubes add a layer of thermal resistance approximately equal to the same volume of fouling uniformly spread around the outside of the tube. Thermal conductivity is taken as 0.1 W/(°C m) [20].

The heat transfer resistance due to milk powder deposition on the front of the tube is difficult to estimate without simplification. The presence of deposits in a heat exchanger are likely to significantly influence the airflow profile and the overall bulk average air velocity in the heat exchanger. The fouling layer acts as a thermal resistance, but it also improves  $h$  and  $A$  by channelling the air flow, which increases the average velocity in the heat exchanger, and enlarging the surface contact area between the air and the tube with fouling.

Fouling on the frontal face of fins has been shown to add little in the way of heat transfer resistance in other industries. Fouling does impact on the air flow resistance and, therefore, the velocity and distribution of the air flow experienced inside the heat exchanger. The added pressure drop can cause a reduction in the volumetric flow rate if the capacity of the fan has reached its zenith. The reduction in air flow through a heat exchanger has been shown to be the root cause of decreases in heat duty for particulate fouling on the frontal face of fins [21].

In this work, attempts are made to stay in heat recovery regions where powder deposition on the frontal face of fins is avoided. Walmsley et al. [22,23] presented a relationship between the velocity through the open area and milk powder stickiness. Using this relationship limits are placed on the outlet temperature of the exhaust heat exchanger, which is the point of greatest powder stickiness, to minimise the likelihood of fouling on the frontal face of fins. As a result only fouling on the frontal face of the tube is considered in the model. Future work will look in detail at the accuracy of this assumption between testing finned tubes of various pitches.

### 3.2.4. The effect of fouling on pressure drop

The effect of fouling pressure drop is estimated based on the experimental pressure drop data for single bare tubes in cross-flow from Walmsley et al. [17]. The experimentally examined fouling build up in Walmsley et al. [17] showed a asymptotic fouling behaviour, which data was analysed using a first order exponential equation containing a characteristic time constant. In this work, the first order approximation is differentiated with respect to obtain

$$\frac{d(\Delta P(\%))}{dt} = \frac{\Delta P_{final}(\%)}{\tau_f} \exp\left(-\frac{t}{\tau_f}\right) \quad (7)$$

For a small time step the change in pressure drop may be numerically estimated in the model using

$$\Delta(\Delta P(\%)) = \frac{\Delta P_{final}(\%)}{\tau_f} \exp\left(-\frac{t}{\tau_f}\right) \Delta t \quad (8)$$

Eq. (8) is applied to estimate how the pressure drop of the exhaust heat exchanger increases overtime. Experimental results of Walmsley et al. [17] yielded a time constant of 420 s based on a powder concentration of 1.8 g of powder per kg of air. In the model, the time constant is proportionally down-scaled to industrial situations where the powder concentration is significantly lower. Linear equations relating the final asymptotic value for the per cent pressure drop increase to stickiness are also obtained from the data presented in Walmsley et al. [17]. These equations are specific to the tube shape.

### 3.3. Utility and capital costing

Utility and capital cost estimates are made based on the parameters presented in Fig. 7. Capital cost equations are built into the spreadsheet and use the cost factor as a Lang factor. Based on these inputs together with the performance predictions, the spreadsheet calculates the cost benefit analysis shown in Fig. 8.

Literature and industrial documentation have very few capital cost estimation equations for finned tube heat exchangers. Furthermore the few equations that are present do not differentiate between heat exchangers with different fin pitches and tube or fin thickness and instead total area is used to estimate a capital cost. As a result the costs of the heat exchangers have been estimated using two different methods. Heat exchanger cost method A is based on calculating the total mass of stainless steel and aluminium required to make the heat exchangers multiplied by individual forming factors that reflect how easy a material will shape. Added to the material and forming costs is the cost of welding the heat exchanger together, which is dependent on the number of tubes in each exchanger, and the cost of putting fins on a tube. The sum of the various cost components relating to the construction of the heat exchanger is multiplied by a Lang factor of 3.5 [24]. Heat exchanger cost method B is based on the total area of the heat exchanger using

$$C_{HX,B} = 500A^{0.815} \quad (9)$$

Eq. (9) was fitted to data collected by the authors for recent industrial finned-tube heat exchanger installations. Capital and utility costs are calculated based on the New Zealand dollar. When simple payback, NPV and IRR are calculated, the spreadsheet uses the higher of the two heat exchanger cost estimates (either HX Cost A or HX Cost B in Fig. 8). Electrical power includes additional electricity consumed by the inlet fan for the new inlet exchanger, by

User Defined Cost Parameters		
Target Inlet Temp	200	°C
Steam Price	\$ 30	/t
Electricity Price	\$ 120	/MWh
$\eta_{\text{Pump/Fan}}$	0.60	
Cost for Cleaning	\$ 5,000	/wash
Production Hours	5000	h/y
Utility Price Rise	5%	/y
Discount Rate	15%	/y
Accounting Period	10	y
Cost Factor	3.37	

Fig. 7. Screenshot from the spreadsheet model showing utility, capital and miscellaneous user defined parameters.

Cost/Benefit		
Estimated Savings	1289	kW
Steam Savings	\$290,001	/y
Inlet Air Heat Req.	10,667	kW
%Main Air Heater Duty	12.1%	
Electrical Power	44	kW
Electrical Cost	\$26,242	/y
Cleaning Cost	\$ 0	/y
Profit	\$ 263,759	/y
HX Cost A	\$ 521,423	/y
HX Cost B	\$ 339,528	/y
Pump & Fan Cost	\$ 33,669	/y
Total Capital Cost	\$555,092	
Payback	2.10	y
Net Present Value	\$ 1,099,282	
IRR	54%	

Fig. 8. Screenshot from the spreadsheet model showing cost/benefit analysis results.

the exhaust fan for the fouled exhaust heat exchanger, and by the water pump.

## 4. Industrial milk powder plant case study

The industrial case study for modelling exhaust heat recovery has an exhaust air temperature of 75 °C with a humidity of 48 g/kg before heat recovery flowing at 153 kg/s on a dry air basis. The inlet air is drawn in at 15 °C on average with a humidity of 10 g/kg at 117 kg/s on a dry air basis. The exhaust air flow includes air flow through the dryer and fluidised beds whereas the inlet air flow is only for the dryer. This same industrial plant was studied by Walmsley et al. [7].

In the analysis, a steam cost of \$45/MWh and an electricity price of \$120/GWh are used. The plant is assumed to operate for 5000 h per year and the dryer is washed every four weeks. At a minimum it is hoped that the exhaust heat exchanger will not require cleaning while the dryer is on product. Project economics are calculated using a typical industrial discount rate of 15% and an accounting period of 10 years. Utility prices are assumed to rise at a constant rate of 5% per year.

## 5. Results and discussion for industrial case study

### 5.1. Modelling heat exchanger performance with fouling

Heat exchanger performance has been modelled for a four week period with estimates for fouling build-up and its associated effects. Three tube types have been selected for comparison. The CF (circular finned tube), CF-9.05-3/4J, was selected from the available correlations in Kays and London [11] because it had the highest Goodness factor, i.e.  $j/f$ . The other tubes analysed include a bare round tube (CB), CB-1.5:1.25, and an EB (elliptical bare tube), EB-1.5:1.25. Fig. 9 plots one case where the inlet heat exchanger has 12 tube rows of CF-9.05-3/4J and the exhaust exchanger has 14 tube rows. Both heat exchangers have a face velocity of 4 m/s.

With no fouling, the finned tube exhaust heat exchanger recovered 3.2 MW, which is equivalent to a 14.4% reduction in steam use for the main dryer air heater. The duty of the finned tube exhaust exchanger system fell to 3.0 MW at the end of the dryer production cycle after fouling. The finned round tube had the greatest amount of deposition resulting in an 8% reduction in heat recovery, which is similar heat transfer reductions experienced in boilers [25], and an increase in pressure drop for the

exhaust exchanger of 5%, which is very modest. The bare round tube exhaust heat exchanger began with a duty of 2.7 MW, which fell to 2.6 MW at the end of the dryer run, and a pressure drop increase of 2%. The elliptical bare tube experienced very little fouling resulting in only a small change to its heat recovery and pressure drop. The low fouling property of elliptical tubes is well established in literature, e.g. Ref. [26], and is derived from the tube's small frontal area to perimeter ratio, which means that on average the particle impact angle is higher than for round tube. The exhaust exchanger with bare round tube recovers 17% less heat than with finned round tube. Fouling on the bare round tube is expected to be less than for the finned tube because the average temperatures experienced in the exhaust heat exchanger are higher due to less heat recovery compared to the finned round tube. The elliptical bare tube has a 41% lower pressure drop and a 3% higher heat recovery compared to the bare round tube. The elliptical tube is low fouling and is not expected to have much fouling after four weeks.

5.2. Optimisation of the liquid coupled loop heat exchanger system

The fouling with its associated effects has been modelled to analyse its impact on key economic indicators. In the optimisation, the tube geometries, number of tube rows in the exhaust exchanger (4–40), and face velocities for the exhaust heat exchanger (2–8 m/s), are methodically varied. In total over 25,000 time steps were modelled and the economics of the exhaust heat recovery system was analysed in terms of NPV and IRR based on average heat recovery and pressure drop values.

Fig. 10 plots the results for the finned round tube, bare round tube and elliptical round tube using the number of tube rows in the exhaust exchanger as the independent variable on the x-axis. Results show it is possible to design an economically favourable heat recovery system with a NPV reaching nearly \$3 million over 10 years and IRR values greater than 50%. The face velocity of the exhaust heat exchanger in Fig. 10 is fixed at 4.0 m/s for all points. Furthermore each point in Fig. 10 takes into account fouling, which overtime lowers heat recovery and increases pressure.

Based on IRR the optimum number of exhaust tube rows is 6 tube rows whereas NPV indicates 12–14 tube rows is most profitable. This difference is important because IRR gives a good indication of the short-term payback of a project and NPV focuses on the long-term profit. As expected the finned tube exhaust heat exchanger offers better IRR and NPV values compared to the bare tubes.

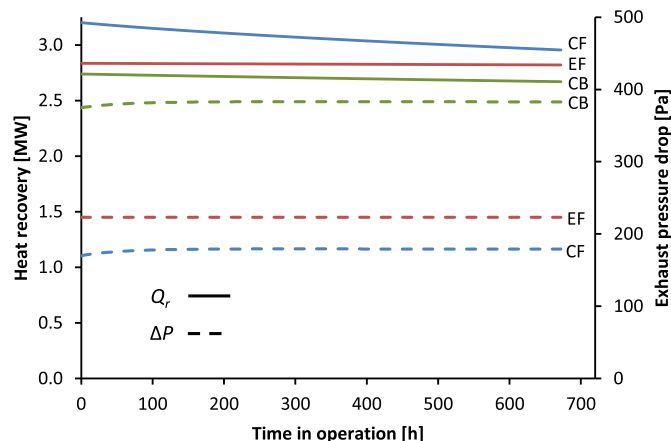


Fig. 9. Estimated heat recovery and pressure drop for a period of four weeks.

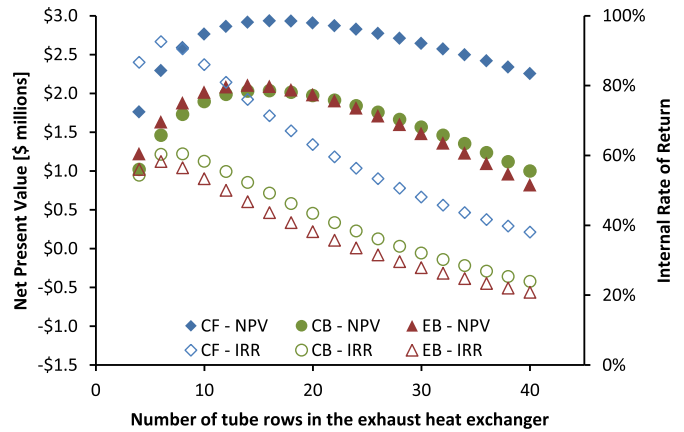


Fig. 10. Number of exhaust tube rows versus NPV and IRR.

The results may be also plotted using the exhaust outlet temperature as the x-axis as shown in Fig. 11. The deposition results on the frontal face of fins from Walmsley et al. [22] suggest fouling on the fins initiates and accelerates for exhaust temperatures below about 55 °C for an absolute humidity of 48 g/kg. In this particular case, the peak of the IRR and NPV curves all occur before 55 °C, which indicates deposition on the front of the fins should not occur. Fig. 11 shows the heat recovery savings achieved by basing the design on NPV is over 40% higher than basing the design on IRR.

Face velocity of the exhaust air heat exchanger is another important design parameter. Fluid velocity is often a parameter that is manipulated to reduce heat exchanger fouling at the expense of increased pressure drop. Fig. 12 plots the peak IRR and NPV values for the three heat exchanger geometries. In all cases the number of rows to achieve the peak IRR value compared to the peak NPV value is different. IRR analysis suggests a face velocity of about 6 m/s is advantageous whereas the NPV values support the selection of 4 m/s. Based on these results, the best LCHE system from a long-term investment viewpoint for the industrial case study is installation of a finned tube heat exchanger (CF-9.05-3/4J) to recover heat from the exhaust air with a face velocity of 4 m/s and 14 tube rows. For this system the NPV is NZ\$2.9 million and an IRR of 71%.

6. Conclusion

Milk spray dryer exhaust heat recovery is economically justifiable based on an industrial case study with an exhaust temperature

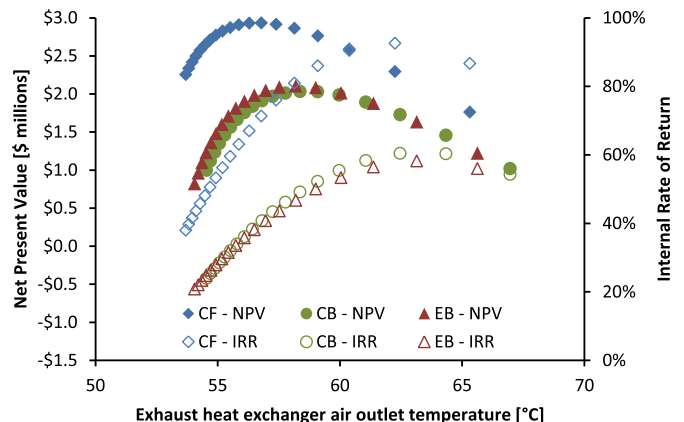


Fig. 11. Exhaust outlet temperature versus NPV and IRR.

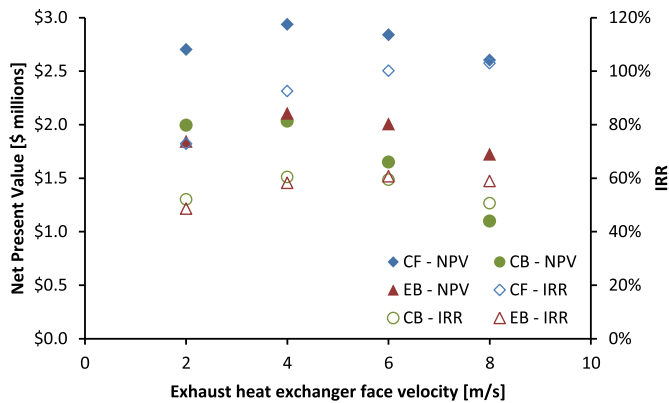


Fig. 12. Heat exchanger face velocity versus the peak NPV and IRR values.

of 75 °C. The exhaust heat recovery model applies literature correlations for finned-tube heat exchangers as the basis for determination of heat transfer and pressure drop. The impact of milk powder fouling in an exhaust heat recovery system is predicted to be able to be limited through smart heat exchanger design. Fouling predications are based on experimental correlations for milk powder deposition and fouling from literature. Results show that 4 m/s face velocity is the best trade-off between reducing fouling while maintaining an acceptable pressure drop. Internal rate of return analysis suggests the exhaust heat exchanger should contain only a few rows of tube (4–6 rows) whereas net present value analysis favours a larger exhaust heat exchanger with 12–14 rows. The developed thermo-economic assessment model has flexibility to be applied to any milk powder plant to optimise the economics of an exhaust heat recovery system.

#### Appendix. Site specific challenges facing economic implementation of milk spray dryer exhaust heat recovery

The economics for dryer exhaust heat recovery are highly site specific. For different industrial case studies, the optimum design of the exhaust heat exchanger may change; however the same thermos-economic analysis method may be applied. The operation, equipment, and construction are slightly different for each milk powder plant and spray dryer. The purpose of this section is to highlight some of the important factors that require consideration for industrial implementation of exhaust heat recovery in New Zealand milk powder plants by drawing upon the authors' collective experiences and observations.

- **Inlet air temperature and humidity to the dryer:** The temperature and humidity of the ambient is location specific. The temperature of the inlet air as the designated heat sink provides essential temperature driving to recovery exhaust heat, which is directly related to the size of the exhaust heat exchanger. The inlet temperature will vary during a day/night and over the production season. Less humidity air is advantageous in terms of dryer capacity, but it also has a lower heat capacity flow rate, which means less recovered heat and steam is needed to raise the temperature of the air to approximately 200 °C.
- **Exhaust air temperature and humidity:** Dryers with higher exhaust temperatures are better candidates for energy recovery due to a larger potential temperature driving force, which results in increase heat recovery and improved economics. Humidity is also an important factor because it affects the stickiness of the milk powder and, therefore, the amount of fouling. For ease of exhaust heat recovery, a lower humidity is

desirable, but from an overall dryer efficiency perspective, lower exhaust temperatures at high humidity maximise the drying capacity of the air.

- **Inlet and exhaust fan capacity:** For existing sites it is important to understand where the inlet and exhaust fans are operating on the respective fan curves. Fans with sufficient spare capacity do not require replacement, which for retrofits is likely to be a significant cost. Where fans are likely pressure drop constrained, it is smarter to design the exhaust and inlet heat exchangers to meet a pressure drop target rather than a heat recovery target.
- **Existing pre-heaters using utility:** at many sites steam is used to preheat air entering the building to 30–35 °C. These heat exchangers are typically a few rows deep with a large frontal area and a low face velocity. Re-piping an existing inlet pre-heater exchanger to use heat from the dryer exhaust is likely the most economical opportunity for some sites.
- **Existing heat recovery to dryer inlet air:** some sites use waste heat from flue gas from the boiler or hot process condensate water to preheat the dryer inlet air. Because exhaust heat recovery is heating in similar temperature ranges, the full benefits of both heat recovery systems are not achievable.
- **Re-usable existing ducting:** if possible it is desirable to avoid the costs of fabricating and installing large sections of new ducting.
- **Price of energy:** heating costs can vary by 30–50% from site to site depending on the fuel source – either coal or natural gas – and the conversion efficiency. The supply of energy can strongly affect the price of energy.
- **Operating and production hours:** heat recovery savings is directly proportional to the hours of production per year.
- **Physical space:** the building housing the dryer needs to have the room for a heat recovery system. Modifications to buildings are very costly and risky potentially causing product contamination.
- **Inlet air heater bottleneck:** where the inlet air heater is the bottleneck to increased production, exhaust heat recovery would provide additional duty to allow for more airflow into the dryer and additional dryer capacity. In this case, exhaust heat recovery may prevent the need for increasing the capacity of the existing steam boiler to meet the higher process heat demand.
- **Bag filters:** efficient removal of milk particles from the exhaust air stream can decrease the risk and potential for exchanger fouling.
- **Good attitude to change:** the site needs a good attitude to change, particularly when a technology is being implemented for the first time.

#### References

- [1] Reay D. A selection of heat recovery applications illustrated by means of case studies. *J Heat Recovery Syst* 1982;2:401–18. [http://dx.doi.org/10.1016/0198-7593\(82\)90028-5](http://dx.doi.org/10.1016/0198-7593(82)90028-5).
- [2] Mercer AC. Improving the energy efficiency of industrial spray dryers. *J Heat Recovery Syst* 1986;6:3–10. [http://dx.doi.org/10.1016/0198-7593\(86\)90166-9](http://dx.doi.org/10.1016/0198-7593(86)90166-9).
- [3] Laurijssen J, De Gram FJ, Worrell E, Faaij A. Optimizing the energy efficiency of conventional multi-cylinder dryers in the paper industry. *Energy* 2010;35:3738–50. <http://dx.doi.org/10.1016/j.energy.2010.05.023>.
- [4] Han X, Liu M, Wang J, Yan J, Liu J, Xiao F. Simulation study on lignite-fired power system integrated with flue gas drying and waste heat recovery – performances under variable power loads coupled with off-design parameters. *Energy* 2014;76:406–18. <http://dx.doi.org/10.1016/j.energy.2014.08.032>.
- [5] Tippyawong N, Tantakitti C, Thavornun S. Energy efficiency improvements in longan drying practice. *Energy* 2008;33:1137–43. <http://dx.doi.org/10.1016/j.energy.2008.02.007>.
- [6] Linnhoff B, Hindmarsh E. The pinch design method for heat exchanger networks. *Chem Eng Sci* 1983;38:745–63.

- [7] Walmsley TG, Walmsley MRW, Atkins MJ, Neale JR. Improving energy recovery in milk powder production through soft data optimisation. *Appl Therm Eng* 2013;61:80–7. <http://dx.doi.org/10.1016/j.applthermaleng.2013.01.051>.
- [8] Walmsley TG, Walmsley MRW, Atkins MJ, Neale JR. Integration of industrial solar and gaseous waste heat into heat recovery loops using constant and variable temperature storage. *Energy* 2014;75:53–67. <http://dx.doi.org/10.1016/j.energy.2014.01.103>.
- [9] Walmsley TG, Walmsley MRW, Atkins MJ, Fodor Z, Neale JR. Optimal stream discharge temperatures for a dryer operation using a thermo-economic assessment. *Chem Eng Trans* 2012;29:403–8. <http://dx.doi.org/10.3303/CET1229252>.
- [10] Atkins MJ, Walmsley MRW, Neale JR. Integrating heat recovery from milk powder spray dryer exhausts in the dairy industry. *Appl Therm Eng* 2011;31:2101–6. <http://dx.doi.org/10.1016/j.applthermaleng.2011.03.006>.
- [11] Kays WM, London AL. *Compact heat exchangers*. 3rd ed. Malabar, USA: Krieger Pub. Co.; 1998.
- [12] Walmsley TG, Walmsley MRW, Atkins MJ, Neale JR, Sellers CM. An experimentally validated criterion for skim milk powder deposition on stainless steel surfaces. *J Food Eng* 2014;127:111–9. <http://dx.doi.org/10.1016/j.jfoodeng.2013.11.025>.
- [13] London AL, Kays WM. The liquid coupled indirect-transfer regenerator for gas turbine plants. *Trans ASME* 1951;73:529–40.
- [14] Walmsley TG, Walmsley MRW, Atkins MJ, Hoffman-Vocke J, Neale JR. Numerical performance comparison of different tube cross-sections for heat recovery from particle-laden exhaust gas streams. *Procedia Eng* 2012;42:1476–90. <http://dx.doi.org/10.1016/j.proeng.2012.07.527>.
- [15] Wang CC, Webb RL, Chi KY. Data reduction for air-side performance of fin-and-tube heat exchangers. *Exp Therm Fluid Sci* 2000;21:218–26. [http://dx.doi.org/10.1016/S0894-1777\(00\)00005-4](http://dx.doi.org/10.1016/S0894-1777(00)00005-4).
- [16] Holmberg RB. Heat transfer in liquid-coupled indirect heat exchanger systems. *J Heat Transf* 1975;97:499–503.
- [17] Walmsley TG, Walmsley MRW, Atkins MJ, Neale JR. Analysis of skim milk powder deposition on stainless steel tubes in cross-flow. *Appl Therm Eng* 2015;75:941–9. <http://dx.doi.org/10.1016/j.applthermaleng.2014.10.066>.
- [18] Nijdam JJ, Langrish TAG. The effect of surface composition on the functional properties of milk powders. *J Food Eng* 2006;77:919–25. <http://dx.doi.org/10.1016/j.jfoodeng.2005.08.020>.
- [19] Pisecky I. *Handbook of milk powder manufacture*. Copenhagen, Denmark: Niro A/S; 1997.
- [20] MAF Quality Management. *Physical properties of dairy products*. 3rd ed. Hamilton, New Zealand: MAF Quality Management; 1996.
- [21] Bell IH, Groll EA. Air-side particulate fouling of microchannel heat exchangers: experimental comparison of air-side pressure drop and heat transfer with plate-fin heat exchanger. *Appl Therm Eng* 2011;31:742–9. <http://dx.doi.org/10.1016/j.applthermaleng.2010.10.019>.
- [22] Walmsley TG, Walmsley MRW, Atkins MJ, Neale JR. Fouling and pressure drop analysis of milk powder deposition on the front of parallel fins. *Adv Powder Technol* 2013;24:780–5. <http://dx.doi.org/10.1016/j.apt.2013.04.004>.
- [23] Walmsley TG, Walmsley MRW, Atkins MJ, Neale JR. An investigation of milk powder deposition on parallel fins. In: *Chemeca 2012*. Wellington, New Zealand: IChemE; 2012.
- [24] Bouman RW, Jensen SB, Wake ML, Earl WB. *Process capital cost estimation for New Zealand 2004*. Wellington, New Zealand: Society of Chemical Engineers New Zealand; 2005.
- [25] Stehlík P. Conventional versus specific types of heat exchangers in the case of polluted flue gas as the process fluid – a review. *Appl Therm Eng* 2011;31:1–13. <http://dx.doi.org/10.1016/j.applthermaleng.2010.06.013>.
- [26] Bouris D, Konstantinidis E, Balabani S, Castiglia D, Bergeles G. Design of a novel, intensified heat exchanger for reduced fouling rates. *Int J Heat Mass Transf* 2005;48:3817–32. <http://dx.doi.org/10.1016/j.ijheatmasstransfer.2005.03.026>.



**Article 6:**

*An experimentally validated criterion for skim milk powder  
deposition on stainless steel surfaces*

**Walmsley, T.G.**, Walmsley, M.R.W., Atkins, M.J., Neale, J.R.,  
Sellers, C.M., 2014.

Journal of Food Engineering 127, 111–119.

DOI: 10.1016/j.jfoodeng.2013.11.025

Elsevier



# An experimentally validated criterion for skim milk powder deposition on stainless steel surfaces



Timothy G. Walmsley\*, Michael R.W. Walmsley, Martin J. Atkins, James R. Neale, Chloe M. Sellers

University of Waikato, Energy Research Centre, School of Engineering, Hamilton, New Zealand

## ARTICLE INFO

### Article history:

Received 13 September 2013  
Received in revised form 19 November 2013  
Accepted 25 November 2013  
Available online 3 December 2013

### Keywords:

Milk powder  
Particle deposition  
Spray drying

## ABSTRACT

Predicting the deposition during the production of milk powder has been identified as a possible avenue to creating new designs and selecting processing conditions that minimise particle deposition. Numerous studies have looked at characterising various aspects of milk powder deposition, agglomeration and caking. Present literature lacks a fundamental and validated criterion that describes the deposition of skim milk powder particle (SMP) impacts with short contact times (<1 s). In this paper standard solutions to the contact mechanics problem of a spherical elastic particle with an adhesive surface impacting a rigid plate at normal and oblique angles form the basis of a derivation of a semi-empirical criterion that describes whether a particle sticks after impacting a wall. To validate the criterion, the determining factors of skim milk powder deposition, which are air temperature, water activity (i.e. relative humidity), plate (or wall) temperature, and particle size, velocity and impact angle, are isolated and experimentally tested using the Particle Gun technique.

© 2013 Elsevier Ltd. All rights reserved.

## 1. Introduction

Predicting dairy and food powder deposition in spray dryers, auxiliary processes and heat recovery equipment using Computational Fluid Dynamics (CFD) has emerged as an area of significant research interest (Jin and Chen, 2010). A key input function to these computer models is a wall boundary condition/criterion that evaluates whether a powder particle sticks or rebounds. Reported in literature is a wide range of experimental powder stickiness characterisation tests (Boonyai et al., 2004), however there is a lack of a detailed and complete criterion that expresses the critical combination of conditions, including air temperature, humidity, impact velocity and angle, particle mass, etc., that results in deposition.

Current criteria for modelling particle deposition using CFD in literature have been simple in nature with critical values being somewhat arbitrarily selected before modelling results are compared to experimental results for validation. Harvie et al. (2002) formulated a simple wall boundary deposition criterion focused solely on a fixed  $(T - T_g)_{crit}$ , where  $T$  is the air temperature and  $T_g$  is the glass transition temperature of the major amorphous component of the powder. Woo et al. (2008) based their wall capture criterion on a fixed critical normal velocity without respect to the surrounding air conditions. Woo et al. also gave no supporting

experimental evidence for the choice of critical normal velocity and coefficient of restitution. Zhao (2009) built on the approach of Woo et al. by applying a critical normal capture velocity that was dependent on the air temperature and humidity, i.e.  $T - T_g$ . However Zhao did not consider the effect of oblique particle impact angles in his criterion. Jin and Chen (2010) applied the concepts of critical pseudo Ohnesorge (a ratio of viscosity to surface tension) and Webber (the fluid's inertia compared to its surface tension) numbers to determine particle attachment. Jin and Chen give no basis for their selection of critical Ohnesorge and Webber numbers other than the modelling trends somewhat follow experimental results.

Besides CFD wall boundary criterion Palzer (2005) applied a classic model for viscoelastic contact to derive a critical contact time, which if exceeded indicated deposition and/or agglomeration would occur. Palzer's model assumed that sintering as described by the Frenkel equation was the relevant process for developing the adhesion force. This model, however, has been shown to be invalid for SMP in situations where the contact times are short (<1 s) as is the case with the experimental tests such as the Particle Gun stickiness test (Murthi et al., 2010).

Whether a particle, such as Skim Milk Powder (SMP), deposits or rebounds is determined by the particle's kinetic energy, which upon contact is transferred to potential elastic energy and plastic deformation, compared to the bond strength between the particle and the surface (or another particle). Numerous studies dating back to the elementary work of Hertz (1881) in the late nineteenth century have studied the theoretical and experimental aspects of

\* Corresponding author. Address: University of Waikato, Gate 8, School of Engineering, Hillcrest Rd, Hamilton, New Zealand. Tel.: +64 78384937.

E-mail address: [tgw7@waikato.ac.nz](mailto:tgw7@waikato.ac.nz) (T.G. Walmsley).

## Nomenclature

### Roman

$a$	dimensionless constant
$a_w$	water activity
$B$	proportionality constant in Eq. (8)
$D_1$	dimensionless constant in Eq. (1)
$D_2$	temperature constant in Eq. (1), °C
$d$	particle diameter, m
$E$	energy, J
$F$	force, N
$G$	shear modulus, Pa
$k$	dimensionless constant in Eq. (2)
$m$	mass, kg
$P$	pressure, Pa
$RH$	relative humidity, %
$r$	particle radius, m
$T$	temperature, °C
$T_g$	glass transition temperature, °C
$W_a$	work of adhesion, J
$Y$	Young's modulus, Pa
$Y^*$	modified Young's modulus, Pa

### Greek

$\gamma$	adhesion bond strength, J/m <sup>2</sup>
$\delta$	penetration depth, m
$\Theta$	impact angle, °
$\lambda$	dimensionless group of properties
$\nu$	Poisson's ratio
$\rho$	density, kg/m <sup>3</sup>

### Subscripts

$a$	adhesion
$crit$	critical
$l$	lactose
$n$	normal
$p$	particle
$pd$	plastic deformation
$rot$	rotational
$s$	sticking
$t$	tangential
$w$	water

the normal impact of spherical balls on plates. This body of literature includes work on elastic (Hertz, 1881), elastic–plastic (Thornton and Ning, 1998), plastic, and viscoelastic spheres (Brilliantov et al., 2007).

The aim of this study is to derive and experimentally validate a criterion that describes the adhesion of SMP onto a flat, polished stainless steel surface. Factors contributing to deposition that are studied include: air temperature and humidity, particle size and mass distribution, impact velocity and angle, and plate temperature. To describe these effects on particle deposition, a simple elastic contact model with adhesion is derived and its constants solved by fitting the model to experimental data. Furthermore, data from several literature sources are reviewed and included when validating the model. This validated deposition criterion may prove useful to be applied as a wall boundary condition in Computational Fluid Dynamics models to predict where deposition will occur in processing equipment for optimising equipment design.

## 2. Theory

### 2.1. Developments in the understanding of SMP surface stickiness

Early experimental studies on the stickiness characteristics of food and dairy powders looked at stickiness development in situations where contact between particles occurred for extended periods of time (Wallack and King, 1988). Focus was given to measuring temperature ( $T$ ) and relative humidity ( $RH$ ) conditions that caused sudden coalescing of dairy powder particles leading to agglomeration and caking (Hennigs et al., 2001). Stickiness tests have also been developed to mimic the operation of various unit operations such as lab-scale spray drying (Chen et al., 1993; Kota and Langrish, 2006), fluidised bed drying (Zuo, 2004), cyclone separation units (Intipunya et al., 2009), and dryer exhaust gaseous heat exchangers (Walmsley et al., 2013b, 2013c). The Particle Gun test, which uses an impingement jet and fires particles at a flat plate, was constructed to simulate shorter contact times and to acutely study the effects of airflow dynamics (Paterson et al., 2007).

The surface stickiness of food and dairy powders is intricately related to the concepts of glass transition temperature and viscosity (Downton et al., 1982). In amorphous materials, such as SMP, the glass transition temperature,  $T_g$ , identifies the boundary

between the material being in a non-sticky glassy state or a sticky rubbery state. The major amorphous component in SMP is Lactose, which accounts for about half of SMP by weight. For air temperatures below  $T_g$ , the viscosity is high and molecular movements of surface lactose are subdued. Above  $T_g$ , molecular mobility rapidly increases while the surface viscosity lowers. Liquid bridges may then readily form between two particles and between particles and solid surfaces. Further temperature increases above  $T_g$  continues to lower viscosity. The amount the air temperature is above  $T_g$ , i.e.  $T - T_g$ , is logarithmically related to viscosity,  $\mu$ , as described by the Williams et al. (1955) equation, where  $D_1$  is a dimensionless constant and  $D_2$  is a temperature constant for a given amorphous composition. Hence,  $T - T_g$  is a non-linear measure of stickiness through viscosity.

$$\text{Log}\left(\frac{\mu}{\mu_g}\right) = \frac{-D_1(T - T_g)}{D_2 + (T - T_g)} \quad (1)$$

The glass transition temperature of a material is strongly dependent on the moisture content and water activity at the surface of the particle. For two component substances Gordon and Taylor (1952) suggested a modified rule of mixtures equation was sufficient to calculate the glass transition temperature of the material, which for SMP may be applied to lactose and water (Hennigs et al., 2001),

$$T_g = \frac{T_{g,l} + kX_{eq}T_{g,w}}{1 + kX_{eq}} \quad (2)$$

where  $T_g$  is the glass transition temperature of SMP,  $X_{eq}$  is the equilibrium moisture content on a dry basis,  $T_{g,l}$  is the glass transition temperature of lactose,  $T_{g,w}$  is the glass transition temperature of water and  $k$  is a constant. Since  $X_{eq}$  is weakly dependent on temperature, Brooks (2000) successfully developed a polynomial model to relate  $a_w$  (or  $RH$ ) to  $T_g$  with high accuracy,

$$T_g = 530.66a_w^3 + 652.06a_w^2 - 366.33a_w + 99.458, \quad [0 < a_w < 0.575] \quad (3)$$

where  $a_w$  is the water activity. However Brooks' equation is limited to the water activity range stated and beyond this range, the model is unreliable. As a result Eq. (2) may be applied, in combination with the appropriate sorption isotherm that links particle moisture

content to air temperature and humidity, as an estimate when the range of Eq. (3) is exceeded.

## 2.2. Deposition criterion for normal and oblique impacts of adhesive amorphous particles

In this section the derivation of a criterion is presented that describes the collision of an adhesive elastic sphere against a solid wall. The criterion is based on the works of Johnson et al. (1971), Savkoor and Briggs (1977) and Thornton and Ning (1998) to describe the contact kinetics of an elastic particle impacting a rigid wall, in combination with the work of Williams et al. (1955) to describe the temperature dependency of the surface viscosity and adhesion energy of a particle. To the best knowledge of the authors the combining of these two bodies of work has generated a functional and novel criterion that describes the attachment of variably adhesive particles, such as SMP.

The energy balance of a particle–surface collision is

$$E_{k,i} = E_{k,f} + W_a + E_{pd} + \Delta E_{rot} \quad (4)$$

where  $E_{k,i}$  and  $E_{k,f}$  are the initial and final kinetic energy of a particle colliding with a surface,  $W_a$  is the work of adhesion,  $E_{pd}$  is the energy of plastic deformation, and  $\Delta E_{rot}$  is change in rotational energy. If it is assumed that  $E_{pd}$  and  $\Delta E_{rot}$  are zero, then a particle sticks when the incoming kinetic energy is less than the work of adhesion, which may be determined by

$$W_a = \int_{\delta_c}^0 F'_n d\delta \quad (5)$$

where  $F'_n$  is the equivalent normal force and  $\delta$  is the penetration depth.

Thornton and Ning (1998) applied numerical integration to find the equivalent expression

$$W_a = 0.9355F_s \delta_{crit} \quad (6)$$

where  $F_s$  is the pull-off force (adhesion force) and  $\delta_{crit}$  is the critical (negative) penetration depth at which separation is imminent. Thornton and Ning (1998) then applied Eq. (6) to normal impacts and produced a model that describes sticking and restitution of a particle. In this work, we extend the application of Eq. (6) to sticking at non-normal impacts, but do not attempt to completely describe the rebound of a particle. It is at this point that the derivation now turns to the work of Savkoor and Briggs (1977) to described when an adhesive elastic sphere sticks at oblique impacts given known normal ( $F_n$ ) and tangential ( $F_t$ ) loadings. Savkoor and Briggs (1977) presented the following condition for sticking to occur

$$9\pi^2 r^2 \gamma_s^2 + 6F_n \pi r \gamma_s - \frac{Y^*}{4G^*} F_t^2 \geq 0 \quad (7)$$

$$\text{where } \frac{1}{Y^*} = \frac{1 - \nu_1^2}{Y_1} + \frac{1 - \nu_2^2}{Y_2}, \quad \frac{1}{G^*} = \frac{2 - \nu_1^2}{G_1} + \frac{2 - \nu_2^2}{G_2}$$

In the above equation,  $\gamma_s$  is the surface adhesion bond strength,  $r$  is the particle radius,  $Y$  is Young's modulus,  $\nu$  is Poisson's ratio,  $G$  is the shear modulus and subscripts 1 and 2 refer to properties of the particle and surface.

As a simplification, in this work it is assumed ratio of the normal and tangential forces are related through the normal impact angle and a proportionality constant  $B$ ,

$$\frac{F_t}{F_n} \approx \frac{dF_t}{dF_n} = -B \tan(\Theta_n) \quad (8)$$

The adhesion pull-off force,  $F_s$ , required to prevent particle detachment at the boundary between stick/rebound is found when Eq. (7) is set equal to zero

$$9\pi^2 r^2 \gamma_s^2 - 6F_s \pi r \gamma_s - \frac{Y^* B^2}{4G^*} \tan^2(\Theta_n) F_s^2 = 0, \quad \text{where } F_s = -F_n \quad (9)$$

which may be rearranged to make  $F_s$  the subject,

$$F_s = \frac{3}{2} \pi r \gamma_s \lambda, \quad \text{where } \lambda = 2 \left( 1 + \sqrt{1 + \frac{Y^* B^2}{4G^*} \tan^2(\Theta_n)} \right)^{-1} \quad (10)$$

Johnson et al. (1971) derived the pull-off force for normal impacts as  $F_{s(0)} = \frac{3}{2} \pi r \gamma_s$ , which solution is obtained by setting  $\Theta_n = 0$  in Eq. (10).

The solution to the critical penetration depth is (Thornton and Ning, 1998),

$$\delta_{crit} = \left( \frac{5\pi\gamma_s r^{1/2} \lambda}{8Y^*} \right)^{2/3} \quad (11)$$

Substituting Eqs. (10) and (11) into Eq. (6) and simplifying gives

$$W_a = 6.913 \left( \frac{r^4 \gamma_s^5 \lambda^5}{Y^{*2}} \right)^{1/3} \quad (12)$$

For sticking, Eq. (12), the effective work of adhesion in the normal direction, must equal to or greater than the kinetic energy of the particle in the normal direction,

$$\frac{1}{2} m v_n^2 \leq 6.913 \left( \frac{r^4 \gamma_s^5 \lambda^5}{Y^{*2}} \right)^{1/3}, \quad \text{where } m = \frac{4}{3} \pi r^3 \rho \quad (13)$$

Eq. (14) is obtained by making  $\gamma$  the subject

$$\gamma_s \geq 0.2442 r \rho^{3/5} v_n^{6/5} Y^{*2/5} \left( 1 + \sqrt{1 + \frac{Y^* B^2}{4G^*} \tan^2(\Theta_n)} \right) \quad (14)$$

In this work the adhesion bond strength,  $\gamma_s$ , is related to  $T - T_g$ , i.e. particle surface stickiness, through viscosity (Eq. (1)). To link  $\gamma_s$  to  $T - T_g$ , the ratio of the adhesion bond strength,  $\gamma_s$ , using the adhesion bond strength at the glass transition temperature as the basis is postulated to be proportional to the inverse of the ratio of the surface viscosity,  $\mu$ , of the particle using the viscosity at the glass transition temperature as the basis such that

$$\frac{\gamma_s}{\gamma_g} = a \left( \frac{\mu}{\mu_g} \right)^{-1} \quad (15)$$

where  $a$  is a dimensionless proportionality constant and subscript  $g$  refers to the property at the glass transition temperature. Viscosity is related to  $T - T_g$  as described by Eq. (1). Combining Eqs. (1) and (15) and rearranging gives

$$\gamma_s = a \gamma_g 10 \left( \frac{D_1 (T - T_g)}{D_2 + (T - T_g)} \right) \quad (16)$$

By equating Eqs. (14) and (16), a model is formed that describes the critical boundary between adhesion and rebound of particles.

$$\begin{aligned} & 0.2442 r \rho^{3/5} v_n^{6/5} Y^{*2/5} \left( 1 + \sqrt{1 + \frac{Y^* B^2}{4G^*} \tan^2(\Theta_n)} \right) \\ & = a \gamma_g 10 \left( \frac{D_1 (T - T_g)_{crit}^*}{D_2 + (T - T_g)_{crit}^*} \right) \end{aligned} \quad (17)$$

Eq. (17) is rearranged to make  $T - T_g$  the subject to obtain

$$(T - T_g)_{crit}^* = \frac{D_2 \log \left( \frac{0.2442 r \rho^{3/5} v_n^{6/5} Y^{*2/5} \left( 1 + \sqrt{1 + \frac{Y^* B^2}{4G^*} \tan^2(\Theta_n)} \right)}{a \gamma_g} \right)}{D_1 - \log \left( \frac{0.2442 r \rho^{3/5} v_n^{6/5} Y^{*2/5} \left( 1 + \sqrt{1 + \frac{Y^* B^2}{4G^*} \tan^2(\Theta_n)} \right)}{a \gamma_g} \right)} \quad (18)$$

In its present form Eq. (18) is a theoretical description of the critical  $T - T_g$  conditions required for a particle to stick. The following

experimental work was carried out to determine the constants  $a$ ,  $D_1$ ,  $D_2$  and  $B$  in Eq. (18) and to validate the functional form of the model. It is important to note that the deposition model derived encompasses a number of simplifications such as particles are assumed to be spherical, incoming rotational energy to the collision is zero, and plastic deformation is zero. These simplifications are considered to be of a low order of magnitude compared to effects of as particle size, velocity, etc.

### 3. Experimental methods

#### 3.1. Particle Gun operation

The Particle Gun is an experimental test that looks at deposition on a flat plate in an impingement jet (Paterson et al., 2007). The Particle Gun delivers air at a controllable temperature (20–90 °C), relative humidity (0–100%) and average jet velocity (0–40 m s<sup>-1</sup>). It functions by bubbling compressed air through a temperature regulated hot water tank. Depending on the tank water temperature and pressure (regulators  $P_2$  and  $P_3$  in Fig. 1), the air moisture content is controlled. Adjusting  $P_3$  controls the air flow rate exiting the tank.

After exiting the tank, moist air passes through a 400 W heater to reach the required temperature. Temperature ( $T_V$ ) and relative humidity ( $RH_V$ ) readings are logged immediately before a Venturi. Immediately following the Venturi, powder is injected through a cone with the aid of a little air suction. A tape heater is wrapped around the powder injection cone to eliminate condensation forming and to increase powder flowability into the air. The particle-laden air then develops along a 1.6 m insulated 11 mm tube (inside diameter), before impacting a target plate. The particle surfaces are assumed to be in equilibrium with the air and impact the plate at the same speed as the jet (Paterson et al., 2007). Air Reynolds numbers ranged from 4200 to 18,800, indicating the air is fully turbulent.

Air temperature and relative humidity are logged before the Venturi. Using this temperature and relative humidity, the absolute humidity is calculated. Air temperature ( $T$ ) is also regularly measured at the end of the tube. By using a water mass balance around the Venturi, the air moisture content in the tube is calculated. This mass balance takes into account ambient air sucked in through the Venturi. Knowing  $T$  and the absolute humidity in the tube, the relative humidity ( $RH$ ) is also determined. At the time of impact with the plate, particles are estimated to have a surface temperature and water activity in equilibrium with  $T$  and  $RH$ . Plate temperature is measured using a K-type thermocouple slotted into

a hole in the aluminium plate. A polished 304 stainless steel plate, 150 mm square, is used as the target plate. Jet velocity is measured using a 15 mm diameter impeller anemometer, 10 mm from the tube end. Anemometer readings are corrected through the aid of PIV analysis to give a more accurate average jet velocity across the 11 mm tube.

Tests performed analyse the effects of plate (or wall) temperature and particle size, velocity and impact angle on deposition and the minimum required  $T - T_g$ , which is a function of air temperature and relative humidity, to achieve deposition. For each test the amount of deposition at the centre of the collection is weighed, which helped reinforce the identification of critical  $T - T_g$  values.

#### 3.2. Particle size distribution analysis

Powders used in the deposition tests include agglomerated and non-agglomerated SMP. Bulk non-agglomerated SMP has a lower particle size distribution whereas agglomerated SMP has a high particle size distribution. These bulk powders were also mechanically sieved to create several size fractions (Table 1). By using both types of powder a wider range of particle size fractions were able to be obtained and tested than if only agglomerated or non-agglomerated powder was sieved. The various size fractions are identified by referring to the medium,  $d_{(0.5)}$ . Particle size distributions were measured in iso-propanol using a Malvern Mastersizer 2000 according to the method outlined by Pisecky (1997).

#### 3.3. Visualisation of impingement jet airflow patterns

A PIV flow visualisation technique has been successfully applied to characterise the impingement jet air flow patterns of the Particle

**Table 1**

SMP particle size distribution parameters used in deposition tests. Particle sizes characterising the distribution are for the 10, 50 and 90 percentiles.

Agglomerated (Y/N)	$d_{(0.1)}$ ( $\mu\text{m}$ )	$d_{(0.5)}$ ( $\mu\text{m}$ )	$d_{(0.9)}$ ( $\mu\text{m}$ )
N	18	30	57
N	31	51	87
N	32	61	140
N	39	104	202
Y	66	108	172
Y	101	170	285
Y	98	268	571
Y	164	303	532
Y	410	686	1159
Y	431	893	1488

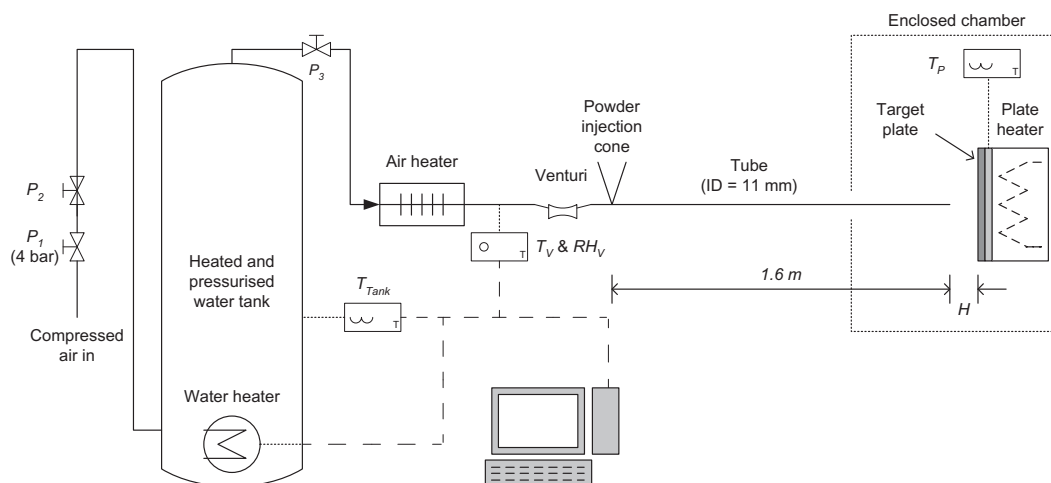


**Fig. 1.** Schematic of the Particle Gun test apparatus.

Gun set-up at average jet velocities of 8.0, 10.0, 15.0, 25.0 and 35.8 m/s. PIV uses a thin laser light sheet orientated parallel to the seeded gas or liquid flow. Dispersion of the light sheet caused by the seeded particles is captured by a camera fixed perpendicular to the sheet. Two images are taken in quick succession ( $\approx 10 \mu\text{s}$ ). These are compared and processed using cross correlation computer algorithms. From this analysis full velocity flow fields are obtained. For further information on PIV, refer to Raffel et al. (2007).

Impingement jet characteristic dimensions for the PIV analysis mirrored those used for the powder adhesion tests. Fine paraffin liquid particles were seeded into the air jet by a Flow Tracker 700 CE fluid atomiser at 1.5 bar. After impacting the wall, some particles were observed to stick to the plate, although enough remained in the air flow to capture the flow field in and around the jet. The light sheet was produced by a Nd:YAG laser (526 nm) and position in the jet centre, parallel to the jet flow. A Nikon FlowSense 4 M MKII camera with resolution  $2048 \times 2048$  pixels was fixed perpendicular to and focused on the light sheet.

For analysis, 200 double frame images at 1 Hz and  $10 \mu\text{s}$  between frames are captured. These are analysed using an average cross correlation method with an interrogation area of 32 pixels square and an overlap of 50% in both the horizontal and vertical directions. A No-DC filter, a peak height ratio filter and a moving average filter were successively applied to remove inconsistent vectors. Interpolation of the neighbouring vectors replaced deleted vectors. Maximum velocities in the jet's centre have been checked using a TSI 8386-M-GB hot wire anemometer.

For comparison of the different average jet velocities, profile cuts 10 mm and 20 mm away from the plate are plotted (Fig. 2). Velocities have been normalised by dividing by the maximum velocity. Both normalised velocity profiles suggest the shape of the jet does not change significantly within the average velocity range of  $8.0\text{--}35.8 \text{ ms}^{-1}$ . Therefore Fig. 3 is representative of all average velocities.

Results increased understanding of air flow interaction with the plate boundary. The normalised velocity contour plot, Fig. 3, shows the jet spreads only a little before interacting with the plate. In the centre of the jet is a stagnation zone.

During deposition testing, the jet velocity was measured using an anemometer and correlated with the aid of PIV to ensure accurate estimate average jet velocity and peak velocity (Fig. 4). All reported jet velocities are the average velocity across the tube exit and they have been corrected using the equations shown in Fig. 4.

In the previous Particle Gun studies by Paterson and co-workers, i.e. (Murti et al., 2010, 2009; Paterson et al., 2007; Zuo et al., 2007), no correction was made to account for the difference in size between the jet and vane anemometer diameters (Paterson, 2011).

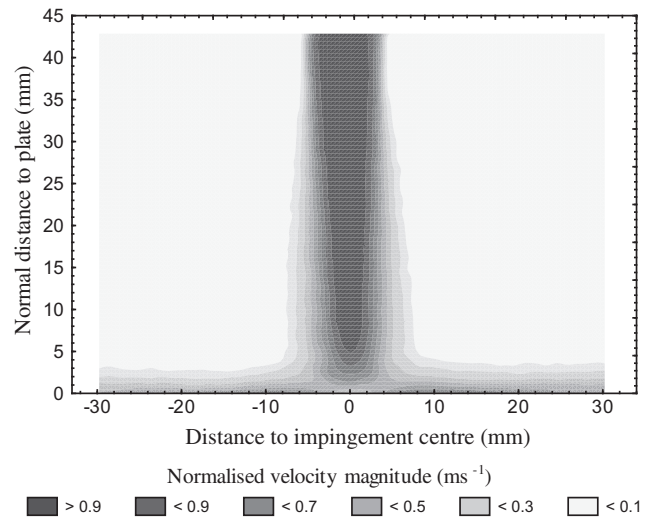


Fig. 3. Normalised velocity magnitude contours of a normal impingement jet.

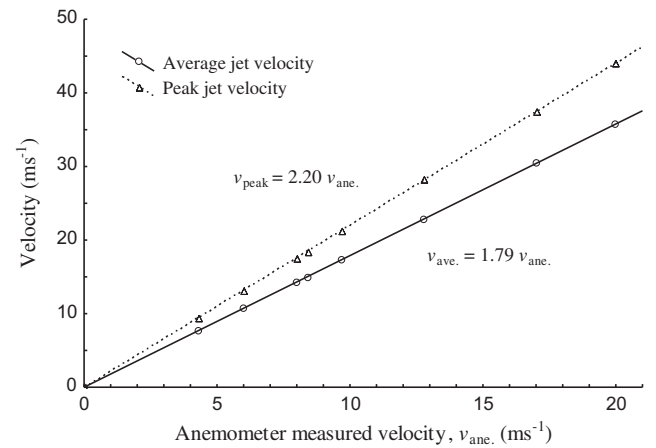


Fig. 4. Correlation between PIV and 15 mm diameter anemometer velocities of a 11 mm air jet.

Corrections to the velocities reported Paterson and co-workers using the understanding gained by PIV analysis are also not possible because they do not report the diameter of their vane anemometer. Zhao (2009) also used PIV to successful correct anemometer readings. As a result it is vital to repeat much of the experimental

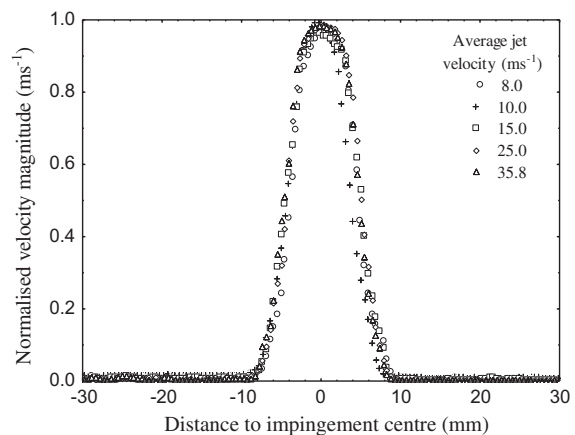
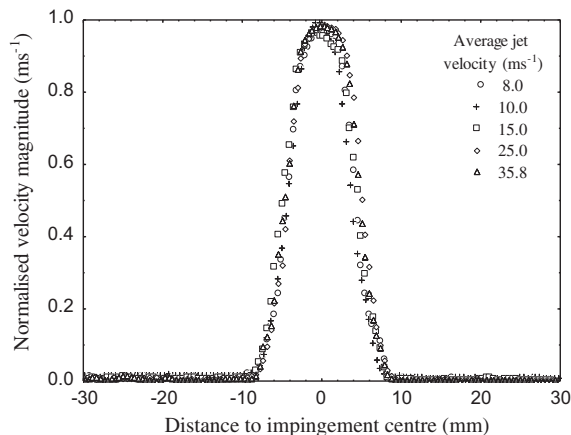


Fig. 2. Normalised velocity profile 10 mm (left) and 20 mm (right) away from and parallel to the plate.

work that has previously been carried out by Paterson and co-workers and Zhao.

### 3.4. Determination of $(T - T_g)^*_{crit}$

The critical  $T - T_g$  is defined as the deposition onset point on a deposition % in the impingement zone versus  $T - T_g$  graph (Fig. 5). Deposition % is the amount of powder deposited divided by the amount of powder injected into the test rig. Deposits located outside the impingement zone (approximately the size of the tube) are not included when measuring the deposition because the conditions, i.e. air temperature, humidity and velocity, causing the powder to stick is unknown and may significantly differ from the impingement jet conditions. Plots similar to Fig. 5 were required to determine the critical  $T - T_g$  for each test condition reported in this study. It is important to note that  $T - T_g$  or stickiness is a function of the combined effects of air temperature and relative humidity.

The determination of  $(T - T_g)^*_{crit}$  is a significant point of difference between this work and previous studies that have employed the Particle Gun test but included any deposit attached to the col-

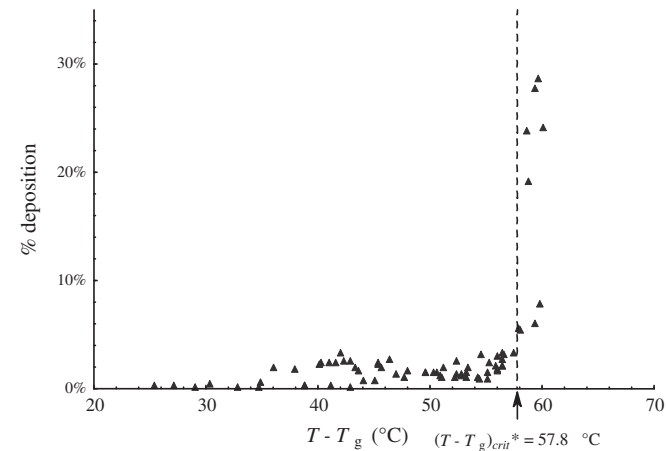


Fig. 5. Effect of  $T - T_g$  on the deposition % at the centre of the plate. Test conditions:  $d_{(0.5)}$  267  $\mu\text{m}$ , average jet velocity 15.0 m/s and normal impingement.

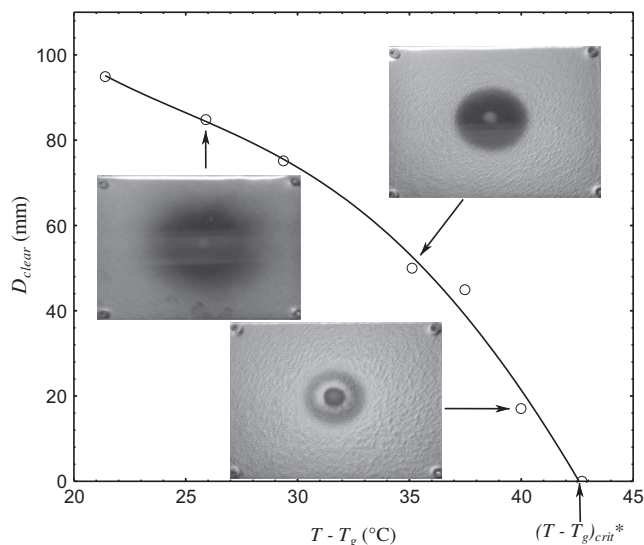


Fig. 6. Effect of  $T - T_g$  on the clear ring diameter. Test conditions:  $d_{(0.5)}$  61  $\mu\text{m}$ , normal impingement and jet velocity 15.0  $\text{ms}^{-1}$ , data from Zhao (2009).

lection plate at the end of a run (Paterson et al., 2007; Zhao, 2009). As a result, the  $(T - T_g)_{crit}$  calculated in this work are differentiated from previous definitions by using a \*.

Using the data of Zhao (2009), Fig. 6 is constructed to illustrate that significant deposition occurs outside the impingement zone at low  $T - T_g$  stickiness values before deposition is concentrated within the impingement zone. It is interesting to note that after heating the target plate to ensure the jet and plate are at the same temperature, the deposition at the periphery of the plate almost completely ceased. Controlling the plate temperature is also a clear point of difference between this work and previous works by Paterson et al. (2007) and Zhao (2009).

## 4. Results and discussion

### 4.1. Factors affecting milk powder deposition

#### 4.1.1. Effect of plate temperature on $(T - T_g)^*_{crit}$

Results show an increase in plate temperature relative to the jet temperature ( $T - T_p$ ), slightly increases  $(T - T_g)^*_{crit}$  and decreases deposition, for air and plate temperatures below 90 °C (Fig. 7). Fig. 7 shows trends for 15.0 and 25.0 m/s jet velocities and an estimate for a lower velocity of 5.4 m/s using the same slope. The estimate shows the relative influence of plate temperature compared to velocity.

When the plate and jet are different temperatures, the region in front of the plate has a temperature and relative humidity gradient. The interaction of this region on stickiness is complex. On a macro-scale, Fig. 7 shows a linear relationship between  $T - T_p$  and  $(T - T_g)^*_{crit}$ . Since the relationship between  $T_g$  and RH is non-linear, the trend in Fig. 7 suggests that the temperature gradient in front of the plate mostly affects the temperature at the surface of the particle; rather than its water activity.

The effect of plate temperature also has significant industrial application. Where processing equipment – dryers, transport ducts, cyclones and fluidised beds – are un-insulated and deposition is a key issue, one possible solution is to insulate the walls. Insulation effectively increases the wall temperature, which increases  $(T - T_g)^*_{crit}$  and is likely to result in reduced deposition, e.g. Chen et al. (1993).

#### 4.1.2. Effect of particle size distribution on $(T - T_g)^*_{crit}$

Fig. 8 shows that smaller particles having significantly lower  $(T - T_g)^*_{crit}$  values. This result is consistent with the well-known

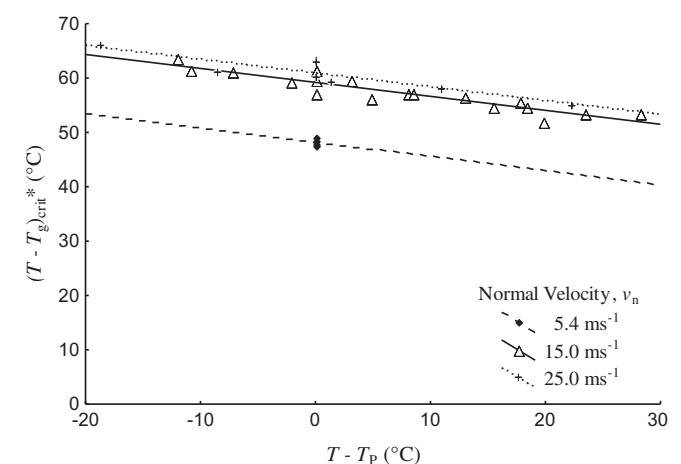


Fig. 7. Influence of plate temperature on  $(T - T_g)^*_{crit}$ . Test conditions:  $d_{(0.5)}$  267  $\mu\text{m}$  and normal impingement.

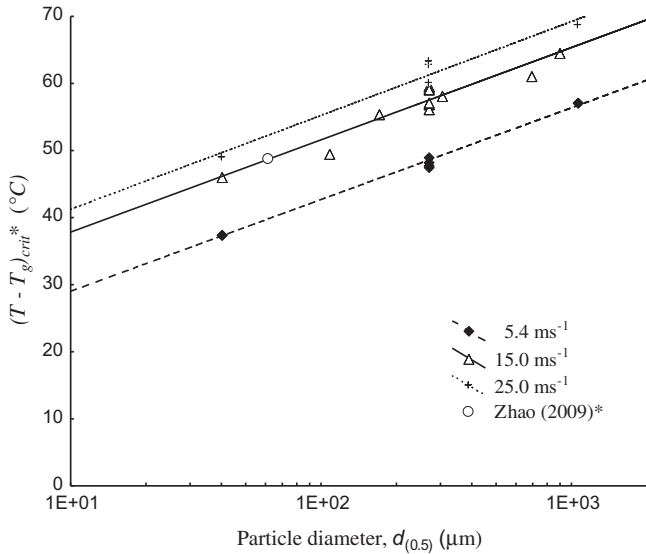


Fig. 8. Effect of particle size on  $(T - T_g)_{crit}^*$  in a normal impingement jet. Trends for 5.4 and 25.0 m/s are estimates.

observation that smaller particles have greater agglomeration and deposition tendencies. Of particular note is the log scale applied to the  $d_{(0.5)}$  axis to yield a straight line for the data. In the formation of trend line equations,  $d_{(0.5)}$  is assumed to be equivalent to a uniform particle diameter,  $d_p$ .

When Zhao (2009) published his results, focus was given to calculation of  $(T - T_g)_{crit}$  values where the deposition % was based on all deposits attached to the target plate. In this study, only deposits at the jet's central zone are included in the deposition %. Photographs of the deposition morphology were taken by Zhao, which has allowed the authors to reanalyse Zhao's results to obtain the data points in Fig. 8 and later in Fig. 9. Since Zhao did not control the temperature of the plate, corrections for a difference in temperature between the plate and jet (23 °C) have also been carried out, as indicated using a \*, according to the slope of the trend line in Fig. 7. Walmsley et al. (2010b) showed that without temperature control, the difference between the jet and plate temperatures, i.e.  $T - T_p$ , is 23.2 °C for the same set-up as Zhao. Fig. 8 also shows

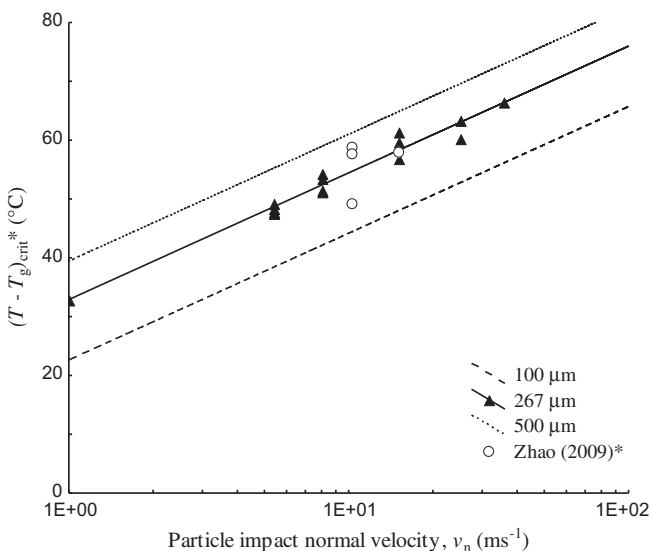


Fig. 9. Effect of normal particle impact velocity on  $(T - T_g)_{crit}^*$  with normal impingement, i.e. an impact angle of zero degrees.

trend estimates for 5.4 and 25.0 m/s, drawn using the same slope as the 15.0 m/s trend line and offset by the few data points measured. It is worthy to note that work by Paterson and co-workers did not focus on the effect of particle size.

4.1.3. Effects of impact velocity and angle on  $(T - T_g)_{crit}^*$

In general, higher particle impact velocities, as a result of higher air flow, result in less deposition. In this analysis it is assumed that particles impact with the same velocity and angle as the jet is positioned relative to the target plate. When the jet is at an angle, then both a normal component and tangential velocity component arise. The effect of normal velocity on  $(T - T_g)_{crit}^*$  is presented in Fig. 9. Of particular note is the log scale on the  $v_n$  axis applied to obtain a straight line. Trend lines for particle size distributions 100 and 500 μm have been estimated using offsets shown in Fig. 8.

The effect of tangential velocity is reported by Murti et al. (2010) and Walmsley et al. (2010b), although both studies used original definition of  $(T - T_g)_{crit}$  rather than the newly defined  $(T - T_g)_{crit}^*$ . However the trends are the same. Fig. 10 shows that increasing the impact angle for a constant velocity magnitude requires an increase in  $(T - T_g)_{crit}^*$  for particles to stick. Alternatively, it may be rephrased that particles impacting at non-normal angles at the same velocity magnitude are less likely to stick. Konstandopoulos (2006) reports that for non-normal impacts there may also exist a critical impact angle beyond which no deposition occurs. However due to operational limitations of the experimental test the applicability of Konstandopoulos' observation could not be ascertained.

4.2. Validation of deposition criterion

The experimental and literature data are applied to Eq. (18) to determine the constants in the model. Materials properties for

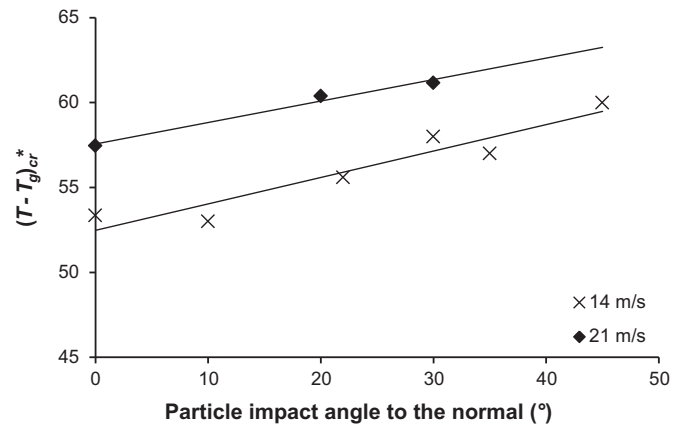


Fig. 10. Effect of impact angle on  $(T - T_g)_{crit}^*$ . Particle size  $d_{(0.5)}$  100 μm.

Table 2

Mechanical properties and constants of stainless steel and amorphous lactose (Murti, 2006; Perkins et al., 2007; Zhang et al., 2006).

Material property	Stainless steel	SMP (lactose)
Particle density, $\rho$ (kg/m <sup>3</sup> )	N/A	1050
Shear modulus, $G$ (GPa)	73.9	3.49
Young's modulus, $Y$ (GPa)	193	3.57
Poisson's ratio, $\nu$	0.305	0.120
Surface tension at low humidity, $\gamma_{g1}$ (J/m <sup>2</sup> )	0.0520	0.0574
$Y^*$ (GPa)	3.56	
$G^*$ (GPa)	0.83	
$\gamma_g$ (J/m <sup>2</sup> ) for $T < T_g$	0.109	

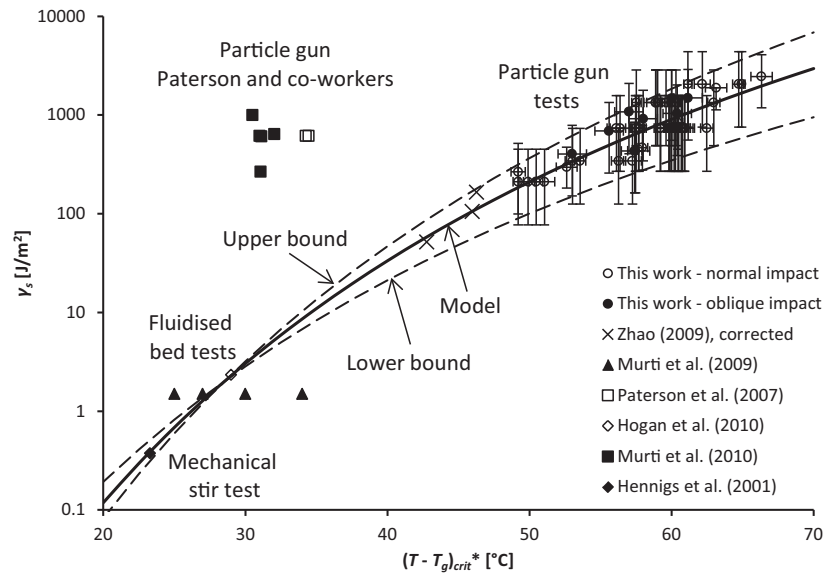


Fig. 11. Combined effect of particle size, impact angle and velocity on deposition. The work of Zhao is corrected (\*) for plate temperature effects.

SMP and stainless steel are provided in Table 2. Materials properties (other than density) for SMP are difficult to locate in literature; consequentially, data for lactose is used in its place. Surface tension energy at the glass transition temperature is estimated from measurements for stainless steel and lactose taken at low humidity.

With estimates for the materials properties in Eq. (18), the remaining unknowns are constants  $a$ ,  $D_1$ ,  $D_2$  and  $B$ . These constants are found by plotting  $\log(\gamma_s)$  against  $(T - T_g)_{crit}^*$  adjusted for  $T - T_p = 0$ . In addition to data collected in this work Fig. 11 includes: fluidised bed deposition data from Murti et al. (2009) and Hogan and O'Callaghan (2010); mechanical stir test data from Hennigs et al. (2001), and Particle Gun test data corrected from Zhao (2009), Paterson et al. (2007), and Murti et al. (2010). Vertical bars indicating the degree of uncertainty in Fig. 11 are estimated from the distribution of particle sizes and impact velocities of the particles and the horizontal uncertainty bars are estimated from non-stick/stick test conditions. By applying a least squares approach in tandem with Excel™ Solver the constants in Eq. (18) are solved and are given in Table 3. Constants for the upper and lower bounds are obtained using the estimated errors for the experimental data in this work.

#### 4.3. Application of deposition criterion

The deposition criterion may be applied to predict the critical stickiness as a function of particle velocity, radius and impact angle for SMP. This equality may be implemented in Computational Fluid Dynamics models to predict where and how much deposition will occur for given processing equipment geometries and airflow patterns. Typically, users may define capture/rebound criterion for interactions between particles and wall boundaries in CFD. At present numerical modelling of food and dairy powder deposition has mainly focused on deposition in the main drying chamber (Jin

and Chen, 2010) and deposition in the Particle Gun test (Walmsley et al., 2010a). The deposition criterion may be also applied to predict the angle at which deposition would stop for a known particle velocity, radius and stickiness. This is applicable to curved and angled geometries, such as round tubes and parallel plates, that are common components of compact heat exchangers. After successful application of powder deposition in CFD it may be possible to inform the design of dairy processing equipment and heat exchangers so that powder deposition is minimised enabling longer times between cleans. Future work will look at application of predicting deposition in compact heat exchangers for heat recovery from milk spray dryer exhaust air flows. At present concerns over powder deposition and fouling of exhaust heat exchangers have prevented the uptake of this technology in the New Zealand dairy industry even though the potential energy savings is significant (Walmsley et al., 2013a).

#### 5. Conclusion

In this study the key factors that cause milk powder to attach to walls or plates have been experimentally investigated. These factors include air temperature, relative humidity, plate temperature, and particle size, velocity and impact angle. Using standard solutions to the contact mechanics problem of a spherical adhesive elastic particle impacting a rigid plate, a semi-empirical criterion is successfully derived and fitted to literature and experimental data. There is significant opportunity to apply this new criterion as a wall boundary condition in Computational Fluid Dynamics models to predict where deposition will occur in processing equipment for optimising equipment design.

#### References

- Boonyai, P., Bhandari, B., Howes, T., 2004. Stickiness measurement techniques for food powders: a review. *Powder Technol.* 145, 34–46.
- Brilliantov, N., Albers, N., Spahn, F., Pöschel, T., 2007. Collision dynamics of granular particles with adhesion. *Phys. Rev. E* 76, 051302.
- Brooks, G.F., 2000. The Sticking and Crystallisation of Amorphous Lactose (M. Tech.). Massey University, Palmerston North, New Zealand.
- Chen, X.D., Lake, R., Jebson, S., 1993. Study of milk powder deposition on a large industrial dryer. *Food Bioprod. Process. Trans. Inst. Chem. Eng. Part C* 71, 180–186.
- Downton, G.E., Flores-Luna, J.L., King, C.J., 1982. Mechanism of stickiness in hygroscopic, amorphous powders. *Ind. Eng. Chem. Fundam.* 21, 447–451.

Table 3  
Constants for SMP deposition model.

Constant	Model	Upper bound	Lower bound
$a$	$7.7 \times 10^{-6}$	$1.2 \times 10^{-4}$	$8.9 \times 10^{-7}$
$B$	9.7	10.4	9.9
$D_1$	14.5	12.2	16.2
$D_2$ (°C)	36.4	38.5	34.8

- Gordon, M., Taylor, J.S., 1952. Ideal copolymers and the second-order transitions of synthetic rubbers. I. Non-crystalline copolymers. *J. Appl. Chem.* 2, 493–500.
- Harvie, D.J.E., Langrish, T.A.G., Fletcher, D.F., 2002. A computational fluid dynamics study of a tall-form spray dryer. *Food Bioprod. Process.* 80, 163–175.
- Hennigs, C., Kockel, T.K., Langrish, T.A.G., 2001. New measurements of the sticky behavior of skim milk powder. *Dry. Technol. Int. J.* 19, 471.
- Hertz, H., 1881. On the contact of elastic solids. *J. Reine Angew. Math.* 92, 156–171.
- Hogan, S.A., O'Callaghan, D.J., 2010. Influence of milk proteins on the development of lactose-induced stickiness in dairy powders. *Int. Dairy J.* 20, 212–221.
- Intipunya, P., Shrestha, A., Howes, T., Bhandari, B., 2009. A modified cyclone stickiness test for characterizing food powders. *J. Food Eng.* 94, 300–306.
- Jin, Y., Chen, X.D., 2010. A fundamental model of particle deposition incorporated in CFD – simulations of an industrial milk spray dryer. *Dry. Technol. Int. J.* 28, 960.
- Johnson, K.L., Kendall, K., Roberts, A.D., 1971. Surface energy and the contact of elastic solids. *Proc. R. Soc. Lond. Math. Phys. Sci.* 324, 301–313.
- Konstandopoulos, A.G., 2006. Particle sticking/rebound criteria at oblique impact. *J. Aerosol Sci.* 37, 292–305.
- Kota, K., Langrish, T.A.G., 2006. Fluxes and patterns of wall deposits for skim milk in a pilot-scale spray dryer. *Dry. Technol. Int. J.* 24, 993–1001.
- Murti, R.A. (2006). The effect of lactose source on the stickiness of dairy powders (M. Engineering). Massey University, Palmerston North, New Zealand.
- Murti, R.A., Paterson, A.H.J., Pearce, D., Bronlund, J.E., 2009. Stickiness of skim milk powder using the particle gun technique. *Int. Dairy J.* 19, 137–141.
- Murti, R.A., Paterson, A.H.J., Pearce, D., Bronlund, J.E., 2010. The influence of particle velocity on the stickiness of milk powder. *Int. Dairy J.* 20, 121–127.
- Palzer, S., 2005. The effect of glass transition on the desired and undesired agglomeration of amorphous food powders. *Chem. Eng. Sci.* 60, 3959–3968.
- Paterson, A.H.J., 2011. Personal Communication.
- Paterson, A.H.J., Bronlund, J.E., Zuo, J.Y., Chatterjee, R., 2007. Analysis of particle-gun-derived dairy powder stickiness curves. *Int. Dairy J.* 17, 860–865.
- Perkins, M., Ebbens, S.J., Hayes, S., Roberts, C.J., Madden, C.E., Luk, S.Y., Patel, N., 2007. Elastic modulus measurements from individual lactose particles using atomic force microscopy. *Int. J. Pharm.* 332, 168–175.
- Pisecky, I., 1997. Handbook of Milk Powder Manufacture. Niro A/S, Copenhagen, Denmark.
- Raffel, M., Willert, C.E., Wereley, S.T., Kompenhans, J., 2007. Particle Image Velocimetry: A Practical Guide, second ed. Springer, New York, USA.
- Savkoor, A.R., Briggs, G.A.D., 1977. The effect of tangential force on the contact of elastic solids in adhesion. *Proc. R. Soc. Lond. Math. Phys. Sci.* 356, 103–114.
- Thornton, C., Ning, Z.M., 1998. A theoretical model for the stick/bounce behaviour of adhesive, elastic–plastic spheres. *Powder Technol.* 99, 154–162.
- Wallack, D.A., King, C.J., 1988. Sticking and agglomeration of hygroscopic, amorphous carbohydrate and food powders. *Biotechnol. Prog.* 4, 31–35.
- Walmsley, M.R.W., Zhao, S.X., Walmsley, T.G., Neale, J.R., Atkins, M.J., Hoffmann-Vocke, J., 2010a. Modelling deposition of amorphous based particles in an impingement jet. In: Proceedings of the 19th International Congress of Chemical and Process Engineering, Prague, CZ.
- Walmsley, T.G., Walmsley, M.R.W., Atkins, M.J., Neale, J.R., 2013a. Improving energy recovery in milk powder production through soft data optimisation. *Appl. Therm. Eng.* 61, 80–87.
- Walmsley, T.G., Walmsley, M.R.W., Atkins, M.J., Neale, J.R., 2013b. Fouling and pressure drop analysis of milk powder deposition on the front of parallel fins. *Adv. Powder Technol.* 24, 780–785.
- Walmsley, T.G., Walmsley, M.R.W., Atkins, M.J., Neale, J.R., Addenbrooke, D.M., 2013c. Critical impact angle for mitigating deposition of skim milk powder on tubes in cross-flow. In: Proceedings of International Conference on Heat Exchanger Fouling and Cleaning – 2013, Budapest, Hungary.
- Walmsley, T.G., Walmsley, M.R.W., Zhao, S., Neale, J.R., Atkins, M.J., 2010b. Effect of angle on particle deposition in an impingement jet. In: Proceedings of the 17th Australasian Fluid Mechanics Conference, Auckland, New Zealand.
- Williams, M.L., Landel, R.F., Ferry, J.D., 1955. The temperature dependence of relaxation mechanisms in amorphous polymers and other glass-forming liquids. *J. Am. Chem. Soc.* 77, 3701–3707.
- Woo, M.W., Daud, W.R.W., Mujumdar, A.S., Wu, Z.H., Talib, M.Z.M., Tasirin, S.M., 2008. CFD – evaluation of droplet drying models in a spray dryer fitted with a rotary atomizer. *Dry. Technol. Int. J.* 26, 1180.
- Zhang, J.X., Ebbens, S., Chen, X.Y., Jin, Z., Luk, S., Madden, C., Patel, N., Roberts, C.J., 2006. Determination of the surface free energy of crystalline and amorphous lactose by atomic force microscopy adhesion measurement. *Pharm. Res.* 23, 401–407.
- Zhao, S.X., 2009. Experimental and Numerical Investigations on Skim Milk Powder Stickiness and Deposition Mechanisms (M. Phil.), University of Waikato, Hamilton, New Zealand.
- Zuo, J.Y., 2004. The Stickiness Curve of Dairy Powders (M. Tech. Thesis), Massey University, Palmerston North, New Zealand.
- Zuo, J.Y., Paterson, A.H.J., Bronlund, J.E., Chatterjee, R., 2007. Using a particle-gun to measure initiation of stickiness of dairy powders. *Int. Dairy J.* 17, 268–273.

**Article 7:**

*Analysis of skim milk powder deposition on stainless steel tubes in cross-flow*

**Walmsley, T.G.**, Walmsley, M.R.W., Atkins, M.J., Neale, J.R., 2015.

Applied Thermal Engineering 75, 941–949.

DOI: 10.1016/j.applthermaleng.2014.10.066

Elsevier



## Research paper

## Analysis of skim milk powder deposition on stainless steel tubes in cross-flow



T.G. Walmsley\*, M.R.W. Walmsley, M.J. Atkins, J.R. Neale

Energy Research Centre, School of Engineering, University of Waikato, Hamilton 3216, New Zealand

## HIGHLIGHTS

- Skim milk powder deposition on round, elliptical and turned squared tubes is tested.
- Powder deposited almost exclusively on the various tubes' front faces.
- Elliptical tube is shown to be naturally low fouling due to its shape.
- The critical impact angle is a function of particle stickiness and air velocity.

## ARTICLE INFO

## Article history:

Received 7 June 2014

Accepted 7 October 2014

Available online 28 October 2014

## Keywords:

Heat exchanger  
Particulate fouling  
Heat recovery  
Powder deposition

## ABSTRACT

Particulate fouling on the gas side of heat recovery equipment is a common industrial problem. The aim of this study is to characterize the deposition of skim milk powder on a single bare tube in cross-flow. A custom built rig is applied to simulate exhaust air conditions that is experienced in an exhaust exchanger. For a constant airflow rate, increasing particle stickiness resulted in greater deposition coverage around the front of the round and elliptical tubes peaking in the middle, whereas the turned square tube tended to be either clear or covered. Results show that the skim milk powder particle impact angle on the tube, as opposed to the wall shear stress, is an important determinant for deposition. During each test and at the conclusion of each test, which was when fouling reached an asymptote, the amount of deposition coverage and build-up on the tube varied depending on the tube shape, particle stickiness, and air velocity.

© 2014 Elsevier Ltd. All rights reserved.

## 1. Introduction

Heat exchanger fouling is costly and affects a wide range of industries [1]. Severe heat exchanger fouling levels significantly degrades thermal and hydraulic performance. Common design techniques to mitigate fouling [2] include (i) increasing velocity, (ii) implanting inserts between or within tubes, (iii) non-standard tube geometries (e.g. elliptical tubes), (iv) non-standard fin geometries, and (v) low surface energy coatings.

Abd-Elhady et al. [3] developed the concept of a dimensionless rolling moment, which is defined as the hydrodynamic rolling moment divided by the adhesion resting moment, to calculate a limiting fouling velocity that theoretically predicts the onset of fouling, and shows close agreement with lab-scale experimental results [4]. The literature contains a variety of methods that reduce fouling by increasing the air turbulence and wall shear stress, such

as placing inserts between tubes [5], adding a non-heat transferring “spoiler” tube row at the front of a compact heat exchanger [6], and using non-standard shaped tubes Paz et al. [7] focused on fouling in diesel exhaust gases and showed the close relationship between wall shear stress and deposition. Using this link between wall shear stress and fouling, Walmsley et al. [8] developed CFD (Computational Fluid Dynamics) models to examine a wide range of tubes for their fouling, heat transfer and pressure drop characteristics.

Heat recovery from milk spray dryer exhaust airflows has the potential to increase the process's heat efficiency by 10–20% [9], but its uptake New Zealand industry has been subdued due to concerns over fouling, effectively causing worst-case economics to be very poor. In the mid-1980's the New Zealand Plains Co-Op Dairy Ltd factory installed a glass tube air-to-air exhaust heat recovery system. Energy surveys of its performance showed heat recovery decreased by 40% after 13 h of operation. In the late 2000's, a new 20+ t/h state-of-the-art spray dryer was built in NZ costing over US\$200 million, which plan to include spray dryer exhaust heat recovery using a liquid coupled loop. The exhaust heat exchanger was built but never installed due to concerns over milk powder

\* Corresponding author.

E-mail address: [timgw@waikato.ac.nz](mailto:timgw@waikato.ac.nz) (T.G. Walmsley).

Nomenclature		$\alpha$	time constant, s
		$\tau$	wall shear stress, Pa
<i>Variables</i>		<i>Subscript</i>	
$a_w$	water activity, dimensionless	1	state 1
$c$	powder concentration, mg/m <sup>3</sup>	2	state 2
$\Delta P$	percent change in differential pressure, %	$a$	adhesion
$k$	material constant in Eq. (2), dimensionless	$b$	bulk
$m$	mass fraction, dimensionless	$f$	fouling
RM	rolling moment, dimensionless	$l$	lactose
$t$	time, s	$p$	particle
$T$	air temperature, °C	$s$	solid
$T_g$	glass transition temperature, °C	$w$	water
$X$	mass fraction of water on a dry basis, dimensionless		

fouling causing disruptions to plant production. Since that time an additional twelve milk powder spray dryers have been built in New Zealand all without exhaust heat recovery.

The aim of this study is to experimentally characterize the deposition of SMP (Skim Milk Powder) on a single bare tube in cross-flow. Tube geometries examined include round, elliptical and turned square tubes. For each test the air temperature and absolute humidity is selected to mimic various locations within an exhaust heat recovery system. Experimental deposition tests are performed using the same rig as reported Walmsley et al. [10]. The experimental results are analysed in terms of localised wall shear stresses [7] and particle impact angle [11] to determine which is important in relation to the deposition of milk powder. Results are compared to the experimentally validated SMP deposition model reported by Walmsley et al. [12] for deposition in an impingement jet on an angled flat plate. The overall goal is to provide empirical evidence that quantifies the effect of fouling on the thermal and hydraulic performance of milk dryer exhaust recuperators and find effective ways to minimise fouling through good heat exchanger selection and design.

## 2. Theory

### 2.1. Particle transport and deposition processes

Deposition of particles may result from a combination of several discrete transport processes and mechanisms [13]. These processes are largely dependent on the dimensionless particle relaxation time ( $t^+$ ), which is a function of the particle's density and radius and the fluid's density, viscosity, and wall shear stress. The particle relaxation time represents the time scale with which the particles respond to changes in the slip velocity. Typically, three general transport regimes are identified: (1) turbulent diffusion ( $t^+ < 0.1$ ), (2) turbulent diffusion-eddy impaction ( $0.1 < t^+ < 10$ ) and (3) particle inertia moderated ( $t^+ > 10$ ). In the turbulent diffusion regime, deposition is a mass transport problem described by Fick's law. The second regime is a transitional regime whereas particles that fall in the particle inertia regime respond slowly to changes in velocity flow field changes as indicated by the large  $t^+$ .

Beyond these fundamental mechanisms of deposition, researchers have attempted to establish important local and global parameters that can be calculated and optimised to minimise fouling.

#### 2.1.1. Critical wall shear stress

Paz et al. [7] attempted to show how the localised wall shear stress provides a better description and tool for predicting when

“rolling” occurs. They define the critical wall shear stress as the minimum shear stress value to cause RM to equal unity. Because the local wall shear stress of a tube in cross-flow varies around the profile of the tube, it is expected that any area with a wall shear stress above the critical value will experience no deposition.

#### 2.1.2. Critical impact angle

The critical impact angle (refer to Fig. 8) is the angle beyond which no particles will stick to a surface resulting in minimal fouling [14]. This concept is based on an energy balance between a particle's tangential kinetic energy of impact and the minimum energy required to break its adhesive contact with the surface. Since the adhesion energy is related to particle stickiness, it is anticipated that the critical impact angle changes depending on the air velocity and conditions, which determine the particle stickiness.

### 2.2. Understanding milk powder stickiness

Many studies have shown that the stickiness behaviour of amorphous powders can be described by the extent to which the air temperature,  $T$ , exceeds the glass transition temperature,  $T_g$ , of the major amorphous components of the material, i.e.  $T - T_g$  [15]. For SMP the main amorphous component is lactose, which is about 52 wt% of SMP.

The glass transition temperature of lactose is usually determined using thermal methods such as DSC (Differential Scanning Calorimetry). Performing DSC on every sample of milk powder at each condition tested would be time consuming and highly impractical. However Brooks [16] developed a third order empirical polynomial model for predicting the  $T_g$  of lactose at a given particle surface water activity ( $a_w$ ), which is assumed to be in equilibrium with the air relative humidity. This model is shown in Eq. (1) and is accurate for  $a_w$  in the range of 0–0.575.

$$T_g = -530.66(a_w)^3 + 652.06(a_w)^2 - 366.33(a_w) + 99.458 \quad (1)$$

For situations where the relative humidity is above 57.5% the Gordon and Taylor equation (Eq. (2)) can be used to predict  $T_g$ . This equation uses the mass fractions of total solids and water ( $m_s$  and  $m_w$  respectively), the glass transition temperatures of lactose ( $T_{gl}$ ) and water ( $T_{gw}$ ), whose values were taken as 103 °C and –137 °C, and a constant,  $k$ , whose value was taken as 6.83.

$$T_g = \frac{T_{gl} + kX_w T_{gw}}{1 + kX_w}, \quad \text{where } X_w = \frac{m_w}{m_s} \quad (2)$$

Once the glass transition temperature has been calculated the parameter  $T-T_g$  is then calculated. This value is correlated to the stickiness of the powder where a higher  $T-T_g$  results in a higher stickiness (adhesiveness).

**3. Methods**

**3.1. Test rig operation**

The experimental setup is schematically shown in Fig. 1. The test rig allows milk powder to be added to an air stream of controlled temperature and humidity. This powder laden air flow is then contacted in cross-flow with various geometries. The air temperature is controlled using three separate thermal operations. First a plate-fin liquid to air heat exchanger circulates heated water to preheat air. The air is drawn in by a fan and blown along the test duct. A small amount of direct steam injection further increases the temperature of the air while achieving the target humidity. Finally an electric heater connected to a VSD (Variable Speed Drive) is used as a trimming element to adjust the final temperature of the air stream.

An orifice plate in the duct provides a pressure drop which is related to the air velocity in the air duct and used to control the fan speed via a PID feedback loop to ensure a constant flow rate through the system as fouling on the tubes occurred. The orifice plate consists of a 10 mm lip on the top-side of the duct. This plate also creates a region of low pressure immediately behind the plate where milk powder is injected, aided by a little suction induced by the orifice plate. The powder laden airflow then travels through the test duct where fully developed turbulent flow is to be achieved before contact with the deposition surfaces. To control the rate of powder injection, a bottle full of powder is mechanically tapped. On average powder was added at 2.4–3.8 g/min and test durations ranged from 20 to 80 min depending on the rate of deposition, i.e.  $dm_f/dt$ . At an air velocity of 4.5 m/s, the concentration of milk powder is approximately 2.0 g/m<sup>3</sup> and for air at 6.5 m/s the concentration is about 2.9 g/m<sup>3</sup>, which is significantly higher than in industry to have an accelerate the test.

By adjusting the direct steam injection valve, it was attempted in the tests to achieve an absolute humidity of 50–60 g H<sub>2</sub>O/kg dry air as this relates directly to the moisture content at industrial milk spray dryer exhausts. The process of setting up the initial temperature and humidity of the test system took anywhere up to 3 h. Rigorous start-up and operation procedures for the equipment were established to prevent condensation on the test section. In the event that condensation was evident, the results were invalidated.

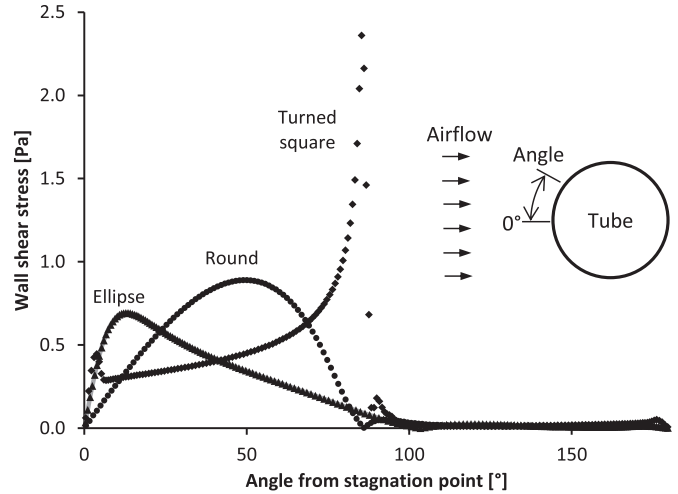


Fig. 2. Wall shear stress for round, elliptical and turned squared tubes using CFD.

Preventing condensation is a key reason why it often took several hours to achieve the desired conditions because temperature and humidity increased had to be done by small increments. Once the desired values were achieved and steadied, powder was added. The time for separate tests varied depending on the rate of deposition.

Throughout the course of the tests, deposition, pressure drop across the tube, and air temperature and humidity are visually observed and/or monitored. In general a test would be stopped when the pressure drop across the tube reached a constant level. Temperature and relative humidity were logged at 1 s intervals and  $T-T_g$  was calculated for each interval and averaged for the entire test period. Two standard deviations of the temperature and relative humidity data for each test are used to estimate uncertainty in  $T-T_g$ . At the conclusion of each test the test assembly was removed from the duct and photographs were taken to show the deposition morphology from various angles.

**3.2. Bare tube test set-up**

Round (25.4 mm), elliptical (22 mm × 39 mm), and turned square (25.4 mm × 25.4 mm) tubes were housed horizontally in a cross-flow fashion in a section with transparent acrylic walls enabling visual inspection of the test. The hydraulic diameters tubes are: round is 25.4 mm, elliptical is 22.9 mm and turned square is 25.4 mm. Each tube was tested individually using various

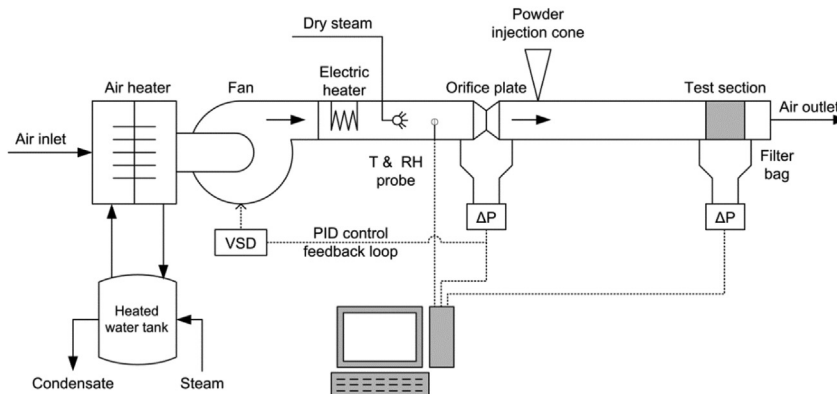


Fig. 1. Deposition test rig schematic.

air temperatures (46 °C–62 °C) to achieve a range of stickiness levels,  $T-T_g$ . Average duct velocities of 4.5 and 6.5 m/s are used in the tests.

Photographs looking down the tubes were taken at regular intervals in an attempt to observe the growth of deposition over time. These images, depending on the clarity of the deposition layer, were later analysed to measure the location of deposition on each tube. Based on the photos, measurements and the tube geometry, the average location for the edge of the fouling layer was calculated using MatLab™. This result was then compared with flow simulation CFD results (Fig. 2) to determine the critical wall shear stress at the location where deposition ceased. CFD models included a single tube in an 80 mm square duct (same as the experimental) using the modelling parameters outlined by Walmsley et al. [8].

### 3.3. Particle size distribution

Non-agglomerated Skim Milk Powder is used in all tests. The particle size distribution was measured in iso-propanol using a Malvern Mastersizer 2000 according to the method of Pisecky [17]. By cumulative volume fraction, the mid diameter of the powder,

$d(50\%)$ , was measured as 104  $\mu\text{m}$ ;  $d(10\%) = 39 \mu\text{m}$  and  $d(90\%) = 202 \mu\text{m}$ .

### 3.4. Determination of $T-T_g^*$

Particle stickiness or  $T-T_g^*$  is defined in the same manner as Walmsley et al. [12] where  $T$  is taken as the air temperature (dry bulb) and  $T_g$  is calculated using the Gordon-Taylor equation (Eq. (2)). Wall temperature effects on  $T-T_g$  are accounted for using the equation presented in Walmsley et al. [12].  $T-T_g^*$  differs from the conventional definition of  $T-T_g$  in that it is corrected for a minor wall temperature effect. This wall temperature effect was quantified by Walmsley et al. [12].

## 4. Experimental results for single tubes in cross-flow

### 4.1. Fouling coverage and location

The stickiness of the milk powder, as quantified by  $T-T_g^*$ , was shown to influence the coverage and morphology of deposits around the front of the tubes. Fig. 3 shows photographs of three tests performed on the round tube at an air velocity of 4 m/s.

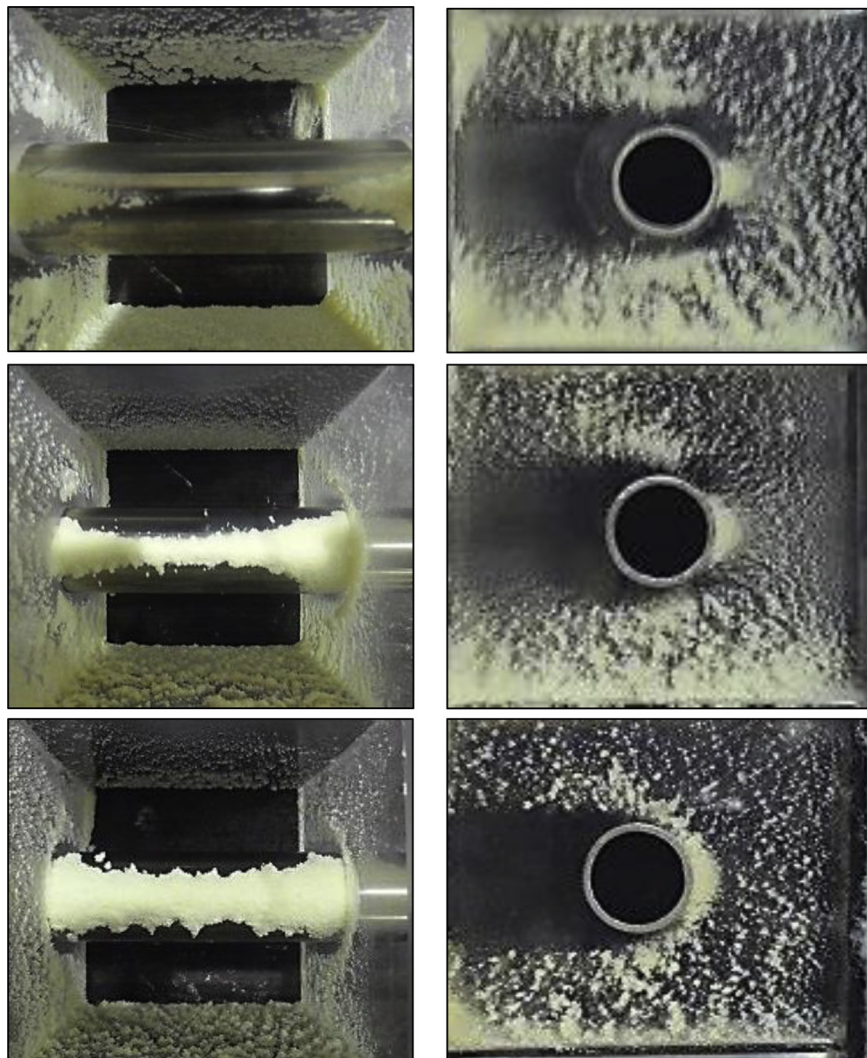


Fig. 3. The effect of increasing stickiness on the frontal deposition for round tube at an air velocity of 4 m/s. From top,  $T-T_g^*$  conditions are 43.3, 47.6 and 52.6 °C. Photographs were taken at the end of the test.

Results are organised so that the top photographs are for the lowest  $T-T_g^*$  condition progressively down to the bottom photograph for the highest  $T-T_g^*$  condition. Increasing the stickiness of the powder is observed to significantly increase the fouling coverage around the front of the tube and the powder layer thickness.

The side angle photographs show the growth of the fouling layer near the wall. An airflow separation point on the front of the round tube is suggested by the deposits attached to the duct wall. Very little deposition was observed during any of the tests (for all three tube geometries) on the rear of the tubes. For each test condition, the wall of the ducting is seen to make an impact on the amount of deposition on the tube near the wall. Since the velocity profile is likely to be fully developed after travelling along a relatively long straight duct, air velocities near the duct wall are slower than in the centre of the duct, being zero at the wall boundary. As a result the particle impact velocity near the wall is progressively slower as particles impact closer to the wall, increasing the chance for particles to deposit.

The elliptical tube required higher  $T-T_g^*$  values to result in similar deposition amounts and coverage levels as the round tube for the same bulk air velocity as shown in Fig. 4. In terms of milk powder fouling properties the elliptical tube is, therefore,

favourable over the round tube. The low fouling property of elliptical tubes has been demonstrated for tube bundles by researchers in other fields. For example Bouris et al. [18] applied both experimental and numerical approaches to conclude elliptical tube bundles were less susceptible to fouling.

Another benefit associated with the elliptical tube is the lower gas side flow resistance resulting in a lower pressure drop. Walmsley et al. [8] numerically evaluated the performance of round and elliptical tube bundles. In the models the same hydraulic air-side diameter and frontal free-flow area for the two sets of tube bundles are constant so that the comparison between the tube geometries was fair. Their models suggested that the pressure drop across an elliptical tube bundle is about half of the pressure across a round tube bundle for the same air side heat transfer coefficient. Although in terms of compactness, the round tube bundle required about 30% less volume (and heat transfer area) than the elliptical tube bundle to achieve the same heat transfer, but experienced a 150% greater pressure drop.

The turned square geometry is characterised by two flat 45° angled sides facing the airflow. It was noticed in testing the turned square tube that no partial deposition occurred at intermediate

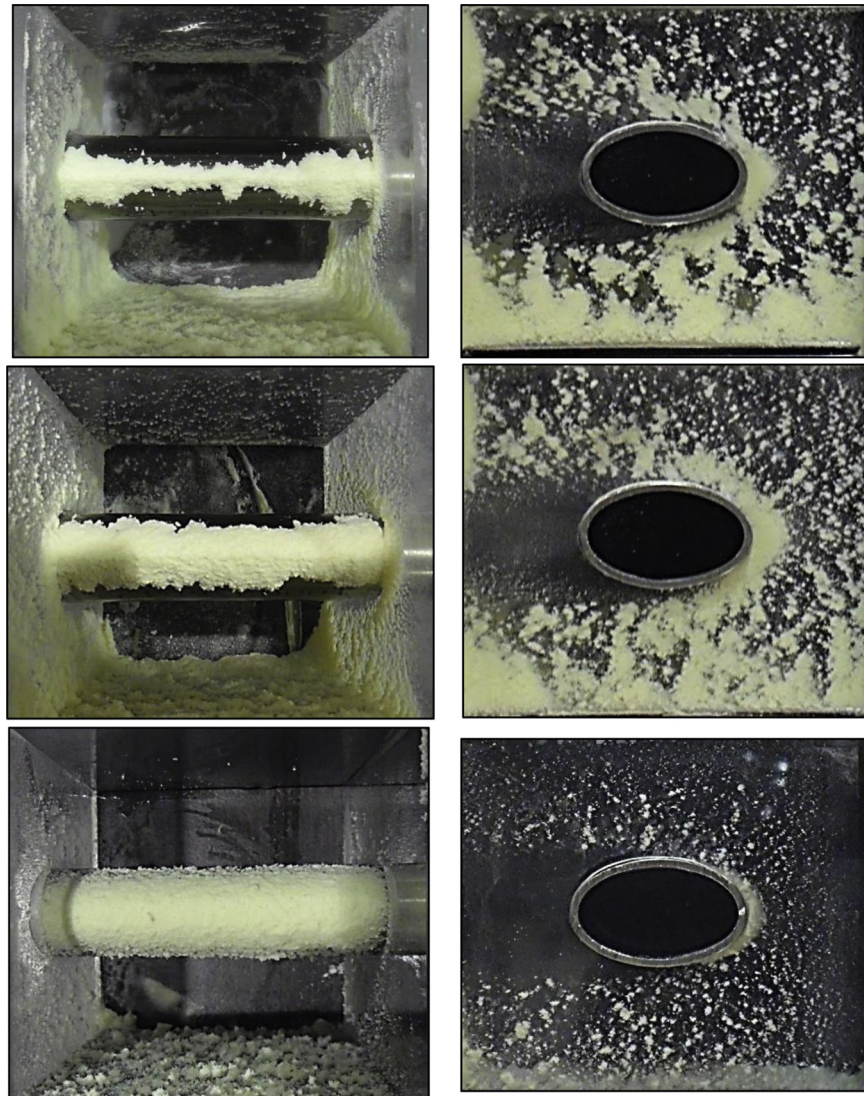
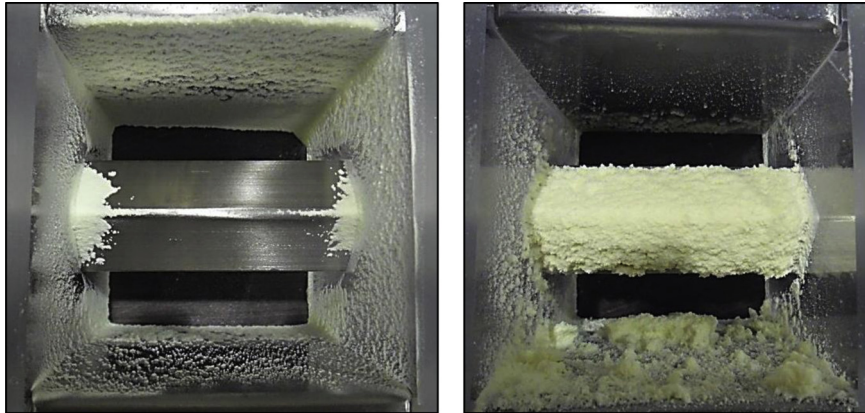


Fig. 4. The effect of increasing stickiness on the frontal deposition for elliptical tubes. From top,  $T-T_g^*$  conditions are 50.0, 54.8 and 62.5 °C. Photographs were taken at the end of the test.



**Fig. 5.** The effect of increasing stickiness on the frontal deposition for turned square tube.  $T-T_g^*$  conditions are 56.7 °C (left) and 61.2 °C. Photographs were taken at the end of the test.

$T-T_g$  values, as was seen for the round and elliptical tubes. Instead, there was either very little deposition (Fig. 5 left), or a fouling layer completely covering the front face of the tube (Fig. 5 right), as the stickiness was increased. These test results suggest there is a critical combination of impact angle (and/or wall shear stress) and particle stickiness that first initiates deposition to cover the surface of the turned square tube. Once again the small amount of deposition in Fig. 5 (left) near the wall is likely the result of wall slowing the air velocity.

Fig. 6 presents photographs of the deposition morphology for round tube and elliptical tube. The surface of the deposition on the front of the tubes typically had a small rounded peak that extended on an angle back to the tube at which point deposition ceased. The angled sides of the deposition were flat but rough. The deposition layer always peaked near the duct walls.

#### 4.2. Critical wall shear stress and critical impact angle

The initial focus of the experimental analysis is to investigate how the local wall shear stress around the profile of various tubes influences particulate deposition. Three observations were expected in relation to this concept. First, it was expected that increasing  $T-T_g^*$  would require a higher wall shear stress to prevent deposition. Second, if wall shear stress is a determining factor for deposition, then it is expected that there is a clear correlation between wall shear stress and  $T-T_g^*$  that may be independent of the tube geometry and average bulk airflow velocity. Third, it was expected that deposition may favour the rear facing side of the tube as

shown by Paz et al. [7] for particulate deposition on tube bundles fouled by a diesel exhaust, which has already been shown to not be the case for milk powder deposition on tubes.

Based on these hypothesises a unique critical wall shear stress should exist for each  $T-T_g^*$  value. To test this hypothesis, the local wall shear stress at the location on the tube where deposition ceased is plotted against  $T-T_g^*$  for round, elliptical and turned square tubes in Fig. 7. Results display no clear correlation for the tests performed at various face velocities. This lack of correlation suggests that the size and momentum of the milk powder particles is sufficient to break through the shear layer around the tubes with little impact. In addition, deposition at the rear of the tube was observed to be minimal. These results imply that the transport regime and mechanism of the bulk of the particles is not diffusion controlled as was the case for Paz et al. [7]. An underlying reason for the difference between this work and Paz et al. is the particle relaxation time. As mentioned earlier, the particle relaxation time milk powder in heat exchangers falls in the particle inertia moderated regime for the transport and deposition mechanism. As a result milk powder particles in heat exchangers respond slowly to changes in velocity flow field changes. In contrast the particle relaxation time in the work of Paz et al. [7] was between 0.1 and 1 s indicating particle transport is turbulent diffusion-eddy impaction controlled.

In the situation where particle motion and direction does not deviate from that of the bulk fluid direction along the duct, particles impact the tube surface at an angle approximately equal to that of the bulk flow direction. The critical impact angle for a given air

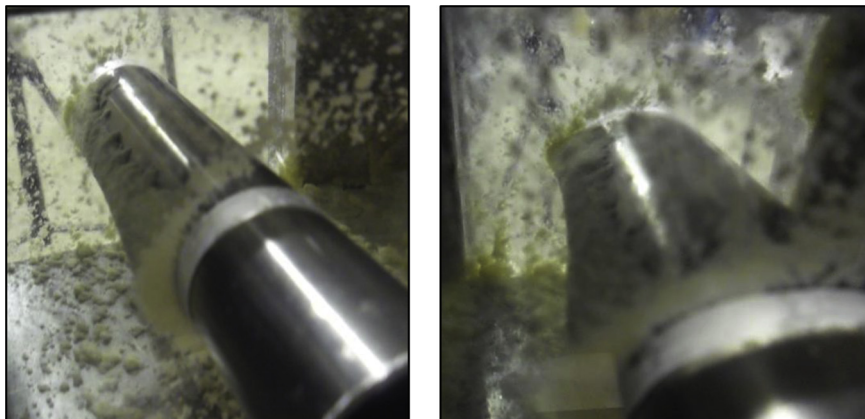


**Fig. 6.** Deposition morphology on round and elliptical tubes.  $T-T_g^*$  conditions are 52.6 °C (left) and 54.8 °C. Photographs were taken at the end of the test.

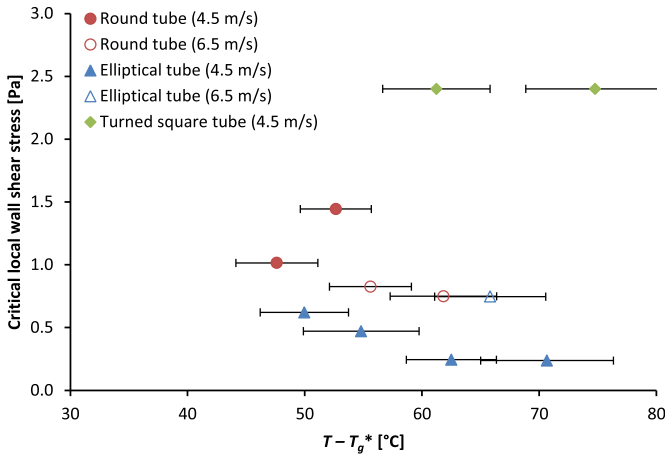


Fig. 7. Critical local wall shear stress plotted against  $T - T_g^*$  for round, elliptical, and turned square tubes.

velocity and powder stickiness may be defined as the angle between the bulk flow direction and the normal to the tube surface at the point where deposition terminates, which is known from the experimental tests, for the round and elliptical tubes where the impact angle varies around the circumference of the tube. The general concept of a critical impact angle was originally suggested by Konstandopoulos [14]. Fig. 8 illustrates how the critical impact angle to the normal is estimated for deposition on the elliptical, round and square tubes. For the round tube this is merely the angle of the polar coordinate at the surface location. For the elliptical tube the angle varies from that of the polar coordinate as illustrated in Fig. 8a. For the turned square tube the angle remains constant at  $45^\circ$  (considering only the positive angles) and as a result the tube was either clear or covered with deposition. The boundary between fouling and no fouling is defined by a critical combination of factors such as air velocity, stickiness, and impact angle. Therefore, in the case of the turned square tube, the critical combination of air velocity, stickiness, and impact angle is determined in the first

instance by varying  $T - T_g^*$ , instead of the impact angle, as can be done in the round and elliptical tube tests.

Fig. 9 plots the critical impact angle relative to the direction of the airflow against particle stickiness,  $T - T_g^*$ . Vertical and horizontal bars in Fig. 9 represent the uncertainty of the measurements. Uncertainty in  $T - T_g^*$  was the result of fluctuating temperature and humidity measurements. Uncertainty in the critical impact angle is due to the non-uniform deposition along the length of the tube. Predictions of the critical impact angle using the deposition model from Walmsley et al. [12] is included in Fig. 9 for comparison. When the uncertainty is taken into account, the deposition model from Walmsley et al. [12] appears to be sufficiently representative of the experimental data for single tubes in cross-flow. At  $T - T_g^*$  below  $65^\circ\text{C}$ , the model provides a close match to the critical impact angle with the exception of the turned square tube; whereas at higher  $T - T_g^*$  the model over predicts the critical impact angle.

In the case of the turned square tube, it was found that either the entire face of the tube was clean or fouled. Increasing  $T - T_g^*$  after the tube fouled therefore gave an apparent “critical” impact angle of  $45^\circ$  since there could be no impacts at angles greater than  $45^\circ$ . The minimum measured  $T - T_g^*$  required to cause the turned square tube to foul was  $61.2^\circ\text{C}$  and the maximum measured  $T - T_g^*$  giving no fouling was  $56.7^\circ\text{C}$ . The critical impact angle for the given air velocity and  $T - T_g^*$  lies, therefore, between  $56.7^\circ\text{C}$  and  $61.2^\circ\text{C}$  for the turned square tube. The model predicts a  $T - T_g^*$  value of  $53.6^\circ\text{C}$ . If the  $T - T_g^*$  uncertainty is taken into account, the measured  $T - T_g^*$  may be as low as  $53.4^\circ\text{C}$ , which marginally encompasses the model.

#### 4.3. Pressure drop

The fouling growth rate and pressure drop across the tube are related. Fig. 10 plots the increase in pressure drop as a percentage for three stickiness levels for the round tube and one stickiness level for the elliptical tube. The data suggests the rate of pressure drop and, therefore, fouling build-up is dependent on the stickiness level, with higher stickiness conditions resulting in faster growth. Fouling was observed to reach an asymptote and this observation is reflected in the pressure drop measurements. When an asymptote

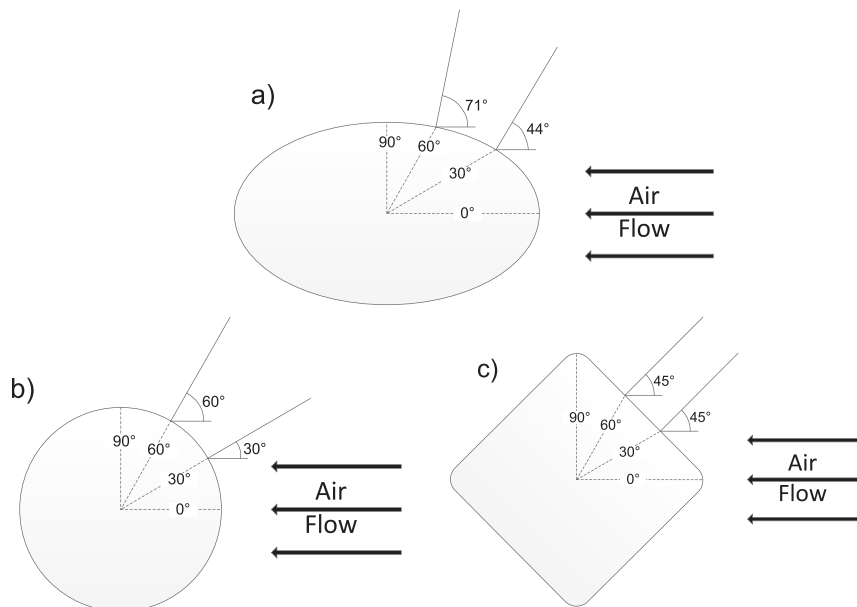


Fig. 8. Schematic showing how the impact angle is defined and how it changes for: a) elliptical tubes; b) round tubes; c) turned square tubes.

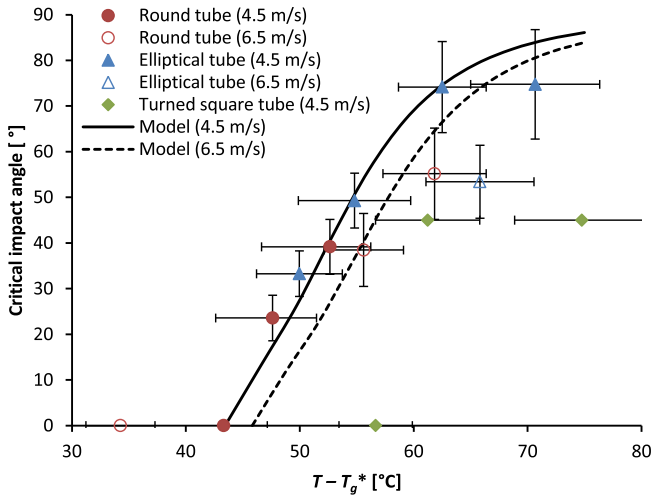


Fig. 9. Estimated critical impact angle for the round, elliptical and turned square tubes. The milk powder deposition model is taken from Walmsley et al. [12] and calculated using a particle diameter of 104 μm.

is reached, it implies the rate of fouling and removal are approximately the same.

A first order exponential approximation of the pressure drop increase with time is also plotted in Fig. 10 using the general equation.

$$\Delta P(\%) = \Delta P_{\text{final}}(\%) \left( 1 - \exp\left(-\frac{t}{\alpha_f}\right) \right) \quad (3)$$

where  $t$  is the time from the start of the test and  $\alpha_f$  is the time constant for the fouling, which is estimated as 420 s. This time constant was similar for the round and elliptical tubes. Since the powder concentration is fairly low and it is unexpected to significantly influence the airflow profiles, it may be assumed that the supply of powder to heat exchanger surfaces is a key limiting factor for the rate of deposition. On the other hand the air velocity and stickiness of the powder determines the equilibrium amount of powder attached to a tube. As a result the final pressure drop increase is a function of stickiness for a given velocity profile and tube geometry whereas the time constant is a function of powder concentration, which may be estimated from the average powder injection rate. For different concentrations of powder the equivalent time constant for the pressure drop rise is estimated using

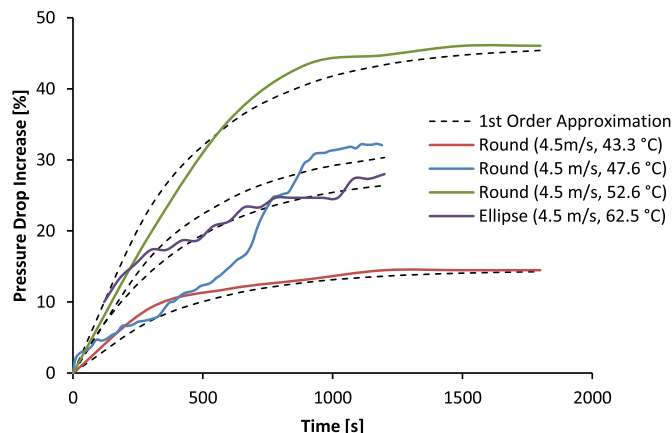


Fig. 10. Pressure drop over time across a single round tube for three levels of stickiness showing a first order exponential approximation with a time constant of 420 s.

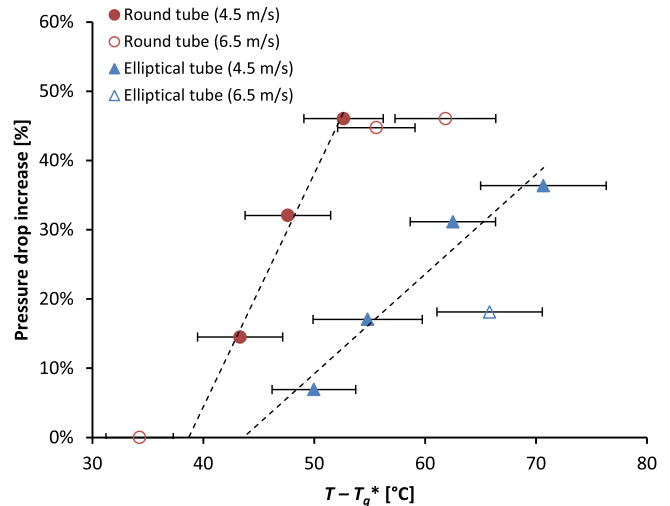


Fig. 11. Final pressure drop versus  $T - T_g^*$  for the round and elliptical tubes.

$$\alpha_{f,2} = \alpha_{f,1} \frac{C_{b,1}}{C_{b,2}} \quad (4)$$

where  $c_b$  is the milk powder concentration in the bulk airflow. The final pressure drop increase percentages are plotted against  $T - T_g^*$  in Fig. 11. The round and elliptical tubes both experience increases in pressure drop with increasing  $T - T_g^*$ . As  $T - T_g^*$  increases, the deposition coverage around the tubes grows adding resistance to the airflow. For the same  $T - T_g^*$  the pressure drop increase for the round tube is greater than for the elliptical tube. This conclusion reinforces the idea that the coverage of the frontal deposition for the round tube is greater than for the elliptical tube at the same  $T - T_g^*$ .

### 5. Conclusion

Deposition results for tubes indicate milk powder deposition is influenced by the impact angle of the milk powder on the tube wall, which angle varies around the circumference for the round and elliptical tubes. Deposition mostly occurs on the front face of the round, elliptical and turned square tubes and decreases around each tube until a critical impact angle to the surface of the tube and deposition ceases. None of the tube geometries contained significant deposition on the rear side of the tube. The critical impact angle may be described by a literature deposition model for SMP and is independent of tube shape. Elliptical tube is shown to be naturally low fouling due to the shape of the tube.

### References

- [1] T.R. Bott, *Fouling of Heat Exchangers*, Elsevier, Amsterdam, The Netherlands, 1995.
- [2] H. Müller-Steinhagen, H. Malayeri, A.P. Watkinson, Heat exchanger fouling: mitigation and cleaning techniques, *Heat Transfer Eng.* 32 (2011) 189–196.
- [3] M.S. Abd-Elhady, C.C.M. Rindt, J.G. Wijers, A.A. Van Steenhoven, E.A. Bramer, T.H. van der Meer, Minimum gas speed in heat exchangers to avoid particulate fouling, *Int. J. Heat Mass Transfer* 47 (2004) 3943–3955, <http://dx.doi.org/10.1016/j.ijheatmasstransfer.2004.03.024>.
- [4] Z. Jegla, B. Kilkovský, P. Stehlík, Calculation tool for particulate fouling prevention of tubular heat transfer equipment, *Heat Transfer Eng.* 31 (2010) 757–765, <http://dx.doi.org/10.1080/01457630903500932>.
- [5] P. Stehlík, Conventional versus specific types of heat exchangers in the case of polluted flue gas as the process fluid – a review, *Appl. Therm. Eng.* 31 (2011) 1–13, <http://dx.doi.org/10.1016/j.applthermaleng.2010.06.013>.
- [6] G. Zhang, T.R. Bott, C.R. Bemrose, Reducing particle deposition in air-cooled heat exchangers, *Heat Transfer Eng.* 13 (1992) 81–87.

- [7] C. Paz, E. Suárez, A. Eirís, J. Porteiro, Experimental evaluation of the critical local wall shear stress around cylindrical probes fouled by diesel exhaust gases, *Exp. Therm. Fluid Sci.* 38 (2012) 85–93, <http://dx.doi.org/10.1016/j.expthermflusc.2011.11.011>.
- [8] T.G. Walmsley, M.R.W. Walmsley, M.J. Atkins, J. Hoffman-Vocke, J.R. Neale, Numerical performance comparison of different tube cross-sections for heat recovery from particle-laden exhaust gas streams, *Procedia Eng.* 42 (2012) 1476–1490, <http://dx.doi.org/10.1016/j.proeng.2012.07.527>.
- [9] T.G. Walmsley, M.R.W. Walmsley, M.J. Atkins, J.R. Neale, Improving energy recovery in milk powder production through soft data optimisation, *Appl. Therm. Eng.* 61 (2013) 80–87, <http://dx.doi.org/10.1016/j.applthermaleng.2013.01.051>.
- [10] T.G. Walmsley, M.R.W. Walmsley, M.J. Atkins, J.R. Neale, Fouling and pressure drop analysis of milk powder deposition on the front of parallel fins, *Adv. Powder Technol.* 24 (2013) 780–785, <http://dx.doi.org/10.1016/j.apt.2013.04.004>.
- [11] R.A. Murti, A.H.J. Paterson, D. Pearce, J.E. Bronlund, The influence of particle velocity on the stickiness of milk powder, *Int. Dairy J.* 20 (2010) 121–127, <http://dx.doi.org/10.1016/j.idairyj.2009.08.005>.
- [12] T.G. Walmsley, M.R.W. Walmsley, M.J. Atkins, J.R. Neale, C.M. Sellers, An experimentally validated criterion for skim milk powder deposition on stainless steel surfaces, *J. Food Eng.* 127 (2014) 111–119, <http://dx.doi.org/10.1016/j.jfoodeng.2013.11.025>.
- [13] A. Guha, Transport and deposition of particles in turbulent and laminar flow, *Annu. Rev. Fluid Mech.* 40 (2008) 311–341.
- [14] A.G. Konstandopoulos, Particle sticking/rebound criteria at oblique impact, *J. Aerosol. Sci.* 37 (2006) 292–305, <http://dx.doi.org/10.1016/j.jaerosci.2005.05.019>.
- [15] S. Palzer, The effect of glass transition on the desired and undesired agglomeration of amorphous food powders, *Chem. Eng. Sci.* 60 (2005) 3959–3968, <http://dx.doi.org/10.1016/j.ces.2005.02.015>.
- [16] G.F. Brooks, *The Sticking and Crystallisation of Amorphous Lactose*, M. Tech, Massey University, 2000.
- [17] I. Pisecky, *Handbook of Milk Powder Manufacture*, Niro A/S, Copenhagen, Denmark, 1997.
- [18] D. Bouris, E. Konstantinidis, S. Balabani, D. Castiglia, G. Bergeles, Design of a novel, intensified heat exchanger for reduced fouling rates, *Int. J. Heat Mass Transfer* 48 (2005) 3817–3832, <http://dx.doi.org/10.1016/j.ijheatmasstransfer.2005.03.026>.

**Article 8:**

*Integrating district cooling systems in Locally Integrated Energy Sectors through Total Site Heat Integration*

Liew, P.Y., **Walmsley, T.G.**, Wan Alwi, S.R., Manan, Z.A., Klemeš, J.J., Varbanov, P.S., 2016.

Applied Energy 184, 1350–1363.

DOI: [10.1016/j.apenergy.2016.05.078](https://doi.org/10.1016/j.apenergy.2016.05.078)

Citations: 11

Elsevier



# Integrating district cooling systems in Locally Integrated Energy Sectors through Total Site Heat Integration



Peng Yen Liew<sup>a,b</sup>, Timothy Gordon Walmsley<sup>c</sup>, Sharifah Rafidah Wan Alwi<sup>a,d,\*</sup>, Zainuddin Abdul Manan<sup>a,d</sup>, Jiří Jaromír Klemeš<sup>e</sup>, Petar Sabev Varbanov<sup>e</sup>

<sup>a</sup> Process Systems Engineering Centre (PROSPECT), Research Institute of Sustainable Environment (RISE), Universiti Teknologi Malaysia, 81310 UTM Johor Bahru, Johor, Malaysia

<sup>b</sup> Department of Environmental Engineering and Green Technology, Malaysia – Japan International Institute of Technology (MJIT), Universiti Teknologi Malaysia, 54100 Kuala Lumpur, Malaysia

<sup>c</sup> Energy Research Centre, School of Engineering, University of Waikato, Hamilton, New Zealand

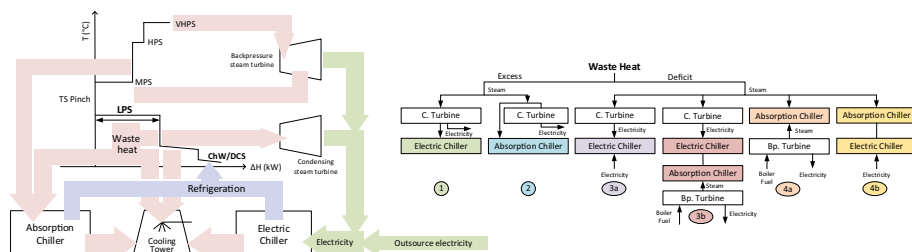
<sup>d</sup> Faculty of Chemical and Energy Engineering, Universiti Teknologi Malaysia, 81310 UTM Johor Bahru, Johor, Malaysia

<sup>e</sup> Faculty of Information Technology and Bionics, Pázmány Péter Catholic University, Práter utca 50/a, 1083 Budapest, Hungary

## HIGHLIGHTS

- Heat integration of district cooling and chilled water network in industrial clusters for low-grade heat utilisation.
- An improved methodology is introduced to incorporate Absorption Chillers and/or Electric Chillers in industrial clusters.
- Simultaneous reduction in fossil fuel-based chilling system in urban area and industrial waste heat venting.
- General equations for annualized operating and capital cost per unit of chilled water generation are proposed.
- Six different chilled water generation system configurations are considered in the study.

## GRAPHICAL ABSTRACT



## ARTICLE INFO

### Article history:

Received 28 December 2015

Received in revised form 7 May 2016

Accepted 14 May 2016

Available online 26 May 2016

### Keywords:

Total Site Heat Integration

Process Integration

District cooling system

Chilled water network

Waste heat

## ABSTRACT

Between 20% and 50% of world energy consumption is lost as waste heat through energy conversion and transportation in manufacturing processes. Within industrial clusters and Locally Integrated Energy Systems (LIES), waste heat recovery for the purpose of heating and power generation has been well established via schemes such as process streams Heat Integration, cogeneration system, district heating integration, boiler feed water preheating and Organic Rankine Cycle. Waste heat can also be used to generate cooling energy via technologies such as the absorption chiller. During the summer season and in tropical countries, space cooling in buildings typically consumes up to 50% of the total energy consumption. Further recovery of waste heat to generate cooling can result in huge energy savings and emission reduction. This paper presents a new Total Site Energy Integration concept that integrates not only heat and power, but also cooling. The waste heat technology considered for cooling generation are Absorption Chiller (AC) and Electric Compression Chiller (EC). As there is actually an economic trade-off between amounts of chilled water generated, cooling water and power consumed, the new framework has been

\* Corresponding author at: Process Systems Engineering Centre (PROSPECT), Research Institute of Sustainable Environment (RISE), Universiti Teknologi Malaysia, 81310 UTM Johor Bahru, Johor, Malaysia.

E-mail address: [shasha@cheme.utm.my](mailto:shasha@cheme.utm.my) (S.R. Wan Alwi).

## Nomenclature

### Abbreviations

AC	absorption chiller
CHP	combined heat and power
ChW	chilled water
COP	coefficient of performance
DCS	district cooling system
EC	electric chiller
GCC	Grand Composite Curve
HPS	high pressure steam
LIES	locally integrated energy system
LP	low pressure
LPS	low pressure steam
MPS	medium pressure steam
MU-PTA	Multiple Utility Problem Table Algorithm
OCC	operating and capital cost per unit of chilled water generated
SUCC	Site Utility Composite Curve
SUGCC	Site Utility Grand Composite Curve
TS	Total Site
TSP	Total Site Profile
TS-PTA	Total Site Problem Table Algorithm
VHP	very high pressure

### Symbols

$\Delta h$	enthalpy difference (kJ/kg)
$\Delta E$	electricity duty (kW)
$\Delta H$	heat duty (kW)
$\Delta Q$	heat content (kW)
$\Delta T_{\min}$	global uniform minimum allowable temperature difference (°C)
$\Delta T_{\min,up}$	minimum allowable temperature difference between utility and process streams (°C)
$\Delta T_{\min,pp}$	minimum allowable temperature difference between process streams (°C)

CC	annualised capital cost (\$/y)
CHR	chilled water demand to waste heat availability ratio
COP	coefficient of performance
$fCC()$	function annualised capital cost for individual equipment (\$/y)
OCC	specific operating and capital cost of a kW of chilled water generation (\$/y)
OH	operating hours in a year (h/y)
mCp	heat capacity flowrate (kW/°C)
$P$	price (\$/kW y)
$T_S$	source temperature (°C)
$T_S'$	shifted source temperature (°C)
$T_T$	target temperature (°C)
$T_T'$	shifted target temperature (°C)
$X$	steam quality
$\eta$	efficiency

### Subscripts

AC	absorption chiller
BFW	boiler feed water
Cond	condensate
Comp	compressor
EC	electric chiller
ele	electricity
exc	excess
LP	low pressure
rec	recoverable/available
c.turb	condensing steam turbine
bp.turb	backpressure steam turbine
vap	vaporization
VHP	very high pressure

proposed to guide users in selecting the most economical waste heat-to-cooling technology for Industrial Clusters and LIES. For the presented case study, the lowest-cost solution used a waste-heat driven AC supplying 4.0 MW of Chilled Water (ChW) and a supplementary EC supplying the remaining 1.0 MW. The electricity demand of the integrated system is loaded by 1.3 MWe through this ChW generation system configuration, while the cooling tower load is increased by 3.3 MW. The ChW is expected to be generated at USD 115.10/kW y compared to USD 270.9/kW y for generating ChW by a conventional EC system without waste heat recovery.

© 2016 Elsevier Ltd. All rights reserved.

## 1. Introduction

Process Integration through Pinch Analysis is one of the alternatives for performing resources conservation study. This concept started with thermal energy conservation during the energy crisis in the late 1970s. Industrial energy efficiency gained attentions for reducing greenhouse gases emission and improving world sustainability. In order to maintain market share, energy efficiency reduces the plant operating cost and consequently enhances profitability margin in industry [1].

Single process Heat Integration has been well developed and successfully applied in industry. To date, most of the industrial processes have energy recovery networks within each process. However, the energy recovery system is normally standalone for each process. The energy (heating or cooling) demands of these individual processes are then satisfied by a utility system. Total Site (TS) Heat Integration is introduced for enhancing the energy

recovery opportunities for an individual process to energy saving between processes [2]. TS Heat Integration aims to recover energy using the utility system as a heat transfer medium across processes [3]. In this concept, process waste heat generates utility for satisfying the utility deficits of other processes. This simultaneously reduces the cooling utility for the removal of waste heat and saves hot utility supply from boiler for fulfilling the heating requirement. Based on industrial experiences, Chew et al. [4] analysed the practical implementation issues of TS Heat Integration.

Heat Integration design and planning could be done using Mathematical Programming and Pinch Analysis techniques [5]. Mathematical Programming has been well developed for simultaneously incorporating various objectives and constraints in designing an optimal site utility system involving multiple processes [6]. On the other hand, Pinch Analysis targeting methodologies can be divided into two main streams, which are the graphical and algebraic methods. Graphical methodology is prioritised in the

methodology development process, because it could be easily understood by users. Algebraic techniques are convenient for obtaining precise solutions, and especially quicker for users without automated targeting tools. Total Site Profile (TSP) is the graphical tool in TS targeting to show the heat sources and sinks available from all single processes. The TSP is constructed based on the heat sources and sinks found in the Grand Composite Curve (GCC) for individual processes [2]. The Site Utility Composite Curve (SUCC) is performed based on the TSP, to determine the quantity of utility generation and consumption in the TS system. Energy saving potentials could be found when the utility generated by the process heat sources could be matched with the utility demand at the same temperature level, and at lower temperature levels [7]. Numerous algebraic targeting methodologies based on the Problem Table Algorithm have been introduced to achieve the similar objectives [8].

Extensive research have been done to improve the accuracy of the targeting results. Global uniform minimum allowable temperature difference ( $\Delta T_{\min}$ ) is typically used in the conventional TS targeting methodologies. The minimum allowable temperature difference between the utility and process streams ( $\Delta T_{\min,up}$ ) is introduced [9] to generate realistic energy recovery targets. In certain cases, boiler feed water sensible heat should be included in the targeting stage for determining the realistic targeting result and increasing the degree of freedom in designing the TS heat exchanger network [10]. Liew et al. [11] proposed a methodology to include the water sensible heat during targeting using the Utility Generation Curve in SUCC. In this case, the energy consumed by boiler feed water heating is eliminated before the utility generation and consumption curve pinches together. Sun et al. [12] introduced an additional methodology for incorporating boiler feed water preheating, which is targeted at the individual process utility targeting step. Chew et al. [13] incorporated the pressure drop issues in the TS targeting methodology, which further led to a more realistic estimation of the TS energy requirement.

Matsuda et al. [14] implemented *R*-curve analysis and TS analysis to identify the theoretical energy saving potential and develop practical energy saving options for a Japanese industrial park. Besides steam as heat transfer medium, Walmsley et al. [15] explored the low temperature heat recovery potential considering thermal storage system of a large multi-plant dairy factory using a hot water loop. Hackl and Harvey [16] demonstrated a practical design and implementation methodology on TS Heat Integration for improving industrial energy efficiency on a chemical cluster at Stenungsund, Sweden. Liew et al. [17] presented a TS retrofit framework for identifying financial-promised heat exchanger network and utility system modification options at petrochemical plant. TS system needs to cope with the process operational variation for all the integrated individual processes, which TS sensitivity analysis is introduced for optimal design of site utility system [18]. The effects of TS process modification options are explored with the changes of TSP for reducing capital cost of process retrofit [19]. The Shifted Retrofit Thermodynamic Grid Diagram [20] and Retrofit Tracing Grid Diagram [21] are introduced recently for aiding Heat Exchanger Network retrofit design.

Co-generation or Combined Heat and Power (CHP) system using steam turbine is very common in site utility system for replacing steam let-down stations. Turbines extract thermal energy from high pressure steam for generating mechanical work, which the work is then converted into power [22]. The co-generation potential in a utility system could be targeted through Site Utility Grand Composite Curve (SUGCC) [3]. Turbine hardware model [23] is a commonly used basis for model development to determine the turbine performance and capacity. However, steam turbine is only capable to recover energy from high temperature heat sources. A lot of efforts are invested in low grade heat recovery as there are

always excess low temperature heat sources in industrial processes [24], even after considering Inter-Process Heat Integration. Kwak et al. [25] further discussed on the low grade waste heat utilisation in process industry through several heat recovery techniques.

Locally Integrated Energy System (LIES) concept had been introduced for incorporating renewable energy and district heating systems with industrial processes [26]. Industrial waste heat utilisation through district heating gained attention as one of the promising options for increasing system-wide energy efficiency [27]. Varbanov and Klemeš [28] introduced the Total Site Cascade for analysing the energy consumptions of LIES considering the energy availability of the commercial or residential buildings, as well as renewable energy sources. Besides district heating, another option would be recovering low grade excess heat through heat pumping to satisfy heat deficit at higher temperature with supplementary work required [29]. Desai and Bandyopadhyay [30] proposed to integrate Organic Rankine Cycle to the separating utility processes for reducing cold utility requirements, while reducing electricity import from the grid. Waste heat driven multi-effect distillation in industrial desalination system could be another option for low grade heat recovery [31]. Miah et al. [32] suggested and demonstrated the upgrade of low grade heat to better heat quality by heat pump for maximising the energy recovery within an industrial zone or process through direct or indirect heat transfer. A methodology is proposed by Oluleye et al. [33] for analysing the potential of industrial waste heat recovery and utilisation for generating power, heat and chilling through different technologies. Hackl and Harvey [34] reported on the integration of bio-refinery with renewable feedstock into petrochemical industry for enhancing the site energy efficiency.

Space cooling system is essentially important for tropical countries, as well as summer in four-season countries. According to IEA [35] report, service and residential buildings consumed generally about 59% of the total energy consumption in South East Asia. For example, CETDEM [36] conducted a small scale research and reported on the average household electricity consumption in Petaling Jaya and Kajang, Malaysia, in which 44% of household electricity usage is attributed to space cooling or air conditioning propose. A huge portion of these consumptions are due to the energy intensive air conditioning system. For this reason, it has been rather obvious that industrial low grade heat powered space cooling system would be beneficial to the community energy system. Absorption chiller (AC) applies the thermodynamic closed-loop system, which is able to utilise waste heat for providing cooling energy or refrigeration. This system has lower Coefficient of Performance (COP) compared to vapour compression cycles. AC has an advantage for utilising low temperature waste heat (<100 °C) to deliver cooling or chilling medium [37]. So far, a number of research has been done on waste heat-driven AC.

However, the integration of district cooling system to TS or LIES system has not been discussed in any previous publications as an option to utilise the industrial low-grade waste heat. The proposed integration system allows an entire region, as opposed to a single site, to benefit from sustainable operation. Such regional approach enhances the effectiveness of the collaborative initiative by enterprises and the authority to address global warming issue. The electricity consumption of the district cooling system for urban buildings could be reduced by implementing the proposed integration scheme that also reduces the waste heat vented to the atmosphere and thereby preventing environmental emissions as well as thermal pollution.

The presented work introduces the Heat Integration of district cooling system and chilled water network in TS industrial system for the utilisation of industrial low-grade heat. This is the first contribution that addresses the use of ACs and/or Electric Chillers (EC)

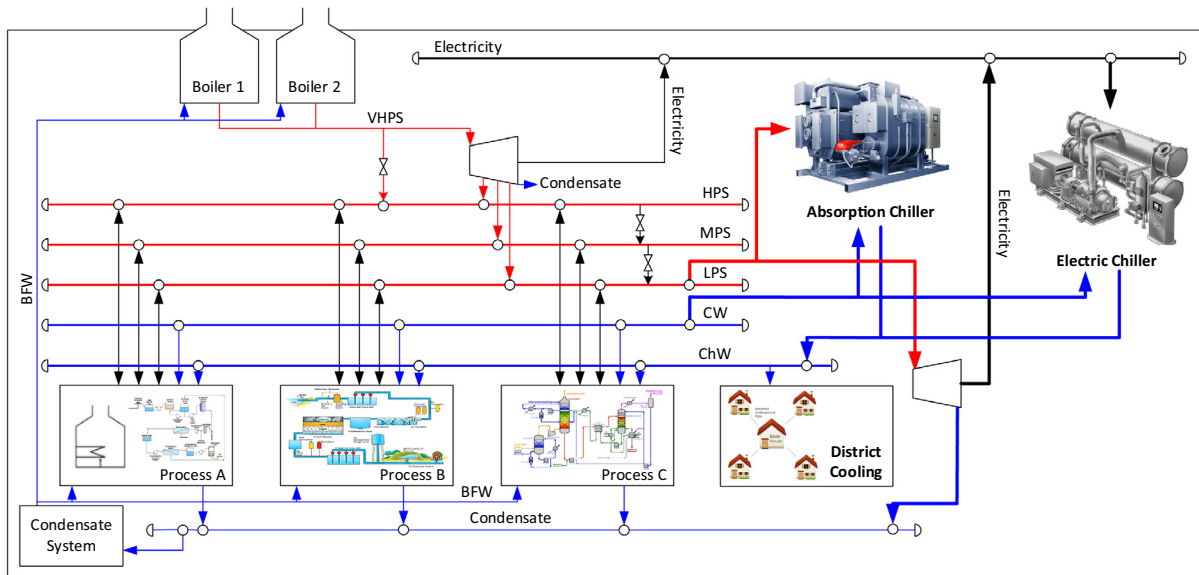


Fig. 1. A Total Site with an integrated centralised cooling system (further developed from Perry et al. [26]).

to power a centralised chilled water network or district space cooling system. The schematic diagram of the system is shown in Fig. 1. An improved TSHI methodology is introduced in this work to incorporate ACs and/or ECs in TS integrated industrial clusters. Besides direct steam utilisation in ACs to generate ChW, the conversion of low-grade heat to electricity through co-generation system is considered in the study for powering the EC units. The proposed methodology considers several possible integrated ChW generation schemes by ACs and/or ECs, based on the waste heat availability of the industrial processes. The objective of the methodology could be summarised as, to utilise the low grade waste heat available from the TS processes for satisfying the ChW requirement by the processes and/or DCS system aided by AC and/or EC unit. General equations for obtaining the annualized operating and capital costs per unit of ChW generated by the AC and EC units are proposed in this work as a guideline for system configuration selection in order to achieve the study objective. Waste heat in this study is defined as additional heat source available in the TS system, which could not be further recovered with any process heat sinks. This system is analogous to tri-generation system operated by fossil fuel, which focuses utilisation of process waste heat to produce heat, cooling and power simultaneously.

This paper continues with the explanation on the general concept of District Cooling System in Section 2, as well as the theories and operations of electric vapour compression and absorption chiller, for understanding the system to be integrated to the TS system. The new TSHI targeting methodology incorporating district cooling system, is then introduced in Section 3. The novel methodology is demonstrated with an illustrative case study in Section 4, followed by a discussion in the last part of the section.

## 2. District Cooling System

The International Institute of Refrigeration (IIR) estimates that the refrigeration and chilling demands consume about 15% of the total electricity generated globally [38]. The energy consumption of air conditioning system could not be under estimated as an opportunity for boosting energy savings and sustainability in society. Saidur [39] reported the typical electricity consumption in commercial or office buildings for several countries located near the equator as in Table 1. These countries mainly use air

Table 1  
Typical electricity consumption breakdown for commercial/office buildings [39].

Country	Air conditioning (%)	Lighting (%)	Other (%)
Malaysia	57	19	24
Indonesia	51	14	26
Thailand	59	21	20
Singapore	59	7	34
Saudi Arabia	50	20	30

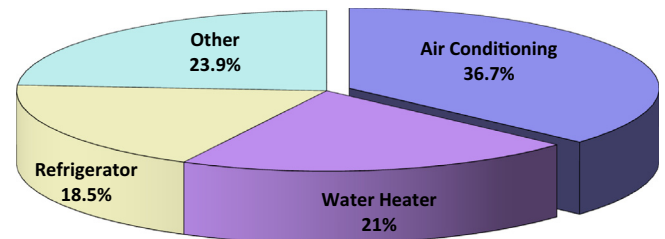


Fig. 2. Typical household electricity consumption in Singapore for year 2012 [40].

conditioning system for space cooling. The results show that air conditioning systems alone consume between 50% and 60% of the total energy consumption in commercial buildings. Household or residential electricity consumptions have a similar trend in tropical countries. Fig. 2 shows the average weighted household electricity consumption in Singapore for 2012, where air conditioning systems are the main electricity consumer.

Air conditioning system is essential for indoor spaces in hot tropical countries, especially in South East Asia, South Asia and South America. In South East Asia, commercial buildings commonly use centralised cooling systems. However, household air conditioning systems are typically decentralised or individual.

Centralised or District Cooling System (DCS) is a system to distribute cooling energy for space chilling to residential commercial and/or industrial consumers [40]. This system type is favourable for high population density buildings or even high building density locations.

Generally, DCSs are larger scale centralised cooling systems, which are connected by the chilled water distribution network. A

centralised chiller plant is responsible for the chilled water generation by vapour compression ECs, ACs or other cooling sources. The chilled water generated is then distributed to individual building cooling systems or user stations through the distribution network. The distribution network supplies the chilled water via insulated pipes and returns the spent chilled water to the centralised chiller plant. Pumps in the network create pressure difference between supplies and returns headers to drive the flow. Direct and indirect connections may be used in the building cooling system. Heat exchange between the chilled water from the DCS and the building's centralised air conditioning system is done for user stations with indirect connections, while chilled water is pumped to the individual air handling units for systems with direct connection configurations.

DCS is well-known for high energy efficiency compared to the conventional centralised air-conditioning system. By reducing the overall energy consumption, the greenhouse gases emission are able to be reduced, while enhancing the community or local sustainability. DCSs reduce the usage of refrigerant due to the load diversity and less standby chillers, which could reduce the pollutant potential due to leakages. The leakages or accidents in the DCS could be controlled and solved properly with well organised maintenance team. The building management team is able to release the responsibility for operating and maintaining the individual centralised chilling system to specialist DCS companies. This approach helps ensure the reliability of the chilled water supply, and reduces the capital investment and maintenance costs on the building's air conditioning system.

### 2.1. Electric vapour compression chiller

Electric Chillers (EC) based on the vapour compression refrigeration cycle is the most commonly used air conditioning system for space cooling in commercial and residential buildings. It is frequently being used to supply ChW to the DCS system. This is a conventional type of air conditioning system, which could be divided into room cooler and centralised system. Room cooler is an individual unit for small space conditioning, which is typically seen in residential buildings. Centralised system is a large-scale vapour compression cycle, which supplies conditioned air to large spaces and buildings.

The vapour refrigerant in the refrigeration cycle is compressed before entering the condenser. At this pressure level, the refrigerant has a saturation temperature above the ambient air temperature, which allows the refrigerant to discharge energy through

the condensation process of the refrigerant in the condenser. The energy released in the condenser is rejected to the outside atmosphere using air-cooled heat exchangers or to cooling water using plate heat exchangers. The liquid refrigerant then adiabatically expands after passing through an expansion valve to the required pressure level of the evaporator. At this pressure, the saturation temperature of the refrigerant is below the air conditioning (or chilled water) temperature and vaporizes by absorbing energy from the air entering the air conditioned space (or the chilled water return line). In large air conditioning systems, the vaporization process is done in an air handling unit, which distributes the conditioned air throughout the building. The heated vapour refrigerant then returns to the compressor to complete the cycle. The working principle of vapour compression chiller is illustrated in Fig. 3 for the generation of chilled water.

Refrigerants commonly used in the vapour compression cycle for conventional air conditioning systems include hydrochlorofluorocarbons (HCFCs), hydrofluorocarbons (HFCs), ammonia, carbon dioxide, sulphur dioxide, and hydrocarbons [41]. These refrigerants have replaced the previously favoured chlorofluorocarbon (CFCs) based refrigerants, which are known to cause significant ozone depletion. Of particular note, ammonia is frequently used in industrial chiller units due to its high COP and minimal Global Warming Potential. Carbon dioxide is an emerging industrial refrigerant with several commercially available options that use a trans-critical vapour compression cycle, which simultaneously produces chilled water and hot water ( $\sim 90^\circ\text{C}$ ). In this study, the EC is powered by the waste heat generated electricity through a condensing steam turbine. The condensing turbine recovers the work potential between steam and condensate at near vacuum condition. However, the exhaust from condensing turbine is not fully condensed. A condenser is needed after the turbine for condensing the remaining steam, which requires additional CW supply to the condenser.

### 2.2. Absorption chiller

AC technology was introduced for generating Chilled Water (ChW) by removing heat from chilled water return and transferring the heat to evaporate a refrigerant [42]. ACs have four major components, which are the generator, condenser, evaporator and absorber. The condenser and generator operate at the same high pressure and the Evaporator and Absorber operate at the same low (vacuum) pressure.

The absorption refrigeration cycle's internal fluid is a mixture of two pure fluids, which act as a refrigerant and an absorbent. The

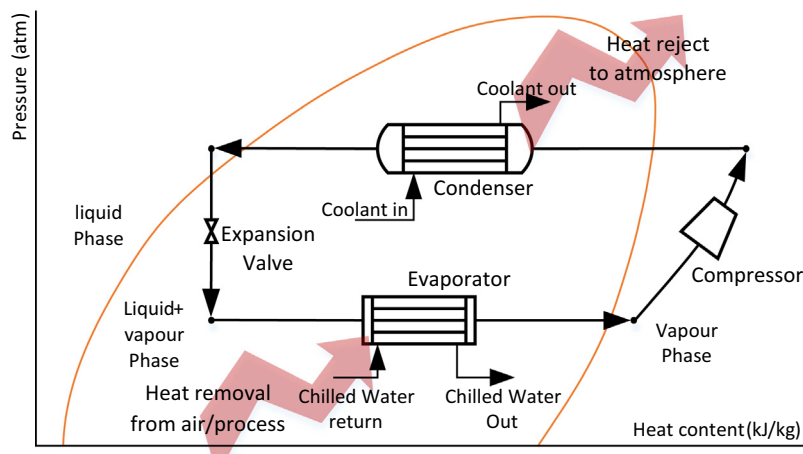


Fig. 3. Basic mechanism in a vapour compression chiller.

refrigerant has lower boiling point compared to the absorbent. External energy, such as recovered LP steam, needs to be supplied to the generator to boil the refrigerant from the refrigerant rich solution which enters the generator from the absorber. After boiling off the refrigerant, the remaining lean solution (in terms of refrigerant) is directed back to the Absorber through a heat exchanger and an expander. With the aid of external cooling, the lean solution then absorbs evaporated refrigerant from the evaporator. The generator and absorber with the associated pump and expansion valve constitute the so-called chemical compressor, which is similar to the conventional vapour compression cycle with a mechanical compressor.

Gaseous state refrigerant rich fluid also exits the Generator and flows to a condenser. The condenser, as well as the absorber, requires cooling from the cooling water system for condensing the vapour refrigerant. The liquid refrigerant is then expanded to the lower pressure level of the chiller. At a deep vacuum pressure condition, the liquid refrigerant is boiled using a low temperature heat source to generate chilled water. In order to maintain the deep vacuum condition in the evaporator, absorbent in the absorber absorbs the refrigerant vapour exiting the evaporator. The absorption process requires cooling water supply. Rich solution of refrigerant and absorbent is pumped to the generator at higher pressure. Heat exchange is performed between the rich and lean solutions in order to enhance the efficiency of the system. The mechanism of an AC is shown in Fig. 4.

Low grade heat could be supplied to operate ACs, which can be harvested from renewables or process waste heat. A key parameter for this technology is the Coefficient of Performance for Absorption Chiller ( $COP_{AC}$ ), which is frequently defined as kW of chilling output per kW of heating input and kW of work input. However, the work input is relatively negligible to the heat input to the chiller system. The typical  $COP_{AC}$  formula is shown as Eq. (1). A typical single-effect absorption chilling system has  $COP_{AC}$  value between 0.70 and 0.76 [37].

$$COP_{AC} = \frac{\text{Chiller Load}}{\text{Generator Input}} = \frac{Q_e}{Q_g} \quad (1)$$

Multi-stage absorption systems are available in the market for utilising heat sources at higher temperature for better performance system. The multi-effect ACs are producing lower temperature refrigerant with better quality heat sources supplied. Multiple generators and condenser are used in a multi-effect absorption chilling

system for more refrigerant to desorb from the absorbent solution [43]. The operating pressure and temperature of the generators and condensers increase with the increment of the number of system's effects. The external heat source is supplied to the highest temperature generator for boiling refrigerant from the weak lean solution. The lower temperature generator is then heated by the refrigerant separated from the higher temperature generator. The  $COP_{AC}$  of a double-effect system typically raises to the range between 1.0 and 1.3 [42] out of an ideal  $COP_{AC}$  of 2, prototype triple-effect system has calculated to have  $COP_{AC}$  in the range of 1.4–1.6 [43].

This system is attractive for industry with similar amounts of low temperature waste heat sources and chilling demands. In order to enhance the  $COP_{AC}$  and reduce the costs of the AC system, research and development works have primarily focused on finding good absorbent and refrigerant working pairs and appropriate advanced absorption refrigeration cycle.

### 3. Total Site targeting

Total Site energy targeting methodology for integrating the district or centralised cooling system in the TS system is proposed in this study. The proposed algorithm is aimed to fully satisfy ChW by utilising the waste heat available from a fully integrated TS system. This work focuses on the integration of new or existing DCS to a properly integrated TS industrial cluster. In this methodology, waste heat is defined as the remaining energy available on-site after the processes are properly integrated in TS concept, before DCS is proposed to be integrated with the processes. The methodology considers a single scenario steady state TS system operation. The part-load chiller characteristics and the base load of standby chillers are not considered in this work, as well as fluctuation of energy supply and demand with time [44]. The methodology is summarised in Fig. 5 and described step-by-step.

#### Step 1: Individual process energy targeting

- (a) Extract process stream data (supply and target temperatures, and duties) for all processes and energy users within the TS (or LIES), including the energy demand for DCS or centralised cooling system.
- (b) Adjust the duty of the energy demand for DCS or centralised cooling system to account for heat loss that may occur during the transport of the ChW.

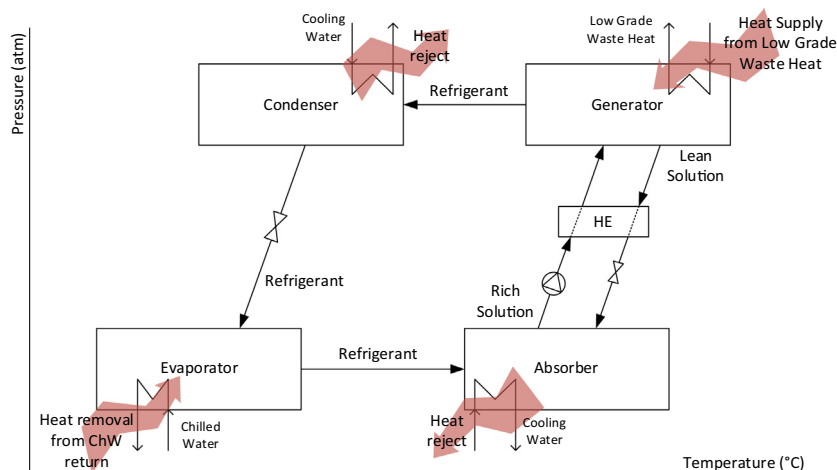


Fig. 4. System configuration of an Absorption Chiller.

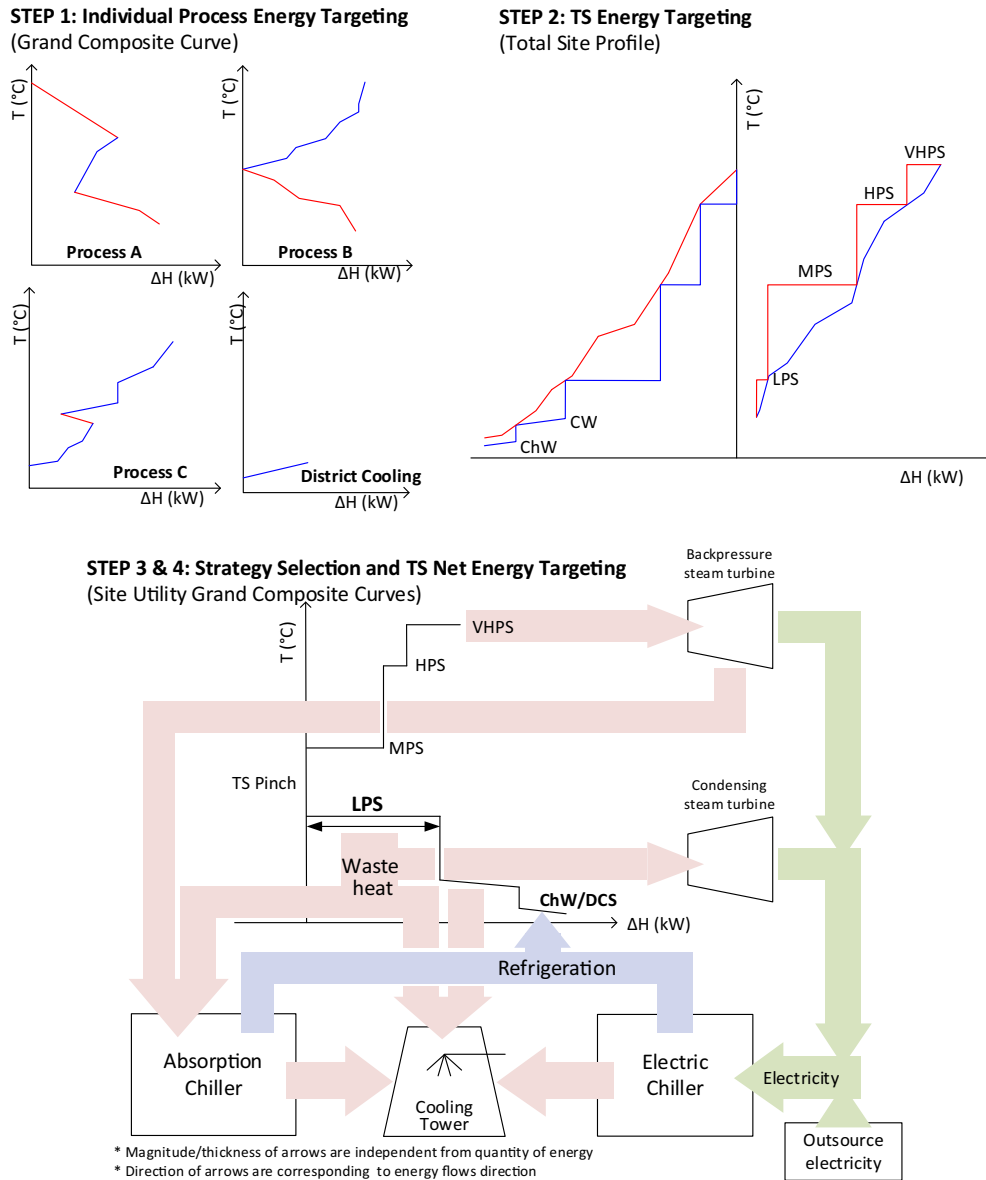


Fig. 5. TS energy targeting with district cooling system or chilled water network.

- (c) Target energy use for each process within the TS (or LIES) system using the Grand Composite Curve (GCC) [45] and/or Multiple Utility Problem Table Algorithm (MU-PTA) [8].

*Step 2: TS energy targeting*

- (d) Target utility heat and power production and use for TS or LIES system using the Total Site Profile (TSP), which includes the district cooling or centralised cooling system demands.
- (e) Construct the Site Utility Grand Composite Curve (SUGCC) [7] and/or calculate the Total Site Problem Table Algorithm (TS-PTA) [8] based the utilities selected from the TSP.
- (f) Identify the TS Pinch region.
- (g) Determine the amount of excess heat that may be recovered from below the TS Pinch region, which is available for use in a waste heat-driven AC or recovered through condensing steam turbine to generate electricity which is later used by an EC to generate ChW.

*Step 3: Strategy selection for chilled water generation*

- (h) Determine the electricity price ( $P_{ele}$ ), fuel price ( $P_{fuel}$ ), cooling water price ( $P_{CW}$ ),  $COP_{AC}$  for the AC unit and  $COP_{EC}$  for the EC unit from literature or supplier data.
- (i) Calculate the CHR, which is the ChW demand and waste heat excess ratio (Eq. (2)) to assess the amount of heat excess to be used for ChW generation.

$$CHR = \frac{\text{Chilled Water Demand}}{\text{Waste Heat Recovered}} = \frac{Q_{ChW}}{Q_{rec}} \quad (2)$$

- (j) Perform cost analysis (Eqs. (3)–(5), supplemented by Eqs. (6)–(19)) for different system configurations to generate ChW. Fig. 6 shows the route map of possible system architectures for ChW generation to satisfy the requirement of DCS, as well as the decision tree for assisting the selection procedure. These routes are the straightforward system design with flexibility on the system configuration. This

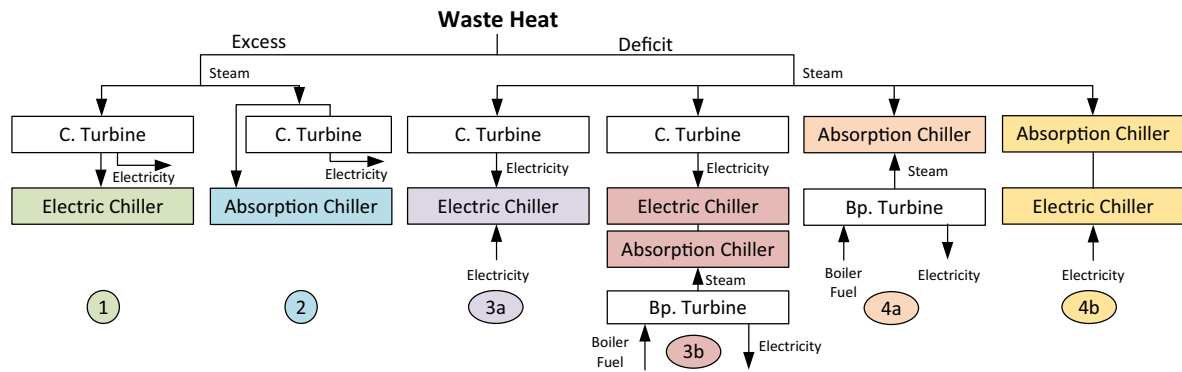


Fig. 6. Chilled water generation strategies utilising waste heat.

configuration selection step could be skipped for sites with specific requirement on the system design for combining AC and EC technology at specific ratio.

Eq. (3) represents the general equation of annualized operating and capital cost ( $OCC_{AC}$ ) for a unit of ChW generated through an AC, while Eq. (4) is the general equation to calculate the unit cost for ChW generated using EC ( $OCC_{EC}$ ). Eqs. (3) and (4) are supplemented by the Eqs. (6)–(19). Noted that the capital cost for EC ( $fCC_{EC}(\Delta Q_{LP(EC)})$ ) could be eliminated from the equations for DCS retrofit problem with existing EC unit. Same thing happen to condensing turbine cost ( $fCC_{c.turb}(\Delta Q_{LP(EC)})$ ) or the backpressure turbine cost ( $fCC_{b.p.turb}(\Delta Q_{LP(EC)})$ ) could also be omitted when there is an appropriate turbine in the industry processes to be used in this system. Eq. (5) calculates the overall OCC for a system configuration with separated OCC calculated for waste heat and supplementary chillers.

If the CHR is zero, the industrial cluster has no waste heat to be recovered by the system. The DCS should operate as a standalone system and not integrate with this industrial TS system, for securing the operational and management flexibility, as well as unnecessary piping cost.

If the CHR is less than (or equal to) the  $COP_{AC}$ , there is sufficient waste heat to generate sufficient ChW for satisfying the requirements using AC. The decision continues to examine if EC is available at the DCS. If there is EC available, the EC would continue its operation for saving in capital cost. The age of the EC would need to be considered for the lifecycle cost-optimum solution of this integration project. There are two possible common and straightforward system configurations to be used when there is sufficient waste heat at below TS Pinch, which are:

- EC only: If the DCS is a new proposed system or the life-span of the existing EC is approaching, and the operating and capital costs of EC unit ( $OCC_{EC}$ ) is lower than AC ( $OCC_{AC}$ ), the heat available should be recovered by a condensing steam turbine to power an EC unit (Route 1, Fig. 6). The excess electricity produced could be sold to the grid or used at other part of the TS system. This option should be chosen if the DCS is equipped with a properly performed EC unit for saving investment cost.
- AC only: If the DCS is a new proposed or the existing EC is reaching its maximum life-span, and the operating and capital costs (OCC) for EC is higher than AC, the ChW demand can be satisfied using an AC (Route 2, Fig. 6). The waste heat is directly utilised by the AC unit. The remaining waste heat could be either vented to atmosphere or recovered by condensing turbine, depending on the situation in the existing plant. Note that the  $OCC_{AC}$  (Eq. (3)) is formulated system to recover excess waste heat using condensing steam turbine. The electricity profit should be eliminated if the plant decided to vent the excess waste heat. In

addition, the excess waste heat could also be recovered through the AC system and sell to other plants out of the TS system boundary. The designer or engineer might modify Eq. (3) by removing the turbine price and inserting the ChW sales price.

If the CHR is greater than the  $COP_{AC}$ , there is insufficient excess heat at below TS Pinch region to produce the required ChW demand. This situation will be discussed using the case study. In the case of insufficient waste heat, the selection is divided into two levels, which the waste heat-operated chiller unit is selected prior to supplementary unit designation. The general  $OCC_{AC}$  (Eq. (3)) and  $OCC_{EC}$  (Eq. (4)) could be used to calculate the OCC for the individual system, while Eq. (4) could be used to calculate the overall OCC of the system configuration. A preliminary guideline for selecting the cost benefit ChW generation system configuration based on the current system setup.

- EC (waste heat chiller): If a new DCS without EC unit is planned to be integrated with a TS industrial processes with limited quantity of waste heat, a condensing steam turbine could be used to transform the waste heat to electricity and operate EC when the  $OCC_{EC}$  is lesser than  $OCC_{AC}$  (Route 3, Fig. 6). The remaining ChW loads are required to be satisfied by a supplementary chiller. The technology to satisfy the ChW supply shortage should be selected using total cost analysis (Eqs. (3) and (4)) for the remaining ChW load.
  - EC only: If the operational and investment cost for supplying the remaining ChW demand is lower for EC, a full ChW capacity EC is required to be installed in the integrated system (Route 3a, Fig. 6). This option also should be chosen for an existing DCS with an appropriate EC unit to be integrated with an industrial TS system.
  - EC + AC: If the  $OCC_{AC}$  for satisfying the remaining ChW demand is lower than  $OCC_{EC}$ , an AC with a backpressure steam turbine could be used as the supplementary chiller for the waste heat-powered EC (Route 3b, Fig. 6). The capital cost involves in this system is very high compared to other routes, as the system involves four equipment (i.e., condensing turbine, backpressure turbine, AC and EC). It could only be feasible when the electricity price is much higher than steam production cost or boiler fuel price.
- AC (waste heat chiller): If the existing ChW generation facility in the DCS is ready to be used or there is no existing facility, an AC could be used for direct utilisation of all waste heat available from the industrial cluster (Route 4, Fig. 6). An AC based waste heat chiller is very attractive when the load for the waste heat chiller higher than the supplementary chiller. The supplementary chilling could be provided by a separate unit of EC or to have a larger capacity AC, as discussed below:

- AC only: If the  $OCC_{AC}$  for supplying the remaining ChW required is lower than the  $OCC_{EC}$  (Route 4a, Fig. 6), an AC with full capacity to satisfy all the ChW demand needs to be installed. This system configuration increases the boiler load, which provides an additional unrecovered cogeneration opportunity for contradicting the boiler fuel cost. This option is reasonable when there is an existing VHP to lower pressure backpressure turbine with sufficient capacity to recover electricity from the enthalpy potential. This option also becomes remarkable when steam generation cost or the fuel price is lower than the electricity.
- AC + EC: A combination of AC and EC should be considered (Route 5, Fig. 6), if the  $OCC_{AC}$  for satisfying the remaining ChW demand is higher than  $OCC_{EC}$ . In this case, AC utilises all the waste heat available to generate maximum amount of ChW, while the remaining load is satisfied by an EC, which operates by electricity from grid or the on-site Combine Heat and Power system. This configuration is preferable when there is a CHR and  $COP_{AC}$  are closed to each other, due to no investment on new turbine system is required and giving higher operational flexibility to the system.

- (k) Select the system configuration to generate ChW in the chilled water network based on the overall OCC for different system configuration.

$$OCC_{AC} = \frac{p_{ele}\Delta E_{net(AC)} + p_{cw}\Delta Q_{out(AC)} + p_{fuel}\Delta Q_{in(AC)} + CC_{AC}}{\Delta Q_{ChW(AC)}} \quad (3)$$

$$OCC_{EC} = \frac{p_{ele}\Delta E_{net(EC)} + p_{cw}\Delta Q_{out(EC)} + CC_{EC}}{\Delta Q_{ChW(EC)}} \quad (4)$$

$$\text{Overall OCC} = \frac{OCC_{EC}\Delta Q_{ChW(EC)} + OCC_{AC}\Delta Q_{ChW(AC)}}{\Delta Q_{ChW}} \quad (5)$$

$$\begin{aligned} \Delta Q_{out(AC)} &= \Delta Q_{CW(AC)} + \Delta Q_{CW,c.turb(AC)} \\ &= \Delta Q_{condenser(AC)} + \Delta Q_{absorber(AC)} + Q_{condens.c.turb(AC)} \\ &\cong \Delta Q_{LP,rec} + \Delta Q_{LP,boiler(AC)} + \Delta Q_{ChW(AC)} + \Delta Q_{pump(AC)} \\ &\quad + \chi_{c.turbine}\Delta Q_{LP,rec} \end{aligned} \quad (6)$$

$$\Delta Q_{LP(AC)} = COP_{AC}\Delta Q_{ChW(AC)} \quad (7)$$

$$\Delta E_{net(AC)} = \Delta E_{pump(AC)} - \Delta E_{LP\rightarrow Cond.exc(AC)} - \Delta E_{VHP\rightarrow LP(AC)} \quad (8)$$

$$\Delta E_{pump(AC)} \cong \Delta Q_{pump(AC)} \quad (9)$$

$$\Delta E_{LP\rightarrow Cond} = \eta_{c.turb} \frac{\Delta Q_{LP}}{\Delta h_{vap,LP}} \Delta h_{LP\rightarrow Cond} \quad (10)$$

$$\Delta E_{VHP\rightarrow LP} = \eta_{bp.turb} \frac{\Delta Q_{LP}}{\Delta h_{vap,LP}} \Delta h_{VHP\rightarrow LP} \quad (11)$$

$$CC_{AC} = fCC_{AC}(\Delta Q_{ChW}) + fCC_{c.turb}(\Delta Q_{LP,rec}) + fCC_{bp.turb}(\Delta Q_{VHP\rightarrow LP}) \quad (12)$$

If  $CHR \leq COP_{AC}$ ,

$$\begin{aligned} \Delta Q_{LP(AC)} &= \Delta Q_{LP,rec(AC)} - \Delta Q_{LP,exc(AC)} \\ \Delta Q_{in(AC)} &= 0 \end{aligned} \quad (13)$$

If  $CHR > COP_{AC}$ ,

$$\begin{aligned} \Delta Q_{LP(AC)} &= \Delta Q_{LP,rec(AC)} + \Delta Q_{LP,boiler(AC)} \\ \Delta Q_{in(AC)} &= \frac{\Delta Q_{VHP,boiler(AC)}}{\eta_{boiler}} = \frac{1}{\eta_{boiler}} \frac{\Delta Q_{LP}}{\Delta h_{vap,LP}} \Delta h_{VHP\rightarrow BFW} \end{aligned} \quad (14)$$

$$\begin{aligned} \Delta Q_{out(EC)} &= \Delta Q_{CW(EC)}\Delta Q_{CW,c.turb(EC)} \\ &= \Delta Q_{condenser(EC)} + \Delta Q_{condenser,c.turb(EC)} \\ &= \Delta Q_{ChW(EC)} + \Delta Q_{comp(EC)} + \chi_{c.turbine}\Delta Q_{LP,rec} \end{aligned} \quad (15)$$

$$\Delta Q_{LP(EC)} = COP_{EC}\Delta Q_{ChW(EC)} \quad (16)$$

$$\Delta E_{net(EC)} = \Delta E_{comp(EC)} - \Delta E_{LP\rightarrow Cond.(EC)} \quad (17)$$

$$\Delta E_{comp(EC)} = COP_{EC}\Delta Q_{ChW(EC)} \cong \Delta Q_{comp(EC)} \quad (18)$$

$$CC_{EC} = fCC_{EC}(\Delta Q_{ChW}) + fCC_{c.turb}(\Delta Q_{LP,rec(EC)}) \quad (19)$$

#### 4. Case study

This case study is modified from the illustrative literature case study used in Liew et al. [18]. In this case study, The DCS system encounters a situation whereby the existing chillers need to be replaced with new chillers and being proposed to integrate with an industrial complex at 3 km away from the DCS. The industrial complex consists of three different industrial processes, which is properly integrated between each other. The management found that there is waste heat in the site, which can be recovered for the use of a new participant in the system.

Table 2 shows the stream data required for the TS analysis, which the district cooling system is represented as one of the processes in the TS system and includes a margin related to heat loss that occurs during transport. The TSP gives visual insight into the effective inclusion of district cooling systems. The minimum temperature difference between the process streams and the utility ( $\Delta T_{min,up}$ ) is assumed to be 10 °C and the minimum temperature difference between the process streams ( $\Delta T_{min,pp}$ ) is 20 °C. Four types of utilities are available in the existing industrial processes, which includes High Pressure Steam (HPS) at 270 °C, Medium Pressure Steam (MPS) at 180 °C, Low Pressure Steam (LPS) at 133 °C, and cooling water (CW) at 25–30 °C. The site boiler system with 75% efficiency uses natural gas fuel, which assumes at the cost of 162.00 USD/kW y. The boiler produces Very High Pressure (VHP) steam at 90 bar and 450 °C. The grid electricity cost is assumed at 701.92 USD/kW y, while the cooling tower operating cost is 28.45 USD/kW y. A Chilled Water (ChW) header is installed to connect the integrated industrial cluster and the district cooling system (DCS) at 8–11 °C for serving the chilling demand. Chiller vendor offers waste heat-driven AC system ( $COP_{AC} = 0.723$ ) and

**Table 2**  
Stream table for case study.

Stream	$T_S$ (°C)	$T_T$ (°C)	$\Delta H$ (kW)	$mCp$ (kW/°C)	$T'_S$ (°C)	$T'_T$ (°C)
<i>Process A</i>						
A1 Hot	200	100	20,000	200	190	90
A2 Hot	150	60	36,000	400	140	50
A3 Cold	50	220	-25,500	150	60	230
A4 Hot	170	150	10,000	500	160	140
<i>Process B</i>						
B1 Hot	200	50	4,500	30	190	40
B2 Hot	200	119	18,630	230	190	109
B3 Cold	35	200	-6,800	40	40	210
B4 Cold	130	150	-3,000	150	140	160
<i>Process C</i>						
C1 Hot	240	100	2,100	15	230	90
C2 Cold	50	250	-4,000	20	60	260
C3 Cold	40	190	-15,000	100	50	200
C4 Cold	109	140	-1,860	60	119	150
<i>District cooling system</i>						
D1 Hot	30	16	5,040	360	20	6

EC ( $COP_{EC} = 3.1$ ) to be considered, which the capital cost would be 350 USD/t and 240 USD/t of ChW generation through AC and EC unit.

#### 4.1. Steps 1 & 2: Individual process and TS energy targeting

TS cascade Pinch Analysis [8] is used in this case study to determine the overall heating and cooling utilities consumption of the TS system. The energy targeting result for this Case Study is shown in a TS-PTA (Table 3). The 'Heat Requirement' column in the table represents the net energy requirements for each utility level in the TS system, which considers the energy recovering within the same utility level. These values have not considered the inter-utility level energy recovery, which may further enhance the energy efficiency.

Heat Cascade in the TS-PTA assess the energy recovery opportunities between utility levels and determine energy flow for recovering energy excess at higher temperature to be supplied to lower temperature level energy demand. The terminology for Heat Cascade is to bring the high temperature energy excess to satisfy the energy demands at lower utility level. The 'Initial Cascade' is assuming no external heating provided to the system, which represents the shutdown of the site boilers. However, this condition would be invalid when there is negative energy flows between the utility levels, because energy excess from low temperature is not able to satisfy the demands at higher temperature. The 'Final Cascade' in the TS-PTA determines the ultimate external heating and cooling requirements of the TS system. The TS Pinch location of the integrated system could also be obtained from the 'Final Cascade', which divides the utility levels into net heat excess and demand region. Utility levels located below the TS Pinch region are considered as net heat excess levels, which consist of process streams to be cooled by cooling utilities. The net heat demand region is located above TS Pinch, which requires heating from the site boiler system.

The distributed energy requirements of the TS system are shown in the 'Utility Requirement' column. This result provides information for providing alternative energy sources to the system for satisfying the heating or cooling requirement at certain utility level. Besides that, cogeneration potential of the utility system could be read from the 'Utility Requirement' determined. The maximum cogeneration potential in this case study at above Pinch region is found at 1.83  $MW_e$ . The implementation of ChW generation technology does not generally effect on the power generation opportunity above Pinch, unless the boiler load is increased to supply supplementary steam to the chiller in Route 3b and 4a (Fig. 6). In this study, the 'Utility Requirement' column is necessary to obtain the quantity and quality of waste heat available on site to incorporate with the ACs. The boiler steam generation demand (highest end of the final cascade) for the TS system in this case

study is 17.1 MW. The system also requires 36.4 MW of cold utility to cool the heat excess at LPS and CW levels (lowest end of the final cascade). More importantly, 5.0 MW of ChW (1,433 t of refrigeration) is demanded by the district cooling system, which should be supplied by electricity- and/or heat-driven chiller systems.

#### 4.2. Step 3: Strategy selection

The excess LPS stream's work potential can be recovered through a waste heat-driven AC to produce ChW, which is more expensive compared to CW, for use in the district cooling system. The ChW demand and waste heat ratio (CHR) for this case study is 0.91 using Eq. (2), which means the ChW demand is 9% less than the excess LPS. The CHR is higher than the given  $COP_{AC}$  of 0.723, which means the ChW demand could not be fully satisfy by the available LP waste heat on-site. Excess LPS available in the TS system limits the production of sufficient ChW for the use in the district cooling system. This case study analyses four different possible solutions, which are:

- Case 1: EC unit fully satisfies the ChW demand from the DCS, while the plant vents the excess low-grade heat at LP level to atmosphere (Table 4).
- Case 2: EC unit fully satisfies the ChW demand from the DCS (Route 3a, Fig. 6), while an LP condensing steam turbine recovers some power at the expense of increased CW load (Table 5).
- Case 3: EC recovers all the process waste heat at LP level, while the remaining ChW demand is satisfied by an AC unit (Route 3b, Fig. 6). This option increases the boiler load, while producing a small amount of electricity through backpressure turbine (Table 6).
- Case 4: AC unit fully satisfies the ChW required by the DCS (Route 4a, Fig. 6), which increases the site boiler load and generates additional electricity through backpressure turbine (Table 7).
- Case 5: AC recovers the process LP waste heat (Route 4b, Fig. 6). Supplementary EC unit supplies the remaining ChW required in the TS system (Table 8).

If a conventional EC is used to satisfy the DCS load (Case 1 – base case) without integration with the industrial processes in the TS, the 'Net Utility Requirement' for the TS may be calculated as illustrated in Table 4. The EC consumes 1.6  $MW_e$  of electricity to drive the vapour compression cycle (based on an ammonia refrigerant with a  $COP = 3.1$ ) and increases the CW consumption ( $Q_{CW(EC)}$ ) by 6.6 MW ( $=Q_{comp(EC)} + Q_{ChW(EC)} = 1.6 + 5.0$ ), which totals to 37.5 MW of CW to satisfy the CW cooling demands. However, according to the result in Table 3, there is an also excess energy source at LPS. The generated LPS is then condensed by cooling water or vented to the environment. In most cases, plant operators

**Table 3**  
Total Site Problem Table Algorithm for the case study.

Utility levels	Heat source (kW)	Heat sink (kW)	Heat requirement (kW)	Initial cascade (kW)	Final cascade (kW)	Final heat requirement (kW)
HPS	0	-10,650	-10,650	0	17,105	10,650
MPS	500	-6,955	-6,455	-10,650	6,455	6,455
LPS	15,490	-9,955	5,535	-17,105	0	(TS pinch) -5,535
CW	30,850	0	30,850	-11,570	5,535	-30,850
ChW	5,040	0	5,040	19,280	36,385	-5,040
				24,320	41,425	

Positive value represents heat demand/deficit; negative value indicates heat excess/surplus/available.

**Table 4**

Case 1 – Net Total Site energy requirement after rejection of LP steam and Electric Chiller integration for entire chilled water load.

Energy type/level	Initial energy requirement (kW)	LP steam rejection (kW)	EC energy requirements (kW)	Net energy requirement (kW)
Electricity	–1,831	0	1,626	–205
HPS	10,650	0	0	10,650
MPS	6,455	0	0	6,455
LPS	–5,535	5,535 <sup>a</sup>	0	0
CW	–30,850	0	–6,666	–37,516
ChW	–5,040	0	5,040	0

Positive value represents heat demand/deficit; negative value indicates heat excess/surplus/available at the respected temperature range.

<sup>a</sup> LP steam vented into the ambient for ‘free’ cooling.**Table 5**

Case 2 – Net Total Site energy requirement after LP steam turbine and Electric Chiller integration for entire chilled water load.

Energy type/level	Energy requirement (kW)	Condensing turbine energy requirements (kW)	EC energy requirements (kW)	Net energy requirement (kW)
Electricity	–1,831	–916	1,626	–1,121
HPS	10,650	0	0	10,650
MPS	6,455	0	0	6,455
LPS	–5,535	5,535	0	0
CW	–30,850	–4,619	–6,666	–42,135
ChW	–5,040	0	5,040	0

Positive value represents heat demand/deficit; negative value indicates heat excess/surplus/available at the respected temperature range.

choose to vent excess recovered LPS to atmosphere as a means of low-cost cooling. The specific operating and capital cost for ChW is 270 USD/kW y to satisfy the ChW load using EC operates by purely electricity supply from grid.

The waste heat chiller can be first assessed in this study for fully utilising the waste heat available from the industrial site. The 5,535 kW of waste heat at LP level produces 4.0 MW of ChW ( $\Delta Q_{ChW} = COP_{AC} \times LPS \text{ excess} = 0.723 \times 5.54$ ) through an AC system or 2.8 MW of ChW ( $\Delta Q_{ChW} = COP_{EC} \times \text{power input} = 3.1 \times 916$ ) through a turbine (916 kW<sub>e</sub>) and EC unit. The unit cost of every 1 kW of ChW generated using AC and EC systems are calculated. The OCC<sub>AC</sub> is obtained at 74.68 USD/y per kW of ChW, while the OCC<sub>EC</sub> is 64.65 USD/y per kW of ChW generation. This result shows that the EC is preferred as the waste heat chiller in this situation. The calculated assumes no appropriate condensing steam turbine could be used for this application, which charged 141,524 USD/y to the OCC<sub>EC</sub>. If the site has a proper condensing turbine to be used, the OCC<sub>EC</sub> would further reduce to a lower cost. However, the operating cost for cooling tower is highly depending on the water and

**Table 6**

Case 3 – Net Total Site energy requirement after LP steam turbine and Electric Chiller integration for entire chilled water load.

Energy type/level	Energy requirement (kW)	Condensing turbine requirements (kW)	EC energy requirements (kW)	AC energy requirements (kW)	Backpressure turbine energy requirements (kW)	Net energy requirement (kW)
Electricity	–1,831	–916	916	0	–1,008 <sup>a</sup>	–2,839
HPS	10,650	0	0	0	0	10,650
MPS	6,455	0	0	0	0	6,455
LPS	–5,535	5,535	0	3,044	0	3,044
CW	–30,850	–4,619	–3,755	–5,245	0	–44,469
ChW	–5,040	0	2,839	2,201	0	0

Positive value represents heat demand/deficit; negative value indicates heat excess/surplus/available at the respected temperature range.

<sup>a</sup> Additional turbine power generation for expanding the steam produced by boiler from VHP to LP level.**Table 7**

Case 4 – Net Total Site energy requirement after Absorption Chiller integration for entire chilled water load including recovery of LPS.

Energy type/level	Energy requirement (kW)	AC energy requirements (kW)	Backpressure turbine energy requirements (kW)	Net energy requirement (kW)
Electricity	–1,831	0	–344 <sup>a</sup>	–2,175
HPS	10,650	0	0	10,650
MPS	6,455	0	0	6,455
LPS	–5,535	6,971	0	1,436
CW	–30,850	–12,011	0	–42,861
ChW	–5,040	5,040	0	0

Positive value represents heat demand/deficit; negative value indicates heat excess/surplus/available at the respected temperature range.

<sup>a</sup> Additional turbine power generation for expanding the steam produced by boiler from VHP to LP level.**Table 8**

Case 5 – Net Total Site energy requirement after both absorption and electric chiller integration for entire chilled water load.

Energy type/level	Energy requirement (kW)	AC energy requirements (kW)	EC energy requirements (kW)	Net energy requirement (kW)
Electricity	–1,831	0	335	–1,490
HPS	10,650	0	0	10,650
MPS	6,455	0	0	6,455
LPS	–5,535	5,535	0	0
CW	–30,850	–9,537	–1,373	–41,760
ChW	–5,040	4,002	1,038	0

Positive value represents heat demand/deficit; negative value indicates heat excess/surplus/available at the respected temperature range.

electricity price. AC unit could be preferred when the CW price is lower than 16.87 USD/kW y.

The heat excess in LPS level can be partially recovered as electricity through a steam turbine for operating the EC (Case 2). Assuming a condensing steam turbine is used in the EC system, the turbine is estimated to generate 916 kW<sub>e</sub> of electricity by the 5.5 MW of excess LPS supplied, which is equivalent to a turbine isentropic efficiency of 70%. The net electricity demand of the chiller system from the electricity grid reduces to 710 kW<sub>e</sub>, which increases the site's overall operating cost. However, the condenser in the condensing turbine requires CW to maintain the low pressure at the exhaust of the turbine. The net CW demand for cooling the excess heat sources increases from 37.5 MW to 42.1 MW (4.6 MW), as recorded in Table 5. The OCC<sub>EC</sub> for the supplementary chiller in this case is determined as 233.28 USD/kW y. Combining with the waste heat operated EC (OCC<sub>EC</sub> = 64.65 USD/kW y), the overall OCC in this system configuration is found at 138.28 USD/kW y.

Besides supplying electricity from grid to the EC, the supplementary chiller can be an AC unit with a backpressure turbine to generate 2.2 MW of ChW (Case 3), which increases the load of the boiler by 1.94 kg/s of VHP steam generation. Backpressure turbine recovers the work potential of the steam generated between the VHP and LP levels, which produce 1.0 MW<sub>e</sub>. The CW requirement increases by 7.0 MW from the base case (Case 1 – 37.5 MW), while the total hot utility requirements increase by 3.0 MW. The supplementary chilling system is found to work with OCC<sub>AC</sub> of 353.72 USD/kW y, which the overall chilling system operates at 190.87 USD/kW y of ChW generated. Although the electricity generated could be sold for profit, this option might not be economical due to more boiler fuel consumed. In addition, this option involves drastic increment in turbine and boiler capacities, which have high possibility for new equipment installation.

One option is to produce additional boiler steam so that the AC can deliver the entire ChW load (Case 4). The AC requires 7.0 MW of LPS supply to generate the ChW demand by the DCS. From the previous TS-PTA analysis, there are 5.5 MW LP waste heat from the integrated processes, which could be directly recovered to the AC. The 'Net Utility Requirement' column suggests the integration of the ACs shifts the TS Pinch region from between the MPS and LPS headers to between the LPS and CW headers. The CW demand from the integrated process and the AC increases from 37.5 MW (Case 1) to 42.8 MW. To satisfy the new LPS demand, the site boiler is assumed to increase the production of VHP steam by 0.66 kg/s. The marginal increase in power generation potential between VHP and LP levels is estimated to be 309 kW<sub>e</sub>, through a backpressure steam turbine. Overall this option increases the total hot utility requirement by 1.4 MW and CW demands by 5.3 MW, as well as generates additional electricity. The annualized unit operating and capital cost (OCC<sub>AC</sub>) for the supplementary chiller and backpressure turbine is found to be 299.76 USD/kW y. The overall annualized unit cost for ChW generation using this system is 121.03 USD/kW y. The capital cost for backpressure turbine is accounted in this option. The cost would be reduced if the existing cogeneration turbine on-site has sufficient capacity to handle this load.

The final option for generating the required ChW for DCS, Case 5, assumes excess LPS from the process is available for use in an AC unit, while the remaining chilled water is satisfied by an EC. The amount of ChW production by the AC from the heat excess available in the TS system is estimated using Eq. (1). It is found that 4.0 MW of ChW could be produced using the 5.5 MW of LPS recovered from the processes. With the 4.0 MW of ChW generated from the AC, the remaining ChW demand of 1.0 MW should be satisfied by ECs, which requires 335 kW<sub>e</sub> of electricity. The OCC<sub>EC</sub> for the

supplementary chiller is found to be 270.99 USD/kW y, while the overall system OCC is resulted at 115.10 USD/kW y. The installation of a waste heat AC, in combination with the EC, increases the CW utility demand from 37.5 MW in Case 1 to 41.8 MW (3.3 MW). In this option, AC fully utilises the waste heat to satisfy the ChW demand partially. Based on the assumptions in this case study, the AC unit is preferred to be the supplementary ChW generator when the electricity-steam price ratio is larger than 3.1. Similar to the previous analysis, the price ratio is assumed to be 3, which implies an EC unit should be used to satisfy the remaining ChW load, i.e. Route 5, which requires additional electricity supply.

The system configuration determination is highly dependent on the availability of waste heat, electricity price and fuel price. It is significant for the electricity price fluctuation when the OCC<sub>AC</sub> and OCC<sub>EC</sub> considers the electricity consumption in Options 2 and 5, as well as the electricity generation potential for the LP condensing steam turbine in Options 3, 4 and 5. Based on the system condition assumed in this case study, the utility consumption for the five considered options are summarised in Table 9. The ChW requirement for all cases are satisfied, while the waste heat at LP level from the process is utilised completely, which aligned to the objectives in this study.

#### 4.3. Discussion

Most of the cases have the boiler load because the motive of this work is to utilise the waste heat at below pinch to satisfy chilling requirement of the processes or (and) DCS system. The distributed heat requirement in Table 9 shows all the waste heat or heat excess from the integrated processes at LPS level is fully utilised in the chillers. Worth to mention that, the LP level in Cases 3 and 4 has consumed all the heat excess from the processes and loads as consumption. The boiler load increases in Cases 3 and 4 for satisfying the insufficient LP steam supply for the chiller system. The increment of boiler load represents the cogeneration potential of the system, which could generate electricity for profit. However, the awareness on the capacity of the existing boiler and turbine is needed for reducing the capital cost involves in the project.

For cooling tower load, the CW consumption of the system depends on the ChW generation strategy selected for the system. Case 1 requires the lowest amount of CW because the excess LPS is vented to atmosphere and only increased for the CW demand from the EC unit. The differences in the CW loads for Cases 2–5 arise from the amount of additional energy input (e.g. electricity use, boiler fuel consumption) to and output (e.g. power production) from the system. The best option of integration is very much

**Table 9**  
Summary of utility consumptions and unit costs for the integrated TS and DCS.

	Industry only	Case 1 (EC + vent)	Case 2 (EC)	Case 3 (EC + AC)	Case 4 (AC)	Case 5 (AC + EC)
<i>Utility requirements (kW)</i>						
Electricity	-1,831	-205	-1,121	-2,839	-2,175	-1,490
Hot utility load	17,105	17,105	17,105	20,149	18,541	17,105
Cooling tower load	30,850	37,516	42,135	44,469	42,861	41,760
<i>Distributed heat requirements (kW)</i>						
HPS	10,650	10,650	10,650	10,650	10,650	10,650
MPS	6,455	6,455	6,455	6,455	6,455	6,455
LPS	-5,535	0	0	3,044	1,436	0
CW	-30,850	-37,516	-42,135	-44,469	-42,861	-41,760
ChW	0	0	0	0	0	0
<i>Unit cost (OCC) of ChW generation (USD/kW y)</i>						
Waste heat chiller	-	-	64.65	64.65	74.68	74.68
Supplementary chiller	-	270.91	270.77	353.72	299.76	270.99
Overall	-	270.91	154.65	190.87	121.03	115.10

depending on the energy availability in the system, equipment performance and the utilities (e.g. fuel and electricity) price.

In general, waste heat chiller has much lower OCC compared to supplementary chiller, which consumes electricity or boiler fuel. The OCC for ChW generation using waste heat operated AC is slightly higher than the EC system. It can be noted that the supplementary chiller using EC with electricity supplied from grid has OCC at about 270.9 USD/kW y. The exact values deviate slightly according to the capacity and the condition of the system. The AC based supplementary chillers have higher OCC due to the high fuel price and capital cost on the turbine.

Based on the operating and capital cost (OCC) per unit of ChW generated, the combination of waste heat-operated AC and grid electricity-supplied EC is favourable as the cost-effective ChW generation system configuration in this case study. The ChW load in waste heat chiller is much higher for Cases 4 and 5, which has much lower OCC compared to the supplementary chiller. As a result, the overall OCC deviates towards the waste heat-operated AC system in Cases 4 and 5. The OCC for Cases 4 and 5 with waste heat-operated AC system is still lower compared to others due to the big gap between the OCC for waste heat and supplementary chillers. However, the OCC would change when there is any new equipment installation is avoided in the project, which might change the competitiveness of certain configurations.

## 5. Conclusion

An effective methodology for the design of chilled water generation systems using waste heat-driven Absorption Chillers (AC) and Electric Chillers (EC) in TS systems has been successfully demonstrated using an illustrative case study. For the case study, there is insufficient waste LPS heat for an AC to supply all the Chilled Water (ChW) needs for a District Cooling Service (DCS). Four different options for ChW generation are compared to the base case where the DCS and the industrial processes are not integrated. Options for using the waste LPS for generation of ChW include conversion to electricity using condensing steam turbines to supply on-site ECs or direct use in ACs. For the case study, the lowest cost solution used a waste-heat driven AC to supply 4.0 MW of ChW and a supplementary EC to supply the remaining 1.0 MW.

Energy/heat targeting methodology (i.e. Pinch Analysis) serves as one of the component in feasibility study, for assessing the thermodynamic feasibility and benefits of a technology towards the existing system. More implementation issues should be explored for the integration of DCS into an industrial TS system, similar to the work published by Chew et al. [4]. For example, the energy losses and pressure drops due to the distance between the waste heat sources and the DCS, as well as operational issue on the integration.

## Acknowledgements

This work received the financial support from the Universiti Teknologi Malaysia (UTM) research university grant No Q.J130000.21A2.02E33 and Faculty of Information Technology and Bionics, Pázmány Péter Catholic University in Budapest. The research funding provided is highly appreciated by the authors.

## References

- [1] Klemeš J. Handbook of Process Integration (PI): minimisation of energy and water use, waste and emissions. Cambridge, UK: Woodhead/Elsevier; 2013.
- [2] Dhole VR, Linnhoff B. Total site targets for fuel, co-generation, emissions, and cooling. *Comput Chem Eng* 1993;17(1):S101–9.
- [3] Raissi K. Total site integration. Manchester, UK: UMIST – University of Manchester Institute of Science and Technology; 1994.
- [4] Chew KH, Klemeš JJ, Wan Alwi SR, Manan Z Abdul. Industrial implementation issues of Total Site Heat Integration. *Appl Therm Eng* 2013;61(1):17–25.
- [5] Klemeš JJ, Kravanja Z. Forty years of heat integration: pinch analysis (PA) and mathematical programming (MP). *Curr Opin Chem Eng* 2013;2(4):461–74.
- [6] Feng X, Pu J, Yang J, Chu KH. Energy recovery in petrochemical complexes through heat integration retrofit analysis. *Appl Energy* 2011;88(5):1965–82.
- [7] Klemeš J, Dhole VR, Raissi K, Perry SJ, Puigjaner L. Targeting and design methodology for reduction of fuel, power and CO<sub>2</sub> on total sites. *Appl Therm Eng* 1997;17(8–10):993–1003.
- [8] Liew PY, Wan Alwi SR, Varbanov PS, Manan ZA, Klemeš JJ. A numerical technique for Total Site sensitivity analysis. *Appl Therm Eng* 2012;40:397–408.
- [9] Varbanov PS, Fodor Z, Klemeš JJ. Total site targeting with process specific minimum temperature difference ( $\Delta T_{min}$ ). *Energy* 2012;44(1):20–8.
- [10] Liew PY, Wan Alwi SR, Klemeš JJ, Varbanov PS, Manan ZA. Utility-heat exchanger grid diagram: a tool for designing the total site heat exchanger network. *Chem Eng Trans* 2014;39:7–12.
- [11] Liew PY, Wan Alwi SR, Lim JS, Varbanov PS, Klemeš JJ, Abdul Manan Z. Total Site Heat Integration incorporating the water sensible heat. *J Cleaner Prod* 2014;77:94–104.
- [12] Sun L, Doyle S, Smith R. Heat recovery and power targeting in utility systems. *Energy* 2015;84:196–206.
- [13] Chew KH, Klemeš JJ, Wan Alwi SR, Abdul Manan Z, Reverberi AP. Total site heat integration considering pressure drops. *Energies* 2015;8(2):1114–37.
- [14] Matsuda K, Hirochi Y, Tatsumi H, Shire T. Applying heat integration total site based pinch technology to a large industrial area in Japan to further improve performance of highly efficient process plants. *Energy* 2009;34(10):1687–92.
- [15] Walmsley TG, Walmsley MRW, Atkins MJ, Neale JR. Integration of industrial solar and gaseous waste heat into heat recovery loops using constant and variable temperature storage. *Energy* 2014;75:53–67.
- [16] Hackl R, Harvey S. From heat integration targets toward implementation – a TSA (total site analysis)-based design approach for heat recovery systems in industrial clusters. *Energy* 2015;90(1):163–72.
- [17] Liew PY, Lim JS, Wan Alwi SR, Abdul Manan Z, Varbanov PS, Klemeš JJ. A retrofit framework for Total Site heat recovery systems. *Appl Energy* 2014;135:778–90.
- [18] Liew PY, Wan Alwi SR, Varbanov PS, Manan ZA, Klemeš JJ. Centralised utility system planning for a Total Site Heat Integration network. *Comput Chem Eng* 2013;57:104–11.
- [19] Chew KH, Klemeš JJ, Wan Alwi SR, Manan ZA. Process modification of Total Site Heat Integration profile for capital cost reduction. *Appl Therm Eng* 2015;89:1023–32.
- [20] Yong JY, Varbanov PS, Klemeš JJ. Heat exchanger network retrofit supported by extended Grid Diagram and heat path development. *Appl Therm Eng* 2015;89:1033–45.
- [21] Nemet A, Klemeš J, Varbanov P, Mantelli V. Heat integration retrofit analysis—an oil refinery case study by Retrofit Tracing Grid Diagram. *Front Chem Sci Eng* 2015;9(2):163–82.
- [22] Bandyopadhyay S, Varghese J, Bansal V. Targeting for cogeneration potential through total site integration. *Appl Therm Eng* 2010;30(1):6–14.
- [23] Mavromatis SP, Kokossis AC. Conceptual optimisation of utility networks for operational variations—I. Targets and level optimisation. *Chem Eng Sci* 1998;53(8):1585–608.
- [24] Broberg Viklund S, Karlsson M. Industrial excess heat use: systems analysis and CO<sub>2</sub> emissions reduction. *Appl Energy* 2015;152:189–97.
- [25] Kwak D-H, Binns M, Kim J-K. Integrated design and optimization of technologies for utilizing low grade heat in process industries. *Appl Energy* 2014;131:307–22.
- [26] Perry S, Klemeš J, Bulatov I. Integrating waste and renewable energy to reduce the carbon footprint of locally integrated energy sectors. *Energy* 2008;33(10):1489–97.
- [27] Eriksson L, Morandin M, Harvey S. Targeting capital cost of excess heat collection systems in complex industrial sites for district heating applications. *Energy* 2015;91:465–78.
- [28] Varbanov PS, Klemeš JJ. Integration and management of renewables into Total Sites with variable supply and demand. *Comput Chem Eng* 2011;35(9):1815–26.
- [29] Bagajewicz MJ, Barbaro AF. On the use of heat pumps in total site heat integration. *Comput Chem Eng* 2003;27(11):1707–19.
- [30] Desai NB, Bandyopadhyay S. Process integration of organic Rankine cycle. *Energy* 2009;34(10):1674–86.
- [31] Rahimi B, Christ A, Regenauer-Lieb K, Chua HT. A novel process for low grade heat driven desalination. *Desalination* 2014;351:202–12.
- [32] Miah JH, Griffiths A, McNeill R, Poonaji I, Martin R, Leiser A, et al. Maximising the recovery of low grade heat: an integrated heat integration framework incorporating heat pump intervention for simple and complex factories. *Appl Energy* 2015;160:172–84.
- [33] Oluleye G, Jobson M, Smith R, Perry SJ. Evaluating the potential of process sites for waste heat recovery. *Appl Energy* 2015;161:627–46.
- [34] Hackl R, Harvey S. Framework methodology for increased energy efficiency and renewable feedstock integration in industrial clusters. *Appl Energy* 2013;112:1500–9.
- [35] IEA. SouthEast Asia energy outlook: world energy outlook special report. Paris, France: International Energy Agency (IEA); 2013.
- [36] CETDEM. Creating awareness on issues related to climate change, energy usage and transport in Kajang and Petaling Jaya (CACCT) Available from:

- <cetdem.org.my/wordpress/?page\_id=2763>2007 (Retrieved 31 October, 2015).
- [37] Somers C, Mortazavi A, Hwang Y, Radermacher R, Rodgers P, Al-Hashimi S. Modeling water/lithium bromide absorption chillers in ASPEN plus. *Appl Energy* 2011;88(11):4197–205.
- [38] Hong D, Tang L, He Y, Chen G. A novel absorption refrigeration cycle. *Appl Therm Eng* 2010;30(14–15):2045–50.
- [39] Saidur R. Energy consumption, energy savings, and emission analysis in Malaysian office buildings. *Energy Pol* 2009;37(10):4104–13.
- [40] Gang W, Wang S, Xiao F, Gao D-c. District cooling systems: technology integration, system optimization, challenges and opportunities for applications. *Renew Sustain Energy Rev* 2016;53:253–64.
- [41] Calm JM. The next generation of refrigerants – historical review, considerations, and outlook. *Int J Refrig* 2008;31(7):1123–33.
- [42] Jaruwongwittaya T, Chen G. A review: renewable energy with absorption chillers in Thailand. *Renew Sustain Energy Rev* 2010;14(5):1437–44.
- [43] New Buildings Institute. Absorption chiller guideline. California, US: New Buildings Institute; 1998.
- [44] Liew PY, Wan Alwi SR, Klemeš JJ, Varbanov PS, Abdul Manan Z. Algorithmic targeting for Total Site Heat Integration with variable energy supply/demand. *Appl Therm Eng* 2014;70(2):1073–83.
- [45] Linnhoff B, Vredeveld DR. Pinch technology has come of age. *Chem Eng Prog* 1984;80(7):33–40.



**Article 9:**

*A Total Site Heat Integration design method for integrated evaporation systems including vapour recompression*

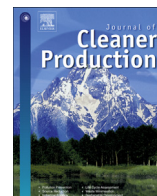
**Walmsley, T.G.**, 2016.

Journal of Cleaner Production 136, Part B, 111–118.

DOI: 10.1016/j.jclepro.2016.06.044

Citations: 7

Elsevier



# A Total Site Heat Integration design method for integrated evaporation systems including vapour recompression



Timothy G. Walmsley

University of Waikato, Energy Research Centre, School of Engineering, Hamilton, New Zealand

## ARTICLE INFO

### Article history:

Received 23 February 2016

Received in revised form

3 June 2016

Accepted 7 June 2016

Available online 16 June 2016

### Keywords:

Process integration

Pinch analysis

Total Site Heat Integration

Evaporation systems

Vapour recompression

Milk processing

## ABSTRACT

This paper presents a new Total Site Heat Integration (TSHI) method for the design of integrated evaporation systems including vapour recompression that minimises energy use and/or cost objective functions. The design of integrated evaporation systems is a common industrial chemical and process engineering problem. The method defines a new hybrid Total Site Profile (TSP) as a key element of the new design method. This profile is a composite of nearby streams that may directly integrate with the evaporation system as well as stream segments from processes that require indirect integration via the utility system. The hybrid TSP plays an important role in the iterative optimisation of evaporation system design parameters including vapour recompression and evaporation load distribution to optimise objective functions such as total cost, total operating cost, and heat recovery. The new TSHI design method for evaporation systems is demonstrated using an industrial milk processing case study.

© 2016 Elsevier Ltd. All rights reserved.

## 1. Introduction

Evaporation systems are commonly needed to concentrate multi-component liquid solutions, suspensions, and emulsions in the food and dairy, pulp and paper, petrochemical, chemical, and pharmaceutical industries. Evaporation systems normally achieve high levels of energy recovery by optimally cascading heat using various multi-effect arrangements (Khanam and Mohanty, 2010) as well as heat integration of evaporation/condensation loads with the heating and cooling needs of other processes (Smith, 2005). Integration of evaporation systems with vapour recompression technologies is a different approach for attaining high levels of energy efficiency, without increasing the number effects. The concept of vapour recompression in evaporation systems is to upgrade low-pressure vapour from an effect's evaporation-side to a higher temperature and pressure for re-injection on the condensation-side of the same or another effect. Mechanical Vapour Recompression (MVR) uses a blower to lift the pressure and temperature of a vapour flow. Thermal Vapour Recompression (TVR) uses a thermo-compressor in conjunction with steam injection for vapour recompression. Of the two techniques, a MVR blower requires higher capital investment, but can greatly reduce

the number of effects and lowering overall energy use and operational cost (Hanneman and Robertson, 2005).

The field of Process Integration (PI) contains systematic methods, such as Pinch Analysis (PA), that can identify cleaner production solutions that minimise energy consumption of individual unit operations and processing sites (Dunn and Bush, 2001). PA, together with Total Site Heat Integration (TSHI) (Liew et al., 2014), are arguably the most universally applied PI techniques. With respect to evaporation systems, PA provides excellent visual tools, e.g. Composite Curves (CC) and the Grand Composite Curve (GCC), for understanding how an evaporation system can efficiently integrate with itself and with other processes on the same site, i.e. background processes (Linnhoff, 1998). Smith and Jones (1990) demonstrated that PA can form the basis for optimising the capital-energy trade-off during the process design and integration of multi-effect evaporation systems.

Westphalen and Wolf Maciel (2000) extended earlier methods to account for a fluid's changes in latent heat of vaporisation with temperature, to represent superheated and subcooled evaporator feeds on a temperature-enthalpy plot, and to optimise vapour bleed duties from each evaporator effect, which further minimised utility use, reduced the number of effects, and led to more favourable economics. Algehed and Berntsson (2003) looked at the TSHI of black liquor evaporators in the Kraft process by using medium-pressure steam and delivering some low-pressure steam back to

E-mail address: [timgw@waikato.ac.nz](mailto:timgw@waikato.ac.nz).

Nomenclature			
<i>Roman</i>		$\Delta$	difference between two states
CP	heat capacity at constant pressure (kJ/[kg °C])	$\eta_o$	compressor efficiency
C	concentration (kg/kg)	<i>Subscripts and Superscripts</i>	
CC	heat exchanger capital cost (\$)	*	shifted
<i>h</i>	specific enthalpy (kJ/kg)	<i>bleed</i>	vapour bleed
<i>k</i>	ratio of specific heats	<i>cond</i>	condensation/condenser
$\dot{m}$	mass flow rate (kg/s)	<i>cont</i>	contribution
<i>P</i>	pressure (kPa)	<i>eva</i>	evaporation
PR	thermo-compressor performance ratio (kg <sub>vap</sub> /kg <sub>steam</sub> )	<i>exit</i>	exit stream
<i>Q</i>	duty (kW)	<i>feed</i>	feed stream
<i>R</i>	gas constant (kJ/[kg K])	<i>fg</i>	fluid-vapour phase change
<i>T</i>	temperature (°C)	<i>l</i>	liquid
TC	total cost (\$/y)	<i>min</i>	minimum
TCC	total capital cost (\$/y)	<i>P1</i>	low pressure
TOC	total operating cost (\$/y)	<i>P2</i>	high pressure
$W_{comp}$	work of compression (kW)	<i>s</i>	supply
<i>Greek</i>		<i>st</i>	steam
$\alpha$	mass fraction of vapour upgraded	<i>t</i>	target
		<i>upg</i>	upgraded low pressure vapour
		<i>ut</i>	utility
		<i>v</i>	vapour

the steam utility system. Walmsley et al. (2016) applied similar PA techniques as Westphalen and Wolf Maciel (2000) in the analysis and possible retro-fit of existing milk evaporation systems that included vapour recompression.

A methodological gap that exists in PA and TSHI literature is a method for targeting and designing an integrated evaporation system where the background process GCC represents opportunities for both direct process–process and indirect process-utility integration. Past studies on integrated evaporation system design have focused on either direct process–process (Walmsley et al., 2016) or indirect process-utility integration opportunities (Algehed and Berntsson, 2003), not both simultaneously. One reason for this gap is the lack of single background heat demand profile that represents both opportunities for direct and indirect integration. This paper seeks to fill this gap by detailing the construction of a hybrid Total Site Profile (TSP).

Recent studies have mostly applied mathematical programming techniques for the optimisation of multi-effect evaporation systems. Druetta et al. (2014) optimised the design of a multi-effect evaporation system for seawater desalination using non-linear mathematical programming techniques. Galván-Ángeles et al. (2015) explored the design and cost trade-offs of integrating TVR into a multi-effect food evaporation system using mixed-integer non-linear optimisation. Han et al. (2015) applied the concept of self-heat recuperation theory in the design of single and multi-stage MVR evaporation systems for concentrating solutions with significant boiling point elevation.

The aim of this study is to develop a new TSHI method for the design of integrated evaporation systems including vapour recompression that minimises energy use and/or cost. This is achieved by maximising both direct process–process and indirect process-utility integration opportunities. The method uses a hybrid TSP as the basis for the new design method. This profile is a composite of streams nearby the evaporation system that may directly integrated as well as streams (or stream segments) from processes that require indirect integration via the utility system. The new profile plays an important role in helping identify how much the evaporation system can integrate across the site. It is also needed to

improve the selection of which vapour recompression technology or combination of vapour recompression technologies are best applied to minimise energy use and/or cost. The new TSHI design method for evaporation systems is demonstrated by an industrial milk processing case study.

## 2. Methodology

A new design method for evaporation systems including vapour recompression is presented in Fig. 1. The method includes calculation of utility, heat recovery, area, and cost targets. The method assumes that vapour recompression is a possible component of the evaporation system. The first half of the method (left-hand side of Fig. 1) details the construction of hybrid TSP, which represents the background processes including possibilities for direct and indirect heat integration with the evaporation system. The second half of the method (right-hand side of Fig. 1) is specific to evaporation systems that require vapour recompression and describes a simple iterative optimisation approach.

### 2.1. Construction of a hybrid Total Site Profile

The left-hand side of Fig. 1 presents the procedure for generating a hybrid TSP. Many of these steps are common to past PA and TSHI literature.

#### Step 1: Evaporation system specifications

Important specifications for the evaporation system include: the dilute feed and concentrate flow rates, temperatures, and concentrations. For new builds, the specification of the general inputs/outputs of the evaporation system enables the design of upstream and downstream processes and unit operations.

#### Step 2: Determine background process stream data

Stream data is extracted from each background process. The stream data includes heat capacity flow rates, supply and target

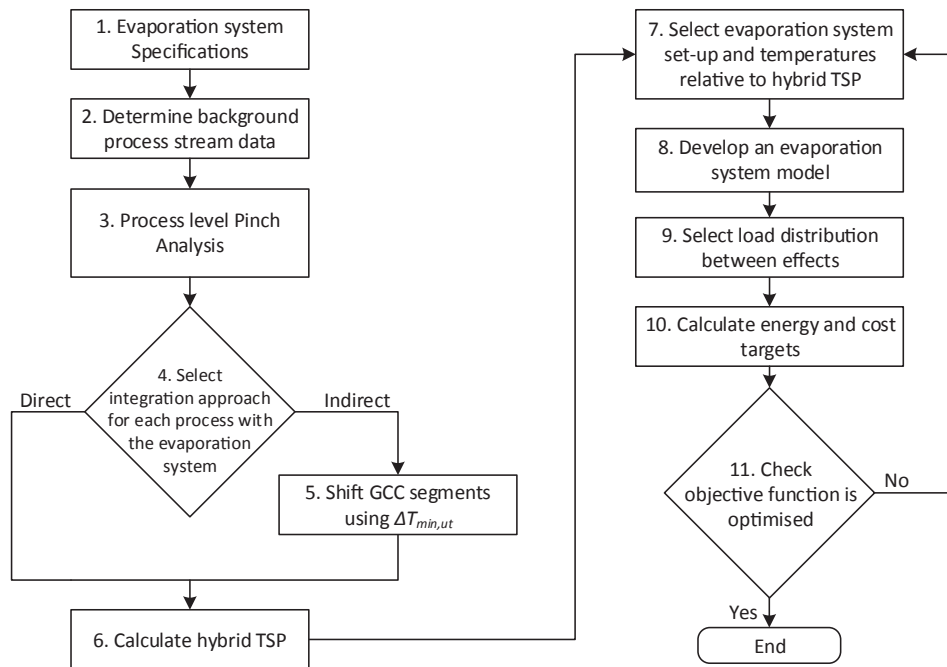


Fig. 1. Integrated evaporation system including vapour recompression design and optimisation method.

temperatures, duties, and contribution minimum approach temperatures ( $\Delta T_{cont,i}$ ) for each stream. The streams are organised by process.

Step 3: Perform process level Pinch Analysis for each process

For the process level PA, supply and target temperatures for each stream are shifted using

$$\text{Process level shift} \begin{cases} T^* = T_i - \Delta T_{cont,i} \in \text{hot process streams} \\ T^* = T_i + \Delta T_{cont,i} \in \text{cold process streams} \end{cases} \quad (1)$$

$$\text{Total Site utility system shift} \begin{cases} T_{evap}^* = T^* - \Delta T_{min,ut} \in \text{hot process streams} \\ T_{evap}^* = T^* + \Delta T_{min,ut} \in \text{cold process streams} \end{cases} \quad (2)$$

The process level PA (Klemeš, 2013) targets the amount of heat recovery within a process as well as the amount of external heating and cooling that is required. A key output from this step is the process GCCs. For existing sites and processes that are considered state-of-the-art, the stream segments heated or cooled by external utility may be composited to effectively form the actual GCC of a process.

Step 4: Select integration approach for each process with the evaporation system

Engineering judgement is applied to decide how each process integrates with the evaporation system. Processes physically nearby the location of the evaporation are good candidates for direct process–process integration. Processes distant from the

evaporation system are best indirectly integration via the utility system using the conventional Total Site approach.

Step 5: Shift GCC segments using  $\Delta T_{min,ut}$

If a process requires indirect heat integration, a second stream temperature shift is needed to account for the intermediate utility that indirectly exchanges heat with the evaporation system. GCC segments requiring indirect integration apply

Step 6: Calculate hybrid TSP

With all process GCC segments on the same temperature scale as the evaporation system, i.e.  $T_{evap}^*$ , individual process GCC segments may be composited using the Total Site Problem Table Algorithm (Klemeš, 2013) into a hybrid TSP. The hybrid TSP differs from the conventional TSP in that it contains stream segments that may be directly integrated with an external operation, which in this case is an evaporation system. A similar approach can also apply to the integrated design of other unit operations and processes.

## 2.2. Evaporation system including vapour recompression design optimisation

The next part of the methodology is specific to integration

optimisation of evaporation systems that include vapour recompression systems. The design method assumes vapour recompression will be required in the evaporation. The inherent assumption of the method and its application is the required evaporation load is an order of magnitude greater than the heating and cooling needs of the background processes within the temperature range of interest for the evaporation system.

Step 7: Select evaporation system set-up and temperatures relative to hybrid TSP

Depending on the desired evaporation temperatures, the evaporation system may be a source for the hybrid Site Sink Profile, a sink for the hybrid Site Source Profile or both a sink and a source that fits in between the two profiles. This is analogous to previous design methods where multi-effect evaporation systems are ideally integrated so that the system fits either above the Pinch as a source, below the Pinch as a sink, or inside a heat recovery pocket of the background processes, in such a way that no extra utility is needed beyond the demands of the background processes (Feng and Smith, 2001).

The most basic set-up of an evaporation system with vapour recompression is a two-effect system, with the first effect integrated using MVR and the second effect integrated using TVR. It is recommended to select a set-up with both MVR and TVR integrated effects where the MVR integrated effect(s) operate at higher temperatures than the TVR integrated effect(s). This is due to TVR units, which are a type of steam ejector, achieving higher efficiencies at lower pressures (El-Dessouky et al., 2002).

For liquids with boiling point elevation ( $>5\text{ }^{\circ}\text{C}$ ), the needed saturation temperature lift ( $>10\text{ }^{\circ}\text{C}$ ) normally require two or more MVR blowers in series. Conventional compressors with much higher compression ratios are not normally used in vapour recompression situations. This is because the vapour is likely to carry entrained droplets, which would damage the compressor. TVR integrated effects benefit from multi-effect arrangements where heat is cascaded through multiple effects before being recompressed using high pressure steam and injected in the condensing side of a higher pressure effect.

Step 8: Develop an evaporation system model

This step involves using computer software such as Excel or process simulation packages, to model the evaporation system set-up, which can then be used to determine the heat demands of the evaporation system. In general effects integrated with vapour recompression are a net heat source for the background processes (Walmsley et al., 2015). In this study, Excel is applied as the platform for constructing a mass and energy balance model of a two-effect evaporation system with MVR and TVR.

Step 9: Select load distribution between effects

In the first instance, the load distribution between MVR and TVR integrated effects may be selected based on experience with similar applications or arbitrarily chosen since this will be optimised. If there are multiple effects integrated with TVR, then the load may be for the entire train.

For successive iterations, if the evaporation system, after integration with the hybrid TSP, remains a net heat source, i.e. requires cooling utility, then some evaporation load should be transferred from the TVR integrated effect(s) to the MVR integrated effect(s). If the evaporation system is a net heat sink, then load is shifted from the MVR integrated effect(s) to the TVR integrated effect(s).

Step 10: Calculate energy and cost targets

The heat demand profile evaporation (excluding the energy inputs of the MVR and TVR units) are graphically pinched against the hybrid TSP to target heat recovery and determined overall utility use and cost. Energy targets and total operating energy cost (TOC) may be calculated using the resultant utility inputs for the evaporation system and the background processes. Area targets for heat transfer between the evaporation system and the background process may be calculated using the BATH formula, from which an estimate for the total capital cost (TCC) including the capital cost of the various vapour recompression units may be determined (Smith, 2005). The total cost,  $TC$ , of the evaporation system is the summation of  $TCC$  and  $TOC$ .

It is important to note that the exclusion of condensate streams from the background heat demand profile is a point of difference between this study and previous studies (Westphalen and Wolf Maciel, 2000). Without integrated vapour recompression in the evaporation system, the recoverable heat from condensate streams is typically very small compared condenser and vapour bleed duties. As a result, the optimisation of condensate stream temperatures could only achieve insignificant benefits. However, once vapour recompression is integrated, the duty of condensate streams becomes increasingly significant. For this study, the PA may be used to determine the target temperature of condensate streams that maximises heat recovery for a given evaporation system design and evaporation load distribution. The target temperature of condensate streams is normally soft because they are often a discharge stream (Walmsley et al., 2013).

Step 11: Check objective function is optimised

The objective cost function may be minimised by adjusting the evaporation system design and/or the distribution of the evaporation load within the system. In this study, both the  $TC$  and the  $TOC$  are used as objective functions. A system with the minimum energy use typically has two or more pinches between the evaporation system and the hybrid TSP or the load distribution has completed shifted to either the MVR or TVR integrated effect(s).

### 3. Integrated evaporation system with vapour recompression case study: milk evaporator

#### 3.1. Background information

An important dewatering stage in the milk powder production

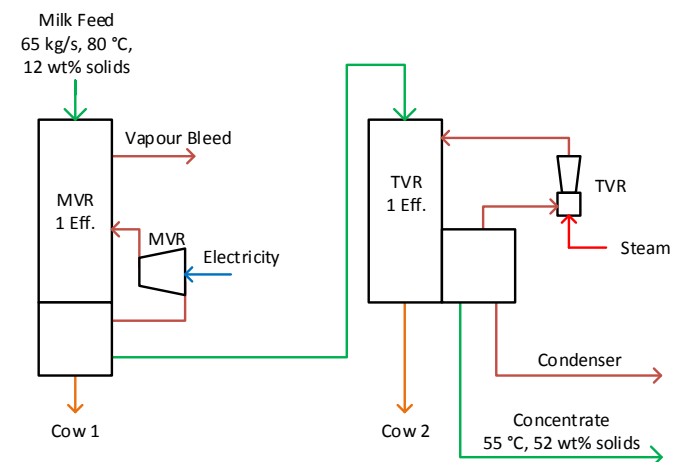


Fig. 2. Typical design of a two-effect milk evaporator system with MVR and TVR.

process is the evaporation system. In this process, a multi-train, multi-effect falling film evaporator system concentrates standardised milk from about 12% to 52% solids (Fig. 2). For continuous spray dryer operation, it is critical that there are multiple trains of evaporators. Each evaporator train is washed clean-in-place (CIP) about every 16 h to maintain food grade processing hygiene, whereas the spray dryer is washed every 2–4 weeks. The operating temperatures of the effects are an important industrial constraint, which restricts integration options. In the evaporation system design, the evaporation temperature of the first effect is limited to a maximum of 65 °C. Each effect has an approach temperature of 5 °C, which is common practice in industry (Walmsley et al., 2015). The evaporation system preceded by a Heat Treatment process (HT) and followed by the Spray Drying process (SD). Other background heat requirements include Site Hot Water (SHW), which is used for direct use applications such as equipment and tanker washing.

### 3.2. Stream and cost data

Stream data for the HT and SD processes and SHW utility are given in Table 1. The contribution minimum approach temperatures,  $\Delta T_{cont}$ , are selected based on the relative heat transfer resistances of different fluids. The HT process and SHW can directly integrate with the evaporation system due to the proximity with the evaporation system, whereas the SD process must indirectly integrate with the evaporation system using a  $\Delta T_{min,HW}$  of 10 °C for a hot water utility loop. The production rate of the plant is 30 t/h of milk powder and it operates for 6000 h/y. Utility prices in New Zealand dollars are \$30/MWh for steam utility, \$120/MWh for electricity, and \$5/MWh for cooling water.

Capital cost estimates in New Zealand dollars for the required heat exchanger (HE) area (including evaporator area), Eq. (3), have been based a correlation from Bouman et al. (2005). This original correlation for a shell and tube heat exchanger has been adjusted for cost index increases over time and multiplied by a Lang factor of 3.5. Capital cost correlations for MVR and TVR units are given in Eqs. (4) and (5) respectively. These correlations have been created based on the best available data from industry and literature (Bouman et al., 2005). Capital costs have been amortised over 10 y at a rate of 10%.

$$CC(HE) = 20,000 + 7,500 A^{0.57} \quad (3)$$

$$CC(MVR) = 17,000 W_{comp}^{0.7} \quad (4)$$

$$CC(TVR) = 680 Q_{ut,st}^{0.7} \quad (5)$$

**Table 1**  
Stream data for background processes. \*Concentrate  $T_s$  is dependent on the temperature of the final effect.

Process	Stream	$T_s$ (°C)	$T_r$ (°C)	CP (kW/°C)	$\Delta Q$ (kW)	$\Delta T_{cont}$ (°C)
HT	Cold milk	8	95	260	22,620	2.5
HT	Milk flash	80	80		-3900	2.5
SD	Concentrate	55*	80	49	1217	2.5
SD	Dryer airflow	10	210	120	24,000	10.0
SD	FB airflow	10	90	65	5200	10.0
SD	HVAC	10	25	50	750	10.0
SD	Dryer exhaust	75	55	204	-4070	10.0
SHW	Site hot water	15	70	21	1150	2.5

### 3.3. Evaporation system model

A heat and mass balance of the two-effect milk evaporator system with one MVR integrated effect and one TVR integrated effect has been implemented in an Excel™ spreadsheet to estimate the heat recovery opportunities from vapour bleed, condenser, and condensate streams. Standard water and steam properties (IAPWS IF-97) and milk properties (MAF Quality Management, 1996) are applied in the model. MVR blowers have an estimated overall efficiency of 70% based on actual performance in the dairy processing industry. Thermo-compressor performance has been modelled using the empirical correlation of Al-Juwayhel et al. (1997).

## 4. Results and discussion

### 4.1. Evaporator design with and without vapour recompression

The milk evaporator case study requires 117 MW of evaporation to remove 50 kg/s of water. If a conventional 4-effect evaporation system is installed, as shown in Fig. 3, the target heat integration between the evaporation system and the background processes is 18.4 MW. However, steam use increases by 9.6 MW beyond the requirements of the background processes, which is represented by the hybrid TSP, while the cold utility increases by 22.3 MW.

An integrated milk evaporation system including vapour recompression is presented in Fig. 4. The MVR effect operates at 65 °C on the tube-side and the TVR effect at 55 °C on the tube-side, both with approach temperatures of 5 °C. The evaporation load distribution between the MVR effect (92%) and TVR effect (8%) has been selected to minimise TOC. The heat recovery from the evaporation system to the background processes is 21.8 MW. The evaporation system requires 2.3 MW of electricity for MVR and 3.7 MW of steam for TVR. In this optimised system, two pinches are observed between the evaporation system and the background processes. The higher Pinch Temperature (67.5 °C) is driven by the shell-side temperature of the MVR effect. Increasing the operating temperature of the pinched effect opens options for improved overall integration between the evaporation system and background processes. The lower hot Pinch Temperature (13 °C) determines the discharge temperature of the condensate streams.

### 4.2. Minimum total operating energy cost design

Three load distribution options with their associated recoverable heat are compared against the hybrid TSP in Fig. 5. An

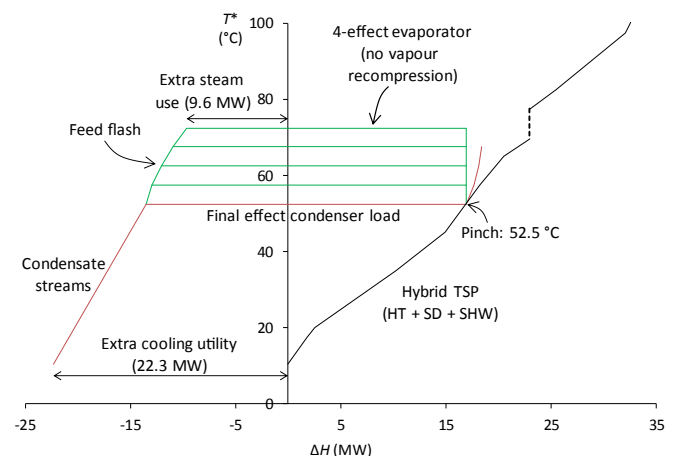


**Fig. 3.** Integrated 4-effect milk evaporator without vapour recompression.

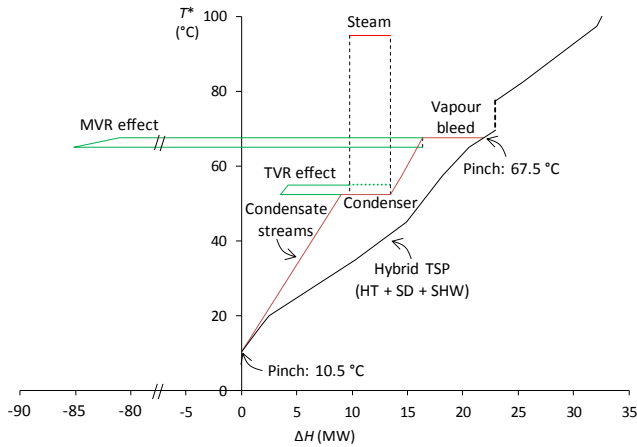


Fig. 4. Integrated 2-effect milk evaporator with MVR and TVR.

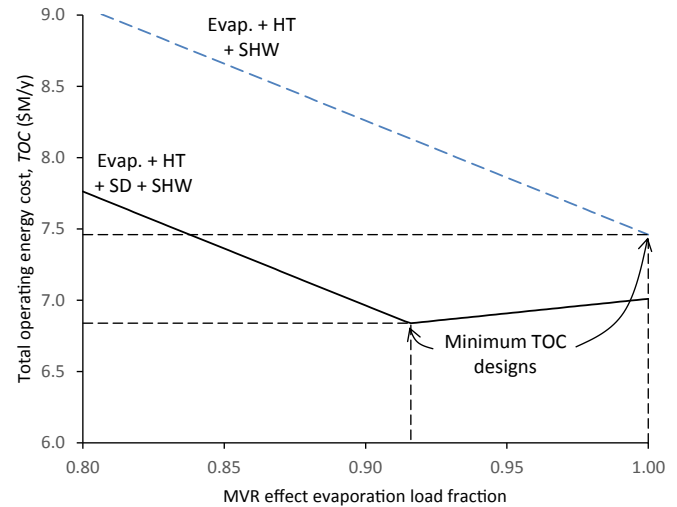


Fig. 6. Effect of evaporation load distribution on total operating cost.

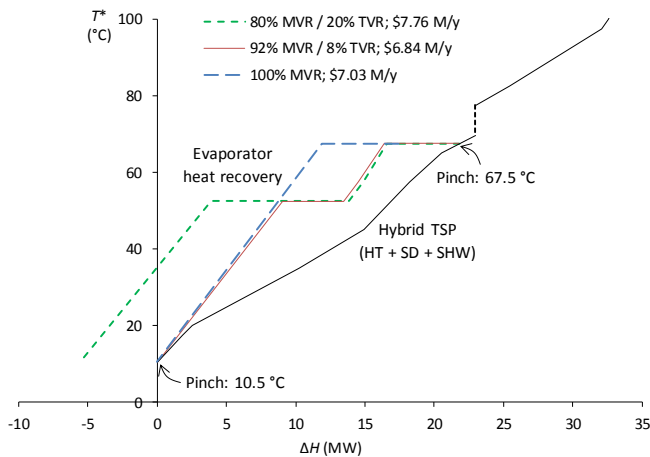


Fig. 5. Evaporation load distribution options and heat recovery for a two-effect milk evaporator system with MVR and TVR. Internal evaporator evaporation and condensation load with each effect is not shown.

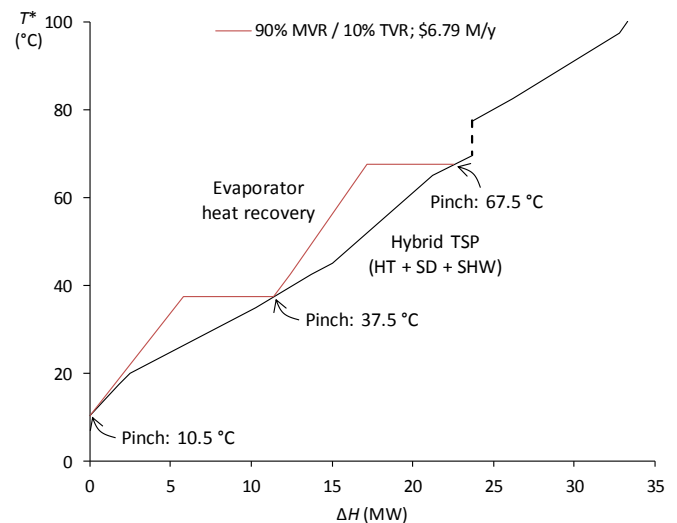


Fig. 7. Minimum energy design of a two-effect milk evaporator system with MVR and TVR.

evaporation loading of 80% MVR effect and 20% TVR effect results in a cold utility target of 5.5 MW. The targeted cold utility can be reduced by increasing the operating temperature of the MVR effect and/or eliminated by selecting a higher soft target temperature (35.2 °C) for condensate streams. Increasing the operating temperature of the MVR effect is not an option for the present case study because it is a process constraint, whereas reselecting the condensate target temperature does not maximise heat recovery nor minimise TOC. The addition of cold utility suggests some evaporation load can be shifted from the TVR effect to the MVR effect to reduce energy input and cost.

At the extreme, a single MVR effect can be used for concentrating milk as presented in Fig. 5. This system creates a Pinch at 10.5 °C with the background processes. In this case, there is an under-utilisation of the required steam for the background processes. The gap between the 100% MVR CC and the background GCC is 4.4 MW, which may be used in a TVR effect to reduce electricity input and, therefore, lower TOC.

The evaporation load distribution between the MVR effect and TVR effect may be optimised to obtain a minimum TOC solution (Fig. 6). For the given background processes, the optimum evaporation load distribution of 92% MVR effect and 8% TVR effect gives a TOC of NZ\$6.84 M/y. The system can be further optimised by lowering the operating temperature of the TVR effect to 40 °C,

which slightly reduces TOC (Fig. 7). This change causes a third Pinch to occur at 37.5 °C and marginally improves the performance of the thermo-compressor. The optimal evaporation load distribution shifts slightly towards such that the split is 90% MVR and 10% TVR. Optimising the operating temperature of the TVR reduces TOC by NZ\$0.05 M/y. However, the small energy cost savings come at the expense of increased capital cost due to reduced overall temperature driving force.

It is also useful to understand the impact that the hybrid TSP of the background processes has on the minimum energy evaporation system. For example, one may consider a stand-alone milk concentrate plant with no SD process. Removing the SD process from the background processes significantly reduces the amount of low temperature heat sinks. As a result, the optimal evaporation system solution only needs an MVR effect (Fig. 6). More generally, Fig. 8 shows how the optimal evaporation load distribution is affected by the amount of heat integration between the evaporation system and the background processes. For this case study, the minimum heat integration for an optimal evaporation system solution to include a TVR effect is 17.8 MW, which is equivalent to

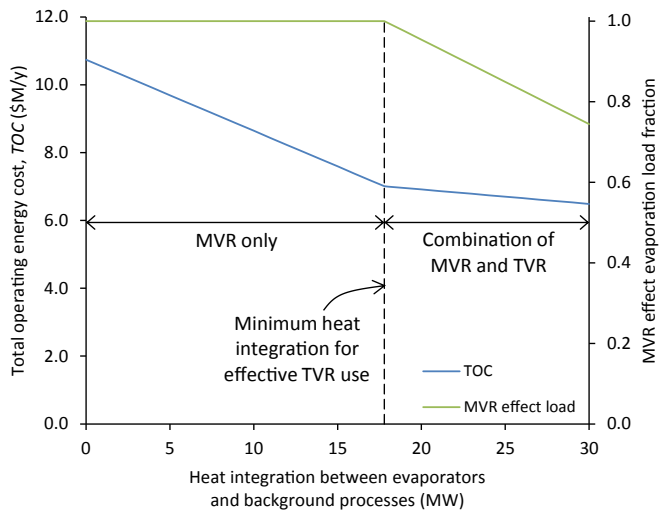


**Fig. 8.** Effect of heat integration between the evaporator system and the background processes on the optimal solution and the total operating cost.

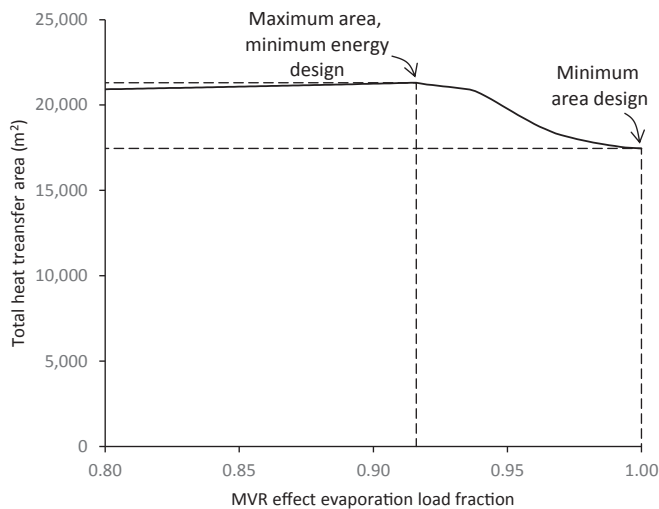


**Fig. 9.** Effect of evaporation load distribution on estimated heat transfer area.

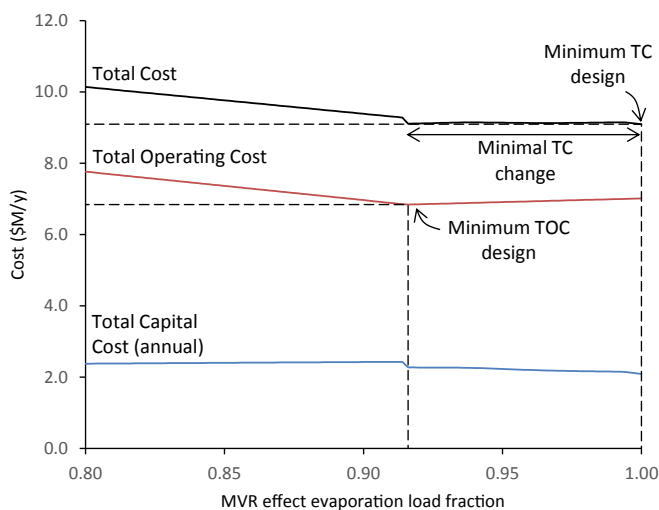


**Fig. 10.** Effect of evaporation load distribution on cost.

357 MJ/tevap. The minimum degree of heat integration can be lowered by increasing the number of effects in the TVR section, thereby improving its energy efficiency.

#### 4.3. Minimum total cost design

Ideally, an evaporation system minimises *TC*, rather than *TOC*. Fig. 9 presents heat transfer area estimates for a range of evaporation load distributions. As is often the case, the minimum energy design results in the maximum estimated area. Selecting an MVR evaporation load above the optimum reduces the amount of estimated area and *TCC* as shown in Fig. 10. For the *TCC* curve, the targeted number of heat exchangers causes a slight discontinuity around the minimum energy design. For evaporation load distributions above the minimum energy design, the increase in operating costs is offset by capital cost savings such that the *TC* curve is very flat. For the milk evaporator case study, the evaporation system with the lowest *TC* is one MVR effect.

## 5. Conclusions

A new design method for evaporation systems including vapour recompression is described and applied to optimise an industrial case study. The new method uses a new hybrid Total Site Profile, which includes opportunities for direct and indirect integration, to target heat recovery and total utility use. The new method helps design minimum energy and cost solutions using vapour recompression technologies. In milk evaporation system case study, the minimum energy solution requires a combination of Mechanical Vapour Recompression (MVR) and Thermal Vapour Recompression, whereas the minimum total cost solution only requires MVR. The method is most valuable for the design of integrated evaporation systems that sit above the Pinch Temperature of the background processes.

## References

- Al-Juwayhel, F., El-Dessouky, H., Ettouney, H., 1997. Analysis of single-effect evaporator desalination systems combined with vapor compression heat pumps. *Desalination* 114, 253–275. [http://dx.doi.org/10.1016/S0011-9164\(98\)00017-4](http://dx.doi.org/10.1016/S0011-9164(98)00017-4).
- Algehed, J., Berntsson, T., 2003. Evaporation of black liquor and wastewater using medium-pressure steam: simulation and economic evaluation of novel designs. *Appl. Therm. Eng.* 23, 481–495. [http://dx.doi.org/10.1016/S1359-4311\(02\)00197-7](http://dx.doi.org/10.1016/S1359-4311(02)00197-7).
- Bouman, R.W., Jensen, S.B., Wake, M.L., Earl, W.B., 2005. *Process Capital Cost Estimation for New Zealand 2004*. Society of Chemical Engineers New Zealand, Wellington, New Zealand.
- Druetta, P., Aguirre, P., Mussati, S., 2014. Minimizing the total cost of multi effect evaporation systems for seawater desalination. *Desalination* 344, 431–445. <http://dx.doi.org/10.1016/j.desal.2014.04.007>.
- Dunn, R.F., Bush, G.E., 2001. Using process integration technology for CLEANER production. *J. Clean. Prod.* 9, 1–23. [http://dx.doi.org/10.1016/S0959-6526\(00\)00021-4](http://dx.doi.org/10.1016/S0959-6526(00)00021-4).
- El-Dessouky, H., Ettouney, H., Alatiqi, I., Al-Nuwaibit, G., 2002. Evaluation of steam jet ejectors. *Chem. Eng. Process. Process Intensif.* 41, 551–561. [http://dx.doi.org/10.1016/S0255-2701\(01\)00176-3](http://dx.doi.org/10.1016/S0255-2701(01)00176-3).
- Feng, X., Smith, R., 2001. Case studies of heat integration of evaporation systems. *Chin. J. Chem. Eng.* 9, 224–227.
- Galván-Ángeles, E., Díaz-Ovalle, C.O., González-Alatorre, G., Castrejón-González, E.O., Vázquez-Román, R., 2015. Effect of thermo-compression on the design and performance of falling-film multi-effect evaporator. *Food Bioprod. Process.* 96, 65–77. <http://dx.doi.org/10.1016/j.fbp.2015.07.004>.
- Han, D., Yue, C., He, W., Liang, L., Pu, W., 2015. Energy saving analysis for a solution evaporation system with high boiling point elevation based on self-heat recuperation theory. *Desalination* 355, 197–203. <http://dx.doi.org/10.1016/j.desal.2014.10.044>.
- Hanneman, H., Robertson, L.J., 2005. *Heat Recovery Systems*, in: *Energy Use Dairy Process*. International Dairy Federation, Brussels, Belgium.
- Khanam, S., Mohanty, B., 2010. Energy reduction schemes for multiple effect evaporator systems. *Appl. Energy* 87, 1102–1111. <http://dx.doi.org/10.1016/j.apenergy.2009.05.003>.
- Klemeš, J.J. (Ed.), 2013. *Handbook of Process Integration: Minimisation of Energy and Water Use, Waste and Emissions*. Woodhead Publishing, Cambridge, UK.

- Liew, P.Y., Wan Alwi, S.R., Lim, J.S., Varbanov, P.S., Klemeš, J.J., Abdul Manan, Z., 2014. Total Site Heat Integration incorporating the water sensible heat. *J. Clean. Prod.* 77, 94–104. <http://dx.doi.org/10.1016/j.jclepro.2013.12.047>.
- Linnhoff, B., 1998. *Introduction to Pinch Technology*. Linnhoff March, Northwich, UK.
- MAF Quality Management, 1996. *Physical Properties of Dairy Products*, third ed. MAF Quality Management, Hamilton, New Zealand.
- Smith, R., 2005. *Chemical Process Design and Integration*. John Wiley and Sons, New York, USA.
- Smith, R., Jones, P.S., 1990. The optimal design of integrated evaporation systems. *Heat. Recovery Syst. CHP* 10, 341–368. [http://dx.doi.org/10.1016/0890-4332\(90\)90086-Y](http://dx.doi.org/10.1016/0890-4332(90)90086-Y).
- Walmsley, T.G., Walmsley, M.R.W., Atkins, M.J., Neale, J.R., 2013. Improving energy recovery in milk powder production through soft data optimisation. *Appl. Therm. Eng.* 61, 80–87. <http://dx.doi.org/10.1016/j.applthermaleng.2013.01.051>.
- Walmsley, T.G., Walmsley, M.R.W., Neale, J.R., Atkins, M.J., 2015. Pinch analysis of an industrial milk evaporator with vapour recompression technologies. *Chem. Eng. Trans.* 45, 7–12. <http://dx.doi.org/10.3303/CET1545002>.
- Walmsley, T.G., Atkins, M.J., Walmsley, M.R.W., Neale, J.R., 2016. Appropriate placement of vapour recompression in ultra-low energy industrial milk evaporation systems using Pinch analysis. *Energy*. <http://dx.doi.org/10.1016/j.energy.2016.04.026>.
- Westphalen, D.L., Wolf Maciel, M.R., 2000. Pinch analysis of evaporation systems. *Braz. J. Chem. Eng.* 17, 525–538. <http://dx.doi.org/10.1590/S0104-66322000000400017>.



**Article 10:**

*A Unified Total Site Heat Integration targeting method for isothermal and non-isothermal utilities*

Tarighaleslami, A.H., **Walmsley, T.G.**, Atkins, M.J., Walmsley, M.R.W., Liew, P.Y., Neale, J.R., 2017.

Energy 119, 10–25.

DOI: 10.1016/j.energy.2016.12.071

Citations: 9

Elsevier



# A Unified Total Site Heat Integration targeting method for isothermal and non-isothermal utilities



Amir H. Tarighaleslami<sup>a</sup>, Timothy G. Walmsley<sup>a,\*</sup>, Martin J. Atkins<sup>a</sup>,  
Michael R.W. Walmsley<sup>a</sup>, Peng Yen Liew<sup>b,c</sup>, James R. Neale<sup>a</sup>

<sup>a</sup> Energy Research Centre, School of Engineering, University of Waikato, Private Bag 3105, Hamilton, 3240, New Zealand

<sup>b</sup> Department of Environmental Engineering and Green Technology, Malaysia-Japan International Institute of Technology (MJIT), Universiti Teknologi Malaysia, 54100, Kuala Lumpur, Malaysia

<sup>c</sup> Process System Engineering Center (PROSPECT), Research Institute of Sustainable Environment (RISE), Universiti Teknologi Malaysia, 81310, UTM Johor Bahru, Malaysia

## ARTICLE INFO

### Article history:

Received 29 April 2016

Received in revised form

17 December 2016

Accepted 18 December 2016

Available online 22 December 2016

### Keywords:

Total Site

Process Integration

Energy targeting

Pinch Analysis

Heat Recovery Loop

## ABSTRACT

This paper presents a new unified Total Site Heat Integration (TSHI) targeting methodology that calculates improved TSHI targets for sites that requires isothermal (e.g. steam) and non-isothermal (e.g. hot water) utilities. The new method sums process level utility targets to form the basis of Total Site utility targets; whereas the conventional method uses Total Site Profiles based excess process heat deficits/surpluses to set Total Site targets. Using an improved targeting algorithm, the new method requires a utility to be supplied to and returned from each process at specified temperatures, which is critical when targeting non-isothermal utilities. Such a constraint is not inherent in the conventional method. The subtle changes in procedure from the conventional method means TSHI targets are generally lower but more realistic to achieve. Three industrial case studies representing a wide variety of processing industries, are targeted using the conventional and new TSHI methods, from which key learnings are found. In summary, the over-estimation of TSHI targets for the three case studies from using the conventional method compared to new method are 69% for a New Zealand Dairy Factory, 8% for the Södra Cell Värö Kraft Pulp Mill, and 12% for Petrochemical Complex.

© 2016 Elsevier Ltd. All rights reserved.

## 1. Introduction

Process Integration (PI) has a key role in addressing energy efficiency and waste heat improvement in process industries [1]. There are three approaches to PI: (1) graphical methods including Pinch Analysis (PA), (2) Mathematical Programming (MP) methods, and (3) hybrid approaches [2]. Application of PI techniques to a wide variety of industries has helped realise meaningful increases in energy efficiency through improved process- and Total Site-level integration [3].

PA is an elegant insight and graphical technique for Heat Integration (HI) targeting and Heat Exchanger Network (HEN) design [4]. It has been well-utilised in the process industry as a tool to maximise energy saving and heat recovery within the individual process units [5]. An important strength of the PA approach to PI is

the targeting stage where important performance targets are determined prior to the design stage. Establishment of meaningful and achievable targets provides critical guidance in the design stage to the engineer of the performance limitations and inherent compromises within a system. On the other hand, Mathematical Programming typically solves network superstructures to find feasible and optimal designs. MP combines algorithmic methods with fundamental design concepts [6]. It is capable of optimising both single- and multi-objective problems including HEN retrofit [7].

Total Site Heat Integration (TSHI) was initially introduced by Dhole and Linnhoff [8] to investigate HI across plants. TSHI is a strategy for the integration of large multi-process sites to improve site-wide energy efficiency that has focused on exploiting the steam utility system to recover and place heat [9]. The method prioritises integration of individual processes and zones (i.e. defined areas of integrity [10]), before integrating across an entire site using the utility system [11]. Total Site (TS) source and sink profiles are composites of shifted Grand Composite Curves (GCC)

\* Corresponding author.

E-mail address: [timgw@waikato.ac.nz](mailto:timgw@waikato.ac.nz) (T.G. Walmsley).

Nomenclature		s	supply
		t	target
<i>Roman</i>		<i>Abbreviations</i>	
CP	heat capacity flowrate (MW/°C)	CC	Composite Curves
H	enthalpy (MW)	ChW	chilled water
Q	heat load (MW)	CTST	Conventional Total Site Targeting
T	temperature (°C)	CW	cooling water
T*	shifted temperature (°C)	GCC	Grand Composite Curve
T**	double shifted temperature (°C)	HI	Heat Integration
<i>Greek</i>		HEN	heat exchanger network
$\Delta$	difference between two states	HOL	hot oil loop
<i>Subscripts</i>		HPS	high pressure steam
cont	contribution	HRL	Heat Recovery Loop
cont,P	contribution, process	HTHW	high temperature hot water
cont,PS(i)	contribution, process streams for process i	LPS	low pressure steam
cont,U	contribution, utility	LTHW	low temperature hot water
cont,U(i)	contribution, utility for utility i	MP	Mathematical Programming
cont,US(i)	contribution, utility streams for utility i	MPS	medium pressure steam
j	utility counter	PA	Pinch Analysis
k	interval counter	PI	Process Integration
m	counter for hot streams	PT	Problem Table
min	minimum	SUGCC	Site Utility Grand Composite Curve
min,P(i)	minimum process for each process i	TS	Total Site
min,PP(i)	minimum process to process for process i	TSHI	Total Site Heat Integration
min,PU(i)	minimum process to utility for process i	TSP	Total Site Profile
n	counter for cold streams	TW	tempered water
		UTST	Unified Total Site Targeting
		VHPS	very high pressure steam

from individual processes and applied to calculate TS targets for heat recovery, utility use, and shaft work/power generation [12]. Shortly after its initial development, Klemeš et al. [9] summarised successful applications of TSHI to an acrylic polymer manufacturing plant, several oil refineries and a tissue paper mill, which all showed utility savings between 20 and 30%. The PhD thesis of Raissi [13] presents much of the early developments of TSHI.

Inter-process integration through TSHI has recently led to increasing utility savings in slaughter and meat processing by 35% [14], large industrial parks in Japan about 53% [15] and Thailand by 28% [16], chemical processing clusters by 42% [17], and Kraft pulp mills about 13% [18]. Notable developments to the TSHI method include: temperature shifting using process [19] and stream [20] specific minimum approach temperatures, application to Locally Integrated Energy Sectors [21], integration of renewables [22], variable energy supply and demand system [23], heat exchange restrictions [24], seasonal energy availability [25], centralised utility system planning [26], retrofit investigations in TS [27], process modifications [28], minimisation of thermal oil flowrate in hot oil loops [29], heat transfer enhancement in site level heat recovery systems [30], variable energy availability [31], and TS utility system targeting [32]. There are also MP approaches to TSHI [33] including its retrofit [34].

Effectively applying TSHI techniques to processing applications and sites that required non-isothermal utilities is complex and economically challenging. The use of a Heat Recovery Loop (HRL) for site-wide heat integration of low temperature processes was investigated by Atkins et al. [35] and later formalised into a comprehensive method by Walmsley et al. [36]. In their work detailed targeting and design considerations for HRLs have included: thermal storage management [37], storage temperature selection [38], storage capacity [35], heat exchanger area sizing

method [39] and performance [40], the integration of industrial solar [41], and the effect of using a nanofluid as the intermediate fluid on heat recovery [42]. Recently, Chang et al. presented the use of MINLP model with economic objectives to optimise HRLs [43].

Liew et al. [44] introduced an algebraic TS energy targeting methodology using cascade analysis. This methodology is developed mainly for targeting isothermal utilities. Non-isothermal utility (e.g. hot water and cooling water) were considered in the grassroots design [44], retrofit [27], and with variable supply and demand [31] case studies by considering only a utility supply temperature and no fixed utility target temperature. This assumption at times generates misleading energy targets for non-isothermal utility because there is no guarantee that the consumption and generation of the non-isothermal utility will maximise heat recovery. Methodology improvement, such as a targeting algorithm for non-isothermal utility, is therefore needed to systematically consider non-isothermal utility with fixed or soft target temperature.

TSHI methodologies are baseline feasibility studies for maximum energy recovery via heat exchanger and utility network. However, there are no network constraints (besides thermodynamics) in conventional TSHI for heat exchanger matches between process and utility streams. This problem was recently recognised by Sun et al. [32]. As the boiler feed water (non-isothermal utility) pinched against the TSP, they recognised that the heat may need to be transferred from multiple processes and that the network, although thermodynamically feasible, might be too complex in practice [32]. Conventional TSHI allows process-utility heat exchanger matches in series from any process for the utility to reach its target temperature and then returned to the central utility system. As a result, conventional TSHI targets for non-isothermal utilities can be overly optimistic. The HRL method, on the other

hand predefines the network structure by having all HRL heat exchangers in parallel to one another (even within a process). Such a tight constraint for the network lowers the inter-plant heat recovery target and often overlooks opportunities to increase energy efficiency [45]. The gap in the literature is, therefore, the lack of an appropriate TSHI method that realistically targets both isothermal and non-isothermal utility consumption.

The aim of this paper is to introduce an improved TSHI method that calculates more realistic and achievable targets for non-isothermal utilities. The new method is referred as the Unified Total Site Targeting Method (UTST). The non-isothermal utilities in this methodology include hot water system for low temperature processes (e.g. food and beverage processing) and intermediate temperature processes (e.g. pulp and paper processing), as well as hot oil system in high temperature processes (e.g. oil refineries). The new method modified the Conventional TSHI Targeting methods, which produces substantially different TS targets for cases when non-isothermal utilities are used in the TS system. Targeting results from the new unified method are compared to the conventional TSHI method using three case studies. The effects of assumptions inherent in both methods that generate targets for TS integration are illustrated and discussed.

**2. The challenge of Total Site Heat Integration targeting for non-isothermal utilities**

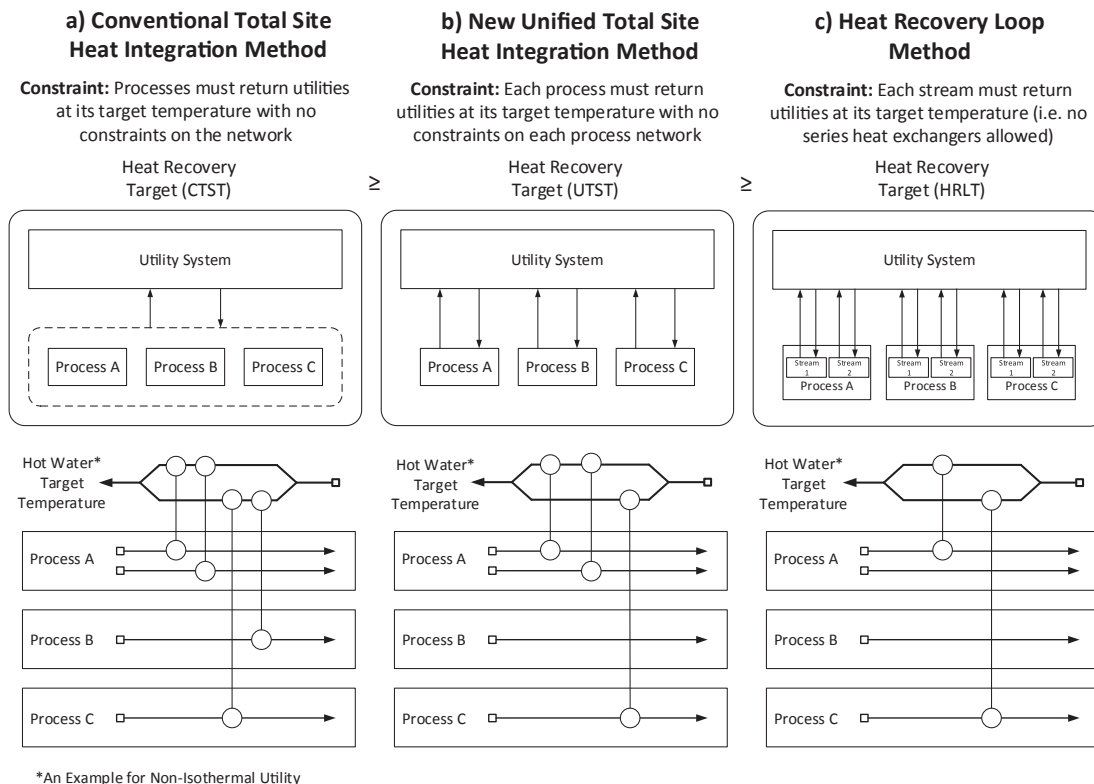
One of the limitations of the conventional TSHI is the treatment of non-isothermal utilities during the targeting process. In these methods, non-isothermal utilities are often treated in the same way as isothermal utilities where the utility supply temperature is the primary constraint. An isothermal utility's temperature remains constant when the utility supplies different processes in a cluster of industrial plants. For non-isothermal utilities that are being

consumed and generated (i.e. TS heat recovery), the utility target temperature may be an additional fixed constraint. Pinching non-isothermal utilities against the TSP presents an economic challenge in designing the utility network.

Few TSHI studies have focused on targeting processes and sites that primarily require non-isothermal utilities; nor have they investigated the possibility of replacing isothermal utilities (e.g. steam) with non-isothermal (e.g. hot oil) to increase heat recovery. A contributing factor for this gap is the lack of a TSHI method that calculates realistic and achievable targets considering both isothermal and non-isothermal utilities. Fig. 1 presents a simple illustration of the problems faced in applying conventional TSHI and HRL targeting methods to a multi-process site that requires non-isothermal utilities.

In each of the three methods (including the new method), the non-isothermal hot water loop is supplied at its supply temperature and must return at its target temperature. The target temperature for non-isothermal utilities can be achieved a number of ways, but is constrained depending on the targeting method. Conventional TSHI inherently allows the target temperature to be met using a single heat exchanger or using heat exchanger matches in series and/or parallel configurations from any process as illustrated in Fig. 1a. In some cases, a series set of heat exchangers may be critical to achieving the TS targets. The Heat Recovery Loop method has an additional constraint that the utility target temperature must be achieved with only one heat exchangers as in Fig. 1c (i.e. it excludes heat exchangers in series). The new method allows heat exchangers in parallel and series to achieve the utility target temperature, if and only if the heat exchangers in series are from the same process as shown in Fig. 1b.

The targets produced using conventional TSHI for non-isothermal utilities are therefore overly optimistic because it allows the target temperature to be achieved using series matches



\*An Example for Non-Isothermal Utility

**Fig. 1.** Comparison of the frameworks and constraints for the conventional TSHI method (a), the new Unified TSHI concept (b), and the Heat Recovery Loop method, including example hypothetical utility network designs (c).

that could (in theory) be from different processes, which is highly likely to be uneconomic and impractical. A similar problem was recognised by Sun et al. [32] in the context of preheating boiler feed water. This creates a dependency on two separate and distinct processes and one of the original rationales for TS was to achieve heat recovery between individual processes without having these types of dependences. These dependencies can cause major operation issues especially in clusters containing non-continuous processes. For example, in Fig. 1a the hot water target temperature on the lower split is achieved by two heat exchangers in series, the first match in Process B and the second from Process C. If there was disturbance in the stream matched from Process B, for example due to its non-continuous nature, the target temperature is unlikely achieved by the match from Process C alone. As a result additional cold utility, such as refrigeration, is consumed to ensure achievement of the target temperature (because this temperature is also its supply temperature as the hot water is regenerated by process streams). If no additional utility is consumed and the water utility is returned to the process for regeneration at a higher temperature than its target, it puts at risk process streams not reaching their target temperature, especially in situations where the exchanger is a utility pinch. As a result in practice, these types of matches would ordinarily be considered impractical as the operational risk and control complexity outweigh the benefits.

To overcome this targeting problem in TSHI, two methodologies have been proposed. Walmsley et al. [46] presented a method for dealing with HI between continuous and non-continuous processes in lower temperatures, such as food and dairy industries, using a dedicated indirect heat recovery system, which is often referred to as a HRL. The trade-off between storage temperature and heat exchanger area in an inter-plant HI using intermediate fluid investigated by Walmsley et al. [40]. They explained all the heat exchangers from HEN connected to the HRL are considered as parallel to each other, as a pre-defined network structure. Fig. 1c illustrates the general framework of how the HRL method allows a dedicated hot water or hot oil system (e.g. a utility sub-system) to interact with individual streams. Such a framework has additional constraints that lowers the inter-process heat recovery target and requires information about process heat exchanger network designs prior to targeting inter-process heat integration.

Another approach is presented by Wang et al. [47], which offers TS targeting as an initial stage followed by HEN design and area targeting, which is solved using Mixed Integer Non-Linear Programming. The methods of Atkins et al. [38] and Walmsley et al. [40] is overly restrictive on the interactions between utility and process streams, whereas the method of Wang et al. [47] is not able to provide the same insights that graphical methods do. Despite the merits of both the above approaches, there is still not an appropriate graphical method to overcome the previously highlighted limitations of conventional TSHI.

It is important to note that besides the challenge of targeting non-isothermal utilities, there are other reasons that are not addressed in this work that cause the conventional TSHI methods to over-estimate TSHI. For example, critical matches may be uneconomic due to (1) long distance between streams, (2) matched streams from different processes may not always be availability hence the system will require a backup heat exchanger at extra cost, (3) stream variability requiring backup utility, (4) safety concerns, (5) fouling concerns, and (6) process control difficulties.

### 3. Methods

#### 3.1. A new Unified Total Site Heat Integration targeting method

This section explains the procedure of the new Unified Total Site

Targeting method. The procedure has three Stages: Data Specification, Process level, and Total Site level. Fig. 2 illustrates the Unified Total Site Targeting method procedure using a flow diagram and Illustrative graphs.

##### 3.1.1. Stage 1 – Data Specification

*Step 1, Extract Stream Data:* Following conventional methodologies, the parameters of process streams are defined using general process data sets (e.g. process flow sheets).

*Step 2, Select  $\Delta T_{min}$  Contribution ( $\Delta T_{cont}$ ):* In this method, due to covering wide range of processes, a stream specific  $\Delta T_{min}$  contribution is used. The minimum temperature difference between process streams in each process ( $\Delta T_{cont,PS(i)}$ ) is  $\Delta T_{cont,P1} + \Delta T_{cont,P2}$ . The selection of stream specific  $\Delta T_{cont}$  should consider the thermo-physical properties of the stream and the energy-capital trade-off through Supertargeting. For example, some process streams may be gases or viscous liquids which have poor heat transfer coefficient, or may be prone to fouling on heat exchanger surfaces. For such cases, the overall heat transfer coefficient of a heat exchanger will be low; therefore, the corresponding heat transfer area will be high. As a result, a relatively high  $\Delta T_{cont}$  should be selected.

##### 3.1.2. Stage 2 – process level targeting

*Step 3, Shift stream temperatures forward to intermediate temperatures ( $T^*$ ):* For each process, supply and target temperatures of hot (source) and cold (sink) streams are shifted using individual process stream  $\Delta T_{cont}$  to the intermediate temperature scale,  $T^*$ , according to Eq. (1),

$$T^* = \begin{cases} T - \Delta T_{cont,P(m)} & \in \text{Sources} \\ T + \Delta T_{cont,P(n)} & \in \text{Sinks} \end{cases} \quad (1)$$

where  $\Delta T_{cont,P(m)}$  and  $\Delta T_{cont,P(n)}$  are minimum allowed temperature contribution for process individual hot and cold streams.

*Step 4, Determine Problem Table (PT), Composite Curve (CC), and GCC for each process:* Problem Table can be calculated to determine the Pinch Temperature, CC, SCC and GCC graphs for each individual process.

*Step 5, Target intra-process heat recovery:* Heat recovery targets for the selected  $\Delta T_{cont}$  values from the CC are obtained for each process. Results include the overall minimum hot and cold utility targets for each process.

*Step 6, Select utilities including temperatures and pressures:* Selection of the utility temperatures/pressure levels affects inter-process heat recovery targets at the TS level. After targeting TS heat recovery, these temperatures may be re-selected (and optimised) to increase inter-process heat recovery targets. In selection of utilities, the idea of soft and hard (fixed) utility target temperatures should be considered. In this step, the minimum temperature difference for each utility ( $\Delta T_{cont,US(i)}$ ) is selected using a similar procedure explained in Step 2. The equivalent  $\Delta T_{min}$  between process and utility streams is  $\Delta T_{cont,P1} + \Delta T_{cont,U1}$ .

*Step 7, Remove pockets:* Following the CIST method, pockets which represent opportunities for intra-process heat recovery, are removed from GCC and heat source and heat sink segments are extracted from GCC for all processes. Therefore, only the net utility demands of the various processes are considered at the TS level.

*Step 8, Target individual process utility generation and consumption:* Targeting the utility generation and consumption in the intra-process targeting stage is an important feature of the new method in targeting non-isothermal utility use where the supply and target temperatures of the utility may be important TS heat recovery constraints. This step is an important difference and improvement from the previous work of Liew et al. [44].

Table 1 shows the general framework for the numerical analysis

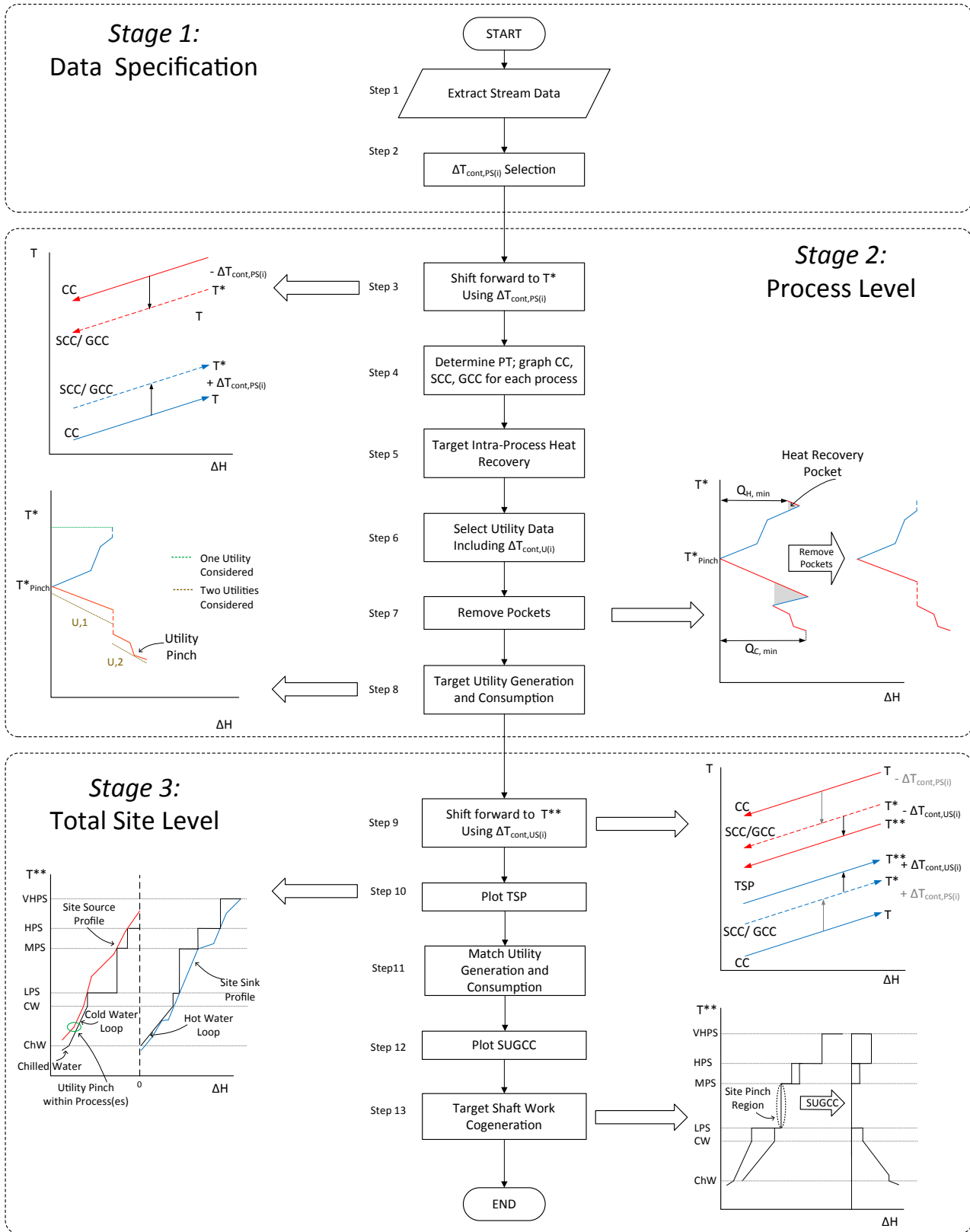


Fig. 2. Unified Total Site Targeting (UTST) procedure.

technique of the utility targeting method. The first column of the framework consists of the shifted temperature levels of the both process streams and utilities, arranged in descending order of

temperature. The inclusion of shifted utility temperatures in the PT formulation is a small but important modification, which allows for the start and end temperature of each utility to be contained in the

**Table 1**

General framework for algebraic technique of the targeting method. Example specific to using cold utilities below the Pinch.

1. Shifted temperature	2. Interval	3. Temperature difference	4. Net heat capacity flowrate	5. Interval heat load	6. Feasible heat loads	7. Heat capacity flowrate for utility $j$	8. Heat capacity flowrate for utility $j+1$
$T_k^*$		$\Delta T_k$	$CP_{net,k}$	$\Delta H_k$	$\sum \Delta H_k$	$CP_{(U,j)k}$	$CP_{(U,j+1)k}$
$T_1^*$	Pinch				$\sum \Delta H_1 = 0$		
$T_2^*$	1	$\Delta T_1$	$CP_{net,1}$	$\Delta H_1$	$\sum \Delta H_2$	$CP_{(U,1)2}$	
$T_3^*$	2	$\Delta T_2$	$CP_{net,2}$	$\Delta H_2$	$\sum \Delta H_3$	$CP_{(U,1)3}$	
$T_4^*$	3	$\Delta T_3$	$CP_{net,3}$	$\Delta H_3$	$\sum \Delta H_4$	$CP_{(U,1)4}$	$CP_{(U,2)4}$
$T_5^*$	4	$\Delta T_4$	$CP_{net,4}$	$\Delta H_4$	$\sum \Delta H_5$	.	$CP_{(U,2)5}$
$\vdots$	$\vdots$	$\vdots$	$\vdots$	$\vdots$	$\vdots$	$\vdots$	$\vdots$
$T_{k-1}^*$	$\vdots$	$\vdots$	$\vdots$	$\vdots$	$\sum \Delta H_{k-1}$	$\vdots$	$CP_{(U,2)k-1}$
$T_k^*$	k	$\Delta T_k$	$CP_{net,k}$	$\Delta H_k$	$\sum \Delta H_k$	$\min(CP_{(U,j)k})$	$\min(CP_{(U,j+1)k})$

PT temperature column. Following the conventional PT method columns 2 to 6 are determined. Column 6 represents the feasible process heat load cascade and columns 7 and 8 help determine the heat capacity flowrate corresponding to each utility (only two utilities shown).

The minimum heat capacity flowrate (CP) value in columns 7 and 8 is the required heat capacity flowrate of each utility, as indicated in the final entry of columns 7 and 8. It is noted that if the utility system contains more utilities then more columns can be added to Table 1. Columns for each utility are ordered from the lowest to highest quality utility (hottest cold utility to the coldest cold utility for below the Pinch and coldest hot utility to the hottest hot utility for above the Pinch). Where supply and target temperatures for two utilities overlap, the calculation in the respective utility CP columns (columns 7 and 8) will also overlap. Table 1 demonstrates the procedure for below the Pinch; however, following the same logic starting from process Pinch Temperature, the table can be calculated for above the Pinch.

To determine the heat capacity flowrate of each utility (i.e. columns 7 and 8), Eq. (2) is applied for non-isothermal utilities. Eq. (2) was derived graphically by finding the equation that determines the maximum CP of a utility based on the utilities target temperature and the each shifted temperature interval, for which the utility may be applied. The minimum of these calculated CP values is the maximum feasible utility CP, which does not violate the Pinch constraint.

Where  $Q$ ,  $\Delta H$  and  $CP$  are respectively the heat load of each utility, enthalpy change of each temperature interval and heat capacity flowrate, and  $T_t^*$  and  $T_s^*$  represent shifted utility target temperature and shifted supply temperature respectively. Subscripts  $U$ ,  $j$  and  $k$  represent number of utility and interval number.

Utility target temperatures can be divided to two categories, fixed (hard) temperatures and soft temperatures. Soft utility target temperatures, in this context, refer to target temperatures that are non-essential to be achieved. Soft temperatures may be changed by varying utility heat capacity flowrates. Hard utility temperatures refer to temperature constraints that should be met. Where a non-isothermal utility will the both consumed and generated in TSHI, the utility supply and target temperatures become important constraints. The optimal temperature selection for each non-isothermal utility will be presented in future work.

### 3.1.3. Stage 3 – Total Site level targeting

*Step 9, Shift intermediate temperatures ( $T^*$ ) forward to the utility temperature scale ( $T^{**}$ ):* Once pockets are removed from the process GCCs (Step 7), the remaining heat load profile represents stream segments that require utility. These stream GCC segments are shift a second time using  $\Delta T_{cont}$ , according to Eq. (4).

$$T^{**} = \begin{cases} T^* - \Delta T_{cont,U(m)} & \in \text{Sources} \\ T^* + \Delta T_{cont,U(n)} & \in \text{Sinks} \end{cases} \quad (4)$$

$$CP_{(U,j)k} = \frac{\min\{\sum \Delta H_1, \sum \Delta H_2, \dots, \sum \Delta H_k\} - \sum(Q_{U,1}, Q_{U,2}, \dots, Q_{U,j-1})}{|T_{t(U,j)}^* - T_k^*|} \quad (2)$$

Eq. (2) applies for the following conditions:

$$\begin{aligned} \sum \Delta H_k &> \sum(Q_{U,1}, Q_{U,2}, \dots, Q_{U,j-1}) \\ T_{s(U,j)}^* &\leq T_k^* < T_{t(U,j)}^* && \in \text{Cold Utility} \\ T_{s(U,j)}^* &\geq T_k^* > T_{t(U,j)}^* && \in \text{Hot Utility} \end{aligned} \quad (3)$$

where  $\Delta T_{cont,U(m)}$  and  $\Delta T_{cont,U(n)}$  are minimum allowed temperature contribution for specific heating and cooling utilities. With a double temperature shift, steam segments are now on the  $T^{**}$  scale, which is the actual utility temperature scale.

*Step 10, Construct Total Site Profiles (TSP):* Process GCC stream segments with a double shift (Step 9) are then composited to form Site Source and Site Sink Profiles using the same methods as CTST. As a result, these profiles are the same for UTST and CTST.

The new UTST transfers utility targets from process GCC (Step 8) to the TS level, whereas CTST targets TS utility use based on Site Source and Site Sink Profiles. This means site hot and cold utility profiles in UTST are composited based on the summation of process GCC utility requirements, which are then plotted on the TSP. This subtle change for determining TS utility targets often results in one or more utility that does not pinch against the TSP where it otherwise does in CTST. This non-pinch at the TS level for a utility indicates that one or more of the process GCCs constrain the use of that utility, i.e. process level utility pinch/pinches. In another words, to achieve the CTST for such a utility, there would be a requirement to route a utility from one process to another process in a series arrangement for the target duty as well as target utility temperature to actually be achieved (Fig. 1a).

*Step 11, Match Utility Generation and Consumption:* With gross TS targets for each utility (Step 10), net TS targets may be determined by matching individual utility generation and consumption targets. This step can be done using a simple table or graphically. For example, TS utility profiles may be pinched against each other using a graphical approach. The overlapping region of the two curves is the TS heat recovery target.

*Step 12, Construct Site Utility Grand Composite Curve:* The Site Utility Grand Composite Curve (SUGCC) is the net utility heat load profile. As such, it is the difference between the TS hot utility load profile pinched against the TS cold utility profile. Important features of the SUGCC include the TS Pinch Temperature region as well as any excess and deficit for each utility level.

*Step 13, Target Shaft Work Cogeneration:* Using the net utility requirements on the SUGCC a target for shaft work generation may be calculated using a turbine model or thermodynamically based on an isentropic expansion efficiency.

### 3.2. Conventional and Unified Total Site Heat Integration targeting methods

Fig. 3 presents the targeting procedures of three conventional TSHI targeting methods as well as the new unified TSHI targeting method. The considered conventional methods are: (1) global method [9], (2) process specific method [19], and (3) stream specific method [20].

Klemeš et al. [9] followed previous the TSHI method of Dhole and Linnhoff [8] by basing targets on a global minimum temperature difference,  $\Delta T_{\min(\text{global})}$  (Fig. 3-1a). This method, as with many others, focused on exploiting the steam utility system to recover heat and produce power for large multi-plant high temperature processing site (e.g. oil refineries). Since steam is considered isothermal in its generation and consumption as a high temperature utility, the design of a TS network, which achieves TSHI targets, is fairly simple.

Later, Varbanov et al. [19] presented a process-specific minimum temperature difference technique, as shown in Fig. 3-1b. This method employed changes in TSP construction algorithms by allowing separate  $\Delta T_{\min}$  specification for process-to-process heat exchange and also process-to-utility heat exchange. The method added a degree of freedom to assign different  $\Delta T_{\min}$  specifications for each process and utility, which resulted in improved targeting. A third sub-set of conventional TSHI methods is presented by Fodor et al. [20]. This method applies stream and utility specific minimum temperature contribution ( $\Delta T_{\text{cont}}$ ), which is presented as Fig. 3-1c. The targeting procedure is similar to previous methods, i.e. global and process specific methods; however, there are significant changes in heat recovery targets and cogeneration potential. The stream and utility specific  $\Delta T_{\text{cont}}$  method provides an even greater number of degrees of freedom to the designer, which can be used to improve the TSHI targets if such detailed data is available. The new

method follows from Fodor et al. [20] in using stream and utility specific  $\Delta T_{\text{cont}}$  as the basis of the procedure.

A critical difference between the new method (Fig. 3-2) and the conventional methods is the level at which utility targeting is performed. The conventional methods (Fig. 3-1) use the TSP, i.e. TS level, to determine the quantity needed of each specified utility. Whereas the new method uses individual process GCCs, i.e. process level, to target utility use, before transferring these targets to the TS level and looking for heat integration within the utility system (Fig. 2). This subtle change allows the engineer to know more about how each utility interacts with individual processes. In the new method, the utility system is constrained to supply utilities to and return utilities from each process at specified temperatures. With respect to non-isothermal utilities, this means sequential utility-process matches are allowed within a process to meet fixed utility supply and target temperatures. Sequential utility-process matches are disallowed between processes, as is inherently acceptable within the conventional TSHI method. This is an important advantage for application of new method to non-continuous processes or for clusters which contain one or more seasonal processes.

## 4. Application of Total Site Heat Integration methods to industrial case studies

This section introduces three case studies to demonstrate the merits of the new TS targeting method for both high and low temperature processes, which require isothermal and non-isothermal utilities, compared to the conventional TS method, CTST. These case studies contain a variety of continuous and non-continuous processes. The CTST and the UTST methods have been implemented into an Excel™ spreadsheet for application to the three case studies.

### 4.1. Case study I: New Zealand dairy processing factory

The first case study illustrates the advantages of the UTST method for targeting of primarily low temperature processes. The case study is based on a large New Zealand dairy factory, which has 15 different processes available for TS integration. Each process has several hot and cold streams, which total 79 streams. Five different utilities are used in the case study to cover the required temperature ranges, as presented in Table 2.

Fig. 4 presents the Total Site Profiles and targets for both the CTST method, in dashed lines, and UTST method, in solid lines, for the dairy case study. A  $\Delta T_{\text{cont}}$  of 2.5 °C for each stream, which is equivalent to  $\Delta T_{\min(\text{global})} = 5$  °C, was assumed for the illustration. As can be seen, LPS demand increases from 1.1 MW in the CTST method to 2.3 MW in the UTST method. HTHW demand slightly decreases from 13.7 MW in the CTST method to 13.6 MW in UTST method. For this case study, Utility Pinches on the TSP that occur in the Conventional TS method, are not present in the UTST method. For the UTST method, Utility Pinches occur on GCCs at the Process Level in the utility targeting step. Utility Pinches are necessary in TSHI to achieve maximum heat recovery. LTHW consumption significantly decreases from 3.3 MW for CTST to 2.0 MW for UTST. On the other hand, LTHW generation decreases from 7.5 MW for CTST to 4.7 MW for UTST. CW targets substantially decreases from 2.9 MW for CTST to 0.2 MW. ChW consumption targets, 7.5 MW, are the same in both methods.

Fig. 5 plots the Site Utility Grand Composite Curves for both the CTST method, in dashed lines, and the UTST method, in solid lines. For this case study, both methods result in the same Site Pinch Region. However, quantity of utilities are different, which impacts on the heat recovery and power generation opportunities related to

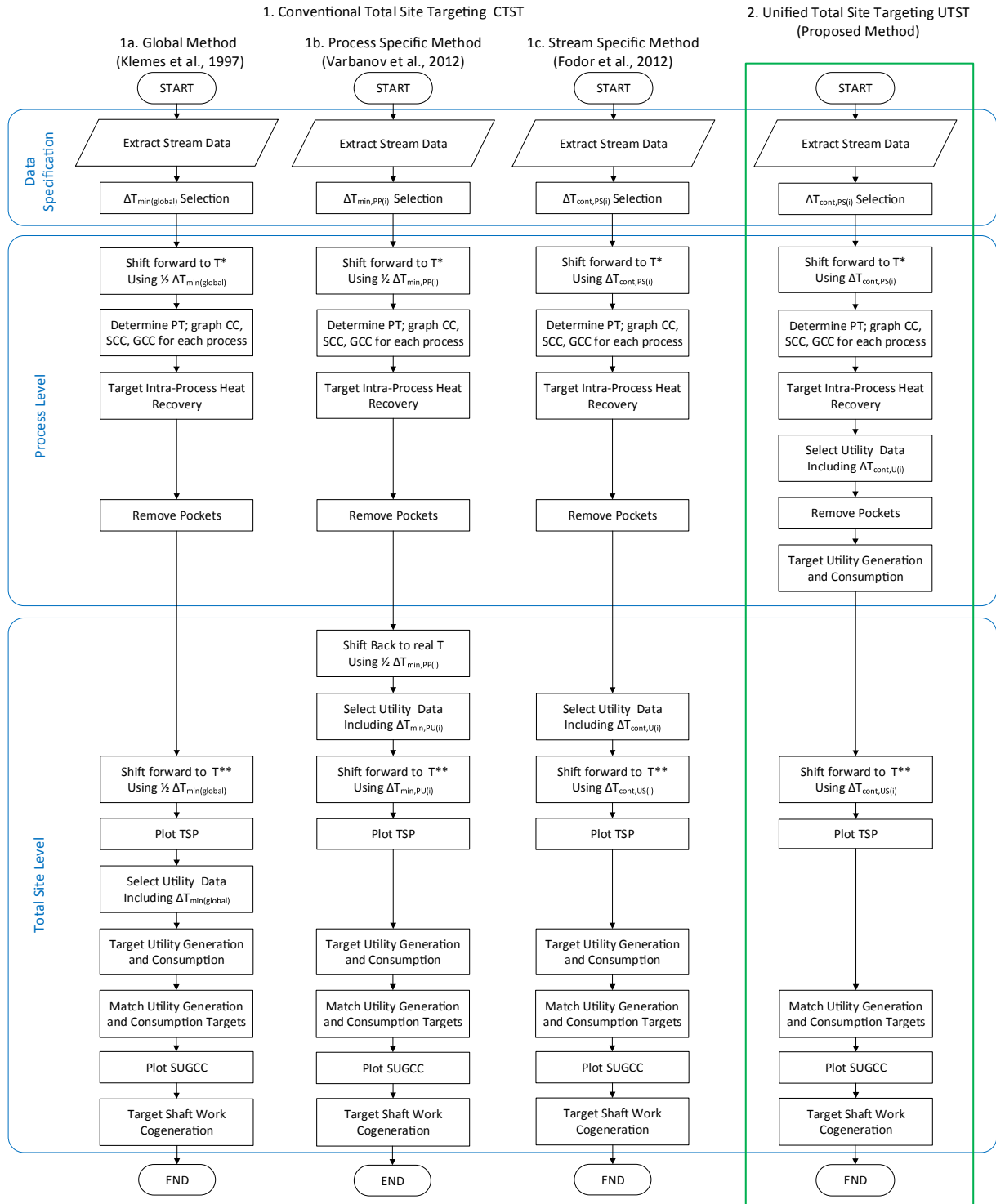


Fig. 3. Comparison between various Conventional and Unified Total Site Heat Integration targeting methods.

Table 2  
Required utilities for Dairy Factory case study.

Utility name	Utility type	Supply temperature (°C)	Target temperature (°C)	Pressure range (bar g)
Low pressure steam (LPS)	Hot	180.0	179.9	10
High temperature hot water (HTHW)	Hot	84.0	64.0 <sup>a</sup>	
Low temperature hot water (LTHW)	Hot	45.0	25.0	
Cooling water (CW)	Cold	24.0	25.0 <sup>a</sup>	
Chilled water (ChW)	Cold	0.0	2.0 <sup>a</sup>	

<sup>a</sup> Soft utility temperature.

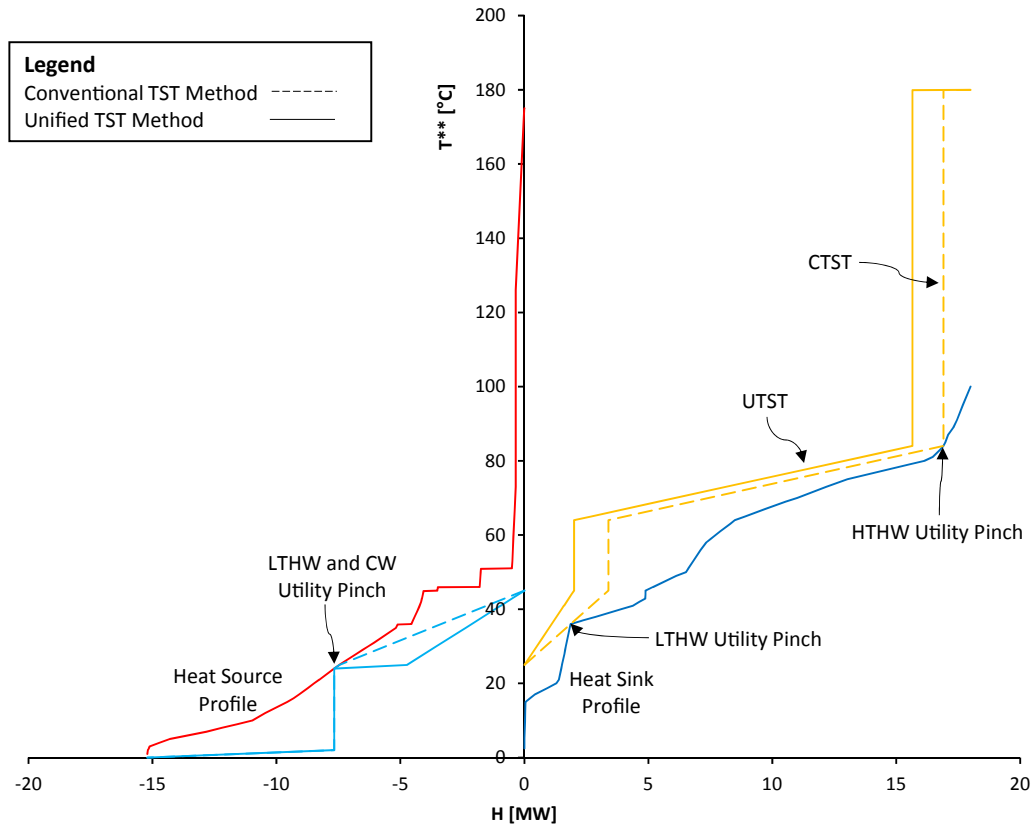


Fig. 4. Total Site Targets for both CTST and UTST methods in Dairy Factory.

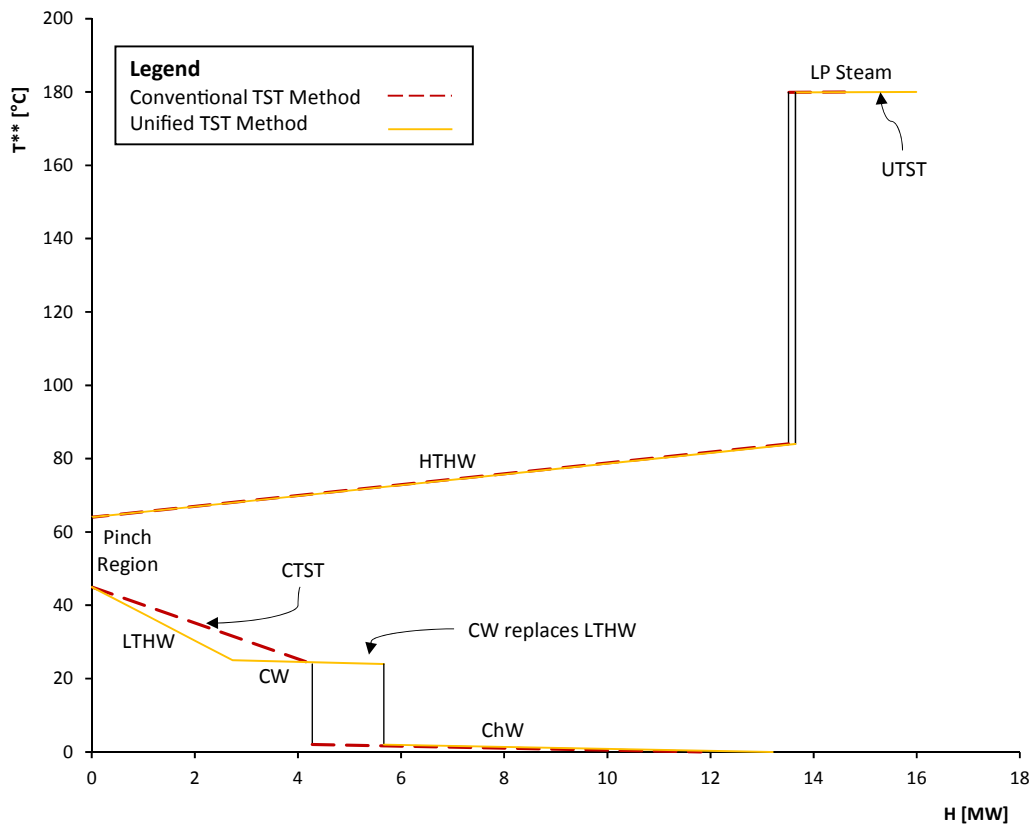


Fig. 5. SUGCC for both CTST and UTST methods in Dairy Factory.

**Table 3**  
Required utilities for Kraft Pulp Mill case study.

Utility name	Utility type	Supply temperature (°C)	Target temperature (°C)	Pressure range (bar g)
High pressure steam (HPS)	Hot	210.0	209.9	15
Low pressure steam (LPS)	Hot	160.0	159.9	9
High temperature hot water (HTHW)	Hot	85.0	60.0	
Low temperature hot water (LTHW)	Cold	25.0	45.0	

each method. In Fig. 5, a difference of 1.3 MW in heat recovery between the methods is seen, where CTST consumes total 14.6 MW of hot utility and 11.9 MW of cold utility versus 16.0 MW of hot utility and 13.3 MW of cold utility in the UTST method. This difference is due to the consumption and generation targets for the LTHW. The more conservative targets for the LTHW system in the UTST method result from the increased constraints around how the non-isothermal utility interacts with the various processes. This constraints cause Utility Pinches to occur within individual processes, rather than on the TSP.

Appendix A presents a comprehensive comparison of gross and net utility consumption and generation targets for both CTST and UTST methods for the dairy processing factory case study.

#### 4.2. Case study II: Södra Cell Värö Kraft Pulp Mill

This case study addresses the merits of UTST method for targeting a non-continuous Kraft mill that spans a wide temperature range where two utility hot water systems are useful for TS heat recovery. The stream data for this case study is taken from Bood and Nilsson [48] and is based on the Södra Cell Värö Kraft Pulp Mill plant in southern Sweden. The Kraft Pulp Mill Plant has 10 different processes with a total of 64 streams available for TS integration.

Minimum temperature difference and individual minimum contribution temperatures are from the same as used by Bood and Nilsson. Several utility streams including HPS, LPS, HTHW and LTHW systems are assumed in this study to cover the required temperature ranges in TSHI as shown in Table 3.

TS targets are presented in Fig. 6 for both CTST and UTST methods. Dashed lines present the CTST method while solid lines present the UTST method. As illustrated in Fig. 6 both methods require the same amount of HPS of 27.7 MW. The LPS demand of UTST is only 2.2 MW higher than CTST method, which is less than 1.5% of entire LPS demand.

The HTHW consumption target decreases from 8.7 MW for CTST to 6.5 MW for UTST and the HTHW generation target reduces from 41.8 MW for CTST to 27.7 MW for UTST. Both methods target the same amount of LTHW utility consumption. However, the LTHW generation target is 79.9 MW for the UTST versus 65.8 MW for the CTST method. The split between HTHW and LTHW in the UTST shows the method tends to require higher quality utilities. TS heat recovery in the UTST method is 2.2 MW lower than the CTST due to the pinched consumption of HTHW and LTHW (Fig. 7). As demonstrated, the UTST method is able to effectively target dual non-isothermal (hot water) utility systems. Appendix A provides a detailed comparison of gross and net utility consumption and

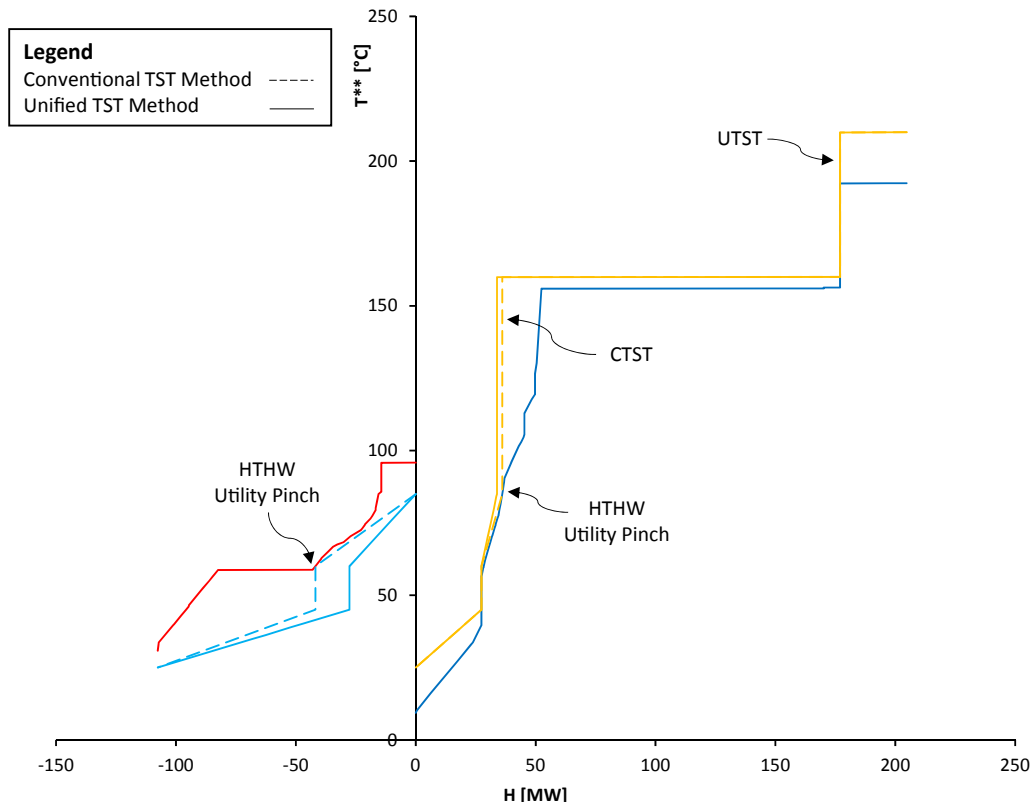


**Fig. 6.** Total Site Targets for both CTST and UTST methods in Kraft Pulp Mill Chemical Cluster.

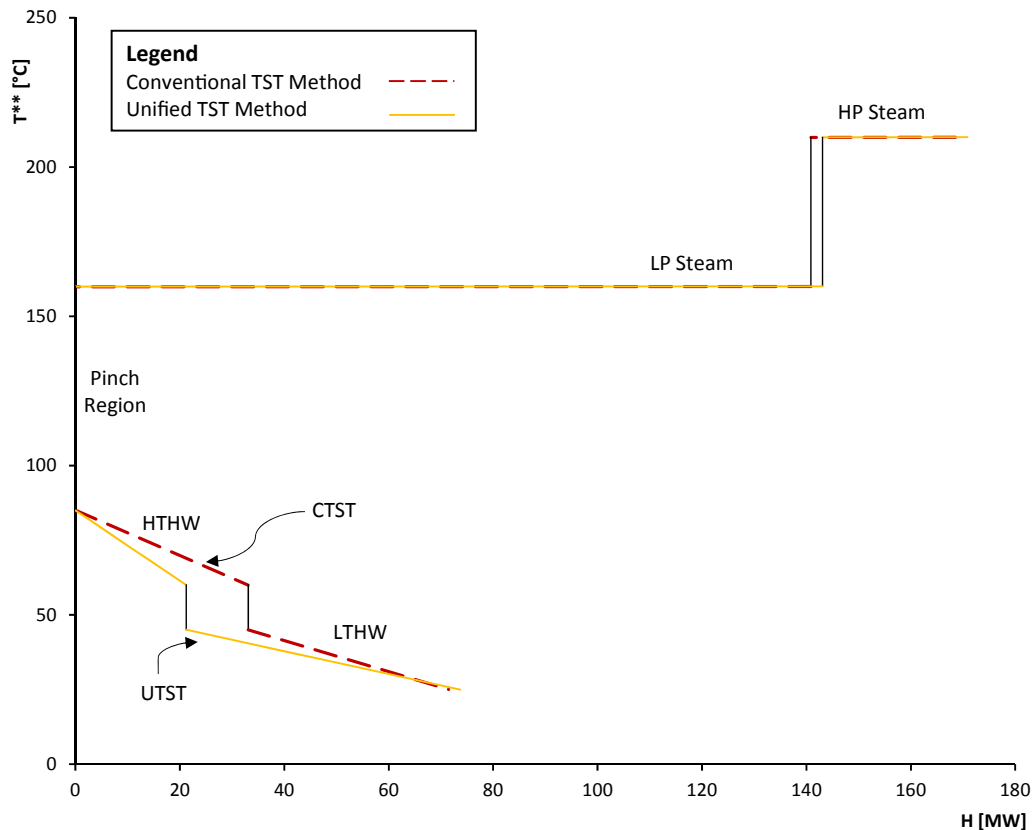


Fig. 7. SUGCC for both CTST and UTST methods in Kraft Pulp Mill Chemical Cluster.

generation targets for both CTST and UTST methods for this case study. The optimal selection of the number and temperatures of utilities for the UTST method will be presented in future work.

#### 4.3. Case study III: A Petrochemical Complex

The third case study is a Petrochemical Complex serviced by a common utility system. Petrochemical Complexes operate continuously with generally higher processing temperatures than Kraft mills and dairy factories and therefore require high pressure steam and very little hot water. This case study addresses the application of the UTST method to higher temperature processes. The petrochemical complex has 8 individual plants and a total of 60 hot and cold streams. Eight different utilities are used to cover the required temperature ranges as shown in Table 4.

In both CTST and UTST procedures, a  $\Delta T_{\text{cont}}$  of 10 °C for each stream has been chosen, which is recommended for Petrochemical, Oil and Gas Refineries [49]. The case study has been analysed using both CTST and UTST methods. Fig. 8 presents the TSP and the utility targets for the UTST method, in solid lines, and for the CTST method, in dashed lines. The UTST method gives very similar utility targets as the CTST method. However, as it can be seen in Figs. 8 and 9, the UTST method presents different non-isothermal utility targets for the TW and CW, which are more likely achievable. The slight utility change in TW and CW of 0.83 MW and 0.80 MW can be observed respectively, while utility targets for HOL, VHPS, HPS, MPS, LPS and ChW are unchanged.

In high temperature processes such as oil and gas refineries, petrochemical and metal processing plants using hot oil loops is common for higher temperatures where it is not possible to use excessively high steam pressures. However, the UTST, due to its advantages in targeting non-isothermal utilities with more realistic

targets, gives the opportunity to consider hot oil loops as a utility for medium temperature ranges (100–300 °C), where steam is normally used. Therefore, an alternate utility design can be investigated for the current case study to include a second hot oil loop (see Fig. 8). The new hot oil loop (HOL2) has a supply temperature of 210 °C and a target temperature of 160 °C. It replaces the MPS, LPS and HPS (generation only) to the new hot oil loop. Fig. 10 illustrates the TS targets for the case study applying CTST method without HOL2, in dashed lines, versus alternate design with the new hot oil loop applying UTST method in solid lines.

The application of the UTST method with the alternate set of utility offers slightly more heat recovery opportunities compared to the CTST method with the original utilities. By analysing both Figs. 10 and 11, UTST increases heat recovery by 0.36 MW, which is 12% increase in inter-process heat recovery, due to the addition of HOL2. For UTST with the alternate utilities, TW and CW increase by 2.4 and 0.8 MW respectively compared to the original case applying the CTST method. The advantage of the alternate case is eliminating two utility lines using a non-isothermal utility, which can be effectively targeted using the UTST method. While in this case study high increase in heat recovery is not illustrated, the possibility of substantial increases in heat recovery for other case studies is likely.

Detailed information for gross and net utility consumption and generation targets for both TS methods are given in Appendix A for both the original and alternative utility levels for Petrochemical Complex.

#### 5. Discussion on the Unified Total Site Heat Integration method

The merits of the new UTST method compared to the

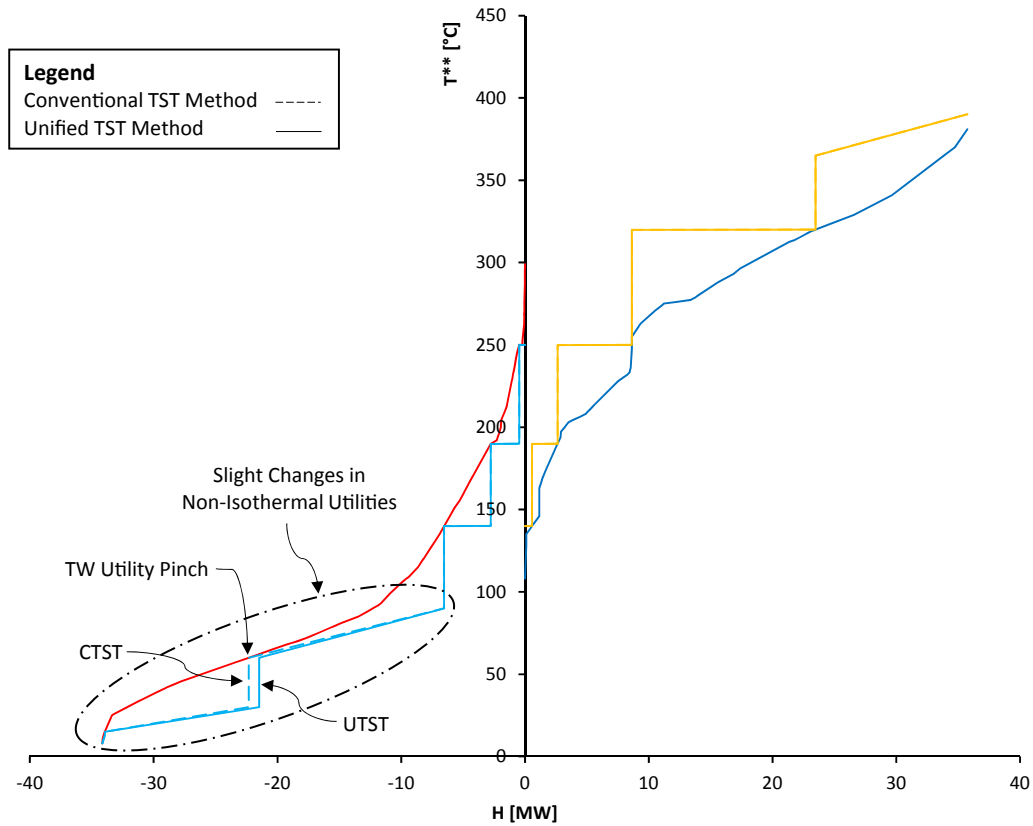


Fig. 8. Total Site Targets for both CTST and UTST methods in Petrochemical Complex.

Table 4

Required utilities for Petrochemical Complex case study.

Utility name	Utility type	Supply temperature (°C)	Target temperature (°C)	Pressure range (bar g)
Hot oil loop (HOL1)	Hot	390.0	365.0 <sup>a</sup>	
Very high pressure steam (VHPS)	Hot	320.0	319.9	65
High pressure steam (HPS)	Hot	250.0	249.9	15
Medium pressure steam (MPS)	Hot	190.0	189.9	9
Low pressure steam (LPS)	Hot	140.0	139.9	5
Tempered water (TW)	Cold	60.0	90.0 <sup>a</sup>	
Cooling water (CW)	Cold	15.0	30.0 <sup>a</sup>	
Chilled water (ChW)	Cold	8.0	13.0 <sup>a</sup>	

<sup>a</sup> Soft utility temperature.

conventional method have been illustrated using three case studies, which represent a diverse range of processing types and temperatures.

Five key learnings from the case studies with regards to the conventional and unified methods are:

- Targets from the new method suggests that the conventional method often over-estimates TSHI potential for non-isothermal utilities

An important element of the new method is the target incorporates the additional constraint for non-isothermal utilities to reach the target temperature within an individual process. By adding this new constraint the calculated targets become more achievable and realistic. The over-estimation of TSHI targets for the three case studies from using the conventional method compared to new method are 69% for a New Zealand Dairy Factory, 8% for the

Södra Cell Värö Kraft Pulp Mill, and 12% for Petrochemical Complex.

- The new method is equally applicable for high and low temperatures processes, and isothermal and non-isothermal utilities

The first case study, the large Dairy Factory, represents low temperature non-continuous processes. The second case study, Kraft Pulp Mill, represents a non-continuous process with a wide range of high to low temperatures. This case study illustrates the similarity of results between the CTST and UTST methods in higher temperature processes and more meaningful targets of UTST method for heat recovery at lower temperatures. In the last case study, non-isothermal utilities at higher temperatures, such as hot oil loops, are common utilities in typical Petrochemical Complexes and Oil refineries. This case study represents the similar outcomes of new method to the Conventional methods in case of traditional

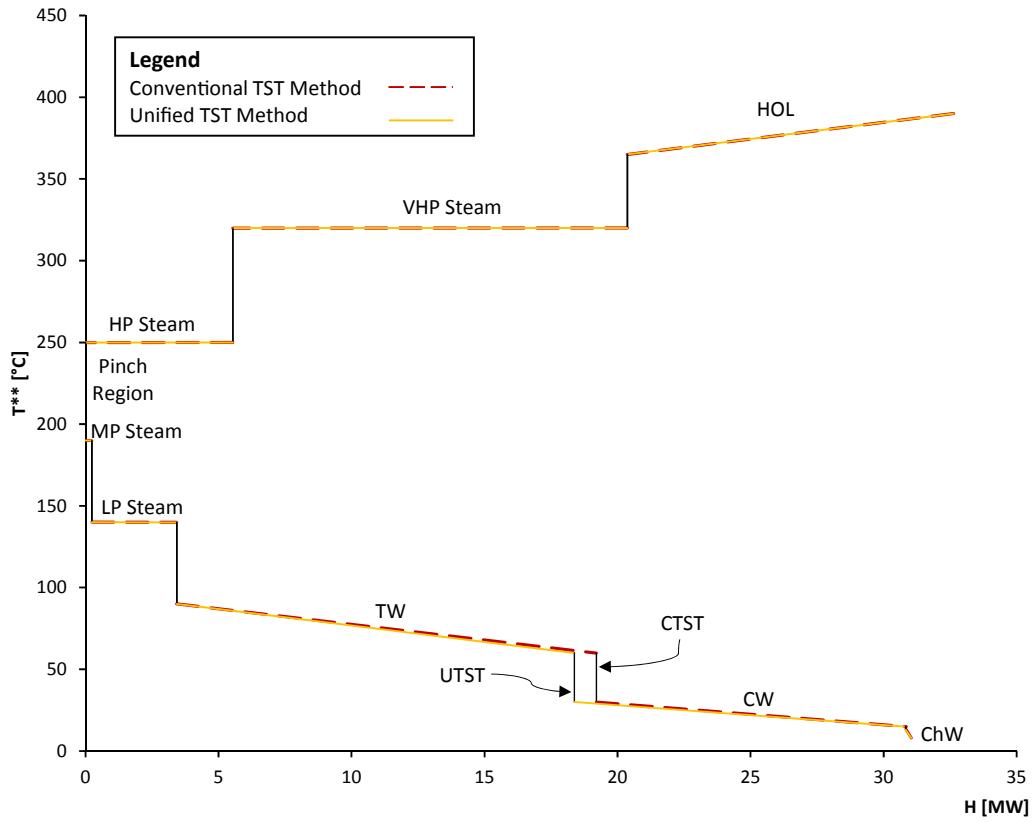


Fig. 9. SUGCC for both CTST and UTST methods in Petrochemical Complex.

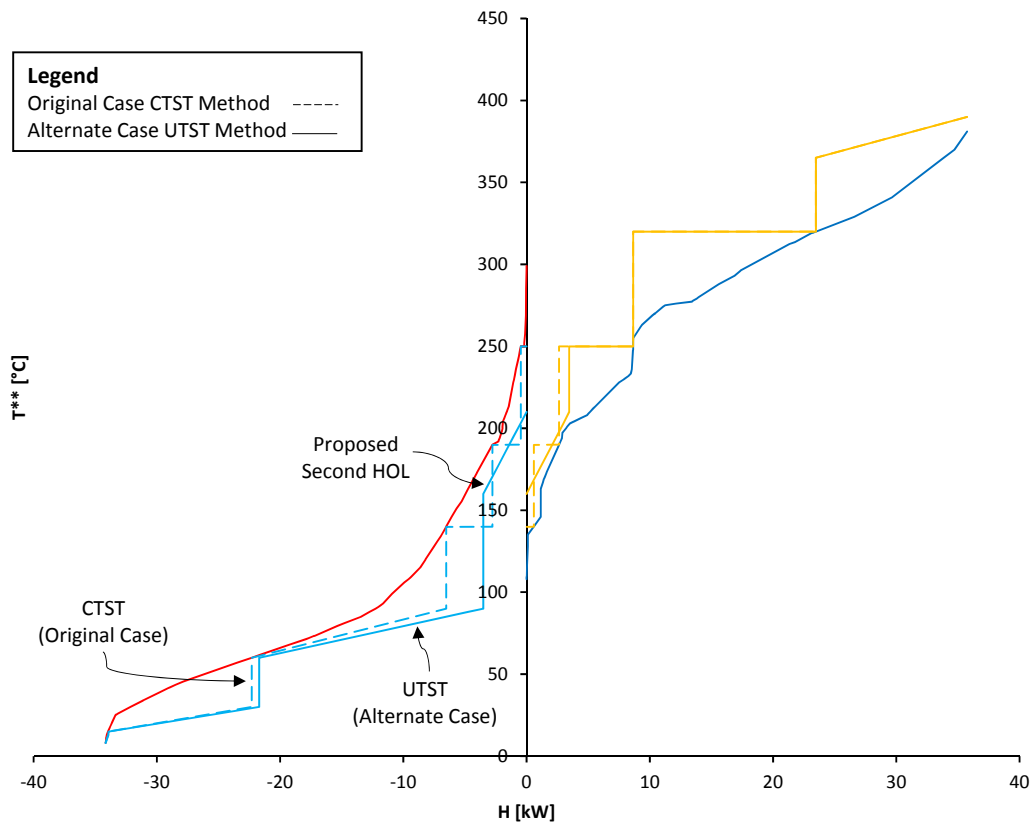


Fig. 10. Total Site Targets for Petrochemical Complex applying CTST method and alternate case applying UTST method.

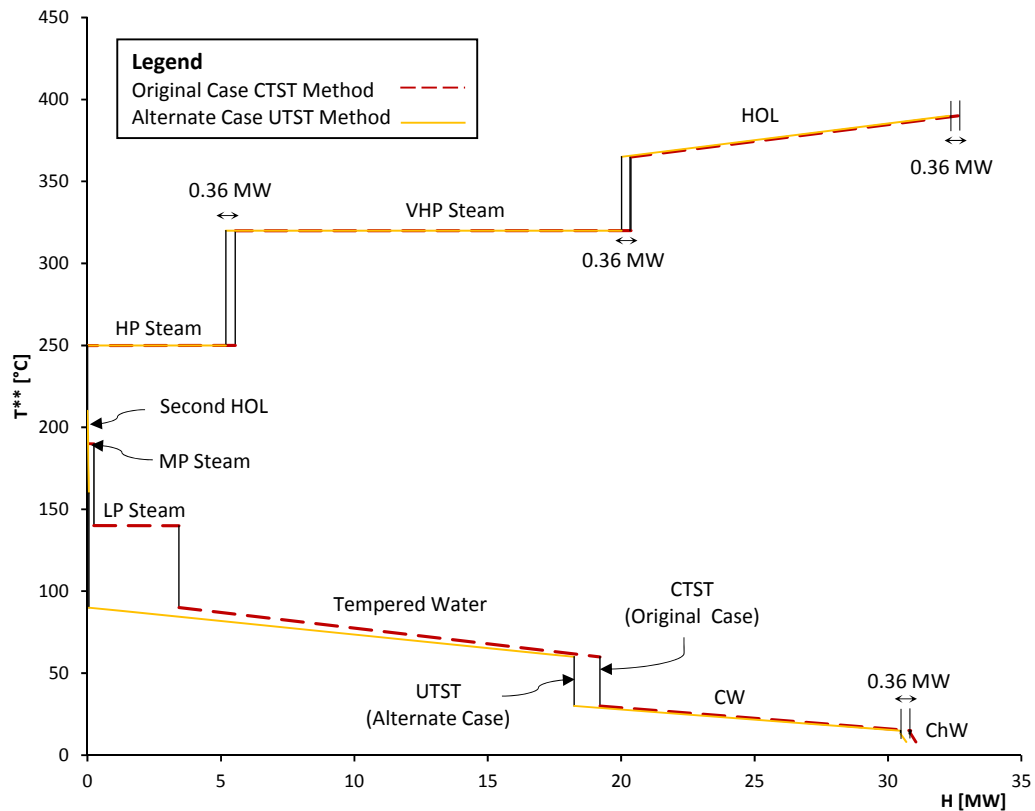


Fig. 11. SUGCC for Petrochemical Complex applying CTST method and retrofit case applying UTST method.

continuous high temperature processes.

- Utilities pinches in the new method are best observed at the process GCC level

After applying the UTST method steam utility demand increases because by introducing the additional constraints, utility pinches occurred within individual processes at the process level, rather than on the TSP, as is always the case with the conventional method. Also, Utility pinches can be seen for isothermal utilities on the TSP, in addition to the process GCCs. However, in case of non-isothermal utilities, the Pinch may not be visible on the TSP (Figs. 4, 6, 8 and 10).

- The new method is advantageous for non-continuous processes

An advantage of the UTST method is it only allows utility heat exchangers in series within the same process to achieve a utility's target temperature, as illustrated in Fig. 1b. As a result, the new method restricts any inter-dependency of utility use between processes, which is important for non-continuous processing clusters that often operate with different schedules and independently.

- The use of hot oil in place of steam utility (HPS, MPS and/or LPS) can increase TS heat recovery

The third case study on a Petrochemical Complex showed the interesting result of increasing TSHI through replacing MPS and LPS with hot oil. Intuitively, the shape of the individual GCCs will dictate the effectiveness of using hot oil instead of steam for increasing heat recovery. However, the increase in targeted heat recovery comes at the expense of a poorer heat transfer since the

heat transfer coefficient of oil is well below that of condensing/evaporating steam.

## 6. Conclusions

A new improved Total Site Heat Integration method has been demonstrated using three industrial case studies. None of the existing conventional TSHI methods addressed non-isothermal utilities targeting incorporated isothermal utilities targeting in the same procedure. The new method calculates more accurate, meaningful and realistic Total Site targets for non-isothermal utilities such as hot and cold water, and hot oil. The advantages of the new method – the Unified Total Site Targeting method – are: (1) the method can be effectively applied to both high temperature and low temperature processes, which use isothermal and non-isothermal utilities, to generate realistic utility targets; (2) although a reduction in Total Site heat recovery targets can be seen in new method, these targets are more achievable with realistic constraints, whereas the conventional method is over-optimistic in targeting non-isothermal utilities; and finally (3) the new method provides the opportunity for the engineer to evaluate different design options, such as replacing one or more isothermal utilities with non-isothermal utilities, which may simplify the utility network and/or increase TS heat recovery.

## Appendix A

A comprehensive comparison of hot and cold utility requirements, amount of heat recovery, and gross and net utility consumption and generation targets for both conventional and unified Total Site targeting methods are presented in the table below for the three case studies.

Case study	Targets										Cold utility consumption <sup>b</sup>														
	$\Sigma Q_{\text{hot}}$					$\Sigma Q_{\text{cold}}$					$\Sigma Q_{\text{HR}}$					Hot utility consumption <sup>a</sup>					Cold utility consumption <sup>b</sup>				
	MW		MW		MW	MW		MW		MW	MW		MW		MW	MW		MW		MW		MW		MW	
Dairy processing factory	CTST (Gross)	17.9	15.2	2.9	—	—	—	—	—	—	—	—	—	—	—	—	—	—	—	—	—	—	—	—	—
	CTST (Net)	14.7	11.9	6.2	—	—	—	—	—	—	—	—	—	—	—	—	—	—	—	—	—	—	—	—	—
	UTST (Gross)	17.9	15.2	2.9	—	—	—	—	—	—	—	—	—	—	—	—	—	—	—	—	—	—	—	—	—
Södra Cell Värö Kraft Pulp Mill	UTST (Net)	16.0	13.3	4.9	—	—	—	—	—	—	—	—	—	—	—	—	—	—	—	—	—	—	—	—	—
	CTST (Gross)	204.7	107.6	66.9	—	—	—	—	—	—	—	—	—	—	—	—	—	—	—	—	—	—	—	—	—
	CTST (Net)	168.6	71.5	103.0	—	—	—	—	—	—	—	—	—	—	—	—	—	—	—	—	—	—	—	—	—
Petrochemical Complex	UTST (Gross)	204.7	107.6	66.9	—	—	—	—	—	—	—	—	—	—	—	—	—	—	—	—	—	—	—	—	—
	UTST (Net)	170.8	73.7	100.8	—	—	—	—	—	—	—	—	—	—	—	—	—	—	—	—	—	—	—	—	—
	CTST (Gross)	35.7	34.1	32.4	12.3	14.8	6.0	—	—	—	—	—	—	—	—	—	—	—	—	—	—	—	—	—	—
Petrochemical Complex (Alternative design)	CTST (Net)	32.6	31.0	35.5	12.3	14.8	5.5	—	—	—	—	—	—	—	—	—	—	—	—	—	—	—	—	—	—
	UTST (Gross)	35.7	34.1	32.4	12.3	14.8	5.1	—	—	—	—	—	—	—	—	—	—	—	—	—	—	—	—	—	—
	UTST (Net)	32.6	31.0	35.5	12.3	14.8	4.7	—	—	—	—	—	—	—	—	—	—	—	—	—	—	—	—	—	—
Petrochemical Complex (Alternative design)	CTST (Gross)	35.7	34.1	32.4	12.3	14.8	4.7	3.9	—	—	—	—	—	—	—	—	—	—	—	—	—	—	—	—	—
	CTST (Net)	31.8	30.2	36.3	12.3	14.8	4.7	0.0	—	—	—	—	—	—	—	—	—	—	—	—	—	—	—	—	—
	UTST (Gross)	35.7	34.1	32.4	12.3	14.8	5.2	3.5	—	—	—	—	—	—	—	—	—	—	—	—	—	—	—	—	—
	UTST (Net)	32.3	30.7	35.8	12.3	14.8	5.2	0.0	—	—	—	—	—	—	—	—	—	—	—	—	—	—	—	—	—

<sup>a</sup> Cold utility generation.

<sup>b</sup> Hot utility generation.

## References

- [1] Klemeš JJ, Varbanov PS, Kravanja Z. Recent developments in process integration. *Chem Eng Res Des* Oct. 2013;91(10):2037–53.
- [2] Klemeš JJ, Kravanja Z. Forty years of Heat Integration: Pinch Analysis (PA) and Mathematical Programming (MP). *Curr Opin Chem Eng* Nov. 2013;2(4):461–74.
- [3] Klemeš JJ. *Handbook of process integration: minimisation of energy and water use, waste and emissions*. First. Cambridge, UK: Woodhead Publishing; 2013.
- [4] Linnhoff B, Hindmarsh E. The pinch design method for heat exchanger networks. *Chem Eng Sci* 1983;38(5):745–63.
- [5] Hackl R, Harvey S. Framework methodology for increased energy efficiency and renewable feedstock integration in industrial clusters. *Appl Energy* Dec. 2013;112:1500–9.
- [6] Biegler LT, Grossmann IE, Westerberg AW. *Systematic methods of chemical process design*. 1 edition. Upper Saddle River, NJ: Prentice Hall; 1997.
- [7] Furman KC, Sahinidis NV. *A Critical Review and Annotated Bibliography for Heat Exchanger Network Synthesis in the 20th Century*. *Ind Eng Chem Res* May 2002;41(10):2335–70.
- [8] Dhole VR, Linnhoff B. Total site targets for fuel, co-generation, emissions, and cooling. *Comput Chem Eng* 1993;17(1):S101–9.
- [9] Klemeš J, Dhole VR, Raissi K, Perry SJ, Puigjaner L. Targeting and design methodology for reduction of fuel, power and CO2 on total sites. *Appl Therm Eng* Aug. 1997;17(8–10):993–1003.
- [10] Ahmad S, Hui DCW. Heat recovery between areas of integrity. *Comput Chem Eng* Dec. 1991;15(12):809–32.
- [11] Hui CW, Ahmad S. Total site heat integration using the utility system. *Comput Chem Eng* Aug. 1994;18(8):729–42.
- [12] Bandyopadhyay S, Varghese J, Bansal V. Targeting for cogeneration potential through total site integration. *Appl Therm Eng* Jan. 2010;30(1):6–14.
- [13] Raissi K. Total site integration. PhD Thesis. Manchester, UK: UMIST; 1994.
- [14] Fritzson A, Berntsson T. Energy efficiency in the slaughter and meat processing industry—opportunities for improvements in future energy markets. *J Food Eng* Dec. 2006;77(4):792–802.
- [15] Matsuda K, Hirochi Y, Tatsumi H, Shire T. Applying heat integration total site based pinch technology to a large industrial area in Japan to further improve performance of highly efficient process plants. *Energy* Oct. 2009;34(10):1687–92.
- [16] Matsuda K, Hirochi Y, Kurosaki D, Kado Y. Application of Area-wide Pinch Technology to a Large Industrial Area in Thailand. *Chem Eng Trans* 2014;39:1027–32.
- [17] Hackl R, Harvey S. From heat integration targets toward implementation – A TSA (total site analysis)-based design approach for heat recovery systems in industrial clusters. *Energy* Oct. 2015;90(Part 1):163–72.
- [18] Bonhivers JC, Svensson E, Berntsson T, Stuart PR. Comparison between pinch analysis and bridge analysis to retrofit the heat exchanger network of a kraft pulp mill. *Appl Therm Eng* Sep. 2014;70(1):369–79.
- [19] Varbanov PS, Fodor Z, Klemeš JJ. Total Site targeting with process specific minimum temperature difference ( $\Delta T_{\text{min}}$ ). *Energy* Aug. 2012;44(1):20–8.
- [20] Fodor Z, Klemeš JJ, Varbanov PS, Walmsley MRW, Atkins MJ, Walmsley TG. Total Site Targeting with Stream Specific Minimum Temperature Difference. *Chem Eng Trans* 2012;29:409–14.
- [21] Perry S, Klemeš J, Bulatov I. Integrating waste and renewable energy to reduce the carbon footprint of locally integrated energy sectors. *Energy* Oct. 2008;33(10):1489–97.
- [22] Nemet A, Klemeš JJ, Varbanov PS, Kravanja Z. Methodology for maximising the use of renewables with variable availability. *Energy* Aug. 2012;44(1):29–37.
- [23] Varbanov PS, Klemeš JJ. Integration and management of renewables into Total Sites with variable supply and demand. *Comput Chem Eng* Sep. 2011;35(9):1815–26.
- [24] Becker H, Maréchal F. Energy integration of industrial sites with heat exchange restrictions. *Comput Chem Eng* Feb. 2012;37:104–18.
- [25] Liew PY, Wan Alwi SR, Klemeš JJ, Varbanov PS, Abdul Manan Z. Total Site Heat Integration with Seasonal Energy Availability. *Chem Eng Trans* 2013;35:19–24.
- [26] Liew PY, Wan Alwi SR, Varbanov PS, Manan ZA, Klemeš JJ. Centralised utility system planning for a Total Site Heat Integration network. *Comput Chem Eng* Oct. 2013;57:104–11.
- [27] Liew PY, Lim JS, Wan Alwi SR, Abdul Manan Z, Varbanov PS, Klemeš JJ. A retrofit framework for Total Site heat recovery systems. *Appl Energy* Dec. 2014;135:778–90.
- [28] Chew KH, Klemeš JJ, Wan Alwi SR, Manan ZA. Process modifications to maximise energy savings in total site heat integration. *Appl Therm Eng* Mar. 2015;78:731–9.
- [29] Bade MH, Bandyopadhyay S. Minimization of Thermal Oil Flow Rate for Indirect Integration of Multiple Plants. *Ind Eng Chem Res* Aug. 2014;53(33):13146–56.
- [30] Tarighaleslami AH, Walmsley TG, Atkins MJ, Walmsley MRW, Neale JR. Heat Transfer Enhancement for site level indirect heat recovery systems using nanofluids as the intermediate fluid. *Appl Therm Eng* July 2016;105:923–30.
- [31] Liew PY, Wan Alwi SR, Klemeš JJ, Varbanov PS, Abdul Manan Z. Algorithmic targeting for Total Site Heat Integration with variable energy supply/demand. *Appl Therm Eng* Sep. 2014;70(2):1073–83.
- [32] Sun L, Doyle S, Smith R. Heat recovery and power targeting in utility systems.

- Energy May 2015;84:196–206.
- [33] Nemet A, Klemeš JJ, Kravanja Z. Mathematical Programming Approach to Total Site Heat Integration. In: P. S. V., Jiří Jaromír Klemeš PYL, editors. *Computer aided chemical engineering* vol. 33. Elsevier; 2014. p. 1795–800.
- [34] Čuček L, Kravanja Z. Retrofit of Total Site Heat Exchanger Networks by Mathematical Programming Approach. In: Martín M, editor. *Alternative energy sources and technologies*. Springer International Publishing; 2016. p. 297–340.
- [35] Atkins MJ, Walmsley MRW, Neale JR. Process integration between individual plants at a large dairy factory by the application of heat recovery loops and transient stream analysis. *J Clean Prod* Oct. 2012;34:21–8.
- [36] Walmsley TG, Walmsley MRW, Atkins MJ, Neale JR. Integration of industrial solar and gaseous waste heat into heat recovery loops using constant and variable temperature storage. *Energy* Oct. 2014;75:53–67.
- [37] Walmsley MRW, Atkins MJ, Riley J. Thermocline Management of Stratified Tanks for Heat Storage. *Chem Eng Trans* 2009;18:231–6.
- [38] Atkins MJ, Walmsley MRW, Neale JR. The challenge of integrating non-continuous processes – milk powder plant case study. *J Clean Prod* Jun. 2010;18(9):927–34.
- [39] Walmsley MRW, Walmsley TG, Atkins MJ, Neale JR. Area Targeting and Storage Temperature Selection for Heat Recovery Loops. *Chem Eng Trans* 2012;29:1219–24.
- [40] Walmsley MRW, Walmsley TG, Atkins MJ, Neale JR. Methods for improving heat exchanger area distribution and storage temperature selection in heat recovery loops. *Energy* Jun. 2013;55:15–22.
- [41] Walmsley TG, Walmsley MRW, Tarighaleslami AH, Atkins MJ, Neale JR. Integration options for solar thermal with low temperature industrial heat recovery loops. *Energy* 2015;90(Part 1):113–21.
- [42] Tarighaleslami AH, Walmsley TG, Walmsley MRW, Atkins MJ, Neale JR. Heat Transfer Enhancement in Heat Recovery Loops Using Nanofluids as the Intermediate Fluid. *Chem Eng Trans* 2015;45:991–6.
- [43] Chang C, Chen X, Wang Y, Feng X. An efficient optimization algorithm for waste Heat Integration using a heat recovery loop between two plants. *Appl Therm Eng* July 2016;105:799–806.
- [44] Liew PY, Wan Alwi SR, Varbanov PS, Manan ZA, Klemeš JJ. A numerical technique for Total Site sensitivity analysis. *Appl Therm Eng* Jul. 2012;40:397–408.
- [45] Atkins MJ, Walmsley MRW, Walmsley TG, Neale JR. Targeting using process integration for large industrial sites operating non-continuously. In: *Chemeca 2012*. Wellington: New Zealand; 2012.
- [46] Walmsley MRW, John Atkins M, Walmsley TG. Application of Heat Recovery Loops to Semi-continuous Processes for Process Integration. In: Klemeš JJ, editor. *Handbook of process integration (PI)*. Cambridge, UK: Woodhead Publishing; 2013. p. 594–629.
- [47] Wang Y, Chang C, Feng X. A systematic framework for multi-plants Heat Integration combining Direct and Indirect Heat Integration methods. *Energy* Oct. 2015;90(Part 1):56–67.
- [48] Bood J, Nilsson L. Energy analysis of hemicellulose extraction at a softwood Kraft pulp mill, case study of Södra Cell Värö. MSc Thesis. Gothenburg, Sweden: Chalmers University of Technology; 2013.
- [49] Kemp IC. *Pinch analysis and process integration*. second ed. Cambridge, UK: Butterworth-Heinemann; 2007.



**Article 11:**

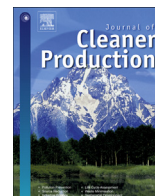
*Total site mass, heat and power integration using process integration and process graph*

Ong, B.H.Y., **Walmsley, T.G.**, Atkins, M.J., Walmsley, M.R.W., 2017.

Journal of Cleaner Production 167, 32–43.

DOI: 10.1016/j.jclepro.2017.08.035

Elsevier



# Total site mass, heat and power integration using process integration and process graph



Benjamin H.Y. Ong<sup>a,\*</sup>, Timothy G. Walmsley<sup>b</sup>, Martin J. Atkins<sup>a</sup>, Michael R.W. Walmsley<sup>a</sup>

<sup>a</sup> Energy Research Centre, School of Engineering, University of Waikato, Private Bag, 3105, Hamilton, New Zealand

<sup>b</sup> Sustainable Process Integration Laboratory – SPIL, NETME Centre, Faculty of Mechanical Engineering, Brno University of Technology - VUT Brno, Technická 2896/2, 616 69, Brno, Czech Republic

## ARTICLE INFO

### Article history:

Received 19 May 2017

Received in revised form

9 July 2017

Accepted 5 August 2017

Available online 9 August 2017

Handling Editor: Yutao Wang

### Keywords:

P-graph

Process integration

Total site integration

Combined heat and power

Optimisation

Mathematical programming

## ABSTRACT

This paper aims to develop a novel method to visualise and solve Total Site Mass, Heat and Power Integration problem using a combination of Process Integration and P-graph techniques. Previous methods dealing with mass, heat and power integration are based on Mathematical Programming, which has the disadvantage of lacking adequate visualisation tools during the construction and optimisation of the problem. It also can face computational issues as problems become increasingly complex. The new method incorporates three important process engineering tools: (1) process modelling of mass and energy balance, (2) Pinch Analysis of individual processes and Total Site Heat Integration of clusters of related processes, and (3) the construction of a Total Site superstructure within the P-graph framework to represent the possible mass, heat, and power interconnections between process and utility systems. To demonstrate the method, a biorefinery case study is investigated. The basis for the biorefinery is a Kraft pulp mill in combination with three potential processes, combined heat and power, and geothermal steam. The three considered new processes are gasification for dimethyl-ether production, simultaneous scarification and co-fermentation of pine for ethanol production, and hydrothermal liquefaction for bio-oil production. Results from the case study show the current optimal solution as a Kraft mill with geothermal heat achieving a profit (revenue less energy and capital costs) of NZD \$283 M/y. A near-optimal solution has hydrothermal liquefaction added to the Kraft mill with geothermal heat with a profit of NZD \$252 M/y.

© 2017 Elsevier Ltd. All rights reserved.

## 1. Introduction

Industrial clustering allows the potential for highly integrated and efficient production of multiple products. The integration could be in the form of material or heat exchange to fully utilise material and energy inputs and re-use waste materials to improve economics. Existing engineering based design methods chiefly focus on site-wide material or heat integration, not both simultaneously. Process Integration, which includes Pinch Analysis, represents a rigorous framework to determine potential and design for reduced energy, waste, and emissions in industrial plants. The framework applies thermodynamic laws to understand the intrinsic nature of industrial production systems with an emphasis on the efficient use of energy and water, and the minimisation of environmental

impacts. As the first major development in PI, Pinch Analysis (PA) marked the beginning of a highly successfully approach to industrial heat integration (Linnhoff and Flower, 1978). PA is now a well-proven technique to identify and design economical heat recovery projects. The Pinch analogy has found application to a wide range of problems, with mass integration being one of the first (El-Halwagi and Manousiouthakis, 1989).

Total Site Integration provides a general framework for expressing the site-level integration of multiple clustered processes and plants with the goal of minimising energy use, resource consumption, and environmental impact. The initial conception of Total Site primarily focused on heat and power integration targets at the site level – Total Site Heat Integration, TSHI (Dhole and Linnhoff, 1993). In carrying out TSHI, the heat demand profiles of individual processes are composited to represent the site source and sink profiles for utility targeting. These profiles give valuable information regarding improvements that are possible at the site-level and how these might be achieved. Typical opportunities

\* Corresponding author.

E-mail address: [bhyo1@students.waikato.ac.nz](mailto:bhyo1@students.waikato.ac.nz) (B.H.Y. Ong).

include replacing a high pressure steam with a lower pressure steam to increase power generation, adding a new steam level to increase heat integration and/or power generation, and introducing renewable energy, such as geothermal heat. Application of the TSHI approach to industrial has proven successful (Klemeš et al., 1997).

TSHI has attracted significant research attention, expanding its application and refining its results (Klemeš, 2013). These developments have chiefly focused on maximising heat and power integration using new approaches and optimising these targets by accounting for additional costs. A sample of studies from the past three years shows the general directions of consideration. Liew et al. (2014) studied the integration of preheating boiler feed water using heat recovery using TSHI. Sun et al. (2014) presented a graphical method for determination of Total Site cogeneration potential through Combined Heat and Power. Chew et al. (2015) investigated the role of process modifications at the process and Total Site levels and the impact of overall energy integration. Liew et al. (2015) looked at the issue of plant layout and its effect on TSHI targets. Nemet et al. (2015) considered how fluctuating utility prices influences the design and retrofit of TSHI networks. Atkins et al. (2016) introduced the idea of using background/foreground analysis to decide synergistic new entrants to a wood processing cluster, which included geothermal heat, and TSHI to quantify the heat savings. Čuček and Kravanja (2016) using a Mathematical Programming (MP) approach to the optimal retrofit design of Total Site heat exchanger networks. Liew et al. (2016) developed an approach to include district cooling systems into TSHI with a focus on local energy sectors. Walmsley (2016) presented a new Total Site level method for the integrated design of evaporation systems including mechanical and thermal vapour recompression. Chang et al. (2016) demonstrated the cost optimisation of Total Site level heat recovery loops considering heat savings, capital investment, and pumping cost. Wang and Feng (2017) showed how the distance between source and sink affects TSHI economics. Tarighaleslami et al. (2017) focused on unifying TSHI for multiple isothermal (steam) and non-isothermal (hot water) utility targeting. Walmsley et al. (2017) described a Total Site integration and optimisation of both process and utility systems using a combination of targeting and process modelling techniques. Hassiba et al. (2017) focused on emissions management at large industrial sites through improved

energy integration.

Total Site problems with simultaneous mass, heat, and power integration, i.e. Total Site Mass, Heat and Power Integration (TSMHPI), as shown in Fig. 1, has received significantly less attention even though this has been viewed as an area of rich potential for a new generation of mega processing sites. Duran and Grossmann (1986) proposed a simultaneous solution for optimal heat integration while optimising the process flow sheet by approximating the non-differentiable optimisation problem and concluded that simultaneous approach is more efficient than the sequential approach in heat integration. Marechal and Kalitventzeff (2003) reported that a variation in process stream properties, production level and product grade lead to different design and operation of the heat exchanger network due to the different possible heat recovery. Simultaneous process synthesis and process integration should be considered when synthesising an industrial cluster. Gassner and Maréchal (2009) presented a superstructure model to produce SNG from woody biomass with sequential mass and energy balance and process integration for optimal materials and utility recovery. Baliban et al. (2011) presented simultaneous process synthesis and power integration in thermochemical coal, biomass and natural gas to liquids facility. The negative side of this approach is the complex mathematical models are more computationally intensive and require more detailed process data. Ng et al. (2012) proposed an approach to simultaneously select the optimum process technologies and production with heat and power integration. Modular optimisation approach was used to break down the complex problem into small models. Kong and Shah (2017) proposed an optimisation model to simultaneously screen for reaction pathways, separation and product separation with heat integration. The proposed method is solved with MILP and improved heat recovery is reported by including the screening of different separation methods. For a biorefinery example, biomass processing is challenging to model. One of the challenges is, biomass processing presents numerous alternative processing routes. By including PI in the pre-selection stage, it introduces an additional layer of combinatorial complexity.

There are some important differences between the advancements for TSHI problems and TSMHPI problems. The complexity of the TSMHPI problem is far greater than the TSHI problem. This has

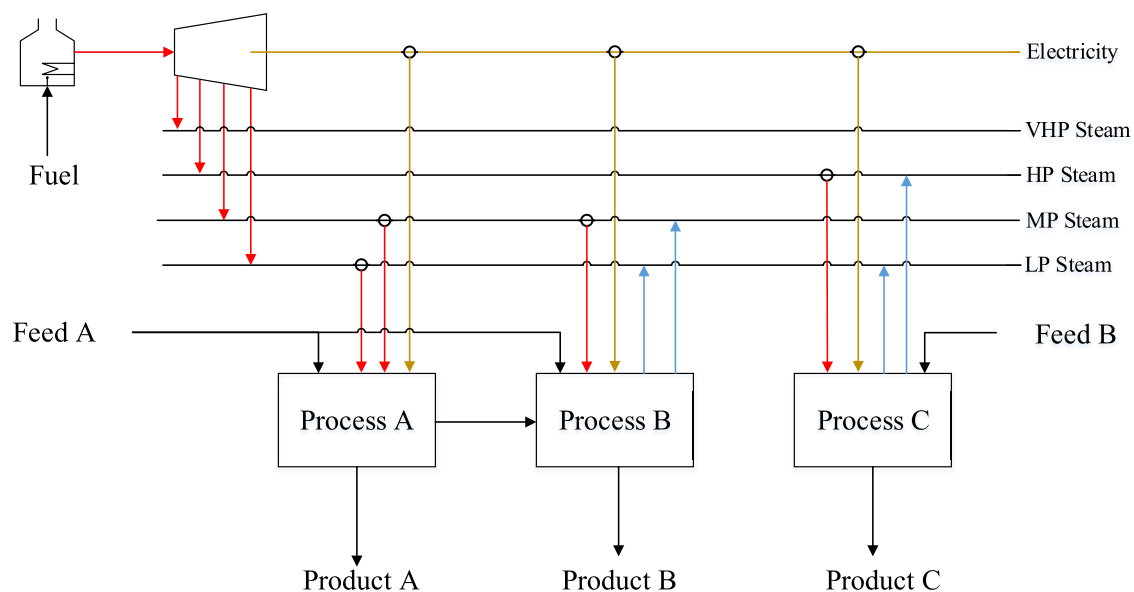


Fig. 1. Total Site Mass, Heat and Power Integration (TSMHPI) problem.

led to TSHI methods comprising both graphical and MP based approaches whereas TSMHPI methods only applied MP. However, the difficulty to solve a Total Site problem by employing MP increases as the size of the problem increases. As a result, the need for specialised MP software and expertise creates a barrier to an increased focus on taking full advantage offered by using a TSMHPI approach. TSHI includes graphical tools such as Total Site Profiles and Site Utility Grand Composite Curves that enable the problem and opportunity to be visualised. Similarly, TSMHPI needs graphical tools to enable visualisation of the problem while maintaining the rigour of optimisation associated with MP.

Process graph (P-graph) methodology is one approach to visualise multi-dimensional network problems using a MP optimisation framework. P-graph employs combinatorial and optimisation algorithms to reduce problem search space size and solve process network synthesis (PNS) problems. P-graph uses a graphical interface to represent the structure of the problem that allows visualisation of the problem, providing a face to the underlying MP. P-graph is more advantageous than other MP approaches as it solves PNS problems through the combinatorial nature of the problem instead of translating the problem into a superstructure with multiple sets of equations. The combinatorial instrument, the five P-graph axioms and the P-graph algorithms, proposed by Friedler et al. (1992), reduces the combinatorial search space by avoiding the infeasible combinations. As the structure of a PNS problem increases, the complexity of the problem increases exponentially. The P-graph methodology generates a superstructure that contains only combinatorially feasible of producing products(s) from raw material(s). Errors that are made during the generation of P-graph model is excluded from the maximal structure. This reduces the free variables from the combinatorially infeasible solutions (Heckl et al., 2010), which is an advantage of P-graph over MP. Another advantage P-graph is, it shows both optimal and near-optimal structures, which finds use in the optimisation of industrial symbiotic networks (Aviso et al., 2015). Voll et al. (2015) suggests that near-optimal solutions are important, as optimal solution is usually an approximation of the optimal real world-solution. With volatile energy prices and demand, near-optimal solutions allow a deeper understanding of the PNS problem for decision making. As an emerging process engineering tool, P-graph has been extended to solve problems such as optimisation of regional supply chains (Lam et al., 2010), heat exchanger network synthesis (Nagy et al., 2001) and efficient energy conversion networks using fuel cells (Varbanov and Friedler, 2008). P-graph has the required elements suitable for adaptation to solving a TSMHPI problem. To date, optimisation of a P-graph model with varying multiple processes with optimisable production rates using multiple levels of hot utility and power generation has not been reported.

The aim of this paper is to develop a novel method to visualise and solve Total Site Mass, Heat and Power Integration (TSMHPI) problem using a combination of Process Integration and P-graph techniques. The new methodology encompasses three distinct engineering tools. First, processes and factories are modelled using sound mass and energy balance modelling (or simulation) techniques. Second, process level PA and Total Site level integration studies of potential processes and factories are undertaken to understand the internal heat recovery potential and the overall heat demand profiles. Third, implementation of potential processes and factories into P-graph. The various process entities in the P-graph model link together through both mass and heat flows while turbines and combined cycles generate power. This paper uses a biorefinery case study to demonstrate the method. The scope of the considered biorefinery processes in this study has been limited to gasification of black liquor (BL), hydrothermal liquefaction (HTL) of biomass and simultaneous scarification and co-fermentation (SSCF)

of biomass, co-located with an existing Kraft Pulp Mill. The superstructure consists of the possibility of material integration between biorefinery processes as well as Total Site Heat Integration through a common steam and hot water utility system.

## 2. Methods

This study aims to develop a novel method that enables visualisation and optimisation of TSMHPI problems. This achieved by combining PI tools and P-graph into a sequential optimisation. The overview of the TSMHPI method is presented in Fig. 2.

The first two steps of the method are the selection of processes and extraction of relevant data from industrial and literature data sources. Ideally, this data should be based on real, full-scale plants but this is not always possible for emerging technologies. The extracted data forms the primary input to the development of process models for the considered processes. The process model should involve a mass and energy balance and be implemented via an Excel™ spreadsheet model, as done in the present study, or via process simulation software. Process data may be gathered directly from existing industrial processes or from literature sources. This study uses both approaches. Mass balance allows the performance of the processes to be analysed, how much product and by-products are produced by the process for each unit of feedstock. Raw materials and products are prepared, heated or cooled and reacted with other materials according to the specifications of the process. Heat balances are carried out to determine overall heating and cooling requirements.

In the steps 4 and 5, stream data are extracted from the process model and utility demand targets are set using established TSHI methods. In the first instance, individual processes are analysed using Process PA to determine heat recovery and utility demand. Minimum approach temperatures,  $\Delta T_{\min}$ , may be based on a global parameter, process-specific basis, or stream-specific basis. The magnitude of  $\Delta T_{\min}$  is appropriately selected for the process or stream depending on the approach. Utility demands are converted to specific terms and assumed to scale with process production rate. These targets may be incorporated directly into the P-graph model or, alternatively, the representation in P-graph may be simplified by combining related processes into a single cluster with a net heat and power demand profile. Net energy demand profiles for multiple utility levels may be determined using the TSHI method of Tarighaleslami et al. (2017) and may be characterised by using Total Site Profiles and Site Utility Grand Composite Curves that are specific to a cluster. Related processes are those that are highly interdependent on one another. Whether two or more processes are related depends on the specific situation and goal. For example, a Kraft pulp mill is a cluster of related processes with the overall aim of producing pulp. As such, a neighbouring paper machine may be considered as independent from the Kraft mill cluster since its goal is to produce paper, not pulp.

The sixth step is to develop a P-graph superstructure of site level process and utility operations including mass, heat, and power interconnections between the operations. This study uses P-graph Studio 5.2 (2017) to implement and solve the TSMHPI problem. A detailed explanation of the method for implementation of the superstructure model to represent the problem is provided in the next three sections. In general, the process and utility systems are represented in P-graph by one or more vertices. These vertices are connected by mass and heat transfer using a superstructure approach where all possible combinations of site level mass and heat integration are drawn. One vertex may also represent a cluster of processes with its net energy demand profile. Once set up, the P-graph algorithms, MSG and SSG, generate the maximal superstructure and all combinatorially feasible individual networks. The

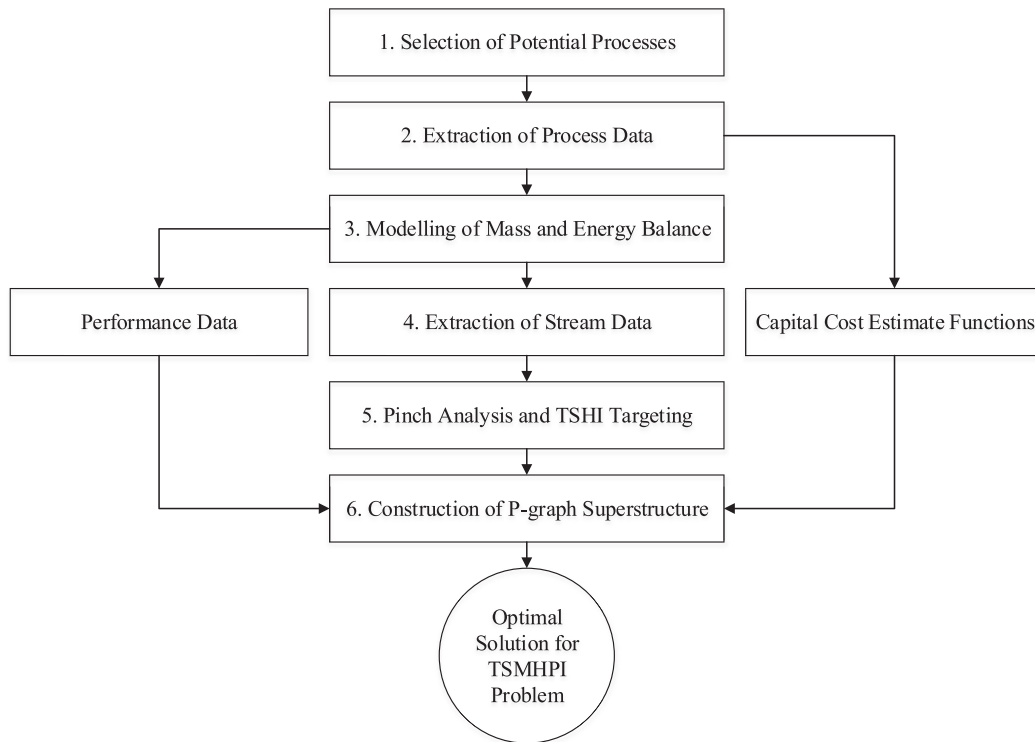


Fig. 2. Total Site Mass, Heat and Power Integration method using process heat integration and P-graph.

ABB algorithm then determines the optimal and near-optimal networks (Friedler et al., 1996). Additional details on how the superstructure is formed and data implemented are explained in the next three sections.

Using the P-graph model a sensitivity analysis should be conducted to understand how variations in input data that reflect its uncertainty affect the final solution. In this study, the final product prices are varied with the range of 0%–100%.

### 2.1. Process operating units and clusters

P-graph is a bipartite graph having two types of vertices, one for operating units and one representing material and/or energy flows (Fig. 3). An arc connecting an operating unit and a material is used to represent the relationship between the operating units and materials. The rectangle vertices are used to represent an operating unit, a process, and/or a cluster of processes. Each operating unit vertex must have at least one input flow and one product output. The input can be raw materials flows (e.g. biomass, black liquor) and utility flows (e.g. steam, geothermal heat, and chilled water). The outputs are the product, by-products and/or utilities generated by the process (e.g. dimethyl-ether, bio-oil, ethanol and electricity). The output may either be a final product, which is represented by a target symbol, or an intermediate product, which is represented by a large solid dot. The performance of the operating unit is specified by the amount of output generated per unit amount of a selected input stream. The performance of the operations is defined by overall conversion factors for feedstock to production while specific utility demand requirements from the heat integration study, capital cost functions for each process and utility operation, and feedstock and final product prices are also added. Some clustered processes can often be represented by a single operating unit vertex while a turbine with multi-stages needs multiple operating unit vertices.

### 2.2. Implementation of feedstock, product and capital cost estimates

The appropriate implementation of cost and price data into P-graph can be non-trivial. P-graph Studio 5.2 limits capital cost functions to linear functions (i.e.  $y = mx + c$ ) and feedstock and product prices to proportional functions (i.e.  $y = mx$ ). This limitation presents a significant problem since capital cost functions are normally non-linear, e.g. power-law functions ( $y = mx^n + c$ ), while feedstock and product prices may depend on volume. Ong et al. (2016) reported an approach to approximate non-linear functions in P-graph using a piece-wise linear approximation split between several operating unit vertices. The approach on how to incorporate nonlinearity in P-graph differs for capital costs, feedstock prices, and product prices.

Capital cost functions are ideally formulated using real plant costs at multiple scales. Since full datasets are rarely available, order of magnitude capital cost estimates based on at least one installation (or detailed cost calculation) may be forecasted using power law estimation for the different scale of productions (Gerrard, 2000), as shown in Eq (1)

$$C = kx^a + b \quad (1)$$

where  $C$  is the cost of the plant at size  $x$ ,  $a$  is the exponent,  $k$  is a constant of the nominal cost of the item at unit scale and  $b$  is the fixed cost. Where historical or published data of the capital cost estimates are unavailable, the capital costs of the different process capacities are estimated with the rule of six-tenths, i.e.  $a = 0.6$ .

The capital costs of all operating units are then translated to Eq (2) to calculate the capital cost in P-graph, as given in Eq (2):

$$CC_{linear} = A_{CC} + B_{CC}x \quad (2)$$

where  $CC_{linear}$  is the investment cost, is estimated using a fixed

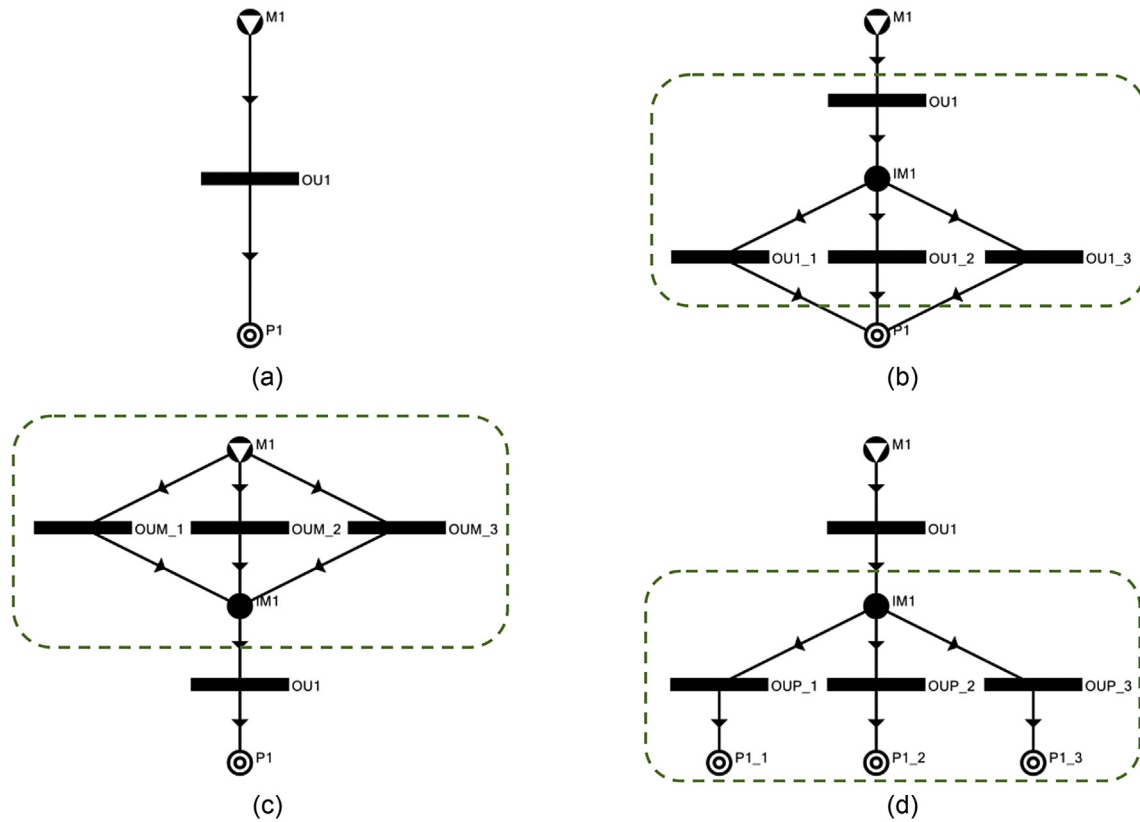


**Fig. 3.** (a) Representation of PNS problem with conventional P-graph framework, (b) approximation of non-linear operating unit costs, (c) approximation of non-linear raw material costs, and (d) approximation of non-linear product costs.

investment cost,  $A_{CC}$ , plus a linear function of plant size (or capital size),  $B_{CC}$ , that is proportional to input material flow rate,  $x$ .

The non-linear cost functions are divided into subintervals using a piecewise linear function. The non-linear cost function is divided into multiple subintervals using equal capacity ranges until the error between the original non-linear cost function and the approximated piece-wise linear cost functions is within the range of error of  $\pm 2.5\%$ . Eq (3) calculates the error of each subinterval,

$$Error = \frac{CC_{actual} - CC_{linear}}{CC_{actual}} \quad (3)$$

where  $CC$  is the investment cost.

For the raw material, the cost of delivered feedstock may also be non-linear, being governed by available volume and distance. For example, higher required wood feedstock volumes increase the average distance travelled from the harvest source to the industrial site, which increases the average delivered cost of biomass. Likewise, the product price may also be non-linear depending on volume and market demand. The non-linear equation of feedstock and product prices depend on the specific situation but can often be modelled using a power-law function such as Eq (1).

The implementation of piece-wise approximation of non-linear functions using multiple linear sub-functions in P-graph Studio requires different approaches for raw materials, operating units and products. Fig. 3 presents illustrative examples of how the linearization is programmed into a P-graph structure, with three subintervals, for operating units (3b), raw materials (3c) and products (3d).

For operating units with non-linear cost functions, additional operating unit(s) representing each subinterval are added to the

original structure with lower and upper capacity multiplier based on the production interval. Since the correlations of the power law are only applicable over fixed range of production size, a limit of the flow raw material into the operating unit is imposed to ensure that the error is minimised. To limit the flow of raw materials into the processes under consideration, an operating unit (OU1 in Fig. 3b) with a fixed upper bound capacity multiplier and an intermediate (IM1) are added. Each interval's linearized fixed and proportional investments cost are assigned to the subinterval's corresponding operating unit.

To incorporate the non-linear cost functions of raw materials, operating units based on the number of subintervals and an intermediate material is added. The cost function is divided and represented by the addition of operating units. The cost for the raw material is added into the proportional operating cost of the operating units. However, in this case, all the lower and upper bounds capacity multiplier is the same throughout the operating units.

For the incorporation of the product cost, the operating units added are dummy operating units. The intermediate material added acts as the output material of the previous operating units that produces the product and distribute them to the different subinterval product cost curve. The cost and flows of the product are added in the product material individually.

### 2.3. Combined heat and power

The P-graph superstructure included a Combined Heat and Power system, which incorporated a boiler, deaerator, and turbine, as shown in Fig. 4. In the model, condensate (blue line) is assumed to return from the processes at a specified temperature (85 °C) and

return percentage. This is combined in the model with make-up water that is preheated to the same temperature using LP steam. The resultant flow becomes the feed to the deaeration process, which also requires steam. The specifications of the deaerator may be based on industry standards, such as [Spirax Sarco Limited \(2007\)](#), which recommend an operating pressure at 0.2 bar at 105 °C with approximately 2% energy loss through the vent. The exit liquid flow from the deaerator is the boiler feed water (BFW). The BFW is then pressurised with a pump and passed to the boiler. Heat from the combustion process is added with the BFW to at the operating unit representing the boiler. The ratio of mass to energy inputs to the boiler defines the superheated steam conditions based on its enthalpy. The superheated steam then passes through multiple operating units, which simulate different stages of the turbine.

A fixed isentropic efficiency is assumed for each extraction stage. The outputs from each stage are lower enthalpy (and pressure) steam and power generation. The output steam flow splits between fulfilling process demands and carrying on to the next turbine stage. All power outputs (orange lines) are collected at an intermediate energy to sum the total power generation.

### 3. Biorefinery case study

The case study considered in this paper is a wood-to-fuel biorefinery, co-locating with an existing Kraft Pulp Mill in Central North Island of New Zealand. Forestry is an important industry in New Zealand. The forestry sector is the third largest export earner, exporting logs, pulp and paper and other residues. A large

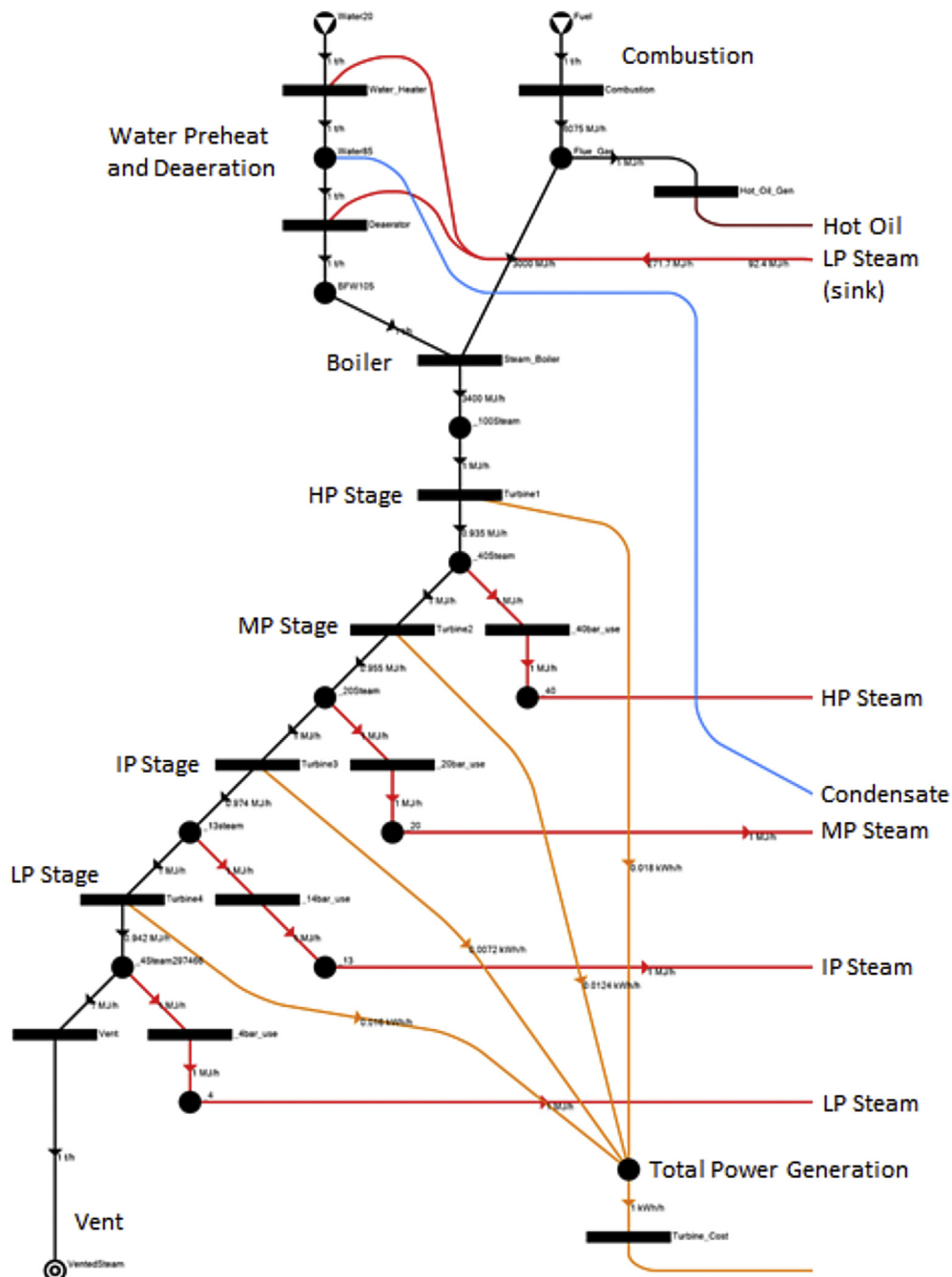


Fig. 4. Implementation of a boiler system with turbine and condensate return in P-graph.

proportion of logs is exported as whole logs. The pulp and paper industry market plummeted when the economic crisis hit in 2009, from which the industry is still recovering to pre-crisis levels (SETIS, 2011). Traditional processing in the pulp mill shows low returns. Increased competition and a volatile foreign exchange rate affect the forestry industry in New Zealand. These pressures are forcing the industry to consider other opportunities to diversify into new, non-traditional products to grow revenue and profit from the same quantum of wood feedstock.

There are several emerging secondary processing technologies that could use wood residues to produce high value bio-based fuels and chemical for rapidly growing markets (de Jong et al., 2012). Only 50% of high value products are extracted from harvested log and others are low value wood residues (Jack et al., 2013). Evolving towards an integrated biorefinery would allow the industry to diversify by manufacturing new high value chemicals, fuels and power, in addition to the traditional core products (van Heiningen, 2006). In principle, co-location of biorefineries with an existing pulp mill allows the potential for highly integrated and efficient production of multiple products by fully utilising material and energy inputs and re-using waste materials. The evolution of a Kraft mill into a biorefinery is an excellent example of a TSMHPI problem and opportunity.

### 3.1. Process selection, data extraction and mass and energy balance

For the biorefinery case study, the raw material is wood biomass with dimethyl-ether (DME), bio-oil and ethanol as potential products. The processes considered in this case are gasification of black liquor, hydrothermal liquefaction (HTL) of biomass and simultaneous scarification and co-fermentation (SSCF) of biomass with a combined heat and power (CHP) on site. The process data for HTL on performance balance model, estimating investment and operational costs were reported by Tews et al. (2014). The process data and conditions for gasification are extracted from Larson et al. (2006), where energy, environment and economic costs and benefits of biorefineries at Kraft pulp and paper mills; the process data of SSCF is from Aden et al. (2002) and Arvidsson and Lundin (2011) carried out the mass balance and energy balance of the process. Process data for the Kraft mill is based on existing mills in the Central North Island of New Zealand.

Mass and energy balances for the processes are calculated using basic conservation principles and the first law of thermodynamics. As such, the models do not include rate based equations. The mass and energy balances in this work are modelled using Excel™. From the mass and energy balance, performance specifications of the processes can be identified and is supplied into P-graph.

### 3.2. Process pinch analysis and total site heat integration

Process stream data for PA and TSHI are extracted from three of the mass and energy balance models, as shown in Table 1. This data covers gasification, HTL, and SSCF. Stream data for the Kraft pulp is withheld due to confidentiality. For this case study, hot oil, steam, cooling water, and refrigerant are the hot and cold utilities. In addition, water is supplied as a utility and hydrogen as a utility from the HTL process.

In this study, a biomass boiler with a multiple steam extraction turbine is considered. The steam exiting the boiler and entering turbine is at 100 bar and 510 °C. The turbine is assumed to have a fixed isentropic efficiency of 80% and a generator efficiency of 98%. Operating steam temperatures and pressures are presented in Table 2. The condensate return of the steam utility is assumed to be returned at atmospheric pressure and 85 °C.

To satisfy the cooling demand, cooling water and refrigeration at

**Table 1**  
Process stream data.

Stream	$T_s$ °C	$T_t$ °C	CP MJ/[t °C]	$\Delta H$ MJ/t
Gasification (DME)				
C1	74	280	1.1	231
C2	−43	25	1.7	116
H1	999.9	730	3.8	1020
H2	729.9	430	5.1	1529
H3	430	429.9	1862.9	186
H4	429.9	350	11.2	898
H5	350	30	2.6	844
H6	280	−50	1.5	508
SSCF (Ethanol))				
C1	30.1	100.0	7.3	512
C2	117.2	117.3	5979.9	598
C3	98.6	110.4	1.3	16
C4	110.4	114.5	120.9	496
C5	114.7	114.8	2189.6	219
C6	175.0	175.1	5142.9	514
C7	220.0	220.1	1102.0	110
H1	145.5	143.5	68.1	136
H10	40.1	35.0	16.1	82
H11	35.1	35.0	1323.1	132
H12	114.8	37.0	0.6	44
H13	79.1	37.0	1.6	67
H2	100.9	99.6	262.8	342
H3	99.5	99.0	26.6	13
H4	100.1	35.0	5.0	323
H5	99.6	37.0	0.9	56
H6	109.4	37.0	1.0	75
H7	87.5	87.4	6591.2	659
H8	62.2	62.1	7177.3	718
H9	60.1	60.0	115.6	12
Hydrothermal Liquefaction (Bio-oil))				
C1	109.0	304.0	7.5	1471
C2	304.0	355.0	7.3	374
C3	116.5	165.6	0.0	2
H1	350.0	144.2	7.4	1516
H2	117.8	60.0	26.5	1532
H3	425.7	396.2	2.0	59
H4	365.8	118.5	0.1	13
H5	118.5	43.3	0.0	3

cryogenic temperatures is required. Cryogenic refrigeration compression work and electricity use was based on the study of Luyben (2017) where 1.0 kW of electricity approximately generated 0.8 kW of cryogenic cooling.

The case study applied a global minimum approach temperature of 10 °C. These approach temperatures are typical of heat exchanger found in industrial pulp mills. Using these data, PI studies of the Kraft pulp mill cluster, gasification, HTL and SSCF are conducted using the same utility supply data.

### 3.3. P-graph model superstructure

A superstructure of the TSMHP problem was implemented in P-graph as shown in Fig. 5. The major processes and utility operations within the superstructure are labelled. Incorporated into the various process and cluster operations are overall performance data that describe the conversion of feedstock to final production. This data is provided in Table 3. The estimated feedstock, fuel and product prices are presented in Table 4. Cost and price data are in New Zealand Dollars (NZD).

In this case study, only HTL has condensate return. The condensate for SSCF is recycled within the system as wash water. The steam and electricity generated in gasification for this case study are supplied directly to the Kraft pulp mill in replacement of steam and electricity generated by burning of black liquor. However, the steam generated by gasification is insufficient for the pulp mill.

**Table 2**  
Steam pressure and temperature specifications.

	High Pressure (HP) Steam	Medium Pressure (MP) Steam	Intermediate Pressure (IP) Steam	Low Pressure (LP) Steam
Pressure (bar)	40	20	13	4
Temperature (°C)	250	212	191	143

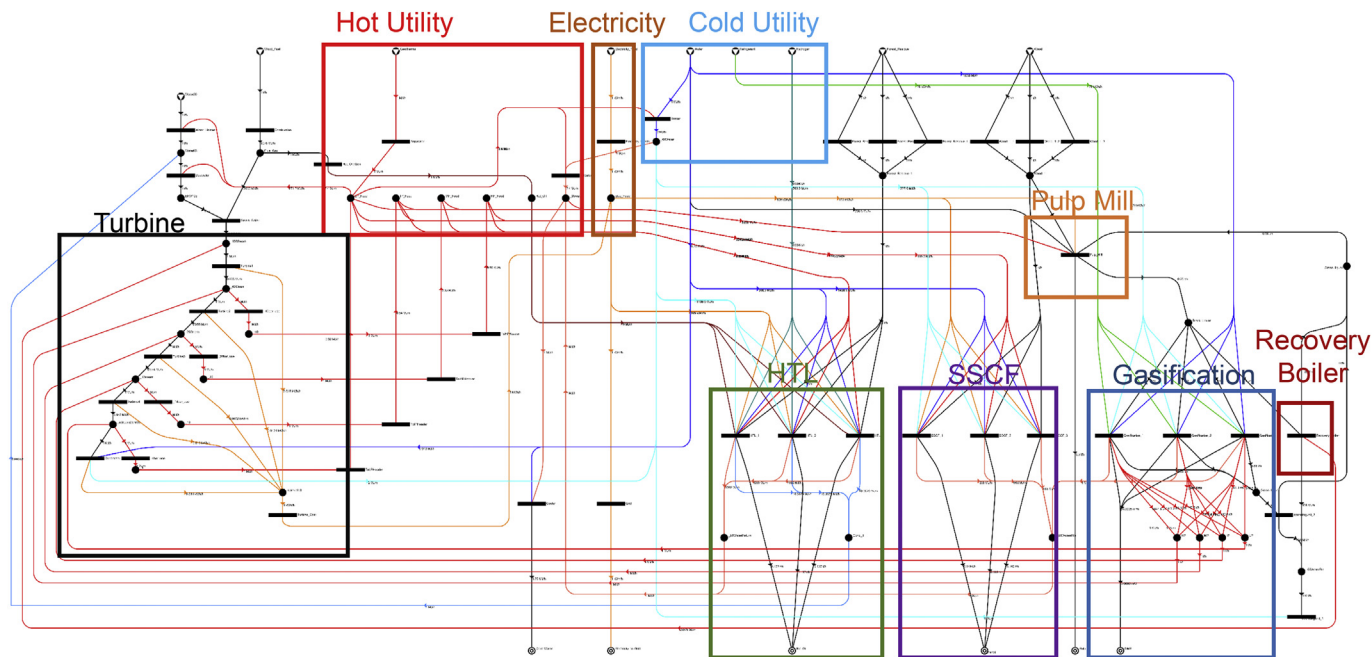


**Fig. 5.** Maximal structure of the P-graph for the biorefinery processing of forest biomass residues.

Capital cost estimation data was derived based on previous plant installations from various sources with similar process pathways using power law cost functions, Eq. (1), for each individual operating unit as presented in Table 5. The lower and upper bound are proportional to input flow rate in t/h. The cost function for pulp and wood biomass are derived for Central North Island, which may differ for different case studies as it is dependent on the

density of the forest, which will, in turn, decide the distance needed to travel from the source to the processing plant. The cost functions were linearized using a piece-wise approach for improved compatibility with P-graph Studio. The selected number of piece-wise subintervals was three. The decision was based on the maximum error of ±2.5% between the piece-wise linear cost curves and the actual cost curve within the lower and upper bounds of the original cost function.

**Table 3**  
Process performance data from process models.

Processes	Overall Conversion
HTL	0.137 t/t
SSCF	0.149 t/t
Gasification	0.0005 m <sup>3</sup> /t
Pulp Mill	0.500 t/t

**Table 4**  
Feedstock, fuel and product prices.

Material Flow	Price	Energy Flow	Price
Boiler Water	\$1.72/t	Geothermal steam	\$5/GJ
Green Wood Fuel	\$30/t	Electricity Import	\$85/MWh (\$23.6/GJ)
Forest Residues	\$27–40/t (for 0–360 t/h)	Electricity Export	\$60/MWh (\$16.7/GJ)
Pulp Wood	\$100–124/t (for 0–450 t/h)	Cooling water	\$0.5/GJ
Pulp	\$1300/t	Hydrogen	\$1000/t
Bio-oil	\$800/t	Refrigeration	\$80/MWh
Ethanol	\$590/t		
DME	\$15,000/m <sup>3</sup>		

## 4. Result and discussion

### 4.1. Heat integration

The Kraft pulp process is a well-established industrial process that has potential to evolve into a multi-product biorefinery. Understanding the hot and cold utility demands of the mill is critical to successful integration and implementation of new technologies and process. Fig. 6 presents the Total Site Profiles and Site Utility Grand Composite Curve for the Kraft mill. Three levels of steam demand are in deficit while hot water is in a net deficit. The hot site Pinch Temperature is 65 °C. Adding processes with Pinch Temperatures above 65 °C is essential to realise Total Site heat integration benefits.

Fig. 7 shows the Grand Composite Curves for the (a) gasification, (b) SSCF, and (c) hydrothermal liquefaction processes. From the GCC, the minimum specific hot and cold demand of the processes are identified as well as targets for each utility level. The process PA in Fig. 7a shows a large excess of high temperature heat for the gasification process forming a threshold problem. It was estimated that the electricity generated by the process using indirect

**Table 5**  
Capital cost estimate functions.

Processes	k (\$/[t/h] <sup>n</sup> )	a	Lower Multiplier Capacity (t/h)	Upper Multiplier Capacity (t/h)
SSCF	9,119,300	0.63	30.0	53.0
HTL	11,339,800	0.60	130.0	210.0
Gasification	25,827,700	0.60	80.0	125.0
Pulp Mill	100	1.30	0	900.0

combined cycle is 132 kWh/t of feed. The electricity generated by gasification serves as a net reduction to the pulp mill power demands. The heat profile of SSCF is significantly different. From Fig. 7b, the Pinch Temperature for SSCF is 90.5 °C. Most of the hot utility demand may be covered using LP steam. In this process, the reboiler and preheater of the beer column are the most energy demanding unit operations, followed by evaporation. In Fig. 7c, the HTL process shows a heat deficit in the range of hot oil utility. Hot oil (or hot flue gas) is required to supply process heat above 300 °C because the required steam pressure (>85 bar) becomes prohibitively costly and dangerous. The cooling demand needed in HTL process is to cool the effluent leaving the reactor.

By carrying out heat integration analysis for each process and cluster, targets for steam consumption and generation may be

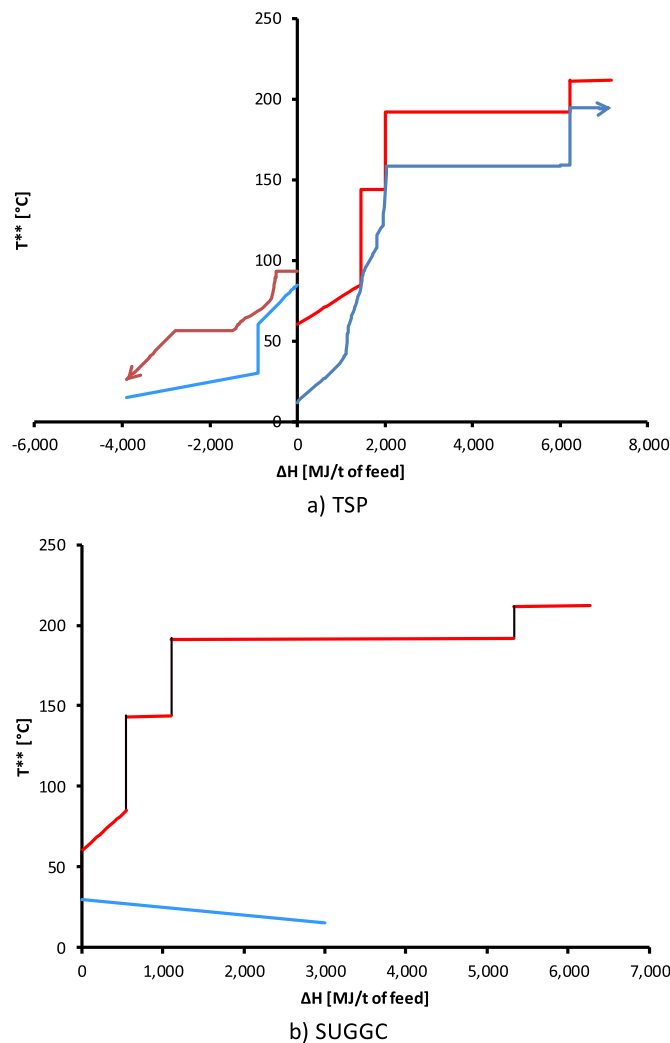


**Fig. 6.** Total Site Profiles (a) and Site Utility Grand Composite Curve (b) of the Kraft pulp mill.

determined and the potential for heat recovery identified. For the considered processes, gasification has significant potential to integrate with the Kraft mill through mass, heat and power integration. HTL and SSCF have potential to generate hot water that may be integrated with the pulp mill while providing an

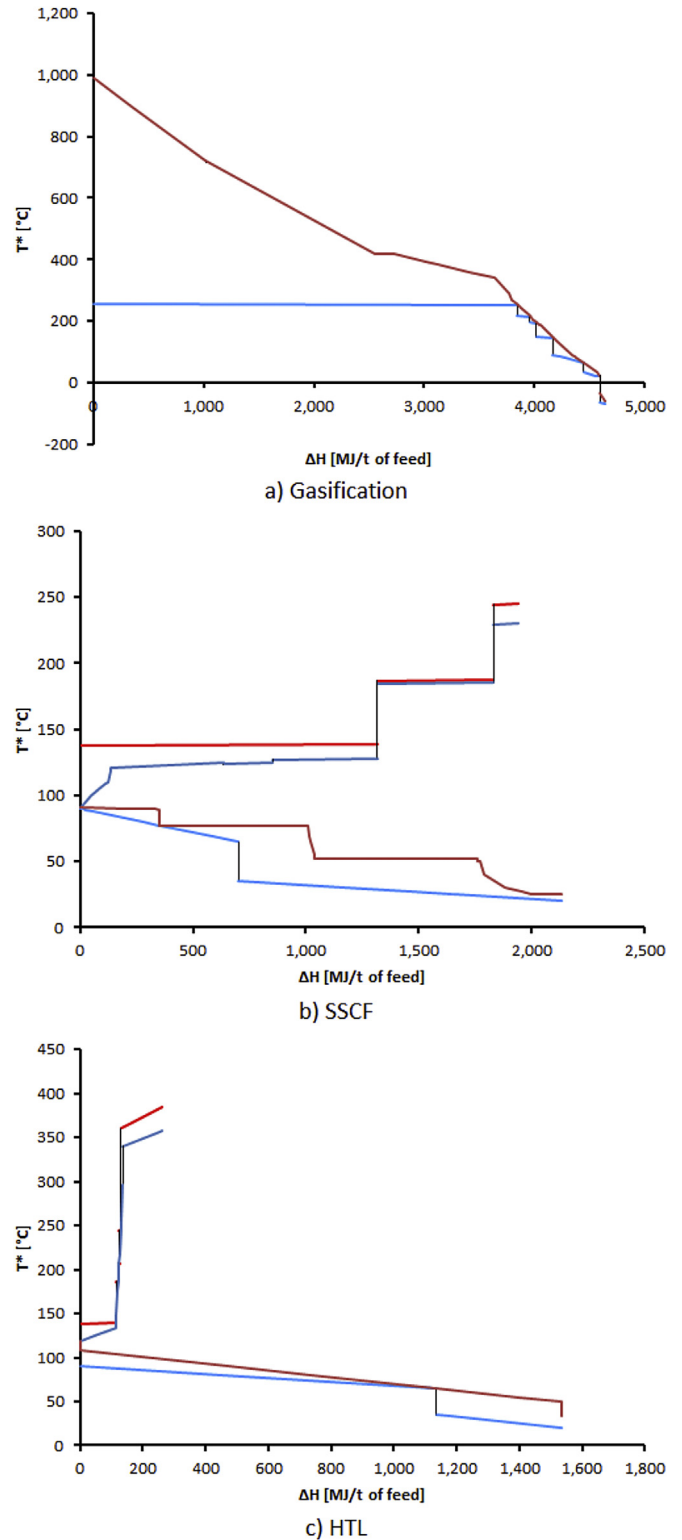


**Fig. 7.** Grand composite curves for (a) gasification of black liquor, (b) simultaneous scarification and co-fermentation of pine, and (c) hydrothermal liquefaction of forest residues.

opportunity to consume geothermal heat and cogenerate power in the biomass boiler. SSCF also benefits from the potential use of relatively inexpensive geothermal heat.

4.2. Simultaneous mass and energy integration using P-graph

The optimal network, the solution with the greatest yearly profit, is shown in Fig. 8 and indicates only Kraft pulp is produced at 600,000 t/y with a yearly profit (revenue less energy and capital costs) of \$283,250,000. Geothermal heat contributes to the optimal solution by increasing profit by \$27,220,000/y. This contribution is determined by comparing the second feasible structure, i.e. the solution with the second highest profit, with the optimal solution. The third feasible structure includes hydrothermal liquefaction in addition to the Kraft mill and geothermal and achieves a profit of \$252,000,000/y. This structure is presented in Fig. 9.

4.3. Sensitivity analysis

For the sensitivity analysis, the price of the biorefinery products are increased individually until the process of the selected product shows profits or appears as Feasible Structure 1, i.e. the optimal solution. Fig. 10 shows what the price of bio-oil must be for HTL to cause its profit to exceed that of a Kraft mill with geothermal steam.

Fig. 10 shows that the price of HTL must be 80% higher than the current price (\$800/t) to be break-even. The increase in revenue is non-linear due to the capital cost function for the HTL plant. SSCF is only feasible when the price of ethanol is at about \$2100 instead of \$590. Gasification on the other hand did not show any feasible structure, even when the product price was increased by one order of magnitude.

One of the reasons why gasification is never in the feasible structure is because of the high capital cost. On the other hand,

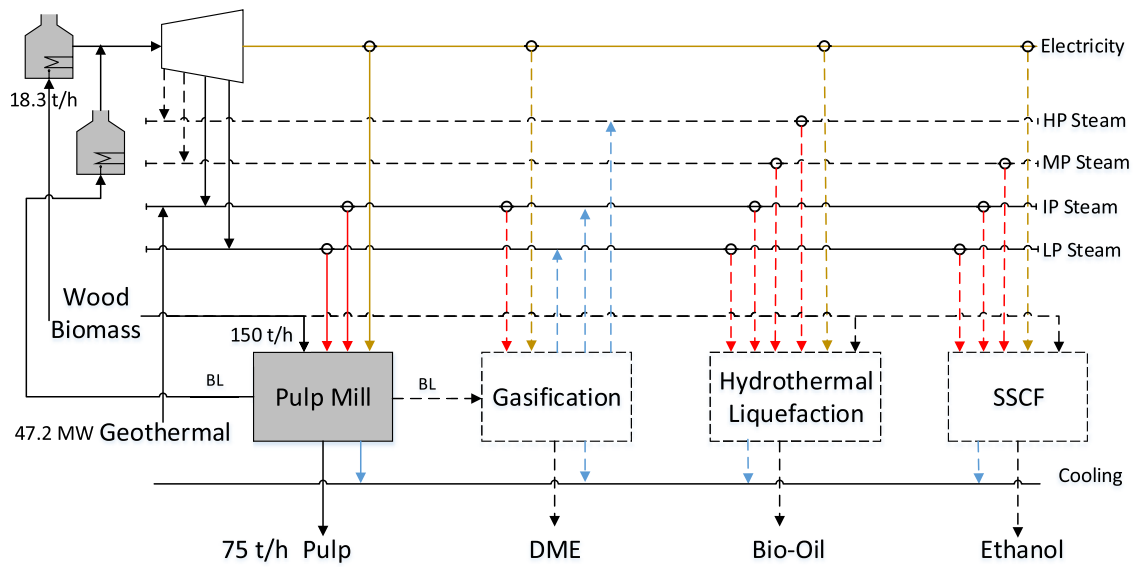


Fig. 8. Optimal network showing Kraft pulp with geothermal as the most profitable processing route.

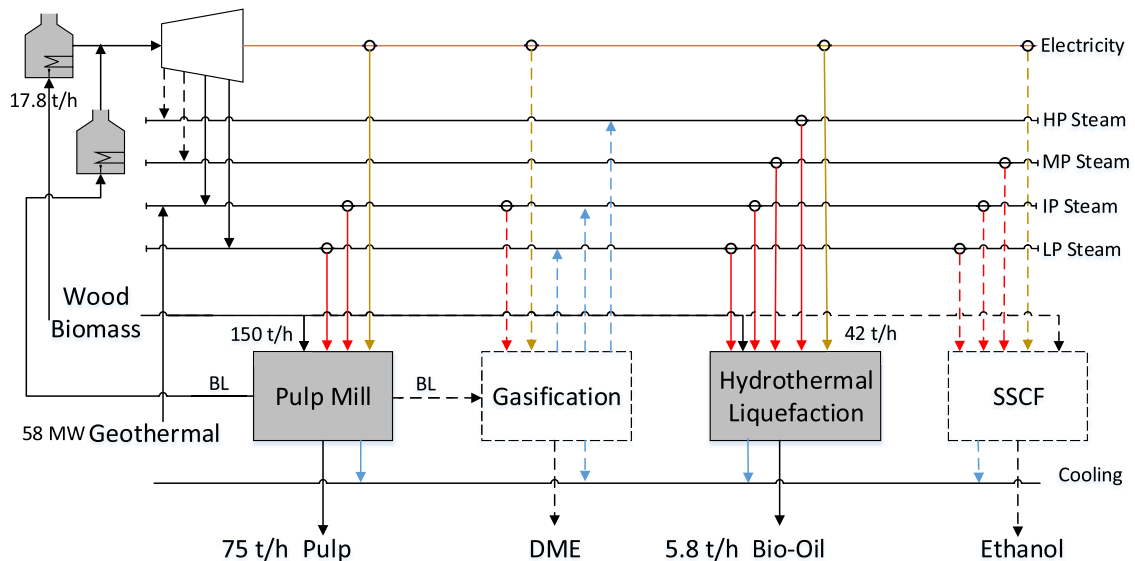


Fig. 9. Near-optimal network showing Kraft pulp, hydrothermal liquefaction and geothermal as the third most profitable processing route.

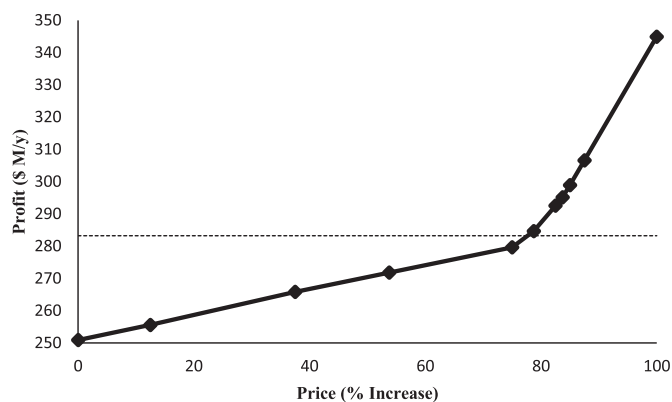


Fig. 10. Sensitivity analysis for HTL product price for bio-ol.

gasification has a large surplus of steam and electricity generated; however, it does not create enough surplus to the pulp mill. SSCF has a low production rate with a higher operating cost with the replenishment of yeast and enzyme.

Hydrothermal liquefaction is a new emerging process. There are more than one type of processing route or biomass feed option. Further analysis of the co-location of hydrothermal liquefaction with Kraft pulp mill, but with black liquor as an additional feedstock should be investigated.

## 5. Conclusions

The innovative combination of Process Integration tools and Process Graph presents a novel graphical method for visualising and optimising integration problems involving mass, heat, and power integration. Specific process level Pinch Analysis and Total Site Heat Integration targets on a per tonne of feed basis have been incorporated into a P-graph superstructure to select the optimal combination of processes including sizes. The novel method has shown great potential through the application of a biorefinery case study where a Kraft mill is used as the platform. By combining PI tools and P-graph, optimal and near-optimal solutions are determined, which allows correlation between different variables that affect the optimality of the problem. Future work of the combination framework can be extended to systematically identify the correlations between variables that affect the solution of the problem.

## Acknowledgements

This research has been supported by the EU project “Sustainable Process Integration Laboratory – SPIL”, project No. CZ.02.1.01/0.0/0.0/15\_003/0000456 funded by EU “CZ Operational Programme Research, Development and Education”, Priority 1: Strengthening capacity for quality research, in collaboration with the University of Waikato, Hamilton, New Zealand.

## Appendix A. Supplementary data

Supplementary data related to this article can be found at <http://dx.doi.org/10.1016/j.jclepro.2017.08.035>.

## References

Aden, A., Ruth, M., Ibsen, K., Jechura, J., Neeves, K., Sheehan, J., Wallace, B., Montague, L., Slayton, A., Lukas, J., 2002. Lignocellulosic Biomass to Ethanol Process Design and Economics Utilizing Co-current Dilute Acid Prehydrolysis and Enzymatic Hydrolysis for Corn Stover (Technical No. NREL/TP-510-32438).

National Renewable Energy Laboratory, Colorado, U.S.A.

Arvidsson, M., Lundin, B., 2011. Process Integration Study of a Biorefinery Producing Ethylene from Lignocellulosic Feedstock for a Chemical Cluster (Master). Chalmers University of Technology, Sweden.

Atkins, M.J., Walmsley, M.R.W., Walmsley, T.G., 2016. Integration of new processes and geothermal into a wood processing cluster. *Clean Technol. Environ. Pol.* 18 (7), 2077–2085.

Aviso, K.B., Chiu, A.S.F., Yu, K.D.S., Promentilla, M.A.B., Razon, L.F., Ubando, A.T., Sy, C.L., Tan, R.R., 2015. P-graph for optimising industrial symbiotic network. *Chem. Eng. Trans.* 45, 1345–1350. <http://dx.doi.org/10.3303/CET1545225>.

Baliban, R.C., Elia, J.A., Floudas, C.A., 2011. Optimization framework for the simultaneous process synthesis, heat and power integration of a thermochemical hybrid biomass. *Comput. Chem. Eng.* 35, 1647–1690.

Chang, C., Chen, X., Wang, Y., Feng, X., 2016. An efficient optimization algorithm for waste Heat Integration using a heat recovery loop between two plants. *Appl. Therm. Eng.* 105, 799–806. <http://dx.doi.org/10.1016/j.applthermaleng.2016.04.079>.

Chew, K.H., Klemeš, J.J., Wan Alwi, S.R., Manan, Z.A., 2015. Process modifications to maximise energy savings in total site heat integration. *Appl. Therm. Eng.* 78, 731–739. <http://dx.doi.org/10.1016/j.applthermaleng.2014.04.044>.

Čuček, L., Kravanja, Z., 2016. Retrofit of total site heat exchanger networks by mathematical programming approach. In: Martín, M. (Ed.), *Alternative Energy Sources and Technologies*. Springer International Publishing, pp. 297–340. [http://dx.doi.org/10.1007/978-3-319-28752-2\\_11](http://dx.doi.org/10.1007/978-3-319-28752-2_11).

de Jong, E., Higson, A., Walsh, P., Wellisch, M., 2012. *Bio-based Chemicals: Value Added Products from Biorefineries*. International Energy Agency, Wageningen, Netherlands.

Dhole, V.R., Linnhoff, B., 1993. Total site TArgets for fuel, Co-Generation, emissions and cooling. *Comput. Chem. Eng.* 17, 101–109.

Duran, M.A., Grossmann, I.E., 1986. Simultaneous optimisation and heat integration of chemical processes. *AIChE J.* 32, 123–138.

El-Halwagi, M.M., Manousiouthakis, V., 1989. Synthesis of mass exchange networks. *AIChE J.* 35, 1233–1244.

Friedler, F., Tarján, K., Huang, Y.W., Fan, L.T., 1992. Graph-theoretic approach to process synthesis: axioms and theorems. *Chem. Eng. Sci.* 47, 1973–1988. [http://dx.doi.org/10.1016/0009-2509\(92\)80315-4](http://dx.doi.org/10.1016/0009-2509(92)80315-4).

Friedler, F., Varga, J.B., Fehér, E., Fan, L.T., 1996. Combinatorially accelerated branch-and-bound method for solving the MIP model of process network synthesis. In: Floudas, C.A., Pardalos, P.M. (Eds.), *State of the Art in Global Optimization*. Kluwer Academic Publishers, Boston, MA, pp. 609–626.

Gassner, M., Marechal, F., 2009. Thermo-economic process model for thermochemical production of synthetic natural gas (SNG) from lignocellulosic biomass. *Biomass Energy* 33, 1587–1604.

Gerrard, A.M., 2000. *Guide to Capital Cost Estimating*, Fourth. ed. Institution of Chemical Engineers (IChemE), Warwickshire, U.K.

Hassiba, R.J., Al-Mohannadi, D.M., Linke, P., 2017. Carbon dioxide and heat integration of industrial parks. *J. Clean. Prod.* 155, 47–56.

Heckl, I., Friedler, F., Fan, L.T., 2010. Solution of separation-network synthesis problems by the P-graph methodology. *Comput. Chem. Eng.* 34, 700–706.

Jack, M., Hall, P., Barry, L., 2013. *WoodScape Study - Summary Report (Summary)*. SCION, Rotorua, New Zealand.

Klemeš, J., Dhole, V.R., Raissi, K., Perry, S.J., Puigjaner, L., 1997. Targeting and design methodology for reduction of fuel, power and CO<sub>2</sub> on total sites. *Appl. Therm. Eng.* 17, 993–1003.

Klemeš, J.J., 2013. *Handbook of Process Integration: Minimisation of Energy and Water Use, Waste and Emissions*, first ed. Woodhead Publishing, Cambridge, UK.

Kong, Q., Shah, N., 2017. Development of an optimization-based framework for simultaneous process synthesis and heat integration. *Ind. Eng. Chem. Res.* 56 (17), 5000–5013.

Lam, H.L., Varbanov, P.S., Klemeš, J.J., 2010. Optimisation of regional energy supply chains utilising renewables: P-graph approach. *Comput. Chem. Eng.* 34, 782–792.

Larson, E.D., Consonni, S., Katofsky, R.E., Iisa, K., Frederick, W.J., 2006. *A Cost-benefit Assessment of Gasification Based Biorefining in the Kraft Pulp and Paper Industry (Final)*. Princeton University, Princeton, California.

Liew, P.Y., Walmsley, T.G., Wan Alwi, S.R., Manan, Z.A., Klemeš, J.J., Varbanov, P.S., 2016. Integrating district cooling systems in locally integrated energy sectors through total site heat integration. *Appl. Energy* 184, 1350–1363.

Liew, P.Y., Wan Alwi, S.R., Lim, J.S., Varbanov, P.S., Klemeš, J.J., Manan, Z.A., 2014. Total Site Heat Integration incorporating the water sensible heat. *J. Clean. Prod.* 77, 94–104.

Liew, P.Y., Wan Alwi, S.R., Manan, Z.A., Klemeš, J.J., Varbanov, P.S., 2015. Incorporating district cooling system in total site heat integration. *Chem. Eng. Trans.* 45, 19–24. <http://dx.doi.org/10.3303/CET1545004>.

Linnhoff, B., Flower, J.R., 1978. Synthesis of heat exchanger networks: I. Systematic generation of energy optimal networks. *AIChE J.* 24, 633–642.

Luyben, W.L., 2017. Estimating refrigeration costs at cryogenic temperature. *Comput. Chem. Eng.* 103, 144–150.

Marechal, F., Kalitventzeff, B., 2003. Targeting the integration of multi-period utility systems for site scale process integration. *Appl. Therm. Eng. Process Integrat. Model Optimisation Energy Sav. Pollut. Reduct.* 23, 1763–1784. [http://dx.doi.org/10.1016/S1359-4311\(03\)00142-X](http://dx.doi.org/10.1016/S1359-4311(03)00142-X).

Nagy, A.B., Adonyi, R., Halasz, L., Friedler, F., Fan, L.T., 2001. Integrated synthesis of process and heat exchanger networks: algorithmic approach. *Appl. Therm. Eng.*

- 21, 1407–1427.
- Nemet, A., Klemeš, J.J., Kravanja, Z., 2015. Designing a Total Site for an entire lifetime under fluctuating utility prices. *Comput. Chem. Eng.* 72, 159–182. <http://dx.doi.org/10.1016/j.compchemeng.2014.07.004>.
- Ng, R.T.L., Tay, D.H.S., Ng, D.K.S., 2012. Simultaneous process synthesis, heat and power integration in a sustainable integrated biorefinery. *Energy Fuel* 26, 7316–7330.
- Ong, B.H.Y., Walmsley, T.G., Atkins, M.J., Walmsley, M.R.W., Neale, J.R., 2016. Approximation of non-linear cost functions in P-graph structures. *Chem. Eng. Trans.* 52, 1093–1098.
- P-graph, 2017. P-Graph [WWW Document]. URL <http://p-graph.com/> (Accessed 18 May 17).
- SETIS, 2011. Energy Efficiency in the Pulp and Paper Industry. Strategic Energy Technologies Information System.
- Spirax Sarco Limited, 2007. The Steam and Condensate Loop, First. ed. Spirax-Sarco Limited, Gloucestershire, U.K.
- Sun, L., Doyle, S., Smith, R., 2014. Graphical cogeneration analysis for site utility systems. *Clean Technol. Environ. Pol.* 16 (7), 1235–1243.
- Tarighaleslami, A.H., Walmsley, T.G., Atkins, M.J., Walmsley, M.R.W., Liew, P.Y., Neale, J.R., 2017. A Unified Total Site Heat Integration targeting method for isothermal and non-isothermal utilities. *Energy* 119, 10–25. <http://dx.doi.org/10.1016/j.energy.2016.12.071>.
- Tews, I.J., Zhu, Y., Drennan, C.V., Elliot, D.C., Snowden-Swan, L.J., Onarheim, K., Solantausta, Y., Beckman, D., 2014. Biomass Direct Liquefaction Options: Technoeconomic and Life Cycle Assessment (No. PNNL-23679). Pacific Northwest National Laboratory, Richland, Washington, USA.
- van Heiningen, A., 2006. Converting a Kraft pulp mill into an integrated forest biorefinery. *Pulp Pap. Can.* 107, 38–43.
- Varbanov, P.S., Friedler, F., 2008. P-graph methodology for cost-effective REDuction of carbon emissions involving fuel cell combined cycles. *Appl. Therm. Eng.* 28, 2020–2029.
- Voll, P., Jennings, M., Hennen, M., Shah, N., Bardow, A., 2015. The optimum is not enough: a near-optimal solution paradigm for energy systems synthesis. *Energy* 82, 446–456.
- Walmsley, T.G., 2016. A total site heat integration design method for integrated evaporation systems including vapour Recompression. *J. Clean. Prod.* 136, 111–118.
- Walmsley, T.G., Atkins, M.J., Walmsley, M.R.W., Philipp, M., Peesel, R.-H., 2017. Process and utility systems integration and optimisation for ultra-low energy milk powder production. *Energy*. <http://dx.doi.org/10.1016/j.energy.2017.04.142>.
- Wang, Y., Feng, X., 2017. Heat integration across plants considering distance factor. In: Kopanos, G.M., Liu, P., Georgiadis (Eds.), *Advances in Energy Systems Engineering*. Springer International Publishing, Cham, Switzerland, pp. 621–648.



**Article 12:**

*Improving energy recovery in milk powder production through soft data optimisation*

**Walmsley, T.G.**, Walmsley, M.R.W., Atkins, M.J., Neale, J.R., 2013.

Applied Thermal Engineering 61, 80–87.

DOI: 10.1016/j.applthermaleng.2013.01.051

Citations: 22

Elsevier



# Improving energy recovery in milk powder production through soft data optimisation



Timothy G. Walmsley\*, Michael R.W. Walmsley, Martin J. Atkins, James R. Neale

University of Waikato, Energy Research Centre, School of Engineering, Hamilton 3216, New Zealand

## ARTICLE INFO

### Article history:

Received 21 November 2012

Accepted 7 January 2013

Available online 22 March 2013

### Keywords:

Process integration

Heat recovery

Pinch analysis

Spray drying

## ABSTRACT

Milk powder production is highly energy intensive and can benefit from the application of Pinch analysis techniques to develop better methods for integrating the process. In this study, process stream data is extracted from an industrial plant and Pinch analysis applied to calculate utility and heat recovery targets. Some of process data is also varied, within small ranges that do not harm product quality or violate environmental regulation, to minimise utility use targets. Using the Pinch design method and the targets as a guide, Maximum Energy Recovery (MER) networks are developed for two cases, where the condenser in the evaporator section of the plant may be directly or indirectly integrating into the remainder of the process. The two MER networks are compared to two heat exchanger network structures commonly found in industry. Results show that there is potential to increase specific heat recovery by over 30%, while reducing total cost by almost 10%, in the best case. To achieve maximum energy recovery, spray dryer exhaust air heat recovery is necessary and should be matched to preheat the dryer inlet air stream.

© 2013 Elsevier Ltd. All rights reserved.

## 1. Introduction

Reducing energy use associated with milk powder production has been the subject of numerous studies. Previous studies have focused on three main areas: (1) heat recovery from the spray dryer exhaust air, including source/sink integration options [1], industrial case studies [2,3], and heat exchanger modelling [4], (2) zonal and total site heat integration of dairy factories, including integration of the milk treatment process that occurs preceding the drying operations [5] and the application [6,7] and design [8] of heat recovery loops to semi-continuous processes, and (3) an overview of good energy efficient practices in spray drying [9]. More recent studies have looked heat recovery targeting methods and heat exchange synthesis between the evaporator and spray dryer unit operations of a powder process [10,11]. This study builds on these previous works by applying Pinch analysis to show how to maximise energy recovery in the evaporator and dryer sections of a milk powder plant.

Traditionally minimising energy use has not been a primary focus in the dairy industry because energy costs represent only a small proportion of the total production cost [12]. However, continuing pressures from rapidly rising fuel costs is providing a greater driver for improving energy efficiency. As a result, advanced thermodynamic approaches, such as Pinch analysis, are being applied to help industry make a step change in energy efficiency.

In the milk powder process, some of the stream data is “soft”, meaning that some flow or temperature set points or target values can vary without impacting the process, product quality and safety. Variations to present stream data may be achieved in several ways, such as by applying new control set-points to the existing process. Designers can use this flexibility to their advantage by varying soft data within a defined range to obtain a minimum energy use target [13,14]. Soft data selection can also significantly impact the development of heat exchanger network structures that are designed to maximise heat recovery.

The aim of this study is to demonstrate how best to integrate an industrial milk powder plant for maximum heat recovery using Pinch analysis. Heat recovery targets are calculated assuming steady stream flow rates and temperatures while on product. Soft stream data is varied to analyse the effect on the targets. After targeting, Heat Exchanger Networks (HEN) are developed for the evaporator and spray dryer sections of a typical site. Hot water for

\* Corresponding author. Tel.: +64 78384937.

E-mail address: [tgw7@waikato.ac.nz](mailto:tgw7@waikato.ac.nz) (T.G. Walmsley).

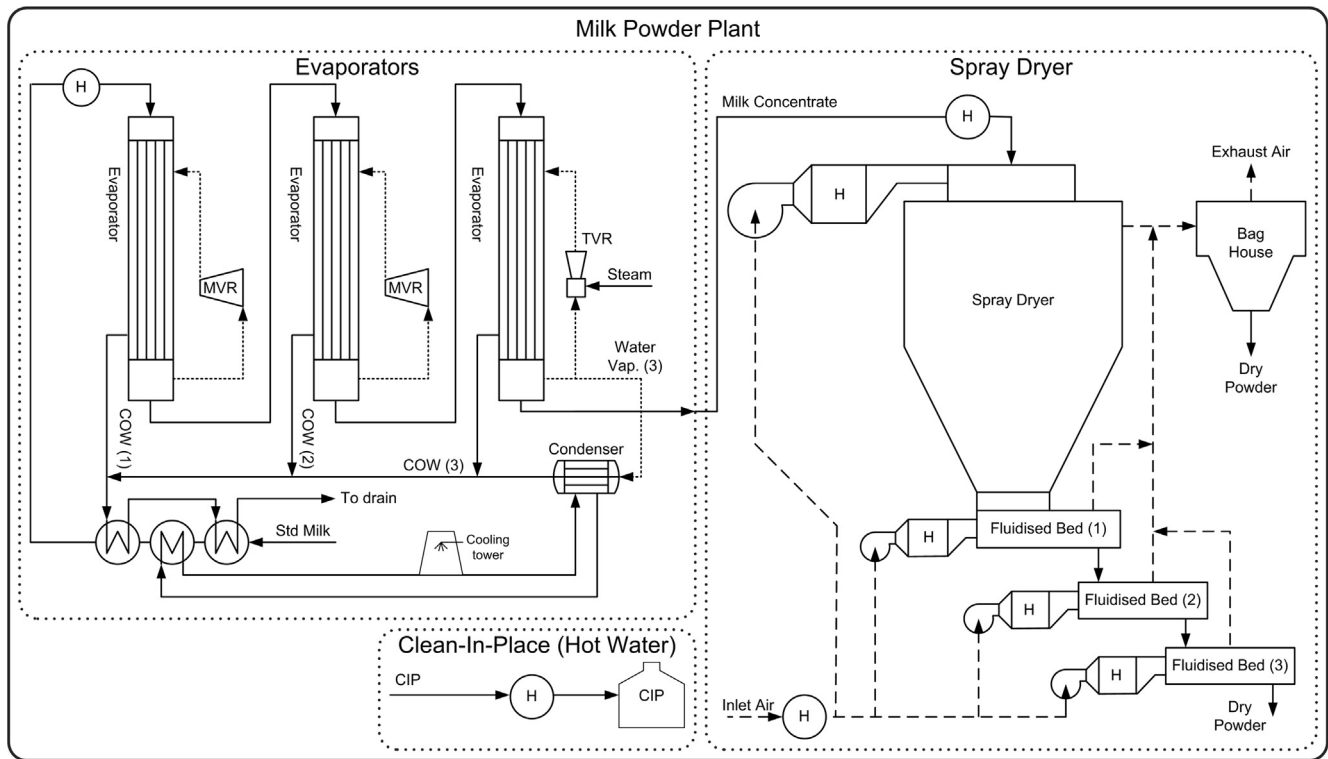


Fig. 1. Milk powder plant schematic including current HEN.

processing equipment, storage silos, and milk tanker truck cleaning, i.e. Clean-In-Place (CIP), is included in the investigation.

## 2. Industrial milk powder production process

An industrial milk powder plant is illustrated in Fig. 1 with evaporator and spray dryer zones, and a common industrial heat recovery network. CIP water is shown as a third zone. It is important to note that standard industry practice for many sites is to not recover heat from the spray dryer exhaust air and to not include CIP water as a heat sink.

### 2.1. Extracted heating and cooling process demands

Specific stream data (using the basis of one tonne of product) for a large industrial milk powder plant that operates for 5000 h/y is presented as Table 1. The streams include the evaporation and condensing streams inside the three evaporator effects. The vapour side streams have been upgraded in temperature using mechanical or thermal recompression. The acronym COW is short for condensate of whey and refers to water that is removed from the milk during the evaporation stages. The heat demand for the four air streams are shown separate although there is opportunity to heat all four air streams collectively and/or the fluidised bed air streams

Table 1

Process stream data extracted for the industrial milk powder plant. Soft temperatures indicated using \*.

Zone	Stream	Hot/cold	State	$T_s$ [°C]	$T_t$ [°C]	CP [MJ/(t <sub>p</sub> °C)]	$\Delta H$ [MJ/t <sub>p</sub> ]
Evap.	Standardised milk	C	Liq.	8.0	63.4	42.7	-2362
Evap.	Effect 1 after MVR (vapour side)	H	Vap.	75.0	74.9		12321
Evap.	Effect 1 (product side)	C	Vap.	69.9	70.0		-12375
Evap.	COW 1 (from effect 1)	H	Liq.	67.5	13.0*	22.3	1215
Evap.	Effect 2 after MVR (vapour side)	H	Vap.	67.0	66.9		7320
Evap.	Effect 2 (product side)	C	Vap.	61.9	62.0		-7353
Evap.	COW 2 (from effect 2)	H	Liq.	61.0	13.0*	13.1	630
Evap.	Effect 3 after TVR (vapour side)	H	Vap.	59.0	58.9		1495
Evap.	Effect 3 (product side)	C	Vap.	53.9	54.0		-1495
Evap.	Condenser vapour	H	Vap.	54.0	53.9		370
Evap.	Condensate (condenser)	H	Liq.	53.9	13.0*	0.7	27
Evap.	COW 3 (from effect 3)	H	Liq.	54.9	13.0*	2.0	81
CIP	CIP hot water	C	Liq.	15.0	55.0	6.0	-238
Dryer	Milk concentrate	C	Liq.	54.0	65.0	6.0	-65
Dryer	Dryer inlet air	C	Gas	15.0	200.0	18.4	-3411
Dryer	FB inlet air (1)	C	Gas	15.0	49.0	1.6	-53
Dryer	FB inlet air (2)	C	Gas	15.0	45.0	2.3	-69
Dryer	FB inlet air (3)	C	Gas	15.0	32.0	1.7	-29
Dryer	Exhaust air – dew point 39 °C	H	Gas	75.0	55.0*	25.7	-513

**Table 2**  
Initial  $\Delta T_{\text{cont}}$  assignment.

State	$\Delta T_{\text{cont}}$ [°C]
Vapour	3.0
Liquid	2.5
Gas	10.0

collectively. Soft data are identified using “\*”. Current site utility prices are: steam utility \$45 per MWh, cooling tower water \$5 per MWh and chilled water \$35 per MWh.

### 3. Methodology

Pinch analysis has been applied to calculate specific utility and recovery targets for milk powder production. Site utility and heat recovery targets are calculated by shifting individual streams by a  $\Delta T_{\text{cont}}$ , which are assigned based on the state of the steam and the best available heat exchanger technology (Tables 2 and 3). The minimum approach temperature,  $\Delta T_{\text{min}}$ , varies depending on which streams are matched and the respective  $\Delta T_{\text{cont}}$ 's of the streams exchanging heat.

For large industrial sites, it is normally most economical to maximise heat recovery within individual zones before transferring heat inter-zonally. Intra-zonal targets are found by applying pinch analysis to each zone. Inter-zonal targets are derived from an analysis of the entire site, where the source and sink sections of the zonal grand composite curves that require utility are combined to form total site source and sink profiles. These profiles can be pinched to provide the maximum heat recovery target for direct inter-zonal heat exchange. Soft stream data is varied within defined limits to minimise utility targets. Preference is given to heat recovery from liquid streams over gaseous streams [10].

HENs are formulated using the pinch design method [15]. Exchanger areas are calculated using the Effectiveness–Number of Transfer Units ( $\epsilon$ -NTU) method using the correlations presented in Table 3 [16,17]. Overall heat transfer coefficients,  $U$ , are taken from Kakaç and Liu [18]. Heat exchanger cost equations as a function of area ( $A$ ) have been adapted from Bouman et al. [19] and multiplied by a Lang factor of 3.5. Cost equation coefficients in Table 3 have been annualised using a discount rate of 10% and an expected life time of 10 years.

#### 3.1. Solution constraints

The limits of the soft target temperatures of the COW and exhaust air streams (Table 1) are presented in Table 4. The liquid COW stream must discharge below 28 °C to meet environmental regulations. The lower limit discharge temperature is determined by the supply temperature of the coldest process stream and the minimum allowable approach temperature.

To prevent excessive fouling, the exhaust air stream must leave a possible recuperator above 55 °C [20]. Exhaust heat must be

**Table 4**  
Soft temperature limits.

Soft stream data	$T_t$ [°C]	
	Lower limit	Upper limit
COW	13	28
Exhaust air	55	75
Exhaust loop return	13	42.5
Cond. loop return	13	38.5

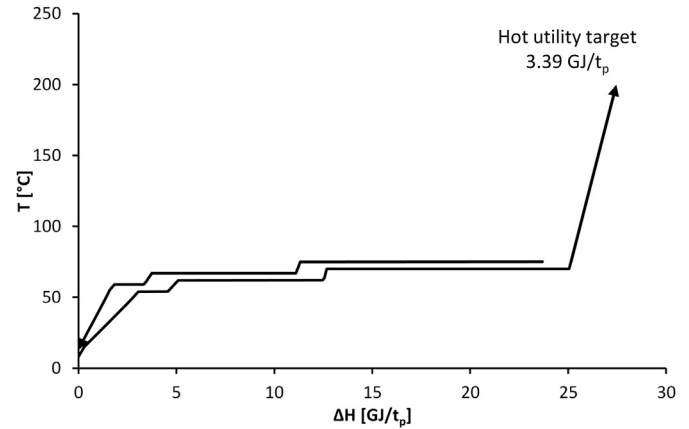


**Fig. 2.** Composite curve for entire site including the evaporators including the MVR and TVR units. Soft temperatures: exhaust air  $T_t$  is 55 °C and COW  $T_t$  is 13 °C. Pinch temperature at 10.5 °C.

recovered indirectly using a liquid couple loop due to the distance between the exhaust ducts and the location of possible heat sinks. The supply temperature of this liquid loop is set at 62.5 °C, which is the exhaust air supply temperature, 75 °C, minus the  $\Delta T_{\text{min}}$  for heat exchange between gas and liquid streams. The return temperature of the loop is a soft temperature.

Direct and indirect heat recovery options from the evaporator condenser are investigated. Direct heat exchange between the condenser vapour and product streams is undesirable due to potential contamination that might occur if the exchanger were to leak. Indirect heat exchanger requires using a liquid water coupled loop. The maximum loop supply temperature is 48.5 °C. The loop return temperature is a soft temperature.

## 4. Stream analysis and energy targeting

### 4.1. Site energy analysis

The composite curves for the entire process, including the evaporation, condensing and temperature upgrading that occurs in the evaporators, is presented in Fig. 2. Soft temperatures have been set at the lower limit values for the respective streams (Table 4). The

**Table 3**  
Heat exchanger overall heat transfer coefficients,  $\epsilon$ -NTU correlations and cost function.

Type	Purpose	$U$ [18] W/(m <sup>2</sup> °C)	Explanation of $\epsilon$ -NTU correlations [16,17]	Cost [19] (\$/y)
Gasket plate heat exchanger	Liq./liq.	2000	Counter flow exchanger	$1800 + 200 A$
Finned tube heat exchanger	Gas/gas	35	Both fluids unmixed crossflow exchanger with two passes	$500 A^{0.815}$
	Gas/liq.	70	Both fluids unmixed crossflow exchanger with two passes	$500 A^{0.815}$
	Gas/vap.	80	One fluid condensing exchanger	$500 A^{0.815}$
Shell and tube condenser	Liq./vap.	1500	One fluid condensing exchanger	$1100 A^{0.57}$

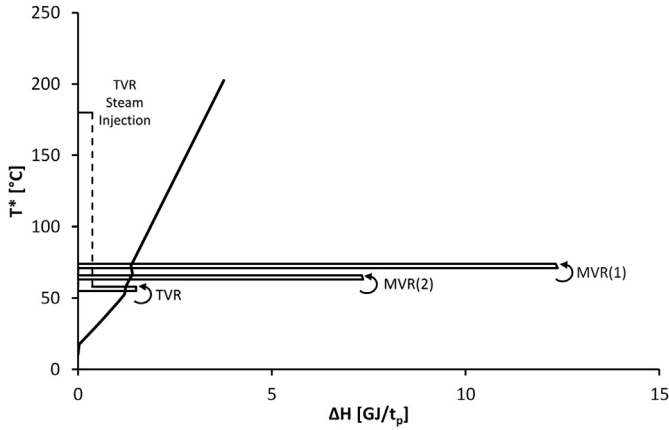


**Fig. 3.** Grand composite curve for evaporators and background process. Soft temperatures: exhaust air  $T_t$  is 55 °C and COW  $T_t$  is 13 °C. Pinch temperature at 10.5 °C.

site pinch is 10.5 °C, although this is not representative of the pinch temperatures in individual zones.

The multi-effect evaporators can be separated from the background process and plotted on a grand composite curve as shown in Fig. 3. Mechanical Vapour Recompression (MVR) and Thermal

Vapour Recompression (TVR) units upgrade vapour removed from the milk to a higher temperature and pressure, which allows the vapour to be recycled to the shell side of the evaporators and boil water on the product side. In the TVR, about two thirds of the vapour leaving the third effect is combined with direct steam injection to increase the temperature. The final third of vapour, not upgraded in the TVR, is sent to a condenser.

4.2. Soft temperature selection

Two soft temperatures are  $T_t$  of the exhaust air and COW streams. In Fig. 4a, the exhaust air  $T_t$  is constant at 75 °C and the COW  $T_t$  is varied with the optimal  $T_t$  at 13 °C. In Fig. 4b, the exhaust air  $T_t$  is varied with the COW  $T_t$  set at 13 °C. The optimal exhaust air  $T_t$  is the lower temperature limit of 55 °C, which was set due to potential fouling. Fig. 4 is valid for both case of directly and indirectly integrating the evaporator condenser.

The effect of the soft condenser loop return temperature ( $T_{CR}$ ) on heat recovery is shown as Fig. 5a. To maintain the maximum heat recovery target,  $T_{CR}$  should be higher than 18.5 °C (Fig. 5a). When  $T_{CR}$  is 18.5 °C, a pinch between the shifted total site profiles occurs (Fig. 6).

The effect of the exhaust loop return temperature ( $T_{ER}$ ) on heat recovery is shown in Fig. 5b. When  $T_{ER}$  is 27.5 °C, a pinch in the

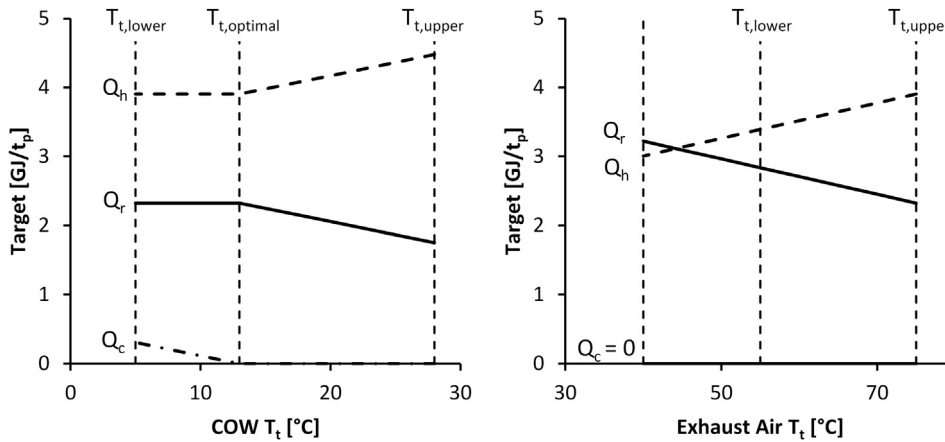


**Fig. 4.** The effect of the soft target discharge temperatures on heat recovery and utility targets. Left graph – exhaust air  $T_t$  is 75 °C and right graph – COW  $T_t$  is 13 °C.

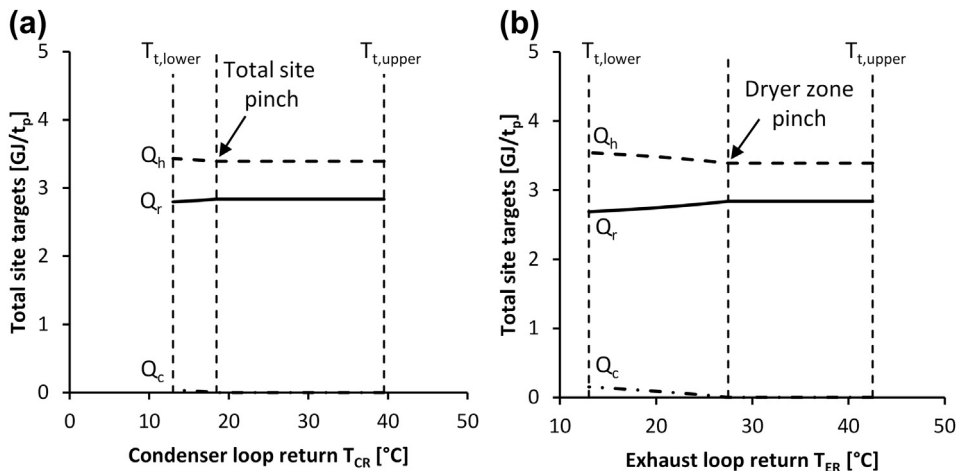


**Fig. 5.** The effect of the soft return temperature on heat recovery and utility targets for the condenser loop (a) and the exhaust loop (b). Soft temperatures: exhaust air  $T_t$  is 55 °C and COW  $T_t$  is 13 °C.

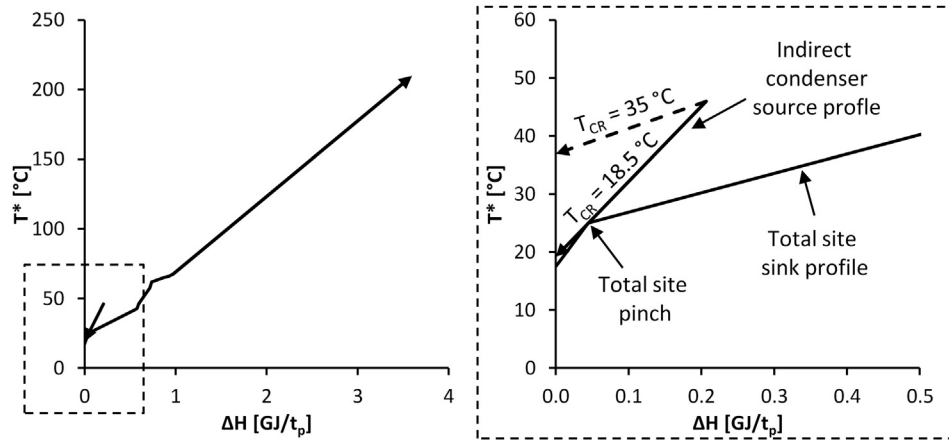


Fig. 6. Total site profiles. Soft temperatures: exhaust air  $T_t$  is 55 °C, COW  $T_t$  is 13 °C, and condenser loop return  $T_t$  is 18.5 °C.

dryer zone occurs between the  $T_s$  of the inlet air streams and the exhaust loop. If  $T_{ER}$  is set below 27.5 °C, cooling utility would be required to reach the specified  $T_{ER}$ .

The final soft temperature is the inlet air entering the building,  $T_t$ . In practice, air is drawn into the processing building from outside and split between the various drying operations. While the air streams are combined there is the possibility of providing some preheat.

#### 4.3. Modified stream data

In summary, the modified stream data of Table 1 are presented in Table 5. The return temperature of the condenser loop is still a soft temperature that may be optimised later in the analysis. The

individual evaporator effects streams have been excluded and the three COW streams have been combined. The stream data may be modified to combine the liquid COW streams into a single stream. A single COW stream would result in a reduction of at least two heat exchangers. Targeting results further suggest that combining the COW streams has no effect on the energy targets or optimum selection of soft temperatures.

#### 4.4. Inter- and intra-zonal targets

Using the modified stream data of Table 5 heat recovery targets for the milk powder plant viewed as a single zone as three separate zones are reported in Table 6. Viewing the problem as a single zone means heat can be transferred between any streams regardless of

Table 5

Modified process stream data. Soft data indicated using \*.

Zone	Stream	Hot/cold	State	$T_s$ [°C]	$T_t$ [°C]	CP [MJ/(t °C)]	$\Delta H$ [MJ/t]
Evap.	Standardised milk	C	Liq.	8.0	63.4	42.7	-2362
Evap.	COW	H	Liq.	64.3	13.0	38.1	1954
Evap.	Condenser vapour (direct) <sup>a</sup>	H	Vap.	54.0	53.9		370
Evap.	Condenser liq. loop (indirect) <sup>a</sup>	H	Liq.	48.5	18.5*	12.3*	370
CIP	CIP hot water	C	Liq.	15.0	55.0	6.0	-238
Dryer	Milk concentrate	C	Liq.	54.0	65.0	6.0	-65
Dryer	Dryer inlet air	C	Gas	15.0	200.0	18.4	-3411
Dryer	FB inlet air (1)	C	Gas	15.0	49.0	1.6	-53
Dryer	FB inlet air (2)	C	Gas	15.0	45.0	2.3	-69
Dryer	FB inlet air (3)	C	Gas	15.0	32.0	1.7	-29
Dryer	Liquid loop from exhaust air	H	Liq.	62.5	27.5*	14.7*	-513

<sup>a</sup> The condenser may be directly or indirectly integrated into the process.

Table 6

Inter- and intra-zonal heat recovery targets.

Target or zone	$T_t$ [°C]	$T_{t,exh}$ [°C]	Intra-zonal $q_r$ [GJ/t <sub>p</sub> ]	Max. inter-zonal exports		
				To evap [GJ/t <sub>p</sub> ]	To CIP [GJ/t <sub>p</sub> ]	To dryer [GJ/t <sub>p</sub> ]
$\Delta T_{min} \rightarrow 0$ °C	8	36	3.923	-	-	-
<i>Totally integrated site</i>	13	55	2.837	-	-	-
Evaporator (condenser directly integrated)	13	-	2.140	-	0.184	0.184 (0.0)
CIP	-	-	0	0	-	0
Dryer	-	55	0.513	0	0	-
<i>Total zonal 1</i>	13	55	2.653	0	0.184	0
Evaporator (condenser indirectly integrated)	13	-	2.117	-	0.170	0.206 (0.037)
CIP	-	-	0	0	-	0
Dryer	-	55	0.513	0	0	-
<i>Total zonal 2</i>	13	55	2.630	0	0.170	0.037

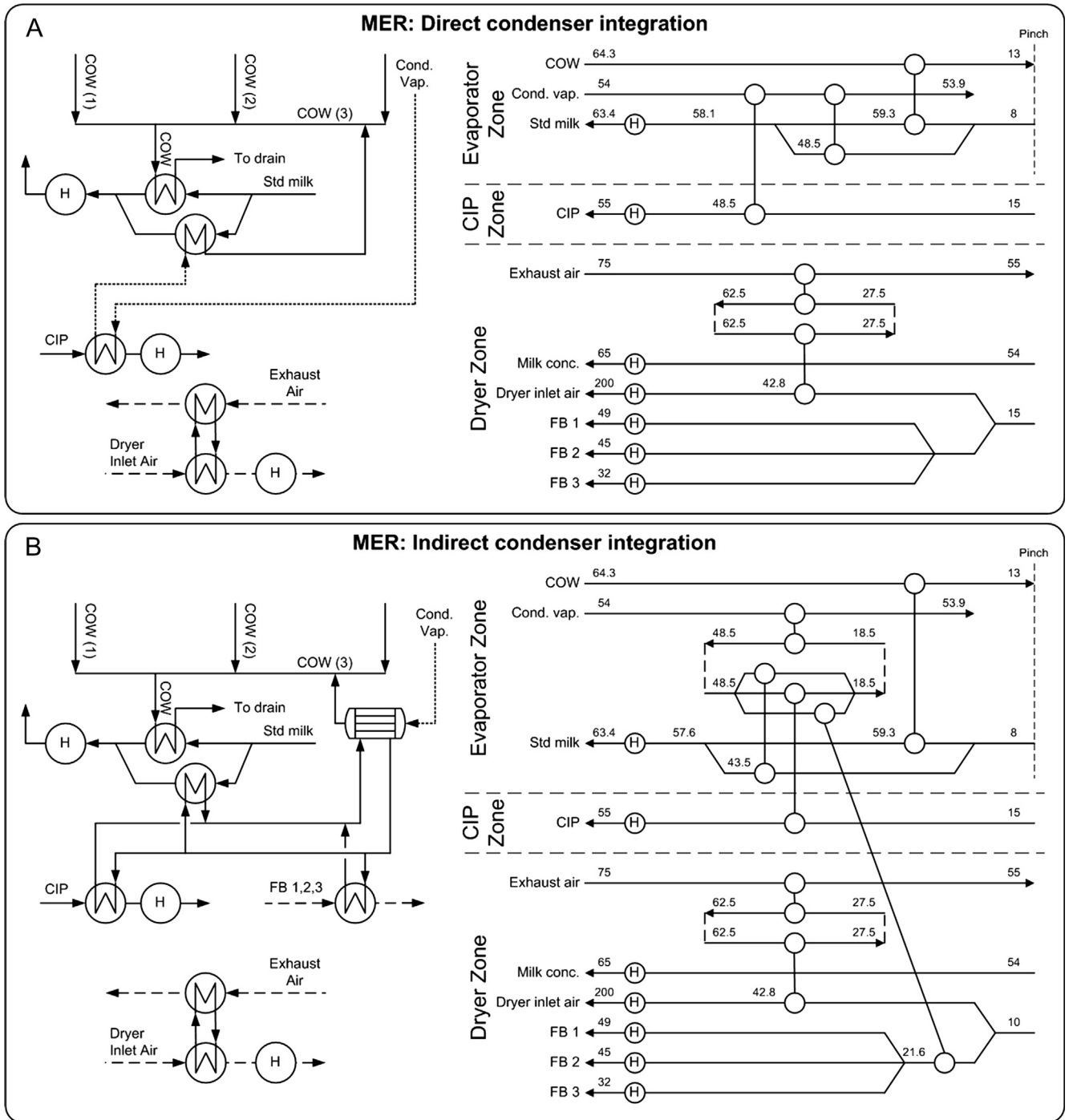


**Fig. 7.** Heat exchanger network grid diagrams and simplified flow sheets for the milk powder plant considering direct (A) and indirect (B) integration of the condenser. Soft temperatures: Exhaust air  $T_i$  is 55 °C, COW  $T_i$  is 13 °C, and condenser loop return  $T_i$  is 18.5 °C.

location. Whereas the zonal approach divides the plant into zones, in which intra-zonal heat recovery is maximised before inter-zonal heat exporting is considered. In addition, the target for the limiting case of  $\Delta T_{cont}$  (or  $\Delta T_{min}$ ) approaching zero is given.

Results suggest that it is possible to achieve heat recovery of 2.84 GJ/ $t_p$ , which is 72.3% of the absolute maximum heat recovery. Without any inter-zonal integration, the total heat recovery targets are 2.65 GJ/ $t_p$  for the case of direct condenser integration, and 2.63 GJ/ $t_p$  for indirect condenser integration. If inter-zonal

integration is allowed between the evaporator and CIP zones, heat recovery can rise to 2.84 GJ/ $t_p$ , with direct condenser integration, and 2.80 GJ/ $t_p$ , with indirect condenser integration. Indirect condenser integration also requires 0.04 GJ/ $t_p$  of heat to be exported from the evaporator zone to the dryer zone. The specific condenser duty is known to vary from plant to plant and so depending on this duty, direct integration of the condenser into the dryer zone may be theoretical required to achieve the heat recovery target, but not required in practice.

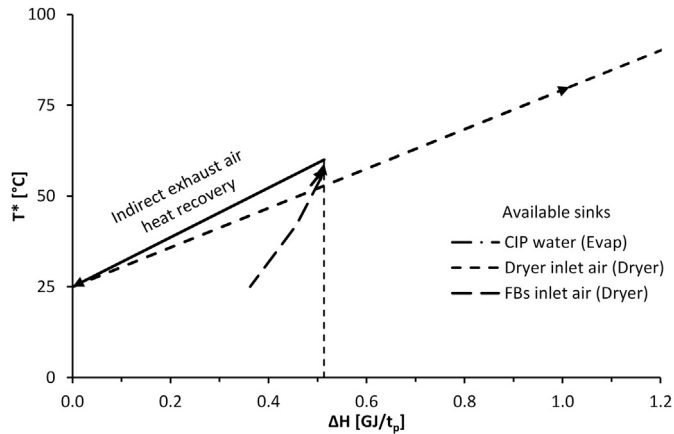


Fig. 8. Heat sink options for indirect exhaust air heat recovery.

### 5. Heat exchanger networks

#### 5.1. Maximum energy recovery networks

Maximum Energy Recovery (MER) heat exchanger networks have been developed for the cases of directly and indirectly integrating the evaporator condenser as shown in Fig. 7. The MER networks were developed using pinch network design rules [15]. Priority was given to maximising zonal heat recovery, before allowing inter-zonal integration. Guidance for this approach was provided by the intra- and inter-zonal heat recovery targets. As suggested in the grid diagram, the air streams enter the building together and there is opportunity to providing some heating while together.

The networks for the cases of direct and indirect integration of the condenser are similar. Both cases match the condenser heat to the split standardised milk stream and the CIP water. In addition to these matches, the indirect condenser integration case also requires heat to be transferred to the dryer zone using a liquid loop.

In the MER networks the exhaust air is matched to the dryer inlet air. Fig. 8 shows the possible sinks for heat recovery from the exhaust air, after integration of the evaporator and CIP zones, and the exhaust air heat source. The best heat sink choice is naturally the dryer inlet air. A second option is to split the exhaust air heat to the dryer and FB air inlet streams. This option would maximise the temperature driving force, but is also capital intensive due to the additional heat exchanger unit(s) and additional ducting and the like.

**Table 7**  
Comparison of proposed maximum energy recovery networks to typical industry practice.

HEN scheme	Production $t_p/y$	Heat recovery $GJ/t_p$	Utility cost $\$/t_p$	Capital cost $\$/t_p$	Total cost $\$/t_p$
MER A	117,500	2.837	41.77	9.90	51.67
MER B	117,500	2.837	42.37	10.53	52.90
Industry A	117,500	2.117	51.65	4.95	56.61
Industry B	117,500	2.172	47.73	6.33	54.06

#### 5.2. Comparison to current industry practice

In the dairy industry there are two common methods for integrating the evaporator and spray dryer sections of the milk powder process as show Fig. 9. Older plants tend to employ method A, whereas newer plants favour method B due to its increased heat recovery. At face value method B may appear highly beneficial. However by preheating the inlet air, the temperature driving force for potential exhaust air heat recovery, which would be a significant step change in energy efficiency, is dramatically reduced and becomes less cost effective.

By applying the same minimum approach temperature difference, the overall heat recovery potential of industry practice may be calculated and compared to the MER networks that were developed (Table 7). Also, using the cost data in Table 3 and the current utility prices, an estimate for the annual utility, capital and total costs may be compared. In terms of raw heat recovery, shifting to one of the MER networks would increase specific heat recovery by 34% over Industry A and 30% over Industry B. Subsequently utility cost decreases, although at the expense of a rise in annual capital cost. Comparing Industry A to MER A, the total cost may be reduced by nearly 10%.

There are some issues that face implementation of MER A and B. Liquid milk process streams have rapid thermophile and microbial growth in the temperature range of 45–60 °C [21]. Short residence times in this temperature range are very important for maintaining product quality over long operating cycles. When excessive thermophile and microbial growth and hold up occurs, product quality degrades and the process must be shut down for cleaning. A second issue is the level of control in the MER network may be costly due to the milk stream split. However, since energy efficiency can be greatly improved through the application of new HEN structures and increased heat exchanger area, the costs of potentially shorter times between cleans and increased control complexity should be investigated more fully.

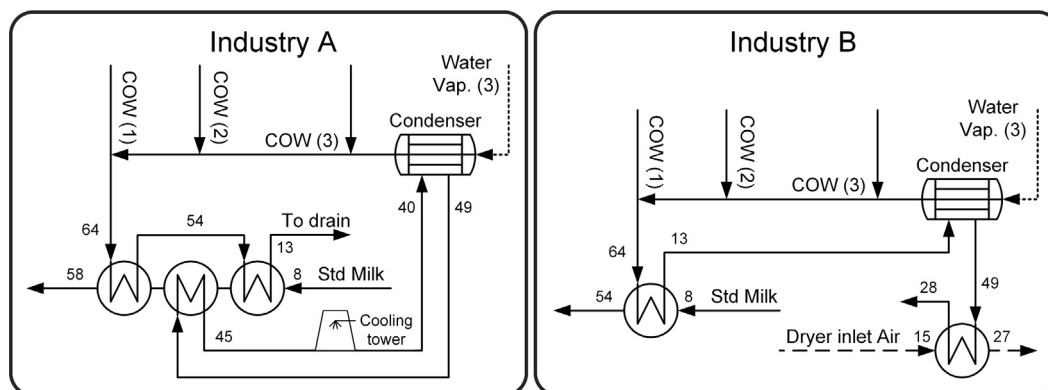


Fig. 9. Schemes for evaporator zone integration including CIP water.

## 6. Conclusion

Heat exchanger networks have been developed that return the maximum energy recovery targets for industrial milk powder production. Comparison to industrial practice has shown that there is potential to economically increase specific heat recovery by at least 30% with a specific cost improvement of 10%. Spray dryer exhaust air heat recovery is necessary to achieve maximum energy recovery and should be matched to preheat the dryer inlet air stream.

## Acknowledgements

The authors would like to thank the Todd Foundation in New Zealand for providing funding for a Ph.D. scholarship and the support of the Energy Research Centre and the School of Engineering at the University of Waikato.

## References

- [1] C.R. Holland, J.B. McCann, Heat recovery in spray drying systems, *International Journal of Food Science & Technology* 15 (1980) 9–23.
- [2] A.C. Mercer, Improving the energy efficiency of industrial spray dryers, *Journal of Heat Recovery Systems* 6 (1986) 3–10.
- [3] J. Miller, The Use of Recovered Heat for Preheating Air to Spray Driers, New Zealand Energy Research and Development Committee Report. Palmerston North, New Zealand, 1987.
- [4] M.J. Atkins, M.R.W. Walmsley, J.R. Neale, Integrating heat recovery from milk powder spray dryer exhausts in the dairy industry, *Applied Thermal Engineering* 31 (2011) 2101–2106.
- [5] C. Robert, Bulletin of the IDF No. 401/2005-Energy Use in Dairy Processing (2005).
- [6] M.J. Atkins, M.R.W. Walmsley, J.R. Neale, The challenge of integrating non-continuous processes – milk powder plant case study, *Journal of Cleaner Production* 18 (2010) 927–934.
- [7] M.J. Atkins, M.R.W. Walmsley, J.R. Neale, Process integration between individual plants at a large dairy factory by the application of heat recovery loops and transient stream analysis, *Journal of Cleaner Production* 34 (2012) 21–28.
- [8] M.R.W. Walmsley, T.G. Walmsley, M.J. Atkins, James R. Neale, Area targeting and storage temperature selection for heat recovery loops, *Chemical Engineering Transactions* 29 (2012) 1219–1224.
- [9] C.G.J. Baker, K.A. McKenzie, Energy consumption of industrial spray dryers, *Drying Technology: An International Journal* 23 (2005) 365–386.
- [10] T.G. Walmsley, M.R.W. Walmsley, M.J. Atkins, Z. Fodor, J.R. Neale, Optimal stream discharge temperatures for a dryer operation using a thermo-economic assessment, *Chemical Engineering Transactions* 29 (2012) 403–408.
- [11] M.J. Atkins, M.R.W. Walmsley, T.G. Walmsley, Z. Fodor, J.R. Neale, Minimising energy use in milk powder production using process integration techniques, *Chemical Engineering Transactions* 29 (2012) 1507–1512.
- [12] J. Klemeš, R. Smith, J.K. Kim, *Handbook of Water and Energy Management in Food Processing*, Woodhead Publishing, Cambridge, UK, 2008.
- [13] J. Zhang, X.X. Zhu, Simultaneous optimization approach for heat exchanger network retrofit with process changes, *Industrial and Engineering Chemistry Research* 39 (2000) 4963–4973.
- [14] J. Klemeš, F. Friedler, I. Bulatov, P. Varbanov, *Sustainability in the Process Industry: Integration and Optimization*, McGraw-Hill, New York, USA, 2010.
- [15] I.C. Kemp, *Pinch Analysis and Process Integration: A User Guide on Process Integration for the Efficient Use of Energy*, Butterworth-Heinemann, Oxford, UK, 2007.
- [16] W.M. Kays, A.L. London, *Compact Heat Exchangers*, third ed., Krieger Pub. Co., Florida, USA, 1998.
- [17] H.A. Navarro, L. Cabezas-Gómez, A new approach for thermal performance calculation of cross-flow heat exchangers, *International Journal of Heat and Mass Transfer* 48 (2005) 3880–3888.
- [18] S. Kakaç, H. Liu, *Heat Exchangers: Selection, Rating, and Thermal Design*, CRC, London, UK, 2002.
- [19] R.W. Bouman, S.B. Jensen, M.L. Wake, W.B. Earl, *Process Capital Cost Estimation for New Zealand 2004*, Society of Chemical Engineers New Zealand, New Zealand, Wellington, 2005.
- [20] T.G. Walmsley, M.R.W. Walmsley, M.J. Atkins, J.R. Neale, An investigation of milk powder deposition on parallel fins, in: *Lecture S02-1, Chemeca 2012*, IChemE, Wellington, New Zealand, 2012.
- [21] B. Rademacher, W. Walenta, H.G. Kessler, Contamination During Pasteurization [of Milk] by Biofilms of Thermophilic *Streptococci*, *International Dairy Federation*, Brussels, Belgium, 1996.



**Article 13:**

*Process and utility systems integration and optimisation for ultra-low energy milk powder production*

**Walmsley, T.G.**, Atkins, M.J., Walmsley, M.R.W., Philipp, M., Peesel, R.-H., 2018.

Energy 146, 67-81.

DOI: [10.1016/j.energy.2017.04.142](https://doi.org/10.1016/j.energy.2017.04.142)

Elsevier



# Process and utility systems integration and optimisation for ultra-low energy milk powder production



Timothy G. Walmsley<sup>a,\*</sup>, Martin J. Atkins<sup>b</sup>, Michael R.W. Walmsley<sup>b</sup>, Matthias Philipp<sup>c</sup>, Ron-Hendrik Peesel<sup>d</sup>

<sup>a</sup> Sustainable Process Integration Laboratory – SPIL, NETME Centre, Faculty of Mechanical Engineering, Brno University of Technology - VUT Brno, Technická 2896/2, 616 69 Brno, Czech Republic

<sup>b</sup> Energy Research Centre, School of Engineering, University of Waikato, Private Bag 3105, Hamilton, New Zealand

<sup>c</sup> Technische Hochschule Ingolstadt, Institute of New Energy Systems, Esplanade 10, 85049 Ingolstadt, Germany

<sup>d</sup> Universität Kassel, Dep. Umweltgerechte Produkte und Prozesse, Kurt-Wolters-Straße 3, 34125 Kassel, Germany

## ARTICLE INFO

### Article history:

Received 10 December 2016

Received in revised form

11 April 2017

Accepted 24 April 2017

Available online 26 April 2017

## ABSTRACT

This study applies a Total Site Heat Integration approach in conjunction with a detailed process and utility model, to develop an innovative ultra-low energy milk powder plant design. The basis for the analysis is a state-of-the-art modern milk powder plant that requires 5265 MJ/t<sub>p</sub> of fuel and 210.5 kWh/t<sub>p</sub> (58.5 MJ<sub>e</sub>/t<sub>p</sub>) of electricity. The model of the modern milk powder plant was validated against industrial data and changes to process and/or utility systems are targeted and implemented into the model to understand the impacts on thermal and electrical demands and emissions. Results show that seven significant changes are beneficial: (1) pre-concentration of milk to 30% using reverse osmosis, (2) a two-stage intermediate concentrate (30%) homogenisation to enable high solids (60%) spray drying, (3) an ultra-low energy Mechanical Vapour Recompression evaporator system, (4) spray dryer exhaust heat recovery, (5) condensing economiser for the boiler, (6) upgrade and integration of chiller condenser heat with hot water utility systems, and (7) recycling of air in the building ventilation system. These changes are estimated to reduce thermal energy use by 51.5%, electricity use by 19.0%, and emissions by 48.6% compared to a modern milk powder plant.

© 2017 Elsevier Ltd. All rights reserved.

## 1. Introduction

Conversion of raw milk into powdered milk is an energy intensive process requiring steam heating, chilling and electrical utilities. The milk powder process has four main processing steps: milk separation, heat treatment, evaporation, and spray drying. Over the past four decades, improved [1] and emerging [2] technologies have increased the energy efficiency of milk powder plants. Specific fuel consumptions have decreased from about 12,000 MJ<sub>f</sub>/t<sub>p</sub> of powder to between 5000 and 6000 MJ<sub>f</sub>/t<sub>p</sub> and specific electricity uses are in the order of 150–400 kWh/t<sub>p</sub> (111 MJ<sub>e</sub>/t<sub>p</sub>) [3]. The absolute fuel and electricity use and split depends on the installed technology, degree of heat integration, scale of production, and utility system efficiency.

Significant improvements in energy efficiency of the core milk

powder processes through redesign and additional heat recovery have been reported in literature. For the milk separation process, Hanneman and Robertson [4] described the industry standard design for a hot milk separation plant where raw milk is separated into skim milk and cream. A key feature of the heat exchanger network design is a stream split of the raw milk for maximising heat recovery from both the hot skim milk and cream. Since this time, new plants have used new technology to perform milk separation while the milk remains cold (8 °C). For the heat treatment and evaporation processes, Walmsley et al. [5] demonstrated the optimal use of vapour recompression technology in an integrated process design based on the application of the appropriate placement principle for a heat pump [6]. The redesigned evaporation system achieved a dramatic 78% reduction in steam (6.40 MW) use at the expense of a 16% increase in electricity (0.36 MW<sub>e</sub>). For spray dryer systems, exhaust heat recovery is another significant opportunity to increase energy efficiency [7]. Walmsley et al. [8] developed a dryer exhaust heat recovery model, which included economic calculations and fouling predictions, and found that a 14%

\* Corresponding author.

E-mail address: [walmsley@fme.vutbr.cz](mailto:walmsley@fme.vutbr.cz) (T.G. Walmsley).

## Nomenclature

### Variables

$\Delta$	Difference between two states
COP	Co-efficient of Performance
Q	Thermal duty (kW)
SEC	Specific Energy Consumption (MJ/ $t_p$ or kWh/ $t_p$ )
W	Work or electrical energy (kW)

### Subscripts

*	Marginal quantity
e	Electricity
f	Fuel
H	Hot
HP	High pressure
LP	Low pressure
p	Powder
rej	Rejected
tot	Total
w	Water removed

reduction in steam through heat recovery was most economical for a particular industrial site.

More opportunities to increase the energy efficiency of milk powder production can be achieved by shifting focus towards the complete Total Site Heat Integration (TSHI) of process and utility systems. TSHI incorporates graphical and mathematical programming methods for the integration of industrial sites [9] and locally integrated energy systems [10]. The framework also enables simultaneous selection, design and integration of unit operations through targeting [11], retrofit of process systems [12], and the integration of renewable energy [13]. The Total Site problem may also be solved using mathematical programming techniques for new design [14] and retrofit [15] problems. Improved site-wide integration through TSHI has led to increasing utility savings in slaughter and meat processing by 35% [16], large industrial parks in Japan about 53% [17] and Thailand by 28% [18], chemical processing clusters by 42% [19], and Kraft pulp mills about 13% [20]. TSHI has been applied to milk powder production in context of stand-alone milk powder plants [5] and multi-plant dairy factories [21] including the optimal integration of industrial solar [22]. However, these studies on milk powder plants have focused on optimising either the process or utility system, not both systems simultaneously.

Energy efficiency improvements in the milk powder process system can be realized through process change available in emerging technologies [23]. One emerging technology is high solids milk concentrate drying. At present, the milk concentrate solids entering the spray dryer are constrained to 53%, above which viscosity becomes prohibitive. Emerging technologies are under development to reduce high solids milk viscosity through ultrasound techniques [24], high-solids steam injection process [25] and two-stage homogenisation of concentrate (20–40%) [26], enabling the drying milk at about 60% solids in the future. Increasing the solids feed to the dryer effectively shifts evaporation load from the spray dryer to the highly integrated evaporator system, which results in significant energy reduction. Another recently commercialised technology is Reverse Osmosis (RO) membrane technology for the pre-concentration of milk up to 30% solids [27]. RO takes evaporation load away from the potentially ultra-low energy evaporator system. As a result the energy reduction opportunity is

suppressed. However, as a retrofit, it is an economic option to boost production, if the evaporator is the processing bottleneck.

For a milk powder plant's utility system, TSHI may be applied to target the minimum boiler flue gas temperature, thus maximising boiler efficiency, and Combined Heat and Power (CHP). A key technology for extracting the maximum heat from boiler flue gas is a condensing economiser. Although the milk powder process can have a low Pinch Temperature, e.g. 10.5 °C [28], very few sites in New Zealand have steam boilers equipped with condensing economisers. Likewise, out of 82 New Zealand dairy processing sites, only four sites have CHP technology installed (New Zealand Heat Plant Database 2015 in Walmsley et al. [29]). Given the low uptake, it is valuable to explore options for maximising CHP as a means for improving and developing a more attractive business case. Such options include raising the initial steam pressure, the addition of new steam pressure levels to improve the overall heat and powder cascade [30], and the optimisation of an integrated CHP system [31].

Another area in the utility system that can contribute to energy cost reduction is waste heat recovery from chiller units. In most instances this opportunity requires an additional compressor unit to increase the pressure of the chiller's condenser, thereby upgrading its heat so that it may be substituted for boiler steam and fulfil process heat deficits. TSHI can aid the selection of the condenser pressure and identify the method for its integration, either direct with process stream and/or via the hot water utility network, using the appropriate placement principle for heat pumps [32]. The final opportunity is the milk powder plant's Heating, Ventilation and Air Conditioning (HVAC) system. At present, the system is a single pass with a steam heater to pre-heat incoming air to 28 °C from an average of 15 °C. After passing through the building air exhausts at about 33 °C. A portion of this air may be recycled to the inlet to reduce thermal energy use.

Combining the multiple process and utility system energy efficiency concepts for milk powder plants, including their coupled interactions, represents the gap in knowledge that this paper fills. The aim of this paper is develop a novel ultra-low energy process design for a milk powder plant that achieves a radical step reduction in thermal and electrical energy use and emissions. To achieve the aim, the new design takes advantage of simultaneous improvements to process and utility systems and quantifies the impacts on energy use and emissions.

In the first instance, a modern milk powder is described and then compared against a future milk powder plant design from literature [32]. Using these designs as a basis, four energy reduction opportunities in the utility system are presented followed by two opportunities in the process system. For the utility system, the investigated opportunities are: (1) increasing boiler efficiency through condensing economisers, (2) waste heat recovery from the chiller unit, (3) recycling of air in the building HVAC system, and (4) Combined Heat and Power (CHP) for electricity production. Changes to the process systems are: (1) pre-concentration of milk using RO up to 30% solids and (2) high solids spray drying up to 60% solids. The context of the study is set in New Zealand with natural gas as the primary fuel and electricity from a grid that has a high share of renewable generation. This work is a culmination and extension of work previously published by the authors [33] over the past several years.

## 2. Industrial milk powder plant designs

### 2.1. Modern milk powder plant – Design 1.0

The milk powder process has four main processing steps: milk separation, heat treatment, evaporation, and spray drying. These

processes are serviced by a common boiler for generating high pressure steam ( $\sim 40$  bar), chiller for generating chilled water, and an air compressor to generate compressed air. After being produced, milk powder is held in cool stores before transportation to market. Fig. 1 presents an overview of a stand-alone milk powder factory.

At modern milk powder factories, the milk separation process separates raw milk from the farm into skim milk and cream, while the fluids are cold ( $\sim 8$  °C). This process requires about 10 MJ/ $t_p$  of hot water and 10 MJ/ $t_p$  of chilled water. Since adopting the new technology the energy use in this section of the plant has become insignificant.

The milk heat treatment process is a combination of holding temperature (80–120 °C) and time (1–60 s), which affects the degree of protein denaturation [34] and the flavour of the milk powder [35]. Milk enters the heat treatment process ( $\sim 8$  °C) and heats to its target heat treatment temperature. During milk heating it is important to recognise that rapid thermophile growth occurs in the temperature range of 45–60 °C [36]. As a result strategies need to be implemented such as parallel processing lines or direct vapour contact exchangers.

The evaporation system follows the heat treatment process and the two processes are closely integrated. These two integrated systems demand 1041 MJ/ $t_p$  of thermal energy (excludes associated boiler losses) and 95.3 kWh/ $t_p$  (26.5 MJ $_e$ / $t_p$ ) of electrical energy. The multi-train, multi-effect falling film evaporation system concentrates standardised milk from about 12% to 53% solids. In this design both Mechanical Vapour Recompression (MVR) and Thermal Vapour Recompression (TVR) are integrated with the evaporation system. Multiple effects improve the energy efficiency of the evaporator and multiple trains enable continuous operation. Each evaporator train is washed clean-in-place (CIP) about every 16 h to maintain food grade processing hygiene. Milk evaporators operate under vacuum with a pressure below 35.5 kPa $_{abs}$  and saturation temperature of 73 °C to avoid further denaturing of proteins and adverse effects on product flavour [36].

The final processing step is the spray dryer system, which is the largest thermal energy use with a SEC demand of 3036 MJ/ $t_p$ . After exiting the final milk evaporator effect, milk is heated ( $\sim 75$  °C) and homogenised before being atomised and sprayed co-currently with hot air (210 °C). Partially dry powder from the main spray dryer

chambers exits through a series of fluidised beds that provides sufficient residence time to complete the drying process and cools the powder from around 80 °C in the main chamber to about 35 °C. Spent dryer air passes through cyclones and/or baghouses to help capture any entrained particles before being exhausted to the atmosphere at about 75 °C.

## 2.2. Future milk powder plant – Design 2.0

The future milk powder plant design adopts an ultra-low energy evaporation system [5] (Fig. 2) and dryer exhaust heat recovery [8] (Fig. 3) to dramatically decrease overall energy use. Other processes remain the same as a modern milk powder plant. Overall these improvements can potentially decrease thermal energy use by 1571 MJ/ $t_p$  (29.8%) in trade-off with an increase in electricity use by 9.7 kWh/ $t_p$  (2.7 MJ $_e$ / $t_p$ , 4.6%). There is also a 26.8% reduction in carbon emissions.

The redesigned low energy evaporator system is presented in Fig. 2. The redesigned evaporator has three important changes compared to a modern evaporator system [5]. These are: (1) both evaporator effects are integrated with MVR resulting in less low grade waste heat, (2) the heat treatment section is integrated with MVR to reduce direct steam injection, and (3) an improved heat exchanger network design that enables maximum extraction of condensate heat, which exits the system at 13 °C (instead of 30 °C).

Dryer exhaust heat recovery uses a liquid coupled loop to indirectly integrate with the dryer inlet air (Fig. 3). A coupled loop system is applied due to the requirement to separate the exhaust air outflow and feed air inflow. The final temperature of the exhaust air should be kept above 55 °C to avoid accelerated powder fouling [37].

In Section 6, a full comparison between the modern milk powder plant (Design 1.0) and potential future low-energy plant designs (Design 2.0–3.0) is presented using thermal and electrical SEC metrics (see Table 3) and specific emissions per tonne of powder produced (see Table 4).

## 3. Methods

A scenario based process and utility systems modelling approach is taken in this paper to determine the extent that energy

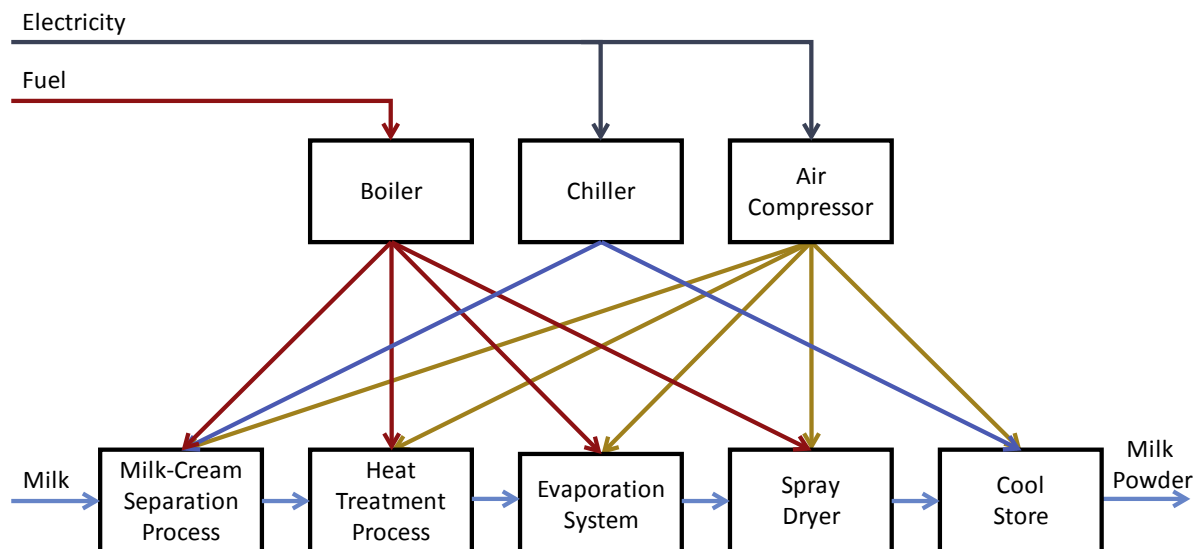


Fig. 1. Modern stand-alone milk powder factory overview.

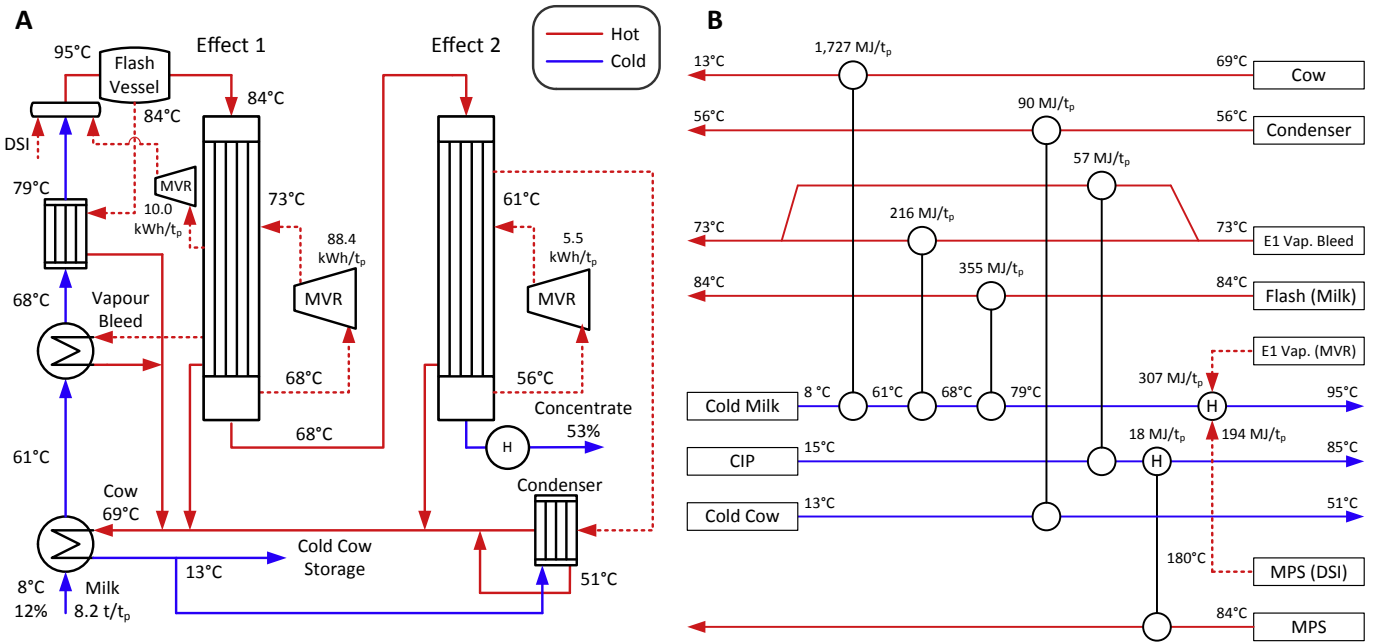


Fig. 2. Ultra-low energy milk evaporation system. Design illustrated using a process flow diagram (A) and grid diagram (B). Process design from Walmsley et al. [5].

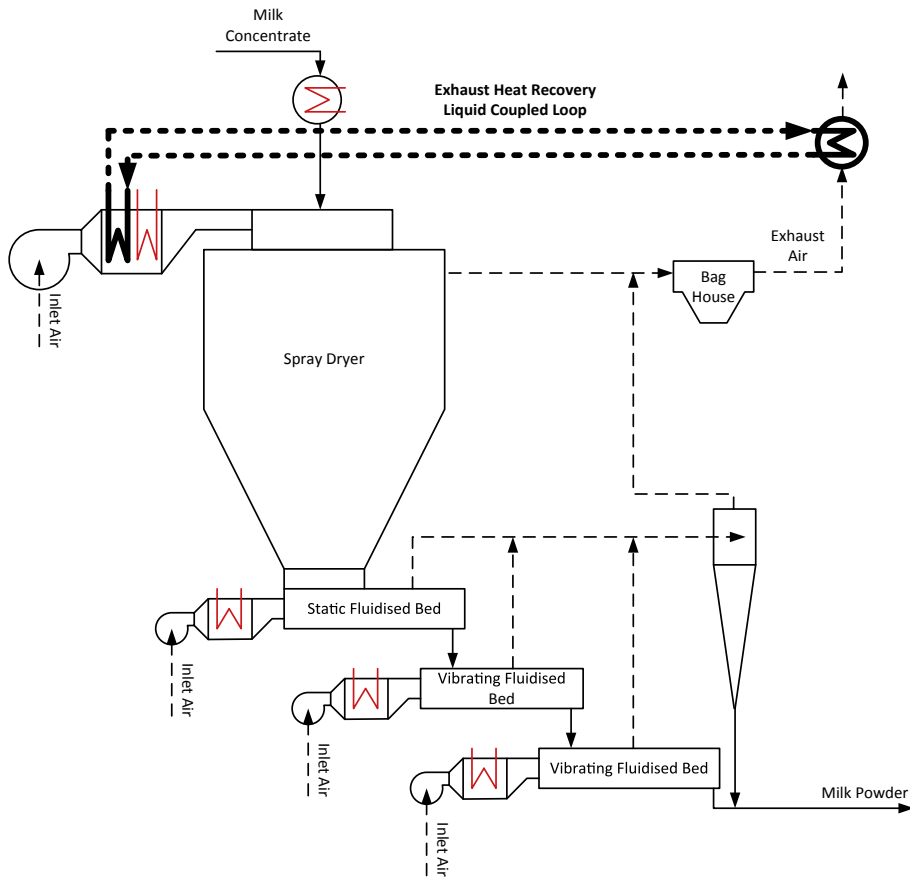


Fig. 3. Milk spray dryer showing indirect exhaust heat recovery using a liquid coupled loop heat exchanger system.

use and emissions may be reduced for milk powder production. As a result, a comprehensive mass and energy process and utility model of a milk powder factory has been implemented in an

Excel™ spreadsheet and validated against industrial data from New Zealand's current milk powder plant design as well as an anticipated future plant design. The model consists of sub-models that

contain process flow and design details for each processing step and utility unit operation. This includes the design of the heat exchanger network for each process, where applicable. The base process models for the milk separation, evaporation and spray drying processing steps were previously developed and reported by Walmsley et al. [5]. This paper reports the extension of the base model, to investigate additional concepts for minimising energy use and emissions across the entire site.

Sub-models within process and utility model are linked through both mass and heat transfer. For example, concentrate exiting the evaporation system is an input to the spray dryer model. Steam generated in the boiler and chilled water from the chilled are driven by the process demands. In general, Fig. 1 presents the major linkages between the various process and utility operations.

Six energy efficiency opportunities within various process and utility operations have been investigated using the milk powder plant process and utility model.

Investigated opportunities in the utility system include:

- (1) increasing boiler efficiency through condensing economisers,
- (2) waste heat recovery from the chiller unit,
- (3) recycling of air in the building HVAC system, and
- (4) Combined Heat and Power (CHP) for electricity production.

Investigated process changes include:

- (1) pre-concentration of milk using RO up to 30% solids, and
- (2) high solids spray drying up to 60% solids.

To investigate these opportunities, new detailed models were needed for: reverse osmosis milk pre-concentration model, two-stage homogenisation model, steam boiler with back pressure steam turbine model, and an ammonia chiller model. These models are described in sections 3.1–3.5. Several process and utility designs result from the investigation. Table 1 summaries the process and utility design changes that are incorporated into Design 2.0–3.0.

TSHI [38] has been applied to target the integration potential for additional energy reduction in the milk powder utility system. Total Site Profiles and Site Utility Grand Composite curve play important roles in targeting additional heat recovery in the utility system. For example, the boiler flue gas is pinched against the Site Utility Grand Composite to target heat recovery and its final temperature. It is important to note that as changes are made to a process, its stream data changes, which then affects its energy generation efficiency or process heat demands. Once the energy efficiency opportunity is targeted, practical design modifications are developed through the application of conventional Pinch heuristics and good engineering judgement. Appendix A provides the stream data for the basis of the Total Site Profiles related to the three generations of design (Designs 1.0–3.0).

In determination of changes to emissions, emissions factors for New Zealand are applied in the analysis to determine the effect on emissions from the various energy efficiency concepts. New Zealand had a grid emissions factor of 0.0359 kg<sub>CO<sub>2</sub>-e</sub>/MJ in 2015 as a result of a high proportion of renewable generation [39]. Process heat from natural gas has an emissions factor of 0.0533 kg<sub>CO<sub>2</sub>-e</sub>/MJ [40].

### 3.1. Principal milk powder process models

The milk separation process in modern milk powder plants operates at the milk storage temperature of about 8 °C. As a result, the process model for this section of the factory splits the raw milk into skim milk (92%) and cream (8%). Separation percentages are based on industrial process flow data.

A detailed heat and mass balance process model of a multi-effect falling film milk evaporator system, including the possibility of both MVR and/or TVR, has been developed. The process design in the model is flexible in that the user can choose the number of evaporation effects (1–3), operating pressures and temperature, heat exchanger network design, as well as the application of MVR and/or TVR technologies. The model applies standard water/steam properties (IAPWS IF-97) and milk properties [41]. Based on industrial data, low pressure mechanical compressors (MVR) have a calculated isentropic efficiency of 80%. TVR (or thermocompressor) performance is determined using the model of Sargolzaei et al. [42], assuming choked flow through the thermocompressor. The process design for the current set-up of evaporation system, which is described in section 2.1 (see Walmsley et al. [5]) has been validated using industrial plant data.

The spray dryer model followed a similar development procedure as the other two process models. A spreadsheet describing its mass and energy flows was constructed and compared with industrial process data for the current dryer set-up, as shown in Fig. 3. Spray dryer exhaust heat recovery is added to improve its energy efficiency, as reported in Walmsley et al. [8]. High solids drying assumes similar dryer chamber and exhaust air outlet temperatures may be achievable and no other process challenges constrain its performance.

### 3.2. Reverse osmosis model for milk pre-concentration

Milk is commercially concentrated using a RO process up to 30% solids for whole milk and 34% solids for skim milk [27]. The recommended operating pressure for industrial RO systems is between 3.1 and 4.1 MPa [43]. Industrial data on the energy performance of RO filtration for milk is difficult to obtain but has been reported in literature to consume 3.9–10.0 kWh/t<sub>w</sub> (1.1–2.8 MJ<sub>e</sub>/t<sub>p</sub>) of water removed [2]. As a result, three cases – high, mid and low energy use – for concentrating milk to 30% are investigated as shown in Table 2.

**Table 1**

Process and utility design changes. \*Utility systems changes investigated using the basis of Design 2.0 and then incorporated into the final design, Design 3.0.

Process Design	Design 2.0	Design 2.1	Design 2.2	Design 2.3	Design 3.0
Ultra-low energy heat treatment & evaporator system	✓	✓	✓	✓	✓
Spray dryer exhaust heat recovery	✓	✓	✓	✓	✓
RO Pre-concentration		✓		✓	✓
High solids spray drying			✓	✓	✓
Boiler condensing economiser	*				✓
Chiller waste heat recovery	*				✓
HVAC air recycle					✓
Combined Heat and Power	*				

**Table 2**

Reverse osmosis specific energy consumptions, per tonne of water removed and per tonne of powder product, for concentrating milk from 12% to 30% solids.

Case	SEC [kWh/t <sub>w</sub> ]	SEC [kWh/t <sub>p</sub> ]
Low	3.9	19.6
Mid	7.0	35.0
High	10.0	50.3

### 3.3. Two-stage homogenisation model for high solids spray drying

Milk concentrate viscosity reduction, which enables high solids spray drying, is achieved using a two-stage homogenisation when the milk reaches a concentration between 20 and 40% solids [26]. The homogenisation process was considered a better option than ultrasound treatment [24] because of its greater potential for viscosity reduction and high-solids steam injection process [25] because of its lower energy demand.

The two stage homogenisation process uses pressures of 14.0 MPa for stage one and 4.0 MPa for stage two as recommended by Bodenstab [26]. Fig. 4 estimates the electricity requirement for homogenising at a range of solids with an assumed pump efficiency of 75%. For milk with the recommended concentration of 35% solids, the electrical use is 8.9 kWh/t<sub>p</sub> (2.5 MJ<sub>e</sub>/t<sub>p</sub>) for stage one and 2.5 kWh/t<sub>p</sub> (0.7 MJ<sub>e</sub>/t<sub>p</sub>) for stage 2. Bodenstab [26] claims this additional processing step can facilitate spray drying using up to a 60% solids concentrate.

### 3.4. Steam boiler and back pressure steam turbine model

The natural gas steam boiler model, including a deaerator, blowdown vessel and feed water pump, was modelled using Excel Add-in JSteam™ ([www.inverseproblem.co.nz](http://www.inverseproblem.co.nz)). TSHI techniques are applied to maximise boiler efficiency. The composite curve of boiler flue gas (initially at 140 °C), after generating steam and preheating combustion air using a standard economiser, is shifted and pinched against the Total Site Source Profile to target the minimum flue gas temperature, which leads to maximising boiler efficiency.

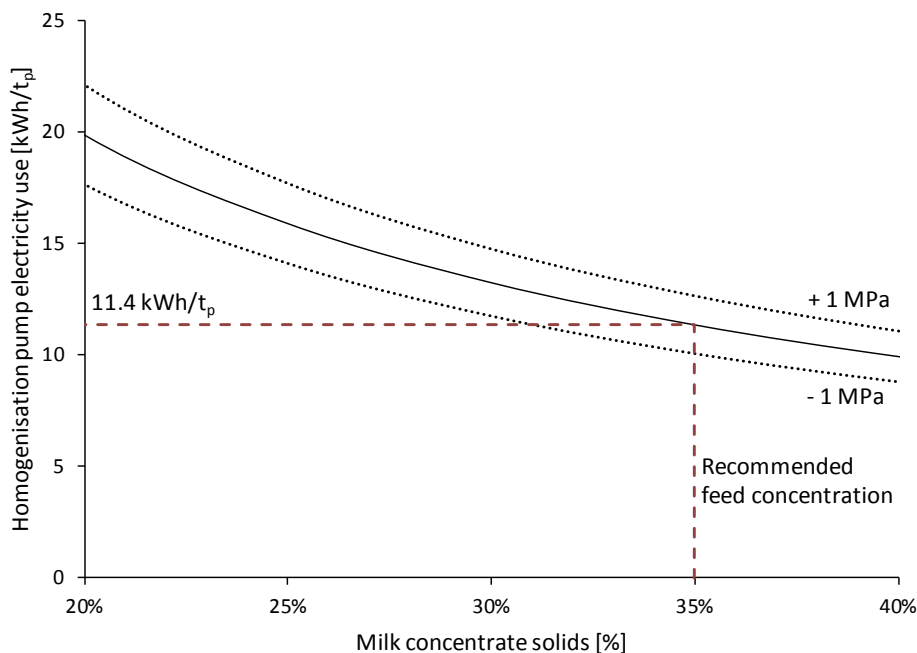


Fig. 4. Milk concentrate two-stage homogenisation process electricity use.

For CHP, the back pressure steam turbine model estimated performance using the M-P turbine model [44], which is the best available empirical correlation for single and multiple extraction turbines. Where a turbine (or steam drive) rating falls below the M-P turbine model's lower limit, the model estimates work assuming an isentropic efficiency of 65%.

### 3.5. Ammonia chiller model

The chiller model uses the vapour compression cycle with ammonia as the working fluid, a compressor efficiency of 53%, a condenser pressure of 2.0 MPa, and a Co-efficient of Performance (COP) of 2.3. Thermophysical properties are called from NIST's REFPROP™. The standard chiller may also generate useful heat (i.e. heat pump) by raising the condenser pressure to 2.6 MPa, which has a saturation temperature of 60 °C. The COP of this unit is 1.8 for chilling and 2.8 for heating. Since the process requires a chiller, it's useful to understand the performance of expending additional electricity to upgrade the condenser heat. The marginal COP\* for heating in the combined system may be defined by:

$$COP_H^* = \frac{Q_{H(HP)} - Q_{rej}}{W_{HP} - W_{LP}} \quad (1)$$

Where subscripts HP refers to a high pressure condenser, LP refers to a low pressure condenser, and rej refers to rejected heat. If all the condenser heat is able to heat process streams (i.e. the rejected heat is zero), then the marginal COP of heating is 13.4.

## 4. Energy efficiency opportunities in the utility system

This section explores four energy efficiency opportunities in the utility system. The basis for the analysis is the future milk powder plant design (Design 2.0). TSHI is applied to target heat integration while the Milk Powder Plant model helped estimate the actual energy change.

#### 4.1. Maximising boiler energy efficiency through condensing economisers

Standard industrial steam boilers for milk powder production operate at 40 bar (250 °C saturated) and are fitted with an economiser. The economiser preheats pressurised boiler feed water before it enters the main evaporation tubes. Depending on the boiler design the flue gas enters the economiser at up to 350 °C and leaves above the acid dew point at 140 °C. An additional condensing economiser can be installed to capture more flue gas heat. There is also a water dew point, which for a natural gas boiler (as considered in this study) is about 60 °C while a coal fired boiler is 40 °C. Extracting additional heat, both sensible and latent (if useful), maximises boiler efficiency and minimises fuel use.

Two sinks within the boiler plant to match with the flue gas in a condensing economiser are the combined condensate return/make-up water flow and the combustion air inlet. The condensate returns from servicing the process at 85 °C, and once combined with the make-up water, the temperature decreases to 68 °C for the current process design and 82 °C for the future design. This difference in temperature is due to current plant design having a lower condensate return percent compared to the expected percent in the future design (74%–94%). The future process design uses less direct steam injection and therefore has a higher condensate return percentage. Matching the combined water flow with the flue gas has a maximum duty of 69 MJ/t<sub>p</sub>. Preheating the combustion is another option, but is undesirable due to poor heat transfer coefficients of gas to gas heat exchange. Further sink options beyond the boiler system may be found using TSHI techniques.

The source profile of the Total Site Profiles together with targeted steam and hot water utility profiles may be pinched with the shifted boiler flue gas flow using a  $\Delta T_{\text{cont}}$  of 12.5 °C. Fig. 5 plots these source, sink and utility profiles for the future process design. The targeted final flue gas temperature is 58.4 °C and the additional heat extraction from the flue gas is 180 MJ/t<sub>p</sub>. The target is influenced by the hot water utility temperature selection. The additional heat extraction from the flue gas has the knock on effect of reducing

boiler fuel consumption to meet the process heat demand, which in turns means the flue gas flow rate slightly decreases. As a result the process and utility model becomes an important tool to capture these coupled effects.

The hot water utility system, as shown in Fig. 5, is one sink option for the condensing economiser. This option would require additional piping from the boiler house to the processing buildings. At present the boiler supplies the process with only two steam pressure levels (using a let-down valve) and returns hot condensate in a separate line. Another sink option that requires minimal additional piping between the boiler and process locations is to return cold condensate (35 °C) by placing the heat in a process sink. For the future process design, the Fluidised Bed air flows may be matched with the hot condensate flows to achieve a duty of 232 MJ/t<sub>p</sub>. The cold condensate, combined with a small amount of make-up water, then extracts an additional 197 MJ/t<sub>p</sub> in a condensing economiser. The overall result is a specific fuel reduction of 227 MJ/t<sub>p</sub>, which is actually greater than the initial integration target.

#### 4.2. Chiller waste heat upgrade and recovery

The chiller system is an essential utility supply operation of chilled water for process cooling. The condenser is normally air-cooled in a closed loop. With ammonia as the working fluid, the condenser operates at 2.0 MPa, which is a saturation temperature of 49 °C. By increasing the compression to 2.6 MPa, the saturation temperature increases to 60 °C and the heat may be integrated into the LTHW, which has a supply temperature of 55 °C. This can be achieved by installing a second compression stage.

Fig. 6 presents how a combine chiller/heat pump system appropriately integrates with the Site Source and Sink Profiles. The Site Sink Profile excludes the portion of heat demand for the Fluidised Bed air streams that is satisfied indirectly through the condensate system using the boiler flue gas. The target boiler heat displacement is 85 MJ/t<sub>p</sub> and its integration results in a specific fuel reduction of 101 MJ/t<sub>p</sub>. Electrical use increases by 1.8 kWh/t<sub>p</sub> (0.5 MJ<sub>e</sub>/t<sub>p</sub>), which is a marginal COP<sub>H</sub> of 13. In the future plant design,

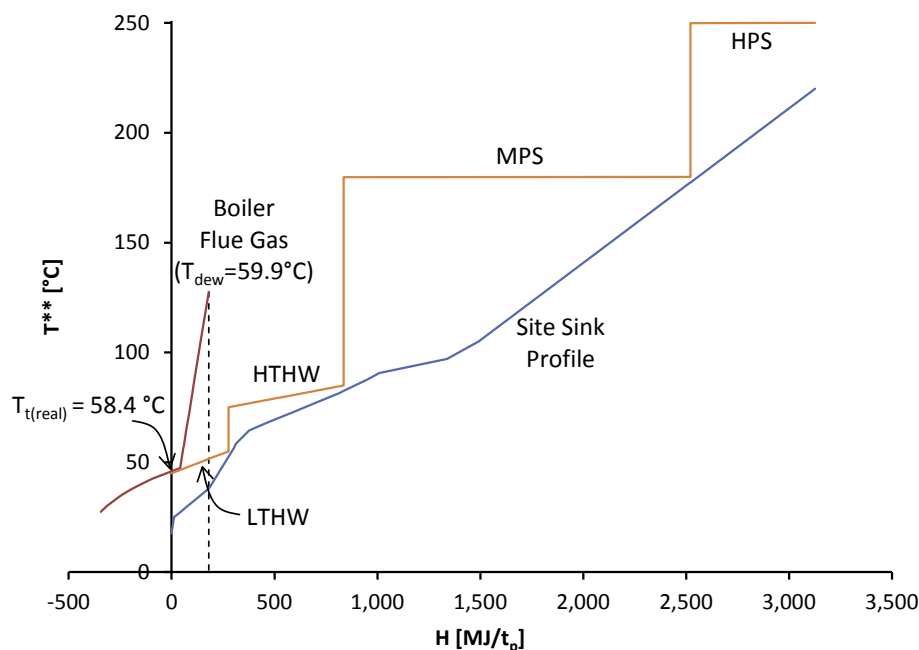


Fig. 5. Target for the minimum boiler flue gas temperature by pinching the flue gas profile with the site hot water utility system.

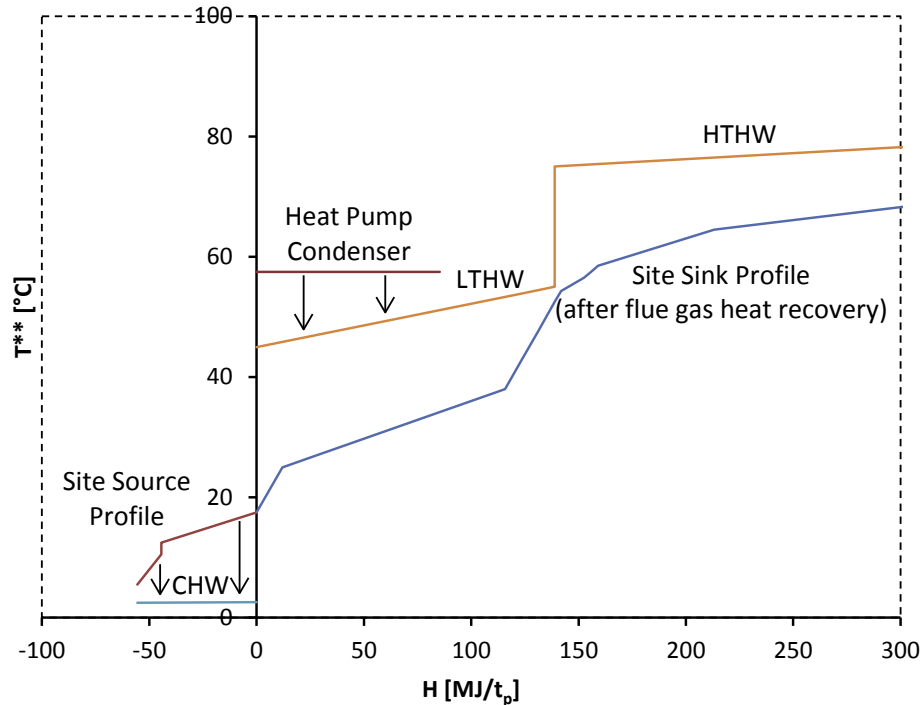


Fig. 6. Combined chiller (through chilled water) and heat pump condenser integration with Total Site Profiles. Note: axes are zoomed; only a portion of the Total Site Profiles is shown.

the LTHW system is used to heat air flows and direct use water applications such as process cleaning, tanker washing, and lactose powder reconstitution.

At some existing dairy factories there is a substantial amount of waste heat, not just from the chiller unit, rejected at about 40 °C. Future work will look at both the integration of heat pumps using chiller and other waste heat, as well as the internal design of the heat pump cycle to match process demand profiles while maximising its COP.

#### 4.3. HVAC air recycle for energy reduction

The thermal energy demand to keep the building that houses the milk powder plant is on average 83 MJ/t<sub>p</sub>. The system operates intermittently depending on the temperature of the incoming fresh air using a temperature control loop. At present, the system is a single pass and a steam heater increases the incoming air temperature from an average of 15 °C–28 °C. After passing through the building air exhausts at about 33 °C through roof ducts. In this opportunity a portion of the exhaust air may be recycled to the inlet as a means of energy recovery. With an exhaust air to fresh air recycle ratio of 2:1, the thermal load decreases to 8 MJ/t<sub>p</sub>.

#### 4.4. Combined heat and power

The final investigated opportunity within the utility system is CHP using a back pressure steam turbine for electricity production. Using the existing two steam levels and a turbine to drop the required steam from 40 bar to 10 bar for the MPS demand gives an electricity production of 46.4 kWh/t<sub>p</sub> (12.9 MJ<sub>e</sub>/t<sub>p</sub>), which for a production rate of 30 t<sub>p</sub>/h is a 1.4 MW turbine, at an isentropic efficiency of 67%. A turbine installation for only 1.4 MW of electricity generation struggles to find economic justification. Alternatively, plant equipment such as fans may be driven by steam

turbines instead of electric motors.

CHP can be increased by adding a VHPS level with superheat and an LPS level. The LPS level requires additional piping to go from the boiler house to the process building. Fig. 7 presents the enhanced CHP system using the Total Site Profiles. These changes to the steam system increases electricity production by 133% to 108.1 kWh/t<sub>p</sub> (30.0 MJ<sub>e</sub>/t<sub>p</sub>). In this case self-generation of electricity reduce grid draw by 49%.

Within the New Zealand context, the adoption of CHP can lead to an increase in emissions. New Zealand's average grid emissions factor of 0.0359 kg<sub>CO<sub>2-e</sub></sub>/MJ is significantly lower than an equivalent fuel-to-electricity emissions factor of 0.0592 kg<sub>CO<sub>2-e</sub></sub>/MJ. The fuel-to-electricity emissions factor is estimated using a 90% efficient fuel-to-thermal generation, which represents the efficiency of a boiler with a condensing economiser. Since the grid emissions is 39% lower, CHP for industrial sites in New Zealand has a negative emissions and environmental impact.

### 5. Energy efficiency opportunities in the process system

This section explores two process system change opportunities for energy reduction. The basis for the analysis is the future milk powder process design (2.0). The Milk Powder Plant model is applied to determine changes in energy use. Tables 2 and 3 provide the break-downs of energy use and emissions for each of the process changes. Table 1 identifies the changes compared to a modern milk powder, Design 1.0, for each design. For each process change it is assumed the total amount of hot water for cleaning is constant.

#### 5.1. Pre-concentration of milk using reverse osmosis – Design 2.1

Implementing a RO milk pre-concentration stage for pre-concentrating milk, assuming the mid SEC of 7.0 kWh/t<sub>w</sub> (1.9 MJ<sub>e</sub>/t<sub>w</sub>), before the MVR evaporators, changes the overall heat and

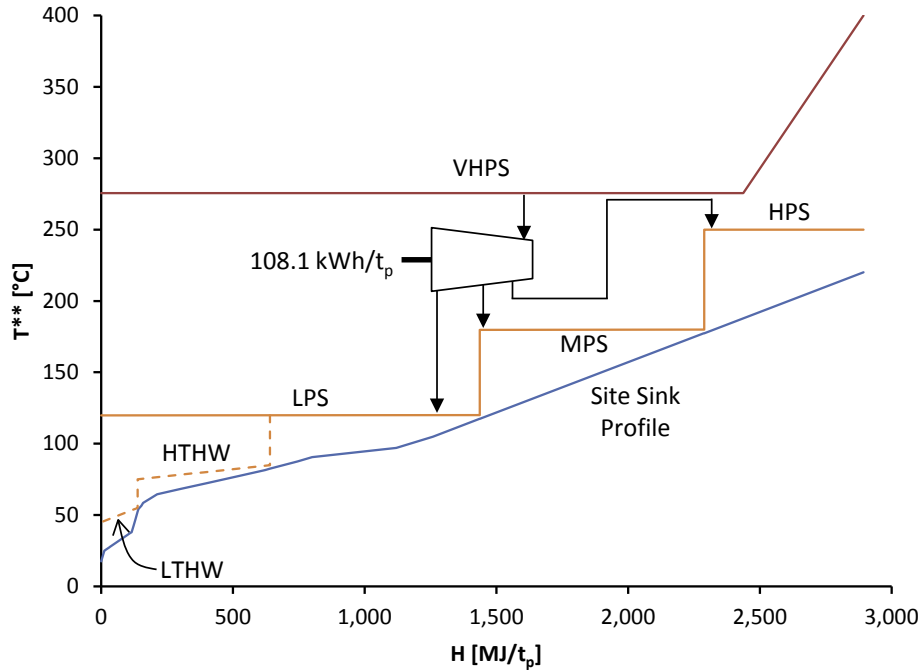


Fig. 7. Combined heat and power system using Total Site Profiles.

Table 3

Break-down of specific thermal and electrical uses in modern milk powder plant design (1.0), future design (2.0), which includes sub-designs with RO pre-concentration (2.1), high solids drying (2.2), and combination of these two process changes (2.3), and the novel ultra-low energy process and utility design (3.0).

Zone	Major Equipment	Thermal Energy Use [MJ/tp]						Electrical Use [kWh/tp]					
		Design 1.0	Design 2.0	Design 2.1	Design 2.2	Design 2.3	Design 3.0	Design 1.0	Design 2.0	Design 2.1	Design 2.2	Design 2.3	Design 3.0
Milk Separation	Cream pasteurisation	11	11	11	11	11	11	–	–	–	–	–	–
	Process pumps	–	–	–	–	–	–	13.1	13.1	13.1	13.1	13.1	13.1
Reverse Osmosis	Process pumps	–	–	–	–	–	–	–	–	35.0	–	35.0	35.0
	Heat treatment	736	194	335	144	184	184	–	10.0	–	11.5	–	–
Heat Treatment & Evaporators	MVR and TVR units	305	–	–	–	–	–	92.7	93.9	20.7	97.1	23.9	23.9
	Process pumps	–	–	–	–	–	–	2.6	2.6	2.6	2.6	2.6	2.6
Spray Dryer	Two-stage homogeniser	–	–	–	–	–	–	–	–	–	11.4	13.3	13.3
	Air heaters	2877	2610	2610	1962	1962	1795	–	–	–	–	–	–
	Feed heater	148	131	131	111	111	111	–	–	–	–	–	–
	Homogeniser feed pump	–	–	–	–	–	–	7.8	7.8	7.8	6.9	6.9	6.9
	Process fans	–	–	–	–	–	–	46.4	46.4	46.4	36.6	36.6	29.1
Utility Services	Product handling	10	10	10	10	10	10	22.1	22.1	22.1	22.1	22.1	22.1
	Cleaning and washing	191	81	130	85	78	78	–	–	–	–	–	–
	HVAC	83	83	83	83	83	8	7.3	7.3	7.3	7.3	7.3	7.3
	Chiller unit	–	–	–	–	–	–	6.7	6.7	6.7	6.7	6.7	8.0
	Compressed air unit	–	–	–	–	–	–	6.8	6.8	6.8	6.8	6.8	6.8
Total Energy Consumption	Boiler pump and fan	–	–	–	–	–	–	4.9	3.4	3.6	2.6	2.7	2.4
	Thermal losses	903	573	624	451	462	357	–	–	–	–	–	–
Total Energy Consumption		5265	3694	3934	2856	2900	2554	210.5	220.2	172.2	224.7	177.0	170.5
Energy Reduction from Design 1.0		–	1571	1330	2409	2365	2711	–	–9.7	38.2	–14.3	33.5	40.0
Energy Reduction from Design 2.0		–	–	–241	837	794	1139	–	–	48.0	–4.5	43.3	49.7
				(–6.5%)	(22.7%)	(21.5%)	(30.8%)			(21.8%)	(–2.1%)	(19.6%)	(22.6%)

electrical balance (Table 3). Fig. 8 shows impact of varying the concentrate solids output from RO on the thermal and electrical energy demands.

For an output of 30% solids, electricity use in Design 2.1

decreases by 21.8% compared to Design 2.0. The electricity use reduction is due to the estimated SEC of the RO process (7.0 kWh/t<sub>w</sub> or 1.9 MJ<sub>e</sub>/t<sub>p</sub>) being lower than MVR evaporators (12.0 kWh/t<sub>w</sub> or 3.3 MJ<sub>e</sub>/t<sub>p</sub>). With the new thermal balance of the MVR evaporator,

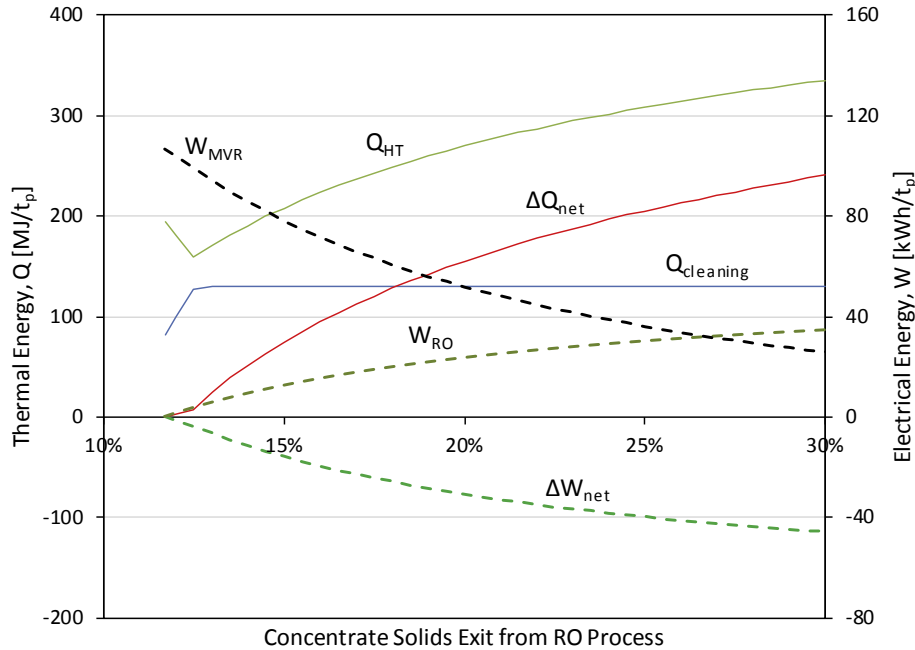


Fig. 8. Effect of RO concentrate solids for Design 2.1 on thermal and electrical energy use for overall use (net), heat treatment process (HT), cleaning, MVR evaporator and RO process.

excess vapour is no longer available for upgrading to integrate with the milk heat treatment process (Fig. 2). This change has the effect of decreasing MVR electricity consumption by 10.0 kWh/t<sub>p</sub> (2.8 MJ<sub>e</sub>/t<sub>p</sub>) and increasing thermal demand in the heat treatment process by 141 MJ/t<sub>p</sub>. There is a second increase to thermal demand of 49 MJ/t<sub>p</sub> for cleaning. These thermal demand increases are caused by a substantially lower quantity of available hot condensate and excess vapour from the lower duty evaporator process. The overall net effect is an increase in thermal load by 6.5% compared to Design 2.0. For a high SEC for RO (10.0 kWh/t<sub>w</sub> or 2.8 MJ<sub>e</sub>/t<sub>w</sub>), there is still a 14.8% reduction in electricity use while for a low SEC for RO (3.9 kWh/t<sub>w</sub> or 1.1 MJ<sub>e</sub>/t<sub>w</sub>) the reduction is 28.8%.

With implementing the RO process, there is a trade-off between thermal and electrical demands. Using the net changes, an equivalent thermal-to-electrical COP<sub>t-e</sub> may be defined

$$COP_{t-e} = \frac{-\Delta W_{net}}{\Delta Q_{net}} \quad (2)$$

The COP<sub>t-e</sub> may be determined for a range of output concentrations from RO and for low and high SEC estimates as shown in Fig. 9. As an isolated process change, a COP<sub>t-e</sub> of 0.68 is excellent if compared with a typical heat engine. However for New Zealand, there is resistance to this isolated process change from a carbon emissions viewpoint. The minimum required COP<sub>t-e</sub> to effect a decrease in emissions is 1.5. As a result, overall carbon emissions rises by 6.6 kg<sub>CO2-e</sub>/t<sub>p</sub> (Table 4).

### 5.2. High solids feed to milk spray dryer – Design 2.2

High solids feed (60%) spray drying of milk greatly reduces thermal load by 22.7% while electricity use increases by 2.1% compared to Design 2.0. Total emissions for satisfying both thermal and electrical energy demands decreases by 19.5%. Thermal energy demand decreases chiefly due to the shifting of evaporation load from the spray dryer process to the MVR evaporator process. The increased electricity use is the result of a combination of changes. In

the heat treatment and evaporator process, electricity use increases by 16.1 kWh/t<sub>p</sub> (4.5 MJ<sub>e</sub>/t<sub>p</sub>), of which the additional two-stage homogenisation process step contributes 71%. The remaining increase results from the high MVR electrical draw for outputting a higher solids product (60%). The electrical-to-thermal COP for this process change is

$$COP_{e-t} = \frac{-\Delta Q_{net}}{\Delta W_{net}} = \frac{837 \text{ MJ/t}_p}{4.5 \text{ kWh/t}_p} = 51.5 \quad (3)$$

This effective COP is high, indicating the proposed change contains substantial benefit. High solids drying of milk is therefore recommended as an area of future research. Further technology development and optimisation may prove whether the patented two-stage homogenisation concept [26] is effective for an industrial process.

### 5.3. Combined process changes – Design 2.3

The third process change concept is a combination of RO milk pre-concentration (based on the mid SEC) and high solids feed (60%) spray drying. This combination of changes, represented as Design 2.3, provides reductions of 21.5% in thermal energy use, 19.6% in electricity use, and 21.3% in emissions compared to Design 2.0. For this design scenario, the positioning of the additional two-stage homogenisation process step for high solids drying is performed using 30% concentrate from the RO process, which is within the recommended operational window [26].

There is a degree of synergy in implementing both process changes. The thermal energy use increase in Design 2.1 is 241 MJ/t<sub>p</sub> compared to Design 2.0. However, after implementing high solids drying (Design 2.2), thermal energy use for Design 2.3 increases by only 44 MJ/t<sub>p</sub>. This synergy is derived from the increased evaporation load on the evaporator system in Design 2.3 compared to Design 2.1. As a result there is additional heat to cascade to preheat milk and generate hot water for cleaning.

These process change concepts also raise the possibility of

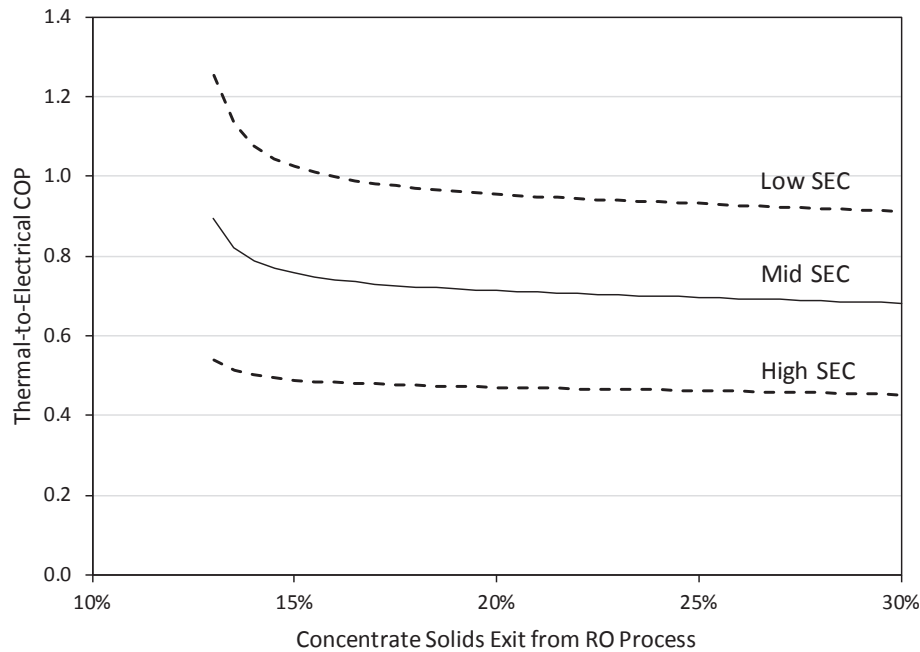


Fig. 9. Effect of RO concentrate solids on equivalent thermal-to-electrical COP given a low, mid, and high SEC for RO.

Table 4

Carbon equivalent emissions arising from thermal and electrical energy demand for various milk powder plant designs.

Process Design	Emissions from Thermal Energy Use [ $\text{kg}_{\text{CO}_2\text{-e}}/\text{t}_p$ ]	Emissions from Electricity Use [ $\text{kg}_{\text{CO}_2\text{-e}}/\text{t}_p$ ]	Total Emissions [ $\text{kg}_{\text{CO}_2\text{-e}}/\text{t}_p$ ]	Percent Emissions Reduction
Design 1.0	280.6	27.2	307.8	–
Design 2.0	196.9	28.5	225.3	26.8%
Design 2.1	209.7	22.3	232.0	24.6%
Design 2.2	152.2	29.0	181.3	41.1%
Design 2.3	154.6	22.9	177.4	42.4%
Design 3.0	136.1	22.0	158.2	48.6%

retrofitting existing milk powder plants to increase both throughput and energy efficiency. Installing a pre-concentration RO system prior to the evaporator system means the evaporator system can handle approximately a three-fold increase in throughput for the same evaporation load. Likewise, reaching a higher solids at the exit of the evaporator decreases the evaporation load on the spray dryer by 25.8%, which means that for the same evaporation load, throughput for the dryer can increase by 34.8%. For this retrofit scenario, the dryer becomes the clear process bottleneck to further increases in production.

## 6. Ultra-low energy milk powder plant – Design 3.0

An ultra-low energy milk powder plant design (Design 3.0) is developed based on simultaneously implementing the following processes and actions: (1) pre-concentration of milk to 30% using RO, (2) high solids (60%) spray drying as a result of a two-stage mild concentrate homogenisation, (3) installation of a condensing economiser for the boiler, indirectly integrated with the fluidised bed air flows through the steam condensate system, (4) upgrade and integration of chiller condenser heat with the hot water utility system, and (5) recycling of air in the building HVAC system. These improvements are added to energy reductions obtained by: (1) an ultra-low energy milk heat treatment and evaporator system and (2) dryer exhaust heat recovery (Table 1). CHP has not been

incorporated into Design 3.0 because for the case study, emissions (a key driving factor) is likely to increase.

The output concentration from the RO process is optimised to ensure reductions in energy and emissions. It was noted in Design 2.1 – RO pre-concentration as an isolated process change – increased overall emissions. A similar investigation for a range of RO concentration outputs has been conducted for Design 3.0 as shown in Fig. 10. For this new design, the minimum thermal and electrical energy requirements occur when the output concentration reaches the imposed limit of 30% solids. Beyond 30% solids, there is a degree of diminishing returns with respect to energy reduction. Future work should incorporate an improved model for the RO process, given reliable data becomes available, where the SEC is a function of concentration.

The combination of proposed process changes influences the optimal design of the heat treatment and evaporator systems. This is chiefly due to the lower quantity of hot condensate for heat integration. Fig. 11 presents the process flow diagram and grid diagram of the new integrated design for the heat treatment and evaporator process, which is implemented as part of the ultra-low energy milk powder plant. Two changes from the previous design of Walmsley et al. [5] (Fig. 2) are: (1) elimination of an integrated MVR unit within the heat treatment process and (2) a shift in load from the condensate heat recovery exchanger to the vapour bleed exchanger. These changes have the benefit of simplifying the

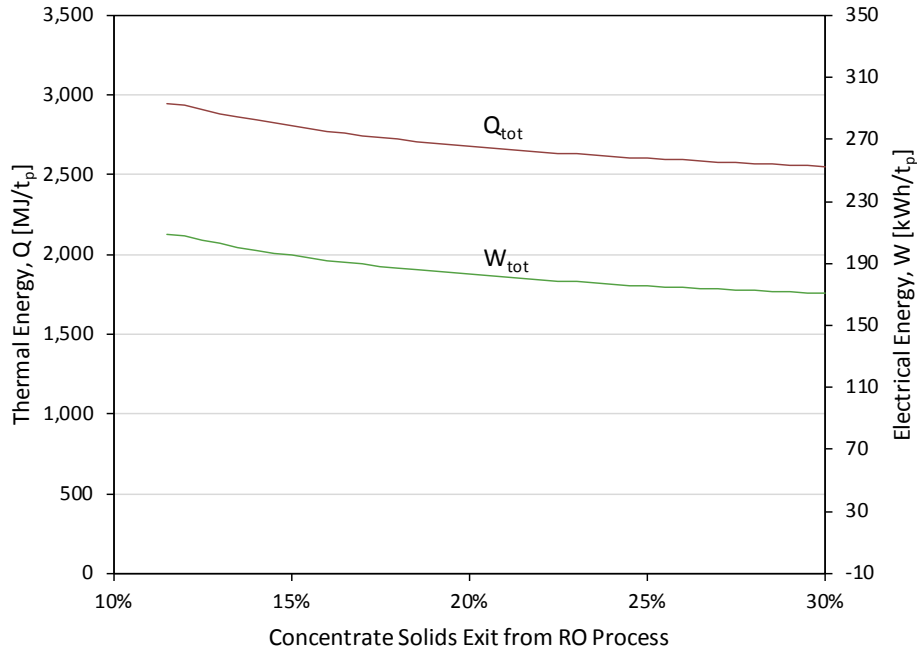


**Fig. 10.** Effect of RO concentrate solids for Design 3.0 on thermal and electrical energy use for overall use (net), heat treatment process (HT), cleaning, MVR evaporator and RO process.

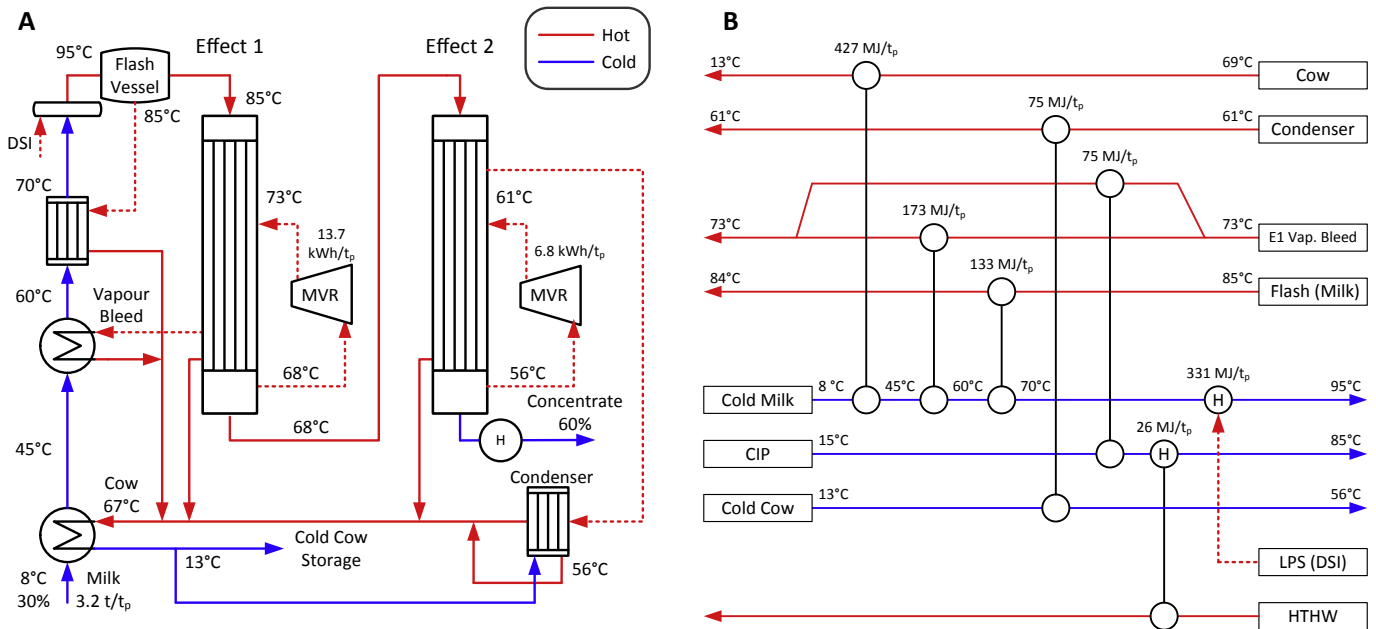


**Fig. 11.** Milk evaporation system design for an ultra-low energy milk powder plant with integrate RO pre-concentration and high solids spray drying. Design illustrated using a process flow diagram (A) and grid diagram (B).

overall system design. It is important to note that the preheat exchanger using vapour from the first effect needs two parallel processing lines for mid-run cleaning to control thermophile growth in the critical temperature range of 45–60 °C.

The process design is compared to a modern milk powder plant (Design 1.0) in Fig. 12 using Sankey diagrams that show where thermal and electrical energy demand occurs within the process, where water is removed, and how much cream and powder are produced. The ultra-low energy design achieves reductions of 51.5%

in thermal energy, 19.0% in electricity use, and 48.6% in emissions compared to the modern milk powder plant. This new design with a step reduction in energy achieves substantially greater energy efficiency than studies in literature, i.e. the optimised evaporation process design of Walmsley et al. [5], the optimised Total Site utility systems design of Walmsley et al. [33], and the best design using emerging technologies by Moejes and van Boxtel [2].

Future experimental research is required to de-risk the proposed milk powder plant design, particularly for high solids drying,

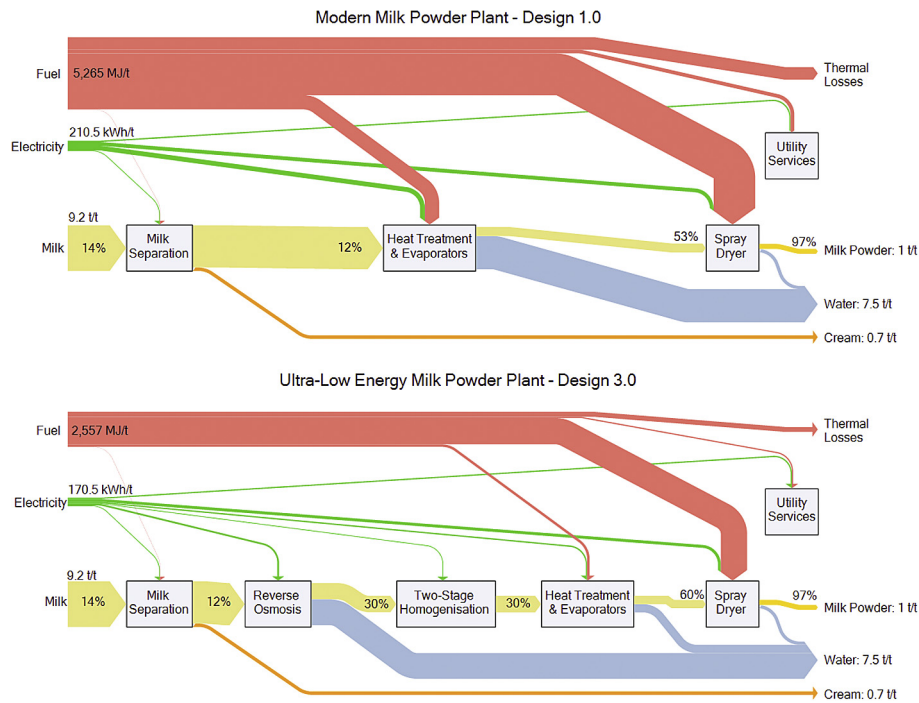


Fig. 12. Sankey diagrams for a modern milk powder plant and an ultra-low energy milk powder plant, comparing energy, water removal, and product flows.

thus enabling full realisation of the energy and emissions savings. A detailed capital cost assessment of the proposed energy efficiency improvements can also be undertaken in future work to determine overall economic justification.

### 7. Conclusions

Process changes and utility systems optimisation, together with improved Total Site integration, has potential to reduce a modern milk powder plant’s thermal energy use by 51.5%, electricity use by 19.0%, and emissions by 48.6%. To achieve this level of energy and emissions savings, the following seven implementations are required: (1) pre-concentration of milk to 30% using reverse osmosis technology, (2) a two-stage 30% concentrate homogenisation for viscosity reduction to enable high solids (60%) spray drying, (3) an ultra-low energy MVR evaporation system, (4) dryer exhaust heat recovery, (5) installation of a condensing economiser for the boiler, (6) upgrade and integration of chiller condenser heat

for use with the hot water utility system, and (7) recycling of air in the building HVAC system. Within the New Zealand context, Combined Heat and Power is not recommended due to an increase in emissions. Future work can focus on de-risking the proposed improvements, especially high solids spray drying, as well as performing a detailed cost-benefit analysis.

### Acknowledgements

This research has been supported by the EU project “Sustainable Process Integration Laboratory – SPIL”, project No. CZ.02.1.01/0.0/0.0/15\_003/0000456 funded by EU “CZ Operational Programme Research, Development and Education”, Priority 1: Strengthening capacity for quality research.

### Appendix 1. Stream data for total site profiles

Table 5  
Stream data for the Total Site Profiles in Design 1.0.

Process	Stream Name	T <sub>s</sub> °C	T <sub>t</sub> °C	CP MJ/(t <sub>p</sub> °C)	Q MJ/t <sub>p</sub>
Milk Treatment	Cream C	80	85	2.2	11
	Cream H	13	8	2.2	11
Heat Treatment and Evaporator	Cold Milk	74	95	32.8	676
	CIP	15	85	1.1	77
	Milk concentrate	53	79	5.7	148
Spray Dryer	Dryer Inlet Air	28	210	14.2	2581
	HVAC	15	28	6.4	83
	FB Inlet Air	28	95	4.4	296
Other	Tanker wash and direct use	15	54	1.3	53
	CIP and reconstitution	15	54	0.3	10
	Cool stores	20	15	8.9	44

**Table 6**  
Stream data for the Total Site Profiles in Design 2.0 and the basis for targeting increased utility integration.

Process	Stream Name	T <sub>s</sub> °C	T <sub>t</sub> °C	CP MJ/(t <sub>p</sub> °C)	Q MJ/t <sub>p</sub>
Milk Treatment	Cream C	80	85	2.2	11
	Cream H	13	8	2.2	11
Heat Treatment and Evaporator	Cold Milk	89	95	32.7	194
	CIP	59	85	1.1	29
Spray Dryer	Milk concentrate	56	79	5.7	131
	Dryer Inlet Air	54	210	14.2	2210
	HVAC	15	28	6.4	83
	FB Inlet Air	15	95	5.0	400
Other	Tanker wash and direct use	15	54	1.3	53
	CIP and reconstitution	15	54	0.3	10
	Cool stores	20	15	8.9	44

**Table 7**  
Stream data for the Total Site Profiles in Design 3.0.

Process	Stream Name	T <sub>s</sub> °C	T <sub>t</sub> °C	CP MJ/(t <sub>p</sub> °C)	Q MJ/t <sub>p</sub>
Milk Treatment	Cream C	80	85	2.2	11
	Cream H	13	8	2.2	11
Heat Treatment and Evaporator	Cold Milk	79	95	32.7	519
	CIP	66	85	1.1	21
Spray Dryer	Milk concentrate	56	79	4.8	111
	Dryer Inlet Air	57	210	10.5	1610
	HVAC	15	28	16.9	219
	FB Inlet Air	41	95	3.4	185
Other	Tanker wash and direct use	15	54	1.3	53
	CIP and reconstitution	15	54	0.3	10
	Cool stores	20	15	11.1	55

## References

- Xu T, Flapper J. Reduce energy use and greenhouse gas emissions from global dairy processing facilities. *Energy Policy* 2011;39:234–47. <http://dx.doi.org/10.1016/j.enpol.2010.09.037>.
- Moejes SN, van Boxtel AJB. Energy saving potential of emerging technologies in milk powder production. *Trends Food Sci Technol* 2017. <http://dx.doi.org/10.1016/j.tifs.2016.10.023>.
- Ramírez CA, Patel M, Blok K. From fluid milk to milk powder: energy use and energy efficiency in the European dairy industry. *Energy* 2006;31:1984–2004. <http://dx.doi.org/10.1016/j.energy.2005.10.014>.
- Hanneman H, Robertson LJ. Heat recovery systems. In: *Energy use in dairy processing*. Brussels, Belgium: International Dairy Federation; 2005.
- Walmsley TG, Atkins MJ, Walmsley MRW, Neale JR. Appropriate placement of vapour recompression in ultra-low energy industrial milk evaporation systems using pinch analysis. *Energy* 2016;116(Part 2):1269–81. <http://dx.doi.org/10.1016/j.energy.2016.04.026>.
- Townsend DW, Linnhoff B. Heat and power networks in process design. Part I: criteria for placement of heat engines and heat pumps in process networks. *AIChE J* 1983;29:742–8. <http://dx.doi.org/10.1002/aic.690290508>.
- Krokida MK, Bisharat GI. Heat recovery from dryer exhaust air. *Dry Technol Int J* 2004;22:1661.
- Walmsley TG, Walmsley MRW, Atkins MJ, Neale JR, Tarighaleslami AH. Thermo-economic optimisation of industrial milk spray dryer exhaust to inlet air heat recovery. *Energy* 2015;90(Part 1):95–104. <http://dx.doi.org/10.1016/j.energy.2015.03.102>.
- Liew PY, Wan Alwi SR, Varbanov PS, Manan ZA, Klemeš JJ. Centralised utility system planning for a total site heat integration network. *Comput Chem Eng* 2013;57:104–11. <http://dx.doi.org/10.1016/j.compchemeng.2013.02.007>.
- Perry S, Klemeš J, Bulatov I. Integrating waste and renewable energy to reduce the carbon footprint of locally integrated energy sectors. *Energy* 2008;33:1489–97. <http://dx.doi.org/10.1016/j.energy.2008.03.008>.
- Walmsley TG. A total site heat integration design method for integrated evaporation systems including vapour recompression. *J Clean Prod* 2016;136(Part B):111–8. <http://dx.doi.org/10.1016/j.jclepro.2016.06.044>.
- Liew PY, Lim JS, Wan Alwi SR, Abdul Manan Z, Varbanov PS, Klemeš JJ. A retrofit framework for Total Site heat recovery systems. *Appl Energy* 2014;135:778–90. <http://dx.doi.org/10.1016/j.apenergy.2014.03.090>.
- Varbanov PS, Klemeš JJ. Integration and management of renewables into Total Sites with variable supply and demand. *Comput Chem Eng* 2011;35:1815–26. <http://dx.doi.org/10.1016/j.compchemeng.2011.02.009>.
- Nemet A, Klemeš JJ, Kravanja Z. Mathematical programming approach to total site heat integration. *Comput Aided Chem Eng* 2014;33:1795–800. <http://dx.doi.org/10.1016/B978-0-444-63455-9.50134-3>.
- Čuček L, Kravanja Z. Retrofit of total site heat exchanger networks by mathematical programming approach. In: Martin M, editor. *Alternative energy sources and technologies*. Springer International Publishing; 2016. p. 297–340. [http://dx.doi.org/10.1007/978-3-319-28752-2\\_11](http://dx.doi.org/10.1007/978-3-319-28752-2_11).
- Fritzson A, Berntsson T. Energy efficiency in the slaughter and meat processing industry—opportunities for improvements in future energy markets. *J Food Eng* 2006;77:792–802. <http://dx.doi.org/10.1016/j.jfoodeng.2005.08.005>.
- Matsuda K, Hirochi Y, Tatsumi H, Shire T. Applying heat integration total site based pinch technology to a large industrial area in Japan to further improve performance of highly efficient process plants. *Energy* 2009;34:1687–92. <http://dx.doi.org/10.1016/j.energy.2009.05.017>.
- Matsuda K, Hirochi Y, Kurosaki D, Kado Y. Application of area-wide pinch technology to a large industrial area in Thailand. *Chem Eng Trans* 2014;39:1027–32. <http://dx.doi.org/10.3303/CET1439172>.
- Hackl R, Harvey S. From heat integration targets toward implementation – a TSA (total site analysis)-based design approach for heat recovery systems in industrial clusters. *Energy* 2015;90(Part 1):163–72. <http://dx.doi.org/10.1016/j.energy.2015.05.135>.
- Bonhivers JC, Svensson E, Berntsson T, Stuart PR. Comparison between pinch analysis and bridge analysis to retrofit the heat exchanger network of a kraft pulp mill. *Appl Therm Eng* 2014;70:369–79. <http://dx.doi.org/10.1016/j.applthermaleng.2014.04.052>.
- Walmsley TG, Walmsley MRW, Atkins MJ, Neale JR. Integration of industrial solar and gaseous waste heat into heat recovery loops using constant and variable temperature storage. *Energy* 2014;75:53–67. <http://dx.doi.org/10.1016/j.energy.2014.01.103>.
- Walmsley TG, Walmsley MRW, Tarighaleslami AH, Atkins MJ, Neale JR. Integration options for solar thermal with low temperature industrial heat recovery loops. *Energy* 2015;90(Part 1):113–21. <http://dx.doi.org/10.1016/j.energy.2015.05.080>.
- Kemp IC. *Pinch analysis and process integration: a user guide on process integration for the efficient use of energy*. Oxford, UK: Butterworth-Heinemann; 2007.
- Zisu B, Schleyer M, Chandrapala J. Application of ultrasound to reduce viscosity and control the rate of age thickening of concentrated skim milk. *Int Dairy J* 2013;31:41–3. <http://dx.doi.org/10.1016/j.idairyj.2012.04.007>.

- [25] Murphy EG, Tobin JT, Roos YH, Fenelon MA. A high-solids steam injection process for the manufacture of powdered infant milk formula. *Dairy Sci Technol* 2013;93:463–75. <http://dx.doi.org/10.1007/s13594-013-0116-7>.
- [26] Bodenstab S. Process for the preparation of milk powder. EP1259117 B1. 2005.
- [27] Pak Tetra. Membrane filtration reverse osmosis. 2016. In: [www.tetrapak.com:80/processing/membrane-filtration/reverse-osmosis](http://www.tetrapak.com:80/processing/membrane-filtration/reverse-osmosis) [Accessed 30 November 2016].
- [28] Walmsley TG, Walmsley MRW, Atkins MJ, Neale JR. Improving energy recovery in milk powder production through soft data optimisation. *Appl Therm Eng* 2013;61:80–7. <http://dx.doi.org/10.1016/j.applthermaleng.2013.01.051>.
- [29] Walmsley MRW, Walmsley TG, Matthews L, Atkins MJ, Neale JR, Kamp PJJ. Pinch analysis techniques for carbon emissions reduction in the New Zealand industrial process heat sector. *Chem Eng Trans* 2015;45:1087–92. <http://dx.doi.org/10.3303/CET1545182>.
- [30] Sun L, Doyle S, Smith R. Cogeneration improvement based on steam cascade analysis. *Chem Eng Trans* 2013;35:13–8. <http://dx.doi.org/10.3303/CET1335002>.
- [31] Manesh MHK, Abadi SK, Ghalami H, Amidpour M, Hamed MH. A new cogeneration targeting procedure for total site. *Chem Eng Trans* 2012;29:1561–6.
- [32] Yang M, Feng X, Liu G. Heat exchanger network design considering the heat pump performance. *Chem Eng Trans* 2014;39:1099–104.
- [33] Walmsley TG, Atkins MJ, Walmsley MRW, Neale JR, Philipp M, Peesel RH, et al. Total Site utility systems optimisation for milk powder production. *Chem Eng Trans* 2016;52:235–40. <http://dx.doi.org/10.3303/CET1652040>.
- [34] Oldfield DJ, Taylor MW, Singh H. Effect of preheating and other process parameters on whey protein reactions during skim milk powder manufacture. *Int Dairy J* 2005;15:501–11. <http://dx.doi.org/10.1016/j.idairyj.2004.09.004>.
- [35] Baldwin AJ, Cooper HR, Palmer KC. Effect of preheat treatment and storage on the properties of whole milk powder. Changes in sensory properties. *Neth Milk Dairy J* 1991;45:97–116.
- [36] Hinton AR. Thermophiles and fouling deposits in milk powder plants [PhD Thesis]. Massey University; 2003. [muir.massey.ac.nz/handle/10179/1861](http://muir.massey.ac.nz/handle/10179/1861) [Accessed 3 July 2012].
- [37] Walmsley TG, Walmsley MRW, Atkins MJ, Neale JR. Fouling and pressure drop analysis of milk powder deposition on the front of parallel fins. *Adv Powder Technol* 2013;24:780–5. <http://dx.doi.org/10.1016/j.apt.2013.04.004>.
- [38] Klemes JJ, Varbanov PS, Wan ASRW, Manan ZA. Process integration and intensification, saving energy, water and resources. Berlin, Boston: De Gruyter; 2014.
- [39] Walmsley MRW, Walmsley TG, Atkins MJ, Kamp PJJ, Neale JR. Minimising carbon emissions and energy expended for electricity generation in New Zealand through to 2050. *Appl Energy* 2014;135:656–65. <http://dx.doi.org/10.1016/j.apenergy.2014.04.048>.
- [40] Ministry for the Environment. Emission factors and methods 2007. Ministry for the Environment; 2007. [mfe.govt.nz/publications/climate/guidance-greenhouse-gas-reporting-2008-09/html/page3.html](http://mfe.govt.nz/publications/climate/guidance-greenhouse-gas-reporting-2008-09/html/page3.html) [Accessed 26 March 2015].
- [41] MAF Quality Management. Physical properties of dairy products. third ed. Hamilton, New Zealand: MAF Quality Management; 1996.
- [42] Sargolzaei J, Pirzadi Jahromi MR, Saljoughi E. Triple-choking model for ejector. *J Therm Sci Eng Appl* 2010;2:021009. <http://dx.doi.org/10.1115/1.4002752>.
- [43] Membrane System Specialists. Reverse osmosis. MSS; 2016. [www.mssincorporated.com/reverseosmosis.htm](http://www.mssincorporated.com/reverseosmosis.htm) [Accessed 1 December 2016].
- [44] Medina-Flores JM, Picón-Núñez M. Modelling the power production of single and multiple extraction steam turbines. *Chem Eng Sci* 2010;65:2811–20. <http://dx.doi.org/10.1016/j.ces.2010.01.016>.

**Article 14:**

*Integration of industrial solar and gaseous waste heat into heat recovery loops using constant and variable temperature storage*

**Walmsley, T.G.**, Walmsley, M.R.W., Atkins, M.J., Neale, J.R., 2014.

Energy 75, 53–67.

DOI: [10.1016/j.energy.2014.01.103](https://doi.org/10.1016/j.energy.2014.01.103)

Citations: 31

Elsevier



# Integration of industrial solar and gaseous waste heat into heat recovery loops using constant and variable temperature storage



Timothy G. Walmsley\*, Michael R.W. Walmsley, Martin J. Atkins, James R. Neale

University of Waikato, Energy Research Centre, School of Engineering, Hamilton, Waikato, New Zealand

## ARTICLE INFO

### Article history:

Received 23 December 2013

Received in revised form

26 January 2014

Accepted 28 January 2014

Available online 22 February 2014

### Keywords:

Heat recovery loop

Low temperature heat recovery

Solar heating

Process integration

## ABSTRACT

Solar is a renewable energy that can be used to provide process heat to industrial sites but require thermal storage. HRLs (heat recovery loops) are an indirect method for transferring heat from one process to another using an intermediate fluid. With HRL's thermal storage is also necessary to effectively meet the stop/start time dependent nature of the multiple source and sink streams. Combining solar heating with HRL's is a cost effective way to share common storage and piping infrastructure. The conventional HRL design method based on a CTS (constant temperature storage) and a new HRL design method using VTS (variable temperature storage) are applied to demonstrate the potential benefits of inter-plant heat integration and installing solar heating. The dairy case study had available 12 source streams including four spray dryer exhausts and six sink streams. The addition of the dryer exhausts as heat sources was a critical factor in gaining a heat recovery of 10.8 MW for the variable temperature storage design, of which 5.1 MW was contributed from exhaust heat recovery. For the same minimum approach temperature the VTS approach achieved 37% more heat recovery compared to the CTS approach. Solar heating also proved to be a valuable source to be integrated into an HRL with a pinch around the cold storage tank with the maximum addition of 0.9 MW of heating on average for the CTS approach and 1.0 MW of heating on average for the VTS approach.

© 2014 Elsevier Ltd. All rights reserved.

## 1. Introduction

Integration of renewable heat sources into chemical processes is increasingly becoming an area of intense research. Solar thermal stands out as viable candidate for providing heating to low pinch temperature processes. However solar heating is often uneconomic due to the large amount of infrastructure needed to ensure constant day and night heat supply. Where multiple low temperature semi-continuous processes are clustered on a single site, inter-plant heat integration may be effectively achieved using a HRL (heat recovery loop) as illustrated in Fig. 1. Heat storage, as a part of the HRL system, is needed to successfully meet the time dependent nature of the source and sink. Seeing that HRL's already have most of the infrastructure needed for solar heating there exists a nexus between the two concepts that may be utilised for their mutual advantage. Typically hot and cold storage temperatures in HRL's are fixed and the source and sink streams heat and cool the intermediate fluid between two storage temperature levels.

Significant improvement in site heat recovery can be achieved through total site heat integration [1]. When low temperature semi-continuous processes, such as those found in dairy factories, are clustered into one large site, the opportunity exists for across plant indirect heat integration. Excess heat from one plant can be transferred to other plants with the aid of an intermediate fluid and thermal storage acting as a heat recovery loop (HRL) system [2] as shown in Fig. 1. Methods for designing indirect heat recovery systems for batch processes have been proposed by numerous authors, e.g. Refs. [3–5]. The methods apply almost exclusively to batch processes, but the principles also apply for semi-continuous processes especially when integrating across multiple plants on the same site [6].

Several recent studies by the authors have considered various parts of the design, operation and optimisation of HRL's including: thermal storage management options such as a stratified tank [7]; changes to storage temperature for seasonal production changes [8]; utilisation and sizing of thermal storage capacity [9]; characterisation of historical stream flow rates for HE (heat exchanger) area sizing [10]; and, the evaluation of different HE sizing methods through simulation of HRL performance for transient stream data [11]. Recently, Chen and Ciou [3] optimised an indirect heat

\* Corresponding author.

E-mail address: [tgw7@waikato.ac.nz](mailto:tgw7@waikato.ac.nz) (T.G. Walmsley).

Nomenclature			
$A$	area ( $\text{m}^2$ )	cont	contribution
$a$	solar loss coefficient in Eq. (12)	l	limiting
$C$	heat capacity flow rate ( $\text{kW}/^\circ\text{C}$ )	lc	cold storage
$H$	enthalpy ( $\text{kW}$ )	lh	hot storage
$h$	heat transfer film coefficient ( $\text{kW}/^\circ\text{C}/\text{m}^2$ )	loop	loop stream
$I$	solar irradiance ( $\text{kW}/\text{m}^2$ )	h	hot
$n$	number	ho	hot stream outlet
NTU	number of (heat) transfer units	min	minimum
$n$	exponent in Eq. (10)	O	optical
$Q$	heat duty ( $\text{kW}$ )	pro	process stream
$Re$	Reynolds number	r	recovery
$T$	temperature ( $^\circ\text{C}$ )	s	supply or solar
$U$	overall heat transfer film coefficient ( $\text{kW}/^\circ\text{C}/\text{m}^2$ )	sp	set point
$\varepsilon$	heat exchanger effectiveness	t	target
$\eta$	efficiency	tot	total
<b>Subscripts/superscripts</b>		<b>Abbreviations</b>	
*	shifted	CIP	clean-in-place
add	additional	CTS	constant temperature storage
amb	ambient	HE	heat exchanger
ave	average	HEN	heat exchanger network
c	cold stream	HRL	heat recovery loop
co	cold stream outlet	PA	pinch analysis
		VTS	variable temperature storage

recovery system for a batch process by allowing the target temperature set points of the intermediate fluid to differ for each HE resulting in a variable temperature storage system, which change offered improved heat recovery. In other areas, methods have been developed for maximising the integration of solar heating for low pinch temperature processes [12] and total site analysis [13]. However the economics of solar heating systems are often poor due to the infrastructure required to not only collect radiation heat, but also to store the heated fluid overnight. The integration of solar heating into an HRL is mutually beneficial because the HRL system provides the heat storage while solar is an additional heat source (Fig. 1).

Conventional control of an HRL is to measure and compare the outlet temperature of the loop fluid from each heat exchanger (HE) to a common hot or cold temperature set point. To achieve the set

point, the flow rate of the loop fluid through the HE is adjusted. An important characteristic of this approach is hot and cold storage temperatures are constant over time. An alternate approach to HRL control is to vary the set points of the HE's depending on their temperature driving force. This alternate approach is characterised by VTS (variable temperature storage) tanks due to mixing of different temperatures entering the tanks.

This paper aims to look at the effects of CTS (constant temperature storage) versus VTS operation of an HRL system with and without including solar as an additional heat source. The VTS approach has not been widely applied to HRLs, even though the possibility exists for improvements in indirect heat recovery from a simple operational change and the reallocation of some area. With this approach, the intermediate fluid flow rate is controlled to give an outlet temperature that is  $\Delta T$  from the supply temperature of

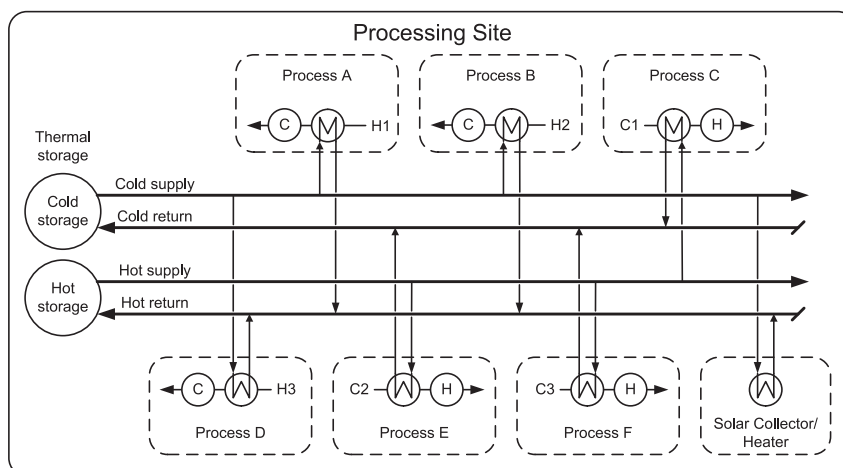


Fig. 1. Heat recovery loop network including the milk powder plant spray dryer.

selected source or sink streams on the loop. Over time the storage tank temperature and volume both vary depending on the thermal loads on the loop and the variability of the streams, which is modelled using the same spreadsheet tool applied by Walmsley et al. [11]. Solar heating may be added to an HRL to increase the quantity and upgrade the quality of heat storage depending on the location of the pinch temperature and the shape of the process Composite Curves.

## 2. Targeting, design and modelling methodologies for HRL's

### 2.1. Targeting and design methods for inter-plant heat integration via an HRL based on average data

In this section a graphical pinch based method for targeting inter-plant heat recovery across multiple semi-continuous plants is presented using a similar method to that proposed by Krummacher and Favrat [5] for batch processes. Like traditional pinch analysis, the Composite Curves form an integral part of the targeting procedure. After zonal or intra-plant heat integration is targeted and heat exchanger networks are designed, streams that still require hot or cold utility are potential candidates for inter-plant integration at the total site level [1].

Inter-plant integration is complicated by the semi-continuous operation of dairy processes. A dairy process often has a number of different operating states such as on product, off product, and CIP (clean-in-place). Variations in production rate, process demand, and season also have an effect on the flow rate and temperature of some process streams. Walmsley et al. [11] demonstrated that an effective method for representing variable stream flow rates for designing an HRL is basing the design on daily time averaged flow rates, which include times in a day when a process is on, off or being cleaned, as opposed to the peak flow rates or median flow rates (Fig. 2). Time average values should only be taken across times when a plant is in regular operation. Daily time averaged stream data can then be used to draw hot and cold Composite Curves that show the daily average heating and cooling enthalpy deficits in each temperature range. How the Composite Curves are brought together and pinched is dependent on the operation – constant or variable temperature – of the storage system.

When targets are obtained from Composite Curves based on time average stream data, the target is for the daily average heat recovery. The targets assume intermediate loop fluid storage is continuously available, which is not always the case in practice. Composites Curves based on typical plant operating values may also be useful in understanding the real time balances between sources and sinks. Time averaged flow rates are lower than stream flow rates while on-product (often referred to as plant design values), therefore determining heat recovery targets from design flows often over predicts what can be recovered especially if there are streams with high flow rates but only operate for a few hours each day.

The algorithms for targeting and designing CTS and VTS HRL's have been developed and implemented into an Excel™ spreadsheet. This targeting and design tool is automated so that a wide range of designs may be generated based on time average stream data.

#### 2.1.1. Constant temperature HRL storage design procedure

For the case of constant temperature storage, Composite Curves may be shifted by a full  $\Delta T_{\min}$  or by  $\Delta T_{\text{cont,pro}} + \Delta T_{\text{cont,loop}}$  since the heat recovery is indirect through an intermediate fluid. A pinch occurs between a limiting supply temperature of a stream and the opposite Composite Curve as shown in Fig. 3. The limiting supply temperature for the hot Composite Curve is the lowest supply temperature of a hot stream and the limiting supply temperature for the cold Composite Curve is the highest supply temperature of a cold stream. The limiting supply temperatures constrain the feasible storage temperature ranges for operating a CTS HRL. The supply temperatures of the streams forming the Composite Curves may be circled to clearly show when a pinch occurs. Once pinched, targets for indirect heat recovery may be calculated. The hot and cold storage temperatures can also be determined directly from the pinched Composite Curves, and a sloped line drawn to span the overlapping heat recovery region represents the average heat capacity flow rate of the HRL intermediate loop fluid. The pinched storage temperature ( $T_{\text{th}}$ ) is fixed while the other storage temperature ( $T_{\text{tc}}$ ) may be varied within a small range without violating the  $\Delta T_{\min}$  constraint. Assuming vertical integration between the hot and cold Composite Curves,  $T_{\text{ho}}$  is the outlet

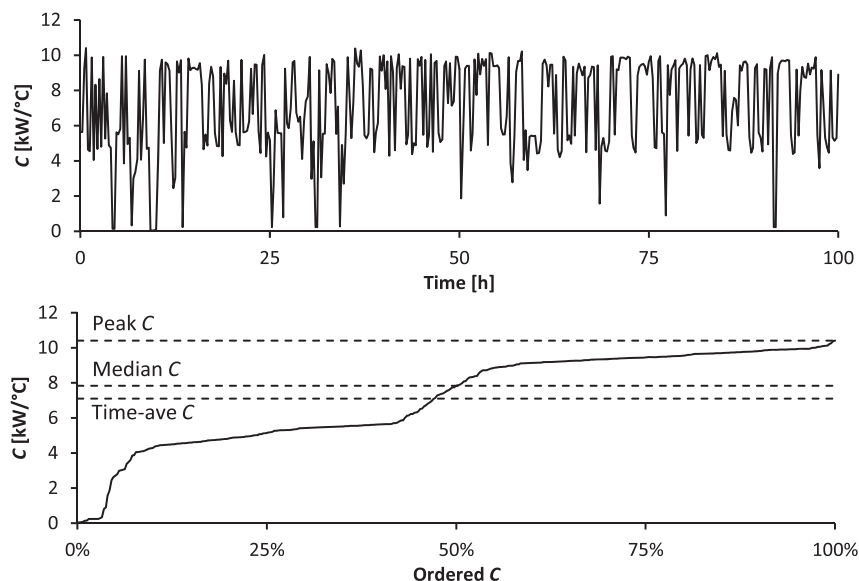


Fig. 2. Example raw and ordered heat capacity flow rate of a stream. Data taken from Walmsley et al. [11].

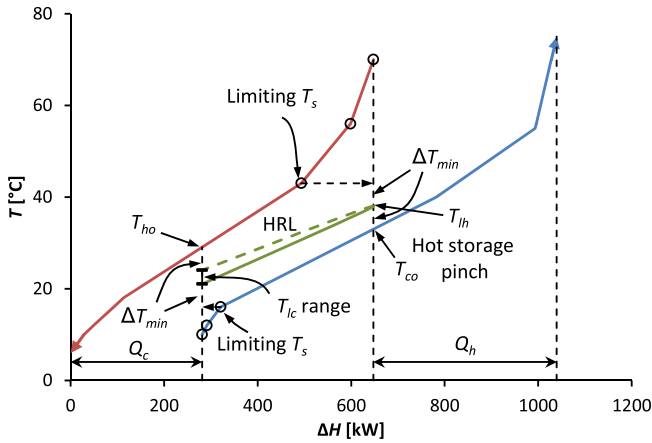


Fig. 3. Inter-plant Composite Curve for indirect heat recovery using an HRL with CTS. Steam data given in Walmsley et al. [11].

temperature of hot streams and  $T_{co}$  is the outlet temperature of the cold streams.

After identifying the HRL storage temperatures on the Composite Curve, heat exchanger areas are calculated using the time average stream data as was recommended by Walmsley et al. [11] for improved heat recovery per unit of area. For constant temperature storage operation, the storage temperatures become the control set-points for the outlet temperature of the loop fluid from heat exchangers on the HRL. Each heat exchanger in the HRL system receives fluid from one storage temperature and is controlled to return the fluid to the other storage tank at its temperature. Designs for a range of heat recovery levels are obtained by selecting new values for  $\Delta T_{min}$ , which leads to new heat exchanger area requirements and new hot and cold storage temperatures.

A comprehensive example of this targeting and design method for HRL's with constant temperature storage is available in Chapter

20, authored by Walmsley et al., of the Handbook of Process Integration [14].

2.1.2. Variable temperature HRL storage design procedure

This section outlines a novel method for targeting and designing an HRL operated using a variable temperature storage system (Fig. 4). The approach is also based on the daily time-average Composite Curve and implemented into an Excel™ spreadsheet.

The targeting and design procedure varies from traditional PA (pinch analysis) in that the cold Composite Curve is shifted under the hot composite curve by a selected feasible  $Q_r$ . After  $Q_r$  is selected, the Composite Curves are shifted together to determine the minimum exchanger approach temperature,  $\Delta T_{min}$ . In this method  $\Delta T_{min}$  and  $\Delta T_{cont}$  is no longer an input variable and therefore a modified method is needed to apply  $\Delta T_{cont}$  for different stream types to account for large differences in film coefficients between streams, e.g. gas versus liquid streams. Where necessary individual streams are shifted by  $\Delta T_{add}$  prior to the construction of the Composite Curve to penalise streams with poor heat transfer coefficients such that

$$T_{s(i)}^* = T_{s(i)} \pm \Delta T_{add} \tag{1a}$$

$$T_{t(i)}^* = T_{t(i)} \pm \Delta T_{add} \tag{1b}$$

where the sign depends on whether the stream is a hot or cold stream. In this study,  $\Delta T_{add}$  for condensing vapour and liquid streams is zero since the respective heat transfer coefficients for these stream types are typically high whereas  $\Delta T_{add}$  for gaseous streams is 10 °C since gas streams normally have very low film coefficients [15]. This same approach for penalising gaseous streams, i.e. the dryer exhaust, may be applied in the CTS method. The Composite Curve is, therefore, partially shifted and the actual minimum approach temperature of a heat exchanger is  $\Delta T_{min} + \Delta T_{add}$ .

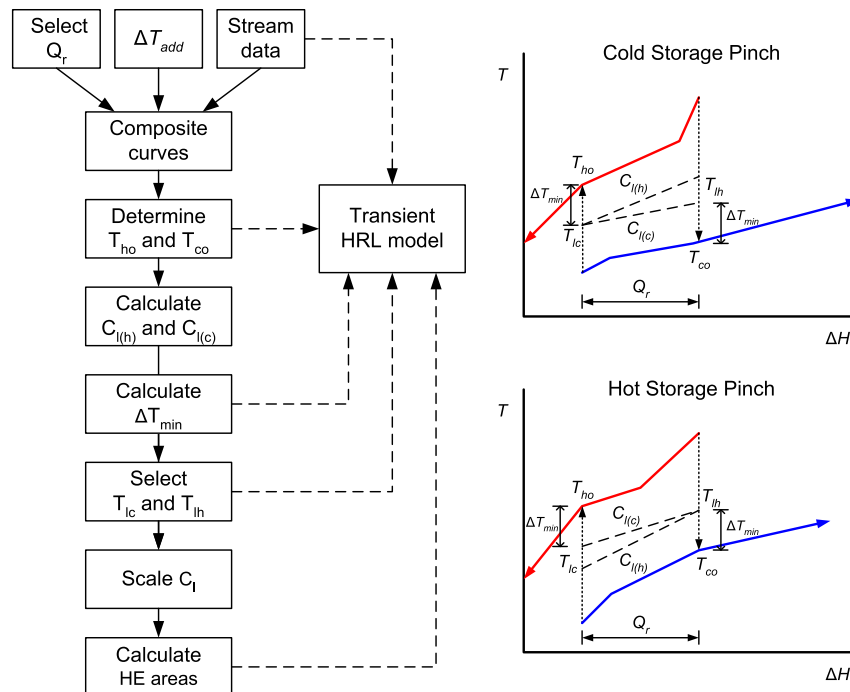


Fig. 4. Procedure for targeting and designing an HRL with VTS.

With the composite curves overlapping by  $Q_r$ , the hot stream outlet temperature, i.e.  $T_{ho}$ , and the cold stream outlet temperature, i.e.  $T_{co}$ , is determined assuming vertical heat integration as shown in Fig. 4. For the same heat recovery level these two outlet temperatures for the CTS and VTS methods are the same. Once these temperatures are found, the limiting combined loop flow rates based on the individual hot streams or the cold streams, i.e.  $C_{l(h)}$  and  $C_{l(c)}$ , are calculated using

$$C_{l(h)} = \sum_{i=1}^{n_h} \frac{Q_i}{T_{s(i)}^* - T_{ho}}, \quad \text{where } Q_i = C_i(T_{s(i)}^* - \max(T_{ho}, T_{t(i)}^*)) \quad (2a)$$

$$C_{l(c)} = \sum_{i=1}^{n_c} \frac{Q_i}{T_{co} - T_{s(i)}^*}, \quad \text{where } Q_i = C_i(\min(T_{co}, T_{t(i)}^*) - T_{s(i)}^*) \quad (2b)$$

where  $n_h$  is the number of hot streams and  $n_c$  is the number of cold streams. If  $C_{l(h)} < C_{l(c)}$ , then the pinch is at the cold storage whereas if  $C_{l(h)} > C_{l(c)}$ , then the pinch is at the hot storage. In some cases  $C_{l(h)} = C_{l(c)}$  and both hot and cold storages are pinched. Streams that start outside the vertical overlapping region of the Composite Curves are not included in the calculation of the limiting heat capacity flow rate. The limiting hot and cold heat capacity flow rates define the minimum and maximum average flow rate boundaries for the VTS HRL system.

As demonstrated in Fig. 4,  $T_{ho}$  is related to  $T_{co}$  through  $\Delta T_{min}$  and the minimum loop temperature difference,

$$T_{co} + \Delta T_{min} = T_{ho} - \Delta T_{min} + \Delta T_{l,min} \quad (3)$$

where the minimum loop temperature difference is a function of the heat recovery level divided by the maximum limiting combined loop flow rate

$$\Delta T_{l,min} = \frac{Q_r}{\max(C_{l(h)}, C_{l(c)})} \quad (4)$$

These equations are rearranged to find an expression for  $\Delta T_{min}$  for a selected  $Q_r$ .

$$\Delta T_{min} = \frac{1}{2} \left( T_{ho} - T_{co} + \frac{Q_r}{\max(C_{l(h)}, C_{l(c)})} \right) \quad (5)$$

The feasible range of average storage temperatures may be calculated using

$$T_{co} + \Delta T_{min} \leq T_{lh} \leq T_{ho} - \Delta T_{min} + \frac{Q_r}{C_{l(h)}} \quad (6a)$$

for the hot storage temperature,  $T_{lh}$ , and

$$T_{co} + \Delta T_{min} - \frac{Q_r}{C_{l(c)}} \leq T_{lc} \leq T_{ho} - \Delta T_{min} \quad (6b)$$

for the cold storage temperature,  $T_{lc}$ .

The designer may choose the average temperature of the non-pinched storage temperature within the range defined in the above equations. The selection may attempt to minimise total heat exchanger area or minimise the loop flow rate; or, one may simply take the mid-point temperature between the upper and lower temperature bounds. With the average storage temperatures ( $T_{lh}$  and  $T_{lc}$ ) and the outlet temperature of the process streams ( $T_{ho}$  and

$T_{co}$ ) decided, the combined average loop flow rate may be calculated

$$C_{l,ave} = \frac{Q_r}{T_{lh} - T_{lc}} \quad (7)$$

Focus is now given to the design of individual heat exchangers in the HRL system. For each heat exchanger, the inlet and outlet temperatures of the process stream and the hot and cold supply temperatures of the loop fluid have been determined. However, the flow rate of the loop through an individual exchanger is not yet known and nor is the outlet (return) temperature of the loop for an individual heat exchanger. As a result an additional equation is needed to fully define each heat exchanger. This equation is based on heat and mass flow rate conservation such that the loop flow rate through a heat exchanger is

$$C_{l(i)} = \frac{Q_i}{T_{s(i)}^* - T_{ho}} \left( \frac{C_{l,ave}}{C_{l(h)}} \right), \quad \text{where } i \in \text{hot streams} \quad (8a)$$

$$C_{l(i)} = \frac{Q_i}{T_{co} - T_{s(i)}^*} \left( \frac{C_{l,ave}}{C_{l(c)}} \right), \quad \text{where } i \in \text{cold streams} \quad (8b)$$

In the above equations, the heat capacity ratio provides a scaling factor for the limiting flow rate for an individual match. Applying the above equations ensure that the average heat and mass flow rates balance. Using the design heat capacity flow rate for a heat exchanger, the outlet/return temperature of the loop fluid may be calculated.

$$T_{l(i),sp} = T_{lh} - (T_{s(i)}^* - T_{ho}) \frac{C_{l(i)}}{C_{l,tot}}, \quad \text{where } i \in \text{hot streams} \quad (9a)$$

$$T_{l(i),sp} = T_{lc} + (T_{co} - T_{s(i)}^*) \frac{C_{l(i)}}{C_{l,tot}}, \quad \text{where } i \in \text{cold streams} \quad (9b)$$

This outlet temperature becomes a temperature set point for the control of the loop fluid through the exchanger. Each heat exchanger will have its own temperature set point returning fluid to the storage tank, which then mixes together. Hence, the HRL has a variable temperature storage system. With each heat exchanger fully defined, its area may be determined using the  $\epsilon$ -NTU heat exchanger design equations [16]. All design parameters of the variable temperature storage HRL are now defined.

## 2.2. Method for transient modelling of actual heat recovery loop performance

An Excel™ based spreadsheet tool has also been developed to simulate the transient performance of an HRL. The tool uses the loop temperature control set points and heat exchanger areas targeted from the steady state design to step-wise calculate the level and temperature of the hot and cold storage tanks. With historical or representative transient stream data, the model may be applied to estimate actual heat recovery for defined volumes of storage. When a stream falls short of its target temperature or storage is unavailable, utility is consumed. In the model, the capacity of the storage tanks and intermediate fluid properties such as density and heat capacity may be specified and the storage tank is assumed to be well-mixed. In this work, the intermediate fluid is water and the effect of storage capacity is investigated.

For this case study the model solves nearly 140,000 counter-current heat exchanger problems. Each problem has an unknown loop heat capacity flow rate, process stream outlet temperature and heat duty. Inlet loop temperatures to the heat exchanger are the

same as the storage temperature from where it is withdrawn. Outlet loop temperatures are the control set point, which is specified in the design. Dynamics relating to process control are not modelled in the spreadsheet. Given a heat exchanger area and overall heat transfer coefficient ( $U$ ), the heat exchanger problems become fully defined. However to calculate the unknowns neither the  $\Delta T_{LM}$  (log-mean-temperature-difference) nor the  $\varepsilon$ -NTU method may be applied. The  $\Delta T_{LM}$  method requires the temperatures in and out of the heat exchanger to be defined; whereas the  $\varepsilon$ -NTU method requires both heat capacity flow rates to be known. Hence an iterative approach was implemented and a generalised solutions table ( $600 \times 600$ ) was generated by iteratively solving a simple, single heat exchanger model. Looking up the solution on the table then enabled the HRL model to solve quickly in about 1 min avoiding the need to iteratively solve thousands of heat exchanger problems, which takes a few hours. To simplify the problem, all heat exchangers, regardless of type, are modelled as a counter current heat exchanger. Cross-flow heat exchangers applied to transfer heat to/from gaseous streams from/to liquid streams normally have multiple liquid passes ( $>6$ ) to produce a near counter flow arrangement [16].

Fluctuations in process stream flow rates and temperature, which are characteristic of semi-continuous processes, are successfully accounted for in the spreadsheet model. Heat exchanger areas are designed according to the time-average flow rate of the process stream. When the flow rate of a stream falls below the design point flow rate,  $U$  and  $Q$  are reduced, and when the flow rate is above,  $U$  and  $Q$  increase. To account for this in the modelling, individual  $U$  values are calculated from the corresponding film coefficients ( $h$ ) for the process and loop streams as a function of Reynolds number ( $Re$ ). Liquids are assigned a design film coefficient of  $4000 \text{ W}/^\circ\text{C}/\text{m}^2$ ; vapours are assigned  $2400 \text{ W}/^\circ\text{C}/\text{m}^2$ ; and gaseous flows are  $71 \text{ W}/^\circ\text{C}/\text{m}^2$ . Assuming the fluids have a constant viscosity, density, and heat capacity, the ratio of the instantaneous  $h$  to the design  $h_{dp}$  is related to the ratio of  $C$  through the Reynolds number, where  $a$  and  $n$  are constants specific to a heat exchanger design,

$$h = a \cdot Re^n \Rightarrow \frac{h}{h_{dp}} = \left( \frac{Re}{Re_{dp}} \right)^n \cong \left( \frac{C}{C_{dp}} \right)^n \quad (10)$$

The spreadsheet model developed for the transient study uses a value of 0.58 for  $n$ , which is specific to a plate heat exchanger [17] but is not out of the range of values for finned tube heat exchangers, 0.52–0.70, calculated from the correlations of Kays and London [16]. Constant  $a$  may be slightly dependent on fluid properties such as the Prandtl number, which is a function of temperature. In this work,  $a$  is assumed to be constant, as is often the case for liquids with relatively small temperature changes. Design point values are based on the average operating flow rate of a stream. Again, to

avoid an iterative solution, a value for  $h$  of the loop side of the heat exchangers was required without first knowing the duty of the heat exchanger and  $C_{l(i)}$ . As a result, the loop side flow rate was approximated by

$$\frac{C_{l(i)}}{C_{pro(i)}} \cong \frac{C_{l(i),dp}}{C_{pro(i),dp}} \quad (11)$$

for the calculation of  $h$  and then  $U$ . In a simple test case, the difference between the estimated and calculated loop  $C$  values was found to be at most 3%.

Included in the HRL model is solar heating based on recorded data from a local weather station. Solar collector efficiency and duty has been modelled using the design equations and constants given by Atkins et al. [12].

$$Q_s = A_s \left( \eta_0 I - a_1 (T_s - T_{amb}) - a_2 (T_s - T_{amb})^2 \right) \quad (12)$$

where  $Q_s$  is the solar heating duty,  $\eta_0$  is the optical efficiency (0.764),  $A_s$  is the area of the solar collector,  $I$  is the solar irradiance,  $a_1$  ( $1.53 \text{ kW}/\text{m}^2/^\circ\text{C}$ ) and  $a_2$  ( $0.0003 \text{ kW}/\text{m}^2/^\circ\text{C}^2$ ) are thermal loss coefficients,  $T_s$  is the average temperature of the collector, and  $T_{amb}$  is the ambient temperature.

### 2.3. Principles for integrating solar heating with HRL's

The integration of solar heating with HRL's is logical because both systems need thermal storage to account for their variable heat supply/demand throughout a day/night cycle. Fig. 5 illustrates the effect of integrating solar heating into two general cases, which may be characterised by the location of the pinch.

In the first case (Fig. 5a) the pinch is at the CS (cold storage) temperature indicating a lack of heat sources. As a result solar heating may be integrated as an additional heat source and either CTS or VTS control may be applied to operate the HRL. It is advantageous to further increase the area of the sink heat exchangers to ensure that the extra heating from solar is fully utilised by the HRL.

The second case (Fig. 5b) is where the pinch is located around the hot storage temperature. Applying solar heating to produce hot water at the pinched hot storage temperature for CTS operation is totally ineffective and inappropriate. This is analogous to adding a hot utility to below the pinch temperature. For VTS operation with a hot storage pinch, the addition of solar heating is like adding a hot utility across the pinch that increases the site's required cooling duty but decreases the site's heating load. To generate benefits from adding solar, the HRL fluid temperature needs to be raised above the pinch temperature and some modifications to the HRL design

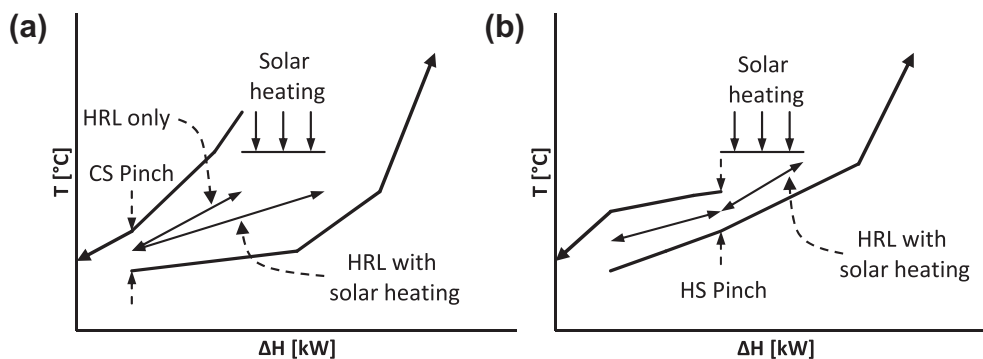


Fig. 5. Composite Curves for the integration of solar heating with HRL's for processes with cold storage pinch (a) and hot storage pinch (b).

may need to be made such as adding a third storage tank with the temperature level as indicated in Fig. 5b.

### 3. Data collection and characterisation

Stream data for four milk powder plants, four other dairy processes, site hot water and two utility units (e.g. compressor) have been obtained from a New Zealand dairy factory for a period of two months during peak processing at intervals of 10 min. Volumetric flow rates were measured by magnetic flow meters and recorded by the company's computer system whereas most temperatures were measured but not logged. As a result historical average temperatures have been used in most cases.

Table 1 presents the stream data for the 18 process streams with the addition of a solar collector. Operating average and daily time average heat capacity flow rates are calculated and temperatures are averaged for while a stream is in operation. The daily time average values include periods when a stream is unavailable throughout a normal day's plant operation due to cleaning and off-product times. Duties based on both heat capacity flow rates are also presented. The solar collector is assigned a supply temperature of 85 °C, and it is assumed that solar heating can heat the intermediate fluid up to 80 °C in evacuated tubes.

Some streams such as the condenser have a high operational duty (993 kW) but only operate for around 8 h/d resulting in a time average duty of 351 kW. The condenser duty is plotted in Fig. 6 using instantaneous values for a 72 h period and ordered values for the entire two months. On the other hand, streams like site hot water are continuously available but its supply temperature and flow rate fluctuates noticeably as shown in Fig. 7.

Solar irradiance and ambient temperature data recorded at a nearby weather station has been downloaded from New Zealand's National Climate Database [18]. Solar irradiance data for the entire two months is plotted in Fig. 8 using time of day as the x-axis and showing the day average (0.43 kW/m<sup>2</sup>), day/night average (0.25 kW/m<sup>2</sup>) and the average of the daily peak (0.97 kW/m<sup>2</sup>).

### 4. Steady state HRL targets and design

#### 4.1. Site composite curves

The site's heating and cooling demand profiles may be determined using the stream data in Table 1 as shown in Fig. 9. The dryer

**Table 1**  
Extracted stream data including the spray dryer exhaust and solar heating.

Stream	Type	T <sub>s</sub> [°C]	T <sub>t</sub> [°C]	Operating		Time-average	
				C [kW/°C]	Q [kW]	C [kW/°C]	Q [kW]
Dryer exhaust A	Hot	75	55	143	2,851	139	2,785
Dryer exhaust B	Hot	75	55	75	1,497	73	1,462
Dryer exhaust C	Hot	75	55	45	898	44	877
Dryer exhaust D	Hot	75	55	29	570	28	557
Utility unit A	Hot	45	30	10	146	8	120
Utility unit B	Hot	45	30	10	146	8	120
Casien A	Hot	50	20	33	999	22	647
Casien B	Hot	50	20	49	1,477	32	956
Casien C	Hot	50	20	49	1,485	32	962
Condenser	Hot	80	79	993	993	351	351
Cheese A	Hot	35	20	120	1,797	98	1,470
Cheese B	Hot	35	20	139	2,074	114	1,691
Solar collector	Hot	85	—	—	—	—	—
Site hot water (SHW)	Cold	16	65	160	7,827	160	7,827
Milk treatment A	Cold	10	50	104	4,159	104	4,159
Milk treatment B	Cold	10	50	104	4,159	104	4,159
Milk treatment C	Cold	11	50	116	4,563	116	4,563
Whey A	Cold	12	45	20	663	16	522
Whey B	Cold	14	45	11	340	9	267

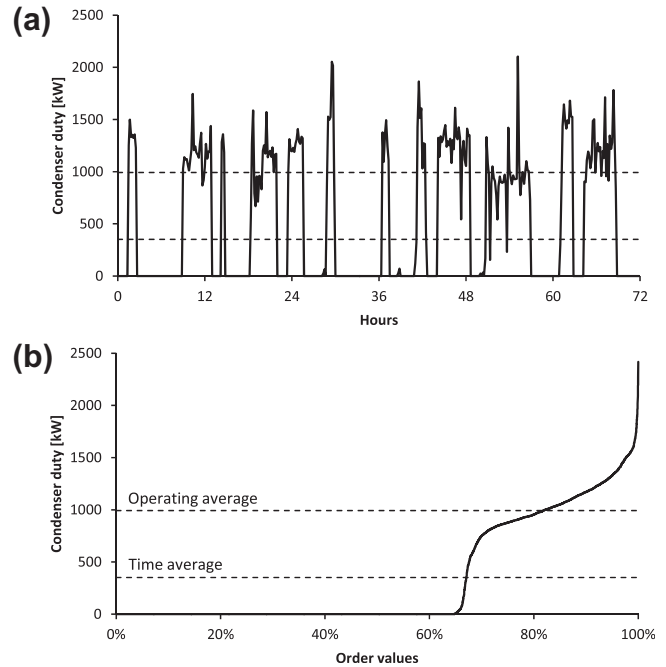


**Fig. 6.** Condenser duty for a 72 h period (a) and as ordered values for the entire two months (b).

exhaust stream has been shifted by 10 °C to reflect its lower heat transfer film coefficient compared to other liquid and condensing vapour streams. The total heating requirement is 21.5 MW on average and the total cooling requirement is 12.0 MW on average.

#### 4.2. Average heat recovery targeting for CTS

Average inter-plant heat recovery achieved by CTS HRL is targeted using a  $\Delta T_{min}$  of 5 °C. As a rule of thumb, liquid/liquid heat

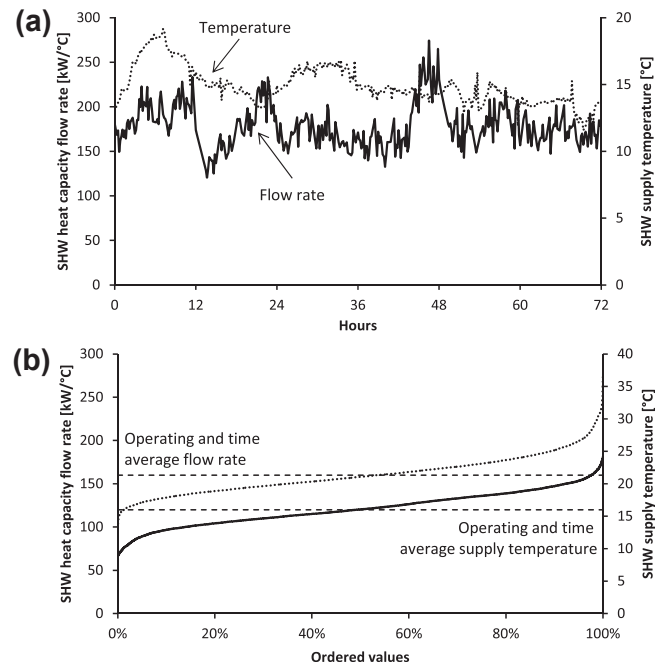


**Fig. 7.** Site hot water supply temperature and heat capacity flow rate for a 72 h period (a) and as ordered values for the entire two months (b).

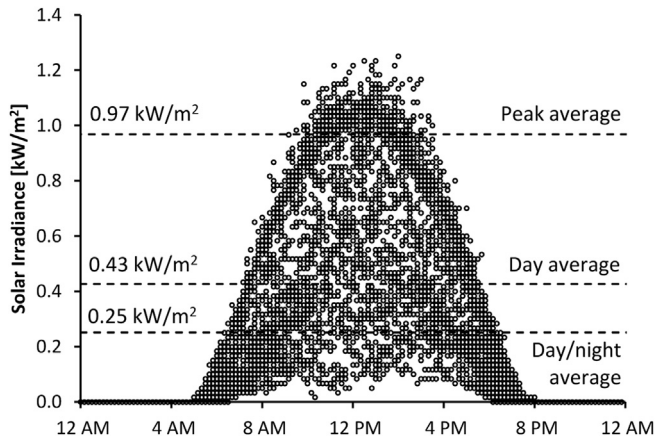


Fig. 8. Solar irradiance recorded by closest weather station the dairy factory [18].

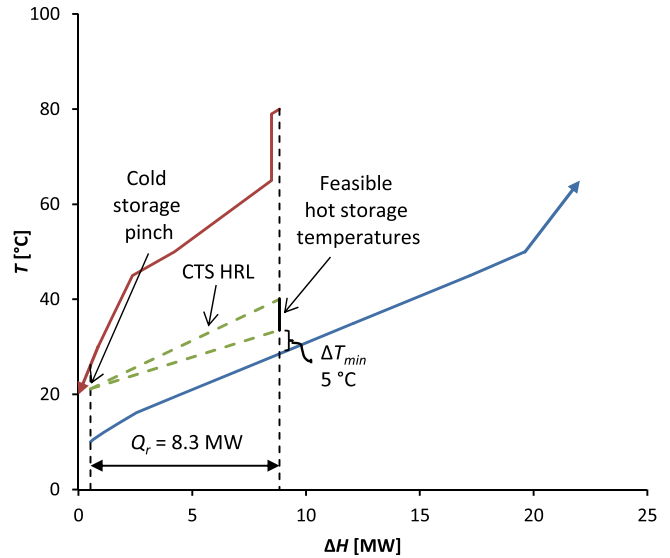


Fig. 10. Heat recovery targeting for CTS based on a  $\Delta T_{\min}$  of 5 °C. Cheese A and B removed from analysis.

recovery using plate heat exchangers tend to be economic at a  $\Delta T_{\min}$  of 5 °C as was demonstrated by Walmsley et al. (2013) for a stand-alone milk powder plant. Fig. 10 presents the pinched Composite Curves for targeting a CTS HRL showing a heat recovery of 8.3 MW. The pinch is around the cold storage temperature caused by site utility unit A's and B's common supply temperatures.

Cheese A and B have been removed from the analysis and the Composite Curve in Fig. 10 to increase heat recovery for a  $\Delta T_{\min}$  of 5 °C. Cheese A and B have the lowest hot stream supply temperature and leaving these streams in the analysis would limit heat recovery to a maximum of 7.5 MW. Above a heat recovery of 7.5 MW, streams Cheese A and B would be encompassed in the overlap region of the Composite Curves causing a hot storage pinch and a  $\Delta T_{\min}$  of less than 5 °C. In general, the stream causing a pinch is removed, which sometimes allows the composite curves to be further overlapped indicating increased heat recovery.

There is a small range of feasible temperatures for the non-pinch hot storage temperature. The effect of varying the hot storage temperature on total area and the loop flow rate is shown in Fig. 11. At the hottest feasible hot storage temperature, the loop flow rate, pressure drop and pumping costs are minimised; whereas

different cold storage temperature minimises total area. From experience, minimising the loop flow rate produces a more practical solution in terms of loop temperature difference and flow rate whereas optimising for the minimum area tends to make less of an impact as indicated by the flatness of the total area curve.

#### 4.3. Average heat recovery targeting for VTS

A heat recovery target for a VTS HRL is determined assuming a  $\Delta T_{\min}$  of 5 °C as shown in Fig. 12. The heat recovery target for the VTS approach is 11.3 MW, which is considerably higher than CTS approach. Fig. 13 presents the effect of hot storage temperature selection where minimising area is at odds with minimising loop flow rate. The CTS method can also recover 11.3 MW, although it requires a lower  $\Delta T_{\min}$  of 0.2 °C and hence a much larger total heat transfer area. To better compare between the

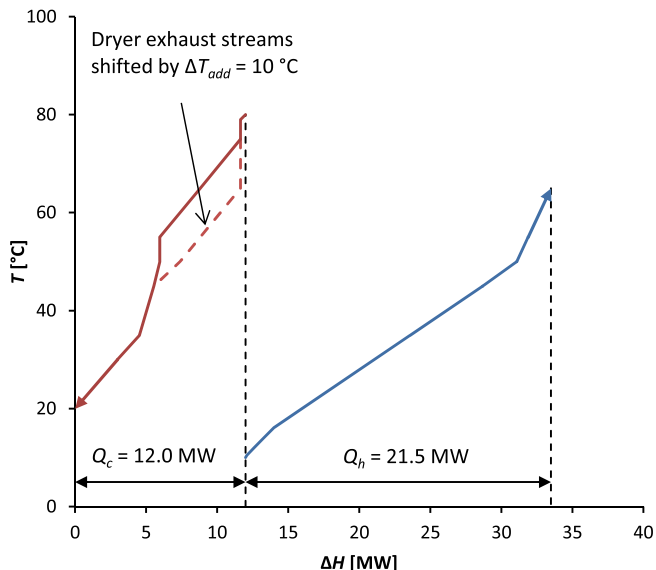


Fig. 9. Time average Composite Curves of available streams for the HRL. Solar heating is not included.

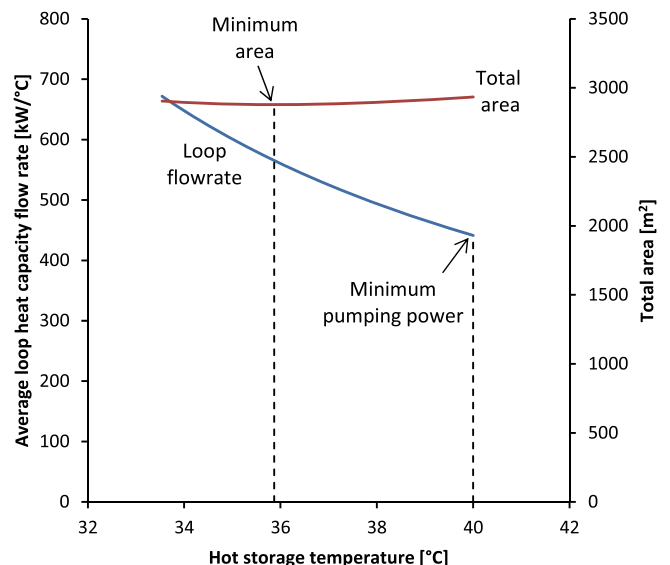


Fig. 11. Effect of cold storage temperature selection on total area and loop flow rate for a CTS HRL based on a  $\Delta T_{\min}$  of 5 °C.

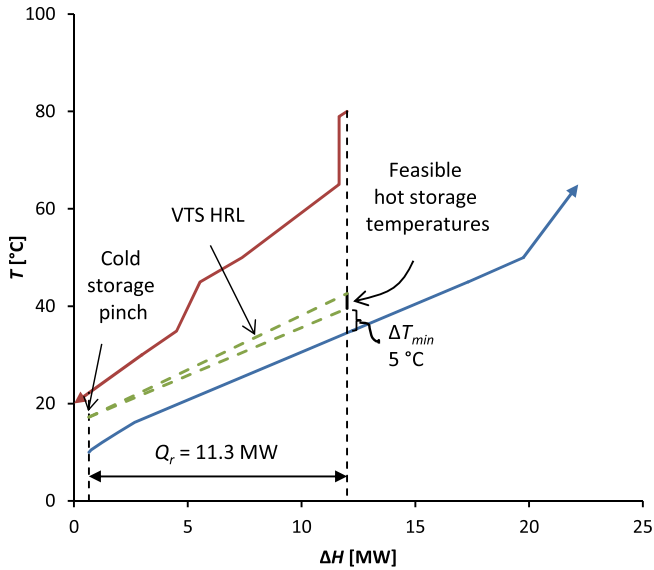


Fig. 12. Heat recovery targeting for VTS based on a  $\Delta T_{min}$  of 5 °C.

two methods, an understanding of the trade-off between heat recovery, total area and average loop flow rate across a broader range is needed.

4.4. Heat recovery, total area and loop flow rate trade-off

In designing an HRL there is an acute trade-off between heat recovery, total area and the loop flow rate. Heat recovery delivers utility savings, heat exchanger area is a capital cost and the loop flow rate determines the pressure drop and pumping costs. The heat recovery performance of CTS and VTS HRL's is compared for a range of  $\Delta T_{min}$  values in Fig. 14. In general the VTS method more effectively distributes temperature driving forces between heat exchangers resulting in higher  $\Delta T_{min}$  values compared to the CTS method. Discontinuities in this graph as well the other graphs in this section are caused by streams being added or removed from the HRL design. For a  $\Delta T_{min}$  of 5 °C, the VTS

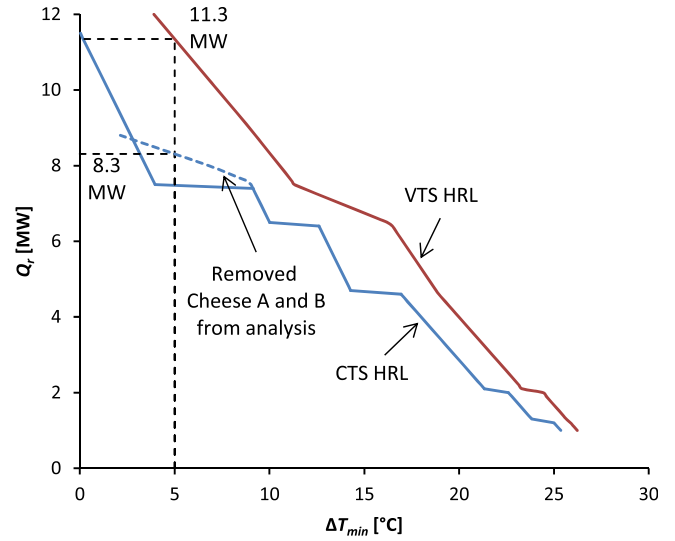


Fig. 14. Heat recovery versus minimum approach temperature.

approach recovers 11.3 MW of heat compared to 8.3 MW for the CTS design.

The heat recovery performance may also be plotted against total network area including the dryer exhaust heat exchanger area as shown in Fig. 15 and total network area excluding the dryer exhaust heat exchanger area as shown in Fig. 16. Black dotted lines are included that correspond to a  $\Delta T_{min}$  of 5 °C for the two design approaches. Below 9.9 MW of heat recovery the CTS approach for this problem provides better heat recovery per unit of area while the VTS approach is advantageous above 9.9 MW of heat recovery if the dryer exhaust area is included. The maximum inter-plant heat recovery for the site, 12.0 MW, is feasible to achieve using the VTS method with a  $\Delta T_{min}$  of 3.9 °C, at which heat recovery level the Composite Curves for a threshold problem. The CTS storage has a maximum heat recovery of 11.5 MW with  $\Delta T_{min}$  approaching zero.

The lower total area achieved by the CTS method below 9.9 MW of heat recovery is mostly due to lower inlet and outlet loop temperatures for the dryer exhaust heat exchangers. The lower

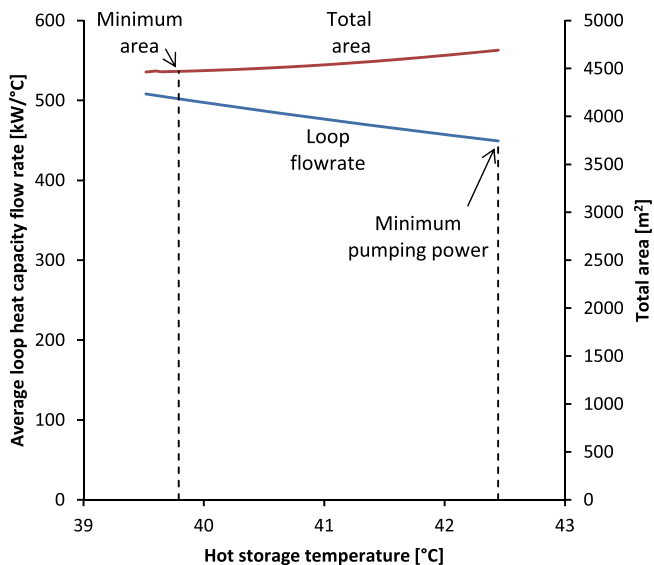


Fig. 13. Effect of cold storage temperature selection on total area and loop flow rate for a VTS HRL based on a  $\Delta T_{min}$  of 5 °C.

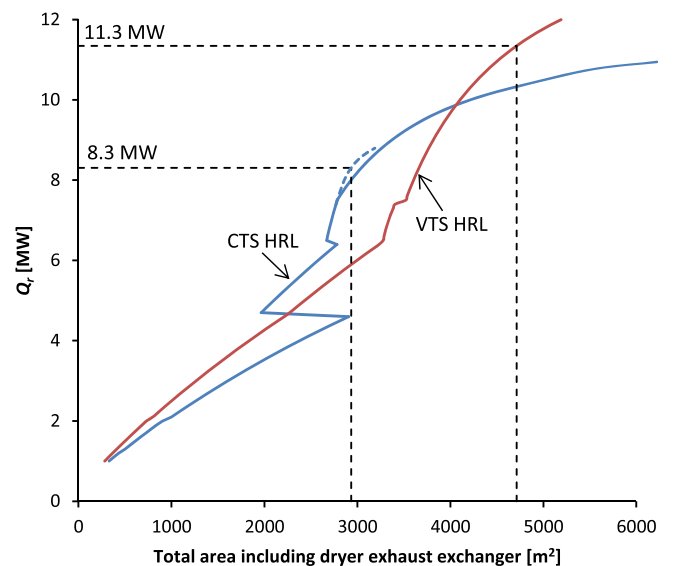


Fig. 15. Heat recovery versus total area including the dryer exhaust exchanger.

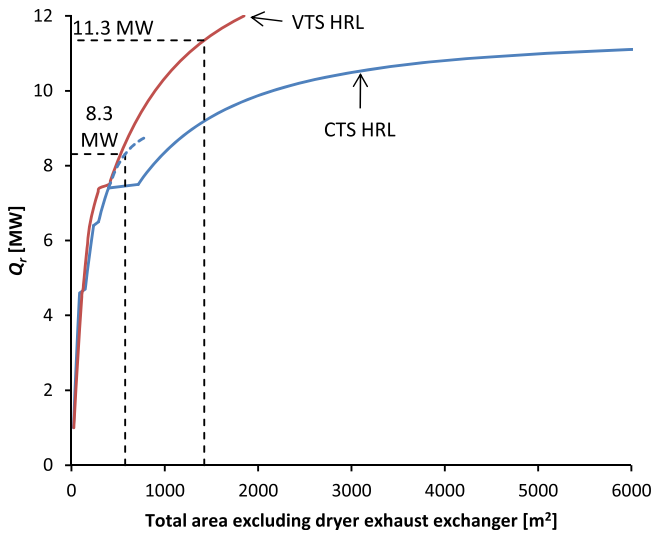


Fig. 16. Heat recovery versus total area excluding the dryer exhaust exchanger.

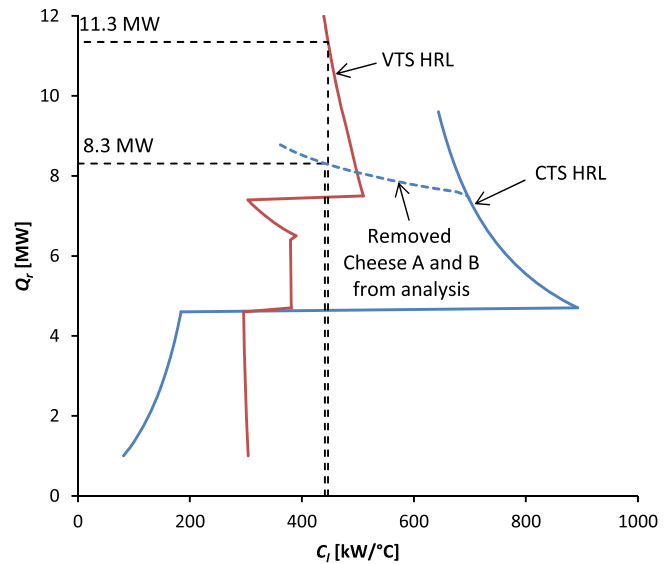


Fig. 17. Heat recovery versus heat capacity flow rate of the loop.

loop temperatures for the CTS design improve the temperature driving force of heat exchangers on the hot side of the loop, which includes the dryer exhaust exchangers. At 9.9 MW of heat recovery the area required for dryer exhaust heat recovery comprises 50% of the total HRL system area, which percentage is higher for heat recovery targets less than 9.9 MW. As a result heat recovery is plotted against the total area excluding the dryer exhaust heat exchangers as presented in Fig. 16. This graph provides a different perspective on which design approach is better. In Fig. 16, the VTS system gives substantially improved heat recovery per unit area for heat recovery greater than 7.5 MW. Below a heat recovery of 7.5 MW, the total area is dominated by the area required for dryer exhaust heat recovery. As a result the CTS approach in Fig. 15 appears to be better at the design stage due to lower loop temperatures maximising the temperature driving force for the dryer exhaust exchanger.

The temperature difference between the hot and cold loop temperatures is a key factor affecting the required loop flow rate (Fig. 17). Small temperature differences require large loop flow rates. When selecting the non-pinched storage temperature, the philosophy has been to minimise the loop flow rate, thus minimising pressure drop and pumping costs. Several additional curves for both CTS and VTS methods could be generated by selecting different non-pinched storage temperatures. When targeting site heat recovery below 5.2 MW, it is possible to remove the stream with the limiting supply temperature from the analysis and improve the final design. As a result Cheese A and B are removed for the CTS design to show this effect while also being able to achieve a  $\Delta T_{\min}$  of 5 °C.

#### 4.5. Integration of solar heating into the HRL design

The integration of solar heating with an HRL is beneficial when the pinch is around the cold storage temperature, which is the case for the CTS and VTS methods with a  $\Delta T_{\min}$  of 5 °C. In this section, the maximum and practical integration of solar heating into the 5 °C  $\Delta T_{\min}$  solutions is investigated.

Fig. 18 shows the maximum amount of solar heat that can be integrated into the CTS HRL without violating the  $\Delta T_{\min}$  constraint whereas Fig. 19 is for a VTS HRL. For these cases the pinch at the hot storage tank is caused by the solar heating. For the CTS approach, the hot storage pinch is between the supply temperature of utility

units A and B and the cold Composite Curve as a result of adding solar to the HRL. For the VTS approach, the second pinch is related to the limiting heat capacity flow rate of the loop based on the hot and cold streams, i.e.  $C_{l(h)}$  and  $C_{l(c)}$ . For a second pinch to occur it is necessary that  $C_{l(h)} = C_{l(c)}$ , where  $C_{l(h)}$  includes solar heating as a hot stream and  $C_{l(c)}$  is based on  $T_{co}$  after solar heating.

Achieving the maximum integration of solar heating is impractical due to the daily solar heating cycle requiring excessive thermal storage. By analysing the solar irradiance data it is found that 65% of the day/night cycle is below the day/night irradiance average of 0.25 kW/m<sup>2</sup>. To account for the cyclic nature of solar availability an estimated 3000 m<sup>3</sup> of thermal storage is required whereas storage for an HRL is typically less than 500 m<sup>3</sup>. If the outlet temperature of the solar collector was higher than 85 °C, which is the value used in this work, the amount of required storage could be lessened. There is an acute optimisation between solar collector temperature, collector heat loss and storage needs that may be analysed as part of future work.

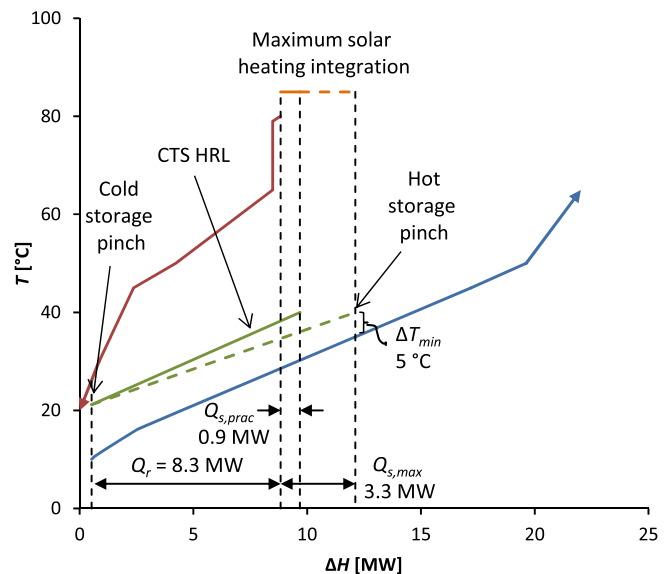


Fig. 18. Maximum and practical average heat recovery and solar heating targets for a CTS HRL based on a  $\Delta T_{\min}$  of 5 °C.

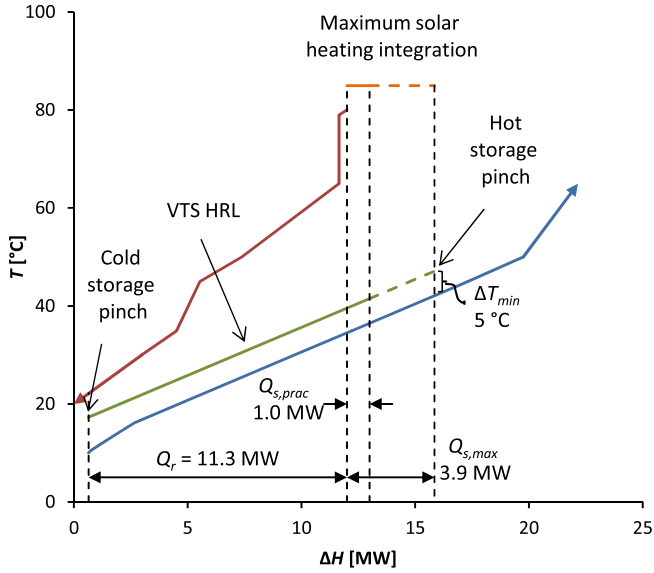


Fig. 19. Maximum and practical average heat recovery and solar heating targets for a VTS HRL based on a  $\Delta T_{min}$  of 5 °C.

A practical amount of solar heating that requires minimal storage can be calculated from  $Q_{s,max}$  assuming that  $Q_{s,max}$  is obtained by the daily average peak solar irradiance, for which there is sufficient sinks on average. As a result this maximum duty is scaled down by the ratio of day/night average to daily average peak solar irradiance ( $I$ ) to obtain a practical average duty of solar heating.

$$Q_{s,prac} = Q_{s,max} \frac{I_{s,ave}}{I_{s,peak}} \quad (13)$$

The practical amount of solar heating is estimated as 0.9 MW for the CTS design and 1.0 MW for the VTS design.

Solar heating duty is a function of the collector area. If the solar collector size is based on the day/night solar irradiance average of 0.25 kW/m<sup>2</sup>, the collector would have insufficient area to achieve the desired average heating duty because the average irradiance value does not take into account the optical and heat losses of the collector. Preliminary analysis of the solar collector suggests that one square meter can average 0.178 kW for the day/night cycle. Without correctly taking into account optical and thermal losses the solar collector would be undersized by 30% for this case and unable to meet its expected design duty. The solar collector needs to be 4776 m<sup>2</sup> for the CTS design and 5606 m<sup>2</sup> for the VTS design.

#### 4.6. Maximum energy recovery HRL designs

The design of an HRL requires the specification of heat exchanger areas and temperature control set points for the return temperature of the loop fluid to storage as provided in Table 2. These design values provide the details for the four HRL designs modelled using transient data. Other parameters such as the operating temperature of the storage units and the loop flow rate may be determined from these two specifications. Heat exchanger areas are sized based on the time average flow rate. Maximum heat recovery HRL designs are targeted to recover 8.3 MW for the CTS design and 11.3 MW for the VTS design with the option of integrating solar heating.

Table 2  
HRL design specifications.

Stream	Loop temperature return set point [°C]				Area [m <sup>2</sup> ]				
	CTS	CTS with VTS solar	VTS with solar	CTS	CTS with VTS solar	VTS with solar	CTS	CTS with VTS solar	VTS with solar
<i>Hot streams</i>									
Dryer exhaust A	40.0	40.0	60.0	60.0	1,156	1,156	1,613	1,613	
Dryer exhaust B	40.0	40.0	60.0	60.0	607	607	847	847	
Dryer exhaust C	40.0	40.0	60.0	60.0	364	364	508	508	
Dryer exhaust D	40.0	40.0	60.0	60.0	231	231	323	323	
Utility unit A	40.0	40.0	40.0	40.0	9	9	7	7	
Utility unit B	40.0	40.0	40.0	40.0	9	9	7	7	
Casien A	40.0	40.0	45.0	45.0	36	36	60	60	
Casien B	40.0	40.0	45.0	45.0	53	53	89	89	
Casien C	40.0	40.0	45.0	45.0	53	53	89	89	
Condenser	40.0	40.0	75.0	75.0	5	5	10	10	
Cheese A	40.0	40.0	29.9	29.9	0	0	125	125	
Cheese B	40.0	40.0	29.9	29.9	0	0	144	144	
Solar collector	40.0	40.0	80.0	80.0	0	4,776	0	5,606	
Total HE area					2,523	2,523	3,822	3,822	
<i>Cold streams</i>									
Site hot water	21.2	21.2	21.7	21.6	127	158	219	257	
Milk treatment A	21.2	21.2	14.7	14.8	85	100	205	230	
Milk treatment B	21.2	21.2	14.7	14.8	85	100	205	230	
Milk treatment C	21.2	21.2	15.3	15.3	94	111	221	249	
Whey A	21.2	21.2	17.0	17.0	13	15	28	32	
Whey B	21.2	21.2	19.2	19.2	7	8	14	16	
Total HE area					411	494	890	1,013	

## 5. Transient modelling of HRL performance

### 5.1. HRL performance with 500 m<sup>3</sup> storage tanks

At any instance the combined heat recovery from the sources may not exactly match the combined heat transfer to the sinks. When that occurs there is a hot and cold imbalance. Most imbalances are short term only lasting for a couple of hours but it is possible that a long term imbalance is sustained for days when plants cease to run due to a lack of milk production from the farms. Short term imbalance is accommodated for by sizing sufficient thermal storage capacity in the HRL system. Long term imbalance results in one of the storage tanks becoming completely empty of fluid.

The instantaneous storage level and hot and cold storage temperatures across a 14 day period is presented in Fig. 20 for the CTS design, Fig. 21 for the CTS with solar design, Fig. 22 for the VTS design and Fig. 23 for the VTS with solar design. These plots demonstrate the real-time transient behaviour of dairy process streams and their associated heating and cooling demands impacting on the HRL operation. Even with 500 m<sup>3</sup> of thermal storage the hot storage tank can quickly fill or empty depending on the mix of streams available. The amount of thermal storage is related to the temperature difference of the hot and cold storage tanks (Table 3). A larger difference on average between the hot and cold storage tanks gives increased thermal density and capacity.

The effect of adding solar heating to the HRL is visible in Fig. 21 for the CTS design and Fig. 23 for the VTS design. For the CTS system, the level of the hot storage tank rises and falls noticeably more than the design without solar. The rise corresponds with daylight hours while the falls relate to night time and the lack of solar heating. The regular cyclic pattern of the hot storage temperature in Fig. 23 for the VTS with solar design is caused by the day/night variations in solar availability. Shorter term variations result from the difference in mixed loop return temperatures from the various heat sources on the HRL. The amplitude of the temperature fluctuations is a function of the amount of hot fluid returned compared to the amount of hot fluid in storage.

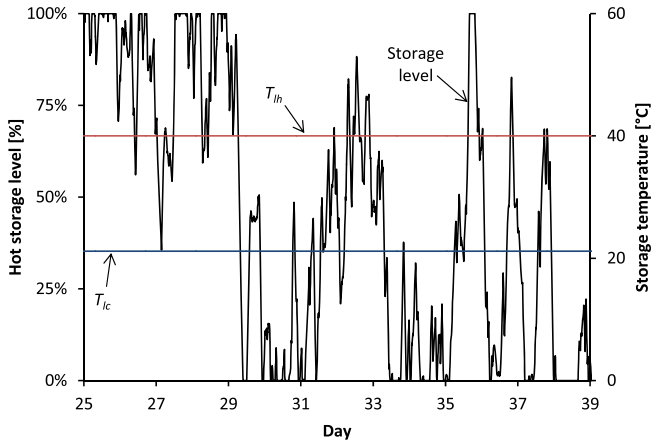


Fig. 20. Thermal storage dynamics for CTS design using 500 m<sup>3</sup> hot and cold storage tanks.

In contrast to the variable hot storage temperature, the cold storage temperature is fairly constant. Many of the sinks at the dairy factory are vital streams for the on-going site operation. These sinks include site hot water, which is constantly being used for washing, and milk treatment streams, which is a necessary process for treating the milk before it is processed into final products. The difference in supply temperature between the sinks is also small (10–16 °C).

The actual combined heat recovery and solar heating with 500 m<sup>3</sup> storage tanks are about 5% less than the targeted values as shown in Table 4. The difference between these two values is a loss that can be attributed to three areas: (1) insufficient heat storage, (2) flow rate variability, and (3) temperature variability. These root causes for the drop in performance of the HRL compared to the targets is analysed in the next three sections.

### 5.2. Effect of storage volume on HRL performance

HRL performance has been modelled for storage capacities between 0 and 1000 m<sup>3</sup> (Fig. 24) as well as the case of infinite storage capacity. HRL performance is characterised by the combination of heat recovery and solar heating that replaces the need for steam and hot water utility. With minimal storage the HRL system recovers a high percentage (92–94%) of the heat recovery for the same design method with infinite storage. Issues relating to stream variability and availability on the required storage appear to be

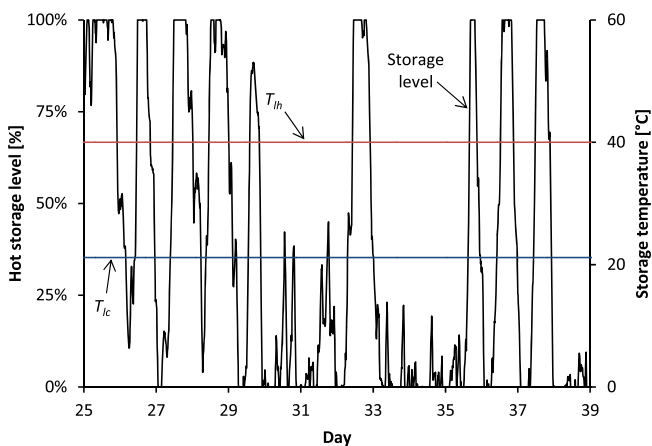


Fig. 21. Thermal storage dynamics for CTS with solar heating design using 500 m<sup>3</sup> hot and cold storage tanks.

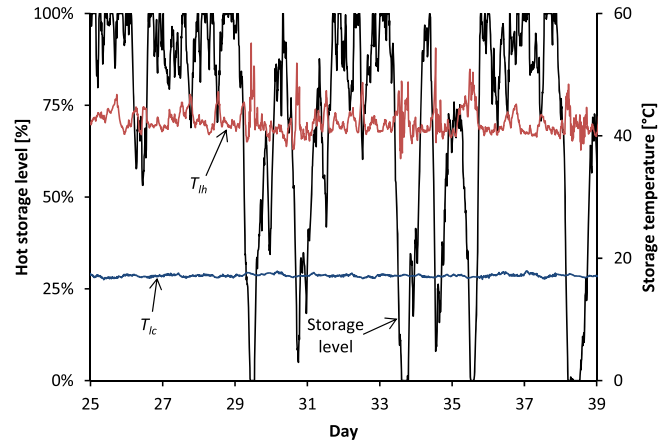


Fig. 22. Thermal storage dynamics for VTS design using 500 m<sup>3</sup> hot and cold storage tanks.

minimised by a number of sources and sinks on the HRL. As more sinks and sources are connected to the HRL degree of source to sink imbalance is reduced lessening the storage requirement. If there were only one source stream and one sink stream in the HRL, then the system would be out of balance whenever one stream is on while the other is off. But when an HRL system has multiple source/sink streams, the degree of imbalance is dampened by the fact the load is spread across more streams.

Actual HRL performance for an effective thermal storage volume may also be characterised as a percentage of the HRL performance with infinite storage (Fig. 25). The VTS designs require much less storage volume to achieve the same HRL performance percentage as the CTS designs. The effective thermal storage energy densities in the VTS systems are higher due to a larger average temperature difference between hot and cold storage temperatures (Table 3).

### 5.3. Effect of off-design process flow rates on heat recovery

As the process stream's flow rate changes, a simple feedback temperature control loop is used to adjust the flow rate of the loop to maintain a constant outlet (return) temperature of the loop fluid. When the process stream's flow rate is above its design value, the heat transfer film coefficients increase due to higher Reynolds numbers for the two fluids exchanging heat. This results in an increased pressure drop and log-mean temperature difference due to a larger approach temperature. The duty of the exchanger is now

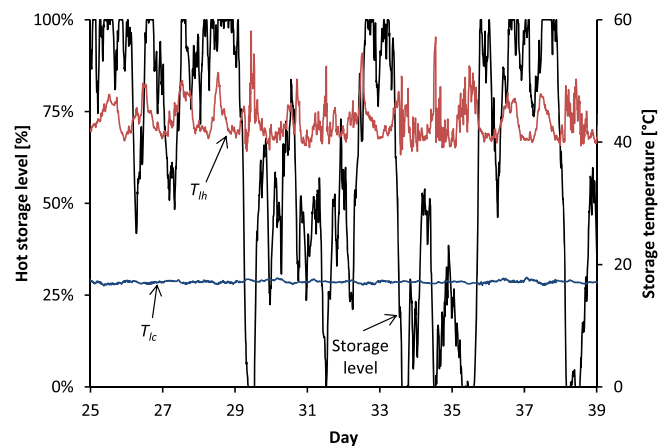


Fig. 23. Thermal storage dynamics for VTS with solar heating design using 500 m<sup>3</sup> hot and cold storage tanks.

**Table 3**

Average hot and cold storage temperatures and the associated impact on thermal storage density and capacity.

Design	Average $T_{ih}$ [°C]	Average $T_{ic}$ [°C]	$T_{ih} - T_{ic}$ [°C]	Thermal storage density increase
CTS	40.0	21.2	18.8	–
CTS with solar	40.0	21.2	18.8	–
VTS	43.3	17.1	26.2	39%
VTS with solar	44.6	17.1	27.5	46%

greater than the design duty, although at the expense of increased pumping power. When the process stream’s flow rate is below the design value,  $h$ ,  $U$ , pressure drop and the log-mean temperature difference are decreased giving a reduced duty.

Fig. 26 plots the actual heat exchanger duty against the heat capacity flow rate of whey B (sink) using the CTS approach. The CTS design is analysed to remove any temperature variability effects. For whey B the supply temperature is an assumed value and is constant for the entire analyse period. The difference between the actual points and the dashed diagonal line ( $n = 1.00$ , Eq. (10)) represents the duty loss/gain caused by variable whey B flow rates. The average actual duty was 117 kW while the time average targeted duty was 125 kW.

The degree to which the exchanger is above and below the targeted duty (diagonal line) is dependent on the  $n$  exponent in Eq. (10). The maximum value of  $n$  is unity. As  $n$  approaches unity, an increase or decrease in  $C$  above the design  $C$  of the process stream results in a proportional increase or decrease in  $U$  and a proportional increase or decrease in  $Q$ . As a result there is no reduction in temperature effectiveness based on the process stream with transient  $C$  values for  $n$  approaching unity as shown in Fig. 27. This implies an important, and perhaps obvious result, that overall heat exchanger performance from transient process streams is always less efficient than from steady process streams with the same time average flow rate and heat exchanger area because  $n$  is always significantly less than one in practice. Fig. 27 also shows that temperature effectiveness increases as the flow rate of the process stream is reduced. In essence, the heat exchanger is oversized for flow rates below the design value and undersized for flow rates above the design value. It may appear that choosing a heat exchanger design with a high exponent  $n$  is advantageous. However the improved performance at higher flow rates will always come at the expense of increased pressure drop and pumping power, which has close to a squared relationship with flow rate.

5.4. Effect of process supply temperature variability on heat recovery

The third reason that the actual HRL performance is lower than the target is temperature variability. Fig. 28 plots the temperature

**Table 4**

Comparison of combined heat recovery and solar heating targets to actual modelled performance highlighting the root causes of the difference.

Design	Combined heat recovery and solar heating [kW]		Root causes of performance reduction [kW]		
	Target	Actual	Insufficient heat storage	Flow rate variability	Temperature variability
CTS	8,310 (100.0%)	7,872 (94.7%)	223 (2.7%)	166 (2.0%)	49 (0.6%)
CTS with solar	9,160 (100.0%)	8,624 (94.1%)	321 (3.5%)	157 (1.7%)	58 (0.6%)
VTS	11,347 (100.0%)	10,777 (95.0%)	126 (1.1%)	350 (3.1%)	94 (0.8%)
VTS with solar	12,345 (100.0%)	11,700 (94.8%)	121 (1.0%)	350 (2.8%)	174 (1.4%)

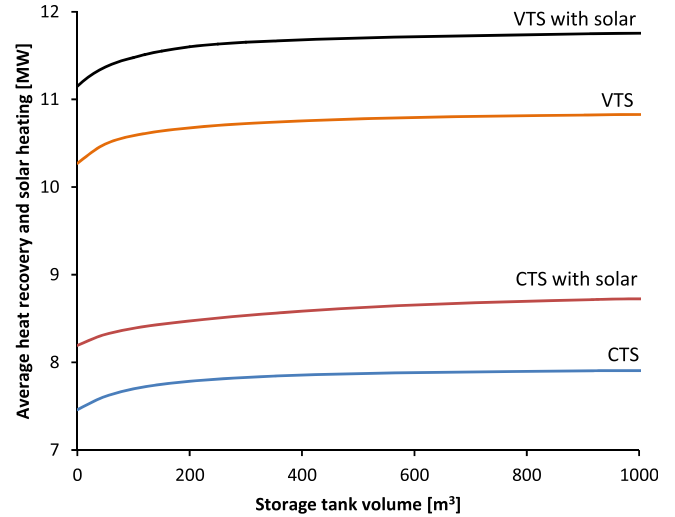


Fig. 24. Effect of thermal storage volume on HRL performance.

effectiveness of the SHW (site hot water) heat exchanger against its inlet temperature. The CTS design is applied to illustrate the effect of process supply temperature variability on heat recovery, which ensures the supply and return temperatures of the HRL are constant. SHW is selected to demonstrate the effect of temperature variability because its inlet temperature is recorded and is known to fluctuate due to changing outside weather conditions as previously shown in Fig. 7.

When the inlet temperature of SHW is less than the loop return set point temperature, the temperature effectiveness of the heat exchanger has some scatter. This scatter is caused by the fact the flow rate of the stream also has variability. To decouple the effects of flow rate variability and temperature variability, exponent  $n$  is set to unity eliminating the effect of flow rate variability from temperature effectiveness as shown by the solid line. Low SHW inlet temperatures have high effectiveness and increased duty, whereas high inlet temperatures have low effectiveness and low duties. At times the actual effectiveness and heat exchanger duty

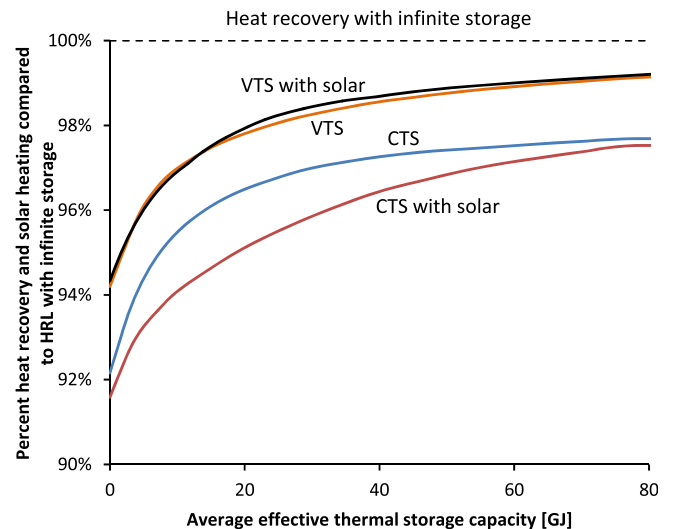


Fig. 25. Effect of average thermal storage capacity on HRL performance as a percentage of the HRL performance with infinite storage.

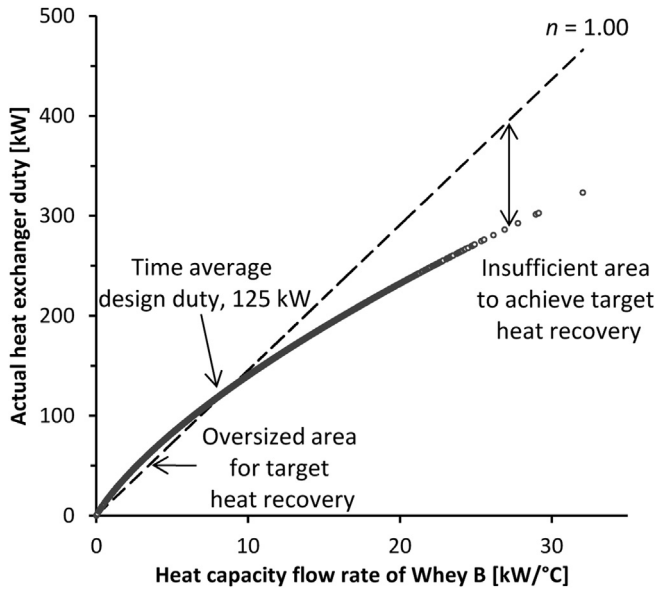


Fig. 26. Actual duty versus heat capacity flow rate of Whey B for CTS design.

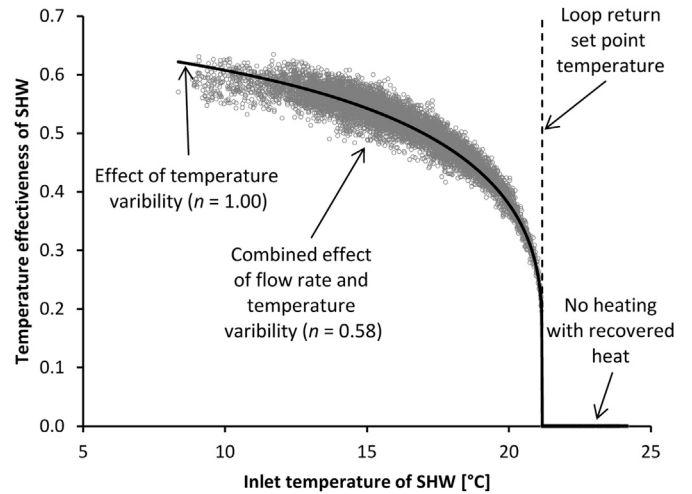


Fig. 28. Temperature effectiveness versus inlet temperature of SHW for CTS design.

are zero because the supply temperature of the process stream exceeds the return temperature set-point of the HRL fluid, which contributes to the amount of decrease HRL performance.

The effect of inlet temperature variability on heat exchanger performance can also be characterised by the outlet temperature of SHW as plotted in Fig. 29. After decoupling the effects of flow rate and temperature variability by setting  $n$  to unity, it is noted that the peak outlet temperature of SHW is achieved when the inlet temperature is equal to the design value. This peak outlet temperature is same as the design outlet temperature. The gap between the solid line in Fig. 29 and the design outlet temperature (28.5 °C) represents, therefore, the loss of duty due to inlet temperature variability for the SHW exchanger. However most (90%) of the heat recovery

loss tied up with the SHW exchanger is the result of high inlet temperatures causing the stream to be incompatible with the operation of the HRL.

### 5.5. The contribution of dryer exhaust heat recovery and solar heating to improving HRL performance and site energy efficiency

The dairy factory has four milk powder plants. Dryer exhaust heat recovery from these plants contribute about 70% of the heat recovery in the CTS designs and about 50% of the heat recovery in the VTS designs (Table 5). Integrating the dryer exhaust with external operations to the milk powder plant is likely advantageous from a capital cost perspective. Dryer exhaust heat recovery represents the key that is able to unlock a new level of energy efficient dairy processing. Linking exhaust heat recovery into a VTS HRL with the added possibility of solar heating can reduce this site's steam demand by 11.7 MW, which is utility cost savings of \$2.6–\$4.0 million/y.

Future work will look at the control dynamics related to running CTS and VTS HRL's. When a process stream's flow rate changes, its outlet temperature is affected causing control action to take place to restore the desired outlet temperature. The dynamics around a single heat exchanger also contribute to the overall dynamics of the

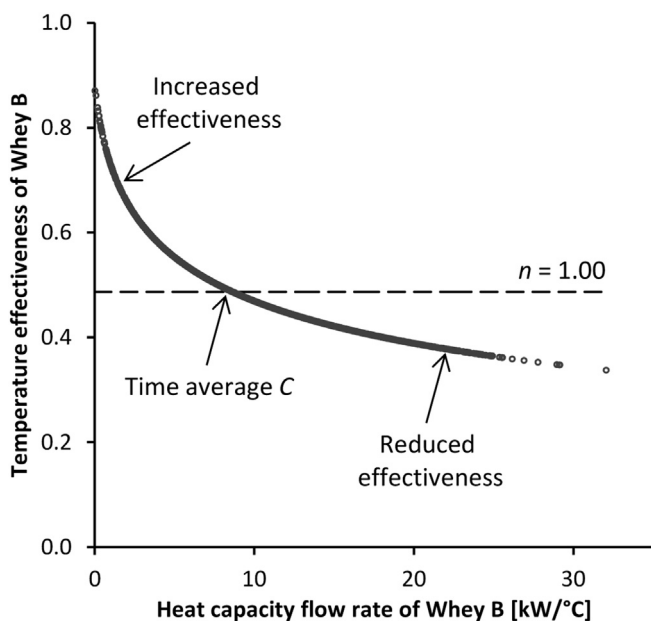


Fig. 27. Temperature effectiveness versus heat capacity flow rate of Whey B for CTS design.

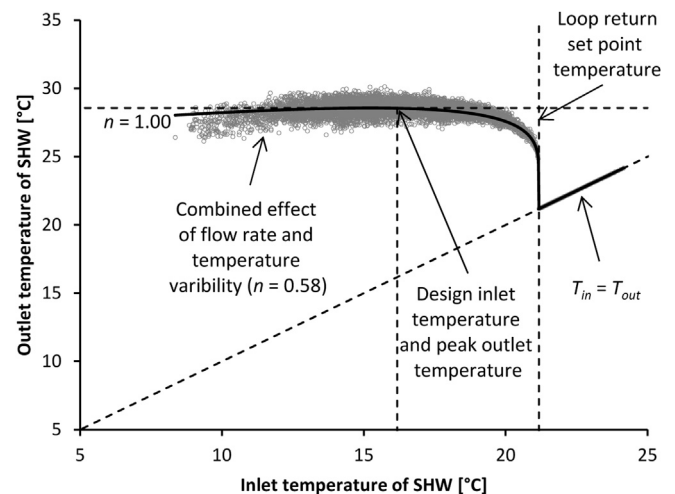


Fig. 29. Outlet temperature versus inlet temperature of SHW for CTS design.

**Table 5**  
Contributions to hot utility reduction assuming 500 m<sup>3</sup> of storage.

Design	Dryer exhaust heat recovery [kW]	Other heat recovery [kW]	Solar heating [kW]	Total [kW]
CTS	5,639	2,233	0	7,872
CTS with solar	5,639	2,134	851	8,624
VTS	5,644	5,134	0	10,777
VTS with solar	5,643	5,139	917	11,700

HRL operation. How these dynamics combine in the heat storage system may prove important for accurately modelling heat recovery.

## 6. Conclusion

Inter-plant indirect heat integration via an HRL combined with renewable solar heating is potentially an economic method for increasing process energy efficiency in large processing sites with a low pinch temperature. How solar heating is integrated depends on the pinch temperature and the shape of the Composite Curves. Where HRL pinch temperatures are located around the cold storage temperature, solar heating can be directly integrated as an additional source without the need for an additional storage tank.

Compared to the conventional HRL design based on a constant temperature storage system, this new method gives solutions with: (1) more effective distribution of temperature driving forces between heat exchangers resulting in higher  $\Delta T_{\min}$  values for the same heat recovery, (2) lower average loop flow rates giving reduced pressure drop and pumping requirements, (3) increased average temperature difference between hot and cold storage temperatures increasing thermal storage density and capacity, and (4) requires less thermal storage. The dairy factory analysed lacked sufficient sources. The addition of the dryer exhausts as heat sources was a critical factor in gaining a heat recovery of 10.8 MW for the variable temperature storage design, of which 5.1 MW was contributed from exhaust heat recovery. Solar heating also proved to be a valuable source with the maximum addition of 0.9 MW of heating on average.

## References

- [1] Klemeš JJ, Dhole VR, Raissi K, Perry SJ, Puigjaner L. Targeting and design methodology for reduction of fuel, power and CO<sub>2</sub> on total sites. *Appl Therm Eng* 1997;17:993–1003.
- [2] Roderer H, Bagajewicz MJ. Targeting procedures for energy savings by heat integration across plants. *AIChE J* 1999;45:1721–42.
- [3] Chen CL, Ciou YJ. Design of indirect heat recovery systems with variable-temperature storage for batch plants. *Ind Eng Chem Res* 2009;48:4375–87.
- [4] Kemp IC, Deakin AW. Cascade analysis for energy and process integration of batch processes. Part 1. Calculation of energy targets. *Chem Eng Res Des* 1989;67:495–509.
- [5] Krummenacher P, Favrat D. Indirect and mixed direct-indirect heat integration of batch processes based on pinch analysis. *Int J Thermodyn* 2001;4:135–43.
- [6] Morrison AS, Walmsley MRW, Neale JR, Burrell CP, Kamp PJJ. Non-continuous and variable rate processes: optimisation for energy use. *Asia Pacific J Chem Eng* 2007;2:380–7.
- [7] Walmsley MRW, Atkins MJ, Riley J. Thermocline management of stratified tanks for heat storage. *Chem Eng Trans* 2009;18:231–6.
- [8] Atkins MJ, Walmsley MRW, Neale JR. The challenge of integrating non-continuous processes – milk powder plant case study. *J Clean Prod* 2010;18:927–34.
- [9] Atkins MJ, Walmsley MRW, Neale JR. Process integration between individual plants at a large dairy factory by the application of heat recovery loops and transient stream analysis. *J Clean Prod* 2012;34:21–8.
- [10] Walmsley MRW, Walmsley TG, Atkins MJ, Neale JR. Area targeting and storage temperature selection for heat recovery loops. *Chem Eng Trans* 2012;29:1219–24.
- [11] Walmsley MRW, Walmsley TG, Atkins MJ, Neale JR. Methods for improving heat exchanger area distribution and storage temperature selection in heat recovery loops. *Energy* 2013;55:15–22.
- [12] Atkins MJ, Walmsley MRW, Morrison AS. Integration of solar thermal for improved energy efficiency in low-temperature-pinch industrial processes. *Energy* 2010;35:1867–73.
- [13] Nemet A, Klemeš JJ, Varbanov PS, Kravanja Z. Methodology for maximising the use of renewables with variable availability. *Energy* 2012;44:29–37.
- [14] Klemeš JJ, editor. *Handbook of process integration: minimisation of energy and water use, waste and emissions*. Cambridge, UK: Woodhead Publishing; 2013.
- [15] Walmsley TG, Walmsley MRW, Atkins MJ, Neale JR. Improving energy recovery in milk powder production through soft data optimisation. *Appl Therm Eng* 2013;61:80–7.
- [16] Kays WM, London AL. *Compact heat exchangers*. 3rd ed. Malabar, USA: Krieger Pub. Co.; 1998.
- [17] Wang L, Sundén B, Manglik RM. *Plate heat exchangers: design, applications and performance*. Wit Pr/Computational Mechanics; 2007.
- [18] NIWA. *The national climate database*; 2013.

**Article 15:**

*Total Site Utility Systems Structural Design Considering  
Electricity Price Fluctuations*

**Walmsley, T.G.**, Philipp, M., Varbanov, P.S., Klemeš, J.J., 2018.

Computer-Aided Chemical Engineering, accepted article.

DOI: in process

Elsevier

## Total Site Utility Systems Structural Design Considering Electricity Price Fluctuations

Timothy G. Walmsley<sup>a\*</sup>, Petar S. Varbanov<sup>a</sup>, Matthias Philipp<sup>b</sup>, Jiří J. Klemeš<sup>a</sup>

<sup>a</sup>*Sustainable Process Integration Laboratory – SPIL, NETME Centre, Faculty of Mechanical Engineering, Brno University of Technology, Brno, Czech Republic*

<sup>b</sup>*Technische Hochschule Ingolstadt, Institute of new Energy Systems, Ingolstadt, Germany*

walmsley@fme.vutbr.cz

### Abstract

This study aims to optimise the structural design of industrial central utility systems while taking full advantage of intra-day electricity spot price fluctuations. Surges in renewable electricity generation uptake have amplified the rises and falls between peak and off-peak electricity prices. Industrial Total Sites and Locally Integrated Energy Sectors can take maximum advantage of periods of both low and high electricity prices through appropriate technology investment. Using P-graph, a Utility Systems Planner superstructure is extended to apply a multi-period analysis to optimally select the fuels, energy conversion technologies, and the requires sizes to install for a representative case study. A key difference between the multi-period solution and the single-period solution is an Electric Boiler that operates when the electricity price is low. This results in a Total Annual Cost saving of 7.5 %.

**Keywords:** Process Integration; Total Site; utility systems; energy planning.

### 1. Introduction

Sustained growth in renewable electricity generation has changed the dynamics of many electricity markets. Large swings between high-peak and low-off-peak electricity prices resulting from the complex interplay between intermittent renewable energy supply, continuously fluctuating electricity demands, and market structure and policy (Aflaki and Netessine, 2017). To maintain a functional grid, electricity spot prices decrease to encourage greater consumption and increase to discourage. Locally Integrated Energy Sectors – LIES (Perry et al., 2008) and Total Sites (Klemeš et al., 1997), i.e. large industrial sites, can profit from periods of both low and high electricity prices through the right technology investments. For example, with Combined Heat and Power (CHP), a site may increase electricity exports when the price is high and, with heat pumps, a site may increase electricity imports when the price is low. The structural design of the central utility system with built-in degrees of freedom (e.g. spare capacity) holds the key to a system becoming responsive to grid dynamics.

Design and optimisation of Total Site central utility systems in literature for both retrofit and greenfield cases have chiefly focused on the operational optimisation of steam and gas turbine networks with some studies considering various uncertainties. For example, Sun et al. (2017) studied the multi-period operational optimisation of an existing utility system that consists of boilers, gas turbines, steam turbines, condensers, and let-down valves, with natural gas as the fuel, under both time- and probability-based uncertainties.

Zhu et al. (2016) applied Mathematical Programming (MP) to optimise a network of complex steam turbines. Luo et al. (2014) applied a multi-objective optimisation to determine a low-emissions utility system using similar technologies as Sun et al. (2017) without emissions abatement, fuelled by coal and natural gas. In other works, forecasting utility price increases over the entire lifetime of a project was considered by Nemet et al. (2015) as part of Total Site system optimisation. These studies, and other similar works, have focused on only a few fuels and energy conversion technologies in an optimisation with highly constrained structures and no consideration was given for how sites can benefit from a variable electricity spot price.

The aim of this study is to optimise the structural design of a Total Site (or LIES) central utility system, which cogenerates heating, cooling and power, considering electricity spot price fluctuations such that Total Annual Cost (TAC) is minimised. The study extends the work of Walmsley et al. (2018) that introduced a new Utility Systems Planner (USP) tool built as a P-graph superstructure. Using a multi-period approach in P-graph (Heckl et al., 2015), the USP is transformed to model electricity price fluctuations and to solve for the cost-optimal utility system structural design. The USP superstructure includes 5 energy sources, 16 energy conversion technologies, and 9 intermediate utility levels. A case study is presented to illustrate the extended USP tool for a LIES case study.

## 2. P-graph

P-graph is a combinatorial optimisation framework specifically for Process Network Synthesis (PNS) problems (Friedler et al., 1996), and the basis of P-graph Studio (2017). Underpinned by five fundamental axioms, P-graph has proven effective at reducing computational burden by very quickly identifying the sub-set of feasible structures for optimising PNS problems with high combinatorial complexity. Three other advantages over standard MP software are: (1) the use a graphical user interface for inputting superstructures and displaying results, (2) the locating of optimal and near-optimal solutions, and (3) the software is free. A key limitation of P-graph Studio is it only allows input of Mixed-Integer-Linear (MIL) type problems, where non-linear functions must be handled using a piece-wise linear approach (Ong et al., 2016). Recent applications of P-graph have included Total Site mass, heat and power integration (Ong et al., 2017) and multi-period optimization of sustainable energy systems (Aviso et al., 2017). P-graph is selected as the optimisation tool for this work due to its excellent visualisation of the problem and its solution as well as its inherent capability to reduce computational burden that helps solve the complex multi-period superstructure.

## 3. Utility Systems Planner - USP

Figure 1 presents the USP superstructure from P-graph Studio. Energy resources (circles) at the top of the superstructure, from left to right, are Electricity Import from the grid, Biomass, Coal, Natural Gas (NG), and Geothermal heat. Located at the bottom are the industrial and district energy users. Considered energy conversion technologies (rectangles) are: solid fuel and gas-fired boilers, NG Combined Cycle Gas Turbine (CCGT), NG Reciprocating Gas Engine (GE), Thermal Vapour Recompression (TVR), Mechanical Vapour Recompression (MVR), Organic Rankine Cycle (ORC), Heat Pump (HP), Absorption Chiller (ACH), Electric Chiller (EC), Steam Turbine, and Let-down Valves (LV). The intermediate energy levels (circles) are Electricity (EL), four steam levels (VHPS, HPS, MPS, LPS), High-Pressure Hot Water (HPHW), Hot Water (HW), Cooling Water (CW), and Chilled Water (CHW). Dark red lines represent electricity

flows, other shades of red and orange lines represent different hot utility levels, blue lines are cold utility, and light blue lines are condensate and water flows. The USP model requires specifying (i) user energy demands, (ii) energy conversion performances ratios, (iii) energy prices, (iv) capital and operating costs, and (vi) GHG emissions factors.

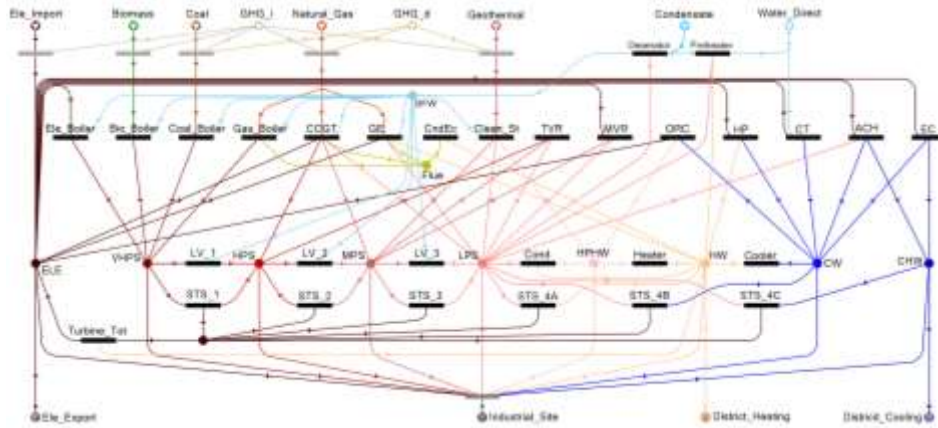


Figure 1: Utility Systems Planner tools – initial superstructure.

#### 4. Method

The optimisation method in this study involved four stages: (1) Analyse historical electricity spot prices. This step included looking at the daily cyclic profile and the ordered value plots for the electricity prices. (2) Determine electricity prices for the multi-period analysis. Multi-period analysis is applied to approximate electricity price variations based on the ordered value plot of the electricity price. This step calculates the average price for each period. (3) Convert the USP superstructure into a multi-period equivalent to include electricity prices variations. This step uses the method of Heckl et al. (2015) to duplicate the initial superstructure (e.g. Figure 1) for  $n$  periods so that different electricity prices may be inputted for each period. Attention must be given to the multi-period superstructure to ensure capital cost is accounted appropriately. (4) Solve the P-graph superstructure for cost-optimal and near-optimal feasible structures. The objective function of the optimisation in P-graph Studio is to minimise TAC in Eq(1).

$$\text{TAC} = \text{UC} + \text{CC} + \text{OM} \quad (1)$$

Where UC is the utility cost, CC is the annualised capital cost, and OM is the operating and maintenance costs.

#### 5. Locally Integrated Energy Sector - LIES Case Study

The considered LIES encompasses a representative industrial chemical processing site and the heating and cooling needs of the surrounding district. Figure 2 presents the Site Utility Grand Composite Curves for the industrial site and the entire LIES. The industrial site has a Utility System Pinch between the MPS and LPS levels, which extends to between the MPS and CW levels once the district heating/cooling demands are included for the LIES. Table 1 presents the prices for energy use while fresh water is 0.2 €/t and on-site GHG emissions are 5 €/t. For details on capital costs and performance ratios of each energy conversion process refer to Walmsley et al. (2018).

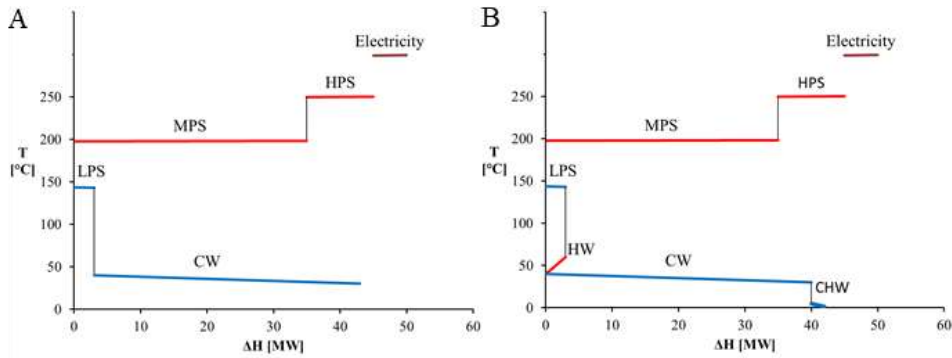


Figure 2: Site Utility Grand Composite Curves for the industrial site (A) and LIES (B).

Table 1: Industrial energy, GHG emissions and water prices and GHG emissions factors (EF).

	Electricity	Biomass	Coal	Natural Gas	Geothermal
Consumption (€/GJ)	22.3*	10.0	5.0	7.0	3.0
Generation (€/GJ)	16.7*	-	-	-	-
GHG emissions (kg/GJ)	-	-	91.4	55.2	1.3

\*Average electricity prices (80.1 €/MWh), minus lines charge for sale (20 €/MWh)

The historical price fluctuations in wholesale electricity index for the EU-28 are presented in Figure 3. The median hourly electricity price trend for a daily cycle shows a low trough (4 a.m.) during the night, a small peak in the morning (8 a.m.) followed by a downturn in the afternoon before rising to a high peak in the evening (7 p.m.). The absolute electricity price is heavily influenced by the season as indicated by the individual trends for the different days. Ordering all electricity price provides a sense of the frequency that each price point arises. A three-period approximation of the ordered electricity price profile can be formulated (Figure 3B). There is a trade-off between the accuracy of the approximation (i.e. more periods) and the computational burden and is an area that may attract attention in future work.

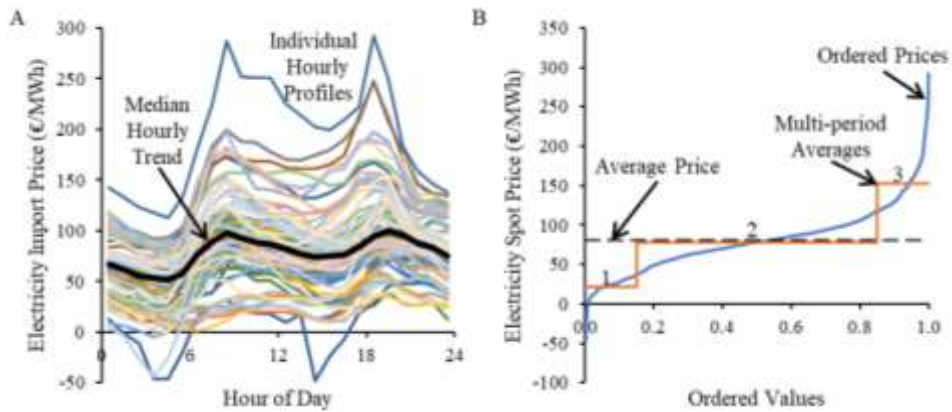


Figure 3: Electricity price with daily profiles for a sample of 84 d in 2017 (A) and by ordered values with single average and multi-period averages (B).

Using the average prices of the three periods from Figure 3B, the USP superstructure may be converted into a multi-period problem. This means the superstructure is replicated

three times. Nodes that represent the physical unit operation and its capital cost connect to each of the three superstructures. This is necessary to ensure that when a unit operation is required in any period, the capital cost is precisely accounted.

Solving the new multi-period superstructure to minimise TAC leads to the structural design as shown in Figure 4. Compared to the base case without multi-period analysis, the TAC savings is 7.5 % but a 90 % increase in GHG emissions due to the export of electricity, 29.3 MW<sub>e</sub>. The final design includes an electric boiler, a gas boiler and a gas engine. When the electricity price is low, the electric boiler is switched on and the gas engine off. As the electricity price rises from period 1 to 2, it becomes uneconomic to use electricity as the heat source rather the site becomes a net electricity exporter. During the two higher electricity price periods, the gas engine runs at peak capacity to maximise electricity exports. The gas boiler has a steady load through all three periods of about 43 MW<sub>f</sub>. The optimal solution suggests that an intensified and integrated gas boiler and engine with electric water heating as a single unit is a key technological solution.

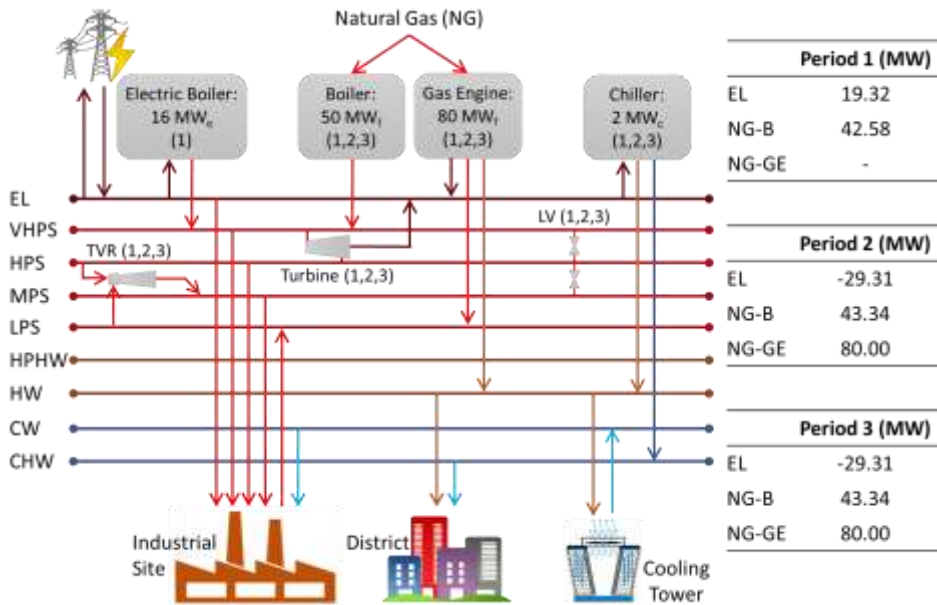


Figure 4: Utility systems structural design with key fuel and equipment for minimum TAC.

## 6. Conclusions

The Utility Systems Planner (USP) model, built using P-graph, incorporated a comprehensive range of possible fuels, resources, energy conversion operations, and auxiliary equipment. This superstructure has been extended in this study to encompass a multi-period analysis. This step forward enabled consideration for considering peak and off-peak electricity prices as part of the utility systems design phase. A comparison of the best utility systems structural designs showed the addition of an Electric Boiler (EB). The installation of an EB unlocked a Total Annual Cost savings of 7.5 % but a 90 % increase in GHG emissions due to an electricity export of 29.3 MW. Future work will focus on applying the USP to additional case studies as well as greater emphasis on environmental concerns beyond GHG emissions.

## Acknowledgement

This research has been supported by the EU project “Sustainable Process Integration Laboratory – SPIL”, project No. CZ.02.1.01/0.0/0.0/15\_003/0000456 funded by EU “CZ Operational Programme Research, Development and Education”, Priority 1: Strengthening capacity for quality research, in a collaboration with the Technische Hochschule Ingolstadt, Germany.

## References

- S. Aflaki, S. Netessine, 2017, Strategic Investment in Renewable Energy Sources: The Effect of Supply Intermittency, *Manufacturing & Service Operations Management*, 19(3), 489–507.
- K.B. Aviso, J.-Y. Lee, J.C. Dulatre, V.R. Madria, J. Okusa, R.R. Tan, 2017, A P-graph model for multi-period optimization of sustainable energy systems, *Journal of Cleaner Production*, 161(Supplement C), 1338–1351.
- F. Friedler, J.B. Varga, E. Fehér, L.T. Fan, 1996, Combinatorically Accelerated Branch-and-Bound method for solving the MIP model of Process Network Synthesis, Chapter In: *State of the Art in Global Optimization*, Springer, Boston, USA, 609–626.
- I. Heckl, L. Halász, A. Szlama, H. Cabezas, F. Friedler, 2015, Process synthesis involving multi-period operations by the P-graph framework, *Computers & Chemical Engineering*, 83(Supplement C), 157–164.
- J.J. Klemeš, V.R. Dhole, K. Raissi, S.J. Perry, L. Puigjaner, 1997, Targeting and design methodology for reduction of fuel, power and CO<sub>2</sub> on Total Sites, *Applied Thermal Engineering*, 17(8–10), 993–1003.
- X. Luo, J. Hu, J. Zhao, B. Zhang, Y. Chen, S. Mo, 2014, Multi-objective optimization for the design and synthesis of utility systems with emission abatement technology concerns, *Applied Energy*, 136(Supplement C), 1110–1131.
- A. Nemet, J.J. Klemeš, Z. Kravanja, 2015, Designing a Total Site for an entire lifetime under fluctuating utility prices, *Computers & Chemical Engineering*, 72(Supplement C), 159–182.
- B.H.Y. Ong, T.G. Walmsley, M.J. Atkins, M.R.W. Walmsley, 2017, Total site mass, heat and power integration using process integration and process graph, *Journal of Cleaner Production*, 167(Supplement C), 32–43.
- B.H.Y. Ong, T.G. Walmsley, M.J. Atkins, M.R.W. Walmsley, J.R. Neale, 2016, Approximation of non-linear cost functions in P-graph structures, *Chemical Engineering Transactions*, 52, 1093–1098.
- S. Perry, J.J. Klemeš, I. Bulatov, 2008, Integrating waste and renewable energy to reduce the carbon footprint of locally integrated energy sectors, *Energy*, 33(10), 1489–1497.
- P-graph Studio, 2017, P-graph Studio, P-graph <p-graph.com> accessed 07.12.2017.
- L. Sun, L. Gai, R. Smith, 2017, Site utility system optimization with operation adjustment under uncertainty, *Applied Energy*, 186(Part 3), 450–456.
- T.G. Walmsley, X. Jia, M. Philipp, A. Nemet, P.Y. Liew, J.J. Klemeš, P.S. Varbanov, 2018, Total Site utility system structural design using P-graph, *Chemical Engineering Transactions*, 63, 31–36.
- Q. Zhu, X. Luo, B. Zhang, Y. Chen, S. Mo, 2016, Mathematical modeling, validation, and operation optimization of an industrial complex steam turbine network-methodology and application, *Energy*, 97(Supplement C), 191–213.



**Article 16:**

*Minimising carbon emissions and energy expended for electricity generation in New Zealand through to 2050*

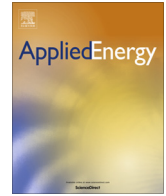
Walmsley, M.R.W., **Walmsley, T.G.**, Atkins, M.J., Kamp, P.J.J., Neale, J.R., 2014.

Applied Energy 135, 656–665.

DOI: 10.1016/j.apenergy.2014.04.048

Citations: 39

Elsevier



# Minimising carbon emissions and energy expended for electricity generation in New Zealand through to 2050



Michael R.W. Walmsley\*, Timothy G. Walmsley, Martin J. Atkins, Peter J.J. Kamp, James R. Neale

Energy Research Centre, School of Engineering, Faculty of Science & Engineering, University of Waikato, Hamilton, New Zealand

## HIGHLIGHTS

- NZ electricity demand is estimated to reach 75 TW h/year (2050) from 43 TW/h (2011).
- New NZ generation for 2050 is best derived from geothermal, wind and hydro.
- The EROI for NZ's electricity sector will decrease from 34 (2011) to 18 (2050).
- Renewable generation is favourable over fossil fuel with CCS for CO<sub>2</sub> reductions.

## ARTICLE INFO

### Article history:

Received 29 December 2013  
Received in revised form 27 March 2014  
Accepted 16 April 2014  
Available online 15 May 2014

### Keywords:

Electricity planning  
Carbon emissions  
EROI  
Renewables

## ABSTRACT

Carbon Emissions Pinch Analysis (CEPA) and Energy Return on Energy Investment (EROI) analysis are combined to investigate the feasibility of New Zealand reaching and maintaining a renewables electricity target above 90% through to 2050, while also increasing electricity generation at an annual rate of 1.5% while allowing for a 50% switch to plug in electric vehicle transportation for personal use vehicles. Under this scenario NZ's electricity demand is anticipated to reach a maximum of between 70 and 75 TW h by 2050. If NZ is carbon emissions constrained to 1990 levels, to minimise energy expended, electricity growth will predominantly come from wind (18 TW h) and geothermal (13 TW h), and hydro (5.6 TW h) to a lesser extent. Renewables resources will produce nearly 95% of electricity generation. The analysis demonstrates that NZ is in a very good position to sustainably meet their future electricity needs while maintaining very low carbon emissions levels and economically desirable EROI levels.

© 2014 Elsevier Ltd. All rights reserved.

## 1. Introduction

New Zealand (NZ) is a remote island country in the South Pacific with a population of 4.4 million, expected to peak at 6 million between 2040 and 2060 [1]. NZ is well endowed with energy resources. Both renewable and non-renewable energy resources are available for electricity generation with hydro, geothermal, wind and biomass accounting for a little less than 80% of generation in 2011. Coal, natural gas and biomass are available for process heat and traditional thermal electricity generation. Liquid fuels for transport and off grid power generation, however, have limited availability domestically and imported crude oil supplies the nations' needs.

There is strong political will within NZ for continued growth in the renewable electricity generation sector. In 2007 the NZ Government set a 90% renewable energy target for the electricity sector to be met by 2025 [2]. To help achieve this goal a 10 year moratorium against new fossil fuel based generation beginning

in 2008 was legislated. The moratorium was repealed in 2008 after a change of Government; although a high renewables target has remained a key strategy for reducing NZ greenhouse gas (GHG) emissions and for creating a more sustainable energy future for NZ.

NZ already has a high proportion of renewable generation mainly due to the large amount of hydro generation (77% in 2011) [3]. However, almost all of the attractive hydro generation capacity has been fully utilised and hydro storage capacity is limited to about two months, which leads to supply concerns during dry years. In 1992 and 2008 there was a severe nationwide drought causing very low hydro lake levels, which then required increased generation from thermal plants. A large pump storage project that triples hydro lake storage capacity to six months has been proposed and detailed hydrological modelling suggests the impacts of the drought in 1992 on the electricity sector could have been averted [4].

It is generally accepted that a high renewables target for electricity generation is a realistic and achievable aspiration for NZ. However, as the best renewable energy sites are utilised first the energy expended to generate the next usable quantity of energy gets progressively higher, and the Energy Return on Energy

\* Corresponding author. Tel.: +64 78384701; fax: +64 78384835.

E-mail address: [m.walmsley@waikato.ac.nz](mailto:m.walmsley@waikato.ac.nz) (M.R.W. Walmsley).

Invested (EROI) will conversely decline. More analysis of the actual effect of a 90% renewables target stretching beyond 2025–2050 on the generation mix, GHG emissions levels, environmental impact/footprint, economic costs and security of supply is needed. Consideration of various scenarios needs to also include the declining EROI for each renewable and non-renewable resource [5].

In addition to economic considerations, environmental impacts of electricity generation through carbon, water [6], and land footprints [7] also play an important role when deciding how best to increase generation. Carbon Emissions Pinch Analysis (CEPA) developed by Tan and Foo [8] is a useful graphical technique to express the impact of electricity generation in terms of carbon footprint for individual plants/resources and for the sector as a whole. Geothermal generation while considered renewable can have a significant carbon footprint depending on the geology and associated geothermal systems of the area. New hydro power can also have a carbon footprint if the hydro lake formed removes large amounts of vegetation from the landscape [9]. These site specific carbon emission or environmental factors need to be accounted for in energy planning analysis. Economic factors that can also affect energy planning include security of supply, amortised total cost, type of electricity market and need for local employment opportunities.

It is anticipated that the declining EROI of fossil fuels will have a significant impact on the economic vitality of national economies [7]. Likewise switching to renewable energy sources with lower EROI values may have a negative impact on economies because of the strong link between EROI and quality of life. Although EROI and CEPA approaches have been separately used for emissions targeting and energy planning, the trade-off between the energy cost and the associated emissions cannot easily be determined. The minimisation of energy costs and environmental targets are usually contradictory objectives which means improving in one objective results in sacrificing the other [9]. A number of approaches have been developed to account for this trade off, including a cost based criterion for carbon emissions/energy production optimisation [10], plus a general modelling approach for optimal planning of energy systems subject to carbon and land footprint constraints [11].

The aim of this paper is to apply CEPA and EROI analysis to planning how NZ can best meet future electricity demand for a population that is anticipated to peak in 2050, while also meeting the goal of 90% renewable generation and lower environmental impacts in terms of carbon footprint. Energy generation methods are analysed through spreadsheet optimisation to determine the 2050 generation mix that meets 1990 or 2011 emissions levels, while minimising energy expended.

The work combines for the first time CEPA and EROI analysis, to a national case study, with and without carbon capture and storage (CCS) as an energy penalty. EROI analysis is extended to include thermal energy required to capture and store carbon emissions so that renewable and non-renewable electricity generation resources/technologies may be compared on a carbon neutral basis. The novel approach enables more realistic economic constraints to be applied to the CEPA planning method. Carbon emissions per capita for NZ are also compared to Australia and the USA. Predicting future electricity demand in NZ includes a growth rate of 1.5%, closure of a NZ aluminium smelter (which is 15% of current electricity consumption in NZ) and the 50% uptake of plug-in electric vehicles in the private transport sector.

## 2. Theory and methods

### 2.1. Carbon emissions pinch analysis

Carbon Emissions Pinch Analysis (CEPA) was first developed by Tan, Foo, and co-workers, and is based on the application of

traditional Pinch Analysis techniques used in heat and mass integration to minimise energy and water usage [8,10,11]. Emissions targeting was originally confined to total site analysis, which focused on optimisation and emissions reduction of industrial sites [12]. CEPA extends the pinch analysis technique from industrial sites to broader macro-scale applications and can be readily applied to the electricity generation sector [13], although it can also be applied to primary energy usage. Sectorial and regional studies can also be conducted for power systems emissions constraint planning with CCS [14] including retrofitting [15] and for multi-period scenarios [16] and variable CO<sub>2</sub> sources and CO<sub>2</sub> sinks [17].

A major aspect of CEPA involves the construction of supply composite curves that plot cumulatively the quantity of electricity generated for the several fuel sources against total equivalent carbon emissions (CO<sub>2</sub>-e) from those sources. The fuel source with the lowest Emissions Factor (EF) (the amount of emissions produced per unit of electricity e.g. kt CO<sub>2</sub>-e/GW h) is plotted first, followed by the next highest and so on. The slope of the supply profile is equal to the emissions factor. The overall Grid Emissions Factor (GEF) is simply the average total emissions factor or specific emissions for the entire system.

An example of the method is presented in Table 1 and Fig. 1. Fig. 1A presents the current supply and demand for electricity and the associated emissions of 1000 kt CO<sub>2</sub>-e. If the new emissions target reduces to 400 kt CO<sub>2</sub>-e (Fig. 1B), the demand profile now meets the supply profile causing a pinch. From the pinch point two options for achieving the emissions target based on Fuel A with renewables and Fuel B with renewables are shown. There are many other combinations of fuels and renewables that can achieve the target, but options A and B are important limits bounding the various combinations. Option A uses renewable energy to lower emissions by 600 kt CO<sub>2</sub>-e whereas option B lowers emissions by switching fuels from B to A and adding renewables. Since option B maximises the use of fuel A, which has the second to lowest emissions factor, this option represents the minimum quantity of renewables needed to be sourced to achieve the emissions target. For further information about CEPA, the reader is referred to Tan and Foo [8] and Atkins et al. [18] for a detailed outline of the method.

### 2.2. Energy returned on energy invested analysis

EROI as a concept is essentially the ratio of the amount of useful energy produced to the amount of energy expended in order to generate the unit of useful energy. The concept was first proposed by American systems ecologist Hall et al. [19]. The useful energy may be in the form of a *primary energy source* such as natural gas (NG), crude oil or coal, or in the form of a *refined energy carrier* such as electricity, gasoline or briquettes [20]. The EROI method traditionally uses a first law of thermodynamic analysis approach

**Table 1**  
Example electricity and emissions scenario.

	Quantity (GW h)	Emissions (kt CO <sub>2</sub> -e)	Emissions Factor (kt CO <sub>2</sub> -e/GW h)
<i>Demand</i>			
Industrial	350	350	1.0
Residential & commercial	650	650	1.0
Total demand	1000	1000	1.0
<i>Supply</i>			
Renewables	300	0	0
Fuel A	400	200	0.5
Fuel B	300	800	2.67
Total supply	1000	1000	1.0

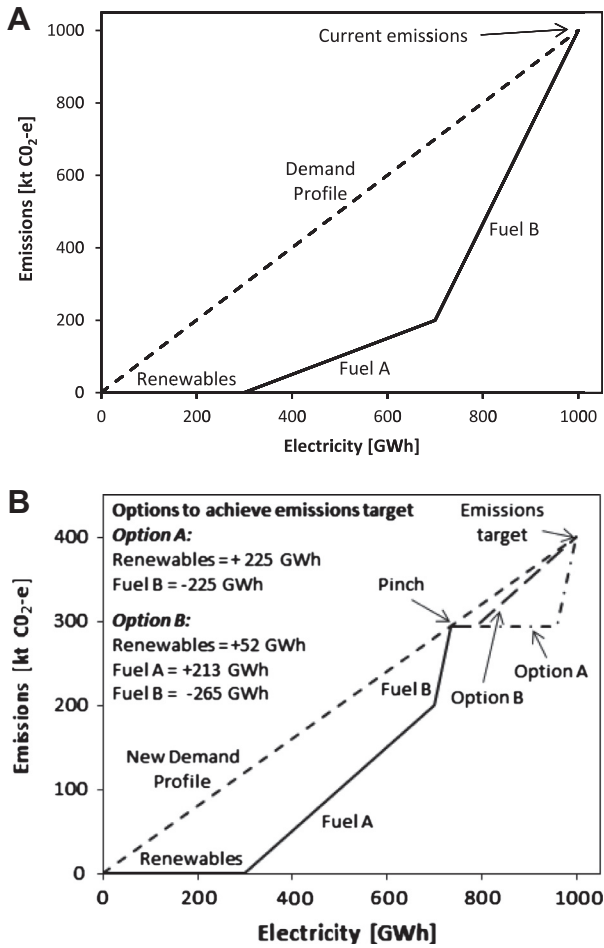


Fig. 1. Example demand and supply composite curves (A) before and (B) after emissions reduction.

and differences in energy quality between heat, work and electricity are not accounted for in the analysis.

For an energy project EROI is defined by Eq. (1) where  $\dot{E}_{gen}$  is the amount of useful or gross energy produced per year,  $t_{life}$  is the expected lifetime of the plant and  $\dot{E}_{exp}$  is the energy expended for extracting ( $\dot{E}_{ex}$ ) and processing ( $\dot{E}_{pro}$ ) the natural resource including construction ( $E_{con}$ ) and decommissioning ( $E_{dec}$ ) of the heat or power plant. The processing energy is also known as the parasitic energy expended.

$$EROI = \frac{\dot{E}_{use}}{\sum \dot{E}_{exp}} = \frac{\dot{E}_{gen}}{\sum (E_{con} + E_{dec})/t_{life} + \dot{E}_{ex} + \dot{E}_{pro}} \quad (1)$$

Fig. 2 illustrates Eq. (1) how energy is both expended and generated through-out the lifetime of a project. Processing conversion losses are not included in useful energy produced. Projects with high EROI are desirable and are typically the first to be implemented. Where the EROI is less than unity, it means that a project has a net energy consumption rather than generation.

While conceptually EROI seems fairly straightforward, the actual determination and consensus of precise definitions is not [20,21]. Several Energy Return Ratios have been used and called EROI. Part of the difficulty is that different authors have drawn different system boundaries for the determination of the EROI while others have sought to also include indirect inputs (e.g. embedded energy resource inputs). Most authors use a gross energy output basis while a few use a net energy output basis, although often it is not clear exactly what basis is used. Recent studies have

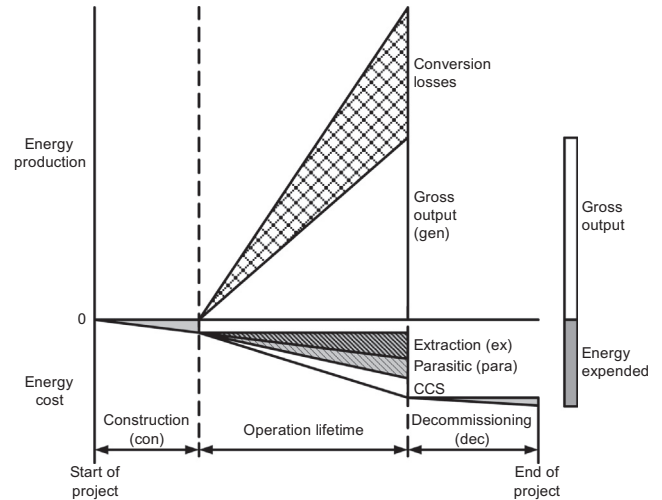


Fig. 2. Analysis of energy generation and expended across the lifetime of a typical energy generation project.

recognised these discrepancies and have sought to construct a clear framework for calculating net energy ratios (NER) and gross energy ratios (GER) with defined system boundaries [21,22]. This study uses a gross energy generated basis for calculating EROI with the system boundary outlined in Fig. 3. Where studies have used a net energy output basis, the equivalent gross energy EROI is estimated by Eq. (2).

$$EROI_{gross} = EROI_{net} + 1 \quad (2)$$

If electricity generation is considered specifically then we can further define an EROI for the fuel ( $EROI_F$ ) as in Eq. (3) and an overall EROI for the electricity ( $EROI_{gen}$ ) as in Eq. (4). The total energy expended ( $\dot{E}_{ED}$ ) is the sum of all the inputs needed in the extraction, processing and distribution operations of the fuel, which includes the direct use of the energy product ( $\dot{E}_{pro}$ ), direct use of external energy ( $\dot{E}_{ext1}$ ), and indirect use of external energy ( $\dot{E}_{ind1}$ ).

$$EROI_F = \frac{\dot{E}_F}{\dot{E}_{ED}} = \frac{\dot{E}_F}{\dot{E}_{pro} + \dot{E}_{ext1} + \dot{E}_{ind1}} \quad (3)$$

When electricity is generated additional energy is required for generation ( $\dot{E}_{pp}$ ), which includes internal electricity use ( $\dot{E}_{para}$ ), direct fuel inputs ( $\dot{E}_{dir}$ ), direct external energy inputs ( $\dot{E}_{ext2}$ ) and indirect energy inputs ( $\dot{E}_{ind2}$ ), some of which is the embedded energy of construction and decommissioning that must be spread over the expected lifetime of the plant.

$$EROI_{gen} = \frac{\dot{E}_{gen}}{\dot{E}_{ED} + \dot{E}_{pp}} = \frac{\dot{E}_{gen}}{\dot{E}_{pro1} + \dot{E}_{ext1} + \dot{E}_{ind1} + \dot{E}_{para} + \dot{E}_{pro2} + \dot{E}_{ext2} + \dot{E}_{ind2}} \quad (4)$$

In the early stages of new technology development, the EROI can often be low, even less than one (Fig. 4). However, as the new technology matures and more efficient extraction and energy generation techniques become available, the EROI for a natural resource to be converted to fuel and/or electricity can vastly improve [23]. Often it is during the technology development phase that Governments and Joint Ventures provide funding to develop the expertise and technology relevant to their country's natural resource profile. As focus shifts from small-scale operation to large-scale operation, a significant reduction in the energy overhead may occur resulting in an increase in EROI. Once the technology is economically competitive with the existing energy

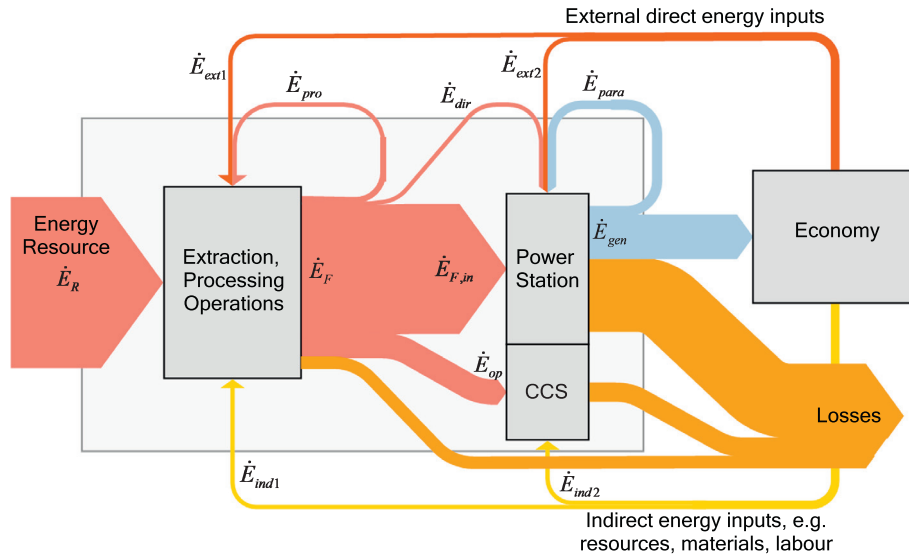


Fig. 3. Sankey diagram of energy flows in electricity generation including Carbon Capture and Storage (CCS).

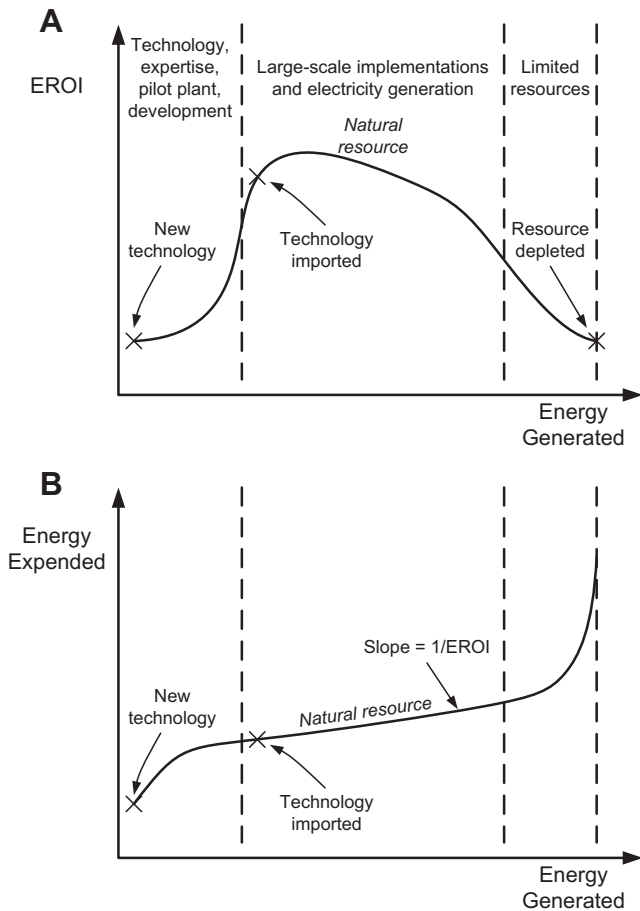


Fig. 4. The influence of technology development and availability of natural resource on (A) EROI and (B) the energy expended to utilise the resource.

generation techniques, large scale implementation occurs. For small countries, such as NZ, the risk and cost associated with the technology development phase can often be too great for significant forward investment and, as a result, technology is often imported.

The first energy generation projects should target projects where the EROI is greatest as these resources/technologies generally have the lowest cost of energy production. As more of a country's available renewable and non-renewable resources are exhausted due to growth in energy demand, projects with lower EROI are implemented until each resource is completely depleted or fully utilised, as is the case for renewable energy. Typically the quality and the ease of extraction of a resource degrade as more of the resource is accessed. However, new exploration that locates high quality resources is always a possibility to again lift the EROI. Fig. 4B plots the energy generation against the energy expended over the life time for a given natural resource. The resulting slope of the curve is the inverse of EROI, where shallower slopes indicate high EROI and steeper slopes represent poor EROI.

EROI can vary greatly depending on the type and quality of the natural resource and the technology used for extraction and conversion [24]. Gupta and Hall discuss these issues and the EROI ranges presented in their review paper have been used to create Fig. 5. To date, there has been little work on EROI in the context of the New Zealand electricity industry and this is an area of future work [25].

Hydro is a renewable resource with the highest and most variable EROI's. Values are highly dependent on geography and climate, and less on conversion technology since the technology is mature. The high EROI reflects the low amounts of expended energy, typically long economic life of a hydro dam, and high conversion efficiency of the generation technology [26]. Other renewables like wind, wave, geothermal and solar are consistently lower than hydro, and have variable EROI values. With these resources location, climate and development of new technology contribute to variable EROI values. Fossil fuel derived electricity EROI values have less spread due to a stronger dependence on technology and less on location and climate, except for extraction of the primary energy source. The EROI of nuclear is disputed in the literature. Nuclear has very low EROI values with some researchers [24] and this is likely to be caused by the strict regulatory and safety requirements around nuclear. However with others the ability to scale up electricity generation from nuclear is attractive due to the extremely high energy density of the nuclear fuel and high EROI values are reported [25].

EROI estimates for NZ's resources are calculated assuming the ratio of EROI to generation cost in NZ\$/MW h is approximately the same for all resources (Table 2 and Fig. 5). Gupta and Hall

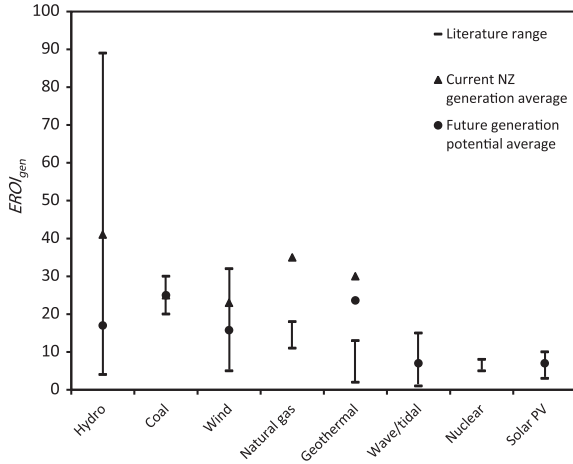


Fig. 5.  $EROI_{gen}$  values and ranges for various resources to produce electricity [24].

[24] report a narrow band of  $EROI_{gen}$  values for coal to electricity and as a result coal assuming an  $EROI_{gen}$  of 25 is used as the basis to estimate the  $EROI$  of other resources using cost ratios. Costs for future generation potential are taken from a key strategy document published by NZ's Ministry of Business, Innovation and Employment [3].

Traditionally,  $EROI$  has been calculated without respect to carbon emissions and any associated energy cost for capturing and storing carbon (CCS). To account for the varying carbon emissions from the energy generation sources, additional energy expended for the capture and storage of carbon emissions may be included to calculate an equivalent carbon reduced or carbon neutral  $EROI$  for electricity (Eq. (5)).

$$EROI_{gen,ccs} = \frac{\dot{E}_{gen}}{\dot{E}_{ED} + \dot{E}_{PP} + \dot{E}_{CCS}} \quad (5)$$

$EROI_{gen,ccs}$  is related to  $EROI_{gen}$  as shown in Eq. (6).

$$\frac{1}{EROI_{gen,ccs}} = \frac{1}{EROI_{gen}} + \frac{\dot{E}_{CCS}}{\dot{E}_{gen}} \quad (6)$$

The energy expended for CCS includes energy used in the CCS process operation ( $\dot{E}_{op}$ ), construction and decommissioning of the CCS plant ( $\dot{E}_{cap}$ ) and extraction of additional fuel for use in CCS ( $\dot{E}_{ED,ccs}$ ).

$$\dot{E}_{CCS} = \dot{E}_{op} + \dot{E}_{cap} + \dot{E}_{ED,ccs},$$

$$\text{where } \dot{E}_{op} = \dot{E}_{gen} \hat{E}_{CCS} (\varepsilon_{tot} - \varepsilon_{acc}), \quad \dot{E}_{cap} = \beta \dot{E}_{PP}, \quad \dot{E}_{ED,ccs} = \left( \frac{\dot{E}_{CCS}}{\dot{E}_{F,in}} \right) \dot{E}_{ED} \quad (7)$$

$$\text{and } \varepsilon_{tot} = \varepsilon_{ele} \left( \frac{\dot{E}_{F,in} + \dot{E}_{CCS}}{\dot{E}_{F,in}} \right), \quad \hat{E}_{CCS} = \frac{\dot{E}_{CCS}}{\dot{m}_{CO_2}}$$

In the above equation  $\varepsilon_{tot}$  is the total  $CO_2$ -e emissions leaving the power plant and CCS process,  $\varepsilon_{ele}$  is the emissions leaving the power plant only,  $\varepsilon_{acc}$  is the acceptable level of emissions,  $\beta$  is the capital factor for the CCS plant compared to the power plant, and  $\hat{E}_{CCS}$  is the specific total energy required (thermal and electrical) for the capture and sequestration of one tonne of  $CO_2$ -e. The value of  $\hat{E}_{CCS}$  is strongly dependent on the CCS technology, the concentration of  $CO_2$  in the flue gas after CCS, and the heat integration of CCS with any neighbouring processes. Based on the amine based capture system of Rao and Rubin [27],  $\hat{E}_{CCS}$  is 1.35 GW h/kt  $CO_2$ -e for 85%  $CO_2$  capture efficiency, which includes a thermal requirement of 1.20 GW  $h_{th}$ /kt  $CO_2$ -e and an electrical requirement of 0.15 GW  $h_{ele}$ /kt  $CO_2$ -e.

Inserting the definitions of  $\dot{E}_{op}$ ,  $\dot{E}_{cap}$  and  $\dot{E}_{ED,ccs}$  into Eq. (7) gives

$$\dot{E}_{CCS} = \dot{E}_{gen} \hat{E}_{CCS} \left( \varepsilon_{ele} \left( \frac{\dot{E}_{F,in} + \dot{E}_{CCS}}{\dot{E}_{F,in}} \right) - \varepsilon_{acc} \right) + \beta \dot{E}_{PP} + \frac{\dot{E}_{CCS}}{\dot{E}_{F,in}} \dot{E}_{ED} \quad (8)$$

Rearranging to make  $\dot{E}_{CCS}$  the subject gives

$$\dot{E}_{CCS} = \dot{E}_{F,in} \frac{\beta \dot{E}_{PP} + \dot{E}_{gen} \hat{E}_{CCS} (\varepsilon_{ele} - \varepsilon_{acc})}{\dot{E}_{F,in} - \dot{E}_{ED} - \dot{E}_{gen} \hat{E}_{CCS} \varepsilon_{ele}} \quad (9)$$

from which an expression for  $\dot{E}_{CCS}/\dot{E}_{gen}$  is obtained.

$$\frac{\dot{E}_{CCS}}{\dot{E}_{gen}} = \frac{\hat{E}_{CCS} (\varepsilon_{ele} - \varepsilon_{acc}) + \beta \dot{E}_{PP}}{\eta_{gen} (\dot{E}_{F,in} - \dot{E}_{ED} - \hat{E}_{CCS} \varepsilon_{ele})}, \quad \text{where } \eta_{gen} = \frac{\dot{E}_{gen}}{\dot{E}_{F,in}} \quad (10)$$

Estimates based on the power station with CCS case study of Rubin et al. [28] for the various components of  $\dot{E}_{CCS}$  suggests  $\dot{E}_{op}$  is about 95% of the energy consumption associated with the CCS life-cycle. A good estimate for  $\dot{E}_{CCS}/\dot{E}_{gen}$  is therefore based on  $\dot{E}_{op}$  alone.

$$\frac{\dot{E}_{CCS}}{\dot{E}_{gen}} \approx \frac{\hat{E}_{CCS} (\varepsilon_{ele} - \varepsilon_{acc})}{1 - \eta_{gen} \hat{E}_{CCS} \varepsilon_{ele}} \quad (11)$$

The idea of a composite curve similar to CEPA may be applied to concepts of  $EROI_{gen}$  and  $EROI_{gen,ccs}$ . The composite curve of the various energy generation resources may be created by plotting cumulative energy expended on the y-axis and energy generated on the x-axis so that the slope of the curve is equal to the inverse of  $EROI$ . The resource with the highest  $EROI$  are plotted first, followed by the second highest  $EROI$  resource and so on to the last resource with the lowest  $EROI$ . This is discussed further in Section 3.3 and examples composite curves are presented.

### 2.3. Optimisation framework for minimising carbon emissions and energy expended for electricity generation

Future electricity generation planning solutions are based on a simple optimisation method. Using CEPA multiple options for meeting a future electricity demand with a carbon emissions cap

Table 2  
Emissions, generation efficiency,  $EROI$  values and additional generation from natural resources for NZ.

Generation type	Emissions factor [kt $CO_2$ -e/GW h]	Electricity generation thermal efficiency	$EROI_{gen}$ for present generation <sup>a</sup>	Additional generation potential <sup>a</sup> [GW h]	Estimated $EROI_{gen}$ for future generation <sup>a</sup>
Hydro	0.000	N/A	41	5600	17
Wind 1	0.000	N/A	23	11,000	18
Wind 2				9000	13
Other renewables	0.000	N/A	7	15,000	7
Geothermal 1	0.128	15%	30	10,000	25
Geothermal 2				3000	19
Natural Gas (NG)	0.422	55%	35	Limited supply	35
Coal	0.733	33%	25	No limit	25

<sup>a</sup> Estimates for  $EROI$  values based on relative costs per MW h of generation compared to coal using the MED data [3].

may be determined as illustrated in Fig. 1. Options are judged based on the estimated total energy expended to achieve the generation and emissions targets with the option with the lowest energy expended being regarded as the best option. In the optimisation method, the total energy expended for electricity generation is identified as the objective function to be minimised. The total expended energy includes energy for CCS if it is required to stay under the emissions cap.

$$\text{Obj. function: } \min \left( \sum \dot{E}_{\text{exp,tot}} \right), \quad \text{where } \sum \dot{E}_{\text{exp,tot}} = \sum \dot{E}_{\text{exp,1}} + \sum \dot{E}_{\text{exp,2}} + \dots + \sum \dot{E}_{\text{exp,n}} \quad (12)$$

The optimisation has two key constraints: (1) the electricity supply must meet the estimated future demand (Eq. (13)) and (2) total emissions must be below an emissions target (Eq. (14)). Constraints for the maximum available extra electricity generation are incorporated into the optimisation. Table 2 presents the emissions factors applied in this study for the various energy sources.

In this work, EROI values are estimated using literature values and NZ government data. Future work will look closer at variable EROI values that are resource and site dependent for New Zealand's electricity generation sector.

$$\dot{E}_{\text{demand}} \leq \dot{E}_{\text{supply}}, \quad \text{where } \dot{E}_{\text{supply}} (\text{GW h}) = \dot{E}_1 + \dot{E}_2 + \dots + \dot{E}_n \quad (13)$$

$$\varepsilon_{\text{tot}} \leq \varepsilon_{\text{tar}}, \quad \text{where } \varepsilon_{\text{tot}} (\text{kt CO}_2\text{-e}) = \varepsilon_1 \dot{E}_1 + \varepsilon_2 \dot{E}_2 + \dots + \varepsilon_n \dot{E}_n \quad (14)$$

### 3. Results and discussion

#### 3.1. New Zealand electricity sector growth analysis

The electricity sector in NZ has experienced consistent growth in demand since 1990 and a corresponding increase in net emissions as illustrated in Fig. 6. The NZ electricity industry also experienced far reaching and significant restructuring since 1990 and these reforms have had a profound effect on the investment behaviour of both generators and distributors [29]. The average yearly growth in demand over the time averaged 1.77% and there has been an increasing trend to higher Grid Emissions Factors. Due to the heavy reliance on hydro the GEF is sensitive to hydro storage lake levels and “dry years” such as 1992 and 2008 can result in a spike in GEF. As a result of the Global Financial Crisis in 2008, the growth in electricity demand has reduced somewhat, however

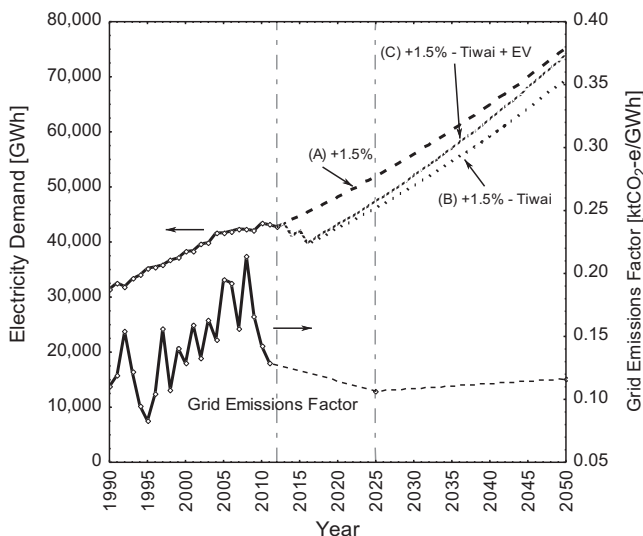


Fig. 6. Projected electricity demand growth in NZ to 2050.

growth rates are expected to return to traditional levels from 2013 due to the relative strength of the NZ economy.

Three scenarios for future demand are also shown in Fig. 6. Scenario (A) a 1.5% per year increase in demand, scenario (B) a 1.5% per year increase and the gradual closure of Tiwai Point Aluminium smelter, and scenario (C) a 1.5% per year increase and the gradual closure of Tiwai Point Aluminium smelter plus a gradual uptake of plug in hybrid electric cars (1,300,000 cars by 2050). The Aluminium smelter at Tiwai Point located in the South Island of NZ used approximately 13% of the electricity generated in NZ in 2012 and the Manapouri hydro-dam alone supplied the smelter. The smelter is nearing the end of its plant life and there is considerable political debate about the merits of using so much of the nation's renewable energy resource on aluminium production mainly for export. For this study the case where the smelter closes within the next 3 years is considered such that the electrical demand from the smelter is halved in 2014 and becomes zero in 2016. Scenario B and C illustrate this affect by the sudden drop in electricity demand and emissions between 2013 and 2016 as the smelter closes.

There is also a strong will in NZ, although not presently mandated by Government, to reduce overall emissions and as a result this study investigates two cases of reducing overall emissions to 1990 and 2011 levels by 2050. These correspond to emissions of 3730 and 5580 kt CO<sub>2</sub>-e in 2050. A total electricity generation target of 75,000 GW h for 2050 is set to meet predicted future demand which is driven by population growth and changes in technology especially in the transport sector. It is noted that the NZ Population is predicted to peak between 2040 and 2050 at 6 million and so a 75,000 GW h total electricity generation target in 2050 may also be the peak.

#### 3.2. Carbon emissions pinch analysis

##### 3.2.1. Emissions per Capita Comparison for New Zealand, Australia and the United States

The electricity generation-carbon emission profile of NZ is compared against Australia (Aus) and the United States (USA) on a per capita basis for 2011 (Fig. 7). A large portion of the generation in the USA and Australia is comprised of traditional fossil fuel based generation (e.g. coal and natural gas), whereas NZ has a much larger share of renewables mainly hydro and geothermal. The USA has lower emissions per capita than Australia due to a significant amount of nuclear generation. The electricity generation profiles for each country are clearly unique and in part a reflection of the range of exploitable energy resources, renewable and non-renewable, available in each country. This is clearly demonstrated by the high utilisation of hydro and geothermal generation in NZ, which has large reserves of easily exploited hydro and geothermal resources and a comparatively small population base. Where easy to exploit or cost effective renewable energy resources are limited, countries are forced to either constrain energy consumption, use more fossil fuel, or install nuclear plants to cover the shortfall. As a result, in these countries the emissions per capita is controlled by the proportion of fossil fuel to nuclear electricity generation. For example, France has the lowest per capita carbon emissions in the developed world due to 75% of its electricity generation coming from nuclear power [30].

##### 3.2.2. Annual electricity emissions for New Zealand in 1990, 2006, 2007 and 2011

Using the CEPA composite curve method the electricity generation mix in NZ for the years 1990, 2006, 2007, and 2011 are illustrated in Fig. 8. The total electricity demand and emissions for NZ in 2011 were 43,138 GW h and 5580 kt CO<sub>2</sub>-e respectively (GEF = 0.129 kt CO<sub>2</sub>-e/GW h) and the generation mix was 57.6% hydro, 18.4% gas, 4.7% coal, 13.4% geothermal, 4.5% wind and

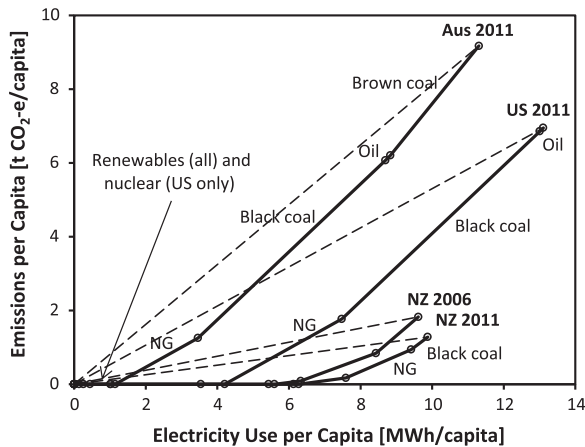


Fig. 7. Comparison of generation mix profiles between NZ, Australia and United States (US) on a per capita basis in 2011, with the addition of NZ's profile in 2006 (peak emissions).

1.5% other renewables. The total amount generated from renewables (including geothermal) was 77%, with the remainder from fossil-fuel based thermal generation. Emissions factors were calculated based on data from New Zealand's Ministry of Economic Development Energy Data Set [3].

It is important to note that although geothermal generation is considered a renewable energy source there are associated GHG emissions. This emissions factor is site specific and can vary by almost two orders of magnitude depending on the geology and fluid circulation within the geothermal field. In this work the aggregate emissions factor for all NZ geothermal generation is used (0.128 kt CO<sub>2</sub>-e/GW h). Individual geothermal fields and the effect on the emissions factor for NZ have previously been reported (Atkins et al., 2010). Renewable generation sources also have emissions due to factors such as construction, materials, maintenance, and the like. A variety of Life cycle emissions factors have been reported and they vary considerably depending on the technology and location of the generation considered but also on the assessment methodology, conversion efficiency, capacity factor and plant life used [31]. Despite the variation, the life cycle estimates for wind and hydro are typically at least one to two orders of magnitude lower than geothermal and fossil-fuel based thermal generation and therefore the life cycle emissions have been ignored in this analysis.

There has been a significant shift in the generation mix between 1990 and 2011. While the mix is still dominated by hydro, the

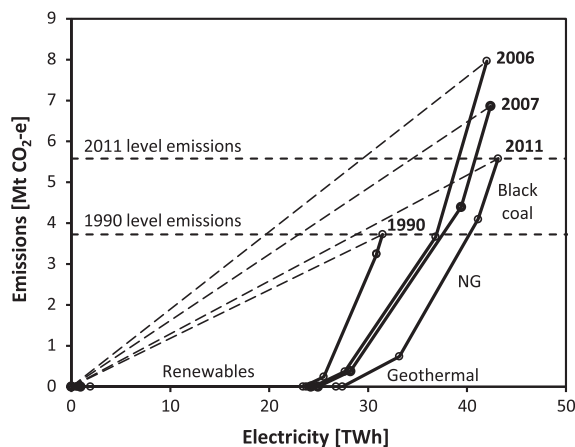


Fig. 8. A comparison of carbon emissions and electricity generation in New Zealand for 1990, 2006, 2007, and 2011.

amount from geothermal doubled between 1990 and 2006 and then roughly doubled again between 2006 and 2011. Wind generation was also added to the generation mix starting in 2004 although is still only a relatively small proportion of the total ( $\approx 4.5\%$  in 2011). The emissions factors for coal and natural gas have also improved slightly since 1990 as a direct result of efficiency improvements and the increased use of combined cycle gas turbines.

Emissions from the electricity sector have almost doubled from 3730 kt CO<sub>2</sub>-e in 1990 to just less than 5580 kt CO<sub>2</sub>-e in 2011. Emissions peaked in 2006 when emissions were over 9000 kt CO<sub>2</sub>-e. There was a 14% reduction in emissions from 2006 to 2007 due to the replacement of coal with natural gas. Emissions continued to decrease from 2007 to 2011, with a further reduction in coal fired generation and a doubling of geothermal generation. The average emissions factor from geothermal generation increased 15% from 0.115 to 0.128 kt CO<sub>2</sub>-e/GW h due to the geology and location of the new geothermal generation.

### 3.3. Energy return on energy invested analysis for the New Zealand electricity sector

A plot of the estimated energy expended in 1990 and 2011 against electricity generation in NZ for each resource is presented in Fig. 9. The energy expended values are estimated using  $EROI_{gen}$  values presented in Table 1. The slopes of the lines in Fig. 9 are the inverse of  $EROI_{gen}$ . In 1990 the average  $EROI_{gen}$  across the electricity sector was 25 and decreased to 20 mainly due to the increase in renewable generation having low  $EROI_{gen}$ . A notable difference between Figs. 8 and 9 is the order and ranking of the resources. In particular, from an energy return point of view, coal is favourable and advantageous, but it comes at the environmental cost of increased CO<sub>2</sub> emissions. As a result, for many resources there is a natural conflict between achieving a high  $EROI_{gen}$  while at the same time minimising emissions.

To account for the differences in environmental impact in terms of carbon emissions/footprint, an additional expended energy term for CCS is included in the calculation of EROI so that all resources are carbon neutral. The  $EROI_{gen}$  profile for 2011 is shown again in Fig. 10 where energy expended including the additional energy to remove carbon emissions is plotted against electricity generation. Including the energy requirement for CCS increases the energy expended by 767% for the same level of electricity production. Energy return favourability shifts in the NZ case towards low emissions renewable resources such as hydro, wind, solar, wave and geothermal. However, it should be noted that there are

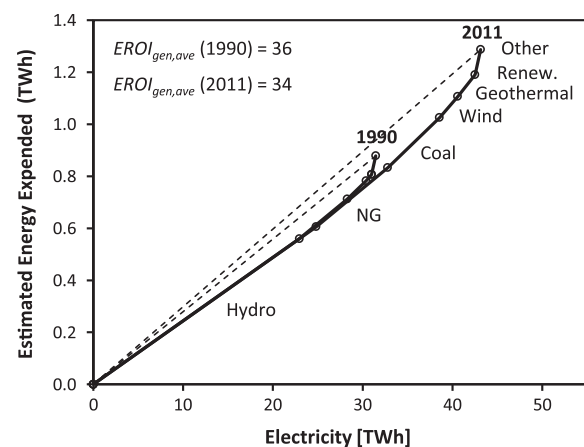


Fig. 9. The estimated annual cumulative energy expended for New Zealand electricity generation in 1990 and 2011.

limitations on the generation capacity of each renewable resources, as they generally take up more land area and are geography dependent.

The effect of CCS on acceptable carbon emissions  $\epsilon_{acc}$  and EROI for each generation type is illustrated in Fig. 11. Carbon emitting sources like geothermal, gas and coal start with high EROI values and reduce sharply to become less economic as CCS energy is implemented and accounted for. Low carbon renewable energy sources like wind, hydro, wave, and other renewables like solar, wave and biomass lie near the y-axis with little emissions. CCS is clearly an undesirable and unnecessary carbon emissions remedy for NZ and even with modest amounts of CCS, the EROI of most renewable generation sources becomes superior to fossil fuel sources.

With pressure to reduce emissions the introduction of CCS for fossil fuel derived generation may be considered necessary for some countries. It is evident from Fig. 11 that introduction of CCS to lower emissions of fossil fuels to acceptable levels causes a significant EROI penalty that will encourage the expansion of renewable generation up to the maximum possible. Without emissions constraint NG combine cycle generation on average is the clear favourite followed by coal, geothermal, hydro and wind for future generation in NZ. Actual generation selection, however, will depend on specific sites and cases as the EROI for renewable can vary considerably for each.

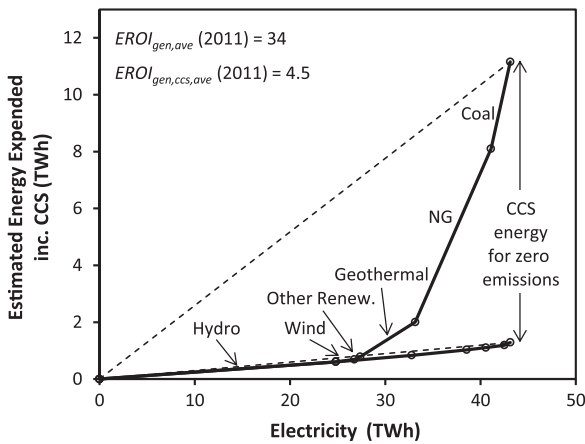


Fig. 10. The estimated annual cumulative energy expended for New Zealand electricity generation in 2011 including additional energy required to operate CCS processes for zero carbon emissions.

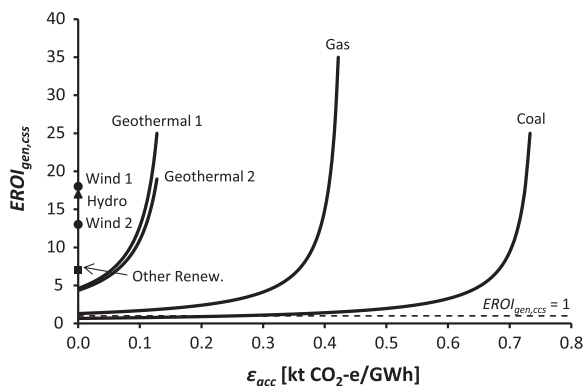


Fig. 11. Effect of CCS emissions reduction on EROI for a variety of non-renewable energy sources compared renewable sources.

3.4. Electricity generation planning for New Zealand through to 2050

Figs. 12 and 13 illustrate the optimal generation mix and minimum expended energy required to meet future electricity demand of 75 TWh in 2050 at 1990 and 2011 emission levels respectively. The optimum values have been determined using a spreadsheet optimisation tool. The optimisation took into account the predicted maximum generation limit for each energy source (Table 2) to ensure the results are meaningful. A variety of generation options are possible for reaching the demand and emissions target. The

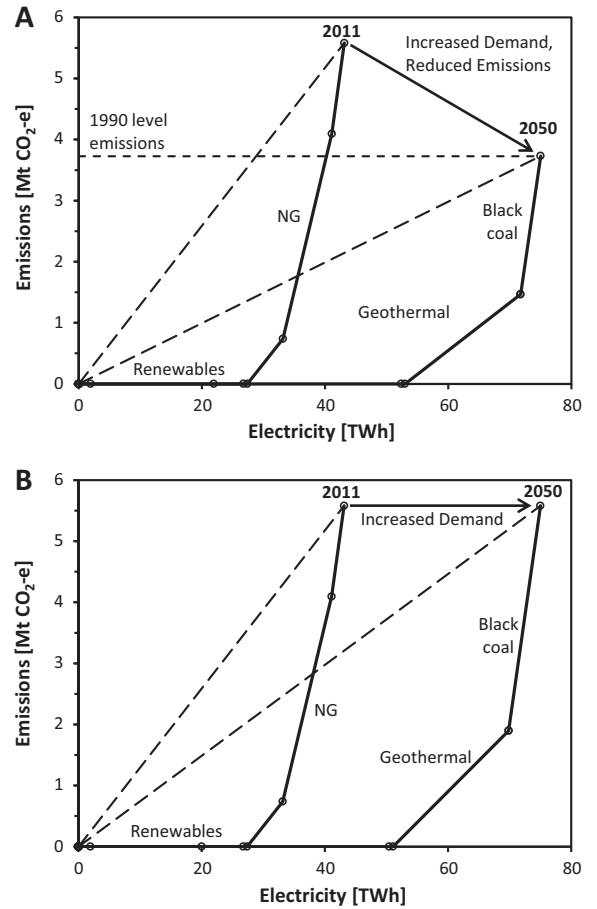


Fig. 12. Emissions composite curves to meet 2050 electricity demand for (A) 1990 and (B) 2011 emissions cap.

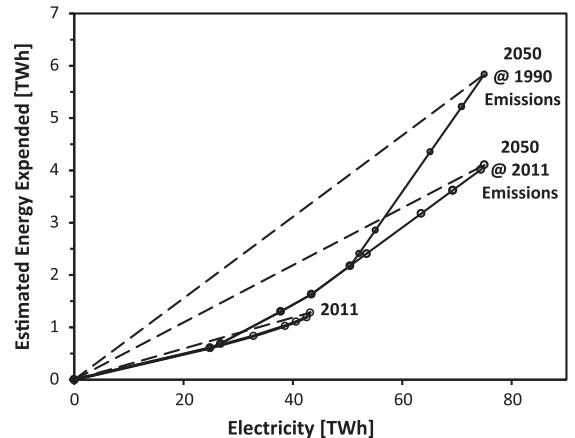


Fig. 13. Energy expended composite curves to meet 2050 electricity demand at 1990 and 2011 emissions cap.

generation mix that minimises expended energy while meeting the other constraints is likely to be the most economic option.

Optimal expansion of generation to meet the increased demand from 2011 to 2050 at 1990 emissions level would require wind to increase to 27% of total generation, hydro is 41%, geothermal is 25% and other renewables like biomass, marine or solar to increase to over 2%. A small degree of CCS is needed to capture a total of 1700 kt CO<sub>2</sub>-e to reach 1990 emissions level. Under this scenario renewable energy is maximised and CCS is applied to obtain 1990 emissions levels. For maintaining 2011 emission limits in 2050, wind, hydro and geothermal are required to increase by the same amount, and other renewables like biomass, marine or solar are not required to increase.

In Fig. 13 the increase in energy expended per unit of electricity produced as a result of emissions caps is illustrated. To meet the increased demand in 2050 the lower 1990 emissions target has a 42% higher estimated expended energy requirement compared to the higher 2011 emissions target. This is evidenced by the decrease

in the average EROI values from 2011 through to 2050 for the different generation mixes to meet the two emissions targets. With a shift away from fossil fuel generation to more renewables, lower EROI values for individual electricity generation projects than for coal have resulted.

Extending the NZ study to simultaneously account for EROI and emissions in generation selection, Fig. 14 summarises the optimised generation mix to reach the electricity target of 75 TWh for a wide range of target emission levels. The relative EROI values of each resource affects when a resource will phase into the generation mix and the range of emissions levels examined provides a sensitivity analysis for how emissions affect the generation mix. Varying EROI values for each resource will modify the results, but only if the relative EROI values change between resources.

With no emission constraint the optimal mix would have coal at 42% of total generation, geothermal at 21%, and wind (3%) and hydro also at present generation levels (33%). In the optimisation

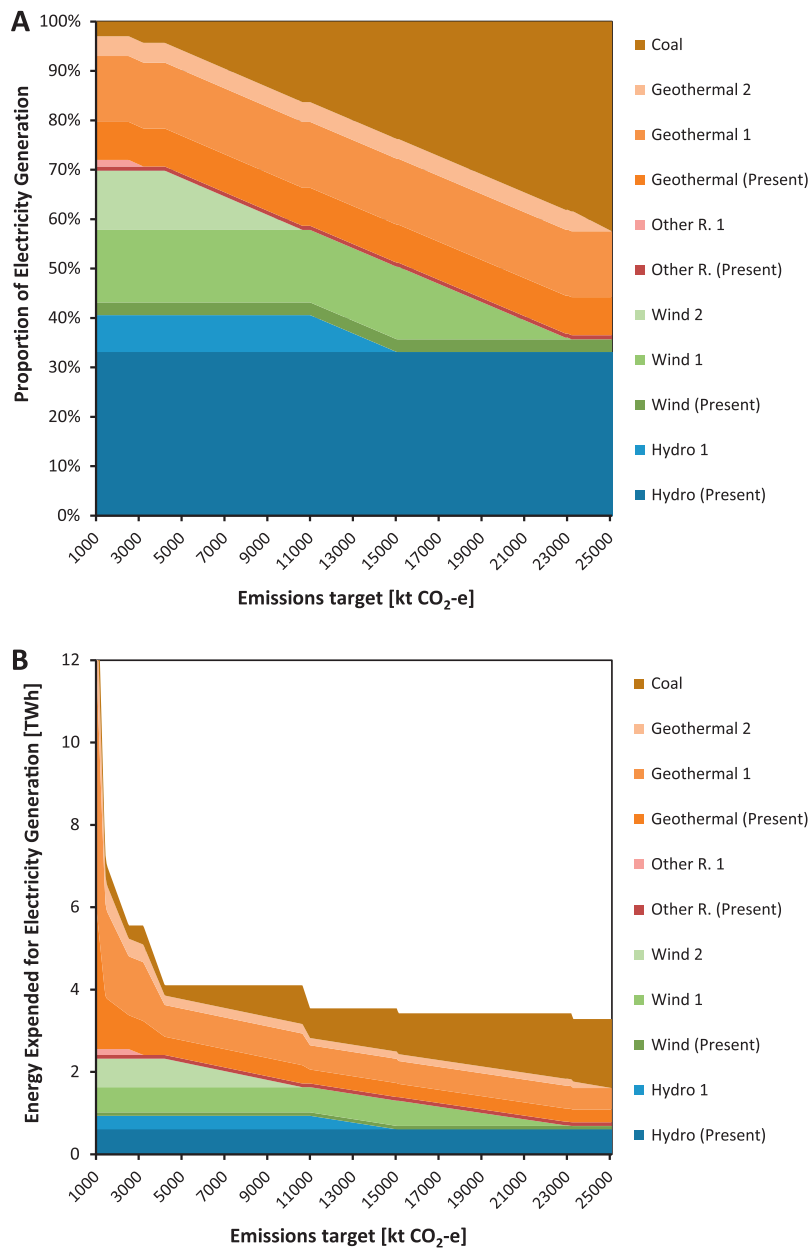


Fig. 14. Summary of (a) optimised generation mix to meet 2050 demand with (b) minimum expended energy.

NG has not been used because it is not certain that new reserves of gas will be discovered and if they are discovered it is likely the gas will be used to make liquid fuels, as liquid fuels will be the most challenging sustainability challenge for NZ once petroleum is scarce.

It is clear from Fig. 14 that NZ is in a very favourable position to maintain a very high renewable generation mix in excess of 90% without a significant energy expended penalty to the nation. With reducing emissions target from 25,000 kt CO<sub>2</sub>-e, the minimum energy expended rises gradually from 3.3 TW h to 5.6 TW h while emissions fall by 90%. Reducing from 2011 emissions to 1990 emissions cap (3730 kt CO<sub>2</sub>-e) in 2050 will come at a 4.6 TW h increase in energy expended, which is likely to also result in an increase in electricity price to the consumer in real terms of a similar percentage. However, maintaining 2011 emissions cap will require a 2.8 TW h increase in energy expended. In either case the emissions per capita for NZ will be highly favourable compared to countries less fruitful in natural energy resources.

Reducing NZ's electricity sector emissions to "zero" is progressively more challenging with the current range of generation technologies available. Marine energy has potential for large scale adoption in the future with NZ being an island country with vast marine energy resource. As marine energy technology moves beyond the technology development and early adopter stage to the large-scale commercial installation stage the EROI may improve and by 2050 some marine energy may be present in the generation mix of NZ if very low emissions are required. Growth in solar thermal is unlikely due to NZ's frequent cloudy weather which limits generation. Some biomass growth is likely but overall growth will be constrained by competing use for land and for use of biomass in sustainable materials production and biofuels.

#### 4. Conclusion

Carbon Emissions Pinch Analysis and carbon equivalent Energy Return on Energy Investment analysis are useful techniques for electricity sector emissions planning and targeting. Applying the methods to the NZ electricity sector demonstrate that renewable generation resources like wind, geothermal and hydro are favourable from both an emissions and energy return on investment point of view. For NZ to meet a 74% increase in electricity demand from 43 TW h in 2011 to 75 TW h by 2050 while maintaining renewable generation above 90%, and emission targets at 1990 levels, fossil-fuel based thermal generation will be required to reduce from 23% to less than 6% of total electricity generation, whereas wind will need to increase to 27%, geothermal to 25% and hydro to 41%. High quality renewable energy resources are available in NZ to maintain a low emissions electricity sector that maintains a 90% renewable generation mix through to at least 2050. However, the challenge of multi-criterion sustainable energy planning that harmoniously weights the factors of carbon, water, land, safety, economics and social viability, is an on-going dialogue that scientists, engineers, politicians, media and the community must engage in.

#### References

- [1] Statistics NZ. National Population Projections: 2011(base) – 2061, Statistics NZ; 2012.
- [2] Ministry of Economic Development (MED), New Zealand Energy Strategy, Ministry of Economic Development; 2008.

- [3] Ministry of Economic Development (MED), New Zealand Energy Strategy, Ministry of Economic Development; 2013.
- [4] Bardsley WE. Note on the pumped storage potential of the Onslow-Manorburn depression, New Zealand. *J Hydrol (NZ)* 2005;44:131–5.
- [5] Murphy DJ. The implications of the declining energy return on investment of oil production. *Phil Trans R Soc A* 2014;372:20130126. <http://dx.doi.org/10.1098/rsta.2013.0126>.
- [6] Bhardwaj AK, Zenone T, Jasrotia P, Robertson GP, Chen J, Hamilton SK. Water and energy footprints of bioenergy crop production on marginal lands. *GCB Bioenergy* 2011;3:208–22. <http://dx.doi.org/10.1111/j.1757-1707.2010.01074.x>.
- [7] Lovins AB. Renewable Energy's "Footprint" Myth. *Electricity J* 2011;24:40–7. <http://dx.doi.org/10.1016/j.tej.2011.06.005>.
- [8] Tan RR, Foo DCY. Pinch analysis approach to carbon-constrained energy sector planning. *Energy* 2007;32:1422–9. <http://dx.doi.org/10.1016/j.energy.2006.09.018>.
- [9] Fearnside P. Do hydroelectric dams mitigate global warming? The Case of Brazil's CuruÁ-una Dam. *Mitigation Adaptation Strategies Glob Change* 2005;10:675–91.
- [10] Foo DCY, Tan RR, Ng DKS. Carbon and footprint-constrained energy planning using cascade analysis technique. *Energy* 2008;33:1480–8. <http://dx.doi.org/10.1016/j.energy.2008.03.003>.
- [11] Lee SC, Sum Ng DK, Yee Foo DC, Tan RR. Extended pinch targeting techniques for carbon-constrained energy sector planning. *Appl Energy* 2009;86:60–7. <http://dx.doi.org/10.1016/j.apenergy.2008.04.002>.
- [12] Linnhoff B, Dhole VR. Targeting for CO<sub>2</sub> emissions for total sites. *Chem Eng Technol* 1993;16:252–9. <http://dx.doi.org/10.1002/ceat.270160407>.
- [13] Crilly D, Zhelev T. Emissions targeting and planning: an application of CO<sub>2</sub> emissions pinch analysis (CEPA) to the Irish electricity generation sector. *Energy* 2008;1498–507. <http://dx.doi.org/10.1016/j.energy.2008.05.015>.
- [14] Ooi REH, Foo DCY, Tan RR, Ng DKS, Smith R. Carbon constrained energy planning (CCEP) for sustainable power generation sector with automated targeting model. *Ind Eng Chem Res* 2013;52:9889–96. <http://dx.doi.org/10.1021/ie4005018>.
- [15] Priya GSK, Bandyopadhyay S. Emission constrained power system planning: a pinch analysis based study of Indian electricity sector. *Clean Technol Environ Policy* 2013;15:771–82. <http://dx.doi.org/10.1007/s10098-012-0541-y>.
- [16] Ooi REH, Foo DCY, Tan RR. Targeting for carbon sequestration retrofit planning in the power generation sector for multi-period problems. *Appl Energy* 2014;113:477–87. <http://dx.doi.org/10.1016/j.apenergy.2013.07.047>.
- [17] Lee J-Y, Tan RR, Chen C-L. A unified model for the deployment of carbon capture and storage. *Appl Energy* 2014;121:140–8. <http://dx.doi.org/10.1016/j.apenergy.2014.01.080>.
- [18] Atkins MJ, Morrison AS, Walmsley MRW. Carbon emissions pinch analysis (CEPA) for emissions reduction in the New Zealand electricity sector. *Appl Energy* 2010;87:982–7. <http://dx.doi.org/10.1016/j.apenergy.2009.09.002>.
- [19] Hall CAS, Cleveland CJ, Kaufmann RK. *Energy and resource quality: the ecology of the economic process*. New York, USA: Wiley; 1986.
- [20] Murphy DJ, Hall CAS. Year in review—EROI or energy return on (energy) invested. *Ann New York Acad Sci* 2010;1185:102–18. <http://dx.doi.org/10.1111/j.1749-6632.2009.05282.x>.
- [21] Mulder K, Hagens NJ. Energy return on investment: toward a consistent framework. *Ambio* 2008;37:74–9.
- [22] Brandt AR, Dale M. A general mathematical framework for calculating systems-scale efficiency of energy extraction and conversion: energy return on investment (EROI) and other energy return ratios. *Energies* 2011;4:1211–45. <http://dx.doi.org/10.3390/en4081211>.
- [23] Prieto PA, Hall CAS. *Solar power in the Spanish electricity grid: the energy returned on energy invested*. New York, London: Springer; 2011.
- [24] Gupta AK, Hall CAS. A review of the past and current state of EROI data. *Sustainability* 2011;3:1796–809. <http://dx.doi.org/10.3390/su3101796>.
- [25] Weißbach D, Ruprecht G, Huke A, Czernski K, Gottlieb S, Hussein A. Energy intensities, EROIs (energy returned on invested), and energy payback times of electricity generating power plants. *Energy* 2013;52:210–21. <http://dx.doi.org/10.1016/j.energy.2013.01.029>.
- [26] Atlason RS, Unnthorsson R. Energy return on investment of hydroelectric power generation calculated using a standardised methodology. *Renew Energy* 2014;66:364–70. <http://dx.doi.org/10.1016/j.renene.2013.12.029>.
- [27] Rao AB, Rubin ES. Identifying cost-effective CO<sub>2</sub> control levels for amine-based CO<sub>2</sub> capture systems. *Ind Eng Chem Res* 2006;45:2421–9. <http://dx.doi.org/10.1021/ie050603p>.
- [28] Rubin ES, Chen C, Rao AB. Cost and performance of fossil fuel power plants with CO<sub>2</sub> capture and storage. *Energy Policy* 2007;35:4444–54. <http://dx.doi.org/10.1016/j.enpol.2007.03.009>.
- [29] Barton B, Redgwell C, Rønne A, Zillman DN. *Energy security: managing risk in a dynamic legal and regulatory environment*. Oxford, UK: Oxford University Press; 2004.
- [30] Ball P. France's nuclear power program continues in force. *MRS Bull* 2011;36:418–21. <http://dx.doi.org/10.1557/mrs.2011.140>.
- [31] Weisser D. A guide to life-cycle greenhouse gas (GHG) emissions from electric supply technologies. *Energy* 2007;32:1543–59. <http://dx.doi.org/10.1016/j.energy.2007.01.008>.



**Article 17:**

*Carbon Emissions Pinch Analysis for emissions reductions in  
the New Zealand transport sector through to 2050*

Walmsley, M.R.W., **Walmsley, T.G.**, Atkins, M.J., Kamp, P.J.J., Neale, J.R., Chand, A., 2015.

Energy 92, Part 3, 569–576.

DOI: 10.1016/j.energy.2015.04.069

Citations: 22

Elsevier



# Carbon Emissions Pinch Analysis for emissions reductions in the New Zealand transport sector through to 2050



Michael R.W. Walmsley, Timothy G. Walmsley\*, Martin J. Atkins, Peter J.J. Kamp, James R. Neale, Alvin Chand

University of Waikato, Energy Research Centre, School of Engineering, Hamilton, New Zealand

## ARTICLE INFO

### Article history:

Received 5 December 2014

Received in revised form

22 April 2015

Accepted 25 April 2015

Available online 21 May 2015

### Keywords:

Carbon Emissions Pinch Analysis

Energy planning

Transport energy sector

## ABSTRACT

The CEPA (Carbon Emissions Pinch Analysis) method for energy planning has been modified for improved application to large transport systems. The modified method is applied to investigate the feasibility of NZ (New Zealand) reaching a 1990 emission levels for transport by 2050. The transportation sector has been traditionally a difficult area to transition to high levels of renewable energy because of the strong dependency on fossil fuels. For New Zealand, possible steps for low carbon emissions from transport are: (1) electrification of all rail, (2) wide-spread adoption of energy efficient vehicle technologies, (3) partial electrification of light passenger vehicles through plug-in hybrid and electric vehicle technologies, and (4), introduction of liquid fuels from biomass as an alternative to liquid fuels from petroleum.

© 2015 Elsevier Ltd. All rights reserved.

## 1. Introduction

Replacement of traditional oil and natural gas based transport fuels with alternatives that are both technically and economically viable and environmentally, socially and politically sustainable is a significant global issue. As transport energy demand rises, especially in developing countries, and as oil and gas reserves become increasingly difficult to find and exploit, energy companies and nations will be driven to convert unconventional energy resources, like tar sands, shale oil, agricultural crops and silviculture forests, into replacement fuels. Increased motivation to address the transports' fuel challenge is derived from the need to lower environmentally harmful emissions, such as carbon and the like emissions, and to reduce air pollution in many of the world's major cities. However converting unconventional energy resources into transport fuels, even after considerable research effort, remains a technical challenge and struggles to economically compete with oil-derived liquid fuels.

Careful energy sector planning using engineering analysis tools, such as CEPA (Carbon Emissions Pinch Analysis) [1] and EROI (Energy Return on Investment) analysis [2], is therefore needed to ensure that the inevitable transition to a low fossil fuel transport

energy sector occurs in a way that minimises the increase in cost and energy expended from the economy to meet the desired demand within the nation's carbon emissions targets. EROI is essentially the ratio of the amount of useful energy produced for society to the amount of energy that has to be expended to obtain the useful energy in the first place. Effective production of energy with high EROI values is crucial to economic growth, industrial manufacturing, employment and the general economic well-being of citizens [3]. CEPA, on the other hand, quantifies the environmental impact in terms of emissions of using energy. CEPA is a graphical method for showing how much carbon emissions are contributed from each part of an energy sector (e.g. electricity, transport) and exploring possible pathways for modifying the energy system to meet fixed emissions targets.

NZ (New Zealand) is well endowed with natural energy resources. Renewable resources such as hydro (58%), geothermal (13%), wind (4%) and biomass (<1%) accounted for 77% of electricity generation in 2011 [2]. Coal, natural gas and biomass are used for process heat and the remaining power generation demand. Imported crude oil accounts for 33.8% of NZ's primary energy needs and 99.8% of NZ's transport fuel needs [4]. NZ has a current population of 4.4 million that is anticipated to reach 5.8 million about 2050 [5]. There is strong political will within NZ for continued growth in the renewable generation sector as a strategy for reducing NZ greenhouse gas (GHG) emissions. Numerous studies

\* Corresponding author.

E-mail address: [timgw@waikato.ac.nz](mailto:timgw@waikato.ac.nz) (T.G. Walmsley).

have been commissioned by the NZ government into alternate transport fuel options for NZ in the biofuels areas [6].

There are also many other studies that are specific to other countries that are in a similar energy and resource position as NZ that may be considered when exploring solutions for NZ. For example, Mathiesen et al. [7] conclude that Denmark should use their abundant renewable electricity generation potential to directly power as much of the future transport fleet as possible. Other transport operations such as aeroplanes and ships that cannot be electrified are anticipated to use liquid fuels from biomass. As a result, they are exploring ways to increase the carbon yield of liquid fuels from biomass through the direct or indirect integration of renewable electricity in the conversion process. These ideas may have merit for countries that have the natural resources to produce large quantities of renewable electricity at reasonably high EROI ratios. Maintaining high EROI levels for transport energy will help minimise the economic and environmental effects of transitioning from fossil fuels to other energy alternatives.

The aim of this paper is to apply a modified CEPA method to explore how NZ can meet its future transport demand in 2050 while reducing the associated carbon emissions to 1990 levels. Various methods for reducing emissions are investigated including production of biofuels, electrification of the transport fleet using renewable resources, and increases in combustion engine efficiency through hybrid systems. For example, we are attempting to define such items as how much biofuels NZ needs to produce, not how much biofuels NZ can produce. There will continue to be technical and economic challenges facing the quantum of biofuels NZ requires by 2050 to help achieve 1990 levels of emissions. As a result, this paper extends the CEPA for analysis of transport sectors where the transport demand can be divided into distinct classes. CEPA has been chiefly applied to electricity sectors in NZ [8] and Ireland [9] and extended to include carbon capture and storage (CCS) [10].

## 2. A modified Carbon Emissions Pinch Analysis framework for transport sectors

CEPA was first developed by Tan, Foo, and co-workers [1], and is based on the application of traditional Pinch Analysis techniques beyond Total Site Analysis for large industrial sites to broader macro-scale applications such as regional and national electricity generation sectors [9]. Sectorial and regional studies have been conducted for power systems emissions constraint planning [11] with CCS [10] including retrofitting [12] and for multi-period scenarios [13] and variable CO<sub>2</sub> sources and CO<sub>2</sub> sinks [14]. In the New Zealand context, CEPA has been applied to the national electricity sector [8] to show how increased electricity demand in 2050 can be met and the generation mix optimised for minimum energy cost [2]. However, the method has not been applied to the transport sector as far as the authors are aware and some degree of modification to the standard method is required to extend CEPA to analysis of a transport system.

In this work the CEPA method is modified for extended application to transport sectors. An underlying tool of CEPA is the construction of composite curves together with identification of the pinch, which is often caused by an emissions target that is lower than the current emissions level. The y-axis of the composite curve graph is carbon emissions equivalent in kt CO<sub>2</sub>-e and the x-axis is the useful transport output in Mt-km, where the tonnes represent people or freight depending on the purpose of the transport operation. The demand curve represents the transport's primary purposes (e.g. freight or passenger), mode (e.g. marine, air, rail) and class (e.g. buses, ships, trains, light passenger vehicles, etc.). The supply curve captures the fuels sources (e.g. petrol, diesel,

electricity, compressed natural gas, etc.) used in the various transport operations, which are stacked beginning with the fuel with the lowest transport fuel emissions factor ( $\epsilon_{TF}$ ) and so on to the one with the highest. The transport fuel emissions factor can be determined by

$$\epsilon_{TF} = \frac{\epsilon_F}{\phi_w \eta_T} \quad (1)$$

where  $\epsilon_F$  is fuel emissions factor in kt CO<sub>2</sub>-e/MJ,  $\phi_w$  is the ratio of useful transport weight to gross vehicle weight in Mt/Mt<sub>gross</sub> and  $\eta_T$  is the gross transport output efficiency in (Mt<sub>gross</sub>-km)/MJ.  $\epsilon_F$  is dependent on the fuel and is not affected by the transport method.  $\phi_w$  is a function of the transport method and its fill-rate.  $\eta_T$  mainly relates to the engine efficiency and its aero- and/or hydro-dynamics.

A generic example of a transport system is presented in Fig. 1 to demonstrate how the CEPA method may be modified for transport systems. Fig. 1A is the conventional CEPA style plot that presents the overall fuel supply and transport demand with an associated emissions of 1000 kt CO<sub>2</sub>-e. The solid black line is the average  $\epsilon_{TF}$  for the entire system and called the overall Transport Emissions Factor (TEF). The new emissions target represents a 20% reduction goal of transport emissions. The point where the dotted diagonal line, which is based on the emissions target, intersects the fuel supply curve is the pinch point.

When considering how to achieve the emissions target, the overall CEPA graph lacks sufficient detail about transport modes and classes to base decisions of where emissions reduction efforts are best focused. The overall transport demand can be broken-down into the individual transport classes with as shown in Fig. 1B. Combinations of transport classes and fuels that contribute a high proportion of the total emissions can now be identified and emissions reductions methods considered. Two options for emissions reduction are presented in Fig. 1C and D. The first option targets improving transport fuel efficiency of class B with fuel C. An example of this option is increasing public transport fill-rates by encouraging their use through measures such as increasing Government subsidies or, in the long-term, market driven increases in petrol prices. The second option switches some of fuel C for A within class B. An example of this can be electrification of the rail network, where electricity is generated using a high proportion of renewables (e.g. hydro). There are many other situational options for reducing emissions such as switching transport classes, which also can be considered.

It is also useful to plot the transport data on an emission versus fuel use in PJ to understand the impact various emissions reduction options have on total fuel use.

## 3. Transport efficiencies and fuel emissions factors

There are a wide variety of transport modes (e.g. marine, air, road, and rail) and many classes of vehicles or vessels within these modes. For example, within the road transport mode there are light trucks, heavy trucks, and light commercial vehicles. Within these classes, there are further subclasses of specific vehicle or vessel makes and models made to common specification and/or performance.

At the vehicle class level, transport fuel use, emissions and useful transport output can be calculated with a reasonable degree of accuracy using the numerous data available from government agencies. This study uses transport data published by the NZ Ministry of Transport [15] and the Ministry of Business, Innovation and Employment [5] and literature values of average transport fuel efficiencies in passenger-km/L and t-km/L [16], which are

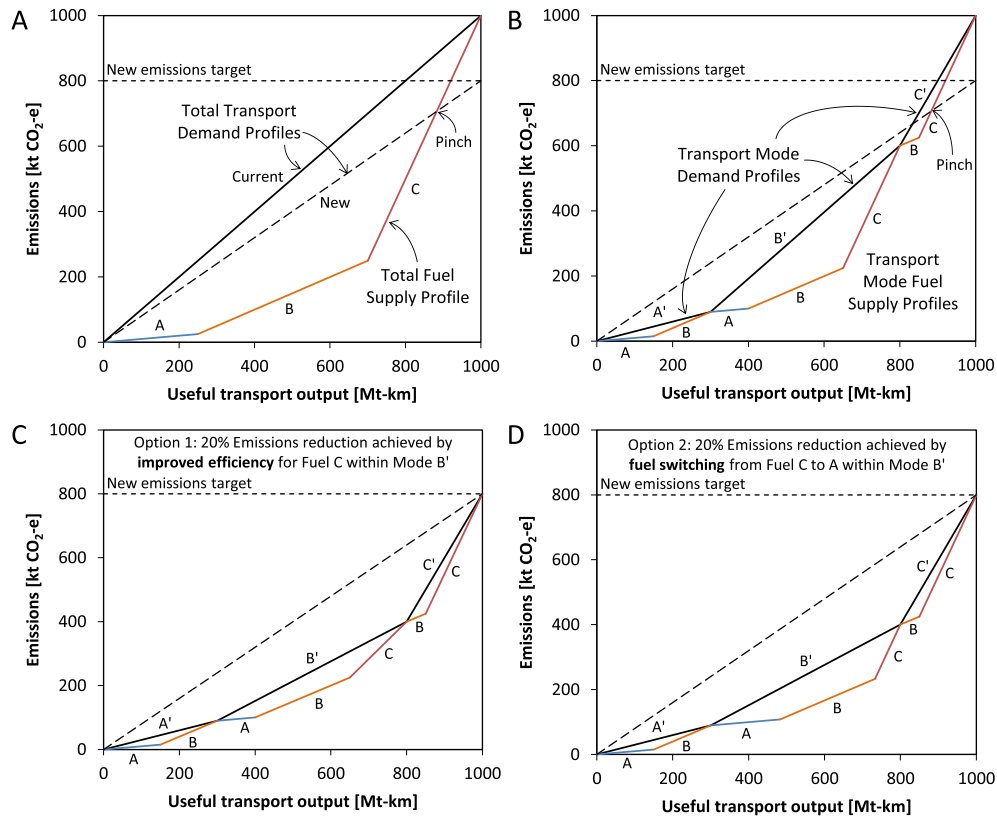


**Fig. 1.** Methods for reducing emissions of a generic transport sector. (A) Total transport demand and fuel supply curves; (B) supply and demand profiles divided by transport classes; and (C and D) two options for reducing emission.

compared in Fig. 2A for passenger transport and Fig. 2B for freight transport. A log scale has been used to enable presentation of a wide range of transport modes on a single graph. Public transport methods like ferry, bus and rail potentially have good efficiencies provided passenger fill rates are high. Fill-rates for NZ's public transport are low likely due to the comparatively low population density of NZ cities. Freight transport exhibits similar trends (Fig. 2B) with ship and rail being the most efficient methods, followed by heavy and light truck, and air. LCV (Light Commercial Vehicles) is less energy efficient transport mode but most convenient.

Transport class emission factors used in this study were calculated based on data from NZ's Ministry of Business, Innovation and Employment energy data set [5] and are presented in Table 1. Useful transport output for passengers has been calculated by assuming passengers have an average mass of 75 kg.

#### 4. New Zealand transport sector fuel and emissions growth projections

The NZ transport sector has experienced significant growth in fuel demand from 1974 to 2008 as illustrated in Fig. 3. Petrol and diesel fuels dominate the growth in fuel use, followed by aviation fuels. Fuel oil declined in the 1980s and again increased in the 1990s. Responses to global recessions, oil price hikes and/or periods of economic restructuring are also evident in the fuel use data. As global oil prices rose in the late 1970s, economies like NZ were forced to spend more on foreign imported oil, which affected their balance of trade, which in turn forced other changes on the economy. The economic restructuring that took place in NZ in the 1980s was in many ways precipitated by the oil crisis of 1979.

The large increase in diesel fuel use and to a lesser extent petrol fuel use, as is seen in Fig. 3, is related to the large increase in LPVs (light passenger vehicle) and LCVs (light commercial vehicle) that occurred during the 1990s and beyond when import regulations were relaxed in the early 1990s, along with road freight transport rules. Light vehicle numbers soared, especially diesel powered vehicles, and imported second-hand vans and trucks increased the overall freight transport supply at the expense of any growth in rail (Fig. 4A).

The contribution of each transport mode to fuel use and emissions from 1990 to 2012 is illustrated in Fig. 4. As discussed previously, road transport has dominated the growth in both fuel use and emissions. International air and international marine have also risen most likely as a result of global tourism increases. Domestic air, domestic marine and rail, have experienced only small increases. Significantly, about half of the international transport emissions are not formally included in NZ's emissions for this study. Only trips that fuel and begin in NZ, e.g. departing international flight, are counted.

Since 2005 annual growth has slowed with negative growth in 2009 after the start of the global recession in 2008. Growth rates are expected to return to traditional levels from 2013 due to a rising population with continued reliance on fossil fuels for transport (Fig. 5). The current population of 4.4 million is rising because of positive net migration and a higher than replacement birth rate of 2.1 [17]. It is projected by Statistics NZ, the country's population is most likely to peak between 6 and 7 million after 2050. The increase in population will put pressure on energy, land and water resources.

For this study we have taken a conservative 'business-as-usual' approach and assumed passenger and freight transport demand

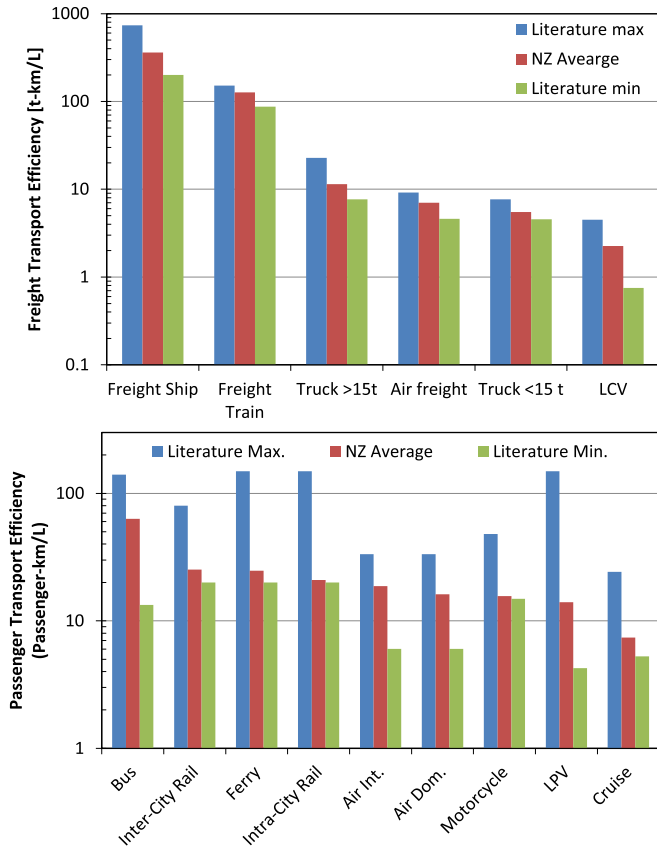


Fig. 2. Freight (top) and passenger (bottom) transport efficiency by transport mode and class for NZ transport [5,15] compared to literature values [16].

will increase proportional with population through to 2050. This gives 2050 targets for CEPA of 107 G(passenger)-km for passenger transport demand and 126 Gt-km for freight transport demand, which equates to approximately 326 PJ of fuel use. Beyond population, transport demand is also closely tied to national and global economic states and the oil price, both of which have seen dramatic fluctuations over the past decade. Between the 1990 and 2005 transport demand per capita in terms of both freight and passenger

Table 1  
Transport fuel emissions factors for fossil fuel energy supply.

Type	Class	$\epsilon_{FT}$ [t CO <sub>2</sub> -e/Gt-km]
<i>Freight transport</i>		
Marine	Cargo ships domestic	9
Marine	Cargo ships international	11
Rail	Freight	18
Road	Truck B (>15 t)	200
Air	Freight	372
Road	Truck A (<15 t)	414
Road	Light commercial vehicles (LCV)	1013
<i>Passenger transport</i>		
Marine	Ferry	21
Marine	Cruise ships international	137
Marine	Cruise ships domestic	137
Road	Bus	452
Rail	Commuter inter-city	902
Air	International (passenger + cargo)	936
Air	Domestic (passenger + cargo)	1327
Rail	Commuter intra-city	1361
Road	Motor cycle	1950
Road	Light passenger vehicles (LPV)	2177

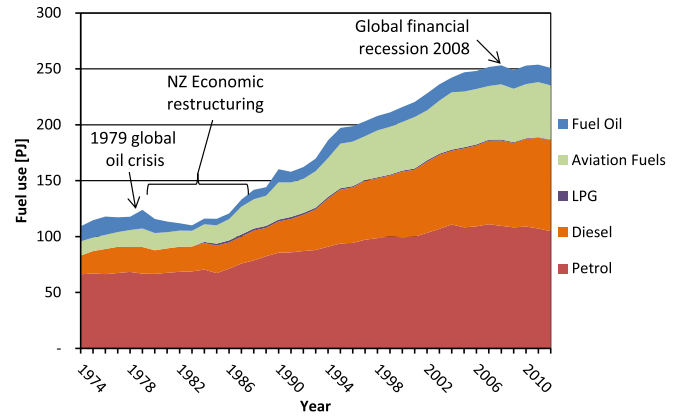


Fig. 3. Transport fuel growth in NZ by fuel type from 1974 to 2013. Data taken from the NZ Ministry of Transport [15].

transport increased by 29% and 25% respectively. From 2005 to 2012 the global financial crisis hit reducing freight and passenger transport demands per capita by 13% and 5% respectively. The future projections of transport demand have therefore a significant degree of uncertainty because of the several forces that come into play that influence total transport demand.

## 5. Results and discussion for New Zealand transport case study

### 5.1. Carbon Emissions Pinch Analysis for the New Zealand transport sector in 2012

Using the CEPA composite curve method the freight and passenger transport demands in NZ for the year 2012 are illustrated in Fig. 6. The fuel supply composite curve has not been included in Fig. 6 because it cannot clearly be distinguished from the demand curve, which is due to all current transport fuels being derived from crude oil with very similar EFs (Emissions Factor) within each vehicle class. Fig. 6 shows passenger transport contributes 12% of the useful transport output but is responsible for 71% of transport emissions. The total freight transport demand and emissions for NZ in 2012 were 95.9 Mt-km and 5.0 Mt CO<sub>2</sub>-e respectively (TEF = 0.052 Mt CO<sub>2</sub>-e/Mt-km). The total passenger transport demand and emissions for NZ were 13.1 Gt-km and 12.4 Mt CO<sub>2</sub>-e respectively (TEF = 0.944 Mt CO<sub>2</sub>-e/Mt-km). In both cases the amount powered from renewable fuels was negligible.

EFs vary depending on the freight or passenger load factor, engine technology and tare weight differences rather than fuel differences. Marine transport is clearly very efficient at transporting both freight and people with marine vessels having the lowest emission factors in both demand classes. Freight rail is equally a low emissions transport method and road freight methods are the highest. It is important to note that although road freight methods have the highest emissions factors, they have additional cost benefits of being flexible giving point-to-point delivery with minimal handling stages.

With passenger transport, LPV (Light Passenger Vehicles) stands out as generating 65% of passenger transport emissions, while delivering only 28% of the useful transport output. High EFs for rail and bus are principally caused by low participation rates as a result of high LPV use, and as a result the useful transport output from these classes is relatively small. Air transport, including domestic and international travel, contributes 27% of passenger transport emissions and provides 25% of the useful transport output.

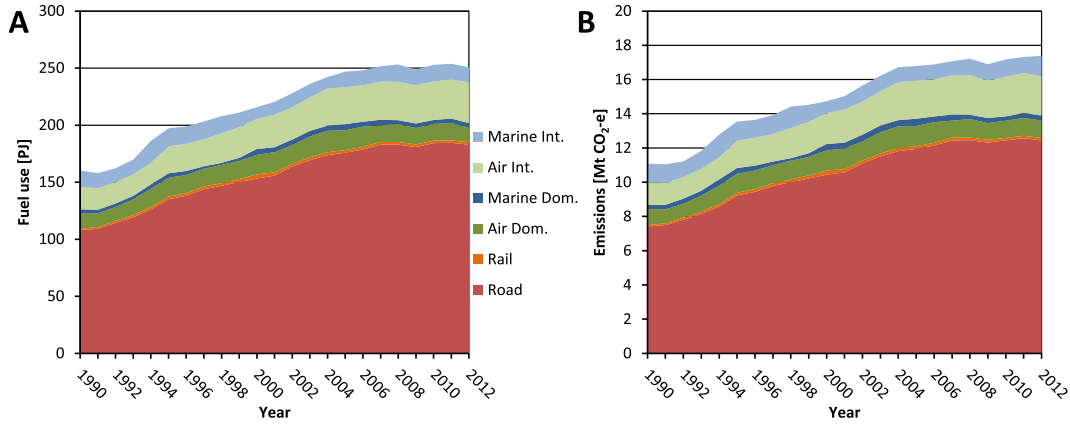


Fig. 4. Transport fuel (A) and emissions (B) in NZ growth by transport mode from 1990 to 2012. Data taken from the NZ Ministry of Transport [15].

5.2. Approaches to reducing CO<sub>2</sub>-e emissions in transport energy sectors

5.2.1. Renewable liquid fuel production

Globally liquid fuels for transport vehicles are nearly exclusive refined from crude oil. This refining process and the eventually fuel combustion emits a substantial amount of emissions. Producing drop-in liquid biofuels from sustainably grown biomass resources can begin to replace oil based fuels in the future when oil reserves are sufficiently low and the price of oil high enough for the economics of biofuel production to be economic. In 2009 Jack and Hall [18] reported a detailed analysis of the potential biofuel production in NZ showing where and how much new afforestation may occur. Their results indicate that with the use of an additional 1.8 million hectares of low productivity land, currently returning less than NZ\$200/(ha y) mainly for sheep and beef farming, to produce woody biomass at a similar return rate, NZ could produce up to 232 PJ or 7.0 billion litres of petrol equivalent biofuel and could be economically competitive with conventional liquid fuels at an oil price of around US\$200 per barrel. Most biofuel conversion technologies are currently in the pre-commercialisation stage and, therefore, the efficiency of biofuel production and its cost competitiveness and rate of return for land use is likely to improve in the future.

5.2.2. Improved vehicle transport fuel efficiency

In the last decade the fuel efficiency of LPVs, LCVs and buses has been significantly improved by hybrid engine technology. HVs (hybrid vehicles) intelligently use a battery and electric motor in conjunction with a combustion engine to achieve high fuel efficiency. Based on data from the NZ Ministry of Transport [15], an estimate of 40% reduction in fuel use can be obtained when switching from a normal combustion engine vehicle to a hybrid vehicle for the same total distance travelled under normal use. With rising fuel prices, it is anticipated that at least half of the LPVs, LCVs and Buses will contain some form of hybrid engine by 2050.

5.2.3. Increased integration of electricity in transport vehicles

Integration of electricity into the transport sector has traditionally focused on the electrification of rail. New Zealand has some opportunities to convert fossil fuel driven rail to electric rail and for purposes of this study it is assumed that by 2050 conversion has taken place. Beyond electrification of rail, there is growing popularity around the future adoption of EV (electric vehicles). Some organisations [19] and politicians [20] have campaigned on the misleading notion that EVs have zero emissions. In this section it is shown the actual emissions from an EV over its life are dependent on the weight of the car and battery, and the overall GEF (Grid

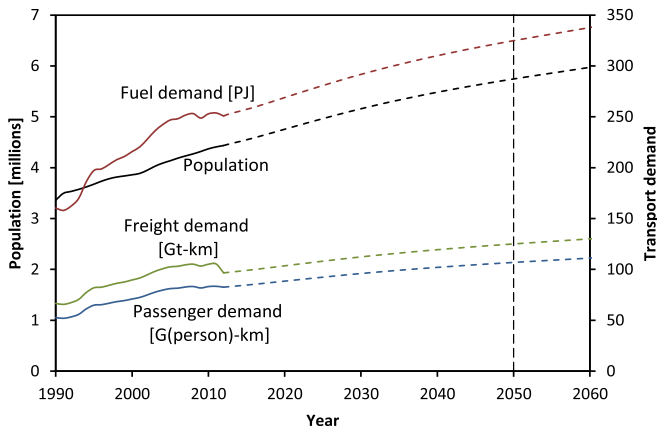


Fig. 5. Projected population and transport demand growth in NZ to 2050 for business as usual.

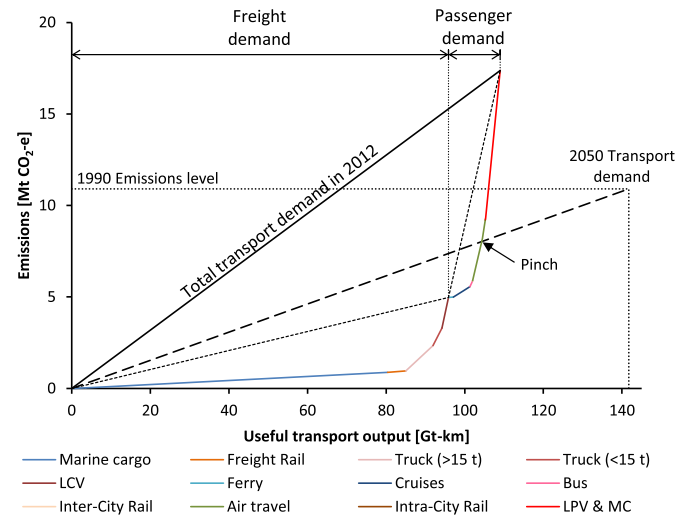


Fig. 6. Combined emissions composite curve for freight and passenger transport demand by transport purpose and class in New Zealand for 2012 and the target for 2050.

**Table 2**  
Estimated emission factors for three light passenger vehicles.

	Embedded car emissions <sup>a</sup> [kt CO <sub>2</sub> -e]	Embedded battery emissions <sup>b</sup> [kt CO <sub>2</sub> -e]	Fuel consumption	Operating emissions factor <sup>c</sup> [kt CO <sub>2</sub> -e/100 km]	Life cycle emissions factor [kt CO <sub>2</sub> -e/100 km]	Operating & battery emissions factor [kt CO <sub>2</sub> -e/100 km]
ICE (internal combustion engine)	7500	–	0.072 L/km	17.57	21.32	17.57
P-HV (plug-in hybrid vehicle)	7500	1800	0.0214 L/km 0.20 kWh/km	5.74	10.39	6.64
EV (electric vehicle)	7800	8100	0.24 kWh/km	1.16	9.11	5.36

<sup>a</sup> Based on 5 kg CO<sub>2</sub>-e/kg<sub>car</sub>.

<sup>b</sup> Based on 15 kg CO<sub>2</sub>-e/kg<sub>bat</sub>.

<sup>c</sup> Based on NZ 2050 GEF 0.049 kg CO<sub>2</sub>-e/kWh, 50% EV mode for P-HV, Petrol EF 2.44 kg CO<sub>2</sub>-e/L.

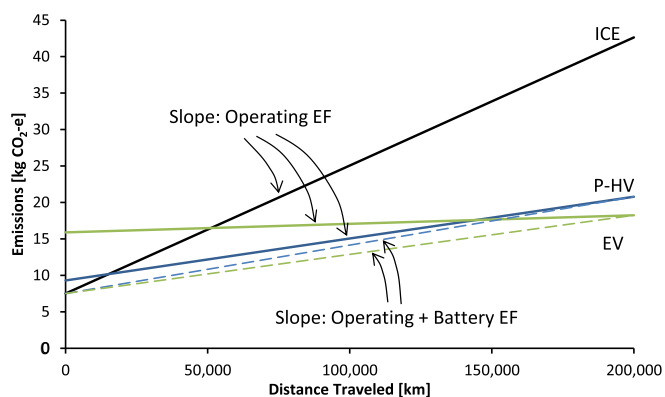


**Fig. 7.** Emissions for LPVs based on the 2050 estimated electricity GEF for NZ (0.049 kg CO<sub>2</sub>-e/kWh).

Emissions Factor) for electricity production in a given country. Where it means that additional coal will be burned to supply electricity to an EV, the overall emissions will be greater than the typical petrol engine car.

It is important when considering alternate LPVs that the life-cycle GHG emissions are included, especially for EVs where increased emissions occur with the manufacture and replacement of the batteries. As the range of the vehicle in electric mode increases the mass of the battery must become greater. There is a large variation in the reported GHG emissions of battery manufacture from 6 kg CO<sub>2</sub>-e/kg<sub>bat</sub> [21] to 22 kg CO<sub>2</sub>-e/kg<sub>bat</sub> [22]. The variation is due in part to the different assumptions and system boundaries used in the LCA (Life Cycle Analysis) studies. A value of 15 kg CO<sub>2</sub>-e/kg<sub>bat</sub> has been used in this study. The GHG emissions associated with the production of the car is assumed to be 5 kg CO<sub>2</sub>-e/kg<sub>car</sub> and is within the range of 4–6.5 kg CO<sub>2</sub>-e/kg<sub>car</sub> reported in the literature [23]. The extra battery emissions will normally be attributed to the country that makes the batteries, but in this analysis these emissions have been included as an operating and battery emissions factor (Table 2).

The emissions as a function of distance for ICE (Internal Combustion Engine) vehicles, P-HV (plug-in hybrids vehicles), and EV (Electric Vehicles) are presented in Fig. 7 based on the 2050 GEF of

0.049 kt CO<sub>2</sub>-e/GWh<sub>e</sub> [2]. The various EFs used to construct Fig. 7 are given in Table 2. The slopes of the solid lines represent the operating EF for each vehicle type. The dashed lines in the figure represent the operating and amortised battery emissions for P-HV and EV, and is used to determine the actual GHG reductions possible by switching from ICE to P-HV and EV. The total reduction in GHG emissions over the total life of the vehicle is 49% and 43% for P-HV and EV respectively. The EV has greater final overall emissions than the P-HV due to the significant increase in the emissions associated with the manufacture and replacement of the batteries. The overall lifecycle contribution of the fuel decreases as vehicles become more electrified. The fuel contribution for the ICE is 82%, while the P-HV and EV have fuel contributions of 55% and 13% respectively.

The slope of the EV line in Fig. 7 is derived from the GEF for electricity production. As the GEF increases, the slope of the EV (and P-HV) line also increases. For countries where the GEF is greater than 0.566 kt CO<sub>2</sub>-e/GWh<sub>e</sub>, the adoption of EVs is counter-productive in terms of reducing overall emissions. At present New Zealand has a GEF for electricity of 0.129 kt CO<sub>2</sub>-e/GWh<sub>e</sub>, Australia has a GEF of 0.811 kt CO<sub>2</sub>-e/GWh<sub>e</sub>, and the USA has a GEF of 0.530 kt CO<sub>2</sub>-e/GWh<sub>e</sub> [2]. Converting significant proportions of the electricity grids in Australia and the USA to renewables (e.g. wind and solar) and/or low carbon emitting fuels and generation technologies (e.g. nuclear power plant and coal power plant with CCS) are needed before EVs present themselves as a viable solution to reducing carbon emissions.

#### 5.2.4. Government policy and intervention

Governments play a critical role in setting policies that encourage the use of more efficient transport methods. New Zealand can learn from methods being employed in other countries as a guide to what implemented government policies are effective for driving good behaviour and lowering transport emissions. For example, many highways in the USA and other countries have car-pool lanes dedicated to high occupancy vehicles (usually two or more people in a vehicle), which aims to increase the fill rate of on-road LPVs. Dedicated bus lanes in inner cities and/or adjacent to highways are also common in major cities as a way to improve the travel time on public buses, which also leads to increased fill rates. In Hasselt, Belgium the city council decided to abolish bus fares in 1997 [24]. This resulted in the number of travellers on buses

**Table 3**  
Options for NZ to meet 1990 emissions level in 2050. Energy units PJ use a thermal basis.

	P-HV and EV fuel savings	Fuel replaced by electrification	Oil and gas fuels	F-T coal	Biofuels needed
Scenario A	77 PJ	49 PJ (5.4 TWh <sub>e</sub> )	155 PJ	–	47 PJ
Scenario B	77 PJ	49 PJ (5.4 TWh <sub>e</sub> )	–	–	169 PJ
Scenario C	–	26 PJ (2.9 TWh <sub>e</sub> )	–	31 PJ	106 PJ

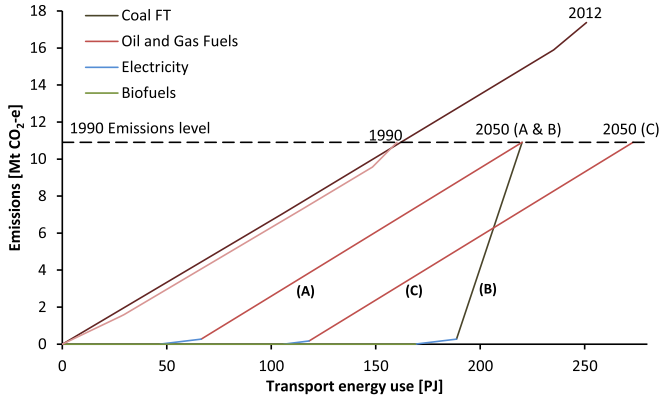


Fig. 8. Emissions – transport energy use composite curves to meet 2050 over all transport demand for a 1990 emissions target.

increasing from 350,000 in 1997 to 4,600,000 in 2007. In 2013, the city revisited the policy and under the weight of an on-going financial recession reverted to charging adults (19 + years) €0.60 per trip. Establishing safe cycle ways is another approach targeted towards reducing the number of single passenger cars on the road. California introduced an effective financial incentive programme to encourage the uptake of P-HVs.

5.3. Transport planning for New Zealand through to 2050 with reduced carbon emissions

Three scenarios are illustrated in Table 3 and Fig. 8 for achieving transport emissions reduction to 1990 levels by 2050 using the CEPA graphical method. A variety of transport fuel mixes are possible for reaching the demand and emissions target.

In Scenarios A and B, it is assumed 40% of the LPV, LCV and bus fleets will be hybrid vehicles, which improves the overall energy efficiency of these classes and results in a fuel savings 77 PJ. Scenarios A and B also assume P-HVs and, to a lesser extent, EVs in the LPV class (~40%) will enable replacement of 46 PJ of liquid fuels with 18 PJ (5.1 TWh) of electricity use. Freight and city rail is also electrified replacing a thermal fuel need of 2.9 PJ with 1 PJ (0.3 TWh) of electricity use. An increase in demand of 5.4 TWh is

equivalent to 7.3% of estimates of the NZ electricity grid (75 TWh) in 2050 [2]. The 2050 electricity demand projection from Walmsley et al. [2] of 75 TWh assumed an uptake of electric powered vehicles of 6.5 TWh, which is close to the estimate in this work. The remainder of the transport demand for Scenarios A is met using oil derived fuels of 155 PJ and the minimum amount of biofuels of 47 PJ that is required to keep within the emissions target based on 1990 levels. In Scenario B, the remainder of the transport demand is met using Fischer–Tropsch (FT) liquid fuels from coal (31 PJ) and biofuels (169 PJ) while keeping under the emissions target. Scenario C is the same as A with the exception of assuming a 20% uptake of HVs, P-HVs, and EVs in the LPV, LCV and bus fleets, which means the energy savings is half the amount that was originally quantified. The lower uptake of energy efficiency technologies means an additional 53 PJ of input energy is needed in Scenario C compared to the first two scenarios (Fig. 8). As a result, the minimum required biofuel production to keep within the emissions target is 106 PJ.

The anticipated transport supply and demand profiles for freight and passenger transport from Scenario A in 2050 are plotted in Fig. 9. Where a transport mode and class requires a liquid fuel, a blended fuel is assumed and its emissions are determined using a weighted emissions factor (53.5 kt CO<sub>2</sub>-e/PJ) for renewable biofuel (zero emissions) and liquid fuel from oil (69.3 kt CO<sub>2</sub>-e/PJ). LPVs benefit significantly from increased overall efficiency from the uptake of hybrid systems and from the integration of electricity as a main power source.

The presented scenarios assume that existing transport modes continue to be used in a similar manner and similar amount per capita as in 2012. Further emissions reduction can be achieved with further transport class switching; for example, more freight by rail and marine rather than truck and LCV and more public transport by light rail and bus, especially in NZ’s largest cities, i.e. Auckland, Wellington, Christchurch and Hamilton. The challenge of meeting the 1990 emissions level in 2050 critically depends on the uptake of energy efficient vehicles and production of biofuels. This needs to be done with the minimum amount of extra energy being expended by the economy to ensure that the transition to a new fuel source does not reduce NZ’s economic competitiveness.

6. Conclusion

Freight and passenger transport demand in New Zealand is anticipated to increase by 30% from 2012 to 2050 due to population growth. An important element of reducing carbon emissions attributed to transport in New Zealand is electrification of all rail and partial electrification of light passenger vehicles through plug-in hybrid and electric vehicle technologies to the degree of 5.4 TWh<sub>e</sub>, which replaces the equivalent of 49 PJ of conventional liquid fuels. New Zealand’s electricity is supplied by a high proportion of hydro and geothermal renewable generation, which in turn can help lower emissions from the transport sector when effectively integrated. With an uptake of 40% for all light passenger vehicles, buses and light commercial vehicles, hybrid engine technology is estimated to reduce liquid fuel use by 77 PJ in 2050 compared to using current transport technologies. In 2050 total transport energy use as a combination of liquid fuels and electricity is calculated to be 220 PJ. To reach the goal of reducing carbon emissions to 1990 levels in 2050, 47 PJ of biofuels is needed together with 174 PJ of conventional liquid fuels from oil.

References

[1] Tan RR, Foo DCY. Pinch analysis approach to carbon-constrained energy sector planning. Energy 2007;32:1422–9. <http://dx.doi.org/10.1016/j.energy.2006.09.018>.

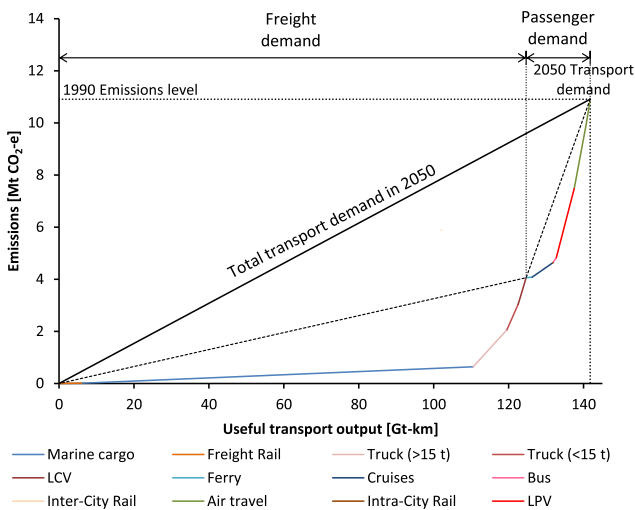


Fig. 9. Combined emissions composite curve for freight and passenger transport supply and demand in New Zealand for 2050 Scenario A, i.e. minimum biofuels production.

- [2] Walmsley MRW, Walmsley TG, Atkins MJ, Kamp PJJ, Neale JR. Minimising carbon emissions and energy expended for electricity generation in New Zealand through to 2050. *Appl Energy* 2014;135:656–65. <http://dx.doi.org/10.1016/j.apenergy.2014.04.048>.
- [3] Hall CAS, Balogh S, Murphy DJR. What is the minimum EROI that a sustainable society must have? *Energies* 2009;2:25–47. <http://dx.doi.org/10.3390/en20100025>.
- [4] MBE. Energy balances. *Minist. Bus. Innov. Employ.*; 2012. <http://www.med.govt.nz/sectors-industries/energy/energy-modelling/data/energy-balances> [accessed 22.05.14].
- [5] Statistics NZ. New Zealand's growing population. *NZ Off Yearb* 2012 2013. [http://www.stats.govt.nz/browse\\_for\\_stats/snapshots-of-nz/yearbook/people/population/7-million.aspx](http://www.stats.govt.nz/browse_for_stats/snapshots-of-nz/yearbook/people/population/7-million.aspx) [accessed 22.05.14].
- [6] Taylor M. Alternative liquid fuels: global availability, economics and environmental impacts. Auckland, New Zealand: EME Consulting; 2007. <http://www.med.govt.nz/sectors-industries/energy/pdf-docs-library/energy-data-and-modelling/technical-papers/alternative-liquid-fuels.pdf> [accessed 22.05.14].
- [7] Mathiesen BV, Lund H, Connolly D, Østergaard PA, Möller B. The design of smart energy systems for 100% renewable energy and transport solutions. [http://vbn.aau.dk/en/publications/the-design-of-smart-energy-systems-for-100-renewable-energy-and-transport-solutions\(5d61152c-f511-48eb-bc0f-a490275fba9c\).html](http://vbn.aau.dk/en/publications/the-design-of-smart-energy-systems-for-100-renewable-energy-and-transport-solutions(5d61152c-f511-48eb-bc0f-a490275fba9c).html); 2013 [accessed 04.12.14].
- [8] Atkins MJ, Morrison AS, Walmsley MRW. Carbon emissions pinch analysis (CEPA) for emissions reduction in the New Zealand electricity sector. *Appl Energy* 2010;87:982–7. <http://dx.doi.org/10.1016/j.apenergy.2009.09.002>.
- [9] Crilly D, Zhelev T. Emissions targeting and planning: an application of CO<sub>2</sub> emissions pinch analysis (CEPA) to the Irish electricity generation sector. *Energy* 2008;1498–507. <http://dx.doi.org/10.1016/j.energy.2008.05.015>.
- [10] Ooi REH, Foo DCY, Tan RR, Ng DKS, Smith R. Carbon constrained energy planning (CCEP) for sustainable power generation sector with automated targeting model. *Ind Eng Chem Res* 2013;52:9889–96. <http://dx.doi.org/10.1021/ie4005018>.
- [11] Priya GSK, Bandyopadhyay S. Emission constrained power system planning: a pinch analysis based study of Indian electricity sector. *Clean Technol Environ Policy* 2013;15:771–82. <http://dx.doi.org/10.1007/s10098-012-0541-y>.
- [12] Priya GSK, Bandyopadhyay S, Tan RR. Power system planning with emission constraints: effects of CCS retrofitting. *Process Saf Environ Prot* 2014;92:447–55. <http://dx.doi.org/10.1016/j.psep.2014.02.010>.
- [13] Ooi REH, Foo DCY, Tan RR. Targeting for carbon sequestration retrofit planning in the power generation sector for multi-period problems. *Appl Energy* 2014;113:477–87. <http://dx.doi.org/10.1016/j.apenergy.2013.07.047>.
- [14] Lee J-Y, Tan RR, Chen C-L. A unified model for the deployment of carbon capture and storage. *Appl Energy* 2014;121:140–8. <http://dx.doi.org/10.1016/j.apenergy.2014.01.080>.
- [15] Ministry of Transport. New Zealand vehicle fleet statistics. *NZ Veh Fleet Stat* 2014. <http://www.transport.govt.nz/research/newzealandvehiclefleetstatistics/> [accessed 22.05.14].
- [16] US Department of Energy. Transportation energy data book. 2013. <http://cta.ornl.gov/data/index.shtml> [accessed 22.05.14].
- [17] Statistics NZ. National population projections: 2011(base) – 2061. *Stat NZ* 2012. [http://www.stats.govt.nz/browse\\_for\\_stats/population/estimates\\_and\\_projections/NationalPopulationProjections\\_HOTP2011/Commentary.aspx](http://www.stats.govt.nz/browse_for_stats/population/estimates_and_projections/NationalPopulationProjections_HOTP2011/Commentary.aspx) [accessed 10.12.13].
- [18] Jack M, Hall P. Bioenergy options for New Zealand: analysis of large-scale bioenergy from forestry. Rotorua, New Zealand: Scion; 2009.
- [19] Emissions Free Cars. All the benefits of electric vehicles. *Emiss. Free Cars*; 2014. <http://emissionsfreecars.com/> [accessed 22.05.14].
- [20] Clegern D. Governors announce bold initiative to put 3.3 million zero-emission vehicles on the road by 2025. *Calif. Environmental Prot. Agency*; 2013. <http://www.arb.ca.gov/newsrel/newsrelease.php?id=520> [accessed 22.05.14].
- [21] Notter DA, Gauch M, Widmer R, Wäger P, Stamp A, Zah R, et al. Contribution of Li-ion batteries to the environmental impact of electric vehicles. *Environ Sci Technol* 2010;44:6550–6. <http://dx.doi.org/10.1021/es903729a>.
- [22] Majeau-Bettez G, Hawkins TR, Strømman AH. Life cycle environmental assessment of lithium-ion and nickel metal hydride batteries for plug-in hybrid and battery electric vehicles. *Environ Sci Technol* 2011;45:4548–54. <http://dx.doi.org/10.1021/es103607c>.
- [23] Hawkins TR, Singh B, Majeau-Bettez G, Strømman AH. Comparative environmental life cycle assessment of conventional and electric vehicles. *J Ind Ecol* 2013;17:53–64. <http://dx.doi.org/10.1111/j.1530-9290.2012.00532.x>.
- [24] Eltis. Hasselt cancels free public transport after 16 years (Belgium). *Eltis*; 2013. [http://www.eltis.org/index.php?ID1=5&id=60&news\\_id=4183](http://www.eltis.org/index.php?ID1=5&id=60&news_id=4183) [accessed 22.05.14].



**Article 18:**

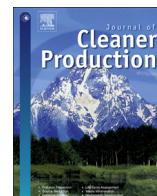
*Energy Return on energy and carbon investment of wind  
energy farms: A case study of New Zealand*

**Walmsley, T.G.**, Walmsley, M.R.W., Atkins, M.J., 2017.

Journal of Cleaner Production 167, 885-895.

DOI: 10.1016/j.jclepro.2017.08.040

Elsevier



# Energy Return on energy and carbon investment of wind energy farms: A case study of New Zealand



Timothy G. Walmsley<sup>a,\*</sup>, Michael R.W. Walmsley<sup>b</sup>, Martin J. Atkins<sup>b</sup>

<sup>a</sup> Sustainable Process Integration Laboratory – SPIL, NETME Centre, Faculty of Mechanical Engineering, Brno University of Technology, Brno, Czech Republic

<sup>b</sup> Energy Research Centre, School of Engineering, University of Waikato, Hamilton, New Zealand

## ARTICLE INFO

### Article history:

Received 12 May 2017

Received in revised form

11 July 2017

Accepted 5 August 2017

Available online 5 August 2017

Handling Editor: Yutao Wang

### Keywords:

Wind energy

Energy ratio analysis

Energy Return on Investment

Life Cycle Analysis

Energy planning

Carbon footprint

## ABSTRACT

This paper analyses the Energy Return on Energy Invested (EROI) and Energy Return on Carbon Emissions (EROC) of current wind energy farms in New Zealand. The weighted average EROI for a New Zealand wind energy farm over a 20 year life span is 34.3, with the highest achieving 57.7, while the lowest is 6.5. These values are higher than wind energy farms in Europe and America, which average about 20, and higher than many other electricity generation methods reported in the literature with hydropower being the main exception. The above-average capacity factor of New Zealand wind energy farms is the primary reason for the higher EROI values. The average EROC value for New Zealand's existing wind energy farms is 477 GJ/t CO<sub>2</sub>-e, which is 56 times the EROC of a combined cycle natural gas power station. The substantial range of EROI values are chiefly driven by two factors: (1) wind speed profile for a given site and (2) the blade diameter of the turbine, where greater values are better. The main drawback of wind energy is variability causing reliability issues and needing hydro power as a renewable buffer to keep emissions low.

© 2017 Elsevier Ltd. All rights reserved.

## 1. Introduction

Sustainability metrics and ratios are important tools to quantify the environmental, social, and economic impact of a wide variety of human activity (Tanzil and Beloff, 2006). Considerable research effort has focused on sustainability improvement through increased process efficiency, integration, and intensification, which may be quantified by sustainability metrics (Klemeš and Varbanov, 2013). A few examples of environmental metrics are carbon, water, energy, emissions, nitrogen, land, and biodiversity footprints (Čuček et al., 2012). Multidimensional metrics and analysis also exist, attempting to describe the total environmental impact and long-term sustainability (Kilkış, 2016). Sustainability analysis attempts to overcome the uncertainty of conventional economic analyses where external factors such as market prices, capital cost competition and government policy have significant effect and environmental and social impacts are difficult to quantify in monetary terms (Mikulčić et al., 2016). As a result, the present study focuses on

analysing wind energy farms that generate electricity through the lens of sustainability ratios based on energy and carbon emissions investments for electricity generation.

Energy Return on Investment (EROI) is an important energy ratio that may be applied to characterise the viability of a natural resource from an energy viewpoint. The ratio compares the amount of useful energy derived to the amount of energy expended to process, generate, and distribute the useful energy. As such, it is effectively the inverse of an energy investment footprint. EROI was proposed by Hall et al. (1992) and continues to find relevance in providing insight to a wide range of problems (Hall, 2017). For electricity production, it is defined as the ratio of the electrical output compared to the summation of all energy inputs (direct and embedded) excluding the primary fuel. Estimates of EROI values for traditional electricity resources range from 25 (coal power stations) up to 41 (hydro power) (Walmsley et al., 2014).

EROI depends on the type and quality of the natural resource, whether it be renewable or non-renewable, and the technologies used for extraction, processing and conversion (Gupta and Hall, 2011). Fossil fuel derived electricity EROI values have less spread due their ongoing abundance, which is expected to taper off in the coming decades, especially if clean coal technology like Carbon Capture and Sequestration (CCS) needs to be employed. Hydro is a

\* Corresponding author.

E-mail address: [walmsley@fme.vutbr.cz](mailto:walmsley@fme.vutbr.cz) (T.G. Walmsley).

### Nomenclature

C	Carbon equivalent emissions (kg CO <sub>2</sub> -e/unit)
D	Blade diameter (m)
E	Energy (GJ/unit)
EROC	Energy return on carbon emissions equivalent (GJ/kg CO <sub>2</sub> -e)
EROI	Energy return on energy investment
H	Height (m)
L	Roading length (m)
m	Mass (t)
n	Number of turbines at a site
P	Power density (W/m <sup>2</sup> )

renewable resource often with the highest but also wide range of EROI values. EROI is chiefly dependent on the water flow, hydraulic head, and geography including the volume and quality of fill needed for the dam, and much less dependent on turbine conversion technology. Other renewables like wind, wave, geothermal and solar are consistently lower than hydro. With these resources, besides geography and climate, the development of new technology significantly contributes to the EROI values. Linking EROI values to the renewable generation technology selection and the key dimensions that effectively characterise a natural resource is important for predicting the EROI performance on future sites.

A second increasingly important ratio is the carbon footprint. As a specific footprint, the numerator is the summation of life cycle carbon emissions while the denominator is the desired output, which for this study is electricity generation. The specific carbon footprint ratio may be inverted to give an Energy Return on Carbon Emissions (EROC), which takes a similar name and form to EROI. EROC expresses the electricity generation per unit of carbon footprint (i.e. GJ/t<sub>CO<sub>2</sub>-e</sub>). Maximising the EROC in turn results in more generation for the same footprint or the same generation for a smaller footprint. EROI and EROC are linked and are both determined using Life Cycle Assessment (LCA).

Several studies have reported detailed LCA of both energy (usually embodied energy) and carbon emissions for wind energy farms (Crawford, 2009). Lenzen and Munksgaard (2002) conducted an extensive review of LCA of wind turbines up to the time of its publication in 2002. Extending this review to include later studies, Kubiszewski et al. (2010) applied a met-analysis approach to the determining EROI of 119 wind turbines, originating from 50 different sources. Most of these primary studies focused on older turbine technology and installations in Europe and North and South America. EROI values ranged from 6.1 to 33.5 for operational turbines. Due to the wide variety of turbine technology and its development, Kubiszewski et al. (2010) concluded EROI and key turbine and site dimensions such as blade diameter and wind speed show a very weak correlation, which is counter-intuitive. Removing turbines with ratings greater than 1 MW, Kubiszewski et al. (2010) showed a good correlation ( $R^2 = 0.641$ ) between EROI and power rating. Weißbach et al., 2013 calculated generic EROI values for wind energy farms in Germany of 16, without buffer storage, and 4, with buffering.

Fernando (2010) determined the embodied energy using LCA of common electricity generation methods including wind energy. Rule et al. (2009) presented the embodied energy and carbon footprint of four wind energy farms in New Zealand. Dale (2013) investigated the levelised energy cost of generation for

renewable electricity generation. He found wind energy farms obtained the lowest energy cost compared to solar PV and concentrating solar power technologies. These LCA studies, some of which determined EROI and/or carbon emissions footprint, investigated several wind energy technologies but the lacked a link between the wind energy technology selection (e.g. number of blades, blade diameter) and characteristics of the natural wind resource with EROI (or embodied energy) and EROC (or carbon emissions footprint). Investigating and correlating the link between each of these elements represents the gap in literature targeted in this study.

The aim of this paper is to develop a simple calculation tool to assess the effects of the wind resource characteristics and the selection of critical design parameters of wind energy farms on EROI and EROC. To achieve the aim, 11 existing and 8 consented wind energy farms in New Zealand are analysed. A simple EROI and EROC calculation tool is developed based on correlations from comprehensive LCA studies to estimate the direct and embodied energy consumptions as well as associated carbon emissions footprints of wind energy farms. This tool is applied to existing sites to estimate EROI and validated against literature EROI values. New Zealand was selected as the case study because the country is a relatively recent adopter of wind energy technology, which avoids the issue of different technology vintages blurring correlations, and has a high proportion of hydro on the grid to balance out intermittent renewable generation. The contributions of this study to the literature are the complete analysis of all existing wind energy farms in New Zealand, the development of a simple calculation tool to estimate EROI and EROC of potential wind energy farm installations, and the validation of the calculation tool against literature values.

## 2. The New Zealand electricity grid and role of wind energy

An overarching goal of the current New Zealand Energy Strategy is to increase the share of renewable electricity generation to greater than 90% by 2025 (MBIE, 2016a). The available renewable generation sources in New Zealand include hydro, wind, geothermal, solar, and biomass. In 2015, renewable hydro, geothermal and wind satisfied 80% electricity demand, which was up from 65% in 2008 (MBIE, 2016b). The New Zealand Government committed to join the 2015 Paris Accord, seeking to reduce carbon emissions to 30% below 2005 levels by 2030. Electricity generation presently accounts for 19% of emissions in New Zealand and so the electricity sector has a role to play in achieving this target.

Renewable energy from hydro, geothermal and wind, 35,465 GWh in 2016, significantly contributes to the New Zealand electricity grid, 42,591 GWh. The generation mix of New Zealand is shown in Fig. 1. In 2016, hydro accounted for 60.4% of the total electricity generation. With significant opposition and growing environmental concerns, the future construction of hydro dams in New Zealand presently appears unattractive as a resource to minimise fossil fuel power stations and to meet demand growth (MBIE, 2017). Geothermal, on the other hand, has dramatically increased from 6.4% of the grid in 2004 to 17.5% in 2016. It is now the country's second largest generation source next to hydro and above natural gas generation at 12.8% (Walmsley et al., 2014). There remains an estimated 850 MW of untapped geothermal capacity that may likely be economic (MBIE, 2016b). This capacity translates to an annual generation of 6600 GWh assuming a capacity factor of 90%. Wind energy currently generates 5.4% of the electricity grid and amounts to a total capacity of 621 MW. It is expected that the contribution of wind generation can peak around 20% of the grid with minimal generation curtailment, additional back-up, and changes to the current grid operation (MBIE, 2016a). Similar results

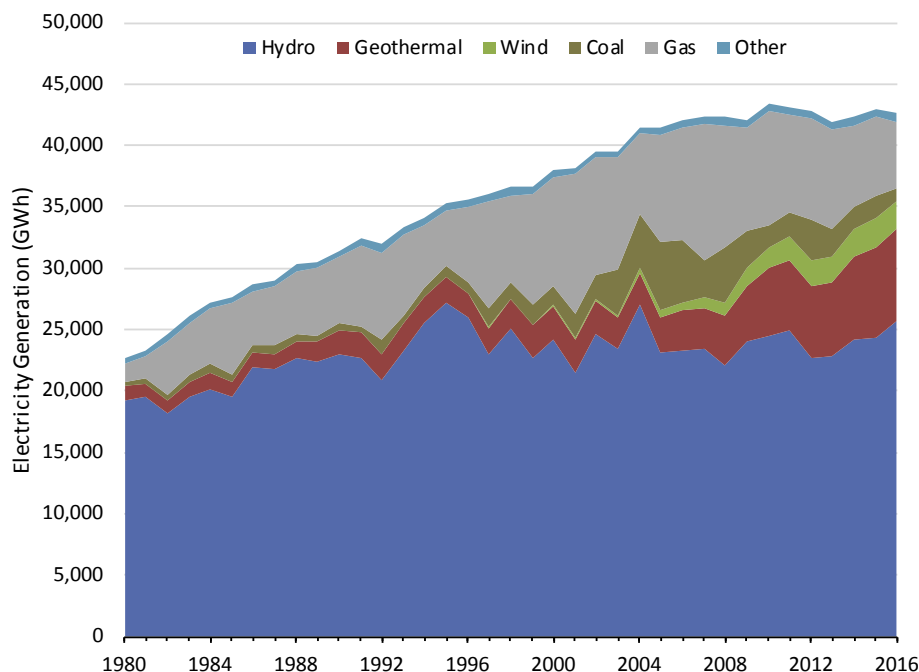


Fig. 1. New Zealand electricity generation 1980 to 2016.

for wind integration have been reported for European and North American electricity grids (Brouwer et al., 2014).

Consistently high average wind speeds are critical to making wind an economically viable generation option. New Zealand has access to excellent wind resources. The current (blue markers) and consented (orange markers) are shown geographically on the terrain map of New Zealand in Fig. 2. For example, the Cook Strait and Manawatu gorge, in the south of the North Island, channels strong winds creating prime locations for electricity generation. Most New Zealand wind energy farms operate at capacity factors greater than 30%, with some individual turbines achieving over 50%. For comparison, Denmark experiences slightly lower capacity factors of 25–30% (Mason et al., 2010). The average capacity factor for wind energy farms in Europe is 21%, with the highest being 57.9% (Boccard, 2009).

Economic analysis of wind energy potential in New Zealand is favourable for many sites. The Long Run Marginal Cost (LRMC) for wind and geothermal is between 80 and 100 NZD and are the two lowest cost options for new generation (MBIE, 2016a). New Zealand has an open market with no direct subsidies or incentives for renewable generation other than the Emissions Trading Scheme (ETS), which requires electricity companies to purchase carbon credits equal to the quantum that is emitted, and market forces. A Government ministry commissioned study projects up to 4120 MW of wind energy may be available across the nation (MBIE, 2017) but not all of this potential will be economic.

### 3. Methods

This investigation calculates EROI and EROC values for individual current and consented wind energy farms in New Zealand using a simple calculation tool. Where possible, the amount of electricity generated is calculated using historic production data, wind speed, and turbine performance models. Correlations from Life Cycle Analysis (LCA) studies are used to estimate the embedded energy and carbon emissions of individual current and consented wind energy farms in New Zealand. The simple calculation tool is

validated against comprehensive LCA data of four wind energy farms in New Zealand and Denmark.



Fig. 2. Wind energy sites and capacities in New Zealand. Existing sites indicated by blue markers and consented sites by orange markers. Map created using Google Maps (2017).

### 3.1. Determination of EROI and EROC

The production of electricity requires the investment and consumption of energy as an input, either directly or embedded in equipment, and life cycle carbon emissions as a by-product. EROI and EROC may therefore be simply defined as

$$EROI = \frac{E_{\text{gen,net}}}{E_{\text{road}} + E_{\text{cable}} + E_{\text{earth}} + E_{\text{materials}} + E_{\text{trans}} + E_{\text{op}}} \quad (1a)$$

$$EROc = \frac{E_{\text{gen,net}}}{C_{\text{road}} + C_{\text{cable}} + C_{\text{earth}} + C_{\text{materials}} + C_{\text{trans}} + C_{\text{op}}} \quad (1b)$$

The electrical output,  $E_{\text{gen}}$ , is the electricity delivered to the grid over the plant's lifetime. Energy input,  $E_{\text{input}}$ , includes the primary energy equivalent (Hall, 2017) of thermal and electrical energy inputs including manufacturing energy for all the necessary materials and parts, transport energy, construction energy, plant operations and maintenance energy, and decommissioning energy. EROI is a dimensionless ratio, meaning the numerator and denominator need to use energy units and the same basis of energy quality. Energy quality is usually accounted using an average value- or exergy-based system. This study applied the value-based approach. As a result, to convert primary and thermal energy into an electrical equivalent, a factor of 0.3 is applied, following the EROI study of Raugei et al. (2012). Carbon equivalent emissions associated with the project,  $C_{\text{plant}}$ , is the summation of all the emissions resulting from constructing, operating, fuelling, and decommissioning the plant, over the life time of the plant. The inverse of EROC is the carbon emissions footprint. The determination of EROI and EROC requires an LCA of the energy project.

In the following sections, the method for determining each component of Equation 1a and b are described.

### 3.2. Estimated electricity generation

Existing New Zealand wind energy farms have public information available about the annual output of the site. To predict the output of future sites, a model was formed which determines the average power output based on the realisable wind potential of the wind at the site. New Zealand's National Institute of Water and

Atmospheric Research (NIWA) maintain a wind energy map of New Zealand (de Vos and Fortuin, 2010). The wind data includes the power density,  $P$ , of the site in  $\text{W/m}^2$  of footprint, based on the Vestas V67 model, assuming  $12.3 \text{ turbine/km}^2$ .

The accuracy of the NIWA map was checked by comparing it with the output electricity data from existing farms as shown in Fig. 3. Although the correlation is weak ( $R^2 = 0.4$ ), the NIWA data is the only available dataset for the basis of a prediction. To account for the poor correlation, a sensitivity analysis is carried out.

Using these datasets, the correlation for predicting specific power output per turbine is

$$E_{\text{gen}}(\text{GJ/turbine}) = 12.7 P \cdot D^2 \quad (2)$$

### 3.3. Life Cycle Analysis for embedded energy and carbon emissions

Life Cycle Analysis (LCA) sums all relevant energy and material inputs and outputs over the lifetime of a product, process, or service. LCA was used to sum all of the material and energy flows and average these over the expected 20 year lifetime of a wind energy farm. Two embedded energy (Fernando, 2010) and emissions (Rule et al., 2009) analyses have been done for New Zealand renewables and these were used as guides for this analysis. The methods for calculating power output, roading, cabling, earth works, turbine materials, transport, and operation, are outlined in the following sections.

#### 3.3.1. Roads

The lengths of access roads,  $L_{\text{main}}$ , for new and existing sites were estimated using satellite images from Google Earth by measuring length of required roads between the wind energy farm and the nearest pre-existing road. The embedded energy of the road per unit length was taken as  $1.86 \text{ GJ/m}$  and the emissions as  $22.6 \text{ kg/m}$  (Elsam Engineering, 2004).

Roading is also needed between individual turbines at a site. A detailed analysis of New Zealand wind energy farms at West Wind, Te Uku, and Tararua was performed to determine an average distance between turbines. The average distance between turbines,  $L_{\text{sub}}$ , for these three farms is  $573 \text{ m}$ . This average distance is applied for future and other existing wind energy farm sites to estimate

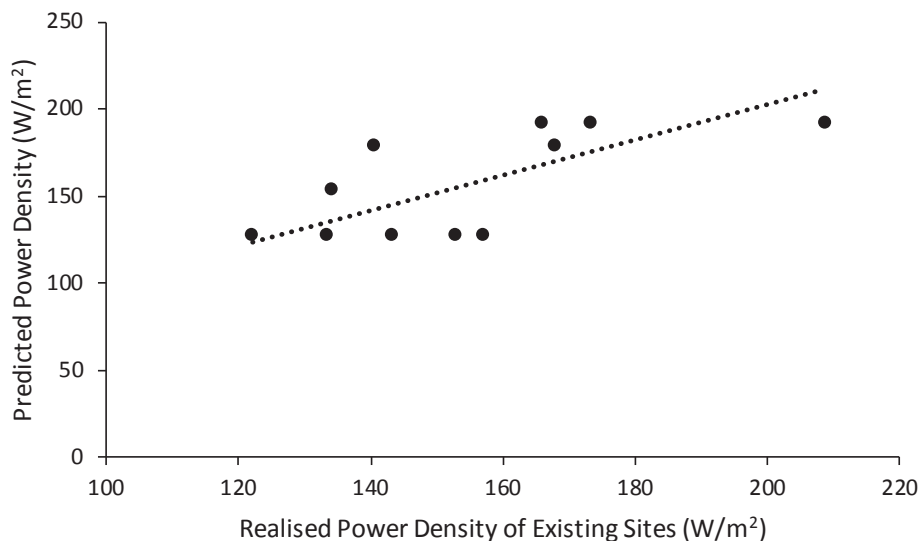


Fig. 3. Comparison of NIWA map with realised power density of existing sites.

total roading requirements. The total embedded energy from roads per turbine ( $E_{road}$ ) and the total carbon emitted per turbine ( $C_{road}$ ) is then calculated using equations (3a) and (3b).

$$E_{road}(\text{GJ/turbine}) = 1.86 \left( \frac{L_{main}}{n} + L_{sub} \right) \quad (3a)$$

$$C_{road}(\text{kg/turbine}) = 22.6 \left( \frac{L_{main}}{n} + L_{sub} \right) \quad (3b)$$

3.3.2. Cables

The length of the required underground cabling was estimated as 1.5 times the distance between turbines (Fernando, 2010). The embedded energy of the cabling is 0.271 GJ/m and the emissions factor is 21.3 kg/m (Rule et al., 2009). The total embedded energy ( $E_{cable}$ ) and carbon emissions ( $C_{cable}$ ) per turbine from cabling is calculated using equations (4a) and (4b).

$$E_{cable}(\text{GJ/turbine}) = 0.407 L_{sub} \quad (4a)$$

$$C_{cable}(\text{kg/turbine}) = 32.0 L_{sub} \quad (4b)$$

3.3.3. Earth works

There is energy associated with earth works at the site, such as digging and flattening. Specific values for embedded energy ( $E_{earth}$ ) and carbon emission ( $C_{earth}$ ) per turbine are taken from Rule et al. (2009) and calculated using equations (5a) and (5b).

$$E_{earth} = 1.1 \text{ GJ/turbine} \quad (5a)$$

$$C_{earth} = 5,600 \text{ kg/turbine} \quad (5b)$$

3.3.4. Turbine materials

The mass and materials of the turbine foundation, tower, blades, nacelle (generator housing) and hub (blade mount) were taken from the manufacturer’s product information (Vestas, 2016). Fig. 4 correlates the tower height with the tower mass based on product specifications given by Vestas.

The nacelle and hub are structural steel with a combine mass of 87 t. The mass of the structural steel may be estimated using

$$m_{steel,1}(\text{kg/turbine}) = 0.0214 H^2 + 0.0845 H + 87 \quad (6a)$$

Simple scaling laws dictate a cubic rise in blade mass with increasing turbine size. Three bladed turbines are the recommended solution. When compared to three blade designs, a 3% loss is incurred for two bladed designs and a 7%–13% loss for one bladed design. A four bladed design offers marginal efficiency increases which do not justify the manufacturing cost of an extra blade (Schubel and Crossley, 2012). Fig. 5 shows the correlation between blade mass and blade diameter, which may be estimated using

$$m_{fibre\ glass}(\text{kg/turbine}) = 1.37 \times 10^{-6} D_{blade}^{3.44} \quad (6b)$$

The applied embodied energy per tonne of material for a gear box and generator are presented in Table 1. The mass of concrete and reinforcing steel used in the foundation was estimated to be proportional to the tower height and the blade length (Rule et al., 2009).

$$m_{concrete}(\text{kg/turbine}) = 0.163 H \cdot D \quad (6c)$$

$$m_{steel,2}(\text{kg/turbine}) = 0.00634 H \cdot D \quad (6d)$$

Combining Equation 6a, b, c, and d with the information in Table 1 gives

$$E_{materials}(\text{GJ/turbine}) = 0.672 H^2 + 2.65 H + 0.248 H \cdot D + 40.1 \times 10^{-6} D_{blade}^{3.44} + 4,320 \quad (7a)$$

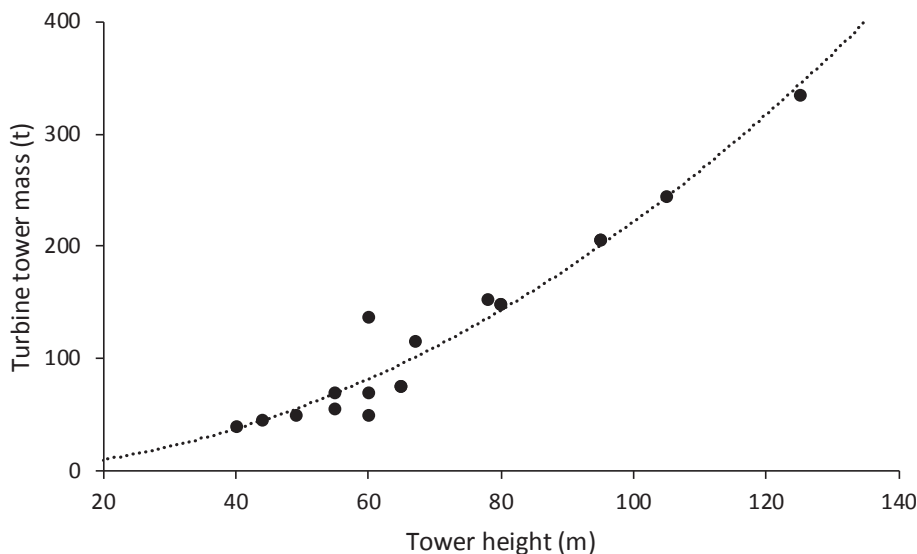


Fig. 4. Relationship for estimating turbine tower mass.

$$C_{\text{materials}}(\text{kg/turbine}) = 26.5 H^2 + 105 H + 26.7 H \cdot D + 0.945 \times 10^{-3} D_{\text{blade}}^{3.44} + 217,000 \tag{7b}$$

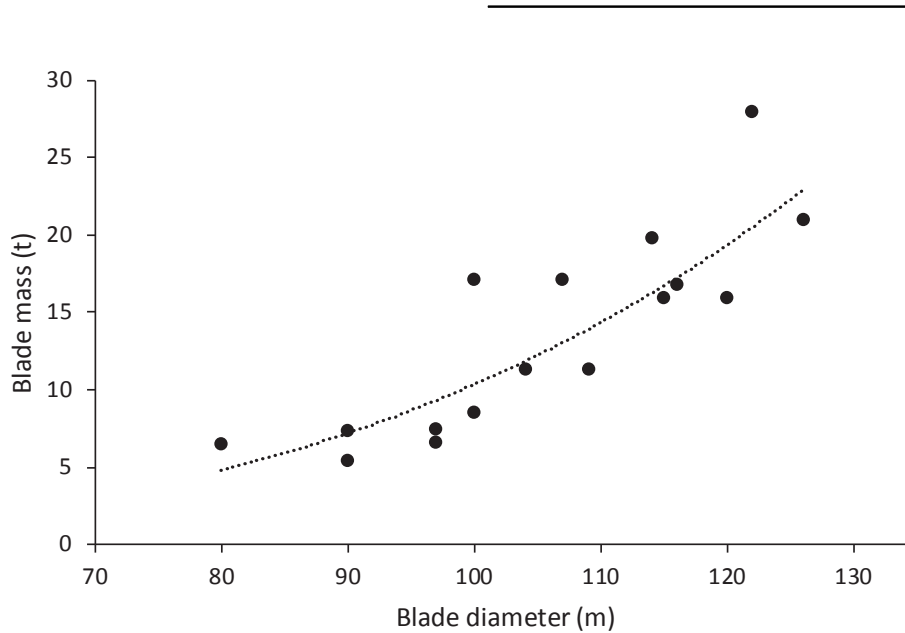


Fig. 5. Power law correlation for estimating turbine blade mass.

3.3.5. Transport

The shipping distance, *S*, and the overland distance, *L<sub>trans</sub>*, were found between each wind site and the manufacturer of the turbines. The predominant supplier is the Danish Vestas, who require 22,000 km to ship the tower and blades from Denmark to New Zealand. Rule et al. (2009) estimated the embodied energy and carbon emissions factors for transport as shown in Table 2.

$$E_{\text{trans}} = (0.00025 S + 0.00125 L_{\text{trans}}) (m_{\text{steel},1} + m_{\text{fibre glass}}) \tag{8a}$$

$$C_{\text{trans}} = (0.000014 S + 0.000068 L_{\text{trans}}) (m_{\text{steel},1} + m_{\text{fibre glass}}) \tag{8b}$$

3.3.6. Operation and maintenance

Wind turbines require electrical power for: (1) yaw mechanisms that keep the blades turned into the wind, (2) blade-pitch controls that meter the spinning rotor, (3) aircraft lights and data-collection electronics, (4) oil heaters, pumps, and coolers for the multi-ton

gearbox, and (5) hydraulic brakes for locking blades down during excessively high wind speeds. In still conditions, the generator is used in reverse, i.e. a motor, to keep the blades moving slowly and prevent damage to the bearings. Using data from Fernando (2010) and self-consumed electricity data from Meridian Energy (New Zealand's leading wind-electricity company), the operation power consumption is estimated to be 1.3% of gross electricity generation. This amount was subtracted from the gross electricity generation to determine the net amount added to the grid. Net electricity generation is applied in calculating EROI and EROC.

Turbines are designed to have a service lifetime of 20 years. It is expected that during the turbine lifetime one reconditioning and/or replaced of half of the gears and the generators will be undertaken, which, at a minimum, comprises a replacement of the sealed bearings (Elsam Engineering, 2004). Additional materials for servicing of the turbines are included in the form of oil changes and gear lubrication and so on. Fernando (2010) estimates the embedded energy due to service and maintenance (*E<sub>op</sub>*) to be 1170 GJ per turbine over its lifetime. This corresponds to carbon emissions (*C<sub>op</sub>*) of 79.7 t per turbine. This includes enough materials to renew half of the gearboxes once in the lifetime of a wind energy farm. This estimate is conservative as several of the gears and the generators will be repaired rather than replaced.

$$E_{\text{op}} = 1,170 \text{ GJ/turbine} \tag{9a}$$

Table 1 Embodied energy factors of wind energy farm materials and components (Rule et al., 2009).

Component	Embedded Energy	Emissions
Steel (Structural)	EF <sub>S,S</sub> 31.4 GJ/t	CF <sub>S,S</sub> 1240 kg CO <sub>2</sub> -e/t
Concrete	EF <sub>C</sub> 1.19 GJ/t	CF <sub>C</sub> 150 kg CO <sub>2</sub> -e/t
Steel (Reinforcing)	EF <sub>S,R</sub> 8.60 GJ/t	CF <sub>S,R</sub> 350 kg CO <sub>2</sub> -e/t
Fibreglass	EF <sub>F</sub> 29.3 GJ/t	CF <sub>F</sub> 690 kg CO <sub>2</sub> -e/t
Gearbox	E <sub>GB</sub> 799 GJ/turbine	C <sub>GB</sub> 54,460 kg CO <sub>2</sub> -e/turbine
Generator	E <sub>GN</sub> 789 GJ/turbine	C <sub>GN</sub> 54,550 kg CO <sub>2</sub> -e/turbine

Table 2 Energy and emissions factors for transport.

Transport mode	Embodied Energy (MJ/t.km)	Emissions (kg/t.km)
Ocean Shipping	0.25	0.014
Land Transport	1.25	0.068

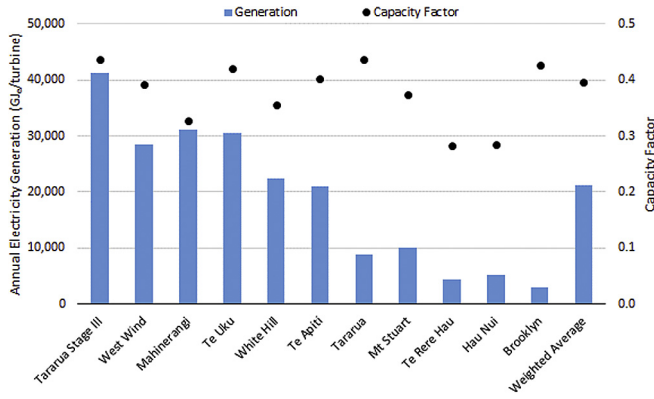


Fig. 6. Annual generation and capacity factor for existing New Zealand wind energy farms.

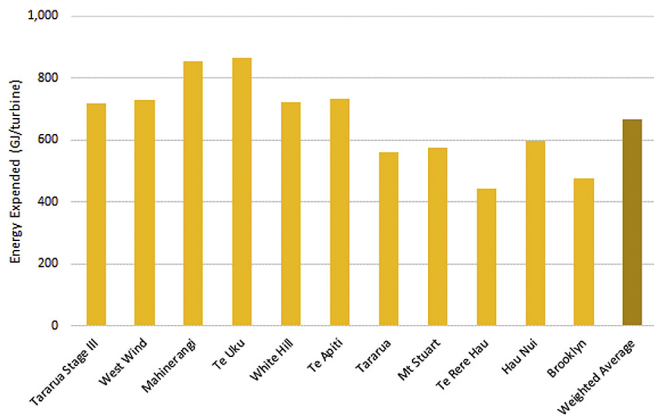


Fig. 7. Estimated total expended energy per turbine for existing sites.

$$C_{op} = 79,700 \text{ kg/turbine} \tag{9b}$$

## 4. Results

### 4.1. Electricity generation and energy expended for existing wind energy farms in New Zealand

The annual generation and calculated capacity factor for the 11 existing wind generation sites are presented in Fig. 6 on a per

turbine basis. Fig. 7 gives the total estimated expended energy for each existing site. The details of the eleven existing New Zealand wind energy farms are summarised in Table 3. The total expended energy for each site can be broken down into five major areas: transport, roads, turbine, base, and operations and maintenances, as shown in Fig. 8.

The results show that blade diameter is a key driver behind electricity generation and embodied input energy for construction of the wind energy farm. The sites with greater generation per turbine correlate well with blade diameter (Table 3). For example, Te Uku with a blade diameter of 101 m and a 30,500 GJ/turbine compared to Tararua, which has a similar capacity factor but only a 47 m blade diameter and produces only 9000 GJ/turbine. The radar plot of the expended energy break-down shows about 60% is attributed to the turbine, followed by the base (16.6% average) and roads (9.4% average). Similar, the blade diameter correlates with energy input. For example, Te Uku with the largest blade diameter required the highest specific energy input.

### 4.2. EROI and EROC for existing wind energy farms in New Zealand

EROI and EROC values for existing New Zealand wind energy farms are shown in Fig. 9. EROI values ranged from 58.4 for the Tararua Stage III wind energy farm to as low as 6.6 for the single Brooklyn Turbine. The variation in EROI values for the different sites is due to the differences in average wind speed, and blade diameter of the turbines. The weighted average EROI (based on electricity production) for New Zealand is 34.7, compared to an average of 19.6 in the literature (Kubiszewski et al., 2010). As expected, EROC values were strongly correlated to EROI values and ranged from 688 to 120 GJ/t CO<sub>2-e</sub> with a weighted average of 477 GJ/t CO<sub>2-e</sub>. In terms of emission factor (the inverse of EROC), the weighted average for New Zealand wind energy farms is 2.1 kg CO<sub>2-e</sub>/GJ (0.0076 t CO<sub>2-e</sub>/MWh). Compared to geothermal at 35.5 kg CO<sub>2-e</sub>/GJ, gas combined cycle at 117 kg CO<sub>2-e</sub>/GJ and coal fired power stations at 204 kg CO<sub>2-e</sub>/GJ (Walmsley et al., 2014), wind energy has a negligible emission footprint while being a renewable source of electricity.

### 4.3. Simple calculation tool validation

To validate the EROI estimation model, four published LCA assessments for wind energy farms both in New Zealand and internationally were used. The two New Zealand wind energy farms were for Te Apati (Rule et al., 2009) and White Hall (Fernando, 2010). The two international farms were Tjareborg (on-shore) and Horns Reef (off-shore) in Denmark (Elsam Engineering, 2004). EROI values based on the data presented in the references were calculated. Inputted model parameters, such as wind speed, blade

Table 3  
Key parameters for existing wind energy farms in New Zealand.

Wind Farm	Installed Capacity [MW]	Annual Generation [GWh]	Capacity Factor	Number of Turbines	Average Wind Speed [m/s]	Hub Height [m]	Blade Diameter [m]	Blade Number	EROI	EROC [GJ/tCO <sub>2</sub> ]
Tararua Stage III	93	360	0.44	31	9.86	65	90	3	57.7	688
West Wind	143	497	0.39	62	8.76	68	82	3	39.0	534
Mahinerangi	36	105	0.33	12	8.39	80	90	3	36.4	513
Te Uku	64.4	240	0.42	28	7.39	80	101	3	35.2	494
White Hill	58	183	0.36	29	7.81	70	80	3	31.1	445
Te Apati	91	325	0.40	55	7.52	70	80	3	28.7	422
Tararua	67	260	0.44	103	7.65	50	47	3	16.0	264
Mt Stuart	7.7	25.6	0.37	9	7.45	45	52	3	17.6	306
Te Rere Hau	48.5	122	0.28	97	7.01	30	33	2	10.1	183
Hau Nui	8.7	22	0.28	15	6.38	46	40	3	8.7	167
Brooklyn	0.23	0.87	0.43	1	6.06	31.5	30	3	6.5	120
Weighted Average	88	195	0.40	52					34.3	470

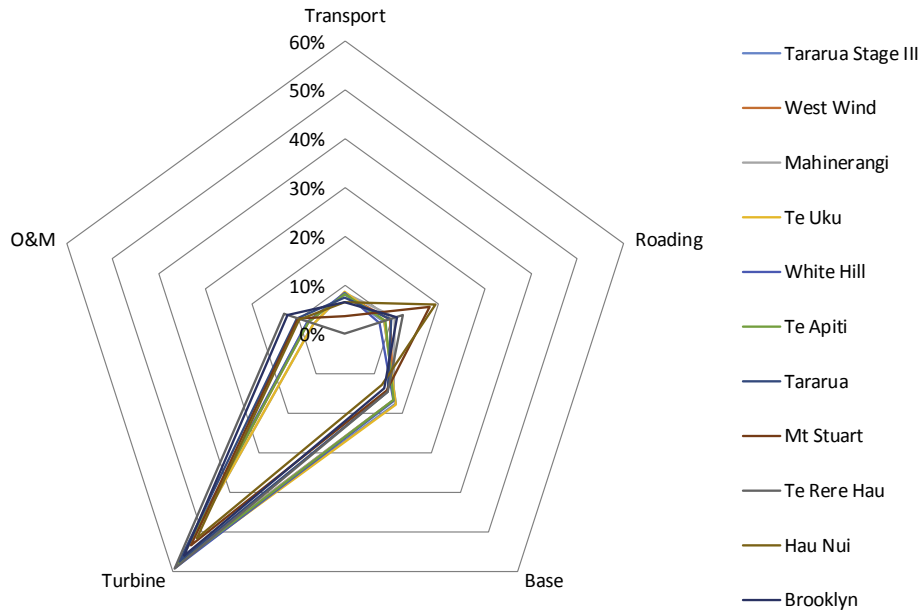


Fig. 8. Breakdown of wind energy farm expended energy.

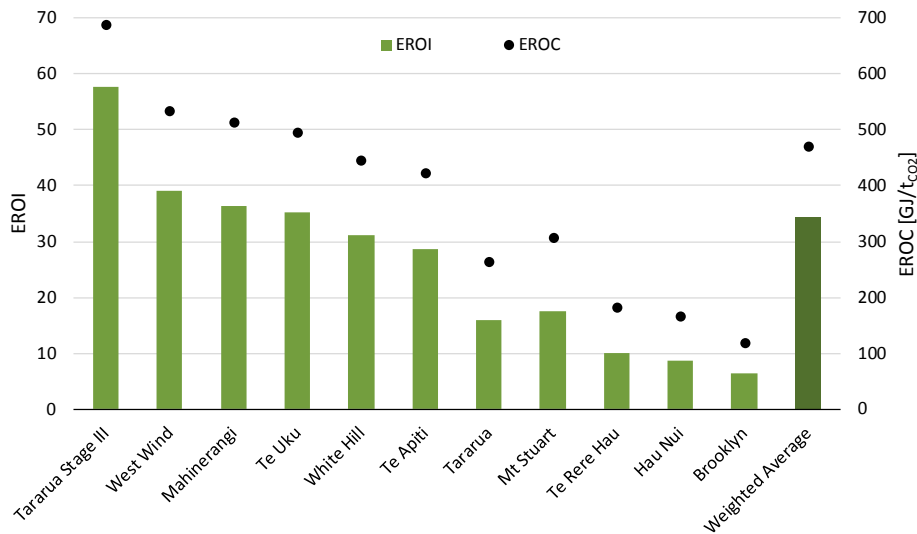


Fig. 9. Energy Return on Investment and Energy Return on Carbon Emissions of existing New Zealand wind energy farms.

diameter and hub height, were then used to estimate EROI values using the model. As shown in Fig. 10, the simple calculation tool tends to slightly over-estimate the reported values that were determined by rigorous LCA studies. However, this difference is within the typical uncertainty that is associated with LCA.

4.4. EROI and EROc for consented wind energy farms in New Zealand

The simple calculation tool estimated the EROI and EROc values for selected wind energy farm proposals that have gone through the New Zealand resource consenting process. Estimates of average wind speed were based on New Zealand's EnergyScape report (de Vos and Fortuin, 2010). The input data and results are summarised in Table 4. EROI values ranged from as high as 48.3 to as low as 11.3. The hub height, blade diameter, and number of blades were all held constant and as a result the main factor effecting EROI was the

wind speed. EROc values ranged from 611 GJ/t<sub>CO2-e</sub> to 191 GJ/t<sub>CO2-e</sub>. Two cases were analysed for each new wind energy site: (1) installed turbines with a hub height of 65 m and blade diameter of 90 m and (2) installed turbines with a hub height of 80 m and blade diameter of 120 m. Both cases assumed three blades per turbine as is standard practice. Based on the simple calculation tool and the limited data for wind speed, the results for EROI and EROc recommend Castle Hill in the Wairarapa, Kaiwera Downs, Turitea, and Mt Cass sites as the most advantageous sites to build New Zealand's next wind energy farm. Although EROI has been shown to correlate with levelised electricity price (Walmsley et al., 2015), the EROI analysis does not replace a required economic analysis rather it helps identify which sites that should receive greatest attention.

4.5. Sensitivity analysis of model inputs

A sensitivity analysis on EROI values was performed on the

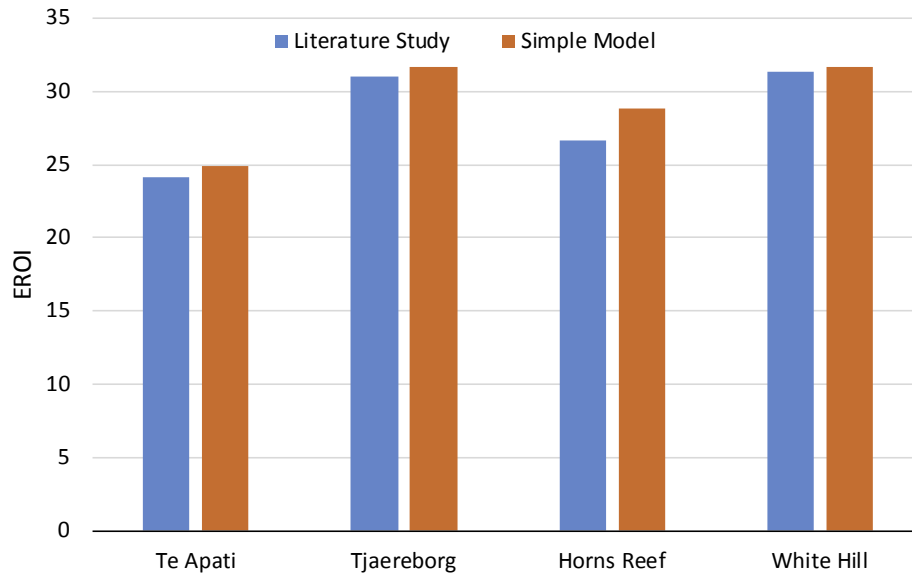


Fig. 10. Simple calculation tool model validation against detailed LCA studies.

Table 4

EROI and EROC estimates for consented New Zealand wind energy farms.

Wind Farm	Max Proposed Capacity [MW]	Number of Turbines	Estimated Average Wind Speed [m/s]	EROI <sup>a</sup>	EROC <sup>a</sup> (GJ/t <sub>CO2</sub> )	EROI <sup>b</sup>	EROC <sup>b</sup> (GJ/t <sub>CO2</sub> )
Castle Hill	800	267	9.00	48.3	611	63.3	728
Kaiwera Downs	240	80	9.00	48.0	611	63.0	728
Hawkes Bay	225	75	7.00	31.1	448	40.2	542
Turitea	180	60	9.00	47.9	611	62.9	727
Puketoi	159	53	7.50	34.8	489	45.3	589
Waitahora	156	52	3.75	11.2	191	13.9	232
Mt. Cass	78	26	9.00	47.2	609	62.2	726
Titiokura	48	16	7.00	30.1	445	39.3	540

<sup>a</sup> Assumptions: hub height = 65 m, blade diameter = 90 m, blade number = 3, capacity factor = 40%.

<sup>b</sup> Assumptions: hub height = 80 m, blade diameter = 120 m, blade number = 3, capacity factor = 40%.

proposed Castle Hill installation. The individual parameters were varied between upper and lower bounds, which depended on the parameter, as shown in Fig. 11. The mid-point at 50% represents the current estimate EROI for Castle Hill based on a 120 m blade diameter (Table 4). Starting with an EROI of 63.3, the wind speed, number of turbines, length of access road, blade diameter, capacity factor, and hub height were each incrementally varied to generate new EROI values using the calculation tool. This analysis shows the most influential variables on EROI are wind speed, blade diameter,

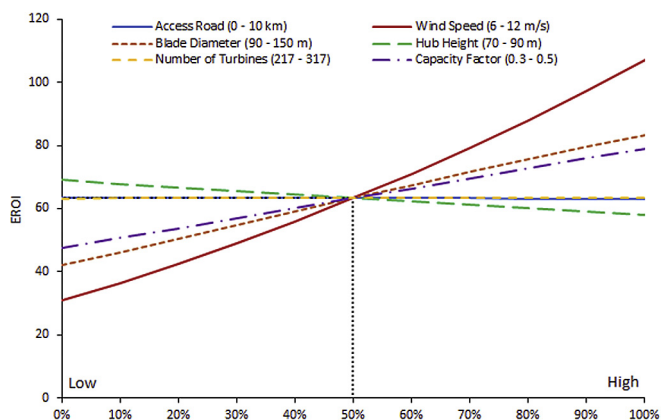


Fig. 11. Sensitivity analysis of EROI.

and capacity factor. Wind speed and capacity factor are characteristics of the natural wind resource while blade diameter is a design variable.

## 5. Discussion

### 5.1. Key factors for increasing EROI and EROC

The New Zealand EnergyScape maps (de Vos and Fortuin, 2010) shows many areas with high wind speeds remain for prospective wind energy sites, such as around Gisborne City (North Island, east coast) and Marlborough region (South Island, north east). Most sites in New Zealand have turbines with 80–90 m blade diameters. Vestas (2016) now produce wind turbines with 120 m diameter blades, indicating that future wind sites may achieve EROI values greater than 60 and EROC greater than 700 GJ/t<sub>CO2-e</sub> due to the technological advance. Along with greater diameters, newer turbines also have lower maintenance requirements than older models. Older turbines have average annual maintenance costs of around 3% of the original cost of the turbine whereas new turbines need only 1.5–2.0% (WMI, 2013).

### 5.2. Technological challenges and drawbacks

High wind speeds are critical to making wind an economical electricity generation option. However, the high average wind speeds, which makes the New Zealand wind resource productive,

are often accompanied by turbulence. These intermittencies in wind speed create variable mechanical loads on the wind turbine structure, causing fatigue and ultimately leading to failure (Katurji, 2011). Turbine operators avoid damage by locking the blades in highly turbulent conditions, to avoid material fatigue and failure, while sacrificing the opportunity to generate power. As the technology improves, so will the turbines ability to operate in turbulent conditions.

The main drawback of wind generation is its variability, which is difficult to accurately predict (Njiri and Söffker, 2016). Smart integration using both supply- and demand-side responses is critical in the uptake of intermittent renewable energy such as wind (Duić, 2015). Variability in generation creates a barrier for companies wanting to sell their electricity to the grid market and an even greater challenge for rural areas without access to a centralised grid (Hossain et al., 2015). On the supply-side, a complementary base-load of reliable electricity is required to offset changes in wind energy. Many of the New Zealand electricity companies also own hydro dams. The high proportion of hydro power on the New Zealand grid positions the country to further increased wind energy generation. Hydro can complement wind as a regulator if the proximity is sufficiently close, which helps minimise the curtailment of total power generation through effective short-term load shifting (Ho et al., 2013). In the New Zealand hydro network, there is around 4000 GWh (14.4 PJ) of storage capacity in the New Zealand hydro network, making it difficult to store wind power over hours and days but there remains potential for pumped storage (Bardsley, 2005). Without hydro, wind energy must rely on fossil fuel power plants to maintain a reliable electricity supply. This pairing does have a negative effect on the thermal efficiency (~4% reduction) of the fossil power station (Brouwer et al., 2014), which should be considered in economic analysis. To an extent, demand-response, such as using residential and industrial hot water systems and electric car batteries, is another approach to countering the intermittency of wind energy.

Wind energy farms have been met with mixed public support. The beauty of New Zealand scenery is central to the country's tourist industry and some people feel that wind turbines are unsightly, while others find them aesthetic and complementary to the landscape (EECA, 2015). Noise is also another deterrent for public support. Under new rules, a strict acoustic noise standard must be met by all prospective wind energy farms. This is often met by locating the wind energy farms away from built up areas. A recent survey showed that 75% of New Zealanders support the development of wind energy farms (EECA, 2015).

## 6. Conclusion

Wind can be a competitive electricity generation resource in terms of both EROI and EROC for New Zealand. This is reflected in the case study where the growth in wind generation in New Zealand has increased from 1.5% of the electricity grid in 2006 to 5.4% in 2016 with many more sites currently consented.

A simple calculation tool has been successfully developed and validated against four detailed LCA studies. The tool can quickly assess the EROI and EROC performance of wind energy farms. The tool requires a minimum number of inputs to determine both EROI and EROC. In comparison, detailed LCA often require micro-details, such as engineering design and materials used, to output sustainability metrics, such as EROI and EROC. In the analysis, the calculation tool is applied to 11 existing and 8 consented wind energy farms in New Zealand. The results for these 19 sites show that these metrics are heavily affected by average wind speed and the blade diameter. EROI values ranged from 58.4 (Tararua Stage III) to as low as 6.6 (Brooklyn Turbine) with an average of 34.7. As expected,

EROC values were strongly correlated to EROI values and ranged from 688 to 120 GJ/t CO<sub>2</sub>-e with a weighted average of 477 GJ/t CO<sub>2</sub>-e. These values favourably compare with EROI and EROC values for wind energy farms in other countries and conventional electricity generation methods, e.g. natural gas combined cycle.

New Zealand has the key advantage of high average wind speeds that result in high capacity factors. New turbine blade technologies have enabled larger blade diameters that is leading to significantly increased EROI and EROC values. As a stand-alone solution, wind energy may be viewed as unreliable due to high generation intermittency. As a result, it is critically important to pair wind generation with flexible baseload generation such as hydro for complementary integration of wind energy farms into national electricity grid, helping overcome wind's intermittency drawback.

## Acknowledgements

This research has been supported by the EU project “Sustainable Process Integration Laboratory – SPIL”, project No. CZ.02.1.01/0.0/0.0/15\_003/0000456 funded by EU “CZ Operational Programme Research, Development and Education”, Priority 1: Strengthening capacity for quality research, in a collaboration with the University of Waikato, New Zealand.

## References

- Bardsley, W.E., 2005. Note on the pumped storage potential of the Onslow-Manorburn depression, New Zealand. *J. Hydrology (NZ)* 44, 131–135.
- Boccard, N., 2009. Capacity factor of wind power realized values vs. estimates. *Energy Pol.* 37, 2679–2688. <http://dx.doi.org/10.1016/j.enpol.2009.02.046>.
- Brouwer, A.S., van den Broek, M., Seebregts, A., Faaij, A., 2014. Impacts of large-scale Intermittent Renewable Energy Sources on electricity systems, and how these can be modeled. *Renew. Sustain. Energy Rev.* 33, 443–466. <http://dx.doi.org/10.1016/j.rser.2014.01.076>.
- Crawford, R.H., 2009. Life cycle energy and greenhouse emissions analysis of wind turbines and the effect of size on energy yield. *Renew. Sustain. Energy Rev.* 13, 2653–2660. <http://dx.doi.org/10.1016/j.rser.2009.07.008>.
- Čuček, L., Klemeš, J.J., Kravanja, Z., 2012. A Review of Footprint analysis tools for monitoring impacts on sustainability. *J. Clean. Prod. Recent Clean. Prod. Adv. Process Monit. Optim.* 34, 9–20. <http://dx.doi.org/10.1016/j.jclepro.2012.02.036>.
- Dale, M., 2013. A comparative analysis of energy costs of photovoltaic, solar thermal, and wind electricity generation technologies. *Appl. Sci.* 3, 325–337. <http://dx.doi.org/10.3390/app3020325>.
- de Vos, R., Fortuin, S., 2010. New Zealand's EnergyScape – Summary of Resource Maps.
- Duić, N., 2015. Is the success of clean energy guaranteed? *Clean. Techn Environ. Policy* 17, 2093–2100. <http://dx.doi.org/10.1007/s10098-015-0969-y>.
- EECA, 2015. Wind Energy [WWW Document]. Energy Efficiency and Conservation Authority. [www.eeca.govt.nz/energy-use-in-new-zealand/renewable-energy-resources/wind/](http://www.eeca.govt.nz/energy-use-in-new-zealand/renewable-energy-resources/wind/) (Accessed 5 November 2017).
- Elsam Engineering, 2004. Life Cycle Assessment of Offshore and Onshore Sited Wind Farms (No. 200128). Elsam Engineering. Fredericia, Denmark.
- Fernando, A.T.D., 2010. Embodied Energy Analysis of New Zealand Power Generation Systems (Master of Engineering). University of Canterbury, Christchurch, New Zealand.
- Google, 2017. Google Maps [WWW Document]. Google Maps. [www.google.cz/maps](http://www.google.cz/maps) (Accessed 5 November 2017).
- Gupta, A.K., Hall, C.A.S., 2011. A review of the past and current state of EROI data. *Sustainability* 3, 1796–1809. <http://dx.doi.org/10.3390/su3101796>.
- Hall, C.A.S., 2017. Energy Return on Investment: a Unifying Principle for Biology, Economics, and Sustainability, Lecture Notes in Energy. Springer International Publishing, Cham, Switzerland. [http://dx.doi.org/10.1007/978-3-319-47821-0\\_1](http://dx.doi.org/10.1007/978-3-319-47821-0_1).
- Hall, C.A.S., Cleveland, C.J., Kaufmann, R.K., 1992. Energy and Resource Quality: the Ecology of the Economic Process. University Press of Colorado, Boulder, USA.
- Ho, W.S., Hashim, H., Lim, J.S., Klemeš, J.J., 2013. Combined design and load shifting for distributed energy system. *Clean. Techn Environ. Pol.* 15, 433–444. <http://dx.doi.org/10.1007/s10098-013-0617-3>.
- Hossain, F.M., Hasanuzzaman, M., Rahim, N.A., Ping, H.W., 2015. Impact of renewable energy on rural electrification in Malaysia: a review. *Clean. Techn Environ. Pol.* 17, 859–871. <http://dx.doi.org/10.1007/s10098-014-0861-1>.
- Katurji, M., 2011. Turbulence and Airflow Variations in Complex Terrain: a Modelling and Field Measurement Approach for Wind Turbine Siting (Ph.D. thesis). University of Canterbury, Christchurch, New Zealand.
- Kılıç, Ş., 2016. Sustainable development of energy, water and environment systems index for southeast european cities. *Journal of cleaner production, special volume: SDEWES 2014-sustainable development of energy. Water Environ. Syst.* 130, 222–234. <http://dx.doi.org/10.1016/j.jclepro.2015.07.121>.

- Klemeš, J.J., Varbanov, P.S., 2013. Process intensification and integration: an assessment. *Clean. Techn Environ. Pol.* 15, 417–422. <http://dx.doi.org/10.1007/s10098-013-0641-3>.
- Kubiszewski, I., Cleveland, C.J., Endres, P.K., 2010. Meta-analysis of net energy return for wind power systems. *Renew. Energy* 35, 218–225. <http://dx.doi.org/10.1016/j.renene.2009.01.012>.
- Lenzen, M., Munksgaard, J., 2002. Energy and CO2 life-cycle analyses of wind turbines—review and applications. *Renew. Energy* 26, 339–362. [http://dx.doi.org/10.1016/S0960-1481\(01\)00145-8](http://dx.doi.org/10.1016/S0960-1481(01)00145-8).
- Mason, I.G., Page, S.C., Williamson, A.G., 2010. A 100% renewable electricity generation system for New Zealand utilising hydro, wind, geothermal and biomass resources. *Energy Pol.* 38, 3973–3984. <http://dx.doi.org/10.1016/j.enpol.2010.03.022>.
- MBIE, 2016a. Electricity Demand and Generation Scenarios 2016 - Ministry of Business, Innovation and Employment [WWW Document]. [www.mbie.govt.nz/info-services/sectors-industries/energy/energy-data-modelling/modelling/electricity-demand-and-generation-scenarios/?searchterm=edgs%202016%2A](http://www.mbie.govt.nz/info-services/sectors-industries/energy/energy-data-modelling/modelling/electricity-demand-and-generation-scenarios/?searchterm=edgs%202016%2A) (Accessed 12 January 2016).
- MBIE, 2016b. Energy Balances [WWW Document]. Ministry of Business, Innovation & Employment. [www.mbie.govt.nz/info-services/sectors-industries/energy/energy-data-modelling/statistics/electricity](http://www.mbie.govt.nz/info-services/sectors-industries/energy/energy-data-modelling/statistics/electricity) (Accessed 6 March 2016).
- MBIE, 2017. Electricity Demand and Supply Generation Scenarios 2016 [WWW Document]. Ministry of Business, Innovation & Employment. [www.mbie.govt.nz/info-services/sectors-industries/energy/energy-data-modelling/modelling/electricity-demand-and-generation-scenarios/edgs-2016](http://www.mbie.govt.nz/info-services/sectors-industries/energy/energy-data-modelling/modelling/electricity-demand-and-generation-scenarios/edgs-2016). (Accessed 1 March 2017).
- Mikulčić, H., Klemeš, J.J., Duić, N., 2016. Shaping sustainable development to support human welfare. *Clean. Techn Environ. Policy* 18, 1633–1639. <http://dx.doi.org/10.1007/s10098-016-1269-x>.
- Njiri, J.G., Söffker, D., 2016. State-of-the-art in wind turbine control: trends and challenges. *Renew. Sustain. Energy Rev.* 60, 377–393. <http://dx.doi.org/10.1016/j.rser.2016.01.110>.
- Raugei, M., Fullana-i-Palmer, P., Fthenakis, V., 2012. The Energy Return on energy investment (EROI) of photovoltaics: methodology and comparisons with fossil fuel life cycles. *Energy Pol.* 45, 576–582. <http://dx.doi.org/10.1016/j.enpol.2012.03.008>.
- Rule, B.M., Worth, Z.J., Boyle, C.A., 2009. Comparison of life cycle carbon dioxide emissions and embodied energy in four renewable electricity generation technologies in New Zealand. *Environ. Sci. Technol.* 43, 6406–6413. <http://dx.doi.org/10.1021/es900125e>.
- Schubel, P.J., Crossley, R.J., 2012. Wind turbine blade design. *Energies* 5, 3425–3449. <http://dx.doi.org/10.3390/en5093425>.
- Tanzil, D., Beloff, B.R., 2006. Assessing impacts: overview on sustainability indicators and metrics. *Environ. Qual. Manage* 15, 41–56. <http://dx.doi.org/10.1002/tqem.20101>.
- Vestas, 2016. Vestas Wind Systems [WWW Document]. Vestas Home Page. [www.vestas.com](http://www.vestas.com) (Accessed 3 June 2016).
- Walmsley, M.R.W., Walmsley, T.G., Atkins, M.J., 2015. Achieving 33% renewable electricity generation by 2020 in California. *Energy Sustain. Dev. Energy Water Environ. Syst.* 92, Part 3, 260–269. <http://dx.doi.org/10.1016/j.energy.2015.05.087>.
- Walmsley, M.R.W., Walmsley, T.G., Atkins, M.J., Kamp, P.J.J., Neale, J.R., 2014. Minimising carbon emissions and energy expended for electricity generation in New Zealand through to 2050. *Appl. Energy* 135, 656–665. <http://dx.doi.org/10.1016/j.apenergy.2014.04.048>.
- Weißbach, D., Ruprecht, G., Huke, A., Czernski, K., Gottlieb, S., Hussein, A., 2013. Energy intensities, EROIs (energy returned on invested), and energy payback times of electricity generating power plants. *Energy* 52, 210–221. <http://dx.doi.org/10.1016/j.energy.2013.01.029>.
- WMI, 2013. Operational and Maintenance Costs for Wind Turbines [WWW Document]. Wind Measurement International. [www.windmeasurementinternational.com/wind-turbines/om-turbines.php](http://www.windmeasurementinternational.com/wind-turbines/om-turbines.php) (Accessed 5 November 2017).